Physics of Atomic Nuclei, Vol. 66, No. 6, 2003, pp. 1009–1014. From Yadernaya Fizika, Vol. 66, No. 6, 2003, pp. 1045–1050.

Exotic Nuclei: From Superheavies to Hyper- and Antimatter*

W. Greiner**

Institut für Theoretische Physik, J.W. Goethe-Universität, Frankfurt am Main, Germany

Received September 9, 2002

Abstract—The extension of the periodic system into various new areas is investigated. Experiments for the synthesis of superheavy elements and the predictions of magic numbers are reviewed. Further on, investigations on hypernuclei and the possible production of antimatter clusters in heavy-ion collisions are reported. Various versions of the meson field theory serve as effective field theories at the basis of modern nuclear structure and suggest structure in vacuum that might be important for the production of hyper- and antimatter. © *2003 MAIK "Nauka/Interperiodica".*

INTRODUCTION

There are fundamental questions in science, like, e.g., "how did life emerge?" or "how does our brain work?" and others. However, the most fundamental of those questions is "how did the world originate?" The material world has to exist before life and thinking can develop. Of particular importance are the substances themselves, i.e., the particles that the elements are made of (baryons, mesons, quarks, gluons), i.e., elementary matter. The vacuum and its structure are closely related to that. We want to report on this, beginning with the discussion of modern issues in nuclear physics.

The elements existing in nature are ordered according to their atomic (chemical) properties in the **periodic system** that was developed by Mendeleev and Meyer. The heaviest element of natural origin is uranium. Its nucleus is composed of $Z = 92$ protons and a certain number of neutrons ($N = 128$–150). They are called different uranium isotopes. The transuranium elements reach from neptunium ($Z = 93$) via californium ($Z = 98$) and fermium ($Z = 100$) up to lawrencium ($Z = 103$). The heavier the elements, the larger their radii and their number of protons. Thus, the Coulomb repulsion in their interior increases, and they undergo fission. In other words, the transuranium elements become more unstable as they get bigger.

In the late 1960s, the dream of superheavy elements arose. Theoretical nuclear physicists around S.G. Nilsson (Lund) and from the Frankfurt school (see [1]) predicted that so-called closed proton and neutron shells should counteract the repelling Coulomb forces. Atomic nuclei with these special **"magic" proton and neutron numbers** and their neighbors could again be rather stable. These magic proton (Z) and neutron (N) numbers were thought to be $Z = 114$ and $N = 184$ or 196. Typical predictions of their lifetimes varied between seconds and many thousands of years. Figure 1 summarizes the expectations at the time. One can see the islands of superheavy elements around $Z = 114$, $N = 184$ and 196, respectively, and the one around $Z = 164$, $N = 318$.

COLD VALLEYS IN THE POTENTIAL

The important question was how to produce these superheavy nuclei. There were many attempts, but only a little progress was made. It was not until the middle of the 1970s that the Frankfurt school of theoretical physics together with foreign guests [R.K. Gupta (India), A. Sandulescu (Romania)] [1] theoretically understood and substantiated the concept of bombarding doubly magic lead nuclei with suitable projectiles, which had been proposed intuitively by the Russian nuclear physicist Yu. Oganessian [1]. The two-center shell model, which is essential for the description of fission, fusion, and nuclear molecules, was developed in 1969–1972 by W. Greiner and his students U. Mosel and J. Maruhn [1]. It showed that the shell structure of the two final fragments was visible far beyond the barrier into the fusioning nucleus. The collective potential energy surfaces of heavy nuclei, as they were calculated in the framework of the two-center shell model, exhibit pronounced valleys, such that these valleys provide promising doorways to the fusion of superheavy nuclei for certain projectile–target combinations (Fig. 2). If projectile and target approach each other through those **"cold" valleys**, they become only minimally excited and the barrier

*This article was submitted by the author in English.

** e-mail: greiner@th.physik.uni-frankfurt.de

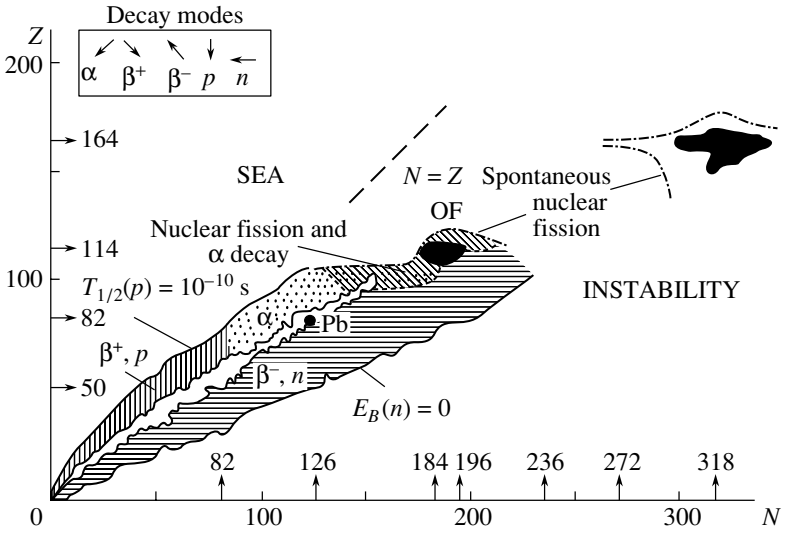

Fig. 1. The periodic system of elements as conceived by the Frankfurt school in the late 1960s. The islands of superheavy elements ($Z = 114$, $N = 184$ and 196 and $Z = 164$, $N = 318$) are shown as dark hatched areas.

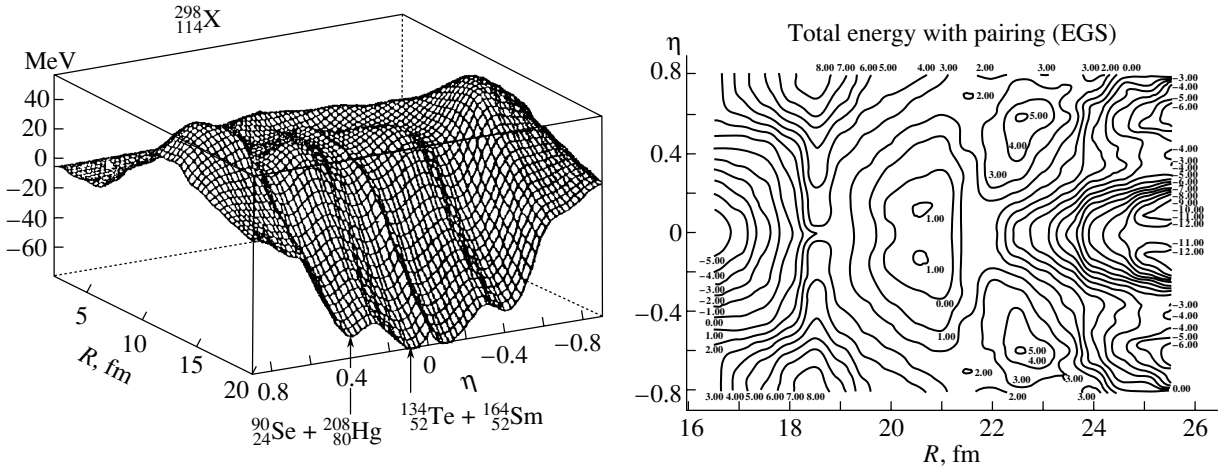

Fig. 2. The collective potential energy surface of $^{184}114$, calculated within the two-center shell model by J. Maruhn *et al.*, shows clearly the cold valleys that reach up to the barrier and beyond. Here, R is the distance between the fragments and $\eta = (A_1 - A_2)/(A_1 + A_2)$ denotes the mass asymmetry: $\eta = 0$ corresponds to a symmetric and $\eta = \pm 1$ to an extremely asymmetric division of the nucleus into projectile and target. If projectile and target approach through a cold valley, they do not "constantly slide off," as would be the case if they approach along the slopes at the sides of the valley. Constant sliding causes heating, so that the compound nucleus heats up and becomes unstable. In the cold valley, on the other hand, the created heat is minimized.

that has to be overcome (fusion barrier) is lowest (as compared to neighboring projectile–target combinations). In this way, the correct projectile and target combinations for fusion were predicted. Indeed, G. Münzenberg and S. Hofmann and their group at GSI [1] have followed this approach. With the help of the SHIP mass separator and position-sensitive detectors, which were especially developed by them, they produced the presuperheavy elements $Z = 106$, 107, . . . , 112, each of them with the theoretically predicted projectile–target combinations, and only with these. Everything else failed. This is an impressive success, which crowned the laborious construction work of many years. Not the last example of this success was the discovery of element 112 and its long α-decay chain. Very recently, the Dubna–Livermore group produced two isotopes of $Z = 114$ element by bombarding ^{244}Pu with ^{48}Ca. Also, this is a cold-valley reaction (in this case due to the combination of a spherical and a deformed nucleus), as predicted by R.K. Gupta, A. Sandulescu, and W. Greiner in 1977. There also exist cold valleys for which both

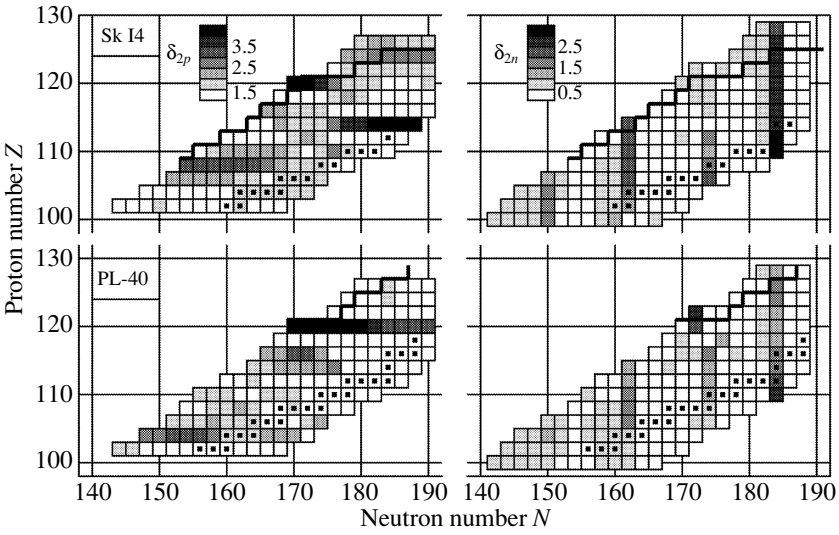

Fig. 3. Gray scale plots of proton gaps (left column) and neutron gaps (right column) in the $N-Z$ plane for deformed calculations with the forces SkI4 and PL-40. Besides the spherical shell closures, one can see the deformed shell closures for protons at $Z = 104$ (PL-40) and $Z = 108$ (SkI4) and the ones for neutron at $N = 162$ for both forces.

fragments are deformed [1], but these have yet to be verified experimentally.

SHELL STRUCTURE IN THE SUPERHEAVY REGION

Studies of the shell structure of superheavy elements in the framework of the meson field theory and the Skyrme–Hartree–Fock approach have recently shown that the magic shells in the superheavy region are very isotope dependent [2]. Additionally, there is a strong dependence on the parameter set and the model. Some forces hardly show any shell structure, while others predict the magic numbers $Z = 114$, 120, 126. Using the heaviest known nucleus hassium $^{264}_{154}108$ as a criterion to find the best parameter sets in each model, it turns out that PL-40 and SkI4 produce its binding energy best. These two forces, though, make conflicting predictions for the magic number in the superheavy region: SkI4 predicts $Z = 114$, 120 and PL-40 $Z = 120$. Most interestingly, $Z = 120$ **as magic proton number seems to be as probable as** $Z = 114$. Deformed calculations within the two models [2] again reveal different predictions: Though both parametrizations predict $N = 162$ as the deformed neutron shell closure, the deformed proton shell closures are $Z = 108$ (SkI4) and $Z = 104$ (PL-40) (see Fig. 3). Calculations of the potential energy surfaces [2] show single-humped barriers, their heights and widths strongly depending on the predicted magic number. Furthermore, recent investigations in a chirally symmetric mean-field theory (see also below) also result in the prediction of these two magic numbers [3, 4]. The corresponding magic neutron numbers are predicted to be $N = 172$ and—as it seems to a lesser extent—$N = 184$. Thus, this region provides an open field of research.

The charge distribution of the $Z = 120$, $N = 184$ nucleus indicates a hollow inside. This leads us to suggest that it might be essentially a fullerene consisting of 60 α particles and one binding neutron per α.

The "cold valleys" in the collective potential energy surface are basic for understanding this exciting area of nuclear physics! It is a master example for understanding the **structure of elementary matter**, which is so important for other fields, especially astrophysics, but even more so for enriching our "Weltbild," i.e., the status of our understanding of the world around us.

EXTENSION OF THE PERIODIC SYSTEM INTO THE SECTIONS OF HYPER- AND ANTIMATTER

Nuclei that are found in nature consist of nucleons (protons and neutrons) which themselves are made of u (up) and d (down) quarks. However, there also exist s (strange) quarks and even heavier flavors, called charm, bottom, and top. The latter has just recently been discovered. Let us stick to the s quarks. They are found in the "strange" relatives of the nucleons, the so-called hyperons (Λ, Σ, Ξ, Ω). The Λ particle, e.g., consists of one u, d, and s quark, and the Ξ particle even of one u quark and two s quarks, while the Ω (sss) contains strange quarks only. If such

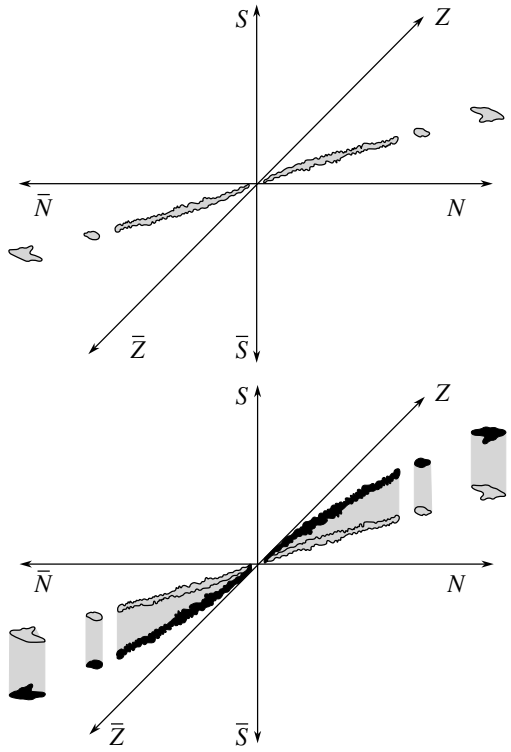

Fig. 4. The extension of the periodic system into the sectors of strangeness (S, $\bar{S}$) and antimatter ($\bar{Z}$, $\bar{N}$). The stable valley winds out of the known proton (Z) and neutron (N) plane into the S and $\bar{S}$ sector, respectively. The same can be observed for the antimatter sector. In the upper part of the figure, only the stable valley in the usual proton (Z) and neutron (N) plane is plotted, however, extended into the sector of antiprotons and antineutrons. In the lower part of the figure, it has been indicated how the stable valley winds out of the $Z-N$ plane into the strangeness sector.

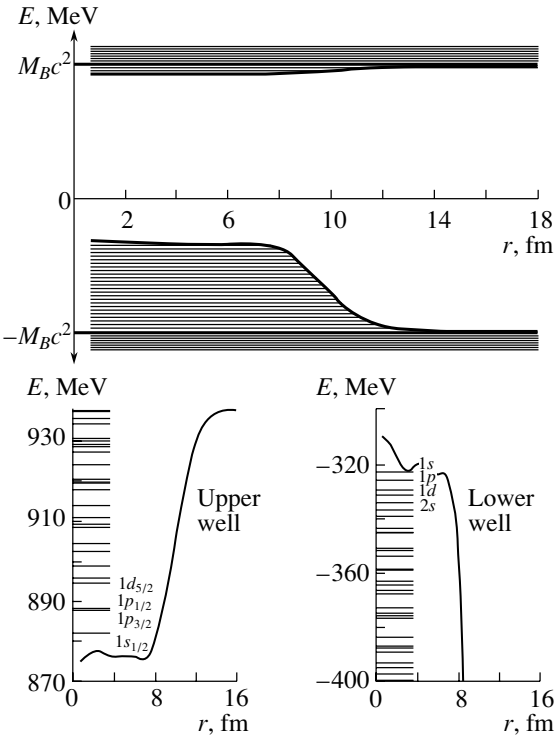

Fig. 5. Baryon spectrum in a nucleus. Below the positive energy continuum exists the potential well of real nucleons. It has a depth of 50–60 MeV and shows the correct shell structure. The shell model of nuclei is realized here. However, from the negative continuum, another potential well arises, in which about 40 000 bound particles are found belonging to the vacuum. A part of the shell structure of the upper well and the lower (vacuum) well is depicted in the lower parts of the figure.

a hyperon is taken up by a nucleus, a **hypernucleus** is created. Hypernuclei with one hyperon have been known for 20 years now and were extensively studied by B. Povh (Heidelberg) [1]. Several years ago, C. Greiner, J. Schaffner, and H. Stöcker [1] theoretically investigated nuclei with many hyperons, **hypermatter**, and found that the binding energy per baryon of strange matter is in many cases even higher than that of ordinary matter (composed only of u and d quarks). This leads to the idea of extending the periodic system of elements in the direction of strangeness.

One can also ask for the possibility of building atomic nuclei out of **antimatter**, which means searching, e.g., for antihelium, anticarbon, antioxygen. Figure 4 depicts this idea. Due to the charge conjugation symmetry, antinuclei should have the same magic numbers and the same spectra as ordinary nuclei. However, as soon as they come into contact with ordinary matter, they annihilate with it and the system explodes.

Now, the important question arises as to how these strange matter and antimatter clusters can be produced. First, one thinks of collisions of heavy nuclei, e.g., lead on lead, at high energies (energy per nucleon $\geq$200 GeV). Calculations with the URQMD model of the Frankfurt school show that, through **nuclear shock waves** [1, 5], nuclear matter gets compressed to 5–10 times of its usual value, $\rho_0 \approx 0.17$ fm^3, and heated up to temperatures of $kT \approx 200$ MeV. As a consequence, about 10 000 pions, 100 Λ, 40 Σ, and Ξ and about as many antiprotons and many other particles are created in a single collision. It seems conceivable that it is possible in such a scenario for some Λ to get captured by a nuclear cluster. This happens indeed rather frequently for one or two Λ particles; however, more of them get built into nuclei with rapidly decreasing probability only. This is due to the low probability for finding the right conditions for such a capture in the phase space of the particles: the numerous particles travel with every possible momenta (velocities) in all directions. The chances for hyperons and antibaryons to meet get rapidly worse with increasing number. In order to produce multi-

Λ nuclei and antimatter nuclei, one has to look for a different source.

In the framework of meson field theory, the energy spectrum of baryons has a peculiar structure, depicted in Fig. 5. It consists of an upper and a lower continuum, as is known from the electrons (see, e.g., [6]). Of special interest in the case of the baryon spectrum is the potential well, built of the scalar and the vector potential, which rises from the lower continuum. It has been known since the time of P.A.M. Dirac (1930) that the negative energy states of the lower continuum have to be occupied by particles (electrons or, in our case, baryons). Otherwise, our world would be unstable, because the "ordinary" particles are found in the upper states, which can decay through the emission of photons into lower lying states. However, if the "underworld" is occupied, the Pauli principle will prevent this decay. Holes in the occupied "underworld" (Dirac sea) are antiparticles.

The occupied states of this underworld including up to 40 000 occupied bound states of the lower potential represent the **vacuum** well. The peculiarity of this strongly correlated vacuum structure in the region of atomic nuclei is that—depending on the size of the nucleus—more than 20 000 up to 40 000 (occupied) bound nucleon states contribute to this polarization effect. Obviously, we are dealing here with a **highly correlated vacuum**. A pronounced shell structure can be recognized [7]. Holes in these states have to be interpreted as bound antinucleons (antiprotons, antineutrons). If the primary nuclear density rises due to compression, the lower well increases, while the upper decreases and soon is converted into a repulsive barrier. This compression of nuclear matter can only be carried out in a relativistic nucleus–nucleus collision with the help of shock waves, which have been proposed by the Frankfurt school (see W. Scheid *et al.* in [1]) and which have since then been confirmed extensively (for references see, e.g., [8]). These **nuclear shock waves** are accompanied by heating of the nuclear matter. Indeed, density and temperature are intimately coupled in terms of the hydrodynamic Rankine–Hugoniot equations. Heating and the violent dynamics cause the creation of many holes in the very deep (measured from $-M_B c^2$) vacuum well. These numerous bound holes resemble antimatter clusters that are bound in the medium; their wave functions have a large overlap with antimatter clusters. When the primary matter density decreases during the expansion stage of the heavy-ion collision, the potential wells, in particular, the lower one, disappear.

The bound antinucleons are then pulled down into the (lower) continuum. In this way, antimatter clusters may be set free. Of course, a large part of the antimatter will annihilate on ordinary matter present in the course of the expansion. However, it is important that this mechanism for the production of antimatter clusters out of the highly correlated vacuum does not proceed via the phase space. The required coalescence of many particles in phase space suppresses the production of clusters, while it is favored by the direct production out of the highly correlated vacuum. In a certain sense, the highly correlated vacuum is a kind of cluster vacuum (vacuum with cluster structure). The shell structure of the vacuum levels (see Fig. 5) supports this latter suggestion. Figure 6 illustrates this idea.

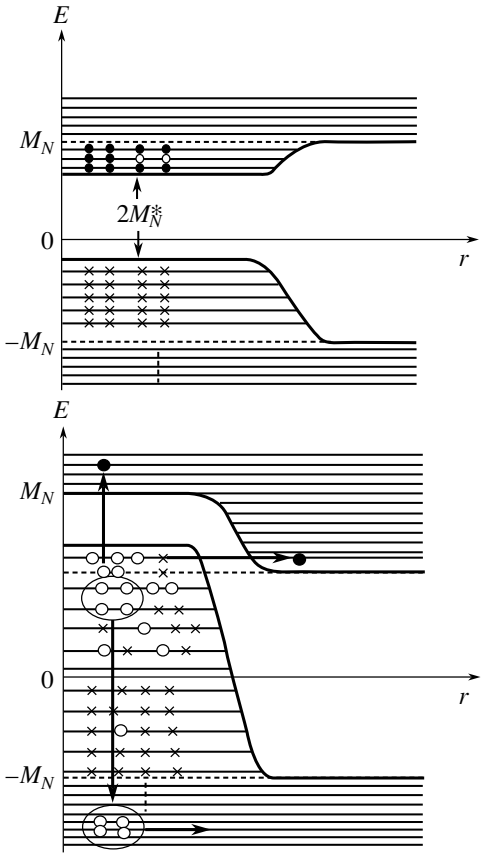

Fig. 6. Due to the high temperature and the violent dynamics, many bound holes (antinucleon clusters) are created in the highly correlated vacuum, which can be set free during the expansion stage into the lower continuum. In this way, antimatter clusters can be produced directly from the vacuum. The horizontal arrow in the lower part of the figure denotes the spontaneous creation of baryon–antibaryon pairs, while the antibaryons occupy bound states in the lower potential well. Such a situation where the lower potential well reaches into the upper continuum is called supercritical. Four of the bound holes states (bound antinucleons) are encircled to illustrate a "quasi-antihelium" formed. It may be set free (driven into the lower continuum) by the violent nuclear dynamics.

The mechanism is similar for the production of multi-hypernuclei (Λ, Σ, Ξ, Ω). Meson field theory also predicts for the Λ-energy spectrum at finite pri-

mary nucleon density the existence of upper and lower wells. The lower well belongs to the vacuum and is fully occupied by Λ.

Dynamics and temperature then induce transitions ($\Lambda\bar{\Lambda}$ creation) and deposit many Λ in the upper well. These numerous bound Λ sit close to the primary baryons: in a certain sense a giant multi-Λ hypernucleus has been created. When the system disintegrates (expansion stage) the Λ distribute over the nucleon clusters (which are most abundant in peripheral collisions). In this way multi-Λ hypernuclei can be formed.

Of course, this vision has to be worked out and probably refined in many respects. This means a much more and thorough investigation in the future. It is particularly important to gain more experimental information on the properties of the lower well by $(e, e'p)$ or $(e, e'pp')$ and also $(\bar{p}_c p_b, p_c \bar{p}_b)$ reactions at high energy ($\bar{p}_c$ denotes an incident antiproton from the continuum, and p_b is a proton in a bound state; for the reaction products, the situation is just the opposite). Also, the reactions $(p, p'd)$, $(p, p'^3\mathrm{He})$, and $(p, p'^4\mathrm{He})$, and others of similar type need to be investigated in this context. Systematic studies of antiproton scattering on nuclei can contribute to clarifying these questions. Various effective theories, e.g., of Walecka-type, on one hand, and theories with chiral invariance, on the other hand, have been constructed to describe dense strongly interacting matter [3]. It is important to note that they seem to give different strengths of the potential wells and also a different dependence on the baryon density.

According to chirally symmetric meson field theories, the antimatter-cluster production and multi-hypermatter-cluster production out of the highly correlated vacuum take place at considerably higher heavy-ion energies compared to the predictions of the Dürr–Teller–Walecka-type meson field theories. This in itself is a most interesting, quasifundamental question to be clarified. In the future, the question of the nucleonic substructure (form factors, quarks, gluons) and its influence on the highly correlated vacuum structure has to be studied. The nucleons are possibly strongly modified in the correlated vacuum: the Δ resonance correlations are probably important. Is this highly correlated vacuum state, especially during the compression, a preliminary stage to the quark–gluon cluster plasma? To what extent is it similar or perhaps even identical to it?

CONCLUDING REMARKS—OUTLOOK

The extension of the periodic system into the sectors of hypermatter (strangeness) and antimatter is of general and astrophysical importance. Indeed, microseconds after the big bang, the new dimensions of the periodic system, we have touched upon, certainly have been populated in the course of the baryo- and nucleogenesis. In the early history of the Universe, even higher dimensional extensions (charm, bottom, top) may play a role, which we did not pursue here. It is an open question how the depopulation (the decay) of these sectors influences the structure and composition of our world today. It should finally be noted that antimatter may also exist within matter for much longer times than what is natively expected [9]. This leads to be cold compression of nuclei, and even dense neutron stars may contain antimatter in the core. Our conception of the world will certainly gain a lot through the clarification of these questions.

REFERENCES

1. W. Greiner, Int. J. Mod. Phys. E **5**, 1 (1996).
2. K. Rutz, M. Bender, T. Bürvenich, *et al.*, Phys. Rev. C **56**, 238 (1997); T. Bürvenich, K. Rutz, M. Bender, *et al.*, Eur. Phys. J. A **3**, 139 (1998); M. Bender, K. Rutz, P.-G. Reinhard, *et al.*, Phys. Rev. C **58**, 2126 (1998).
3. B. D. Serot and J. D. Walecka, Adv. Nucl. Phys. **16** (1986); J. Theis, G. Graebner, G. Buchwald, *et al.*, Phys. Rev. D **28**, 2286 (1983); S. Klimt, M. Lutz, and W. Weise, Phys. Lett. B **249**, 386 (1990); I. N. Mishustin, in *Proceedings of International Conference "Structure of Vacuum and Elementary Matter", Wilderness, South Africa, 1996* (World Sci., Singapore), p. 499; P. Papazoglou, D. Zschiesche, S. Schramm, *et al.*, Phys. Rev. C **59**, 411 (1999); I. N. Mishustin, L. M. Satarov, H. Stöcker, and W. Greiner, Phys. Rev. C **62**, 034901 (2000).
4. P. Papazoglou, PhD Thesis (University of Frankfurt, 1998); Ch. Beckmann, P. Papazoglou, D. Zschiesche, *et al.*, Phys. Rev. C **65**, 024301 (2002).
5. H. Stöcker, W. Greiner, and W. Scheid, Z. Phys. A **286**, 121 (1978).
6. W. Greiner, B. Müller, and J. Rafelski, *QED of Strong Fields* (Springer-Verlag, Heidelberg, 1985); W. Greiner and J. Reinhardt, Supercritical Fields in Heavy-Ion Physics, in *Proceedings of the 15th Advanced ICFA Beam Dynamics Workshop on Quantum Aspects of Beam Physics* (World Sci., Singapore, 1998).
7. I. N. Mishustin, L. M. Satarov, J. Schaffner, *et al.*, J. Phys. G **19**, 1303 (1993); P. K. Panda, S. K. Patra, J. Reinhardt, *et al.*, Int. J. Mod. Phys. E **6**, 307 (1997); N. Auerbach, A. S. Goldhaber, M. B. Johnson, *et al.*, Phys. Lett. B **182**, 221 (1986).
8. H. Stöcker and W. Greiner, Phys. Rep. **137**, 279 (1986).
9. T. Bürvenich, L. M. Satarov, I. N. Mishustin, *et al.*, Phys. Lett. B **542**, 261 (2002).

Physics of Atomic Nuclei, Vol. 66, No. 6, 2003, pp. 1015–1019. From Yadernaya Fizika, Vol. 66, No. 6, 2003, pp. 1051–1055.

Calculated Masses of Heaviest Nuclei*

I. Muntian, Z. Patyk, and A. Sobiczewski**

Soltan Institute for Nuclear Studies, Warsaw, Poland

Received November 11, 2002

Abstract—Masses of heaviest nuclei are calculated within a macroscopic–microscopic approach. Even–even, odd-A, and odd–odd nuclides are considered. A large region of nuclei with proton and neutron numbers of $Z = 82$–128 and $N = 126$–192, respectively, is analyzed. The results are compared with those of other macroscopic–microscopic and of recent microscopic Hartree–Fock–BCS calculations. Alpha-decay energies are also given. © *2003 MAIK "Nauka/Interperiodica".*

1. INTRODUCTION

The objective of this paper is to extend our previous macroscopic–microscopic calculations of nuclear masses [1]. The extension consists mainly in the inclusion of odd-A and odd–odd nuclei. A large region of nuclei with proton and neutron numbers of $Z = 82$–128 and $N = 126$–192, respectively, is considered.

A specific feature of our model is a smaller number of terms and of adjustable parameters in the macroscopic part of mass than in other macroscopic–microscopic models (e.g., [2]). More specifically, we omit the Wigner term and the asymmetry term, $c_a(N - Z)$, with respect to [2]. This is certainly connected with our description of masses in a specific region of nuclei. In particular, the region is far from the line $N = Z$, in the neighborhood of which the Wigner term is important.

The method of the calculations is described in Section 2. Section 3 gives the results of the calculations and a comparison of the calculated masses with experimental values. A comparison of our masses with the results of other macroscopic–microscopic calculations [2] and of recent microscopic Hartree–Fock–BCS calculations [3] is presented in Section 4.

2. METHOD OF THE CALCULATIONS

The ground-state mass of a nucleus is calculated within a macroscopic–microscopic approach. The Yukawa-plus-exponential model [4] is used for the calculation of the macroscopic part of mass, and the Strutinski shell correction is taken for its microscopic part. The Woods–Saxon single-particle potential, with the "universal" variant of its parameters found in [5] and also specified explicitly in [6], is used as a basis for the shell correction.

Values of parameters of the macroscopic part of mass are taken to be the same as in [1], where they were adjusted to experimental masses [7] of even–even heaviest nuclei with atomic number $Z \geqslant 84$.

To describe the microscopic contribution of an odd nucleon to the ground-state mass of a nucleus, its (lowest) quasi-particle energy $E_\nu = \sqrt{(e_\nu - \lambda)^2 + \Delta^2}$ in a single-particle state $|\nu\rangle$ is added to the microscopic part of the mass. Here, e_ν is the energy of the odd nucleon in the state $|\nu\rangle$ and Δ is the pairing-energy gap parameter, calculated in

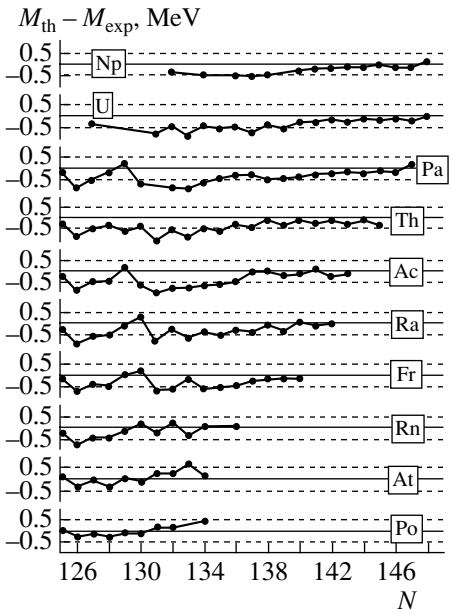

Fig. 1. Difference between calculated, M_{th}, and measured, M_{exp}, masses of nuclei with proton number $Z = 84$–93.

*This article was submitted by the authors in English.

** e-mail: adam.sobiczewski@fuw.edu.pl

Table 1. Equilibrium deformation parameters β_λ^0, $\lambda = 2, 4, 6, 8$, mass $M_{\rm th}$, and α-decay energy $Q_\alpha^{\rm th}$ (both in MeV), calculated for nuclei specified by proton, neutron, and mass numbers (Z, N, and A, respectively)

N	A	β_2^0	β_4^0	β_6^0	β_8^0	$M_{\rm th}$	$Q_\alpha^{\rm th}$	N	A	β_2^0	β_4^0	β_6^0	β_8^0	$M_{\rm th}$	$Q_\alpha^{\rm th}$
$Z = 110$								$Z = 112$							
156	266	0.234	−0.044	−0.030	0.021	133.83	12.40	164	276	0.208	−0.087	0.007	0.017	150.12	12.22
157	267	0.234	−0.050	−0.028	0.023	134.50	12.21	165	277	0.208	−0.093	0.012	0.015	151.70	12.11
158	268	0.232	−0.057	−0.024	0.023	134.05	11.93	166	278	0.204	−0.093	0.015	0.013	152.46	11.86
159	269	0.232	−0.063	−0.022	0.027	134.84	11.63	167	279	0.200	−0.097	0.021	0.011	154.32	11.60
160	270	0.228	−0.067	−0.017	0.024	134.59	11.36	168	280	0.197	−0.098	0.024	0.009	155.29	11.40
161	271	0.230	−0.072	−0.017	0.028	135.51	11.07	169	281	0.165	−0.072	0.012	0.006	157.46	11.21
162	272	0.226	−0.077	−0.012	0.025	135.47	10.74	170	282	0.145	−0.057	0.006	0.005	158.33	10.68
163	273	0.221	−0.083	0.001	0.020	137.17	11.10	171	283	0.135	−0.054	0.007	0.004	160.40	10.16
164	274	0.217	−0.081	−0.002	0.019	138.18	11.57	172	284	0.129	−0.056	0.011	0.003	161.43	9.76
165	275	0.213	−0.086	0.004	0.016	140.29	11.45	173	285	0.122	−0.059	0.015	0.001	163.63	9.49
166	276	0.208	−0.085	0.007	0.014	141.46	11.09	174	286	0.100	−0.045	0.010	0.001	164.90	9.35
167	277	0.206	−0.090	0.013	0.011	143.83	10.79	175	287	0.095	−0.049	0.013	0.000	167.14	8.97
168	278	0.201	−0.089	0.014	0.009	145.22	10.54	176	288	0.093	−0.053	0.017	−0.001	168.81	9.04
169	279	0.197	−0.095	0.022	0.006	147.82	10.24	177	289	0.077	−0.045	0.014	−0.001	171.60	9.19
170	280	0.163	−0.068	0.009	0.006	149.25	9.91	178	290	0.011	0.001	0.000	0.000	173.37	8.98
171	281	0.137	−0.051	0.004	0.005	151.71	9.30	$Z = 113$							
172	282	0.128	−0.052	0.007	0.003	153.13	8.89	166	279	0.203	−0.100	0.020	0.013	159.19	12.16
173	283	0.107	−0.049	0.007	0.001	155.74	8.54	167	280	0.204	−0.107	0.028	0.011	160.77	11.91
174	284	0.104	−0.046	0.009	0.001	157.34	8.34	168	281	0.200	−0.107	0.030	0.009	161.56	11.69
175	285	0.098	−0.048	0.012	0.001	159.99	8.03	169	282	0.196	−0.111	0.042	0.007	163.41	11.47
176	286	0.095	−0.053	0.015	−0.001	161.96	7.99	170	283	0.149	−0.066	0.012	0.005	164.26	11.12
$Z = 111$								171	284	0.138	−0.061	0.011	0.004	166.17	10.68
160	271	0.222	−0.069	−0.013	0.021	142.03	11.79	172	285	0.132	−0.063	0.016	0.002	167.01	10.21
161	272	0.227	−0.078	−0.011	0.028	142.77	11.55	173	286	0.128	−0.067	0.019	0.001	169.04	9.98
162	273	0.224	−0.084	−0.005	0.024	142.43	11.20	174	287	0.095	−0.043	0.009	0.001	170.14	9.85
163	274	0.226	−0.082	0.000	0.026	143.87	11.53	175	288	0.093	−0.048	0.014	0.000	172.23	9.57
164	275	0.216	−0.089	0.005	0.018	144.61	12.04	176	289	0.091	−0.054	0.017	−0.001	173.74	9.57
165	276	0.212	−0.092	0.009	0.016	146.44	11.94	177	290	0.066	−0.036	0.011	−0.001	176.33	9.65
166	277	0.210	−0.093	0.012	0.013	147.44	11.64	178	291	0.013	0.003	0.001	0.000	178.08	9.58
167	278	0.207	−0.098	0.018	0.011	149.51	11.30	179	292	0.029	−0.001	0.000	0.000	180.63	9.12
168	279	0.202	−0.097	0.020	0.009	150.71	11.08	180	293	0.023	0.002	0.000	0.000	182.46	8.85
169	280	0.200	−0.103	0.027	0.006	153.07	10.77	$Z = 114$							
170	281	0.147	−0.050	0.000	0.000	154.38	10.48	168	282	0.186	−0.099	0.028	0.011	166.97	12.09
171	282	0.132	−0.052	0.006	0.004	156.64	9.85	169	283	0.194	−0.113	0.039	0.007	168.57	11.83
172	283	0.126	−0.051	0.008	0.003	157.86	9.38	170	284	0.149	−0.073	0.017	0.005	169.24	11.53
173	284	0.119	−0.053	0.011	0.002	160.24	8.91	171	285	0.130	−0.051	0.002	0.003	170.99	11.11
174	285	0.109	−0.048	0.010	0.001	161.74	8.78	172	286	0.086	−0.021	−0.002	0.002	171.61	10.86
175	286	0.093	−0.047	0.012	0.000	164.26	8.51	173	287	0.088	−0.028	0.001	0.002	173.38	10.56
176	287	0.087	−0.048	0.013	−0.001	166.08	8.47	174	288	0.086	−0.037	0.008	0.001	174.18	10.32
177	288	0.081	−0.041	0.005	−0.002	169.08	8.60	175	289	0.088	−0.047	0.013	0.000	176.10	10.04
178	289	0.052	−0.024	0.006	−0.001	171.19	8.53	176	290	0.000	0.000	0.000	0.000	177.39	10.07

Table 1. (Contd.)

N	A	β_2^0	β_4^0	β_6^0	β_8^0	M_{th}	Q_α^{th}	N	A	β_2^0	β_4^0	β_6^0	β_8^0	M_{th}	Q_α^{th}
177	291	0.028	−0.009	0.002	0.000	179.67	10.10				$Z = 117$				
178	292	0.001	0.000	0.000	0.000	180.83	9.60	172	289	0.077	−0.013	−0.004	0.002	190.29	11.75
179	293	0.000	0.000	0.000	0.000	183.33	9.31	173	290	0.078	−0.020	0.000	0.001	191.57	11.61
180	294	0.000	0.000	0.000	0.000	184.90	9.11	174	291	0.074	−0.028	0.006	0.001	191.89	11.58
181	295	0.001	0.000	0.000	0.000	187.66	9.10	175	292	0.078	−0.039	0.012	0.001	193.39	11.42
182	296	0.000	0.000	0.000	0.000	189.62	9.13	176	293	0.063	−0.028	0.007	0.000	194.14	11.53
183	297	0.004	0.000	0.001	0.000	192.63	9.08	177	294	0.052	−0.023	0.006	0.000	195.96	11.43
184	298	0.000	0.000	0.001	0.000	194.91	9.09	178	295	0.032	−0.010	0.002	0.000	196.82	11.40
				$Z = 115$				179	296	0.027	−0.009	0.002	0.000	198.79	11.26
170	285	0.065	0.009	−0.009	0.001	176.12	12.14	180	297	0.016	−0.004	0.001	0.000	199.97	11.38
171	286	0.071	0.000	−0.009	0.002	177.54	11.70	181	298	0.009	−0.001	0.000	0.000	202.26	11.36
172	287	0.066	−0.004	−0.005	0.001	177.89	11.21	182	299	0.000	0.001	0.000	0.000	203.73	11.35
173	288	0.072	−0.016	−0.001	0.001	179.54	10.95	183	300	0.000	0.001	0.001	0.000	206.30	11.31
174	289	0.067	−0.022	0.003	0.001	180.18	10.74	184	301	0.000	0.001	0.000	0.000	208.10	11.29
175	290	0.056	−0.015	0.001	0.000	182.11	10.65	185	302	0.009	−0.001	0.000	0.000	212.02	12.34
176	291	0.034	−0.002	−0.001	0.000	182.99	10.43	186	303	0.000	0.002	0.001	0.000	213.89	12.08
177	292	0.035	−0.006	0.001	0.000	185.11	10.45				$Z = 118$				
178	293	0.018	0.006	−0.001	0.000	186.17	10.01	172	290	0.080	−0.025	0.002	0.002	196.61	12.40
179	294	0.021	0.001	0.000	0.000	188.47	9.72	173	291	0.081	−0.029	0.004	0.002	197.67	12.24
180	295	0.014	0.003	0.000	0.000	189.96	9.45	174	292	0.079	−0.037	0.010	0.001	197.78	12.15
181	296	0.012	0.003	0.000	0.000	192.57	9.51	175	293	0.082	−0.046	0.015	0.001	199.00	11.93
182	297	0.007	0.004	0.000	0.000	194.38	9.50	176	294	0.077	−0.046	0.016	0.000	199.65	12.11
183	298	0.008	0.003	0.000	0.000	197.25	9.44	177	295	0.067	−0.040	0.013	0.000	201.36	12.22
184	299	0.003	0.003	0.000	0.000	199.39	9.44	178	296	0.039	−0.017	0.004	0.000	202.15	12.06
				$Z = 116$				179	297	0.027	−0.010	0.002	0.000	203.95	11.91
170	286	0.078	0.004	−0.012	0.002	181.79	12.39	180	298	0.017	−0.004	0.001	0.000	204.96	11.98
171	287	0.081	−0.004	−0.010	0.002	183.00	12.00	181	299	0.005	0.000	0.000	0.000	207.07	11.98
172	288	0.077	−0.009	−0.005	0.002	183.21	11.54	182	300	0.000	0.000	0.000	0.000	208.38	11.98
173	289	0.080	−0.022	−0.001	0.002	184.64	11.22	183	301	0.000	0.000	0.000	0.000	210.78	11.95
174	290	0.076	−0.030	0.006	0.001	185.12	11.08	184	302	0.000	0.000	0.000	0.000	212.41	11.95
175	291	0.084	−0.043	0.014	0.000	186.71	10.91	185	303	0.000	0.000	0.000	0.000	216.15	12.99
176	292	0.056	−0.024	0.006	0.000	187.66	11.06	186	304	0.000	0.000	0.000	0.000	217.82	12.71
177	293	0.043	−0.018	0.004	0.000	189.61	11.09	187	305	0.010	0.009	0.004	0.005	221.82	12.57
178	294	0.009	0.000	0.000	0.000	190.56	10.74	188	306	0.000	0.000	0.000	0.000	223.77	12.51
179	295	0.020	−0.004	−0.001	0.000	192.67	10.57				$Z = 119$				
180	296	0.000	0.000	0.000	0.000	193.97	10.71	172	291	0.083	−0.035	0.006	0.003	204.54	12.89
181	297	0.000	0.000	0.000	0.000	196.40	10.65	173	292	0.083	−0.034	0.008	0.002	205.42	12.73
182	298	0.000	0.000	0.000	0.000	198.03	10.70	174	293	0.081	−0.041	0.012	0.003	205.33	12.62
183	299	0.000	0.000	0.001	0.000	200.74	10.66	175	294	0.082	−0.049	0.017	0.002	206.38	12.38
184	300	0.000	0.000	0.001	0.000	202.69	10.65	176	295	0.083	−0.052	0.020	0.002	206.87	12.55
185	301	0.007	−0.001	0.000	0.000	206.82	11.76	177	296	0.072	−0.046	0.017	0.001	208.47	12.65
186	302	0.000	0.000	0.001	0.000	208.83	11.50	178	297	0.000	−0.033	−0.001	0.000	209.42	12.86

Table 1. (Contd.)

N	A	β_2^0	β_4^0	β_6^0	β_8^0	$M_{\rm th}$	$Q_\alpha^{\rm th}$	N	A	β_2^0	β_4^0	β_6^0	β_8^0	$M_{\rm th}$	$Q_\alpha^{\rm th}$
179	298	0.027	−0.011	0.000	0.000	210.98	12.59	175	295	0.089	−0.052	0.017	0.003	213.10	13.01
180	299	0.000	−0.004	0.000	0.000	211.88	12.63	176	296	0.085	−0.056	0.023	0.003	213.43	13.23
181	300	0.015	−0.004	0.001	0.000	213.82	12.60	177	297	0.076	−0.048	0.019	0.002	214.91	13.49
182	301	0.000	0.000	0.000	0.000	214.99	12.59	178	298	0.054	−0.030	0.010	0.000	215.52	13.44
183	302	0.000	0.003	0.000	0.000	217.24	12.56	179	299	0.029	−0.012	0.001	0.000	217.01	13.23
184	303	0.000	0.002	0.000	0.000	218.72	12.56	180	300	0.009	−0.001	0.000	0.000	217.69	13.11
185	304	0.010	−0.002	0.000	0.000	222.24	13.51	181	301	0.002	0.000	0.000	0.000	219.48	13.11
186	305	0.000	−0.001	0.001	0.000	223.79	13.27	182	302	0.000	0.000	0.000	0.000	220.46	13.08
187	306	0.012	0.008	0.004	0.005	227.61	13.16	183	303	0.000	0.000	0.000	0.000	222.55	13.05
188	307	0.000	0.004	0.000	0.000	229.40	13.09	184	304	0.000	0.000	0.000	0.000	223.87	13.07
$Z = 120$								185	305	0.008	−0.001	0.000	0.000	227.20	13.99
172	292	0.087	−0.040	0.009	0.005	211.88	13.46	186	306	0.000	0.000	0.000	0.000	228.56	13.73
173	293	0.085	−0.040	0.010	0.004	212.58	13.34	187	307	0.009	0.008	0.005	0.006	232.22	13.65
174	294	0.084	−0.047	0.015	0.003	212.27	13.24	188	308	0.000	0.000	0.000	0.000	233.81	13.56

the BCS approximation. Pairing interaction of the monopole type, with the same strength parameters as in [1], is taken. No blocking is used.

The equilibrium deformation parameters β_λ^0 of a nucleus are found by minimization of its mass in a large deformation space. The seven-dimensional space β_λ, $\lambda = 2, 3, \ldots, 8$, is used.

3. RESULTS

Comparison between calculated, $M_{\rm th}$, and experimental, $M_{\rm exp}$, masses is shown in Figs. 1 and 2 for all nuclei with atomic number $Z \geqslant 84$ and neutron number $N \geqslant 126$ for which the experimental mass is known [7].

Table 2. Root-mean-square values of the discrepancy between masses calculated in this paper and in [2, 3] and experimental ones [7] for Z–N: even–even, odd–even, even–odd, odd–odd, and all considered nuclei with measured mass

Type and number of nuclei	This paper	[2]	[3]
Even–even: 75	0.286	0.476	0.720
Odd–even: 57	0.413	0.520	0.714
Even–odd: 59	0.408	0.426	0.698
Odd–odd: 47	0.381	0.511	0.676
All: 238	0.370	0.482	0.705

One can see the following:

(i) The discrepancy between $M_{\rm th}$ and $M_{\rm exp}$ is contained within the range ± 0.5 MeV for almost all of the nuclei. Only for some isotopes of the elements with $Z = 86$–92, is the calculated mass smaller than the measured one by more than 0.5 MeV. In particular, it seems that the calculated (negative) shell correction to mass of magic nuclei ($N = 126$) of these elements is too large (in absolute value) by more than 0.5 MeV.

(ii) The theoretical description of mass is better for heavier nuclei than for lighter ones. Probably one can state a more general rule that a better description is obtained for better deformed (i.e., with larger deformation energy) nuclei. In other words, the more distant a nucleus from (spherical) magic numbers, the better the description of mass.

(iii) Calculated masses show a good isotopic dependence. This is especially well seen in a long chain of masses of well-deformed plutonium nuclei.

(iv) From masses of Cm, Cf, and Fm, one can see that effect on mass of a deformed shell at $N = 152$ is well reproduced. It would be very interesting to know if this is also the case for a more strongly deformed shell at $N = 162$ predicted by theory. Unfortunately, masses of nuclei with N around 162 are not yet measured.

(v) Masses of odd-A and odd–odd nuclei, in the calculation of which no additional adjustable

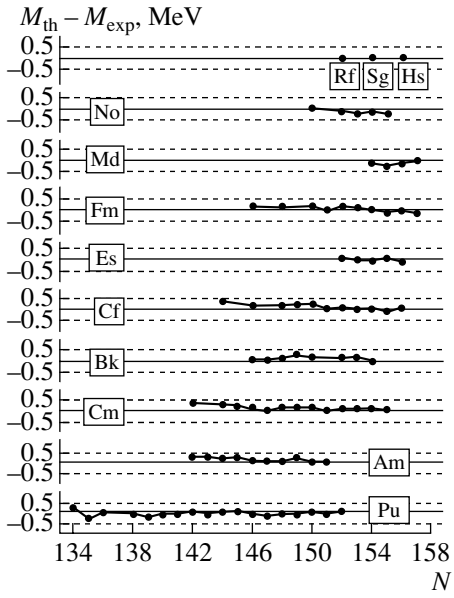

Fig. 2. As in Fig. 1, but for $Z = 94$–108.

parameters were used, are reproduced similarly well as those of even–even nuclei. For lighter nuclei, some staggering effect is observed. Calculated masses of nuclei with odd number of neutrons disagree more with measured values than for neighboring nuclei with even neutron number. It seems that masses of these nuclei are too small because pairing correlations, when treated in the BCS approach without any projection or blocking, are too strong for them.

Table 1 gives equilibrium deformations β_λ^0 and mass $M_{\rm th}$ calculated for nuclei with $Z = 110$–120; α-decay energy $Q_\alpha^{\rm th}$, obtained directly from $M_{\rm th}$, is also given. As the space in this article is too small to show these quantities for all considered nuclei, we decided to give them for nuclei in the region that has been investigated very little experimentally up to present and, thus, for which predictions are more needed. The mass of a nucleus is a basic quantity, from which a number of other quantities, important for synthesis (cf., e.g., [8–12]) or decay of a nucleus, can be obtained.

We have found in the calculations that the odd-multipolarity components β_λ^0, $\lambda = 3, 5, 7$, of the equilibrium deformations of nuclei considered in Table 1 are zero. This is the reason that only even-multipolarity components, $\lambda = 2, 4, 6, 8$, are given in the table.

4. A COMPARISON WITH OTHER CALCULATIONS

In this section, we compare the quality of our description of the mass of the nuclei considered here with that by other macroscopic–microscopic results [2] and recent microscopic Hartree–Fock–BCS results [3]. The comparison is shown in Table 2, where root-mean-square values of the discrepancy between calculated and experimental results are given.

One can see that the macroscopic–microscopic descriptions are better than the microscopic one for all kinds of heaviest nuclei. Among the two macroscopic–microscopic calculations, those of the present paper give smaller discrepancies. This is understandable as parameters of the present model are adjusted to the (smaller) region of (heaviest) nuclei considered in the present paper, while those of [2] are fitted to all nuclei. One may expect then that the results of [2] may be better for far extrapolations, while those of the present paper may be more realistic for less distant nuclei. The latter, however, are more important for experiments presently being done and to be done in the nearest future (cf., e.g., [13–15]).

ACKNOWLEDGMENTS

Support by the Polish State Committee for Scientific Research (KBN), grant nos. 2 P03B 003 22 and 2 P03B 039 22, and the Polish–JINR (Dubna) Cooperation Program is gratefully acknowledged.

REFERENCES

1. I. Muntian, Z. Patyk, and A. Sobiczewski, Acta Phys. Pol. B **32**, 691 (2001).
2. W. D. Myers and W. J. Świątecki, Nucl. Phys. A **601**, 141 (1996).
3. F. Tondeur, S. Goriely, J. M. Pearson, and M. Onsi, Phys. Rev. C **62**, 024308 (2000).
4. H. J. Krappe, J. R. Nix, and A. J. Sierk, Phys. Rev. C **20**, 992 (1979).
5. S. Ćwiok, J. Dudek, W. Nazarewicz, *et al.*, Comput. Phys. Commun. **46**, 379 (1987).
6. Z. Patyk and A. Sobiczewski, Nucl. Phys. A **533**, 132 (1991).
7. G. Audi, O. Bersillon, J. Blachot, and A. H. Wapstra, Nucl. Phys. A **624**, 1 (1997).
8. N. V. Antonenko, E. A. Cherepanov, A. K. Nasirov, *et al.*, Phys. Rev. C **51**, 2635 (1995).
9. E. A. Cherepanov, Pramana, J. Phys. **53**, 619 (1999).
10. G. Giardina, S. Hofmann, A. I. Muminov, and A. K. Nasirov, Eur. Phys. J. A **8**, 205 (2000).
11. V. I. Zagrebaev, Y. Aritomo, M. G. Itkis, *et al.*, Phys. Rev. C **65**, 014607 (2002).
12. A. S. Zubov, G. G. Adamian, N. V. Antonenko, *et al.*, Phys. Rev. C **65**, 024308 (2002).
13. S. Hofmann, Acta Phys. Pol. B **30**, 621 (1999).
14. Yu. Ts. Oganessian, Yad. Fiz. **63**, 1391 (2000) [Phys. At. Nucl. **63**, 1315 (2000)].
15. S. Hofmann and G. Münzenberg, Rev. Mod. Phys. **72**, 733 (2000).

Physics of Atomic Nuclei, Vol. 66, No. 6, 2003, pp. 1020–1025. From Yadernaya Fizika, Vol. 66, No. 6, 2003, pp. 1056–1061.

The Study of Superheavy Elements at SHIP: Results and Plans*

S. Hofmann

Gesellschaft für Schwerionenforschung, Darmstadt, Germany

Received September 4, 2002

Abstract—The nuclear shell model predicts that the next doubly magic shell closure beyond ^{208}Pb is at a proton number between $Z = 114$ and 126 and at a neutron number $N = 184$. The outstanding aim of experimental investigations is the exploration of this region of spherical "superheavy elements." This article describes the experiments that were performed at the GSI SHIP. They resulted in an unambiguous identification of elements 107 to 112. They were negative thus far in searching for elements 113, 116, and 118. The measured decay data are compared with theoretical predictions. Some aspects concerning the reaction mechanism are also presented. © *2003 MAIK "Nauka/Interperiodica".*

1. EXPERIMENTAL RESULTS

In this section, results are presented dealing with the discovery of elements 110 to 112 using cold fusion reactions based on lead and bismuth targets. A detailed presentation and discussion of the decay properties of these elements was given in previous reviews [1, 2].

Element 110 was discovered in 1994 using the reaction ^{62}Ni + ^{208}Pb → ^{269}110 + 1n [3]. The main experiment was preceded by a thorough study of the excitation functions for the synthesis of ^{257}Rf and ^{265}Hs using beams of ^{50}Ti and ^{58}Fe in order to determine the optimum beam energy for the production of element 110. The data revealed that the maximum cross section for the synthesis of element 108 was shifted to a lower excitation energy, different from the predictions of reaction theories. The heavier isotope ^{271}110 was synthesized with a beam of the more neutron-rich isotope ^{64}Ni [1]. The important result for the further production of elements beyond meitnerium was that the cross section was enhanced from 2.6 to 15 pb by increasing the neutron number of the projectile by two, which gave hope that the cross sections could decrease less steeply with more neutron-rich projectiles. However, this expectation was not proven in the case of element 112.

The even–even nucleus ^{270}110 was synthesized using the reaction ^{64}Ni + ^{207}Pb [4]. A total of eight α-decay chains were measured during an irradiation time of seven days. Decay data were obtained for the ground state and a high-spin K isomer, for which calculations predict spin and parity 8^+, 9^-, or 10^- [5]. The new nuclei ^{266}Hs and ^{262}Sg were identified as daughter products after α decay. Spontaneous fission of ^{262}Sg terminates the decay chain.

Element 111 was synthesized in 1994 using the reaction ^{64}Ni + ^{209}Bi → ^{273}111*. A total of three α chains of the isotope ^{272}111 were observed [6]. Another three decay chains were measured in a confirmation experiment in October 2000 [7].

Element 112 was investigated at SHIP using the reaction ^{70}Zn + ^{208}Pb → ^{278}112* [8]. The irradiation was performed in January–February 1996. Over a period of 24 days, a total of 3.4×10^{18} projectiles were collected. One α-decay chain, shown on the left side of Fig. 1, was observed resulting in a cross section of 0.5 pb. The chain was assigned to the one-neutron-emission channel. The experiment was repeated in May 2000, aiming to confirm the synthesis of ^{277}112 [7]. During a similar measuring time, but using slightly higher beam energy, one more decay chain was observed, also shown in Fig. 1. The measured decay pattern of the first four α decays is in agreement with the one observed in the first experiment.

A new result was the occurrence of fission that ended the second decay chain at ^{261}Rf. A spontaneous-fission branch of this nucleus was not yet known; however, it was expected from theoretical calculations. The new results on ^{261}Rf were proven in a recent chemistry experiment [9], in which this isotope was measured as a granddaughter in the decay chain of ^{269}Hs.

A reanalysis of all decay chains measured at SHIP since 1994 (a total of 34 decay chains were analyzed) revealed that the previously published first decay chain of ^{277}112 [8] (not shown in Fig. 1) and the second of the originally published four chains

*This article was submitted by the author in English.

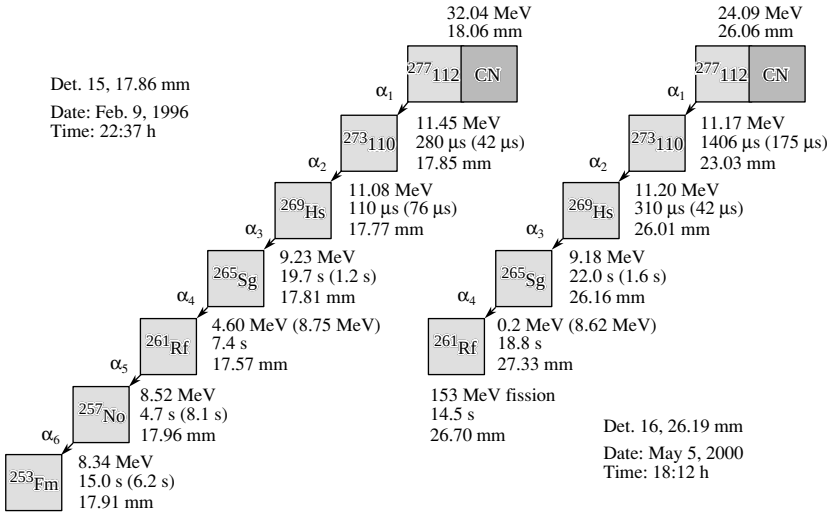

Fig. 1. Two decay chains measured in experiments at SHIP in the cold fusion reaction ^{70}Zn $+^{208}$ Pb $\rightarrow^{278}$ 112*. The chains were assigned to the isotope ^{277}112 produced by evaporation of one neutron from the compound nucleus. The lifetimes given in parentheses were calculated using the measured α energies. In the case of escaped α particles the α energies were determined using the measured lifetimes.

of ^{269}110 [3] were spuriously created. Details of the results of the reanalysis are given in [7].

Results from an experiment at the 88-in. cyclotron in Berkeley aiming to synthesize element 118 were published in 1999 [10]. In order to confirm the data obtained in Berkeley, the same reaction, ^{86}Kr + ^{208}Pb $\rightarrow$ ^{293}118*, was investigated at SHIP in the summer of 1999. The experiment is described in detail in [2]. During a measuring time of 24 days, a beam dose of 2.9×10^{18} projectiles was collected, which was comparable to the Berkeley value of 2.3×10^{18}. No event chain was detected, and the cross-section limit resulting from the SHIP experiment for the synthesis of element 118 in cold fusion reactions was 1.0 pb. The Berkeley data were retracted in the summer of 2001 after negative results of a repetition experiment performed in the year 2001 in Berkeley itself and after a reanalysis of the data of the first experiment, which showed that the three reported chains were not in the 1999 data [11].

2. NUCLEAR STRUCTURE AND DECAY PROPERTIES

The calculation of the ground-state binding energy provides the basic step to determine the stability of superheavy elements (SHEs). In macroscopic–microscopic models, the binding energy is calculated as the sum of a predominating macroscopic part (derived from the liquid-drop model of the atomic nucleus) and a microscopic part (derived from the nuclear shell model). This way, more accurate values for the binding energy are obtained than in the cases of using only the liquid-drop model or the shell model. The shell correction energies of the ground state of nuclei near closed shells are negative, which results in further decreased values of the negative binding energy from the liquid-drop model—and thus increased stability. An experimental signature for the shell-correction energy is obtained by subtracting a calculated smooth macroscopic part from the measured total binding energy.

The shell-correction energy is plotted in Fig. 2*a* using data from [12]. Two equally deep minima are obtained, one at $Z = 108$ and $N = 162$ for deformed nuclei with deformation parameters $\beta_2 \approx 0.22$, $\beta_4 \approx -0.07$ and the other one at $Z = 114$ and $N = 184$ for spherical SHEs. Different results are obtained from self-consistent Hartree–Fock–Bogolyubov calculations and relativistic mean-field models [13, 14]. They predict for spherical nuclei shells at $Z = 114$, 120, or 126 (indicated as dashed lines in Fig. 2*a*) and $N = 184$ or 172.

The knowledge of ground-state binding energies, however, is not sufficient for the calculation of partial spontaneous fission half-lives. Here, it is necessary to determine the size of the fission barrier over a wide range of deformation. The most accurate data were obtained for even–even nuclei using a macroscopic–microscopic model [15]. Partial spontaneous fission half-lives are plotted in Fig. 2*b*. The landscape of fission half-lives reflects the landscape of shell-correction energies, because in the region of SHEs the height of the fission barrier is mainly determined by the ground-state shell correction energy, while the contribution from the macroscopic liquid-drop part approaches zero for $Z = 104$ and beyond.

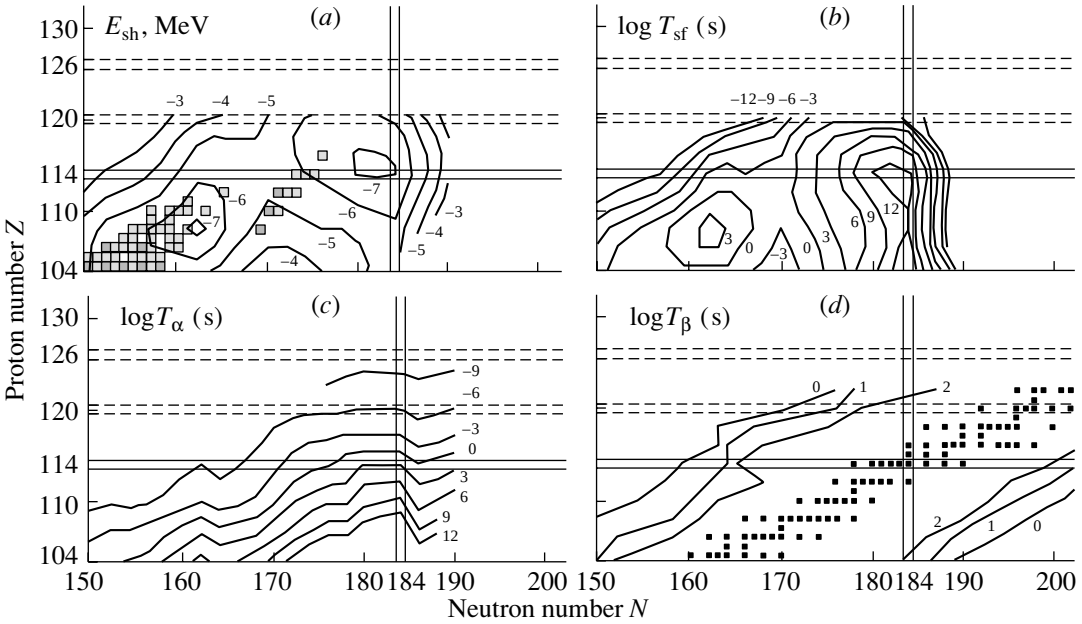

Fig. 2. Shell-correction energy (*a*) and partial spontaneous fission and α and β half-lives (*b*–*d*). The squares in (*a*) mark the nuclei presently known or under investigation. The predicted values in (*a*–*c*) are from [12], and in (*d*) from [16].

Nevertheless, we see a significant increase in spontaneous fission half-life from 10^3 s for deformed nuclei to 10^{12} s for spherical SHEs. This difference originates from an increasing width of the fission barrier which becomes wider in the case of spherical nuclei.

Partial α half-lives decrease almost monotonically from 10^{12} s down to 10^{-9} s near $Z = 126$ (see Fig. 2*c*). The valley of β-stable nuclei passes through $Z = 114$, $N = 184$. At a distance of about 20 neutrons away from the bottom of this valley, β half-lives of isotopes drop down to values of one second [16] (see Fig. 2*d*).

The interesting question arises as to whether and to what extent uncertainties related to the location of proton and neutron shell closures will change the half-lives of SHEs. Partial α and β half-lives are only insignificantly modified by shell effects, because their decay process occurs between neighboring nuclei. This is different for fission half-lives which are primarily determined by shell effects. However, the uncertainty related to the location of nuclei with the strongest shell effects, and thus the longest partial fission half-life at $Z = 114$, 120, or 126 and $N = 172$ or 184, is irrelevant concerning the longest "total" half-life of SHEs. All regions for these SHEs are dominated by α decay. Alpha-decay half-lives will only be modified by a factor of up to approximately 100 if the double shell closure is not located at $Z = 114$ and $N = 184$.

The line of reasoning is, however, different concerning the production cross section. The survival probability of the compound nucleus is determined among other factors significantly by the fission barrier. Therefore, with respect to an efficient production yield, the knowledge of the location of minimal negative shell-correction energy is highly important. However, it may also turn out that shell effects in the region of SHEs are distributed across a number of subshell closures. In that case, a wider region of less deep shell-correction energy would exist with corresponding modification of stability and production yield of SHEs.

3. NUCLEAR REACTIONS

The main features that determine the fusion process of heavy ions are (i) the fusion barrier and the related beam energy and excitation energy; (ii) the ratio of surface tension vs. Coulomb repulsion, which determines the fusion probability and which strongly depends on the asymmetry of the reaction partners (the product Z_1Z_2 at fixed $Z_1 + Z_2$); (iii) the impact parameter (centrality of collision) and related angular momentum; and (iv) the ratio of neutron evaporation and of γ emission vs. the fission of the compound nucleus.

In fusion reactions toward SHEs, the product Z_1Z_2 can reach extremely large and the fission barrier extremely small values. In addition, the fission barrier itself is fragile, because it is solely built up from shell effects. For these reasons, the fusion of SHEs is hampered twofold: (i) in the entrance channel by a high probability for reseparation and (ii) in the exit channel by a high probability for fission. In contrast,

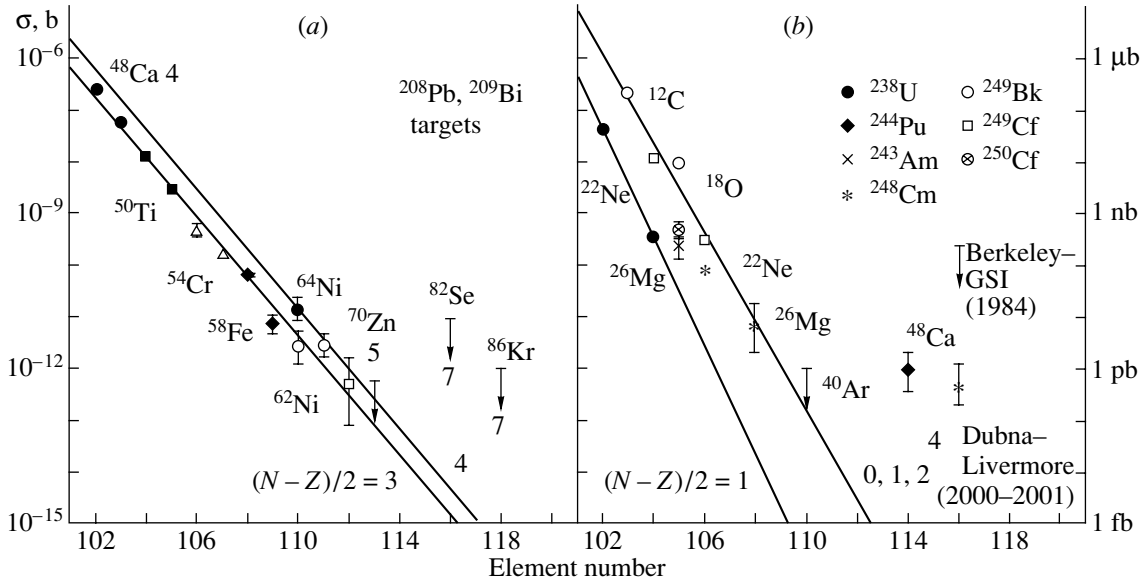

Fig. 3. Measured cross sections and cross-section limits for reactions using ^{208}Pb and ^{209}Bi targets and one-neutron evaporation (*a*) and for reactions using actinide targets and four-neutron evaporation (*b*).

the fusion of lighter elements proceeds unhindered through the contracting effect of the surface tension and the evaporation of neutrons instead of fission.

The effect of Coulomb repulsion on the cross section starts to act severely for fusion reactions to produce elements beyond fermium. From there on, a continuous decrease in cross section was measured from microbarns for the synthesis of nobelium down to picobarns for the synthesis of element 112. Data obtained in reactions with ^{208}Pb and ^{209}Bi for the $1n$-evaporation channel at low excitation energies of about 10–15 MeV (therefore named *cold fusion*) and in reactions with actinide targets at excitation energies of 35–45 MeV (*hot fusion*) for the $4n$ channel are plotted in Figs. 3*a* and 3*b*, respectively.

Some features that the data reveal are pointed out in the following:

(i) Thus far, no data have been measured below cross-section values of about 0.5 pb. This is the limit presently set by experimental constraints. Considering the already long irradiation time to reach a cross-section limit of 0.5 pb (approximately four weeks), it seems impractical to perform systematic studies on this cross-section level or even below it. Further improvement of the experimental conditions is mandatory. Note in this context that the experimental sensitivity has increased by three orders of magnitude since the 1984 search experiment for element 116 using the hot fusion reaction $^{48}\mathrm{Ca} + {}^{248}\mathrm{Cm} \rightarrow {}^{296}116^{*}$ [17, 18].

(ii) The cross sections for elements lighter than 113 decrease by factors of 4 and 10 per element in the case of cold and hot fusion, respectively. This decrease is explained as a combined effect of increasing probability for reseparation of projectile and target nucleus and fission of the compound nucleus. Theoretical consideration and empirical descriptions (see, e.g., [19, 20]) suggest that the steep fall of cross sections for cold fusion reactions may be strongly linked to increasing reseparation probability at high values of Z_1Z_2, while hot fusion cross sections mainly drop because of strong fission losses at high excitation energies. Extremely small values result from extrapolating these data into the region of element 114 and above. However, strong shell effects for SHEs with spherical nuclear shapes could lead to an increase in the fission barrier and thus to an increase in the survival probability of the compound nucleus. The relatively high values measured in Dubna for the synthesis of elements 114 and 116 would be in agreement with this argumentation. In the case of cold fusion, cross-section limits are known only for the synthesis of elements 116 and 118.

(iii) Locally, an increase in the cross section by a factor of 5.8 was measured for element 110 in cold fusion reactions when the beam was changed from ^{62}Ni to ^{64}Ni. It was speculated that this increase could be due to the increased value of the projectile isospin. However, the assumption could not be confirmed in the case of element 112, which was synthesized using the most neutron-rich stable zinc isotope with mass number 70.

It was pointed out in the literature [21] that closed shell projectile and target nuclei are favorable for synthesizing SHEs. The reason is not only a low

reaction Q-value and thus a low excitation energy, but also that fusion of such systems is connected with a minimum of energy dissipation. The fusion path proceeds along cold fusion valleys, where the reaction partners maintain kinetic energy up to the closest possible distance. In this view, the difference between cold and hot fusion is not only a result of gradually different values of excitation energy, but there exists a qualitative difference, which is, on one hand (cold fusion), based on a well-ordered fusion process along paths of minimum dissipation of energy and, on the other hand (hot fusion), based on a process governed by the formation of a more or less energy equilibrated compound nucleus. The use of doubly magic ^{48}Ca and actinide targets seems to proceed via an intermediate fusion process, possibly along a fusion valley less pronounced than in the case of cold fusion. Triggered by the recent experimental success of heavy element synthesis, a number of theoretical studies are in progress aiming to obtain a detailed understanding of the processes involved [22–28].

Due to the great uncertainty concerning the influence of the various steps in the fusion of heavy elements, more and more precise experimental data are needed. It is especially important that various combinations of projectile and target be investigated, from very asymmetric systems to symmetric ones, and that excitation functions be measured. This provides information on how fast the cross section decreases with increasing energy due to fission of the compound nucleus and how fast cross sections decrease on the low-energy side due to the fusion barrier. From both slopes, information about the "shape" of the fission and the fusion barriers can be obtained. At a high enough cross section, these measurements can be complemented by in-beam γ-ray spectroscopy using the recoil-decay tagging method in order to study the influence of angular momentum on the fusion and survival probability [29–31].

4. SUMMARY AND OUTLOOK

The experimental work of the last two decades has shown that cross sections for the synthesis of the heaviest elements decrease almost continuously. However, recent data on the synthesis of element 114 and 116 in Dubna using hot fusion seem to break this trend when the region of spherical superheavy elements is reached.

Progress toward the exploration of the island of spherical SHEs is difficult to predict. However, despite the exciting new results, many questions of a more general character are still awaiting an answer. New developments will not only make it possible to perform experiments aimed at synthesizing new elements in reasonable measuring times, but will also allow for a number of various other investigations covering reaction physics and spectroscopy.

One can hope that, during the coming years, more data will be measured in order to promote a better understanding of the stability of the heaviest elements and the processes that lead to fusion. A microscopic description of the fusion process will be needed for an effective explanation of all measured phenomena in the case of low dissipative energies. Then, the relationships between fusion probability and stability of the fusion products may also become apparent.

An opportunity for the continuation of experiments in the region of SHEs at decreasing cross sections afford, among others, further accelerator developments. High-current beams and radioactive beams are options for the future. At increased beam currents, values of tens of particle μA may become accessible, the cross-section level for the performance of experiments can be shifted down into the region of tens of femtobarns, and excitation functions can be measured on the level of tenths of picobarns. High currents, in turn, call for the development of new targets and separator improvements. Radioactive ion beams, not as intense as the ones with stable isotopes, will allow for approaching the closed neutron shell $N = 184$ at lighter elements. Interesting will be the study of the fusion process using radioactive neutron-rich beams.

The half-lives of spherical SHEs are expected to be relatively long. Based on nuclear models, which are effective predictors of half-lives in the region of the heaviest elements, values from microseconds to years have been calculated for various isotopes. This wide range of half-lives encourages the application of a wide variety of experimental methods in the investigation of SHEs, from the safe identification of short-lived isotopes by recoil-separation techniques to atomic physics experiments on trapped ions, and to the investigation of chemical properties of SHEs using long-lived isotopes.

ACKNOWLEDGMENTS

The recent experiments at SHIP were performed in collaboration with D. Ackermann, F.P. Heßberger, B. Kindler, J. Kojouharova, B. Lommel, R. Mann, G. Münzenberg, S. Reshitko, and H.J. Schött (GSI, Darmstadt); A. Popeko and A. Yeremin (JINR, Dubna); S. Antalic, P. Cagarda, and S. Saro (University of Bratislava); and M. Leino and J. Uusitalo (University Jyväskylä).

REFERENCES

1. S. Hofmann, Rep. Prog. Phys. **61**, 639 (1998).
2. S. Hofmann and G. Münzenberg, Rev. Mod. Phys. **72**, 733 (2000).
3. S. Hofmann *et al.*, Z. Phys. A **350**, 277 (1995).
4. S. Hofmann *et al.*, Eur. Phys. J. A **10**, 5 (2001).
5. S. Cwiok *et al.*, Phys. Rev. Lett. **83**, 1108 (1999).
6. S. Hofmann *et al.*, Z. Phys. A **350**, 281 (1995).
7. S. Hofmann *et al.*, Eur. Phys. J. A **14**, 147 (2002).
8. S. Hofmann *et al.*, Z. Phys. A **354**, 229 (1996).
9. Ch. E. Düllmann *et al.*, Nature **418**, 859 (2002).
10. V. Ninov *et al.*, Phys. Rev. Lett. **83**, 1104 (1999).
11. V. Ninov *et al.*, Phys. Rev. Lett. **89**, 039901 (2002).
12. R. Smolanczuk and A. Sobiczewski, in *Proceedings of the XV Nuclear Physics Divisional Conference on Low Energy Nuclear Dynamics, St. Petersburg, Russia, 1995*, Ed. Yu.Ts. Oganessian *et al.* (World Sci., Singapore, 1995), p. 313.
13. S. Cwiok *et al.*, Nucl. Phys. A **611**, 211 (1996).
14. K. Rutz *et al.*, Phys. Rev. C **56**, 238 (1997).
15. R. Smolanczuk *et al.*, Phys. Rev. C **52**, 1871 (1995).
16. P. Möller *et al.*, At. Data Nucl. Data Tables **59**, 185 (1995).
17. P. Armbruster *et al.*, Phys. Rev. Lett. **54,** 406 (1985).
18. Yu. Ts. Oganessian, Phys. At. Nucl. **64**, 1349 (2001).
19. W. Reisdorf and M. Schädel, Z. Phys. A **343**, 47 (1992).
20. M. Schädel and S. Hofmann, J. Radioanal. Nucl. Chem. **203**, 283 (1996).
21. R. K. Gupta *et al.*, Z. Phys. A **283**, 217 (1977).
22. V. Yu. Denisov and S. Hofmann, Phys. Rev. C **61**, 034606 (2000).
23. V. Yu. Denisov and W. Nörenberg, Eur. Phys. J. A **15**, 375 (2002).
24. Y. Aritomo *et al.*, Phys. Rev. C **59**, 796 (1999).
25. V. I. Zagrebaev, Phys. Rev. C **64**, 034606 (2001).
26. G. Giardina *et al.*, Eur. Phys. J. A **8**, 205 (2000).
27. R. Smolanczuk, Phys. Rev. C **63**, 044607 (2001).
28. G. G. Adamian *et al.*, Nucl. Phys. A **678**, 24 (2000).
29. P. Reiter *et al.*, Phys. Rev. Lett. **82**, 509 (1999).
30. P. Reiter *et al.*, Phys. Rev. Lett. **84**, 3542 (2000).
31. R.-D. Herzberg *et al.*, Phys. Rev. C **65**, 014303 (2002).

Physics of Atomic Nuclei, Vol. 66, No. 6, 2003, pp. 1026–1032. From Yadernaya Fizika, Vol. 66, No. 6, 2003, pp. 1062–1068.

An Idea for Predicting the Evaporation Residue Cross Section in Superheavy Mass Region*

M. Ohta[1)**] **and Y. Aritomo**[2),3)]

[1)] *Department of Physics, Konan University, Okamoto, Japan*

[2)] *Department of Physics, University of Tokyo, Tokyo, Japan*

[3)] *Flerov Laboratory of Nuclear Reactions, Joint Institute for Nuclear Research, Dubna, Moscow oblast, 141980 Russia*

Received September 6, 2002

Abstract—A trial to clarify the main contributors to the evaporation residue cross section in the superheavy mass region is presented. The precise analysis of these factors enables us to understand more clearly the trend of experimental data decreasing exponentially when the atomic number of the residue nucleus increases. It is found that almost all of the experimental data producing nuclei with $Z = 104$ to 114 are fitted with a common parameter set within a reasonable allowance, i.e., ± 0.7 order. In this sense, this model has a reliable predictability for the synthesis of new elements. © *2003 MAIK "Nauka/Interperiodica"*.

1. INTRODUCTION

It is discussed that, at the present stage, we have no confirmative theory to estimate the evaporation residue (ER) cross section in the superheavy mass region, where the atomic number of compound nucleus (CN) is larger than 104 (e.g., [1–3]).

It is also believed that one of the ways to estimate the ER cross section is to solve the time evolution of the reaction system. From an approaching stage of colliding partner to a final stage after evaporation of several neutrons, the time evolution should be solved by using a stochastic differential equation such as the Langevin equation. In combination with the traditional statistical model for the evaporation process, some hybrid attempts along this line have been made [4–7]. A more sophisticated calculation is reported [8], and a model limiting the path of the time evolution is also proposed [9] based on the dinucleus model [10, 11].

However, if we want to search for the time evolution of a nuclear shape more precisely, the dimension of the shape parameter space inevitably increases and the dimension of the stochastic equation also increases, which makes the calculation more time consuming. We also have less knowledge to describe the transition of the potential energy surface from a two-body system to unified nucleus. The way of setting the potential energy surface greatly affects the estimation of the formation probability of the CN, and this is an important and current problem [12, 13]. In addition, we do not have much confirmed knowledge about the frictional force that is an essential physical quantity in the stochastic calculation.

Usually, the fusion evaporation residue reaction process is treated as two successive stages from the viewpoint of the time scale. They are the formation probability to produce a CN in an excited state and the survival probability for the CN to reach its ground state after neutron evaporation.

In this paper, the formation probability $P_{\rm for}$ (sometimes written as the product of the penetrability and the CN producing probability: $\sum T_l P_{\rm CN}^{(l)}$) is given by a function that is inferred from several numerical results obtained by the three-dimensional Langevin calculation. The survival probability $P_{\rm sur}$ is estimated by means of the traditional statistical model with respect to the recent work of Reisdorf and Schädel [14] in which the ER cross section with Z up to 106 was analyzed.

So far as we know now about the reaction mechanism, we have to permit a lot of ambiguity in the estimation of both probabilities. However, our fundamental aim is to pick up the main contributors to the ER cross section. Through systematic analysis, we have classified several factors that contribute nearly independently to the cross section. They are expressed as an exponent of 10, and *synthesis index* (SI) [15, 16] is defined as the sum of these factors. By introducing an adjustable factor A, we get an expression for the ER cross section: $\sigma_{\rm ER} = 10^{{\rm SI}+A}$ [pb]. Almost all of the experimental data for the production of elements

*This article was submitted by the authors in English.

**e-mail: masaota@konan-u.ac.jp

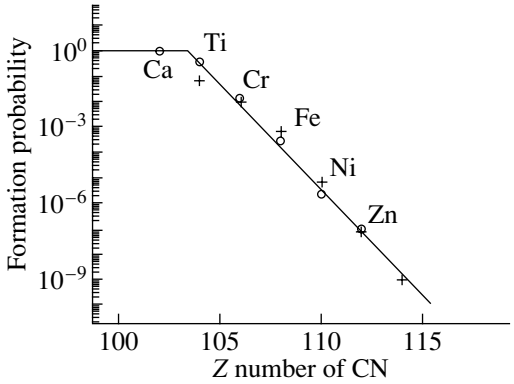

Fig. 1. Formation probability for Pb-target reaction. We plot the experimental data at the excitation energy corresponding to the Bass barrier height by open circles. The name of the element attached to the marks is the projectile. The values of function (1) are shown by crosses.

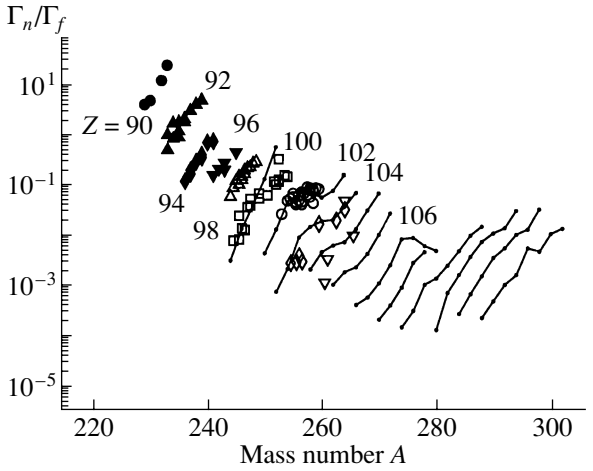

Fig. 2. Isotope dependence of Γ_n/Γ_f at the excitation energy corresponding to the $1n$ or $2n$ channel. The connected lines are our calculation. On an average, the slope of the calculation can be expressed as $(N - N_0)/5$; here, N_0 is a reference number.

from $Z = 104$ to 114 are explained consistently by using a common value of A. This means that the model presented here gives a useful understanding about the trend of the maximum cross section of ER and a more reliable predictability for the synthesis of new elements.

2. FORMATION PROBABILITY

In the present analysis, the logarithm of the formation probability of forming a CN is given by [16]

$$\log P_{\rm for}(Z,\alpha,E^*) = -\frac{3.2+[(E^*-E_B^*+5)^{-1/2}+0.085](Z-100)}{1+\exp[(\alpha-0.55)/\Delta]}, \quad (1)$$

where Z and E^* are the atomic number and the excitation energy of the CN, respectively; and α is the entrance channel mass asymmetry, $\alpha = |A_1 - A_2|/(A_1 + A_2)$, A_1 and A_2 being the mass number of target and projectile. The corresponding excitation energy to the Bass potential barrier [17] is denoted by E_B^* and $\Delta = 0.05$. Note that this formula is valid for $Z \geq 104$, because the function in Eq. (1) is derived under the assumption that the liquid-drop part of the fission barrier is less than 1 MeV. The guiding principle of the derivation of this functional form is based on the probability of overcoming a potential barrier ΔV by thermal diffusion connected with a heat bath of temperature T [18]:

$$P \sim \exp(-\Delta V/T)h(Z,\alpha). \quad (2)$$

Here, we assume that, in order to form a CN, the colliding partners contacting each other have to overcome an extra barrier ΔV along a fusion path; ΔV is mainly a function of Z and α. The function $h(Z,\alpha)$ indicates the probability that the system reaches the CN after overcoming the barrier ΔV. This function should be investigated by means of the exact calculation of the dynamical evolution of the system [13]. But in the present work, this probability is not treated separately. We consider this function to be effectively included in Eq. (1) in the process of data fitting. The dependence of the excitation energy in Eq. (1) comes from the temperature T according to the relation $E^* = aT^2$.

The potential difference between the contact point and the ridge of the potential energy surface located slightly inside of the contact point is investigated by means of the two-center model [19]. We have obtained the following regularity:

$$\Delta V(Z,\alpha) \propto \frac{Z-100}{1+\exp((\alpha-0.55)/0.05)}. \quad (3)$$

The substitution of the relation (3) into Eq. (2) leads to Eq. (1) by introducing some constant factors to reproduce the experimental data. Figure 1 shows the experimental formation probability (open circles) [20] at the energy corresponding to the Bass barrier compared with the value given by Eq. (1) (crosses). The trend depending on Z number is well reproduced for the Pb target reaction series. It is noted that, if E_B^* is less than the effective fission barrier, i.e., the absolute value of the shell correction energy of CN, the value of E_B^* in Eq. (1) is replaced by $|\delta_{\rm shell}|$.

3. SURVIVAL PROBABILITY

The survival probability is calculated by means of the traditional statistical model [21, 22]. We want to

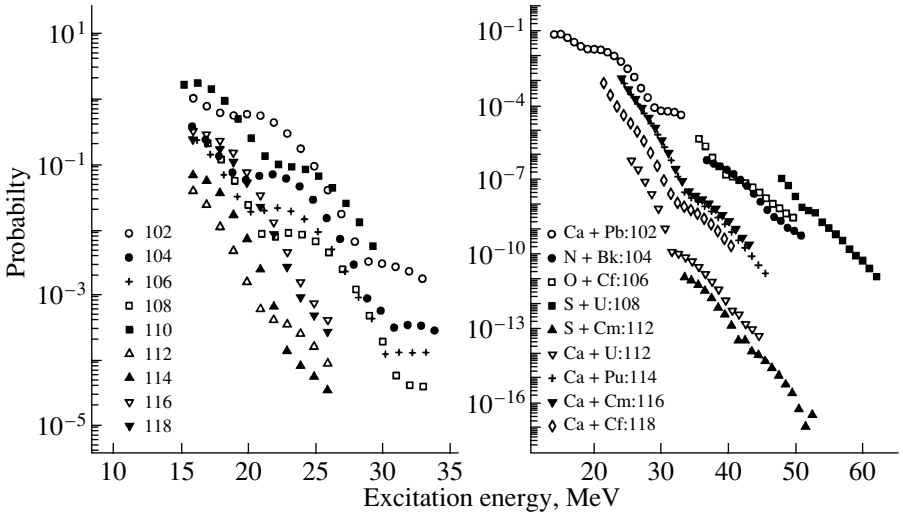

Fig. 3. Excitation energy dependence of survival probability. In the left panel, the symbols for $Z = 112$ (△), 114 (▲), 116 (▽), and 118 (▼) show steeper slopes compared with that for $Z = 102$ (○), 104 (●), 106 (+), and 108 (□). A CN with Z number less than 110 is in general deformed. Therefore, the collective enhancement factor appearing in Eq. (5) enhances the value of Γ_n/Γ_f, and as a result the slope of $P_{\rm sur}$ becomes mild. The same situation can be seen for the case of an actinide target as shown in the right panel. On average, the slope parameter a is determined from the data. For a spherical CN with $\beta_2^{\rm gr} < 0.1$, $a = 0.36$, and for $\beta_2^{\rm gr} > 0.1$, $a = 0.2$.

obtain the probability of finding ER nuclei in competition with the fission process:

$$P_{\rm sur} = \prod_{i=1}^{N} \Gamma_n^{(i)}/(\Gamma_n^{(i)} + \Gamma_f^{(i)}), \qquad (4)$$

where N is the number of neutrons emitted, and $\Gamma_n^{(i)}$ and $\Gamma_f^{(i)}$ are the decay widths of neutron evaporation and fission before the ith neutron emission, respectively. The essential quantity for evaluating the survival probability is Γ_n/Γ_f at any excitation energy of CN [21, 22]:

$$\frac{\Gamma_n}{\Gamma_f} = \frac{k_{\rm coll}({\rm g.s.})}{k_{\rm coll}({\rm saddle})k_{\rm K}} A_0 \qquad (5)$$
$$\times \exp\left[2\sqrt{a_n E_n^*} - 2\sqrt{a_f E_f^*}\right],$$

where $E_n^* = E_{\rm int}^* - B_n$, $E_f^* = E_{\rm int}^* - B_f$, $A_0 = 4A^{2/3}a_f E_n^*/\left(K_0 a_n\left[2\sqrt{a_f E_f^*} - 1\right]\right)$, and $K_0 \equiv \hbar/(2mr_0^2)$. The factor $k_{\rm coll}$(g.s.) and $k_{\rm coll}$(saddle) are added as a collective enhancement factor for the level density of ground state and saddle shape, respectively, and the Kramers factor [18] is expressed as $k_{\rm K} = (\hbar\omega_1/\sqrt{E_{\rm int}^*})(\sqrt{1+x^2} - x)$, where $x = \gamma/(2\omega_0)$; ω_0 and ω_1 are the curvatures of potential energy surfaces at ground state configuration and saddle shape, respectively. The strength of one-body friction is expressed by γ. Our calculation depends on angular momentum. The survival probability $P_{\rm sur}$ is defined [8, 15, 16] as $P_{\rm sur} = \sum_{i=1}^{40}(2l+1)P_{\rm sur}^{(l)}$, assuming that, in this angular momentum range, the formation probability is nearly independent of the angular momentum.

In the following, we check the sensitivity of the survival probability on various physical quantities. It is found that, when the shell correction energy is modified artificially by ±1 MeV, that is, the effective fission barrier is modified by ±1 MeV, the survival probability changes by ±1 order [16, 23]. Thus, the contribution to the index is the ground state shell correction energy itself with a minus sign: $-\delta_{\rm shell}$.

The isotope dependence of Γ_n/Γ_f is presented in Fig. 2, where the excitation energy corresponds to around the $2n$ channel and the experimental data are taken from Ter-Akopyan *et al.* [24]. From these results, on average, we can extract how the survival probability depends on the neutron number of CN. As can be seen from Fig. 2, an increase of five neutrons yields about a one order increase in Γ_n/Γ_f. Therefore, the contribution to SI is $(N - N_0)/5$; here, N_0 is a reference number, which is discussed later.

The excitation energy dependence of the survival probability is one of the important elements to estimate the ER cross section. This is classified into two cases. As can be seen from Eq. (5), the value of Γ_n/Γ_f varies by one order or more depending on whether the CN is well deformed or not [15, 16]. We found that, for the case of spherical-like CN, the slope of the survival probability against the excitation energy is steeper than that for the case of deformed CN. The resultant contribution to SI becomes $a(E - E_0)$, where $a =$

0.36 for $\beta_2^{\rm gr}({\rm CN}) < 0.1$ and $a = 0.2$ for $\beta_2^{\rm gr}({\rm CN}) \geq 0.1$, and E_0 is again a reference energy. The slope parameter a is determined from the calculation of $P_{\rm sur}$ as shown in Fig. 3, where the excitation energy dependence of $P_{\rm sur}$ for the Pb- and actinide-target reactions are shown. In general, the CN whose charge number is greater than 110 has a compact shape with $\beta_2^{\rm gr}$ less than 0.1. As can be seen from Fig. 3, the slope of $P_{\rm sur}$ is classified into two kinds depending on whether $\beta_2^{\rm gr}$ is greater or less than 0.1. Even if the slope is similar, the absolute value is different. This difference comes from the difference of the neutron number and the shell correction energy of the CN. Therefore, the information on the term $a(E - E_0)$ is almost independent of the term $(N - N_0)/5$ and $\delta_{\rm shell}$.

We have to add one more factor to SI. That is the penetrability when the incident energy is less than the Bass barrier height. We assume the inverted parabola with the strength of $\hbar\omega$ as the barrier. Therefore, the contribution to SI is $\log T_B = \log(1 + \exp(-2\pi\Delta E/\hbar\omega))^{-1}$, where $\Delta E(<0)$ is the difference of the Bass barrier and the incident energy.

$\hbar\omega$ is a parameter here, since the early stage of the fusion reaction is still an open problem in superheavy mass region, because the fusion hindrance seems to overwhelm the subbarrier enhancement. Even though the entrance mass asymmetry is near the Bussinaro–Gallone point, the fusion hindrance after the capture of projectile is almost two orders of magnitude [13]. The important point in this model is how to improve Eq. (1) by using new experimental fusion data and to find the theoretical basis to treat the fusion mechanism.

4. RESULTS AND DISCUSSIONS

Summing up the main contributors to the ER cross section, we can define the SI by following relation:

$$\begin{aligned} {\rm SI} = \log P_{\rm for} - \delta_{\rm shell} + (N - N_0)/5 \\ - a(E - E_0) + \log T_B + N_G; \end{aligned} \qquad (6)$$

here, $N_G = \log(\pi/k^2)$ and k is the wave number of an incident channel. Adding an adjustable factor A, we can reproduce almost all of the experimental maximum cross section by $\sigma_{\rm ER} = 10^{{\rm SI}+A}$ [pb]. Throughout the analysis, common values for N_0, E_0, and A are used: $E_0 = 18$ MeV, $A = 0$, and N_0 is chosen for each Z so that the CN with (Z, N_0) has an average neutron separation energy of 7.5 MeV, as shown in Fig. 4. This is a reason why the neutron number dependence in $\sigma_{\rm ER}$ should be estimated from a standard point of view, where the emission rate of neutrons is almost the same. For information about the mass, the shell correction energy, and the ground state deformation, Möller's table [25] is used.

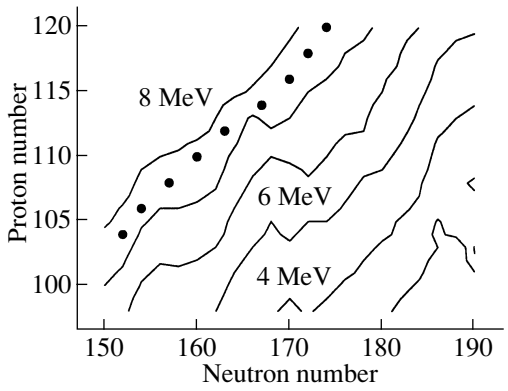

Fig. 4. Contour map of average neutron separation energy $\overline{B_n}$, which is defined by the average of the separation energy in successive four-neutron emission: $\sum_{i=1}^{4} N_n^{(i)}/4$. The reference number of neutrons N_0 for each Z is indicated by points.

In this paper, our attention is focused on the hot fusion reaction system. In Fig. 5, the maximum ER cross sections at excitation energy around 35 MeV, which corresponds to the $3n$ or $4n$ channel, are shown for targets of ^{238}U, ^{244}Pu, ^{248}Cm, and ^{248,249}Cf. The abscissa of the figures is the atomic number of CN. In all cases, the most neutron-rich projectiles that are available in experiments are chosen. They are ^{18}O, ^{19}F, ^{22}Ne, ^{23}Na, ^{26}Mg, ^{27}Al, ^{30}Si, ^{31}P, ^{34}S, ^{37}Cl, ^{40}Ar, ^{41}K, ^{48}Ca, ^{45}Sc, ^{50}Ti, ^{50}V, ^{54}Cr, ^{55}Mn, and ^{58}Fe. It can be seen that the experimental data (indicated by dots) [26–41] entwine well with the band of the prediction. The upper limit of the band is $10^{{\rm SI}+A} \cdot 5$ and the lower one is $10^{{\rm SI}+A}/5$. In the lower right panel in Fig. 5, the cross section for the ^{249}Cf target is drawn by the solid line. In the lower left panel, the prediction for the cross section at $E^* = 45$ MeV which corresponds to the ^{248}Cm(HI, $4n$–$5n$) reaction is drawn by the solid line. The excitation energy corresponding to the Bass potential energy is scattered around 40 MeV in these reaction systems. Therefore, the cross sections at $E^* = 35$ and 45 MeV are comparable, as shown in Fig. 5. The same predictions for the reaction by ^{243}Am and ^{249}Bk targets are drawn in Fig. 6. In the production of even Z elements in Fig. 6, since proton number of both target and projectile are odd, the shell correction energy of CN with even Z is smaller than that for odd Z and the Bass potential barrier is also higher for even Z than for odd Z. Therefore, we can see an enhanced even–odd difference.

As can be seen in Fig. 5, the ^{249}Cf target gives a larger cross section by about a factor of 4 than the ^{248}Cf target. This difference comes from the larger

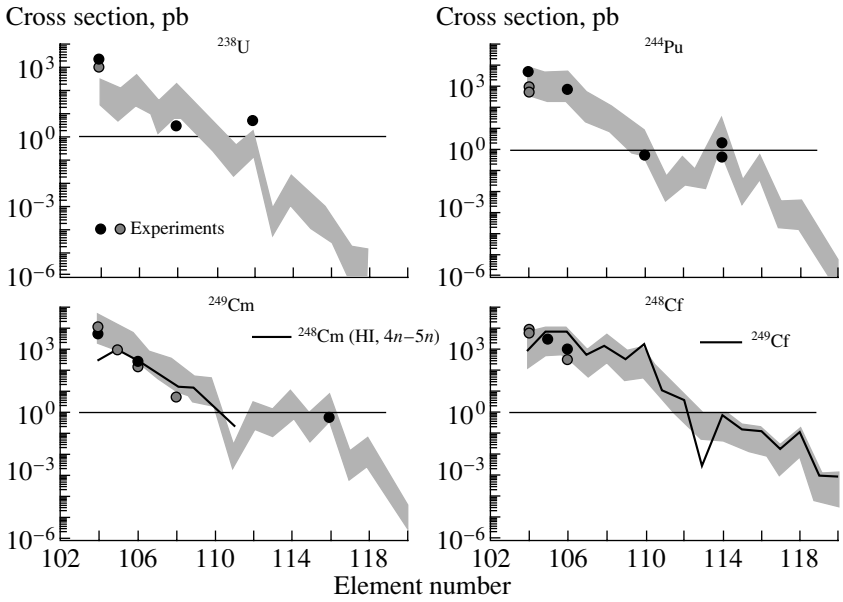

Fig. 5. Maximum cross sections for the synthesis of elements from 104 to 120 using ^{238}U, ^{244}Pu, ^{248,249}Cm, and ^{248,249}Cf targets. For ^{238}U, ^{244}Pu, ^{249}Cm, and ^{248}Cf targets, the prediction at the excitation energy of 35 MeV, which corresponds to (HI, $3n$–$4n$) reaction, is indicated by the band. The upper and the lower limit of the band are $10^{\mathrm{SI}+A} \cdot 5$ and $10^{\mathrm{SI}+A}/5$, respectively. In the lower left panel, the prediction at 45 MeV for ^{248}Cm target is drawn by the solid line. The solid line in the lower right panel shows the prediction for ^{249}Cf target at $E^* = 35$ MeV. In all cases, the most neutron-rich projectile usable in experiments is taken (see text). Points show the experimental data.

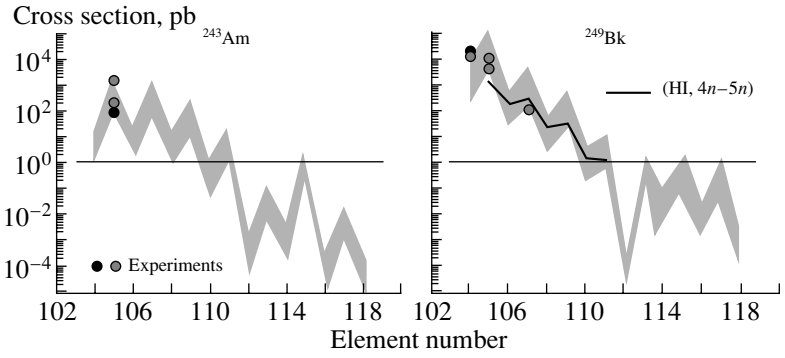

Fig. 6. Maximum cross sections for the synthesis of elements from 104 to 120 using ^{243}Am and ^{249}Bk targets. The excitation energy of CN is around 35 MeV, which corresponds to (HI, $3n$–$4n$) reaction. In the case of ^{249}Bk target, the prediction at the excitation energy of 45 MeV is shown by the solid line. Points show the experimental data.

shell correction energy in the ^{249}Cf case by about 0.4 MeV and the richness of one neutron. Also, in Fig. 5, we can appreciate a bump in the region of element number from 112 to 118 for the case of Pu and Cm target. In the case of Cf target, the bump is not so appreciable. In the middle of the bump, the enhanced cross section by Ca projectile is appreciable due to the strongest shell correction energy of CN compared with the other reaction system, as will be shown in Fig. 7, which will be explained later. On the contrary, the cross section monotonically decreases for the case of U target. This situation can be understood from a precise inspection of Fig. 7.

In Fig. 7, the components of SI corresponding to reactions shown in Fig. 5 are plotted. The term P_{for} (closed square) monotonically changes as Z_{CN} increases. The degree of the decrease in P_{for} becomes mild when the target nucleus becomes heavier because of the slight change of mass asymmetry. The large shell correction energy (closed circles) can be seen around $Z_{\mathrm{CN}} = 114$, 116, and 118 for the Pu, Cm, and Cf target, respectively. The term $-a(E - E_0)$ (open circles) fluctuates since the excitation energy

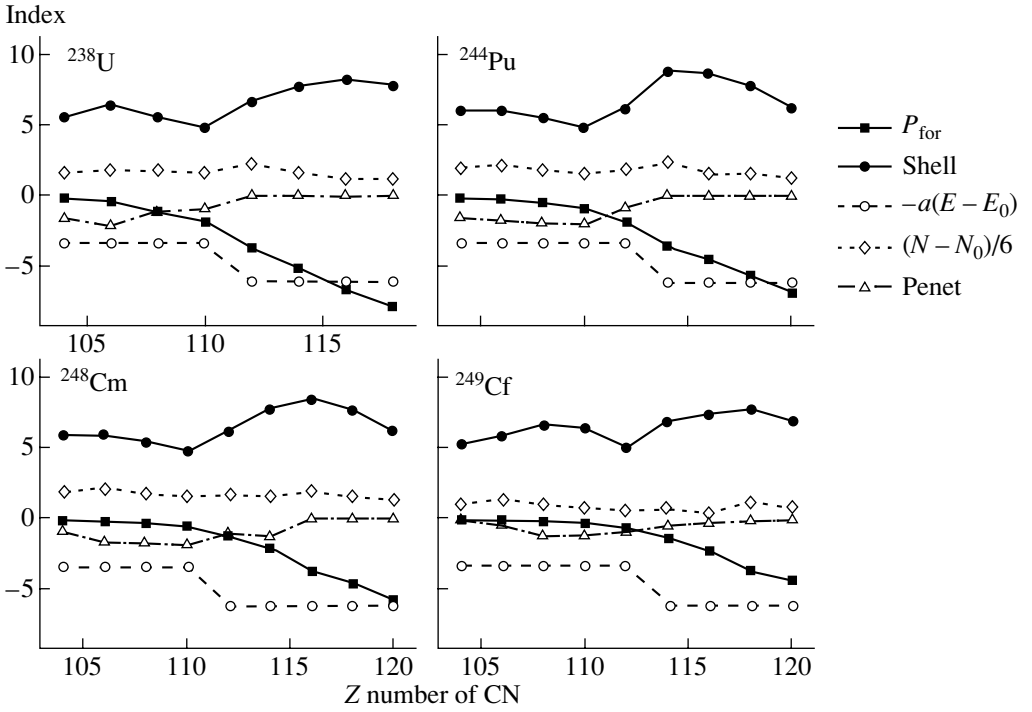

Fig. 7. Component of SI for the fusion reaction with ^{238}U, ^{244}Pu, ^{248}Cm, and ^{249}Cf targets, which correspond to the prediction presented by the band in Fig. 5. The abscissa is the Z number of CN. The formation probability P_{for} (closed squares) and the shell correction energy of CN (closed circles) show an important behavior that controls the cross section. The survival probability (open circles) shifts to a lower value around $Z = 112$ because the ground state deformation of CN changes drastically beyond $Z \geq 110$.

at the maximum cross section is different and the ground state deformation of CN is nearly equal to zero for $Z_{CN} \geq 110$. Here, the different slope parameter a is used whether the ground state of CN is spherical or not, i.e., whether the deformation β_2^{gr} of CN is greater than 0.1 or not [42]. The barrier penetrability indicated by Penet (open triangles) becomes near zero for $Z_{CN} \geq 114$ because of the decrease in the Bass barrier height. The main components making a bump around $Z_{CN} = 114$ for the Pu, Cm, and Cf targets are P_{for} and the shell correction energy. In the case of the U target, the term P_{for} decreases very steeply at large Z_{CN} and the enhancement of the shell correction energy does not appreciate much, so that the trend of σ_{ER} drawn in Fig. 5 shows a monotonic decrease with no enhancement around $Z_{CN} = 114$. The enhancement due to the neutron richness in the ^{48}Ca projectile is about factor 3–4 for the case of Pu, Cm, and Cf targets.

Finally, we mention a prediction for the production of element 118 by using Cf isotopes. By means of the model, we estimate the ER cross section at $E^* =$ 30 MeV for ^{248,249,250,251,252}Cf + ^{48}Ca. Since the Bass barrier heights for these reaction system are 27.5, 27.9, 27.7, 28.3, and 28.4 MeV, respectively, the optimum cross section is assumed to be obtained around the excitation energy of 30 MeV. The predictions for the cross section are listed in the table. Some of the component of SI are also included in the table. The component $(N - N_0)/5$ monotonically increases due to the increase in the neutron number of the target. The absolute value of the shell correction energy has the maximum at the target mass of 249. Another component of SI is nearly constant over the isotopes. Therefore, as a result, the cross section has an enhanced value for the targets ^{249}Cf and ^{251}Cf. Similar systematic predictions have already been in-

Prediction for the maximum cross section for Cf isotope target by ^{48}Ca projectile; the components of SI for the shell correction energy and the neutron-number-dependent part are listed

Mass of Cf	σ_{ER}, pb	δ_{shell}, MeV	$(N - N_0)/5$
248	0.34	7.91	1.2
249	1.21	8.28	1.4
250	0.87	7.84	1.6
251	1.21	7.85	1.8
252	0.53	7.25	2.0

vestigated for the cold fusion system with Pb and Bi targets down to Ba and Xe ones, and the paper is now being prepared.

In conclusion, it is noted that the main contributors to the ER cross section are the formation probability of CN and the shell correction energy, i.e., the effective fission barrier. In this model, the formation probability is estimated in a phenomenological way using the experimental data. As a property of the function for P_{for}, no individual nature of projectile and target is included except the Q value determining the Bass barrier height. And only the shell effect of CN is taken into account in the calculation of the survival probability. However, the trend in experimental data is well fitted to the predicted value. It is surprising because we expected some deviation from the predicted trend due to the individual shell property of projectile and target nucleus. This means that the strong shell effect of the projectile or the target may be smeared out in the early stage of the collision by a nucleon transfer, or other dissipative process.

REFERENCES

1. S. Hofmann, Rep. Prog. Phys. **61**, 639 (1998).
2. P. Armbruster, Rep. Prog. Phys. **62**, 465 (1999).
3. S. Hofmann and G. Munzenberg, Rev. Mod. Phys. **72**, 733 (2000).
4. Y. Abe, Y. Aritomo, T. Wada, and M. Ohta, J. Phys. G **23**, 1275 (1997).
5. Y. Aritomo, T. Wada, M. Ohta, and Y. Abe, Phys. Rev. C **55**, R1011 (1997).
6. Y. Aritomo, T. Wada, M. Ohta, and Y. Abe, Phys. Rev. C **59**, 796 (1999).
7. M. Ohta, K. Okazaki, T. Wada, *et al.*, Acta Phys. Hung. New Ser.: Heavy Ion Phys. **10**, 253 (1999).
8. V. I. Zagrebaev, Y. Aritomo, M. G. Itkis, *et al.*, Phys. Rev. C **65**, 014607 (2002).
9. V. V. Volkov, in *Proceedings of the International Workshop on Fusion Dynamics at the Extremes, Dubna, 2000*, Ed. by Yu. Ts. Oganessian and V. Zagrebaev (World Sci., Singapore, 2001), p. 174.
10. N. V. Antonenko, E. A. Cherepanov, A. K. Nasirov, *et al.*, Phys. Lett. B **319**, 425 (1993).
11. N. V. Antonenko, E. A. Cherepanov, A. K. Nasirov, *et al.*, Phys. Rev. C **51**, 2635 (1995).
12. V. I. Zagrebaev, this Conference.
13. Y. Aritomo, this Conference.
14. W. Reisdorf and M. Schädel, Z. Phys. A **343**, 47 (1992).
15. M. Ohta, in *Proceedings of the International Workshop on Fusion Dynamics at the Extremes, Dubna, 2000*, Ed. by Yu. Ts. Oganessian and V. Zagrebaev (World Sci., Singapore, 2001), p. 110.
16. M. Ohta and Y. Aritomo, J. Nucl. Sci. Tech. (in press).
17. R. Bass, Nucl. Phys. A **231**, 141 (1974).
18. H. A. Kramers, Physica (Utrecht) **7**, 284 (1940).
19. K. Sato, A. Iwamoto, K. Harada, *et al.*, Z. Phys. A **288**, 387 (1978).
20. Yu. Ts. Oganessian, Yad. Fiz. **63**, 1391 (2000) [Phys. At. Nucl. **63**, 1315 (2000)].
21. R. Vandenbosh and J. R. Huizenger, *Nuclear Fission* (Academic, New York, 1973), p. 233.
22. A. V. Ignatyuk, K. K. Istekov, and G. N. Smirenkin, Yad. Fiz. **30**, 1205 (1979) [Sov. J. Nucl. Phys. **30**, 626 (1979)].
23. M. Ohta and Y. Aritomo, in *Proceedings of the International Symposium on Exotic Nuclei* (World Sci., Singapore, 2002), p. 67.
24. G. H. Ter-Akopyan *et al.*, Nucl. Phys. A **255**, 509 (1975).
25. P. Möller, J. R. Nix, W. D. Myers, and W. J. Swiatecki, At. Data Nucl. Data Tables **59**, 185 (1995).
26. A. N. Andreyev *et al.*, Z. Phys. A **345**, 389 (1993).
27. Yu. A. Lazarev *et al.*, Ann. Rep. JINR-FLNR (Joint Inst. for Nucl. Res., Dubna, 1995/1996), p. 43.
28. Yu. A. Lazarev *et al.*, Phys. Rev. C **54**, 620 (1996).
29. E. K. Hulet *et al.*, J. Inorg. Nucl. Chem. **42**, 70 (1980)
30. L. P. Sommerville *et al.*, Phys. Rev. C **31**, 1801 (1985).
31. Yu. Ts. Oganessian *et al.*, Nature **400**, 242 (1999).
32. Yu. Ts. Oganessian *et al.*, Phys. Rev. Lett. **83**, 3154 (1999).
33. Yu. Ts. Oganessian *et al.*, Phys. Rev. C **63**, 011301 (2001).
34. V. K. Utyonkov *et al.*, in *Proceedings of the VII School–Seminar "Heavy Ion Physics," Dubna, 1997*, p. 400.
35. M. R. Lane *et al.*, Phys. Rev. C **53**, 2893 (1996).
36. A. Ghiorso *et al.*, Phys. Rev. Lett. **22**, 1317 (1969).
37. C. E. Bemis *et al.*, Phys. Rev. C **23**, 555 (1981).
38. Z. G. Gan *et al.*, Eur. Phys. J. A **10**, 21 (2001).
39. M. R. Lane *et al.*, Phys. Rev. C **58**, 3413 (1998).
40. A. Ghiorso *et al.*, Phys. Rev. Lett. **33**, 1490 (1974).
41. M. Schädel and A. Türler, private communication.
42. A. R. Junghaus, M.de Jong, H.-G. Clerc, *et al.*, Nucl. Phys. A **629**, 635 (1998).

Physics of Atomic Nuclei, Vol. 66, No. 6, 2003, pp. 1033–1041. From Yadernaya Fizika, Vol. 66, No. 6, 2003, pp. 1069–1077.

Fusion–Fission Dynamics and Perspectives of Future Experiments*

V. I. Zagrebaev**, **M. G. Itkis, and Yu. Ts. Oganessian**

Flerov Laboratory of Nuclear Reactions, Joint Institute for Nuclear Research, Dubna, Moscow oblast, 141980 Russia

Received September 2, 2002

Abstract—The paper is focused on reaction dynamics of superheavy-nucleus formation and decay at beam energies near the Coulomb barrier. The aim is to review the things we have learned from recent experiments on fusion–fission reactions leading to the formation of compound nuclei with $Z \geq 102$ and from their extensive theoretical analysis. Major attention is paid to the dynamics of formation of very heavy compound nuclei taking place in strong competition with the process of fast fission (quasifission). The choice of collective degrees of freedom playing a fundamental role and finding the multidimensional driving potential and the corresponding dynamic equation regulating the whole process are discussed. A possibility of deriving the fission barriers of superheavy nuclei directly from performed experiments is of particular interest here. In conclusion, the results of a detailed theoretical analysis of available experimental data on the "cold" and "hot" fusion–fission reactions are presented. Perspectives of future experiments are discussed along with additional theoretical studies in this field needed for deeper understanding of the fusion–fission processes of very heavy nuclear systems. © *2003 MAIK "Nauka/Interperiodica".*

1. INTRODUCTION

The interest in the synthesis of superheavy nuclei has grown lately due to new experimental results [1–3] demonstrating a real possibility of producing and investigating the nuclei in the region of the so-called "island of stability." The new reality demands more substantial theoretical support of these expensive experiments, which will allow a more reasonable choice of fusing nuclei and collision energies as well as a better estimation of the cross sections and unambiguous identification of evaporation residues (ERs).

A whole process of superheavy-nucleus formation can be divided into three reaction stages. At the first stage, colliding nuclei overcome the Coulomb barrier and approach the point of contact $R_{\rm cont} = R_1 + R_2$. Quasielastic and deep-inelastic reaction channels dominate at this stage, leading to formation of projectile-like and target-like fragments (PLF and TLF) in the exit channel. At subbarier energies, only a small part of incoming flux with low partial waves reaches the point of contact. Denote the corresponding probability as $P_{\rm cont}(l, E)$. Experiments on deep-inelastic collisions and our knowledge about nuclear friction forces allow us to conclude that, at the contact point, nuclei have almost zero kinetic energy. At the second reaction stage, touching nuclei evolve into the configuration of an almost spherical compound mononucleus. For light or very asymmetric nuclear systems, this evolution occurs with a probability close to unity. Two touching heavy nuclei after dynamic deformation and exchange by several nucleons may reseparate into PLF and TLF or may go directly to fission channels without formation of a compound nucleus. The later process is usually called quasifission. Denote a probability for two touching nuclei to form the compound nucleus (CN) as $P_{\rm CN}(l, E)$. At the third reaction stage, the CN emits neutrons and γ rays, lowering its excitation energy and finally forming the residual nucleus in its ground state. This process takes place in strong competition with fission (normal fission), and the corresponding survival probability $P_{xn}(l, E^*)$ is usually much less than unity even for a weakly excited superheavy nucleus.

Thus, the production cross section of a cold residual nucleus B, which is the product of neutron evaporation and γ emission from an excited compound nucleus C, formed in the fusion process of two heavy nuclei $A_1 + A_2 \to C \to B + xn + N\gamma$ at c.m. energy E close to the Coulomb barrier in the entrance channel, can be decomposed over partial waves and written as

$$\sigma_{\rm ER}^{xn}(E) \approx \frac{\pi\hbar^2}{2\mu E}\sum_{l=0}^{\infty}(2l+1)P_{\rm cont}(E,l) \qquad (1.1)$$
$$\times P_{\rm CN}(A_1 + A_2 \to C; E, l)P_{xn}(C \to B; E^*, l).$$

Different theoretical approaches are used for analyzing all three reaction stages. However, the dynamics of the intermediate stage of the CN forma-

*This article was submitted by the authors in English.

**e-mail: valeri.zagrebaev@jinr.ru

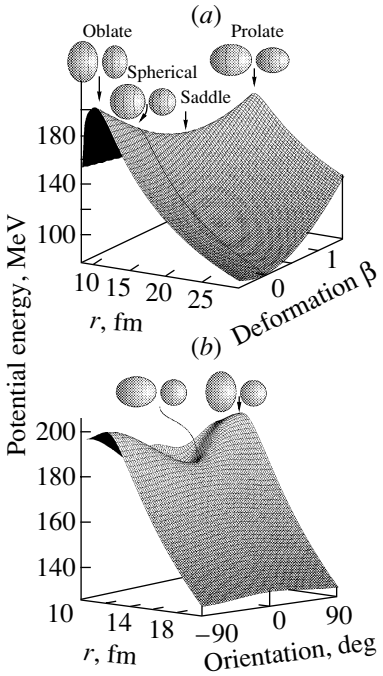

Fig. 1. (*a*) Potential energy of ^{48}Ca + ^{208}Pb depending on distance and quadrupole dynamic deformations of both nuclei. (*b*) Potential energy of ^{48}Ca + ^{238}U depending on orientation of statically deformed ^{238}U nucleus ($\beta_2^{\text{g.s}} = 0.215$).

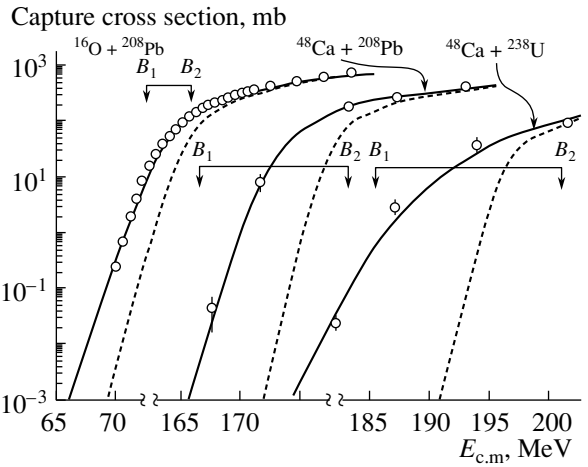

Fig. 2. Capture cross sections in the ^{16}O + ^{208}Pb [9], ^{48}Ca + ^{208}Pb [10], and ^{48}Ca + ^{238}U [3] fusion reactions. Dashed curves represent one-dimensional barrier penetration calculations with the Bass barriers. Solid curves show the effect of dynamic deformation of nuclear surfaces (first two reactions) and orientation of statically deformed nuclei (^{48}Ca + ^{238}U case). The arrows marked by B_1 and B_2 show the positions of the corresponding Coulomb barriers (see the text).

tion is the most vague. It is due to the fact that, in the fusion of light and medium nuclei, in which the fissility of the CN is not very high, the colliding nuclei having overcome the Coulomb barrier form a CN with a probability $P_{\text{CN}} \approx 1$. Thus, this reaction stage does not influence the yield of ER at all. However, in the fusion of heavy nuclei, it is the fission channels (normal and quasifission) that substantially determine the dynamics of the whole process; the P_{CN} value can be much smaller than unity, while its accurate calculation is very difficult. Setting $P_{xn} = 1$ in (1.1), we get the cross section of CN formation σ_{CN}, which can be measured by detection of ERs and fission fragments forming in normal fission (if they are distinguished from quasifission fragments and from products of deep-inelastic collision). Setting in addition $P_{\text{CN}} = 1$ in (1.1), we get the capture cross section σ_{cap}, which can be measured by detection of all fission fragments (if they are distinguished from products of deep inelastic collision). It is clear that, for symmetric fusion reactions, σ_{CN} and σ_{cap} cannot be measured experimentally.

2. CAPTURE CROSS SECTION

The Bass approximation of the potential energy of the interaction between two heavy spherical nuclei [4] is widely used and reproduces rather well the height of the potential barrier. Coupling with the excitation of nuclear collective states (surface vibrations and/or rotation of deformed nuclei) and with nucleon transfer channels significantly influences the capture cross section at near-barrier energies. In Fig. 1, the potential energy is shown depending on dynamic deformation of spherical nuclei ^{48}Ca + ^{208}Pb and on mutual orientation of deformed nuclei ^{48}Ca + ^{238}U($\beta_2^{\text{g.s}} = 0.215$). The incoming flux has to overcome, in fact, a multidimensional ridge with its height depending on orientation and/or dynamic deformation. This means that we have to talk not about one barrier B but rather about a "barrier distribution."

In [5, 6], a semiempirical approach was proposed for calculating the penetration probability of such multidimensional potential barriers. Calculating the barriers B_1 and B_2 for two limit configurations [in the case of statically deformed nuclei, they correspond to the tip and side orientations, otherwise they correspond to the so-called saddle dynamic deformation (see Fig. 1*a*) and spherical configuration], we may approximate the barrier distribution function [7] by an asymmetric Gaussian centered at $B_0 = (B_1 + B_2)/2$. Approximating the radial dependence of the barrier by a parabola and using the Hill–Wheeler formula [8] for the penetration probability of the one-dimensional potential barrier, we may estimate the quantum pen-

etrability of the multidimensional barrier as follows:

$$P_{\rm cont}(E,l) = \int f(B)\Bigg[1+\exp\left(\frac{2\pi}{\hbar\omega(l)}\right. \qquad (2.1)$$
$$\times\left.\left[B+\frac{\hbar^2}{2\mu R_B^2(l,B)}l(l+1)-E\right]\right)\Bigg]^{-1}dB.$$

Here, $\hbar\omega_B$ is defined by the width of the parabolic barrier, R_B defines the position of the barrier, and the barrier distribution function satisfies the normalization condition $\int f(B)dB = 1$.

The capture cross sections calculated within this approach are shown in Fig. 2 for the three reactions (solid curves). They are compared with theoretical calculations made within a model of one-dimensional barrier penetrability for spherical nuclei (dashed curves). In all three cases, a substantial increase in the barrier penetrability is observed in the subbarrier energy region. However, the character of this increase significantly changes: the shift of the barrier and the distribution width, in particular, grow with the increase in the masses of fusing nuclei. An additional decrease in the ^{48}Ca + ^{238}U capture cross section at above-barrier energies as compared with its geometrical limit is explained by a much shallower potential pocket and, thus, by a much smaller value of the critical angular momentum.

Good agreement between the calculated and experimental capture cross sections allows us to believe that we may get a rather reliable estimation of the capture cross section for a given projectile–target combination if there are no experimental data or if these data cannot be obtained at all (symmetric combinations). However, we should realize that some uncertainty nevertheless remains in choosing the parameters defining the multidimensional potential barrier and the capture cross section [6]. The role of the neutron exchange is also not clear yet. Thus, in the cases of fusion of very heavy nuclei and especially for symmetric fusion reactions, the accuracy of our current predictions of the capture cross sections in the subbarrier energy region is about one order of magnitude. At above-barrier energies, this accuracy is much better.

3. FUSION–FISSION DYNAMICS

The processes of the CN formation and quasifission are the least studied stages of the heavy-ion fusion reaction. To solve this problem, we have to answer very fundamental questions. What are the main degrees of freedom playing most important role at this reaction stage? What is the corresponding driving potential and what is an appropriate equation of motion for description of time evolution of the nuclear system at this stage? Today, there is no consensus for the answers and for the mechanism of the compound nucleus formation itself, and quite different, sometimes opposite in their physics sense, models are used for its description.

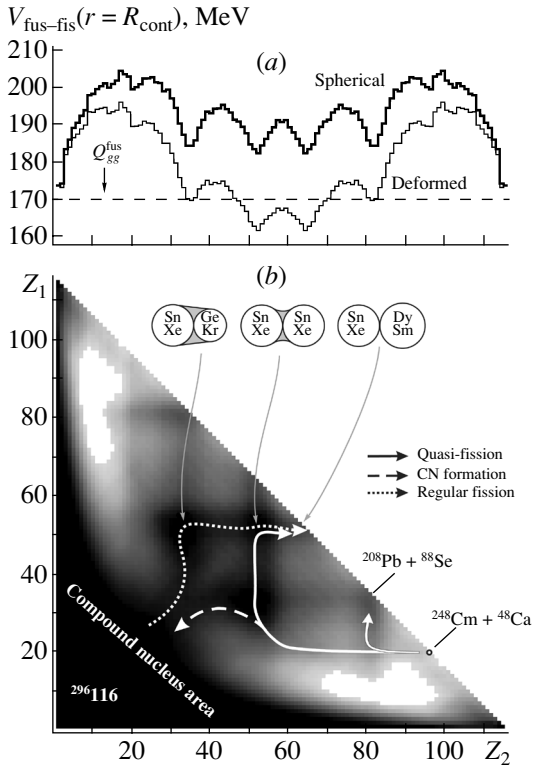

Fig. 3. Driving potential $V_{\rm fus-fis}(Z_1, Z_2)$ of the nuclear system consisting of 116 protons and 180 neutrons. (*a*) Potential energy of two touching nuclei at $A_1 + A_2 = A_{\rm CN}$, $\Delta A = 0$, i.e., along the diagonal of the lower figure. The thick line corresponds to the case of spherical nuclei, whereas the thin line corresponds to $\delta_1 + \delta_2 = 0.3$. (*b*) Topographical landscape of the driving potential on the plane (Z_1, Z_2) (zero deformations). The dark regions correspond to the lower potential energies (more compact configurations).

In [5, 11], a new approach was proposed for description of fusion–fission dynamics based on a simplified semiempirical version of the two-center shell model idea [12]. It is assumed that, on a path from the initial configuration of two touching nuclei to the CN configuration and on a reverse path to the fission channels, the nuclear system consists of two cores (Z_1, N_1) and (Z_2, N_2) surrounded by a certain number of common (shared) nucleons, $\Delta A = A_{\rm CN} - A_1 - A_2$, moving in the whole volume occupied by the two cores. The processes of CN formation, fission, and quasifission take place in the space $(Z_1, N_1, \delta_1; Z_2, N_2, \delta_2)$, where δ_1 and δ_2 are the dynamic deformations of the cores. The compound nucleus is finally formed when two fragments A_1 and

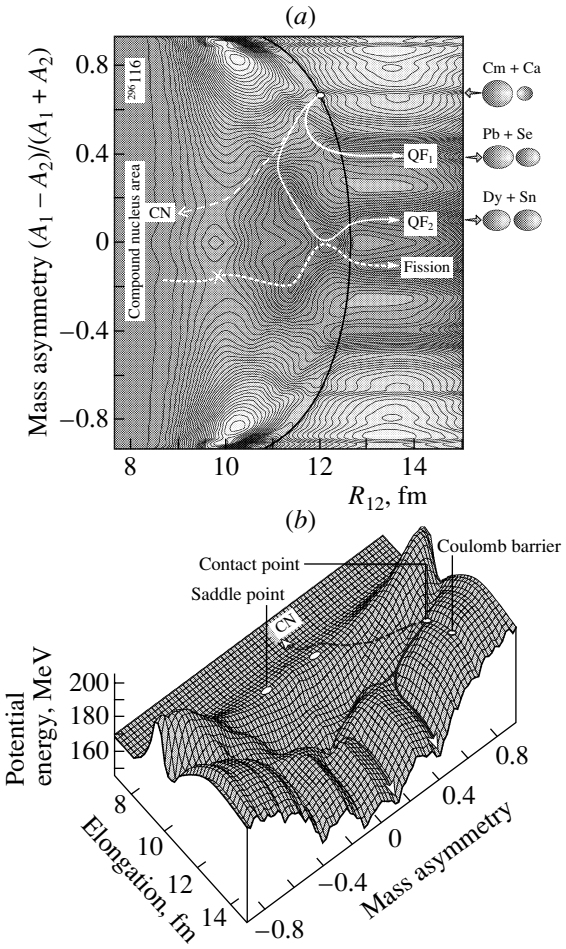

Fig. 4. Driving potential $V_{\text{fus–fis}}$ as a function of mass asymmetry and distance between centers of two nuclei with the deformations $\delta_1 + \delta_2 = 0.3$, topographical landscape (a) and three-dimensional plot (b). The black solid curve in (a) shows the contact configurations. The paths QF_1 and QF_2 lead to the asymmetric and near-symmetric quasifission channels, the dashed curve shows the most probable way to formation of the compound nucleus, and the dotted curve corresponds to normal (regular) fission. See the conformity with Fig. 3.

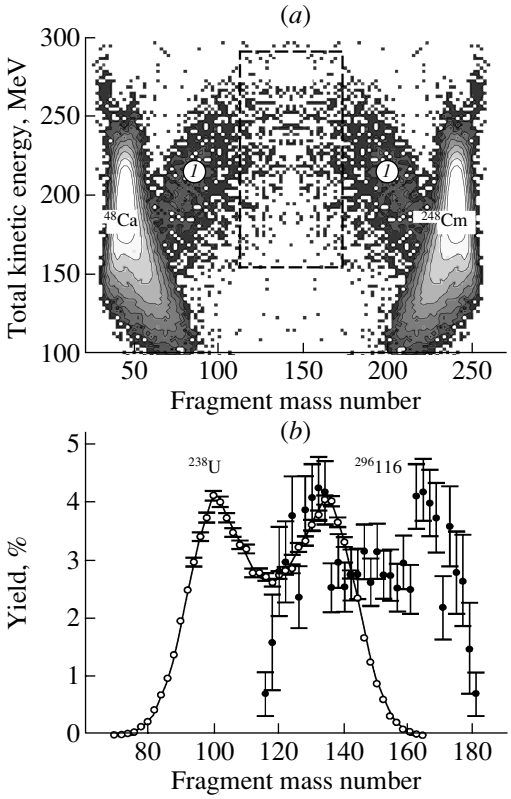

Fig. 5. (a) Two-dimensional TKE–mass plot. The asymmetric quasifission process (QF_1 path in Fig. 4) contributes mainly to the regions marked by *1*. Normal fission and near-symmetric quasifission (QF_2 path in Fig. 4) contribute to the region marked by dashed quadrangle. (b) Mass distribution of near-symmetric fission fragments [dashed quadrangle on panel (a)] detected in the ^{48}Ca + ^{248}Cm reaction at excitation energy of $E^* =$ 33 MeV compared with the fission of ^{238}U measured at approximately the same excitation energy [13].

A_2 go into its volume, i.e., at $R(A_1) + R(A_2) = R_{\text{CN}}$ or at $A_1^{1/3} + A_2^{1/3} = A_{\text{CN}}^{1/3}$.

The corresponding driving potential $V_{\text{fus–fis}}(r, Z_1, N_1, \delta_1; Z_2, N_2, \delta_2)$ was derived in [5] and is shown in Fig. 3 as a function of Z_1, Z_2 (minimized over N_1, N_2 and at fixed values of $\delta_1 + \delta_2$). It was found that the microscopic two-center shell model calculations give very close values of potential energy, though slightly less structural. There are several advantages of the proposed approach. The driving potential is derived on the basis of experimental binding energies of two cores, which means that the "true" shell structure is taken into account (see Fig. 3). The driving potential is defined in the whole region $R_{\text{CN}} < r < \infty$, it is a continuous function at $r = R_{\text{cont}}$, and it gives a realistic Coulomb barrier at $r = R_B > R_{\text{cont}}$. At last, instead of using the variables (Z_1, N_1; Z_2, N_2), we may easily recalculate the driving potential as a function of mass asymmetry $(A_1 - A_2)/(A_1 + A_2)$ and elongation $R_{12} = r_0(A_1^{1/3} + A_2^{1/3})$ (at $r \geq R_{\text{cont}}$, $R_{12} = r = s + R_1 + R_2$, where s is the distance between nuclear surfaces). These variables along with deformation $\delta_1 + \delta_2$ are commonly used for description of the fission process. The corresponding driving potential is shown in Fig. 4.

As can be seen from Figs. 3 and 4, the shell structure, clearly revealing itself in the contact of two nuclei (Fig. 3a), is also retained at $\Delta A \neq 0$ ($R_{12} < R_{\text{cont}}$) (see the deep minima in the regions of $Z_{1,2} \sim 50$ and $Z_{1,2} \sim 82$ in Fig. 3b). Following the fission path (dotted curves in Figs. 3b and 4a), the system overcomes a multihumped fission barrier, which is well known in fission dynamics. The

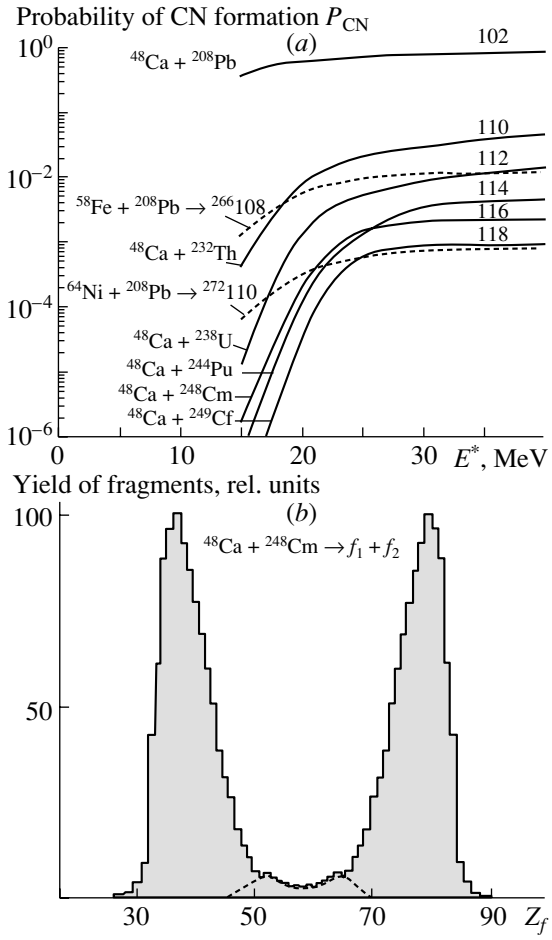

Fig. 6. (*a*) Probability of compound-nucleus formation for the "hot" (solid curves) and "cold" (dashed curves) fusion reactions. (*b*) Charge distribution of quasifission fragments in the $^{48}Ca + ^{248}Cm$ fusion reaction at $E^* = 40$ MeV (linear scale, relative units). The main peaks correspond to the path QF_1 in Fig. 4 (see region *1* in Fig. 5*a*), whereas the small near-symmetric peaks correspond to the path QF_2.

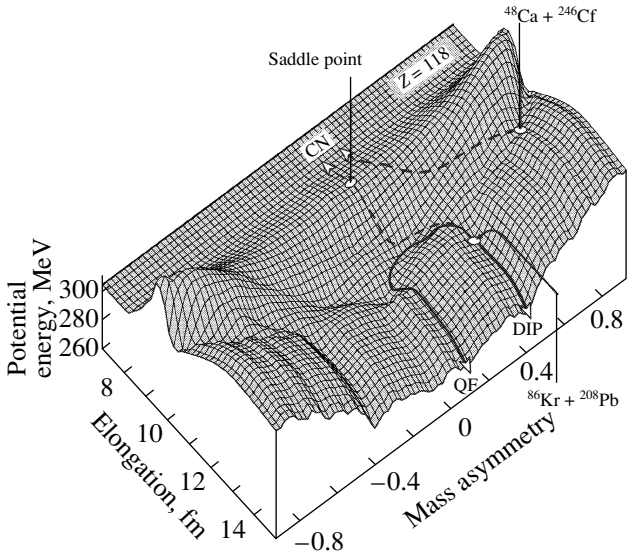

Fig. 7. Fusion–fission driving potential for the nucleus $^{294}118$ formed in the $^{86}Kr + ^{208}Pb$ and $^{48}Ca + ^{246}Cf$ fusion reactions.

intermediate minima correspond to the shape isomer states. From our analysis, we may definitely conclude that these isomeric states are nothing else but two-cluster configurations with magic or semimagic cores (see Fig. 3*b*).

As regards the superheavy compound nucleus formation in the fusion reaction $^{48}Ca + ^{248}Cm$, one can see that, after the contact, the nuclear system may easily decay into the quasifission channels (mainly asymmetric: Se + Pb, Kr + Hg; also near-symmetric: Sn + Dy, Te + Gd)—solid arrow lines in Figs. 3*b* and 4. Only a small part of the incoming flux reaches a CN configuration (dashed-arrow line). An experimental two-dimensional total kinetic energy (TKE) mass plot for the $^{48}Ca + ^{248}Cm$ fusion–fission reaction [3] is shown in Fig. 5. The experimental data are quite understandable qualitatively in terms of multidimensional potential energy surface shown in Figs. 3 and 4.

Using the driving potential $V_{\text{fus–fis}}(Z_1, N_1, Z_2, N_2, \delta_1, \delta_2)$, we may determine the probability of CN formation $P_{CN}(A_1 + A_2 \rightarrow C)$, being part of expression (1.1) for the cross section of the synthesis of superheavy nuclei. It can be done, for example, by solving the master equation [14] for the distribution function $F(Z_1, N_1, Z_2, N_2, \delta_1, \delta_2; t)$. The probability of CN formation is determined as an integral of the distribution function over the region $R_1 + R_2 \leq R_{CN}$. Similarly, one can define the probabilities of finding the system in different channels of quasifission, i.e., the charge and mass distribution of fission fragments measured experimentally.

Results of such calculations performed with a restricted number of variables are shown in Fig. 6. For the "hot" fusion reactions, based on using ^{48}Ca as a projectile, the probability of CN formation at first falls very sharply with increasing Z_{CN}, but then it remains at the level of 10^{-3} for $Z_{CN} = 114–118$ at excitation energies $E^* \geq 30$ MeV. Such behavior of P_{CN} reflects the fact of insignificant changes of $V_{\text{fus–fis}}$ for all these reactions. In contrast with that, for the "cold" fusion reactions, based on using ^{208}Pb as a target, the probability of CN formation decreases very fast with increasing Z_{CN} (see dashed curves in Fig. 6*a*). A qualitative explanation of that can be made again in terms of potential energy surface. In Fig. 7, the driving potential is shown for the synthesis of nucleus $^{294}118$ in the "cold" fusion reaction $^{86}Kr + ^{208}Pb$. Due

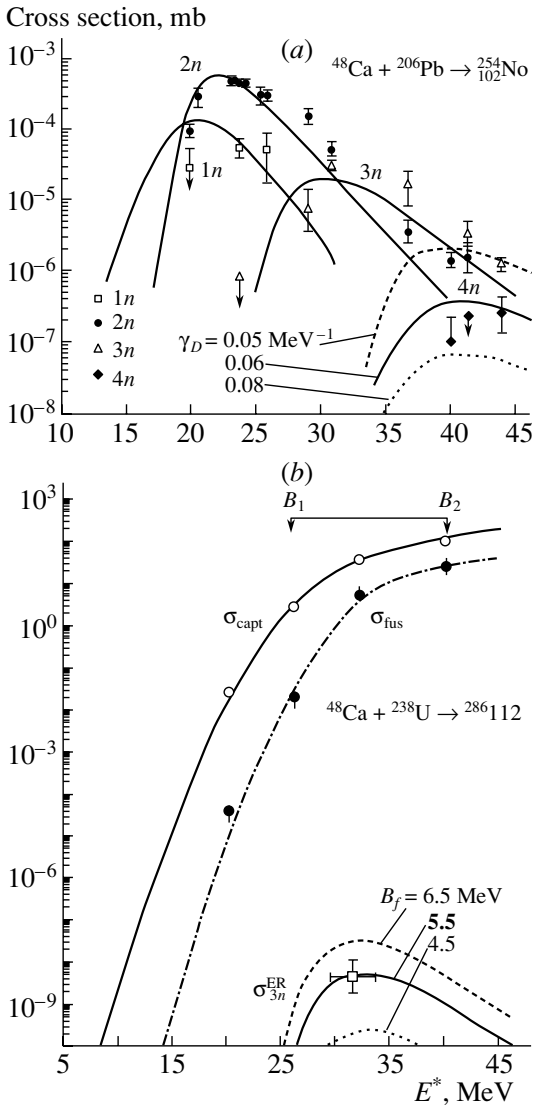

Fig. 8. (*a*) Cross sections of the evaporation residue production for different xn channels in the ^{48}Ca+^{206}Pb fusion reaction. The experimental data are from [17]. The solid curves correspond to the calculations with the damping factor $\gamma_D = 0.06$ MeV^{-1}, whereas the dashed and dotted curves for the $4n$ channel are calculated with $\gamma_D = 0.05$ and 0.08 MeV^{-1}, respectively. (*b*) The capture cross section (all fission fragments, open circles), the total yield of near-symmetric fission fragments with $A = A_{CN}/2 \pm 20$ (solid circles), and the evaporation residue production cross section in the $3n$ channel of the ^{48}Ca + ^{238}U reaction. The arrows show the Coulomb barriers for two ultimate orientations of the deformed target nucleus. The cross section of evaporation residue formation was calculated with a fission barrier of 4.5 (dotted curve), 5.5 (solid curve), and 6.5 MeV (dashed curve).

to dynamic deformation of both nuclei, the potential energy at the point of contact is even lower than the energy of the CN ground state. The nuclear system has to evolve upward on the potential energy surface to reach the CN configuration. It is possible only at sufficiently high excitation energy. Disappearance of the locked Coulomb barrier makes the system unstable against reseparation into the deep-inelastic and quasielastic channels, which have to dominate in this reaction at low energies. In contrast with that, in more asymmetric case of ^{48}Ca + ^{246}Cf fusion reaction leading to the same CN, the potential energy at the point of contact is above the ground state of the CN, and the nuclear system evolves down along the potential energy surface. Of course, the main flux goes to the quasifission valley (Kr + Pb), but nevertheless a small part of it reaches the CN configuration (dashed line in Fig. 7).

Exploration of the multidimensional fusion–fission driving potential itself and of the corresponding evolution of a heavy-nuclear system along its surface is a very promising and fruitful experimental problem. For that purpose, one may perform, for example, fusion–fission and ER measurements on formation of the same easily fissile ^{224}U nucleus in different projectile–target combinations: ^{20}Ne + ^{204}Pb (very asymmetric, behind the Businaro–Gallone barrier), ^{64}Ni + ^{160}Gd (less asymmetric, in front of the Businaro–Gallone barrier), ^{88}Sr + ^{136}Xe and ^{100}Mo + ^{124}Sn (symmetric, inverse to fission process), ^{86}Kr + ^{138}Ba (closed shell nuclei, suppressed deep-inelastic channels), and ^{76}Ge + ^{148}Nd (deformed, dependence on orientation).

4. FISSION BARRIERS OF SUPERHEAVY NUCLEI

The survival probability $P_{xn}(l, E^*)$ of a cooling excited compound nucleus can be calculated within a statistical model [6, 15]. The most uncertain parameter here is the fission barrier. For nuclei with $Z > 100$, which cannot be used as a target material, experimental measurement of the fission barriers is not possible. Calculating the fission barrier for the atomic nucleus (mainly its microscopic component) is also a very complicated puzzle faced with the necessity of solving a many-body quantum problem. The exact solution to that problem is currently unobtainable, and the accuracy of the approximations in use is rather difficult to estimate. As a result, the fission barriers for superheavy nuclei calculated within the different approaches differ greatly (by several megaelectronvolts). Any experimental information on the fission barriers of those nuclei seems to be highly valuable.

An important property of the fission barrier is that it has a pronounced effect on the survival probability of an excited nucleus in its cooling by emitting neutrons and γ rays in competition with fission. It

is this property that may be taken advantage of to make an estimate of the fission barrier of a superheavy nucleus if it is impossible to measure the fission barrier directly. Higher sensitivity may be obtained if such competition is tested several times during the evaporation cascade ("hot" fusion reactions). In this case, the cross section $\sigma_{\mathrm{ER}}^{xn}(E)$, which is proportional roughly to $(\Gamma_n/\Gamma_f)^x$, happens to be more sensitive to the value of the fission barrier since it increases in importance by a factor of x. For the experimental value of the survival probability of the superheavy nucleus to be deduced, it is necessary to measure the cross section of weakly excited CN production in the near-barrier fusion of heavy ions as well as the cross section for the yield of a heavy evaporation residue. It was experiments of this kind that were carried out at FLNR (JINR, Dubna) recently [1–3] as part of a series of experiments on the production of nuclei with $Z = 112$, 114, and 116 formed in the $3n$ and $4n$ evaporation channels.

The fission barriers are usually calculated according to the formula $B_f(J=0) = B_{\mathrm{LD}} - \delta W e^{-\gamma_D E^*}$, where B_{LD} is the liquid-drop fission barrier [16], which is negligibly small for nuclei with $Z > 112$; δW is the shell correction for the ground-state energy; and γ_D is the damping parameter, which accounts for the fact that shell effects fall off as the excitation energy of the CN increases. The value of this parameter is especially important in the case of superheavy nuclei, whose fission barriers are mainly determined just by the shell corrections for their ground states. In the literature, one can find close but slightly different values for the damping parameter, and we paid special attention to the sensitivity of the calculated cross sections to this parameter. Figure 8*a* shows how much the cross section for the $4n$ channel is sensitive to a change in the damping parameter. Simultaneous analysis of a great number of "hot" fusion reactions used for producing heavy elements allows the conclusion that the value of this parameter lies in the range $\gamma_D^{-1} = 14$–18 MeV.

After calculating the value of $P_{\mathrm{cont}}(E, l)$ in such a way as for the measured capture cross section to be reproduced and parametrizing the CN production probability P_{CN} in such a way as for $\sigma_{\mathrm{CN}}^{\mathrm{exp}}$ to be reproduced, fission barriers for the nuclei of the evaporation cascade can be chosen in such a way as for the corresponding measured cross section of the yield of a heavy evaporation residue nucleus to be reproduced with the help of (1.1). The calculated results are shown in Fig. 8 for the case of the $^{48}\mathrm{Ca} + {}^{238}\mathrm{U} \to {}^{286}112$ fusion reaction. Taking account of the fact that fission barriers vary not so much from nucleus to nucleus in an evaporation cascade, as well as making the procedure for assessing them simpler, the same value B_f was used for these nuclei. The typical sensitivity of the calculated production cross section for the ER to a change in the value of the fission barrier is shown in Fig. 8. It is the fact that this sensitivity is high which allows one to expect the value of the fission barrier to be deduced to an accuracy of the order of ± 0.5 MeV with allowance made for the experimental error in measuring this cross section and the uncertainty of some parameters used in the calculations [6]. Since, as discussed above in Section 3, the production probability for a true compound nucleus may really be less than the value of $\sigma_{\mathrm{CN}}^{\mathrm{exp}}/\sigma_{\mathrm{capt}}^{\mathrm{exp}}$, then comparing the measured and calculated cross sections for the evaporation residues allows one to deduce in fact the lower limits for the fission barriers of the corresponding nuclei. Final results are presented in the table.

The lower limits of the heights of fission barriers

Nucleus	E^*, MeV	σ_{capt}, mb	σ_{fus}, mb	σ_{ER}, pb	$\langle B_f \rangle$, MeV
$^{286}112$	31.5	40	≤ 5	$5.0^{+6.3}_{-3.2}$ $(3n)$	≥ 5.5
$^{292}114$	36.5	30	≤ 4	$0.5^{+0.8}_{-0.3}$ $(4n)$	≥ 6.7
$^{296}116$	34.8	30	≤ 2	$0.5^{+0.8}_{-0.3}$ $(4n)$	≥ 6.4

The analysis of the available experimental data on the fusion and fission of the nuclei of $^{286}112$, $^{292}114$, and $^{296}116$ produced in the reactions $^{48}\mathrm{Ca} + {}^{238}\mathrm{U}$, $^{48}\mathrm{Ca} + {}^{244}\mathrm{Pu}$, and $^{48}\mathrm{Ca} + {}^{248}\mathrm{Cm}$ [3], as well as experimental data on the survival probability of those nuclei in evaporation channels of three- and four-neutron emission [1, 2], enables the quite reliable conclusion that the fission barriers of those nuclei are really quite high, which results in their relatively high stability. The lower limits that we have obtained for the fission barriers of nuclei of $^{283-286}112$, $^{288-292}114$, and $^{292-296}116$ are 5.5, 6.7, and 6.4 MeV, respectively [18].

5. CROSS SECTIONS OF SUPERHEAVY-ELEMENT PRODUCTION

Calculating the capture cross sections and the probability for CN formation as described above and using the fission barriers based on the ground-state shell corrections of Möller *et al.* [19], we estimated the cross sections of superheavy element formation in the "hot" and "cold" fusion reactions leading to heavy nuclei with $Z_{\mathrm{CN}} \geq 102$ (Fig. 9). The cross sections for formation of superheavy nuclei with $Z = 114$–118 in the $3n$ and $4n$ evaporation channels of the "hot"

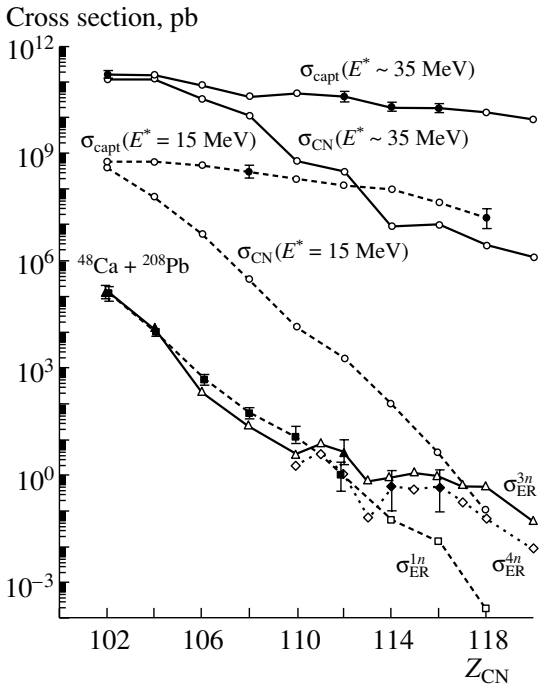

Fig. 9. Capture, fusion, and evaporation residue formation cross sections. For "hot" fusion reactions, the triangles show maximal values of σ_{ER} in the $3n$ evaporation channel, and the diamonds correspond to the $4n$ evaporation channel. Evaporation residue cross sections for the "cold" fusion reactions ($1n$ evaporation channel) are shown by squares. The closed symbols correspond to the experimental values, whereas the open ones correspond to the calculated cross sections. For the "hot" fusion reactions the following projectile–target combinations are used: ^{48}Ca + ^{208}Pb, ^{12}C + ^{249}Cf, ^{18}O + ^{249}Cf, ^{26}Mg + ^{248}Cm; for $110 \le Z_{CN} \le 118$, ^{48}Ca is used as a projectile and ^{232}Th, ^{231}Pa, ^{238}U, ^{237}Np, ^{244}Pu, ^{243}Am, ^{248}Cm, ^{247}Bk, and ^{249}Cf are the targets. The last combination leading to $Z_{CN} = 120$ is ^{58}Fe + ^{244}Pu. For the "cold" fusion reactions, ^{208}Pb is used as a target and the projectiles are the heaviest isotopes of the corresponding stable nuclei (from ^{48}Ca to ^{86}Kr).

fusion reactions were found to be at the level of 0.1–1.0 pb. For the available experimentally "cold" fusion reactions, the cross sections for formation of the same elements in the $1n$ evaporation channel are much lower. A gain of about three orders of magnitude in the survival probability, $P_{1n}(E^* \approx 15\ \text{MeV})/P_{3n}(E^* \approx 35\ \text{MeV}) \approx 10^3$, is compensated here by a loss of two orders of magnitude in the capture cross sections and more than two orders of magnitude in the probability of CN formation.

6. CONCLUSION

From the analysis of the multidimensional fusion–fission driving potential, we may conclude that, in the fission process, a weakly excited heavy nucleus on its way from the ground state to the scission point passes through the optimal configurations with minimal potential energies (shape isomer states), which are nothing else but the two-cluster configurations with magic (closed shell) cores. Analysis of the experimental data on the fusion and fission of the nuclei of ^{286}112, ^{292}114, and ^{296}116, as well as experimental data on the survival probability of those nuclei in evaporation channels of three- and four-neutron emission, enables us to make the quite reliable conclusion that the fission barriers of those nuclei are really quite high, which results in their relatively high stability. The lower limits that we have obtained for the fission barrier heights of $^{283-286}$112, $^{288-292}$114, and $^{292-296}$116 nuclei are 5.5, 6.7, and 6.4 MeV, respectively. This makes the synthesis of superheavy nuclei with $112 \le Z \le 120$ in asymmetric fusion reactions experimentally attainable (see Fig. 9). The choice of appropriate projectile–target combination is very important here. For example, using the fission barriers predicted in [19], we found that the ER cross section for production of element 116 in the $3n$ evaporation channel of the ^{48}Ca + ^{247}Cm fusion reaction should be about 1.5 pb at 35 MeV of initial excitation energy of the CN. That is due to more favorable evaporation of two odd neutrons with lower separation energies compared with a synthesis of the same element in the ^{48}Ca + ^{248}Cm reaction.

ACKNOWLEDGMENTS

The work was supported by INTAS, grant no. 00-655.

REFERENCES

1. Yu.Ts. Oganessian, A. V. Yeremin, A. G. Popeko, *et al.*, Nature **400**, 242 (1999).
2. Yu. Ts. Oganessian, V. K. Utyonkov, Yu. V. Lobanov, *et al.*, Yad. Fiz. **63**, 1769 (2000) [Phys. At. Nucl. **63**, 1679 (2000)].
3. M. G. Itkis, Yu. Ts. Oganessian, A. A. Bogatchev, *et al.*, in *Proceedings of the International Workshop on Fusion Dynamics at the Extremes, Dubna, 2000,* Ed. by Yu. Ts. Oganessian and V. I. Zagrebaev (World Sci., Singapore, 2001), p. 93.
4. R. Bass, *Nuclear Reactions with Heavy Ions* (Springer-Verlag, Berlin, 1980), p. 326.
5. V. I. Zagrebaev, Phys.Rev. C **64**, 034606 (2001).
6. V. I. Zagrebaev, Y. Aritomo, M. G. Itkis, *et al.*, Phys. Rev. C **65**, 014607 (2002).
7. N. Rowley, G. R. Satchler, and P. H. Stelson, Phys. Lett. B **254**, 25 (1991).
8. D. L. Hill and J. A. Wheeler, Phys. Rev. **89**, 1102 (1953).
9. C. R. Morton, D. J. Hinde, J. R. Leigh, *et al.*, Phys. Rev. C **52**, 243 (1995).

10. M. G. Itkis, Yu. Ts. Oganessian, E. M. Kozulin, *et al.*, Nuovo Cimento A **111**, 783 (1998).
11. V. I. Zagrebaev, J. Nucl. Radiochem. Sci. **3**, 13 (2002).
12. U. Mosel, J. Maruhn, and W. Greiner, Phys. Lett. B **34B**, 587 (1971); J. Maruhn and W. Greiner, Z. Phys. **251**, 431 (1972).
13. A. Goverdovski, private communication.
14. L. G. Moretto and J. S. Sventek, Phys. Lett. B **58B**, 26 (1975).
15. A. V. Ignatyuk, *Statistical Properties of Excited Atomic Nuclei* (Energoatomizdat, Moscow, 1983).
16. W. D. Myers and W. J. Swiatecki, Ark. Fys. **36**, 343 (1967).
17. Yu.Ts. Oganessian, V. K. Utyonkov, Yu. V. Lobanov, *et al.*, Phys. Rev. C **64**, 054606 (2001).
18. M. G. Itkis, Yu. Ts. Oganessian, and V. I. Zagrebaev, Phys. Rev. C **65**, 044602 (2002).
19. P. Möller, J. R. Nix, W. D. Myers, and W. J. Swiatecki, At. Data Nucl. Data Tables **59**, 185 (1995).

Physics of Atomic Nuclei, Vol. 66, No. 6, 2003, pp. 1042–1052. From Yadernaya Fizika, Vol. 66, No. 6, 2003, pp. 1078–1088.

The Upgrade of the Kinematic Separator VASSILISSA—Experimental Results and Plans*

A. V. Yeremin[1)], A. V. Belozerov[1)], M. L. Chelnokov[1)], V. I. Chepigin[1)], V. A. Gorshkov[1)], A. P. Kabachenko[1)], O. N. Malyshev[1)], Yu. Ts. Oganessian[1)], A. G. Popeko[1)], R. N. Sagaidak[1)], A. I. Svirikhin[1)], S. Hofmann[2)], G. Berek[3)], I. Brida[3)], and S. Saro[3)]**

[1)] *Flerov Laboratory of Nuclear Reactions, Joint Institute for Nuclear Research, Dubna, Russia*

[2)] *Gesellschaft für Schwerionenforschung, Darmstadt, Germany*

[3)] *Department of Physics, Comenius University, Bratislava, Slovakia*

Received September 12, 2002

Abstract—Within the past twelve years, the recoil separator VASSILISSA has been used for the investigations of evaporation residues produced in heavy-ion-induced complete fusion reactions. In the course of the experimental work, fourteen new isotopes have been identified by the parent–daughter correlations in the region of elements with $92 \leq Z \leq 94$. The study of the decay properties and formation cross sections of the isotopes of elements 110, 112, and 114 was performed using high-intensity ^{48}Ca beams and ^{232}Th, ^{238}U, and ^{242}Pu targets. At the beam energies corresponding to the calculated cross-section maxima of the $3n$ evaporation channels, the isotopes ^{277}110, ^{283}112, and ^{287}114 were produced and identified. For further experiments aimed at the synthesis of the superheavy element isotopes ($Z \geq 110$) with the use of intensive ^{48}Ca extracted beams, improvements in the ion optical system of the separator and the focal plane detector system have been made. © *2003 MAIK "Nauka/Interperiodica".*

1. INTRODUCTION

In the synthesis of transfermium nuclei using heavy-ion fusion reactions, two parameters play the limiting role: decay properties of nuclei to be investigated and their formation cross sections. Modern experimental setups, so-called recoil separators, could be used for the synthesis of heavy nuclei having half-lives of more than 1 μs and less than tens of minutes. The limit of the formation cross section that could be reached in experiments lasting 3–4 months is about 0.2–0.5 pb. In the course of planning new experiments, one should have a possibility of predicting decay properties (decay mode and half-life) as well as formation cross section of heavy nuclei with maximal accuracy.

The decay properties of heavy nuclei strongly depend on the shell structure effects. These stabilizing effects manifest themselves significantly in closed proton and neutron shells. Beyond uranium, the stability of nuclei decrease rapidly with increasing element number Z. According to the macroscopic–microscopic theory, the next spherical shell closure for neutrons beyond $N = 126$ is predicted at $N = 184$. The stability of the superheavy nuclei could increase sharply when their neutron number approaches this spherical shell closure [1–3]. Due to the spherical ground-state and strong ground-state shell-correction energy, the fission barrier is wider and higher than that for deformed nuclei, which is the reason for the expected increased stability against spontaneous fission (SF). For the synthesis of spherical superheavy nuclides, it is of importance to select reaction partners with the highest possible number of neutrons in order to approach the shell $N = 184$ as close as possible [4]. For these reasons, the projectile ^{48}Ca is of special interest in the production of the heaviest elements. Due to its neutron excess, it allows access to compound nuclei that are closer to the predicted magic neutron numbers 178–184. Its doubly magic structure allows synthesizing relatively cold compound nuclei at energies close to the fusion barrier. Also, the ^{48}Ca shell structure could reduce the fusion hindrance, observed for symmetric reactions leading to heavy elements.

A method for the investigation of consistent α decays, the so-called α–α correlation analysis, has long been employed for the identification of new radionuclides. It has already been used in the works to discover and study the decay properties of elements from 102 (α-recoil milking experiments [5])

*This article was submitted by the authors in English.

**e-mail: eremin@sunvas.jinr.ru

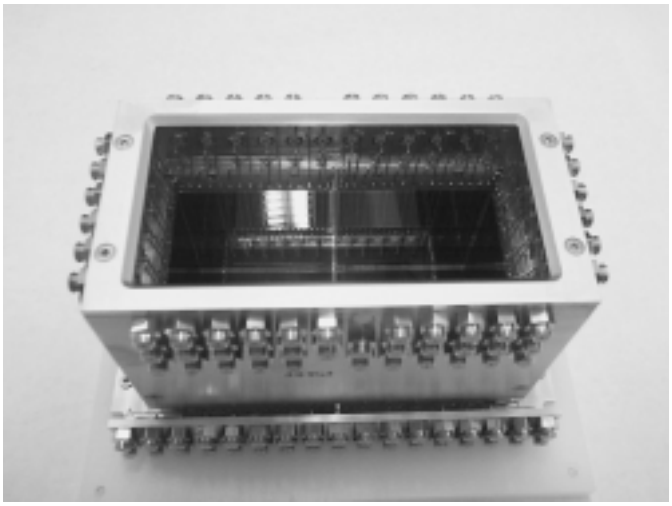

Fig. 1. The new focal plane detector system.

to 105 (delayed α-correlation method [6, 7]). Later, this method was developed and successfully used for the identification and study of decay properties of elements 107–112 with a modern experimental setup and detection module (position sensitive detectors array) [8]. This method is based on the fact that a decay chain starting from an unknown isotope should be ended in the known region of isotopes with known decay properties. If the statistics allow one to be sure that no members in the decay chains were missed, it is possible, starting from the known nuclei, to go back to the beginning of the chain and to make an assignment of what isotope of what element was synthesized.

In the case when the neutron-rich isotope ^{48}Ca is used as a bombarding beam, we have found ourselves in a completely unknown region where all decay chains are started and finished with isotopes having unknown decay properties. According to the calculations [2, 3], the decay chains starting from neutron-rich ($N = 171$–175) isotopes of elements 112–114 after a few α decays should be terminated by SF in the region of elements 104–110. As a first step in an attempt to solve the problem with the newly synthesized isotope identification, we plan a number of experiments, each experiment being a basis for the following one. One of the possibilities was to use targets that differ by an α particle. It means that the isotopes which can be produced in a subsequent experiment should decay to the isotopes which were obtained in the previous experiments. These two-step experiments could be the following ones: $^{48}\mathrm{Ca} + {}^{232}\mathrm{Th} \rightarrow {}^{280}110^*$ and $^{48}\mathrm{Ca} + {}^{236}\mathrm{U} \rightarrow {}^{284}112^*$, $^{48}\mathrm{Ca} + {}^{238}\mathrm{U} \rightarrow {}^{286}112^*$ and $^{48}\mathrm{Ca} + {}^{242}\mathrm{Pu} \rightarrow {}^{290}114^*$, $^{48}\mathrm{Ca} + {}^{244}\mathrm{Pu} \rightarrow {}^{292}114^*$ and $^{48}\mathrm{Ca} + {}^{248}\mathrm{Cm} \rightarrow {}^{296}116^*$.

An additional (in some cases perhaps the main) possibility of distinguishing the isotopes produced in complete fusion reactions from multinucleon transfer reaction products and identifying new nuclides is a method of measuring the atomic mass number of the evaporation residues (ERs), synthesized during the experiment. If the mass resolution of the experimental setup reaches a value of less than 0.5% (for the heavy nuclei with masses in the region of 270–290 amu), one can make a direct identification of the obtained isotope on the basis of its mass measurement. But such a mass resolution can be realized with rather big magnetic systems having deflection angles of $\geq 90°$. Another possibility is the use of simpler and more compact systems that allow one to have the mass resolution at the level of 1.5–3%. For the mass region 270–290 amu, it leads to an accuracy of 3–6 amu. In this case, one can establish the belonging of the newly synthesized nuclide to the region of superheavy nuclei formed from the compound nuclei as a result of a complete fusion reaction between the heavy ion and the target nucleus.

For further experiments aimed at the synthesis of the superheavy element isotopes ($Z \geq 110$) using intensive ^{48}Ca extracted beams, improvements in the ion optical system of the separator and the focal plane detector system have been made.

2. EXPERIMENTAL SETUP

Aiming at the continuation of the experiments on the synthesis and study of decay properties of superheavy nuclei, the separator VASSILISSA [9, 10] was upgraded. For that purpose a new dipole magnet, having a deflection angle of 37°, was installed behind the separator VASSILISSA replacing the old

8° magnet. The new magnet provides an additional suppression of unwanted reaction products by a factor of about 100 and a possibility of having the mass resolution at the level of 1.5–2% for heavy nuclei with masses of about 300 amu. Its bending radius is 1.08 m, the effective length is 69.8 cm, and the vertical gap is 114 mm. The entrance and exit boundaries of the magnetic dipole have the values of 46° and −43°, respectively. To reduce chromatic abberations, the entrance and exit boundaries of the pole have a radius curvature of +0.5 m and −0.5 m.

For the detection of heavy ERs at the focal plane of the new dipole magnet, a new detector system having a 32-strip detector assembly 60 × 120 mm in size and surrounded by backward detectors was also developed (see Fig. 1). It is planned to retain the old detector system [10] including the 8° dipole magnet behind new the 37° magnet, thus organizing a second detection area. Due to the compact configuration of this detector system, it is possible to surround it by ^{3}He counters, thus creating a neutron detector with a high (about 50%) detection efficiency. For this purpose, it will be necessary to build around the detector chamber an array with 200 ^{3}He counters.

Calculations show that the separator has a focal plane inclination of ≈ 24°, the mass (energy) dispersion $D_x = 3.9$ mm/%, and the horizontal magnification $M_x = 1$. Measurements showed good stability (∼ 0.1%) of the effective length of the dipole up to the magnitude of the magnetic field $H = 1.15$ T. The results of the tests with a ^{226}Ra α source showed that the energy dispersion of the new magnet was about 3.8 mm/% and the resolution was about 2%.

3. EXPERIMENT

Within the experimental program of separator VASSILISSA, "hot" fusion reactions leading to compound nuclei with atomic numbers $Z \geq 83$ were intensively studied. In particular, more than 30 heavy-ion–target-nucleus combinations were studied starting from ^{40}Ca + ^{151}Eu → ^{191}Bi* and finishing at ^{26}Mg + ^{208}Pb → ^{234}Pu* for $83 \leq Z \leq 94$ (see Table 1).

Complete fusion reactions with heavy ions studied with the VASSILISSA separator and leading to compound nuclei with atomic numbers $Z \geq 100$ are listed in Table 2.

Excitation functions of the xn ($1 \leq x \leq 12$) evaporation channels were measured for a number of reactions yielding compound nuclei with $Z \geq 83$ in an excitation energy range 20–140 MeV. Figure 2 shows measured formation cross sections obtained for the same ERs but formed after the evaporation of a different number of neutrons. Those cross sections corresponding to the maxima of the excitation curves were derived from the data presented in Tables 1 and 2. An analysis of the xn reactions with $x \geq 4$ reveals that the maximum formation cross sections for the ERs formed after the evaporation of $x + 2$ and x neutrons (in the case of the ^{189}Bi ER, $x + 6$ and x neutrons) remain almost constant in the whole range of isotope mass numbers and in a broad range of the compound nucleus excitation energy. This inference is valid in a broad range of the maximal cross sections (one can see from Fig. 2 that, at the transition from ^{200}At to ^{246}Fm, the cross section decreases by the factor of $\sim 10^8$). This implies a small value of the partial fission width Γ_f, independent of the excitation energy, at the initial steps of the deexcitation cascade.

It follows from the above considerations that, for the compound nuclei in the excitation energy range of 40–120 MeV, the fission time is longer than the neutron evaporation time by about one order of magnitude and reaches $(3–5) \times 10^{-20}$ s [11, 12]. The obtained large value of $\Gamma_n/\Gamma_{\text{tot}}$ for the initial stages of the compound-nucleus evaporation cascade shows a small contribution of fission in the decay of heavy compound nuclei at the excitation energy of 40–120 MeV.

The cross-section trends of the $1n$ ("cold" fusion, $E^* \leq 15$ MeV), $3n$ ("warm" fusion, $E^* \approx 30$ MeV), and $4n$ and $5n$ ("hot" fusion, $E^* \geq 40$ MeV) are plotted in Fig. 3. To guide the eye, three solid lines corresponding to the three fusion reaction types are drawn though the data. In the case of the "hot" fusion reactions, the formation cross sections are lower by no more than one order of magnitude in spite of the higher excitation energy of compound nuclei because of the low fission probability at the initial stages of the deexcitation process. Extrapolation of the lines into the region of heavier elements results in cross sections of about 0.1 pb for the synthesis of elements 112, 114, and 116 using those three fusion reaction types, respectively. Higher cross sections could be expected if the trend of the data in increasing the cross sections with increasing the isospin $T_z = (N - Z)/2$ of the incident particle will continue. This effect was proved with the use of ^{20,22}Ne and ^{24,26}Mg bombarding particles (see Table 1) and in the production of element 110 using the projectiles ^{62,64}Ni [8]. Typically, for the "hot" fusion reactions, the incident particles with $T_z = 1, 2$ are used; for the "cold" fusion reactions, those with $T_z = 3, 4$; and for "warm" fusion reactions, those with $T_z = 4$. But the systematics of the increasing cross sections with increasing isospin T_z of bombarding particle was not confirmed in the synthesis of element 112 using the $T_z = 5$ ^{70}Zn projectile (no enhancement in the cross section). The cross section trend is changed in the synthesis of

Table 1. List of complete fusion reactions with heavy ions studied with the separator VASSILISSA and leading to the compound nuclei with atomic numbers $83 \leq Z \leq 94$

Reaction	CN	$\sigma_{\max}$									
		$3n$	$4n$	$5n$	$6n$	$7n$	$8n$	$9n$	$10n$	$11n$	$12n$
$^{40}Ca + ^{151}Eu$	^{191}Bi	2.6 μb	0.9 μb								
$^{40}Ca + ^{153}Eu$	^{193}Bi	23 μb	30 μb	8 μb							
$^{40}Ar + ^{159}Tb$	^{199}Bi		16 mb	6 mb	4.25 mb	0.68 mb	320 μb	40 μb	9.5 μb		
$^{31}P + ^{169}Tm$	^{200}Po	1.04 mb	4.51 mb	2.63 mb	146 μb	10 μb	5 μb				
$^{27}Al + ^{175}Lu$	^{202}Po	2.2 mb	17 mb	30 mb	8.4 mb	1.6 mb	0.22 mb	2.5 μb	0.4 μb		
$^{40}Ca + ^{159}Tb$	^{199}At	3.6 μb									
$^{40}Ar + ^{165}Ho$	^{205}At			11.5 mb	2 mb	400 μb	35 μb	3.5 μb			
$^{24}Mg + ^{181}Ta$	^{205}At			30 mb	4.5 mb	850 μb	54 μb				
$^{26}Mg + ^{181}Ta$	^{207}At		14 mb	40 mb	20 mb	8 mb					
$^{22}Ne + ^{190}Os$	^{212}Rn					27.7 mb	7.7 mb	3 mb	520 μb	58 μb	3.6 μb
$^{35}Cl + ^{175}Lu$	^{210}Ra			0.3 μb							
$^{31}P + ^{181}Ta$	^{212}Ra		43 μb	41 μb							
$^{22}Ne + ^{194}Pt$	^{216}Ra		11 mb*		3 mb*		90 μb*				
$^{22}Ne + ^{196}Pt$	^{218}Ra		5.05 mb	23.7 mb	18.1 mb*		1.9 mb*		56 μb		
$^{22}Ne + ^{198}Pt$	^{220}Ra			27.3 mb	35 mb	20.2 mb	10.5 mb*		1.07 mb*		0.04 mb*
$^{20}Ne + ^{197}Au$	^{217}Ac	145 μb	2520 μb*		240 μb*		2.6 μb*				
$^{22}Ne + ^{197}Au$	^{219}Ac		3 mb	6.5 mb	2 mb						
$^{48}Ca + ^{174}Yb$	^{222}Th	71 ± 28 μb	85 ± 40 μb	21 ± 9 μb	16 ± 6.5 μb						
$^{48}Ca + ^{176}Yb$	^{224}Th	198 ± 79 μb	806 ± 244 μb								
$^{16}O + ^{208}Pb$	^{224}Th	5208 ± 501 μb	$11\,900^{+9780}_{-3250}$ μb								
$^{24}Mg + ^{197}Au$	^{221}Pa	200 nb	910 nb	600 nb	130 nb						
$^{26}Mg + ^{197}Au$	^{223}Pa			2800 nb	1180 nb						
$^{22}Ne + ^{205}Tl$	^{227}Pa	42 μb	96 μb	57 μb	31 μb						
$^{40}Ar + ^{182}W$	^{222}U			$1^{+0.9}_{-0.6}$ nb							
$^{27}Al + ^{197}Au$	^{224}U			4.7 ± 1.9 nb	1.6 ± 1.1 nb						
$^{20}Ne + ^{208}Pb$	^{228}U		800 ± 400 nb	500 ± 300 nb							
$^{22}Ne + ^{208}Pb$	^{230}U		6 ± 2 μb	2.5 ± 1 μb							
$^{22}Ne + ^{209}Bi$	^{231}Np		300 ± 120 nb	70 ± 40 nb							
$^{24}Mg + ^{208}Pb$	^{232}Pu		4 ± 2 nb								
$^{26}Mg + ^{207}Pb$	^{233}Pu		30 ± 15 nb								
$^{26}Mg + ^{208}Pb$	^{234}Pu		100 ± 50 nb	17 ± 8 nb							

* Formation cross sections are presented as sums of the $(4–5)n$, $(6–7)n$, and $(8–9)n$ evaporation channels, respectively.

Table 2. List of complete fusion reactions with heavy ions studied with the separator VASSILISSA and leading to the compound nuclei with atomic numbers $Z \geq 100$

Reaction	CN	σ_{max}, nb							
		$1n$	$2n$	$3n$	$4n$	$5n$	$6n$	$7n$	$8n$
$^{20}Ne + ^{232}Th$	^{252}Fm					10 ± 3	6.0 ± 2.5		
$^{22}Ne + ^{232}Th$	^{254}Fm							15 ± 5	3 ± 1
$^{44}Ca + ^{208}Pb$	^{252}No		$0.85^{+0.35}_{-0.27}$	$0.17^{+0.22}_{-0.10}$					
$^{48}Ca + ^{204}Pb$	^{252}No		$5.2^{+0.93}_{-0.80}$	$1.36^{+0.53}_{-0.41}$					
$^{48}Ca + ^{206}Pb$	^{254}No	100	500	30	$0.2^{+0.2}_{-0.1}$				
$^{48}Ca + ^{208}Pb$	^{256}No	120	2×10^3	100	$2^{+1.0}_{-0.7}$				
$^{22}Ne + ^{236}U$	^{258}No				7 ± 4	25 ± 7	15 ± 5		
$^{26}Mg + ^{232}Th$	^{258}No				6 ± 2	9 ± 5	8 ± 3		
$^{22}Ne + ^{238}U$	^{260}No						15 ± 7		1.2 ± 0.8
$^{27}Al + ^{232}Th$	^{259}Lr					1.7 ± 0.5	1.3 ± 0.5		
$^{27}Al + ^{238}U$	^{263}Db					0.45 ± 0.20	$0.075^{+0.05}_{-0.06}$		
$^{31}P + ^{232}Th$	^{263}Db					0.12 ± 0.10			
$^{48}Ca + ^{232}Th$	$^{280}110$			$(2^{+4.6}_{-1.7}) \times 10^{-3}$ *					
$^{48}Ca + ^{239}U$	$^{286}112$			$(5^{+6.3}_{-3.2}) \times 10^{-3}$ *					
$^{48}Ca + ^{242}Pu$	$^{290}114$			$(2.5^{+3.3}_{-1.6}) \times 10^{-3}$ *					

* Measurements were performed at a fixed beam energy; therefore, the cross section could be measured not at the maximum of excitation function.

elements 112, 114, and 116 using the $T_z = 4$ ^{48}Ca projectile (upper line in Fig. 3). A possible explanation may reside in both strong shell effects at $N = 28$, $Z = 20$ for ^{48}Ca and $N \geq 170$, $Z = 112$–116 (isospin of ER's $T_z \approx 30$, in comparison with $T_z \approx 25$ in the cases of "hot" and "cold" fusion). The complete fusion reactions induced by ^{48}Ca projectiles seem to be a compromise between "hot" fusion reactions having higher fusion probability and "cold" fusion reactions having higher survival probability at the exit channel.

It is obvious now that formation cross sections of heavy evaporation residues produced in heavy-ion complete fusion reactions depend on the shell structure in both reaction partners (incident ion and target nucleus) and also in the final evaporation residue. The influence of closed neutron and proton shells in the entrance and exit channels of ER formation is obvious but not simple to understand. One of the best examples is a very large enhancement in ER formation cross sections in the case of two doubly magic reaction partners, i.e., ^{48}Ca and ^{208}Pb. A change or removal of a few nucleons in the bombarding ion or target nucleus leads to a decrease in the ER formation cross section by one to two orders of magnitude. The effect of the shell structure in reaction partners is demonstrated in Fig. 4. The data for ^{176}Yb, ^{208}Pb, ^{232}Th, ^{238}U, and ^{242}Pu are from [13–17] (VASSILISSA separator), for ^{248}Cm from [18], and for other targets from [19] (upper panel of Fig. 4). The data for ^{16}O, ^{22}Ne, ^{26}Mg, and ^{48}Ca are from [12, 14, 20, 21] (VASSILISSA separator), for ^{40}Ar from [22], and for other bombarding ions from [8] (lower panel of Fig. 4). One should keep in mind that, in Fig. 4, for every complete fusion reaction, the maximum cross sections were chosen among all the evaporation channels. The number of evaporated neutrons is indicated by symbols.

Comparison of excitation functions of the ERs measured for different mass-asymmetry reactions but leading to the same compound nucleus allows us to analyze how important the effect of the shell structure is in the incident particle and/or target nucleus in the

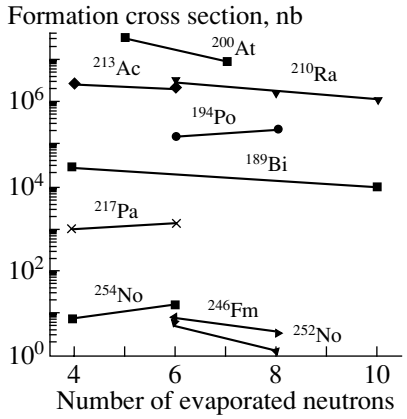

Fig. 2. Experimental cross sections for the same ERs formed after the evaporation of a different number of neutrons.

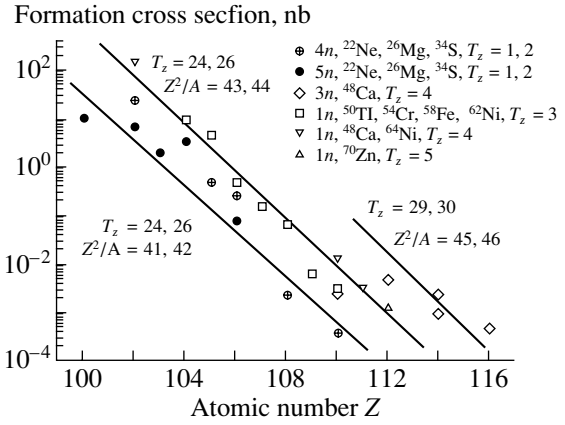

Fig. 3. Experimental cross sections for the ERs formed in "cold," "warm," and "hot" complete fusion reactions.

entrance channel of a fusion reaction with massive nuclei.

In the present work, we consider a set of experimental data on the production of ERs in the reactions ^{48}Ca + ^{204}Pb and ^{44}Ca + ^{208}Pb with different entrance channel asymmetries, but leading to the same compound nucleus ^{252}No*. The reactions ^{48}Ca + ^{206}Pb and ^{48}Ca + ^{208}Pb were used for testing the new detector system and calibrations using previously measured data. Experimental conditions are described in detail in [23].

4. RESULTS

4.1. Decay Properties of Neutron Deficient Isotopes ^{249,250}No

As was already mentioned, the targets ^{206,208}Pb were used to check the transmission of the separator and energy and position calibrations of the focal plane detector assembly. At the beam energy $E_{1/2} = 212.1 \pm 2$ MeV in the half-thickness of the ^{206}Pb target, more than one hundred SF events corresponding to the decay of ^{252}No were collected. The half-life measured from the ER–SF correlation analysis was $T_{1/2\,\mathrm{SF}} = 2.38^{+0.26}_{-0.22}$ s (compare 2.30 ± 0.22 s [24] and 2.44 ± 0.12 s [25]) and the SF branching ratio for ^{252}No was $\mathrm{BR_{SF}} = (32 \pm 3)\%$ (compare $(26.9 \pm 1.9)\%$ [24] and $(32.2 \pm 0.5)\%$ [25]). At the beam energy $E_{1/2} = 234.5 \pm 2$ MeV in the half-thickness of the ^{206}Pb target, two SF events with lifetimes of 8 and 9 μs were detected (time difference between ER implantation and SF decay). The half-life for the two events is $5.9^{+10.7}_{-2.3}$ μs and they can be attributed to the decay of ^{250}No formed in the $4n$ evaporation channel. Earlier, the half-life values of 250 ± 50 μs [26] and 36^{+11}_{-6} μs [25] were reported for the isotope ^{250}No.

The ^{204}Pb target was irradiated with ^{48}Ca at four beam energies $E_{1/2} = 219.4$, 225.6, 231.4, and 236.1 MeV. At the first three energies, a total of 72 SF events were detected. These events can be distributed into three groups according to their lifetimes (see Fig. 5). A fitting procedure with the use of the formalism from [27] yields three half-life values $T_{1/2} = 5.6^{+1.07}_{-0.79}$ μs (42 events), $54.2^{+14.7}_{-9.5}$ μs (22 events), and $2.4^{+1.1}_{-0.6}$ s (10 events).

Calculated α-decay properties of the ^{248}No and ^{250}No nuclei are $Q_\alpha = 9.28$ and 8.99 MeV and $T_\alpha = 21$ and 160 ms, respectively. These results were presented in [28]. As for $T_{1/2\,\mathrm{SF}}$, which is more probable for these nuclei, estimates made in a way described in [29] lead to values of about 0.5 and 15 μs, respectively [30].

The events with the half-life $T_{1/2\,\mathrm{SF}} = 2.4$ s could be attributed to the decay of ^{252}No, produced in the reaction of ^{48}Ca and ^{206}Pb contamination in the ^{204}Pb target. The events with the half-life $T_{1/2\,\mathrm{SF}} = 5.6$ μs (two events with the same half-life from the irradiation of the ^{206}Pb target at the highest beam energy should be added) could be attributed to the decay of ^{250}No, and the events with the half-life $T_{1/2\,\mathrm{SF}} = 54.2$ μs, to the decay of even–odd isotope ^{249}No.

No ER–α–α correlations corresponding to the decay of the ^{250}No isotope into the well-known ^{246}Fm and ^{242}Cf daughter nuclei nor for that of the ^{249}No isotope into the ^{245}Fm and ^{241}Cf daughter nuclei were detected. Proceeding from the nonobservation of such correlations, the upper limits for the α-branching ratio have been estimated as $\mathrm{BR}_\alpha < 10\%$ and $\mathrm{BR}_\alpha < 20\%$ for ^{250}No and ^{249}No, respectively.

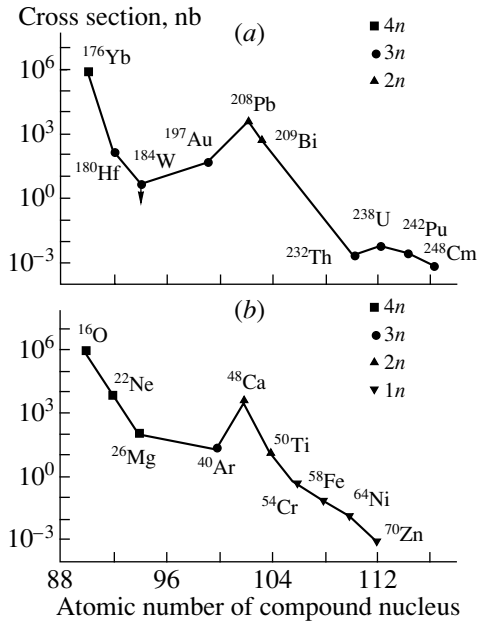

Fig. 4. (*a*) Experimental ER formation cross sections for the reactions with ^{48}Ca and different target nuclei. (*b*) Experimental ER formation cross sections for the reactions with the ^{208}Pb target and different bombarding ions.

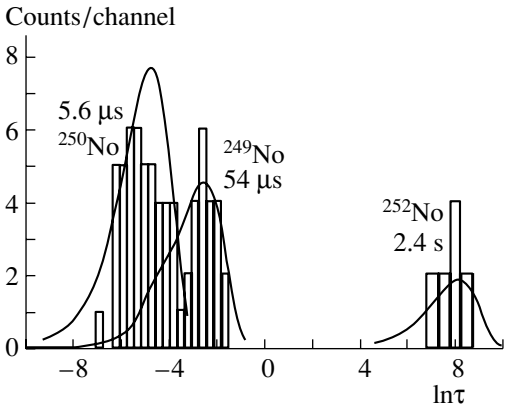

Fig. 5. Time distribution τ (in ms) of the ER–SF correlated events collected in the irradiations of ^{204}Pb target with ^{48}Ca ions.

At the highest beam energy $E_{\rm lab} = 236.1$ MeV, when ^{248}No could be observed as a result of the $4n$ evaporation, the integral flux of 7×10^{16} ions was collected and no SF events were detected. It corresponds to the upper limit of the production cross section of $\sim$ 0.2 nb (for nuclei with $T_{1/2} \geq 2$ μs). In the case of SF of nuclei ($T_{1/2} \leq 2$ μs) in flight through the separator, ERs will not reach the focal plane detectors and will be lost. If ERs undergo a fast α decay in flight, the probability that the daughter nucleus will reach the focal plane detector is decreased by a factor of 5–10 as compared with a nondecaying (relatively long-lived) nucleus. Daughter nucleus ^{244}Fm undergoes spontaneous fission with $T_{1/2} = 3$ ms. Taking into account the relatively low value of the cross section estimated for the $4n$ evaporation channel (see the next section) and the time of flight of ER through the separator, we estimate the upper limit for the half-life of ^{248}No as $T_{1/2} < 1$ μs. This result is in agreement with theoretical predictions.

Table 3. Decay properties of neutron deficient nobelium isotopes

Isotope	Number of events	$T_{1/2\ \rm SF}$, μs	BR$_\alpha$, %
^{250}No	56	$5.6^{+0.9}_{-0.7}$	$\leq$10
^{249}No	24	$54.0^{+13.9}_{-9.2}$	$\leq$20
^{248}No	–	$\leq$1.0	–

With the use of accelerated ^{44}Ca ions, a ^{208}Pb target was irradiated at three beam energies 216.9, 212.5, and 206.2 MeV, and a ^{206}Pb target was irradiated at the beam energy of 214.7 MeV. In the reaction ^{44}Ca+^{208}Pb, a total of 13 SF events were detected. These events can be distributed into two groups according to their lifetimes, with the half-life values equal to $T_{1/2} = 5.4^{+2.3}_{-1.25}$ μs (11 events) and $T_{1/2} = 48^{+87.4}_{-18.9}$ μs (68- and 71-μs lifetime). These values agree well with the data obtained for the reaction ^{48}Ca+^{204}Pb.

In reaction the ^{44}Ca+^{206}Pb at the beam energy $E_{1/2} = 214.7$ MeV, in which ^{248}No, the product of the $2n$ evaporation channel, could be observed, the integral flux of 1.3×10^{17} ions was collected and one SF event with the lifetime $\tau = 29$ μs was detected. This decay can be attributed to ^{250}No formed in the reaction of ^{44}Ca and ^{208}Pb contamination in the ^{206}Pb target. The upper limit of the cross section value for the production of ^{248}No is about 0.1 nb (if $T_{1/2} \geq$ 2 μs). This value is less than that estimated with the use of our data for the ^{208}Pb(^{44}Ca, $2n$) reaction. Thus, the upper limit for the half-life of ^{248}No, as in the previous case, does not exceed the value of 1 μs.

From the data collected in all the irradiations, the decay properties of the neutron deficient nobelium isotopes could be defined; these values are presented in Table 3.

An explanation of the difference in the results of our work and [25, 26] can lie in the long dead time that was present in the measurements in previous experiments. In [26], the complete fusion reaction ^{22}Ne + ^{233}U $\rightarrow$ ^{250}No + $5n$ was investigated; the

rotating wheel technique with mica detectors for SF events detection and time distribution analysis were used. The starting point of time measurements was 100 μs. In [25], the complete fusion reactions ^{48}Ca + ^{206}Pb $\rightarrow$ ^{250}No + $4n$ and ^{48}Ca + ^{204}Pb $\rightarrow$ ^{250}No + $2n$ were studied using the gas-filled recoil separator, ERs were implanted into the focal plane detector, and ER–SF correlations were analyzed. The dead time of the electronics used for ER–SF correlation measurements was about 80 μs.

4.2. Mass Estimates for the Observed SF Activities

We attempted to identify the observed SF activities more definitely using mass determination with the 37° dipole magnet. The basic relations for the mass determination are as follows: $B\rho \sim \sqrt{AE}/Q$ and $E \sim Av^2$, where $B\rho$, A, E, Q, and v are the magnetic rigidity, mass, energy, ion charge, and velocity of the detected ER. Combining these relations, one can get the expression for the mass determination: $A/Q = 9.6525B\rho\,[\mathrm{T\ m}]/v\,[\mathrm{cm/ns}]$. Thus, we have to measure the velocity or time of flight (TOF) and magnetic rigidity (position on the focal plane—strip number) for the implanted ER having the ion charge Q. In these coordinates ($B\rho$–TOF), different ion charge numbers of ER are well resolved.

An ability of the system to determine the masses was tested using ^{198}Po produced in the ^{164}Dy(^{40}Ar, $6n$) reaction and ^{246}Fm produced in the ^{208}Pb(^{40}Ar, $2n$) reaction. The data were collected, and after their sorting, the "magnetic rigidity (strip number)–TOF" for the implanted nuclei (based on their known decay properties) were derived. For ^{198}Po ($E_\alpha = 6.125$ MeV), we observed the charge states $Q = 16$–19 and determined the mass number as one close to 198. Comparing our production rate for ^{246}Fm ($E_\alpha = 8.24$ MeV) with that published earlier [22, 31, 32], we estimated the transmission for ER as $\simeq 20\%$, which is close to the calculated value [33]. The mass number was estimated as one close to 246.

A similar procedure was applied to the data collected in the Ca + Pb studies. Using ER–SF correlations, positions of the implanted ER and corresponding TOFs (attributed to a certain SF decay half-life) were extracted. The results are shown in Fig. 6 in the form of a number of counts corresponding to definite A/Q values for different ranges of time distributions for ER–SF correlations. For all the observed SF activities, a joint multi-Gaussian fit with the width parameter fixed (curves in the figure) allows us to obtain the most probable atomic mass values for the most probable charge states assumed for ER. These values correspond to our simulation based on the approximations describing the energy

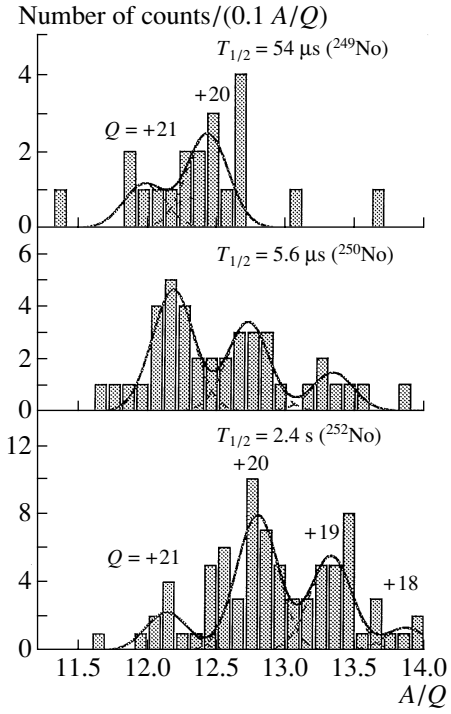

Fig. 6. A/Q distributions for the 5.6-μs, 54-μs, and 2.4-s SF activities observed in the ^{44,48}Ca+^{204,206}Pb reactions (histograms) and the results of a joint multi-Gaussian fit to the data (curves). Assumed charge states for ER are designated in the upper and bottom panels.

and charge distributions for ER [34, 35]. The results of the fit are shown in Table 4, where the atomic mass numbers corresponding to the assumed charge states of ER are given for the observed SF activities. The mean weighted values of the numbers are also given in Table 4.

Note that the offset in the charge states per one unit of charge to the higher and lower states leads to significant overestimates and underestimates, respectively, in the mass numbers within about ± 10 units. So, one can conclude that averaged masses of the observed SF activities are not far from masses of the compound nuclei formed in the corre-

Table 4. Atomic mass numbers of the SF activities observed in the ^{44,48}Ca + ^{204,206}Pb reactions

Charge state	^{249}No	^{250}No	^{252}No
18			249.6 ± 2.4
19		253.3 ± 1.8	253.1 ± 0.8
20	248.2 ± 1.5	254.3 ± 1.1	255.8 ± 0.7
21	251.0 ± 2.9	255.5 ± 0.9	254.9 ± 1.3
Averaged mass	248.8 ± 1.3	254.8 ± 0.7	254.5 ± 0.9

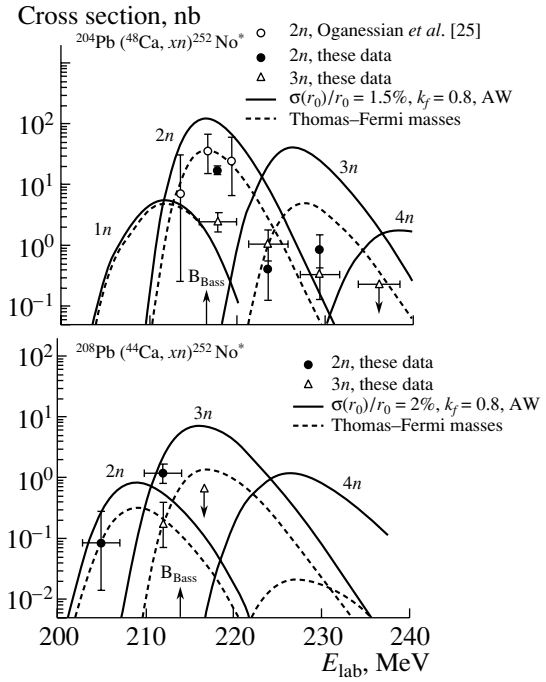

Fig. 7. Cross sections for the 5.6- and 54-μs SF activities produced in the ^{48}Ca + ^{204}Pb and ^{44}Ca + ^{208}Pb reactions leading to the same compound nuclei ^{252}No* and assigned to the 2n (●) and 3n (△) evaporation channels, respectively, in comparison with the calculated excitation functions [36] (curves) and data obtained recently for the 36-μs SF activity [25] (○).

sponding reactions and masses of nuclei produced in a few nucleon evaporation channels.

4.3. The ^{204}Pb(^{48}Ca, xn) and ^{208}Pb(^{44}Ca, xn) Excitation Functions

The obtained cross section data for the 5.6- and 54-μs SF activities are shown in Fig. 7. These activities were assigned to the 2n and 3n evaporation channels leading to ^{250}No and ^{249}No, respectively. In the estimates of the production cross section values, their time of flight through the separator was taken into account.

As can be seen in Fig. 7, the 5.6-μs SF activity corresponds quite satisfactorily to the calculated excitation function for the 2n evaporation channel of both reactions, whereas the energy dependence for the 54-μs SF activity seems to differ slightly from that for the 5.6-μs activity. It implies a possible SF from an isomeric state for one of them and SF from the ground state for another one arising from the ^{250}No nucleus. This possibility must not be rejected on the basis of this data. At the same time, the yield of the 54-μs SF activity observed in our ^{48}Ca + ^{204}Pb experiments is an order of magnitude lower than the yield of the 36-μs SF activity observed in similar experiments [25] (see Fig. 7), in which the latter was identified as ^{250}No.

Continuation of the experiments with the ^{44}Ca beam at energies above the fusion barrier is needed for the final identification of the observed SF activities. At the same time, note that the 5.6-μs SF activity corresponds quite well to the calculated 2n evaporation channel for both reactions induced by ^{44}Ca and ^{48}Ca (see Fig. 7). The observed suppression in the yield of this activity at the transition from ^{48}Ca to ^{44}Ca is connected with about 8 MeV of additional excitation energy of the ^{252}No* compound nuclei at the nominal fusion barrier [37] due to different Q values in the ^{44}Ca reaction. It makes the (^{44}Ca, 2n) reaction a subbarrier one and resembles a similar suppression of the 2n channel at the transition from ^{48}Ca to ^{40}Ar in the reactions with Pb nuclei.

5. SUMMARY AND CONCLUSIONS

In the course of our experiments aimed at the investigation of the ^{44,48}Ca + ^{204,206,208}Pb reactions, two new short-lived SF activities have been observed. One of them, with the half-life $T_{1/2} = 54^{+14}_{-9}$ μs, seems to be similar to the SF activity, with the half-life $T_{1/2} = 36^{+11}_{-6}$ μs, which was observed in similar experiments performed recently [25]. The yield of the 54-μs SF activity observed in our ^{48}Ca+^{204}Pb experiments is an order of magnitude lower than the yield of the 36-μs SF activity observed in similar experiments [25], in which the latter was identified as ^{250}No. The second new SF activity never observed before has the half-life $T_{1/2} = 5.6^{+0.9}_{-0.7}$ μs and the yield is more than 5 times higher than that for the 54-μs SF activity at the energy corresponding to their maximum production yields. On the basis of the mass measurement with the use of the new dipole magnet as well as using the yields and energy dependences for these activities, we have attributed them to ^{250}No ($T_{1/2} = 5.6^{+0.9}_{-0.7}$ μs) and ^{249}No ($T_{1/2} = 54.0^{+13.9}_{-9.2}$ μs). At the same time, we do not exclude a possible existence of two SF emitters in the case of the ^{250}No nucleus.

Despite some disagreement with the previous work [25], our data confirm a drastic decrease in the nuclear stability with distance off the $N = 152$ deformed neutron shell and correspond to the linear (on a log scale) extrapolation of partial SF half-lives to the neutron-deficient side. Such a drastic decrease in the nuclear stability can apparently be explained by a corresponding reduction in the shell correction energy for the fission barriers with decreasing N.

Lowering the shell correction energy explains a drastic decrease in the production cross section values for the neutron-deficient No isotopes observed

in the $^{48}Ca + ^{204,206}Pb$ experiments. The 0.5-MeV reduction in the shell correction energy provided by the Thomas–Fermi nuclear masses leads to general agreement of the calculated cross section values with the measured ones. The observed suppression of the 5.6-μs SF-activity yield at the transition from ^{48}Ca to ^{44}Ca can be explained by the extra excitation energy of the $^{252}No^*$ compound nuclei at the fusion barrier for the latter.

The first test experiments have been performed with the new 37° dipole magnet installed behind the recoil separator VASSILISSA. The results obtained are very promising; it is possible now to define masses of the synthesized ERs with an accuracy of 5–6 amu. This provides an additional reliability of the identification in the experiments aimed at the synthesis of superheavy nuclei in complete fusion reactions between transactinide targets and ^{48}Ca accelerated beams.

With the use of the upgraded separator VASSILISSA, we plan to continue the experiments aimed at the synthesis of superheavy nuclei in the vicinity of predicted spherical shells in complete fusion reactions between $^{34,36}S$ and ^{48}Ca ions and ^{232}Th, $^{236,238}U$, and $^{24,244}Pu$ targets. Odd-Z isotopes that could be obtained in reactions with ^{237}Np and ^{243}Am targets may have even longer half-lives than those of even-Z elements 112 and 114. After the upgrade of the separator, the search for long correlations (up to few hours) becomes possible.

The experiments performed with ^{48}Ca beams are the first step in a long-term program aimed at the synthesis and study of decay properties of superheavy nuclei with neutron numbers close to the predicted spherical shell. The relatively long half-lives of the new isotopes with $Z = 112$, 114 (even–odd and odd–odd isotopes that could be obtained in reactions with ^{237}Np and ^{243}Am targets could have even longer half-lives), synthesized in the reactions with ^{48}Ca ions, dictate the need for upgrading the existing experimental setups and developing new ones, thus providing the possibility of direct mass measurements with an accuracy of 1 amu, and, on the other hand, open new prospects for the investigation of chemical properties of superheavy elements.

ACKNOWLEDGMENTS

We thank A.N. Shamanin and E.N. Voronkov for the maintenance of the VASSILISSA separator and the U-400 crew for providing the stable beams of high intensity.

This work was performed partially under financial support from the Russian Foundation for Basic Research, project no. 02-02-16116.

REFERENCES

1. A. Sobiczewski *et al.*, in *Proceedings of the International Conference on Nuclear Physics "Shells 50", Dubna, Russia, 1999*, Ed. by Yu. Ts. Oganessian and R. Kalpakchieva (World Sci., Singapore, 2000), p. 211.
2. R. Smolańczuk, Phys. Rev. C **56**, 812 (1997).
3. P. Möller *et al.*, At. Data Nucl. Data Tables **59**, 185 (1995).
4. Yu. Ts. Oganessian, in *Proceedings of the International Conference Nuclear Physics at the Turn of the Millenium "Structure of the Vacuum and Elementary Matter", Wilderness, South Africa, 1996* (World Sci., Singapore, 1997), p. 11.
5. B. A. Zager *et al.*, At. Energ. **20**, 230 (1966).
6. A. Ghiorso *et al.*, Phys. Rev. Lett. **22**, 1317 (1969).
7. V. A. Druin *et al.*, Yad. Fiz. **13**, 251 (1971) [Sov. J. Nucl. Phys. **13**, 139 (1971)].
8. S. Hofmann, Rep. Prog. Phys. **61**, 639 (1998).
9. A. V. Yeremin *et al.*, Nucl. Instrum. Methods Phys. Res. B **126**, 329 (1997).
10. A. V. Yeremin *et al.*, Nucl. Instrum. Methods Phys. Res. A **440**, 86 (2000).
11. A. N. Andreyev *et al.*, Nucl. Phys. A **620**, 229 (1997).
12. R. N. Sagaidak *et al.*, J. Phys. **24**, 611 (1998).
13. R. N. Sagaidak *et al.*, Heavy Ion Physics, FLNR JINR Sci. Report 1999–2000 (Joint Inst. for Nucl. Res., Dubna, 2001), p. 48.
14. A. V. Yeremin *et al.*, JINR Rapid Commun., No. 6 [92]-98, 21 (1998).
15. Yu. Ts. Oganessian *et al.*, in *Proceedings of the International Workshop on Fusion Dynamics at the Extremes, Dubna, Russia, 2000*, Ed. by Yu. Ts. Oganessian and V. I. Zagrebaev (World Sci., Singapore, 2001), p. 167.
16. Yu. Ts. Oganessian *et al.*, Eur. Phys. J. A **5**, 63 (1999).
17. Yu. Ts. Oganessian *et al.*, Nature **400**, 242 (1999).
18. Yu. Ts. Oganessian *et al.*, Phys. Rev. C **63**, 011301(R) (2001).
19. H. W. Gäggeler *et al.*, Nucl. Phys. A **502**, 561 (1989).
20. R. N. Sagaidak *et al.*, in *Proceedings of the VI International School–Seminar Heavy Ion Physics, Dubna, Russia, 1997*, Ed. by Yu. Ts. Oganessian and R. Kalpakchieva (World Sci., Singapore, 1998), p. 323.
21. A. N. Andreyev *et al.*, Z. Phys. A **337**, 231 (1990).
22. G. Münzenberg *et al.*, Z. Phys. A **302**, 7 (1981).
23. A. V. Belozerov *et al.*, submitted to Eur. Phys. J. A.
24. W. Westmeier and A. Merklin, Phys. Daten 29 (1) (1985).
25. Yu. Ts. Oganessian *et al.*, Phys. Rev. C **64**, 054606 (2001).
26. G. M. Ter-Akopyan *et al.*, Nucl. Phys. A **255**, 509 (1975).
27. K.-H. Schmidt, Z. Phys. A **316**, 19 (1984).

28. R. Smolańczuk and A. Sobiczewski, in *Proceedings of the XV EPS Nuclear Divisional Conference "Low Energy Nuclear Dynamics", St. Petersburg, 1995*, Ed. by Yu. Ts. Oganessian, R. Kalpakchieva, and W. von Oertzen (World Sci., Singapore, 1996), p. 313.
29. R. Smolańczuk, J. Skalski, and A. Sobiczewski, Phys. Rev. C **52**, 1871 (1995).
30. A. Sobiczewski, private communication.
31. H. Gäggeler *et al.*, Z. Phys. A **316**, 291 (1984).
32. F. P. Heßberger *et al.*, GSI Scientific Report No. 87-1 (Darmstadt, 1986), p. 17.
33. A. G. Popeko, O. N. Malyshev, R. N. Sagaidak, and A. V. Yeremin, Nucl. Instrum. Methods Phys. Res. B **126**, 294 (1997).
34. M. Dahlinger, W. Bonin, E. Kankeleit, and H. Backe, Nucl. Instrum. Methods Phys. Res. A **219**, 513 (1984).
35. R. N. Sagaidak and A. V. Yeremin, Nucl. Instrum. Methods Phys. Res. B **93**, 103 (1994).
36. W. Reisdorf, Z. Phys. A **300**, 227 (1981); W. Reisdorf and M. Schädel, Z. Phys. A **343**, 47 (1992).
37. R. Bass, Phys. Rev. Lett. **39**, 265 (1977); in *Proceedings of the Symposium on Deep Inelastic and Fusion Reactions with Heavy Ions, West Berlin, 1979*, Lect. Notes Phys. **117**, 281 (1980).

Physics of Atomic Nuclei, Vol. 66, No. 6, 2003, pp. 1053–1056. From Yadernaya Fizika, Vol. 66, No. 6, 2003, pp. 1089–1092.

Effect of Nuclear Shell Structure on Fusion Reaction*

H. Ikezoe**, **K. Satou**, **S. Mitsuoka**, **K. Nishio**, and **S. C. Jeong**[1)]

Advanced Science Research Center, Japan Atomic Energy Research Institute, Tokai, Japan

[1)] *Institute of Particle and Nuclear Studies, KEK, Tsukuba, Japan*

Received August 28, 2002

Abstract—The dependence of the fusion reaction on the nuclear shell structure was investigated for the two reaction systems ^{82}Se + ^{138}Ba and ^{82}Se + ^{134}Ba, where the nucleus ^{138}Ba has a closed neutron shell $N = 82$, while the nucleus ^{134}Ba has a neutron number 78. Evaporation residues for these fusion reactions were measured near the Coulomb barrier region. The measured evaporation residue cross sections for the reaction system ^{82}Se + ^{138}Ba were two orders of magnitude larger than those for the reaction system ^{82}Se + ^{134}Ba in the excitation energy region of 20–30 MeV. The evaporation residue cross sections were compared with those of the other reaction systems that produce the same compound nucleus as the present systems. It was found that the fusion reaction ^{82}Se + ^{138}Ba occurs without hindrance, while that of ^{82}Se + ^{134}Ba is considerably hindered, as commonly observed in the massive reaction system with the charge product $Z_pZ_t > 1800$ of projectile and target. This suggests the importance of the shell closure $N = 82$ in the heavy-ion fusion reaction. © *2003 MAIK "Nauka/Interperiodica".*

1. INTRODUCTION

The fusion process between massive nuclei has been extensively investigated thus far. It is well known that the fusion probability between massive nuclei depends on the charge product Z_pZ_t of projectile and target. When the charge product is less than 1800, its fusion cross section is well reproduced by the one-dimensional barrier penetration model. When the charge product is larger than 1800, its fusion cross section is hindered compared with the model calculation. This fact means that the interacting nuclei cannot always fuse to make a compound nucleus even if the system overcomes the entrance channel fusion barrier. Extra kinetic energy is needed so that the system can reach the saddle point after surmounting the fusion barrier.

The fusion between massive nuclei depends on not only the charge product but also the nuclear structure of projectile and target. It is reported that the number of a valence nucleon outside a major shell affects the fusion probability [1, 2]. Recently, Oganessian *et al.* [3] measured the evaporation residues in the fusion reactions ^{86}Kr + ^{136}Xe and ^{86}Kr + ^{130}Xe, where the nucleus ^{136}Xe has a closed neutron shell $N = 82$ and the neutron number of the nucleus ^{130}Xe is 76. They found that the measured evaporation residue cross sections for the fusion reaction ^{86}Kr + ^{136}Xe are almost 2–3 orders of magnitude larger than those for the fusion reaction ^{86}Kr + ^{130}Xe near the Coulomb barrier region. The enhancement of the evaporation residue cross sections between ^{208}Pb and ^{48}Ca is also pointed out in [4]. This experimental evidence suggests that the shell structure also plays an important role in the low-energy fusion process.

In this paper, we report the isotope dependence on the fusion reactions ^{82}Se + ^{138}Ba and ^{82}Se + ^{134}Ba [5], where the nucleus ^{138}Ba has the neutron closed shell $N = 82$ and the number of neutrons in the nucleus ^{134}Ba is 78, four neutrons less than the closed shell.

2. EXPERIMENTAL RESULTS AND DISCUSSIONS

Evaporation residues for the fusion reactions ^{82}Se + ^{138}Ba and ^{82}Se + ^{134}Ba were measured by using ^{82}Se beams from the JAERI tandem booster accelerator. The targets of ^{134}Ba and ^{138}Ba, whose thickness were 0.41 and 0.50 mg/cm^2, respectively, were mounted on a rotating frame and rotated at 100 rpm during the beam irradiation to prevent the targets from breaking due to the beam heating. The evaporation residues emitted in the beam direction from a target foil were separated in-flight from the primary beam by the JAERI-recoil mass separator (JAERI-RMS) [6]. The separated evaporation residues were passed through two microchannel plate detectors (MCP) and implanted into a double-sided

*This article was submitted by the authors in English.

**e-mail: ikezoe@popsvr.tokai.jaeri.go.jp

1063-7788/03/6606-1053$24.00

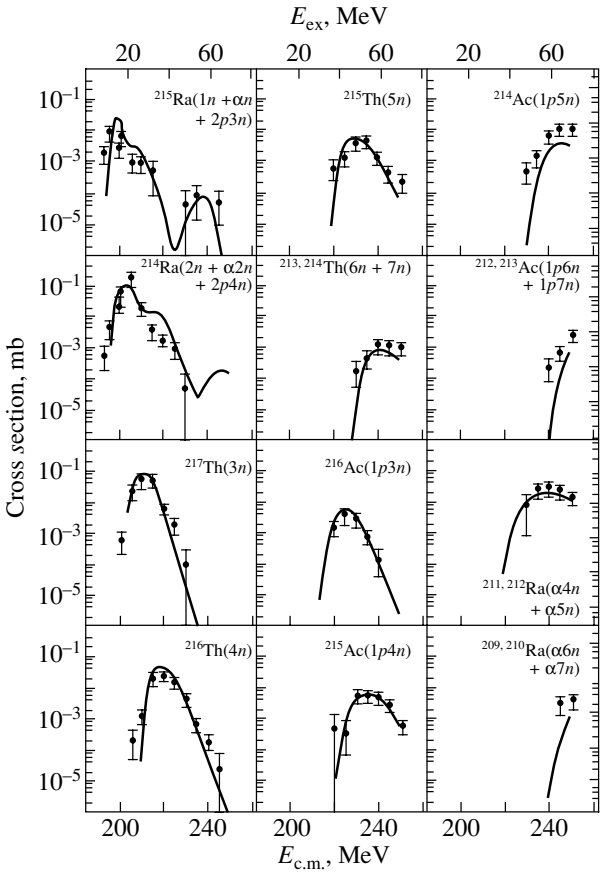

Fig. 1. Evaporation residue cross sections for the reaction ^{82}Se + ^{138}Ba together with the calculated results (solid curves) of the statistical model using the HIVAP code.

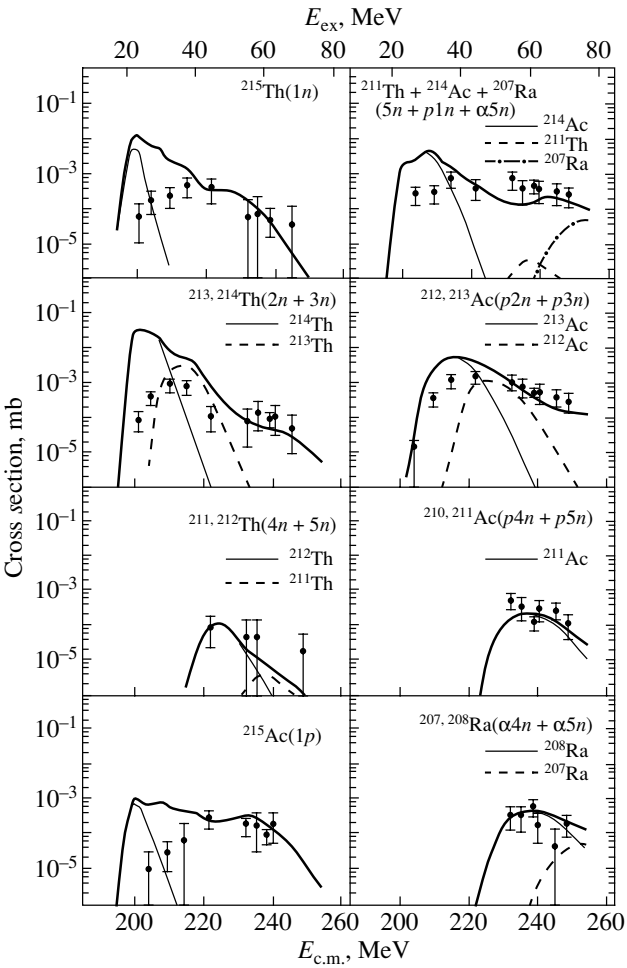

Fig. 2. The same as in Fig. 1, but for the reaction ^{82}Se + ^{134}Ba. The thick curve in each channel is the calculated result including the components originating from the fusion reactions ^{82}Se + ^{135,136,137,138}Ba. The percentage of the barium isotopes 135, 136, 137, and 138 in a ^{134}Ba target were 15.24, 4.03, 1.94, and 5.26%, respectively. The thin curve shows the component originating from the fusion reaction ^{82}Se + ^{134}Ba.

position-sensitive strip detector (DPSD) mounted at the focal position of the JAERI-RMS. The energies and the positions of incoming particles and their subsequent α-particle decays were measured by the DPSD. The typical energy resolution was 75 keV (FWHM).

All evaporation residues produced in the present fusion reactions decay by emitting α particles. Their α-decay energies and half-lives are known from the literature [7]. The identification of each evaporation residue was made event by event by measuring its subsequent α-decay energy and the time interval between the implanted evaporation residue and its decay event. In order to obtain the absolute cross sections, the transport efficiency of the evaporation residue through the JAERI-RMS was estimated by the methods described in [8].

The obtained evaporation residue cross sections for the present reactions are plotted in Figs. 1 and 2 as a function of c.m. energy determined in the middle of the target layer together with the calculated results using the statistical model code HIVAP [9]. As shown in Fig. 1, the maximum evaporation residue cross sections of the $2n$ and $3n$ channels in the fusion reaction ^{82}Se + ^{138}Ba are about 100 μb and are quite consistent with the calculated cross sections for these channels. The details of the statistical model calculation are described in [8]. The excellent agreement between the measured evaporation residue cross sections and the calculated results means that the fusion in the reaction ^{82}Se + ^{138}Ba occurs without any hindrance. This is not true for the so-called extrapush systematics of Quint *et al.* [1], where the extra-extrapush energy increases as a function of the charge product Z_pZ_t. We expect an extra-extrapush energy around $\sim$10–15 MeV for the present reaction ^{82}Se + ^{138}Ba from this systematics. This effectively makes the fusion barrier high and

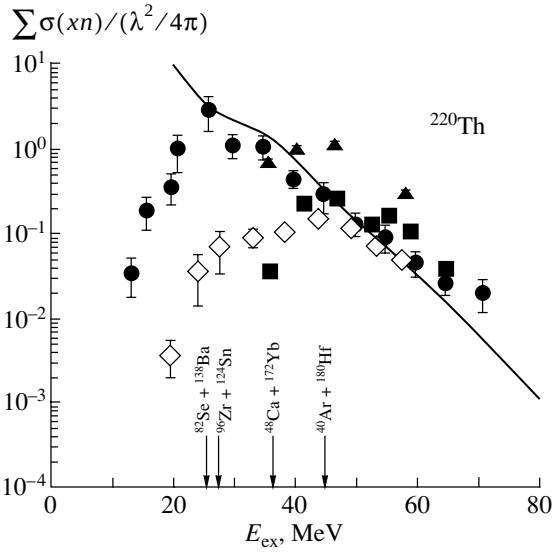

Fig. 3. Reduced cross sections of the sum of all xn channels measured in the several reaction systems that produce the same compound nucleus ^{220}Th as the present reaction system. The closed points show the present data. The data for the reactions ^{48}Ca + ^{172}Yb (closed triangles) [10], ^{40}Ar + ^{180}Hf (closed squares) [11], and ^{96}Zr + ^{124}Sn (open diamonds) [10] are also plotted. The vertical arrows indicate the Bass barrier for each reaction system. The solid curve is the calculated result of the statistical model assuming a partial cross section with a sharp cutoff distribution of the angular momentum.

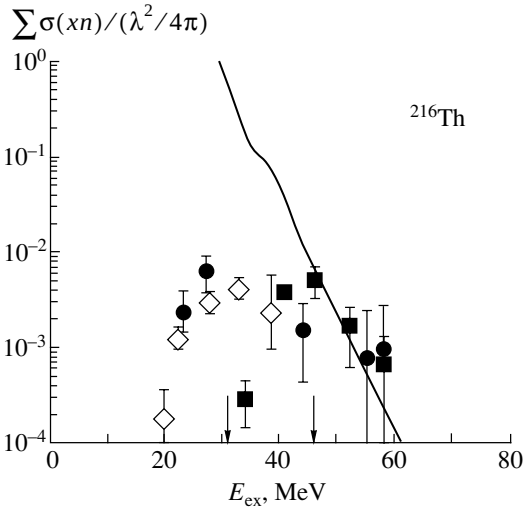

Fig. 4. The same as in Fig. 3, but for the compound nucleus ^{216}Th. The closed points show the present data. The data for the reactions ^{40}Ar + ^{176}Hf (closed squares) [11] and ^{92}Zr + ^{124}Sn (open diamonds) [10] are also plotted. The Bass barrier positions for these reaction systems are shown as arrows (E_{ex} = 31.1 MeV for ^{82}Se + ^{134}Ba and also ^{92}Zr + ^{124}Sn, and 46.2 MeV for ^{40}Ar + ^{176}Hf). The solid curve is the calculated result of the statistical model (see the caption of Fig. 3).

considerably decreases the cross sections of the $1n$ and $2n$ channels in the low-excitation-energy region less than 30 MeV. There is no such evidence seen in the excitation function shown in Fig. 1.

On the other hand, the measured evaporation residue cross sections in the fusion reaction ^{82}Se + ^{134}Ba show clear deviations from the calculated cross sections mainly in the low-excitation-energy region less than 30 MeV as shown in Fig. 2. Since the present target of ^{134}Ba has the admixture of the other isotopes of barium as indicated in the caption of Fig. 2, we can see that a sizable contribution of the fusion contributions mainly concentrate on excitation energies E_{ex} higher than 40 MeV, except for the residues ^{211,212}Th, ^{210,211}Ac, and ^{207,208}Ra. According to the present calculation, these residues are produced only by the fusion reaction ^{82}Se + ^{134}Ba in the energy region $50 < E_{ex} < 70$ MeV. Large deficits of the evaporation residue cross sections are seen in the $1n$, $2n + 3n$, and the $1p$ channels at $E_{ex} \simeq 20$–30 MeV, where the main contribution is ascribed to the fusion reaction ^{82}Se + ^{134}Ba. The observed cross sections corresponding to the maximum of the $2n + 3n$ channels are $\sim$0.1–0.5 μb, which are more than two orders of magnitude smaller compared with the maximum cross section of the $2n$ or $3n$ channel in the fusion reaction ^{82}Se + ^{138}Ba.

Figure 3 shows the reduced cross sections of the sum of all xn channels measured in the several reaction systems that produce the same compound nucleus ^{220}Th as the present reaction systems. The present data for the fusion reaction ^{82}Se + ^{138}Ba shows the largest cross section among the other reaction systems. We see that the reduced cross section for the fusion reaction ^{82}Se + ^{138}Ba bends at the Bass barrier and coincides with other fusion data above the Bass barrier. This comparison of the present data with the other fusion data directly shows that there is no fusion hindrance in the reaction ^{82}Se + ^{138}Ba above the Bass barrier.

The reduced cross section of the sum of all xn channels for the fusion reaction ^{82}Se + ^{134}Ba is shown in Fig. 4 together with the other fusion systems that produce the same compound nucleus ^{216}Th as the present reaction system. We see that the reduced cross section bends at an energy of $\sim$ 10–15 MeV above the Bass barrier. This trend means that the fusion is hindered and the fusion barrier is shifted to a high energy in the amount of $\sim$10–15 MeV. This is consistent with the extrapush systematics of Quint *et al.* [1].

The present result suggests that the fusion process after surmounting the fusion barrier may be different in the reactions ^{82}Se + ^{138}Ba and ^{82}Se +

^{134}Ba. The nucleus ^{138}Ba has the closed neutron shell $N = 82$, and the nucleus ^{134}Ba has the neutron number 78. The calculated subbarrier fusion enhancement due to the coupling of the inelastic excitations of 2^+ and 3^- states is almost the same in both of the present reactions, because the deformation parameters β_2 and β_3 are similar to each other for ^{134}Ba and ^{138}Ba. In the present calculation, the coupling to the neutron transfer channel was not included. The Q values for one- and two-neutron transfers are negative for the reaction ^{82}Se + ^{138}Ba, while the Q value for two-neutron transfer is positive, 0.79 MeV, for the reaction ^{82}Se + ^{134}Ba. This may result in the more subbarrier enhancement in the fusion reaction ^{82}Se + ^{134}Ba than in the case of the fusion reaction ^{82}Se + ^{138}Ba. This expectation contradicts the present experimental results.

Myers and Swiatecki [12] pointed out that the shell energy resists neck growth at the time of contact between projectile and target, and then the projectile nucleus can go deeply into the target nucleus with a small kinetic energy dissipation. In the present reaction systems, the sum of the shell energy for projectile and target is −4.01 and −0.43 MeV for the reaction systems ^{82}Se + ^{138}Ba and ^{82}Se + ^{134}Ba, respectively. This difference of the shell energy may cause the fusion enhancement for the former reaction system compared with the later reaction system.

Oganessian *et al.* [3] suggest the important relation between the fusion process and the fission process. In the case of the fusion reaction ^{86}Kr + ^{136}Xe, the compound nucleus ^{222}Th has the asymmetric fission components close to the nuclei ^{86}Kr and ^{136}Xe. The compound nucleus ^{220}Th, which is produced in the fusion reaction ^{82}Se + ^{138}Ba, also has the asymmetric fission component close to the nuclei ^{82}Se and ^{138}Ba. On the other hand, the compound nucleus ^{216}Th, which is formed in the fusion reactions ^{86}Kr + ^{130}Xe and also ^{82}Se + ^{134}Ba, has no such asymmetric fission component. The present data together with the data obtained by Oganessian *et al.* show that the reaction partners close to the asymmetric fission fragments have a large fusion cross section.

3. CONCLUSIONS

Evaporation residues from the reactions ^{82}Se + ^{138}Ba and ^{82}Se + ^{134}Ba were measured to investigate the dependence of the fusion reaction on the nuclear shell structure of the colliding nuclei. The evaporation residue cross sections measured in the reaction ^{82}Se + ^{138}Ba was almost two orders of magnitude larger near the Coulomb barrier region than those for the reaction ^{82}Se + ^{134}Ba. This large difference is ascribed to the entrance channel of the fusion process. The present data were compared with the other reaction systems that produce the same compound nuclei as the present reactions. From this comparison, we conclude that there is no fusion hindrance for the reaction ^{82}Se + ^{138}Ba, while the fusion for the reaction ^{82}Se + ^{134}Ba is considerably hindered near the Coulomb barrier region. The present result suggests that the fusion of massive reaction systems strongly depends on the shell structure of colliding partners. It is important to realize theoretically the energy dissipation due to the friction after contact by taking into account the shell structure of projectile and target nuclei. Further experimental investigation is needed to make the relation between fusion and fission clear.

ACKNOWLEDGMENTS

We thank the crew of the JAERI tandem booster facility for the beam operation.

REFERENCES

1. A. B. Quint, W. Reisdorf, K.-H. Schmidt, *et al.*, Z. Phys. A **346**, 119 (1993).
2. K.-H. Schmidt and W. Morawek, Rep. Prog. Phys. **54**, 949 (1991).
3. Yu. Ts. Oganessian, *Heavy Elements and Related New Phenomena*, Ed. by W. Greiner and R. K. Gupta (World Sci., Singapore, 1999), Vol. 1, p. 43.
4. Yu. Ts. Oganessian, V. K. Utyonkov, Yu. V. Lobanov, *et al.*, Phys. Rev. C **64**, 054606 (2001).
5. K. Satou, H. Ikezoe, S. Mitsuoka, *et al.*, Phys. Rev. C **65**, 054602 (2002).
6. H. Ikezoe, Y. Nagame, T. Ikuta, *et al.*, Nucl. Instrum. Methods Phys. Res. A **376**, 420 (1996).
7. R. B. Firestone, in *Table of Isotopes*, Ed. by V. S. Shirley (Wiley, New York, 1996).
8. S. Mitsuoka, H. Ikezoe, K. Nishio, and J. Lu, Phys. Rev. C **62**, 054603 (2000).
9. W. Reisdorf and M. Schädel, Z. Phys. A **343**, 47 (1992).
10. C.-C. Sahm, H.-G. Clerc, K.-H. Schmidt, *et al.*, Nucl. Phys. A **441**, 316 (1985).
11. H.-G. Clerc, J. G. Keller, C.-C. Sahm, *et al.*, Nucl. Phys. A **419**, 571 (1984).
12. W. D. Myers and W. J. Swiatecki, Phys. Rev. C **62**, 044610 (2000).

Physics of Atomic Nuclei, Vol. 66, No. 6, 2003, pp. 1057–1064. From Yadernaya Fizika, Vol. 66, No. 6, 2003, pp. 1093–1100.

Theory of Fusion for Superheavy Elements*

Y. Abe[1], C. W. Shen[2),3),4)], G. I. Kosenko[4),5)], and D. Boilley[6)]

[1)] *Yukawa Institute for Theoretical Physics, Kyoto University, Japan*
[2)] *Department of Nuclear Physics, China Institute of Atomic Energy, Beijing, China*
[3)] *Laboratori Nazionale di Sud, INFN, Catania, Italy*
[4)] *RIKEN, Wako, Saitama, Japan*
[5)] *Department of Physics, University of Omsk, Omsk, Russia*
[6)] *GANIL, Caen, France*

Received September 10, 2002

Abstract—A new model is proposed for fusion mechanisms of massive nuclear systems, where so-called fusion hindrance exists. The model describes the whole process in two steps: two-body collision processes in an approaching phase and shape evolutions of an amalgamated system into the compound nucleus formation. It is applied to ^{48}Ca-induced reactions and is found to reproduce the experimental fusion cross sections extremely well, without any free parameter. A schematic case is solved in an analytic way, the results of which shed light on fusion mechanisms. Combined with statistical decay theory, residue cross sections for superheavy elements can be readily calculated. Examples are given. © *2003 MAIK "Nauka/Interperiodica".*

1. INTRODUCTION: WHY TWO STEPS?

The heaviest element that exists in nature is now known to be uranium with atomic number Z being 92. But the discovery of magic numbers in atomic nuclei and their understanding by the shells of nucleonic motion [1] suggest that much heavier atomic nuclei might exist, stabilized by the extrabinding due to possible shells next to the largest known, i.e., $Z = 82$ and $N = 126$. Actually, many theoretical calculations have been made, predicting the next double closed shell nucleus for $Z = 114$, 120, or 126 and $N = 184$ [2]. Naturally, enormous experimental efforts have been devoted to finding traces of existence of corresponding superheavy atomic nuclei and to synthesizing them with nuclear reactions, especially with heavy-ion fusion reactions [3]. But what combination of ions that is favorable as incident channels and what incident energy that is the optimum for residues are not predicted well, and thus, experiments have been performed more or less empirically, i.e., according to the systematic data available thus far. This is due to our lack of knowledge of reaction mechanisms. Based on the theory of compound nucleus reactions, the residue cross sections are given as follows:

$$\sigma_{\rm res} = \pi\lambda\!\!\!^{-2} \sum_J (2J+1) P^J_{\rm fus}(E_{\rm c.m.}) P^J_{\rm surv}(E^*), \quad (1)$$

where $\lambda\!\!\!^{-}$ is the inverse of the wave number and J is the total angular momentum quantum number; $P_{\rm fus}$ and $P_{\rm surv}$ denote the fusion and the survival probabilities, respectively. The latter is given by the statistical theory of decay, i.e., by competitions between neutron emission and fission decay. Although there are ambiguities in the parameters in the properties of heavy and superheavy nuclei that give rise to uncertainties in calculating the survival probability, essentially unknown is the fusion probability, i.e., the fusion mechanism of massive systems. In lighter systems, the fusion probability is well determined by the barrier defined with the Coulomb and the nuclear attraction between nuclei in the incident channel, though there are effects of quantum tunneling and of couplings to collective excitations of ions, etc. [4]. But in massive systems, the situation is not so simple. It has been well known experimentally that there is fusion hindrance [5], which is often described with so-called extrapush energy which is required for the system to fuse in addition to the barrier height [6]. A physical origin or mechanism is not yet well clarified. There are two possible interpretations proposed. They both attribute it to energy dissipations; one is due to the dissipation of the incident kinetic energy during two-body collisions passing over the barrier [7], while the other is due to the dissipation of the energy of collective motions that would lead the amalgamated system to a spherical compound nucleus [6]. It is natural to consider that both mechanisms exit. We,

*This article was submitted by the authors in English.

1063-7788/03/6606-1057$24.00

thus, propose a new theoretical framework for fusion, i.e., a two-step model that incorporates both of them properly [8]. In an approaching phase of passing over the barrier, we describe the system as collision processes under frictional forces, up to the contact point of two incident nuclear substances, and then, we describe dynamical evolutions of the amalgamated mononuclear system toward a spherical shape under frictional forces acting in collective motions of excited nuclei. As is given below, both dynamical processes are described by Langevin equations that include random forces associated to the respective frictions. It would be worth mentioning here that the fluctuations due to random forces are crucially important in problems of small probability such as in the synthesis of the superheavy elements (SHEs), because we have to investigate cases where mean trajectories never reach a spherical shape. Since the two steps are connected successively, the results of the first step naturally give a probability for the incident ions to stick to each other (sticking probability $P_{\rm stick}$) as well as give initial conditions for the second step. In massive systems, there is a conditional saddle point, or a ridge line between the amalgamated configuration and the spherical shape on the potential energy surface calculated with the liquid-drop model (LDM), which could be considered to be another barrier inside and makes most trajectories return back to reseparation (quasifission, etc.), i.e., gives rise to a small probability for forming a spherical shape (formation probability $P_{\rm form}$). Thus, the fusion probability in massive systems is given by the product of the two probabilities,

$$P^J_{\rm fus}(E_{\rm c.m.}) = P^J_{\rm stick}\left(E_{\rm c.m.}\right)P^J_{\rm form}(E_{\rm c.m.})\,. \quad (2)$$

In order to calculate the probabilities, we employ the surface friction model (SFM) [9] for the approaching phase and the one-body wall-and-window formula [10] of the dissipation for the shape evolutions, i.e., for the second step.

2. CONTACT DYNAMICS OF MASSIVE SYSTEMS

As for the approaching phase, as stated above, we follow exactly the prescription of SFM proposed by Gross and Kalinowski [9], although it might be better to improve their treatments and modify their values of the parameters because it does not include so-called rolling friction between incident ions, which surely is expected to play a role in angular momentum transfer. The equation of motion is only for the radial degree of freedom and the orbital angular momentum and is given below,

$$\frac{dr}{dt} = \frac{1}{\mu}p, \quad (3)$$

$$\frac{dp}{dt} = -\frac{dV}{dr} - \frac{\partial}{\partial r}\frac{\hbar^2 L(t)^2}{2\mu r^2} - C_r(r)\frac{p}{\mu} + R_r(t),$$

$$\frac{dL(t)}{dt} = -\frac{C_L(r)}{\mu}(L(t) - L_{\rm st}) + R_L(t),$$

where μ is the reduced mass of the collision system and V is the sum of the Coulomb potential V_c and the nuclear potential V_n. $C_i(r)$ is the radial or the tangential friction coefficient, which is assumed to have the following form factor:

$$C_i(r) = K^0_i\left(\frac{dV_n}{dr}\right)^2, \quad (4)$$

where $K^0_r = 0.035$ and $K^{0\prime}_r = 0.0001$ in units of 10^{-21} s/MeV. $R_i(t)$ denotes a random force associated with the friction for $i = r$ or L and is assumed to be Gaussian and to satisfy the following property:

$$\langle R_i(t)\rangle = 0, \quad (5)$$

$$\langle R_i(t)R_j(t')\rangle = 2\delta_{ij}\delta(t-t')C_i\left(r(t)\right)T^J(t),$$

where the last equation is the fluctuation–dissipation theorem with temperature $T^J(t)$, J being an incident orbital angular momentum, i.e., a total angular momentum of the system. For the case where i and j are equal to T (tangential), $r(t)^2$ is factored on the right-hand side of the last equation. The quantity $L_{\rm st}$ stands for the limiting orbital angular momentum under friction, which is the so-called sliding limit in the SFM and is equal to $(5/7)L$. We calculate many trajectories over relevant impact parameters and obtain probabilities for their reaching the contact point, respectively. Figure 1*a* shows the calculated sticking probability for $L = 0$ for the case of the ^{48}Ca + ^{238}U system. The incident energy is given relative to the barrier height. It is readily seen that, at energies just above the barrier, there is almost no probability. This is due to the fact that the form factor assumed in SFM stretches over outside the barrier top position in massive systems. The results already appear to explain the fusion hindrance and at least partially the extrapush energy, while the second step is also expected to give rise to an additional contribution to the extrapush energy. In order to know the physical situation at the contact point, we analyze the radial momentum distribution as well as that of the orbital angular momentum. Surprisingly, the radial momentum distribution is found to be almost purely Gaussian, as shown in Fig. 1*b*. Its width is consistent with the temperature of the heat bath of nucleons, which is supposed to absorb the incident kinetic energy through the friction force. An example is shown for $J = 0$, but the other angular momentum cases behave in the same way. Therefore, the calculated distribution $S^J(p_0, E_{\rm c.m.})$ is given as follows for each angular momentum:

$$S^J(p_0, E_{\rm c.m.}) = P^J_{\rm stick}(E_{\rm c.m.})g^J(p_0, \bar{p}^J_0, T^J_0), \quad (6)$$

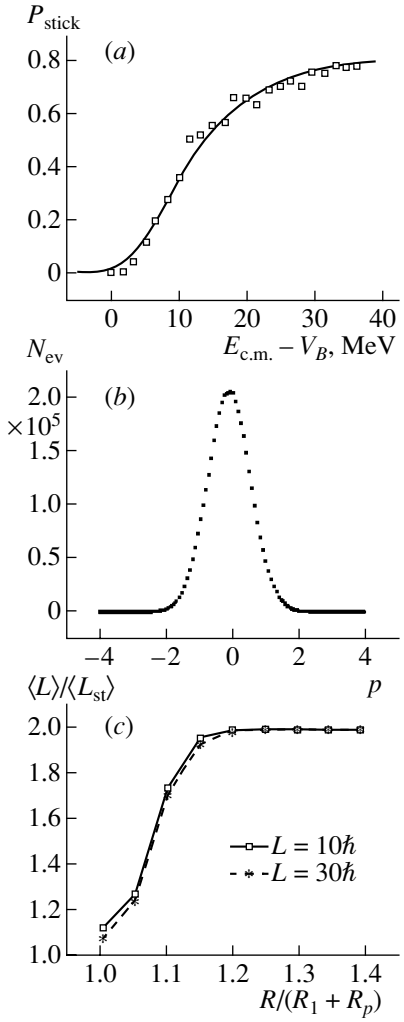

Fig. 1. Results on ^{48}Ca + ^{238}U system with SFM. (*a*) The sticking probability for $L = 0$, (*b*) the radial momentum distribution (in unit of 10^{-21} s MeV/fm), and (*c*) the average orbital angular momentum vs. the relative distance.

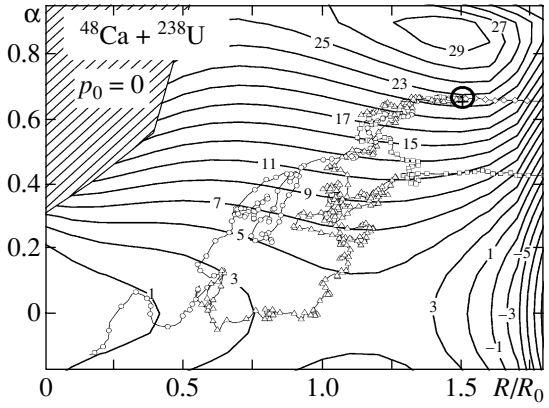

Fig. 2. Examples of trajectories are displayed with the same initial radial momentum being equal to zero. Random force gives rise to a variety of trajectories. The circle in the upper right corner corresponds to the touching configuration reached by the first step, from which dynamical evolutions of shape start (R_0 being the radius of the spherical ground state).

where the Gaussian distribution $g^J(p_0, \bar{p}_0^J, T_0^J)$ is given generally so as to include an average mean momentum left, which is almost equal to zero in the present case. This distribution is used as the initial inputs to the dynamical evolutions at the second step, i.e., to Eq. (8) (see below). T_0^J denotes the temperature of the amalgamated system. The total energy available for the compound nucleus E^* is written by energy conservation as follows:

$$E^* = E_{\rm c.m.} + Q = U_0 - E_{\rm shell} + \varepsilon_0 + k_0, \quad (7)$$

where Q denotes the Q-value of the fusion reaction, U_0 is the LDM potential energy, $E_{\rm shell}$ is the shell correction energy of the ground state, ε_0 is the intrinsic excitation, and k_0 is the radial kinetic energy left at the contact point. The latter two are on average given as $a(T_0^J)^2$ and $(\bar{p}_0^J)^2/2\mu + T_0^J/2$, respectively, with the level density parameter a that is calculated according to Töke and Swiatecki [11]. The orbital angular momentum is also analyzed. The average value is plotted as a function of the radial distance in Fig. 1*c*. It is seen that it approaches the dissipation limit $L_{\rm st}$ about the contact point, which indicates that the incident system reaches the sticking limit, if the rolling friction is properly taken into account. We, thus, can consider that the relative motion is completely damped and reaches thermal equilibrium with the heat bath at the contact point, i.e., that the incident ions form an amalgamated mononuclear system, though the probability is extremely small just above the barrier. It should be noted here that $\bar{p}_0^J = 0$ does not always hold, for example, in the ^{100}Mo+^{100}Mo system.

3. SHAPE EVOLUTION FROM THE CONTACT TO THE SPHERICAL SHAPE

Shape evolutions of the pear-shaped mononucleus formed with the incident ions are described by the multidimensional Langevin equation which is the same as that used for dynamical studies of fission [12],

$$\frac{dq_i}{dt} = (m^{-1})_{ij} p_j, \quad (8)$$

$$\frac{dp_i}{dt} = -\frac{\partial U^J}{\partial q_i} - \frac{1}{2}\frac{\partial}{\partial q_i}(m^{-1})_{jk} p_j p_k - \gamma_{ij}(m^{-1})_{jk} p_k + g_{ij} R_j(t),$$

$$g_{ik} g_{jk} = \gamma_{ij} T^J,$$

where summation is implicitly assumed over repeated indices. The collective mass tensor m_{ij} is the hydrodynamical one and the potential U^J is calculated by

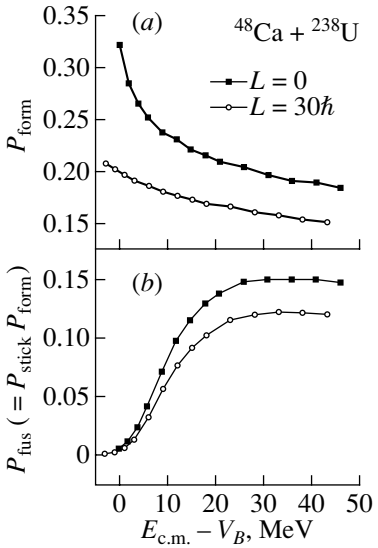

Fig. 3. Calculated formation (a) and fusion probabilities (b).

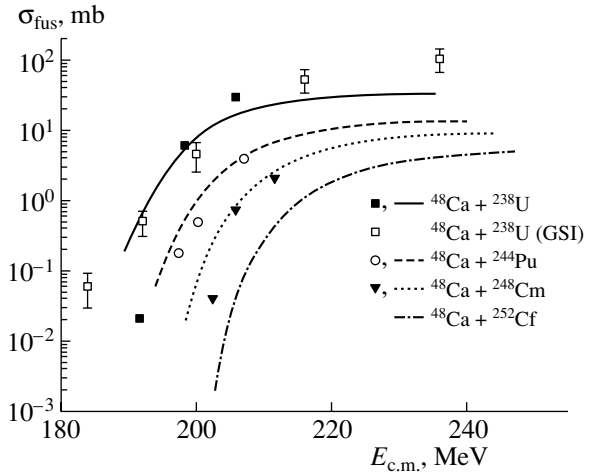

Fig. 4. Calculated excitation functions of fusion reactions for the ^{48}Ca + ^{238}U, ^{48}Ca + ^{244}Pu, ^{48}Ca + ^{248}Cm, and ^{48}Ca + ^{252}Cf systems, together with the available experimental data for GSI [16] and for Dubna [17].

the finite range LDM with two-center parametrization of nuclear shapes [13], added with the rotational energy of the system calculated with the rigid body moment of inertia. The random force $R_i(t)$ is again Gaussian with the normalization 2, and the tensor g_{ij} is now related to the friction tensor γ_{ij}, as is given in the last equation, i.e., the generalized fluctuation–dissipation theorem in the multidimensional case. The friction tensor is calculated with the wall-and-window formula [10]. It is better to take the temperature T^J of the heat bath as that at the conditional saddle point, but it is approximated with that at the contact point, i.e., T_0^J. They are close to each other for the ^{48}Ca-induced reactions. In the present calculations, we only use the relative distance R and the mass asymmetry coordinate α with the other degrees of freedom being frozen. For example, the necking parameter is taken to be 0.8, based on our experiences that it does not change very much while passing over the conditional saddle point in the three-dimensional calculations (though in mass symmetric systems such as ^{100}Mo + ^{100}Mo, the neck degree of freedom appears to play an important role [14]). Figure 2 shows examples of the trajectories on the LDM potential for the ^{48}Ca + ^{238}U system for initial radial momenta and, thus, initial energies being equal to zero. Calculations of many trajectories, starting with various initial radial momenta give a distribution of formation probability $F^J(p_0, T^J)$. By making a convolution of it with the Gaussian distribution of the initial momentum $g^J(p_0, \bar{p}_0^J, T_0^J)$, we obtain the formation probability $P_{\rm form}$:

$$P_{\rm form}(E_{\rm c.m.}) = \int dp_0 F^J(p_0, T^J) g^J(p_0, \bar{p}_0^J, T_0^J). \tag{9}$$

Figure 3a shows the calculated formation probability for the ^{48}Ca + ^{238}U system for $L = 0$ and $30\hbar$. It decreases slowly as the incident energy increases, but stays at very small values even at rather high energies! One could consider this to be an origin of the fusion hindrance, but one should keep in mind that the Gaussian distribution g obtained in the first step plays a crucial role in the second step here. At the first glance, the decreasing energy dependence seems to be peculiar, but the energy dependence of the passing-over probability delicately depends on the friction strength, the potential landscape on the inner side of the conditional saddle point, etc. A detailed analysis with the one-dimensional model will be given elsewhere [15]. In Fig. 3b, the final fusion probability is plotted vs. incident energy. It should be mentioned here that the present model is completely classical, and so there is no quantum tunneling effect included, which limits the lowest energy to be reached.

4. APPLICATION: FUSION LEADING TO SUPERHEAVY ELEMENTS

Fusion cross sections are calculated as usual with the fusion probability,

$$\sigma_{\rm fus} = \pi\lambda^2 \sum_J (2J+1) P_{\rm fus}^J(E_{\rm c.m.}), \tag{10}$$

and are shown in Fig. 4 for the four systems with a ^{48}Ca beam, together with some available measured

cross sections [16, 17]. It is extremely surprising that the calculations reproduce well the experiments on the ^{48}Ca + ^{238}U system without any adjustment, even in the higher energy region. The systematic reproduction of the measured data of the other two systems is also impressive. The only approximation made here is the two-dimensional treatment of the shape evolutions with the neck parameter fixed at 0.8. Experimental measurements are highly desirable in other heavy systems for comparisons with the present calculations.

5. ANALYTICAL METHOD: ONE-DIMENSIONAL SCHEMATIC MODEL [18]

In order to clarify a physical origin of the fusion hindrance, we discuss the simplest case of one-dimension with a parabolic potential around the saddle point and with constant mass m and friction γ. Then, the Langevin Eq. (8) is reduced as follows:

$$\frac{d}{dt}\begin{pmatrix} q \\ p \end{pmatrix} = \begin{pmatrix} 0 & 1/m \\ m\omega^2 & -\beta \end{pmatrix}\begin{pmatrix} q \\ p \end{pmatrix} + \begin{pmatrix} 0 \\ R \end{pmatrix}, \quad (11)$$

where q and p denote the collective coordinate and its conjugate momentum; ω is the frequency of the parabola calculated for each angular momentum state and β is the reduced friction γ/m calculated with the one-body model; and R denotes the random force associated with the friction γ that satisfies the fluctuation–dissipation theorem. Since the equation is linear, we can solve it and obtain an analytical expression of the distribution function in the phase space at any time t, and then, the probability for the system to reach the spherical shape is obtained by integrating the distribution function over the momentum space and the right-half coordinate space of the saddle point. It is a function of time t and of a given initial radial momentum p_0 at the contact point q_0,

$$F^J(T^J, t;\, q_0, p_0) \quad (12)$$
$$= \int_0^\infty \frac{dq}{\sqrt{2\pi}}\,\frac{1}{\sigma_q(t)}\exp\left[-\frac{(q-\langle q(t)\rangle)^2}{2\sigma_q(t)^2}\right],$$
$$\langle q(t)\rangle = A(t)q_0 + B(t)p_0,$$

where $A(t)$ and $B(t)$ are given by the friction strength γ and the frequency ω of the potential at the saddle point. It corresponds to $F^J(p_0, T^J)$ in Eq. (9) as $t \to \infty$. The Gaussian form on the right-hand side of Eq. (12) is due to the Gaussian nature of the random force $R(t)$ assumed in Eq. (11). Since the radial momentum at the contact point has the Boltzmann distribution as obtained in Section 2 with the SFM, the formation probability $P^J_{\rm form}$ at $E_{\rm c.m.}$ is given by folding F^J with the distribution g^J from the right-hand side of Eq. (6) as in Eq. (9) and taking the limit of t to infinity,

$$P^J_{\rm form}(E_{\rm c.m.}) \quad (13)$$
$$= \lim_{t\to\infty}\int_{-\infty}^{\infty} dp_0 F^J(T^J, t; q_0, p_0) g^J(p_0, \bar{p}_0^J, T_0^J)$$
$$= \frac{1}{2}\mathrm{erfc}\left[\left\{\left(x+\sqrt{1+x^2}\right)\sqrt{B_s} - \sqrt{\bar{K}}\right\}\Big/\sqrt{T_0^J + T^J\cdot 2x\left(x+\sqrt{1+x^2}\right)}\right],$$

where $x = \beta/2\omega$ and $\bar{K} = \bar{p}_0^2/2m$ denotes the average remaining radial kinetic energy at the contact point, and $B_s = U_{\rm saddle} - U_{\rm cont}$, i.e., the height of the saddle point $U_{\rm saddle}$ measured from the contact point energy $U_{\rm cont}$. The two temperatures T and T_0 are generally different. The former would be well approximated by the temperature at the saddle, while T_0 is that at the contact point and can be calculated with energy conservation on average.

The SFM without rolling friction and the one-dimensional model for shape evolution would not be realistic enough, but yet we expect that we can understand characteristic aspects of the fusion hindrance observed in experiments.

As is shown in Section 2, the energy dependence of $P_{\rm stick}$ already indicates a necessity of an extrapush energy for the fusion probability to reach 1/2, but according to Eq. (2), the fusion probability is not simply $P_{\rm stick}$, but the product of $P_{\rm stick}$ and $P_{\rm form}$. The latter is given above, and we can easily see that $P_{\rm form}$ itself requires some additional energy for it to reach 1/2. For that, the remaining kinetic energy $\bar{K}$ should be equal to $(x+\sqrt{1+x^2})^2 B_s$ due to the error function of Eq. (13). By the total energy conservation, the additional energy $E_{\rm add} = E_{\rm c.m.} - V_B$, with V_B being the height of the usual barrier as given in the SFM, is simply given by the following formula:

$$E_{\rm add} = (x+\sqrt{1+x^2})^2 B_s + \varepsilon_0 + T_0/2 \quad (14)$$
$$+ U_{\rm cont} - Q - V_B.$$

It should be emphasized here that the friction at the saddle point dramatically enhances the $E_{\rm add}$ through x as is seen in the first term of the right-hand side of Eq. (14). Then, by combining the two formulas given by Eqs. (6) (for $P_{\rm stick}$) and (13), we can analyze the fusion hindrance observed by the experiments. For example, so-called extrapush energy is, roughly speaking, the larger of the additional energies required for $P_{\rm stick}$ and $P_{\rm form}$ to reach 1/2, respectively.

Calculated maximum residue cross sections of the three systems ^{48}Ca + ^{244}Pu, ^{48}Ca + ^{248}Cm, and ^{48}Ca + ^{252}Cf (the factor 1/3 for Møller masses is rather arbitrarily chosen)

System	Prediction of $\Delta E_{\rm shell}$, MeV		$\sigma_{\max}$, pb	E^*, MeV	$\sigma_{\max}$, pb	E^*, MeV
			$3n$		$4n$	
^{48}Ca+^{244}Pu	Liran	−0.23	0.018	30.6	0.018	36.5
	Møller (1/3)	−2.96	7.39	30.1	6.00	35.3
^{48}Ca+^{248}Cm	Liran	−1.37	0.254	31.1	0.045	37.8
	Møller (1/3)	−2.86	4.56	30.4	2.98	35.6
^{48}Ca+^{252}Cf	Liran	−3.24	1.057	32.7	0.095	38.2
	Møller (1/3)	−2.41	0.216	28.8	0.086	33.5

Note: In the experiment for the ^{48}Ca + ^{244}Pu system, the following values are obtained in the $3n$ and $4n$ channels: $\sigma_{\max} \approx 1$ pb and $E_{\rm lab} = 236$ MeV.

Another interesting point for discussion is the cases with extremely small fusion probabilities, in other words, when the mean trajectory is far away from the saddle point. This means that the argument of the error function of Eq. (13) is very large, i.e., the first term is much larger than $\sqrt{\bar{K}}$. Then,

$$P^J_{\rm form}\,(E_{\rm c.m.}) \simeq \frac{1}{\sqrt{4\pi}}\sqrt{\frac{T^J}{B_s}}\exp\left[-\frac{B_s}{T^J}\right], \qquad (15)$$

where we assume $T^J_0 \simeq T^J$. This appears to be similar to Kramers formula [19], but it would be more suitable to call it the inverse Kramers formula, considering the physical situation. Anyhow, such simplification depends on $\bar{K}$ and T_0, which is irrelevant in the Kramers case.

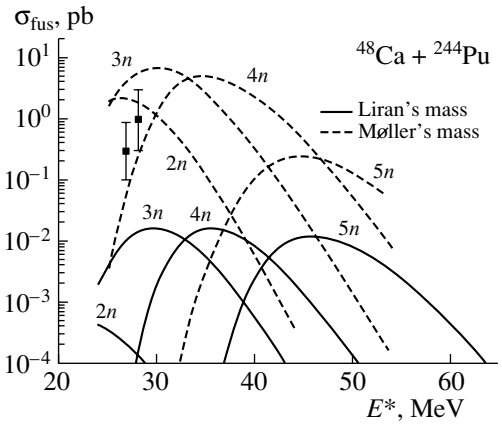

Fig. 5. Calculated excitation functions of xn reactions for the ^{48}Ca + ^{244}Pu system. Møller's shell correction energies are rather arbitrarily reduced by a factor of 1/3.

Sometimes, people use or are tempted to use an approximate formula $\exp[-B_s/T^J]$ for $P_{\rm fus}$ [20]. But as is clearly shown above, only under an extreme condition is $P_{\rm form}$, not $P_{\rm fus}$, given as being proportional to $\exp[-B_s/T^J]$. With such an extreme condition, $P_{\rm stick}$ shows a strong energy dependence, as is exemplified in Fig. 3*a*. Therefore, for $P_{\rm fus}(E_{\rm c.m.})$, we have to take into account both factors, i.e., $P_{\rm stick}$ and $P_{\rm form}$. Otherwise, treatments are physically inconsistent.

6. STATISTICAL DECAY, COMPARISONS WITH RESIDUE CROSS SECTIONS, AND DISCUSSION

In order to predict residue cross sections according to Eq. (1), we need to calculate the survival probability $P_{\rm surv}$. It is essentially given by the ratio between the neutron emission width and the total width, which is almost equal to the fission width,

$$P^J_{\rm surv}(E^*) = \Gamma^J_n(E^*)/(\Gamma^J_n(E^*) + \Gamma^J_f(E^*)). \qquad (16)$$

The neutron width is calculated with the Weisskopf formula, while the fission width is calculated with the Bohr–Wheeler formula [21]. In higher excitations, where more than one neutron can be emitted, we need to use Eq. (16) repeatedly and have to take into account emissions of the other particles. This can be done by the computer programs available. We employ the statistical decay part of HIVAP [22] with the standard parameters, where we take into account neither the collective enhancements [23] nor the Kramers factor [18] in the calculation of fission width in order to avoid introducing additional ambiguities. The former depends on the saddle point deformation, which is supposed to be small in SHEs,

and would cancel with the latter to a certain extent. The LDM fission barrier heights are replaced with those given by the empirical formula [24], though they are negligibly small. The level density parameters are calculated with the Töke–Swiatecki formula [11], but we take into account the dependence of a (for the spherical shape) on the shell correction energy, following the prescription proposed by Ignatyuk [25] with the damping energy E_d being 18 MeV (standard value in HIVAP). Actually, the shell correction energies are the most crucial quantities in residue calculations, because they effectively give the fission barriers for SHEs which have almost zero LDM barriers. But as a matter of course, they are not known experimentally. Of course, there are several theoretical predictions available, which depend essentially on their prediction of the next magic number for proton. Møller predicts $Z = 114$, using single-particle levels of the Saxon–Woods potential, while the mean-field calculations predict $Z = 120$ and 126 [2]. Liran [26] predicts masses, assuming the next magic number to be $Z = 126$. We take those by Møller [27] and Liran as typical examples of mass predictions to calculate residue cross sections for $Z = 114$, 116, and 118 and compare them with the recent Dubna experiments [28]. Figure 5 shows the results for the ^{48}Ca + ^{244}Pu system with two different mass predictions, though we reduced Møller's shell correction energy by a factor of 1/3; otherwise, the absolute values of the residues are a few orders of magnitude larger than the experimentally conceivable one. With the same procedures, we also calculate the residue cross sections for the other two systems. They are summarized in the table. The relative magnitudes are essentially due to the differences in the shell correction energies, though fusion probabilities also depend a little on the systems, as will be seen in Fig. 4. It would be worth making a remark here on an accuracy of the Bohr–Wheeler formula in situations where the temperature is close to the barrier height. Actually, it is the case at least in the beginning of the decay before the shell correction energy is restored to a certain extent. The dynamical studies made numerically show (i) that there are large transient decays (overshooting) and (ii) that the stationary limit is larger than Bohr–Wheeler [29]. The present calculations thus underestimate the fission width and thereby overestimate the residues, which might explain the reason why we need small values of the shell correction energy. But in view of the fact that the problem is on the orders of magnitude, it would not change the situation dramatically. Another way to take into account the features is to calculate the whole process dynamically, at least from the formation to the end of the decay process dynamically, but it requires a huge calculational task over a long time range. It would be difficult to perform even with a modern supercomputer and with the new algorithm developed for the present calculations [30].

In brief, the new two-step model has been found to be extremely successful in reproducing the available fusion data of ^{48}Ca-induced reactions. By combining the present fusion probabilities with the standard statistical decay calculations, we have obtained residue cross sections for $Z = 114$, 116, and 118, which are in good agreement with the recent Dubna experiments, with rather small shell correction energies, much smaller than previously thought. Furthermore, the model is now being applied to other massive systems, such as ^{100}Mo + ^{100}Mo.

ACKNOWLEDGMENTS

We are indebted to B. Bouriquet, B.G. Giraud, and T. Wada for interesting discussions. One of us (D.B.) thanks JSPS for its support and Yukawa Institute for its warm hospitality.

This work is partly supported by the grant-in-aids of JSPS (no. 13640278).

REFERENCES

1. M. G. Mayer and J. H. D. Jensen, *Elementary Theory of Nuclear Shell Structure* (Wiley, New York, 1955).
2. P. Møller and R. Nix, J. Phys. G **20**, 1681 (1994); S. Cwiok *et al.*, Nucl. Phys. A **611**, 211 (1996); M. Bender *et al.*, Eur. Phys. J. A **7**, 467 (2000).
3. S. Hofmann, Rep. Prog. Phys. **61**, 639 (1998); P. Armbruster, Annu. Rev. Nucl. Part. Sci. **50**, 411 (2000).
4. A. B. Balantekin and N. Takigawa, Rev. Mod. Phys. **70**, 77 (1998); M. Dasgupta, D. J. Hinde, N. Rowley, and A. M. Stefanini, Annu. Rev. Nucl. Part. Sci. **48**, 401 (1998).
5. A. B. Quint *et al.*, Z. Phys. A **346**, 199 (1993).
6. W. J. Swiatecki, Phys. Scr. **24**, 113 (1981); S. Bjornholm and W. J. Swiatecki, Nucl. Phys. A **391**, 471 (1982).
7. P. Fröbrich *et al.*, Nucl. Phys. A **406**, 557 (1983).
8. Y. Abe *et al.*, in *Proceedings of YKIS01*, Prog. Theor. Phys. Suppl., No. 146, 104 (2002); C. W. Shen, G. Kosenko, and Y. Abe, Phys. Rev. C **66**, 061602(R) (2002).
9. D. H.E. Gross and H. Kalinowski, Phys. Rep. **45**, 175 (1978).
10. J. Blocki *et al.*, Ann. Phys. (N.Y.) **113**, 330 (1978).
11. J. Töke and W. J. Swiatecki, Nucl. Phys. A **372**, 141 (1981).
12. T. Wada *et al.*, Phys. Rev. Lett. **70**, 3538 (1993).
13. K. Sato *et al.*, Z. Phys. A **290**, 145 (1979).
14. J. Bao, D. Boilley, and Y. Abe (in press).
15. D. Boilley, J. D. Bao, and Y. Abe, submitted to Eur. Phys. J.
16. W. Q. Shen *et al.*, Phys. Rev. C **36**, 115 (1987).
17. M. G. Itkis *et al.*, Nuovo Cimento A **111**, 783 (1998).

18. Y. Abe, D. Boilley, B. Giraud, and T. Wada, Phys. Rev. E **61**, 1125 (2000); see also [8, 14, 15].
19. H. A. Kramers, Physica **VII**(4), 284 (1940).
20. M. Ohta, this Proceedings.
21. Y. Abe *et al.*, Phys. Rep. **275** (2–3) (1996).
22. W. Reisdorf, private communication.
23. G. Hansen and A. S. Jensen, Nucl. Phys. A **406**, 236 (1983).
24. M. Dahlinger *et al.*, Nucl. Phys. A **376**, 94 (1982).
25. A. V. Ignatyuk *et al.*, Sov. J. Nucl. Phys. **21**, 255 (1975).
26. S. Liran, A. Marinov, and N. Zeldes, Phys. Rev. C **62**, 047301 (2000).
27. P. Møller *et al.*, At. Data Nucl. Data Tables **59**, 185 (1995).
28. Yu. Oganessian *et al.*, Phys. Rev. Lett. **83**, 3154 (1999) (and private communication).
29. X. Z. Wu *et al.*, in *Proceedings of NIKKO91,* AIP Conf. Proc. **250**, 245 (1992).
30. C. W. Shen and Y. Abe (in press).

Physics of Atomic Nuclei, Vol. 66, No. 6, 2003, pp. 1065–1070. From Yadernaya Fizika, Vol. 66, No. 6, 2003, pp. 1101–1106.

The Mechanism of Compound Nucleus Formation in Complete Fusion of Two Massive Nuclei*

V. V. Volkov

Joint Institute for Nuclear Research, Dubna, Moscow oblast, 141980 Russia

Received August 28, 2002

Abstract—Using a comparative analysis of modern approaches to the description of the complete fusion process and their predictions on the synthesis of heavy and superheavy elements, an attempt has been made to reveal a realistic picture of the mechanism of the compound nucleus formation in complete fusion of two massive nuclei. © *2003 MAIK "Nauka/Interperiodica".*

1. INTRODUCTION

In the paper, the mechanism of the compound nucleus formation in complete fusion of two massive nuclei is discussed. Major attention is paid to the reactions used for the synthesis of superheavy elements (SHE).

Figure 1 shows a schematic picture of the complete fusion process according to different theoretical approaches. In the Macroscopic Dynamical Model (MDM) [1], it is a process of fusion of two drops of viscous nuclear liquid. In contrast to that, according to the DiNuclear System Concept (DNSC) [2], the nuclei of an evolving nuclear system keep their individuality throughout the entire fusion process. In the Fluctuation–Dissipation Model (FDM) [3], again two drops of viscous nuclear liquid are fused as in the MDM. However, the shape of the nuclear system evolving into a compound nucleus is different. Figure 1*d* shows the process of the nucleon collectivization in complete fusion of two nuclei, according to the Model of Collectivization of Nucleons (MCN) [4]. Such a wide variety of ideas on the complete fusion process attest to the fact that the mechanism of the compound nucleus formation remains a problem still to be solved.

Why so far is there no clear picture of this important nuclear process? There are two serious difficulties in solving this problem.

The first one consists in the closed character of the process of complete nuclear fusion. Fusing nuclei do not send any signals that would allow one to reveal the mechanism of the compound nucleus formation. Experimentalists detect products of decay of compound nuclei. But a compound nucleus "forgets" the history of its formation.

The second difficulty is the very high complexity of the theoretical analysis of this process. Fusion of two multinucleon nuclear systems into a new one is a very complicated problem for theoreticians.

How do theoreticians act in such situation? They create theoretical models using some simplifications of reality. A theoretical model may be considered as

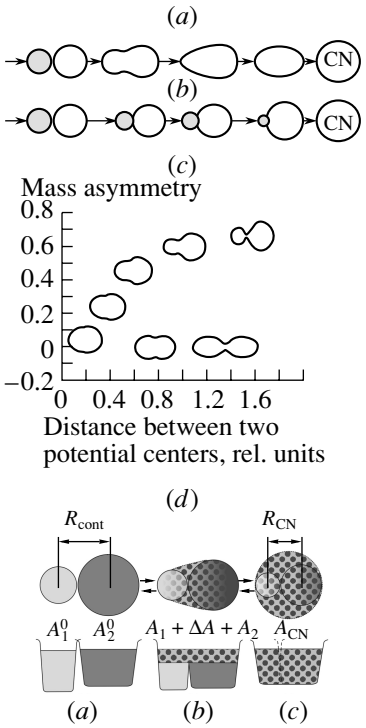

Fig. 1. Schematic illustration of the process of the compound nucleus formation in the framework of different approaches: (*a*) macroscopic dynamical model [1], (*b*) dinuclear system concept [2], (*c*) fluctuation–dissipation model [3], and (*d*) model of collectivization of nucleons [4].

*This article was submitted by the author in English.

1063-7788/03/6606-1065$24.00

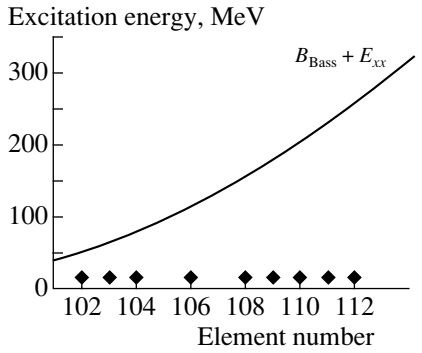

Fig. 2. The excitation energy of compound nuclei of the 102–112 elements synthesized in cold fusion reactions (HI, $1n$); diamonds are the experimental data [5], and the curve is the result of calculations with the use of the MDM [6].

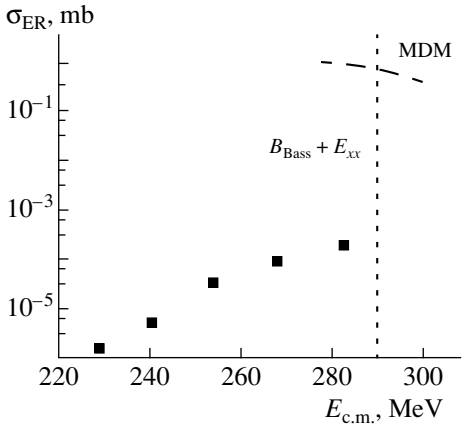

Fig. 3. The evaporation residue cross section in the reaction ^{110}Pd + ^{110}Pd; squares are the experimental data [7], and the dashed curve is the result of calculations with the use of the MDM [2].

some theoretical image of the real nuclear process. Simplifications can be made in different ways, and as a result, we obtain several theoretical pictures of one and the same nuclear process. As time goes, we get accustomed to theoretical images and begin to take them for reality. However, reality and its theoretical image may differ quite greatly.

2. THE MACROSCOPIC DYNAMICAL MODEL

The MDM [1] was the first model that described the whole history of complete fusion of two nuclei starting from the contact of their surfaces and ending by the compound nucleus formation.

In this model, two important simplifications of the reality were used. The first one was that colliding nuclei containing protons and neutrons and having shell structures were replaced by drops of a hypothetical viscous nuclear liquid. The second simplification was that the fusion of two nuclei was considered as a purely dynamical process and was described by classical equations of motion.

The MDM revealed such important aspects of fusion of two massive nuclei as quasifission, extra-push, and extra-extrapush. However, serious difficulties were encountered in attempts to describe reactions used for the synthesis of superheavy elements.

Figure 2 shows the excitation energies of compound nuclei with the charge numbers Z from 102 to 112 synthesized in cold fusion reactions. The experimental data are shown by the diamonds, and the solid curve shows calculation results obtained with the use of the MDM [6]. The calculated data reflect enormous values of the extra-extrapushes in these reactions.

Figure 3 shows the evaporation residue cross section $\sigma_{ER}(E)$ in the reaction ^{110}Pd + ^{110}Pd. Experimental data are marked by the squares, and the curve represents results of calculations with the use of the MDM [2]. The difference between the experiment and calculations reflects the influence of the quasifission channel, which dominates in this reaction. However, in the MDM, competition between the complete fusion and quasifission channels is not possible. If the bombarding energy is higher than the sum of the Coulomb barrier and the extra-extrapush, the complete fusion process is realized; if it is lower, the quasifission process is realized [1].

3. THE DINUCLEAR SYSTEM CONCEPT

The DNSC is not a traditional theoretical model. The DNSC gives a qualitative picture, the scenario of the complete fusion process, similarly to the compound nucleus concept giving a qualitative characteristic of properties of excited compound nuclei.

The DNSC is based on the statement: "Complete fusion of nuclei and deep-inelastic-transfer reactions (DITR) are similar nuclear processes." Indeed, in both processes, full dissipation of the collision kinetic energy occurs and the same conservative and dissipative forces act. On the collision angular momentum scale, there is a section where both processes can be realized. These two processes differ only in one aspect: the nucleus–nucleus potential $V(R)$ has a "pocket" in the complete fusion process; in DITR, there is no such "pocket."

What does the statement on the similarity of the complete fusion process and DITR give us? In contrast to the complete fusion process, DITR are open reactions. The study of mass, charge, energy, and angular distribution of DITR products permits one to reveal a realistic picture of nuclear interaction in deep inelastic collisions, in which the relative velocity

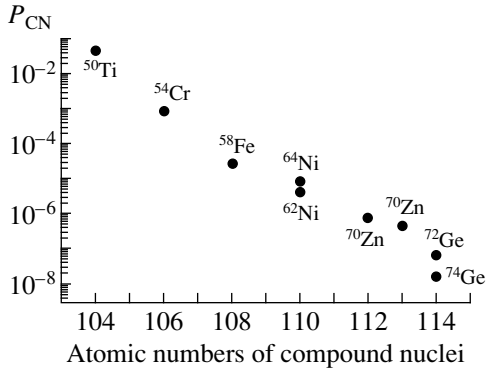

Fig. 4. The probability of complete fusion in the competition with quasifission, P_{CN}, in the cold fusion reactions (HI, $1n$) [18].

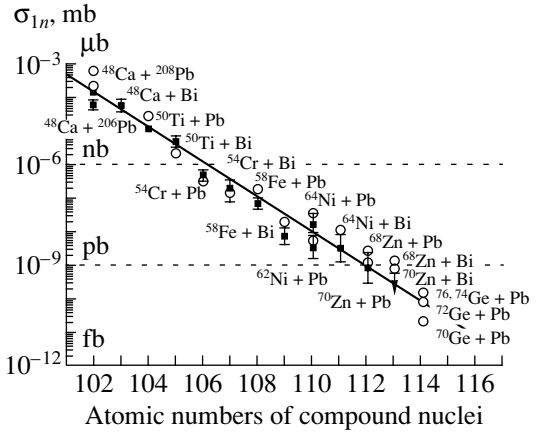

Fig. 5. The production cross section of elements with Z from 102 to 114 synthesized in cold fusion reactions. The closed squares are experimental data, and the circles are the data calculated in accordance with the DNSC [15].

of nuclei drops to zero [8]. It is this unique information about the interaction between two nuclei in the dinuclear system (DNS) that is used to reveal the mechanism of the compound nucleus formation [2].

According the DNSC, the scenario of the processes of complete nuclear fusion and quasifission is the following [9]:

(i) At the capture stage, after the full dissipation of the collision kinetic energy, a DNS is formed.

(ii) A DNS evolves in time by means of nucleon transfer from one nucleus to another. There are two ways of the system's evolution: the first one leads to complete fusion of nuclei; the second one, to the symmetric shape of the system. The first way is terminated by the compound nucleus formation. The second way is terminated by the DNS decay into two nearly equal fragments. It means that the quasifission process takes place.

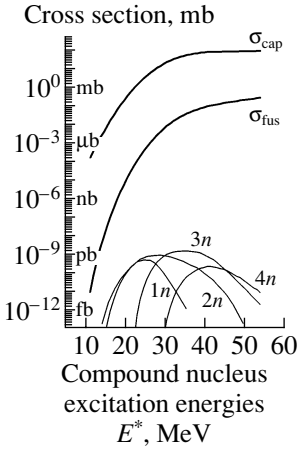

Fig. 6. Calculations of the production cross section of element 114 synthesized in the reaction ^{244}Pu + ^{48}Ca; σ_{cap} is the capture cross section, σ_{fus} is the cross section of the compound nucleus formation, and the lower curves reflect the competition between fission and emission of different numbers of neutrons in the excited compound nucleus [15].

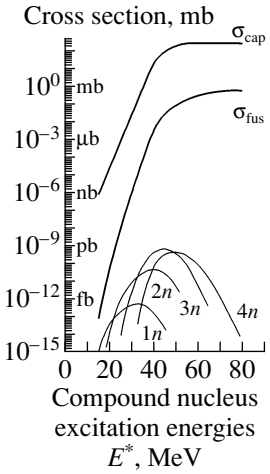

Fig. 7. The same as in Fig. 6, but for the synthesis of element 116 in the reaction ^{248}Cm + ^{48}Ca [13].

(iii) The DNS nuclei retain their individuality during the DNS evolution. This important peculiarity of the DNS evolution is the consequence of the shell structure of nuclei.

The DNSC reveals two important peculiarities in complete fusion of massive nuclei [9]:

(i) The existence of the inner fusion barrier B^*_{fus} on the way to complete fusion. The value of B^*_{fus} determines the energy threshold for the fusion of two massive nuclei. The DNS initial excitation energy E^*_i has to be higher than B^*_{fus}, $E_i \geq B^*_{fus}$.

(ii) The competition between the complete fusion and quasifission channels in the initial DNS, which

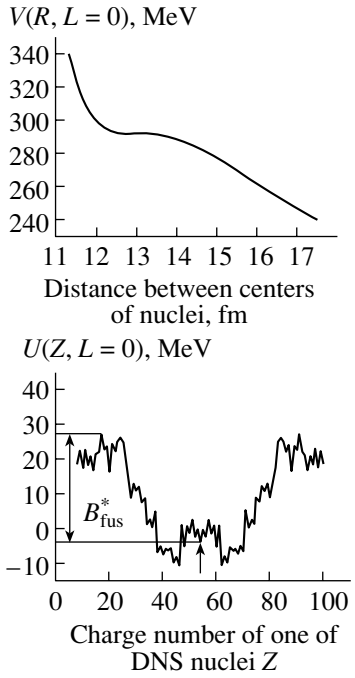

Fig. 8. The nucleus–nucleus potential (above) and the DNS potential energy (below) in the reaction $^{136}Xe + {}^{136}Xe$ [18].

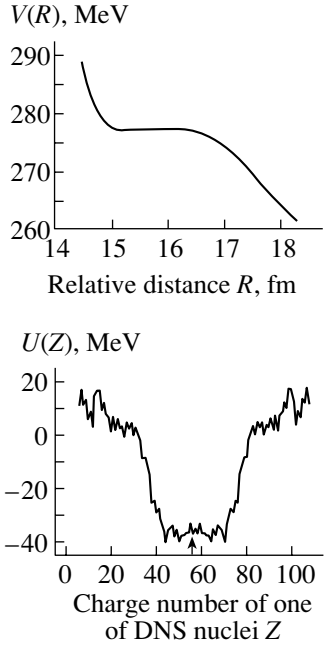

Fig. 9. The nucleus–nucleus potential (above) and the DNS potential energy (below) in the reaction $^{149}La + {}^{149}La$ (calculations by G.G. Adamian and N.V. Antonenko).

is formed at the capture stage. The competition between these two channels is the consequence of the statistical nature of the DNS evolution.

On the basis of the DNSC, models of competition between complete fusion and quasifission [2, 10, 11] and models of mass distribution in quasifission [12, 13] were created. Using these models, all important aspects of the synthesis of heavy and superheavy elements have been analyzed:

production cross sections in the cold and warm synthesis of heavy and superheavy elements have been calculated, and the decisive role of quasifission in cold synthesis has been revealed [14–16];

excitation energies of compound nuclei with atomic number from 102 to 114 synthesized in cold fusion reaction have been estimated [17, 18];

a sharp decrease in the production cross section in symmetric reactions between massive nuclei has been revealed [17, 18];

the role of shell effects in the mass distribution of quasifission fragments in reactions used for the warm synthesis of SHE has been interpreted and described [12, 13].

Figure 4 shows the probability of complete fusion in the competition with quasifission in cold fusion reactions. These data demonstrate that quasifission is the main factor in decreasing the production cross section with Z of a compound nucleus in cold fusion reactions.

In Fig. 5, experimental data on the production cross sections of elements with atomic numbers from 102 to 112 synthesized in cold fusion reactions are compared with the calculated data. One can see satisfactory agreement.

Figure 6 demonstrates calculations of the production cross section of element 114 in the reaction $^{244}Pu+{}^{48}Ca$. The upper curve is the capture cross section, and the curve next to it represents the compound nucleus production cross section. The lower curves reflect the competition between fission and neutron emission in the course of deexcitation of the compound nucleus. The experimental data on the production cross section of $^{288}114$ ($4n$ channel) is equal to $0.5^{+0.6}_{-0.3}$ pb [19]. The calculations were made while the experiment was still in progress. Figure 7 shows the same calculations for the reaction $^{248}Cm + {}^{48}Ca$ used for the synthesis of element 116. The experimental data on the production cross section of $^{292}116$ ($4n$ channel) is equal to $0.5^{+0.8}_{-0.3}$ pb [20]. From Fig. 8, one can see why symmetric reactions are not promising for the synthesis of SHE.

One can say that, in the framework of the DNSC and models created on its basis, it is possible to interpret and describe all main properties of the process of complete fusion of two massive nuclei.

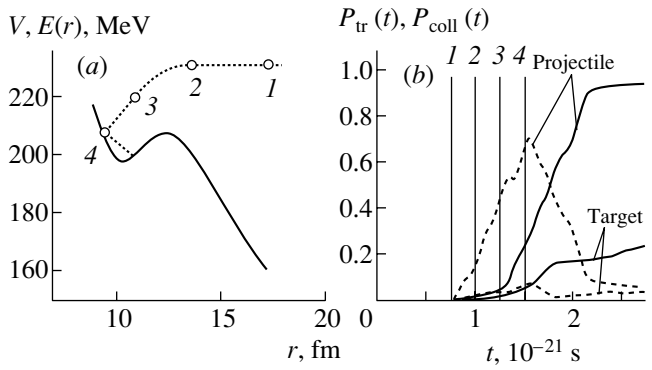

Fig. 10. (*a*) The interaction potential and relative motion trajectory for the collision of ^{48}Ca and ^{248}Cm at the energy $E_{cm} = 230$ MeV. (*b*) Probabilities of the valence neutron transfer (dashed curve) and neutron collectivization (solid curve) [4].

4. THE FLUCTUATION–DISSIPATION MODEL

In the FDM [3], the same simplification for nuclei as in the MDM [1] is used. Nuclei are considered as drops of viscous nuclear liquid. However, two new important factors have been introduced into the description of the fusion process: statistical fluctuation in the interaction of colliding nuclei and shell corrections in the calculation of the nuclear system potential energy. These improvements permit one to describe

production cross sections of SHE in warm fusion reactions;

mass distributions of fission and quasifission products;

a contribution to the symmetric part of the fragment mass distribution from quasifission and fission of a compound nucleus.

However, there is an aspect in which predictions of the FDM cause some doubt. It is the use of symmetric reactions for the synthesis of SHE. The authors of the FDM suggested that the reaction $^{149}_{57}$La + $^{149}_{57}$La $\rightarrow$ ^{198}114 should be used for the synthesis of element 114 [3]. In their calculations, they obtained the optimal excitation energy of the compound nucleus ^{198}114 20 MeV and the production cross section $\sigma_{ER} \sim 10$ pb.

The analysis of this reaction in terms of the DNSC shows that B^*_{fus} is equal to $\sim$50 MeV and the quasifission barrier B_{qf} is lower than 1 MeV (see Fig. 9). The probability of the compound nucleus formation—the factor P_{CN}—is equal to 10^{-15} and the compound nucleus formation cross section will be $\sim 10^{-4}$ pb.

However, we cannot check this prediction of the FDM since the target nucleus and the projectile are radioactive nuclei with half-lives equal to 1 s. If we used an extrapolation of experimental data to the production cross section of symmetric reactions between massive nuclei [21], we could obtain a value of less than 1 fb for the reaction ^{149}La + ^{149}La.

5. THE CONCEPT OF COLLECTIVIZATION OF NUCLEONS IN THE FUSION OF TWO NUCLEI

In works of Prof. Zagrebaev [4], a new concept of the complete fusion process was proposed—the concept of collectivization of nucleons of two fused nuclei. This concept is based on a rather simple model. Each nucleus has an inert core and one valence neutron. After the dissipation of the collision kinetic energy, two cores come into close contact for a certain period of time and the neutron can easily transit from one nucleus to another. It becomes a neutron in common. Figure 10, taken from Prof. Zagrebaev's publications, shows the collectivization of valence neutrons in the reaction ^{248}Cm + ^{48}Ca (230 MeV). The probability of collectivization of a valence neutron of ^{48}Ca reaches a value equal to unity rather quickly.

But what happens in reality? From the figure, one can see that the DNS excitation energy is higher than 20 MeV. The major part of the excitation energy is concentrated in the ^{248}Cm nucleus. The ^{248}Cm level density is very high, with the levels overlapping very strongly. The ^{248}Cm nucleus will turn out to be a nuclear labyrinth for the transferred neutron and this neutron will not find its way back to the ^{48}Ca nucleus.

The level density in the excited ^{248}Cm nucleus will be orders of magnitude higher than that in the ^{48}Ca nucleus. This means that a "common" neutron spends much more time in the ^{248}Cm nucleus than in the ^{48}Ca nucleus.

In the case of a proton transfer from ^{48}Ca to ^{248}Cm, the DNS potential energy decreases by approximately 5 MeV. A proton finds itself in an excited state. It very quickly loses its excitation energy and transits to lower states. From the lower states, a proton never returns to the calcium nucleus.

Proceeding from these considerations, one can say that the interaction of two nuclei after the dissipation of collision kinetic energy and formation of a DNS

is characterized by the privatization of nucleons but not by their collectivization. In complete fusion, a heavy nucleus privatizes all the nucleons of a lighter nucleus. In quasifission, a lighter nucleus privatizes part of the nucleons of a heavy nucleus.

6. CONCLUSIONS

(i) The DNSC is based on information on the interaction of two massive nuclei in a deep-inelastic collision, which has been obtained in the study of deep-inelastic transfer reactions.

(ii) In the framework of the DNSC and models created on its basis, it became possible to interpret and successfully describe all important aspects of complete fusion of two massive nuclei.

(iii) One can say that today the DNSC gives the most realistic picture of the complete fusion process of massive nuclei and the mechanism of the compound nucleus formation.

ACKNOWLEDGMENTS

I would like to thank G.G. Adamain, N.V. Antonenko, E.A. Cherepanov, A.K. Nasirov, and W. Scheid for the fruitful discussion of the problem of complete fusion of massive nuclei.

REFERENCES

1. W. J. Swiatecki, Phys. Scr. **24**, 113 (1981); S. Bjornholm and W. J. Swiatecki, Nucl. Phys. A **391**, 471 (1982); J. P. Blocki, H. Feldmeier, and W. J. Swiatecki, Nucl. Phys. A **459**, 145 (1986).
2. V. V. Volkov, Izv. Acad. Nauk SSSR, Ser. Fiz. **50**, 1879 (1986); N. V. Antonenko, E. A. Cherepanov, A. K. Nasirov, *et al.*, Phys. Lett. B **319**, 425 (1993); Phys. Rev. C **51**, 2635 (1995).
3. Y. Aritomo, T. Wada, M. Ohta, and Y. Abe, Phys. Rev. C **55**, R1011 (1997); **59**, 796 (1999).
4. V. I. Zagrebaev, Phys. Rev. C **64**, 034606 (2001).
5. S. Hofmann, in *Proceedings of the VI International School–Seminar on Heavy Ion Physics, Dubna, 1997*. Ed. by Yu. Ts. Oganessian and R. Kalpakchieva (World Sci., Singapore, 1998), p. 385.
6. A. G. Popeko, Nuovo Cimento A **110**, 1137 (1997).
7. W. Morawek, T. Ackermann, T. Brohn, *et al.*, Z. Phys. A **341**, 75 (1991).
8. V. V. Volkov, Phys. Rep. **44**, 93 (1978); *Nuclear Reactions with Deep-Inelastic Transfer* (Énergoizdat, Moscow, 1982).
9. V. V. Volkov, E. A. Cherepanov, N. V. Antonenko, and A. K. Nasirov, in *Proceedings of the XV Nuclear Physics Divisional Conference "Low Energy Nuclear Dynamics", St. Petersburg, 1995*, Ed. by Yu. Ts. Oganessian, R. Kalpakchieva, and W. von Oertzen (World. Sci., Singapore, 1995), p. 336.
10. E. A. Cherepanov, V. V. Volkov, N. V. Antonenko, and A. K. Nasirov, in *Proceedings of the International Conference "Heavy Ion Physics and Its Application", Lanzhou, China, 1995*, Ed. by Y. X. Luo, G. M. Jin, and J. Y. Liu (World Sci., Singapore, 1996), p. 272.
11. G. G. Adamian, N. V. Antonenko, W. Scheid, and V. V. Volkov, Nucl. Phys. A **627**, 361 (1997).
12. A. Díaz-Torres, G. G. Adamian, N. V. Antonenko, and W. Scheid, Phys. Rev. C **64**, 024604 (2001).
13. E. A. Cherepanov, in *Proceedings of the International Workshop on Fusion Dynamics at the Extremes, Dubna, 2000,* Ed. by Yu. Ts. Oganessian and V. I. Zagrebaev (World Sci., Singapore, 2001), p. 186.
14. V. V. Volkov, in *Proceedings of the 4th International Conference on Dynamical Aspects of Nuclear Fission, Častá-Papiernička, Slovak Republic, 1998,* Ed. by Yu. Ts. Oganessian, J. Kliman, and Š. Gmuca (World Sci., Singapore, 2000), p. 324.
15. E. A. Cherepanov, Pramana, J. Phys. **53**, 619 (1999).
16. G. G. Adamian, N. V. Antonenko, W. Scheid, and V. V. Volkov, Nucl. Phys. A **633**, 409 (1998).
17. V. V. Volkov, G. G. Adamian, N. V. Antonenko, *et al.*, Nuovo Cimento A **110**, 1127 (1997).
18. V. V. Volkov, G. G. Adamian, N. V. Antonenko, *et al.*, in *Proceedings of the VI International School–Seminar on Heavy Ion Physics, Dubna, 1997,* Ed. by Yu. Ts. Oganessian and R. Kalpakchieva (World Sci., Singapore, 1998), p. 423.
19. Yu. Ts. Oganessian, V. K. Utyonkov, Yu. V. Lobanov *et al.*, Phys. Rev. Lett. **83**, 3154 (1999); Phys. Rev. C **62**, 041604 (2000); Yad. Fiz. **63**, 1769 (2000) [Phys. At. Nucl. **63**, 1679 (2000)].
20. Yu. Ts. Oganessian, V. K. Utyonkov, Yu. V. Lobanov, *et al.*, Phys. Rev. C **63**, 011301 (2001); Yu. Ts. Oganessian, V. K. Utyonkov, and K. J. Moody, Yad. Fiz. **64**, 1427 (2001) [Phys. At. Nucl. **64**, 1349 (2001)].
21. P. Armbruster, Rep. Prog. Phys. **62**, 465 (1999).

Physics of Atomic Nuclei, Vol. 66, No. 6, 2003, pp. 1071–1085. From Yadernaya Fizika, Vol. 66, No. 6, 2003, pp. 1107–1121.

Synthesis of Heavy and Superheavy Elements by Reactions of Massive Nuclei*

G. Fazio[1], G. Giardina[1], A. Lamberto[1], R. Ruggeri[1], F. Bonsignore[2], R. Palamara[3], A. I. Muminov[4], A. K. Nasirov[4]***, B. Benoit[5], F. Hanappe[5], T. Materna[5], and L. Stuttgé[6]**

[1] *INFN, Sezione di Catania; Dipartimento di Fisica dell'Università di Messina, Italy*

[2] *Dipartimento di Fisica della Materia e Tecnologie Fisiche Avanzate dell'Università di Messina, Italy*

[3] *Dipartimento PAU dell'Università di Reggio Calabria, Italy*

[4] *Heavy Ion Physics Department, Institute of Nuclear Physics, Tashkent, Uzbekistan*

[5] *Université Libre de Bruxelles, Belgium*

[6] *Institut de Recherches Subatomiques, Strasbourg, France*

Received November 11, 2002

Abstract—By comparing theoretical and experimental excitation functions of evaporation residues resulting from the same compound nucleus or heavy and superheavy nuclei, it is possible to understand the effect of the entrance channel and the shell structure of reacting nuclei on the fusion mechanism. The competition of complete fusion with the quasifission process is strongly related to the intrinsic fusion barrier $B^*_{\rm fus}$ and the quasifission barrier $B_{\rm qf}$, as well as the size of the well in the nucleus–nucleus potential. In our calculations of the excitation functions for capture, fusion, and evaporation residues, we use the relevant variables such as mass asymmetry of nuclei in the entrance channel, potential energy surface, driving potential, spin distribution, and surviving probability of compound nucleus that are responsible for the mechanism of the fusion–fission process. As a result, we obtain a beam energy window for the capture of the nuclei before the system fuses and the Γ_n/Γ_f ratio at each step along the deexcitation cascade of the compound nucleus. Calculations performed in the framework of the model taking into account the nuclear shell effect and shape of colliding nuclei allow us to reach useful conclusions about the mechanism of the fusion–fission process and the production of the evaporation residues. We analyze the ^{40}Ar + ^{176}Hf, ^{86}Kr + ^{130}Xe, and ^{124}Sn + ^{92}Zr reactions leading to ^{216}Th*; the ^{32}S + ^{182}W and ^{60}Ni + ^{154}Sm reactions leading to ^{214}Th*; the ^{48}Ca + ^{248}Cm reaction leading to the ^{296}116 compound nucleus; and the ^{48}Ca + ^{249}Cf reaction leading to the ^{297}118 compound nucleus. © *2003 MAIK "Nauka/Interperiodica"*.

1. INTRODUCTION

Comparison of excitation functions of evaporation residues (ERs) measured for different mass-asymmetry reactions but leading to the same compound nucleus (CN) allows us to analyze the importance of the entrance channel effect on the fusion–fission reaction mechanism in collisions of massive nuclei. Often, excitation functions of ERs measured in various reactions leading to the same CN are different not only in the position of the maximum but also in the value of their maxima. The question of what characteristics of nuclei or what relevant degrees of freedom of the fusion–fission process are responsible for such a difference in ER cross sections is a well-known problem in the search for optimal conditions for the synthesis of new superheavy elements.

The difference between measured data on the cross section of ERs for reactions leading to the same CN can be explained by the difference in the excitation functions of fusion or survival probability of the excited CN. A decrease in fusion cross sections is connected with an increase in events coming to the quasifission process. Quasifission reactions are binary processes that exhibit some of the characteristics of fusion–fission events, such as a full relaxation of the relative kinetic energy and a considerable transfer of mass between the two fragments. The basic difference between fusion–fission and quasifission is that CN formation is not achieved in the latter mech-

*This article was submitted by the authors in English.

** e-mail: giardina@nucleo.unime.it

*** Also at Bogolyubov Laboratory of Theoretical Physics, JINR, Dubna, Russia; Institut für Theoretische Physik der Justus-Liebig-Universität, Giessen, Germany.

anism. Quasifission can be thought of as a bridge between deep-inelastic scattering, where the relative kinetic energy between the fragments can be fully damped, but the mass asymmetry of the entrance channel is mostly preserved, and CN fission reactions, where all memory of the entrance channel is lost [1–8]. The entrance-channel dependence of the distribution of reaction strength has been studied for three systems, namely, $^{32}S + {}^{182}W$, $^{48}Ti + {}^{166}Er$, and $^{60}Ni + {}^{154}Sm$, which all lead to the compound system ^{214}Th in complete-fusion reactions [8]. The maximum contribution of complete-fusion–fission processes to the fissionlike cross section is estimated on the basis of expected angle–mass correlations for such reactions. The results show a strong entrance-channel dependence as predicted by the extrapush model.

An increase in the role of entrance-channel effects was noted in [9], where the reactions with ^{40}Ar and ^{84}Kr led to the same CN, ^{200}Po. Comparison of the measured excitation functions for the isotopes $^{200-xn}Po$ produced in the $^{40}Ar + {}^{160}Dy$ and $^{84}Kr + {}^{116}Cd$ reactions showed that the (Ar, xn) cross sections are larger by factors of ~ 2 to ~ 4 than the corresponding (Kr, xn) values. In the experiment of this group studying of the formation and decay of ^{158}Er produced in reactions with either ^{40}Ar or ^{84}Kr, the deexcitation of that CN by neutron evaporation was independent of its production mode [10]. In reactions of massive projectile and target nuclei, the competition between complete fusion and quasifission appears at the stage of CN formation, in addition to the increase in its fission probability. Even in the case of mass-asymmetric collisions, an inhibition in the fusion was recently observed in the experiment by Hinde and his colleagues [11]. The $^{12}C + {}^{204}Pb$, $^{19}F + {}^{197}Au$, and $^{30}Si + {}^{186}W$ reactions leading to the same ^{216}Ra nucleus have been studied. The authors stressed that there is a significant inhibition of the reduced fusion cross section ($\tilde{\sigma} = \sigma/\pi\lambda^2$) for reactions with ^{19}F and ^{30}Si, being 0.64 ± 0.09 and 0.57 ± 0.08, respectively, of those for ^{12}C.

The dinuclear system (DNS) concept [12] reveals the reason for the strong decrease in the fusion cross section for a massive system or for a symmetric entrance channel. In calculations of the excitation function of ERs, the choice of suitable parameters allows a description of experimental data, but the peculiarity of the reaction mechanism of projectile–target pairs with different mass asymmetry is still unclear. It is well known that it is difficult to measure the fusion cross section directly due to the fact that establishing the origin of fusion–fission reaction fragments is ambiguous.

Calculations based on the DNS concept show [13] that entrance-channel effects are important to describe the experimental data in the case of collisions of massive nuclei. It allows us to estimate the decrease in fusion probability due to an increase in the quasifission process. In the present work, we consider a set of experimental data on the production of ERs in the reactions with a different entrance-channel asymmetry, but leading to the same $^{216}Th^*$ and $^{214}Th^*$ CN. We also give the results on the $^{296}116$ and $^{297}118$ CN and the excitation functions of the ER formation.

It will be shown that competition between complete fusion and quasifission depends on mass asymmetry and peculiarities of shell structure.

The aim of this paper is to establish these effects and to analyze the role of the intrinsic fusion barrier, the quasifission barrier, and the excitation energy of both the DNS and the CN. The partial capture cross sections are calculated by solving equation of motions for relative distance and orbital angular momentum taking into account dissipation of collective kinetic energy [13, 14]; i.e., the value of critical angular momentum at which capture occurs at a given beam energy is calculated dynamically. The partial fusion cross section (spin distribution of CN) is calculated from the capture cross section taking into account competition between complete-fusion and quasifission processes. The competition is determined by a factor P_{CN} which is calculated statistically. The validity of using of the statistical method is justified due to the fact that, in quasifission, a full relaxation of the relative kinetic energy and mass (charge) asymmetry between the two fragments takes place [2–8].

The fact that calculation of the competition between complete-fusion and quasifission processes in the framework of the model under discussion includes the nuclear shell effect and shape of colliding nuclei allows us to reach useful conclusions about the mechanism of the fusion–fission process. The possibility of collisions of nuclei by different orientations of their axial symmetry axis is considered.

2. CAPTURE, FUSION, AND EVAPORATION RESIDUE PRODUCTION IN THE DNS CONCEPT

According to the DNS concept, the complete fusion between heavy ions is a complete transfer of all the nucleons of the projectile (lighter) nucleus into the target (heaviest) nucleus forming a CN of complete shape. Due to the large inertia parameter of deformation, the change in nuclear shape is not so large and the size of the overlapping region of nuclei is small: it is about 5–6% of the total volume. The nucleons of the interacting nuclei form a shell structure that is retained during interaction. Fusion

is considered as a two-stage process. The first step is overcoming the Coulomb barrier in motion along the axis connecting nuclear centers by nuclei at the incoming stage of collision and formation of a nuclear composite (molecular-like so-called dinuclear system). This stage is called capture. The second one is transformation of the DNS into a more compact CN, overcoming the intrinsic barrier ($B^*_{\rm fus}$) on the potential energy surface during evolution on the mass charge-asymmetry axis. In the DNS concept, the potential energy surface is built as a function of the mass charge-asymmetry and relative distance between centers of nuclei forming DNS.

For light and intermediate nuclear systems or for heavy nuclear systems with larger mass asymmetry, this barrier is equal to zero and capture immediately leads to fusion. Therefore, in those cases, the fusion cross section is calculated in the framework of well-known models [15–18]. The $B^*_{\rm fus}$ is determined by the difference between the maximum value of the driving potential ($U(Z, A, R_m)$) and its value at the point corresponding to the initial charge asymmetry of the considered reaction (Fig. 1). If the excitation energy of the dinuclear system, $E^*_{\rm DNS} = E_{\rm c.m.}V(R_m, \ell)$, is not sufficient to overcome $B^*_{\rm fus}$, then the DNS decays into two fragments; i.e., it undergoes quasifission. Quasifission occurs due to motion along relative internuclear distance R and depends on the $V(R)$ nucleus–nucleus interaction potential [see below Eq. (7)]. At capture, the DNS is in a potential well (Fig. 1, bottom). Thus, for quasifission, it is necessary to overcome the barrier ($B_{\rm qf}$) which is equal to the depth of well of $V(R)$. The driving potential is significant in considerations of the fusion process as the motion of a system along the charge (mass) asymmetry degree of freedom.

Here, $U(Z, A, R_m)$ becomes more important to the process. The $U(Z, A, R_m)$ is extracted from the potential energy surface $U(A, Z; R, \ell)$ [see below Eq. (1)], which is a function of the masses (charges) A_1, A_2 ($A_2 = A_{\rm tot} - A_1$) of fragments forming the DNS at the values R_m of the internuclear distance corresponding to the minimum of their nucleus–nucleus potential $V(R)$. The distribution of neutrons between two fragments by the given proton numbers Z_1 and Z_2 (or ratios A_1/Z_1 and A_2/Z_2 for both fragments) was determined by minimizing the potential $U(A_1, Z_1; R)$ as a function of A_1 for each Z_1:

$$U(A, Z; R, \ell) = U(A, Z, \ell, \beta_1, \alpha_1; \beta_2, \alpha_2) \quad (1)$$
$$= B_1 + B_2 + V(Z, \ell, \beta_1, \alpha_1; \beta_2, \alpha_2; R)$$
$$- (B_{\rm CN} + V_{\rm CN}(\ell)).$$

Here, B_1, B_2, and $B_{\rm CN}$ are the binding energies of the nuclei in a DNS and of the CN, respectively,

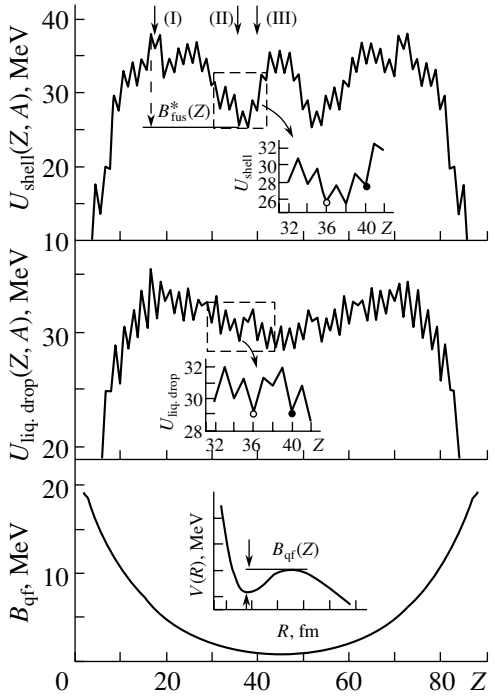

Fig. 1. Driving potential $U(Z, A, R_m; \ell = 0)$ as a function of the charge number Z of a fragment of a DNS calculated by (1) using binding energies from the nuclear data in [19] (top panel) and those obtained with the liquid-drop model (middle panel). The vertical arrows indicate the initial charge number of light nuclei in the ^{40}Ar + ^{176}Hf (I), ^{86}Kr + ^{130}Xe (II), and ^{124}Sn + ^{92}Zr (III) reactions leading to ^{216}Th. The intrinsic $B^*_{\rm fus}$ (top panel) and quasifission $B_{\rm qf}$ (bottom panel) barriers are shown as a function of the charge number of a DNS fragment.

which were obtained from [19, 20]; β_i are the fragment deformation parameters and α_i are the orientations relative to the beam direction; $V_{\rm CN}(\ell)$ is the rotational energy of the CN. R_m is the position of this minimum (bottom of the pocket) on the R axis for a given mass asymmetry A_1. The smallest excitation energy value of the CN is determined by the absolute maximum value of the driving potential lying on the way to fusion ($Z = 0$) from the point corresponding to the initial charge asymmetry (Fig. 1). Note that this value of the excitation energy depends on the mutual orientation of the interacting nuclei. The shapes of the potential energy surface and driving potential depend on the orientations of nuclei relative to the axis connecting the centers of interacting nuclei. The results presented were obtained by averaging the contributions of different orientations. Quasifission is the decay of the DNS without reaching a compact shape. The decay is considered as the motion of a system in the $V(Z, \ell, \beta_1, \alpha_1; \beta_2, \alpha_2; R)$ nucleus–nucleus interaction potential [see below Eq. (7)] along the internuclear axis R. Thus, for quasifission, it is nec-

essary to overcome the barrier of $B_{\rm qf}(\ell)$ on the R axis; the value of $B_{\rm qf}(\ell)$ is defined as a depth of potential well which depends on the orbital angular momentum of entrance channel [Fig. 1 (bottom panel) and Fig. 4 (see below)]. Thus, the DNS concept reveals the reason for the strong decrease in the fusion cross section for a massive system or for a symmetric entrance channel.

2.1. Method of Calculation

In the DNS concept [12], the ER cross section is factorized as follows:

$$\sigma_{\rm ER}(E) = \sum_{\ell=0}^{\ell_d}(2\ell+1)\sigma_\ell^{\rm fus}(E,\ell)W_{\rm sur}(E,\ell). \quad (2)$$

Here, the effects connected with the entrance channel are included in the partial fusion cross section $\sigma_\ell^{\rm fus}(E)$, which is defined by the expressions

$$\sigma_\ell^{\rm fus}(E) = \sigma_\ell^{\rm capture}(E)P_{\rm CN}(E,\ell), \quad (3)$$

$$\sigma_\ell^{\rm capture}(E) = \frac{\lambda^2}{4\pi}\mathcal{P}_\ell^{\rm capture}(E), \quad (4)$$

where λ is the de Broglie wavelength of the entrance channel, $P_{\rm CN}(E,\ell)$ is a factor taking into account the decrease in the fusion probability due to breakup of the DNS (quasifission), and $\mathcal{P}_\ell^{\rm capture}(E)$ is the capture probability which depends on the collision dynamics and is determined by the number of partial waves (ℓ_d) leading to capture.

The number of the partial waves ℓ_d was obtained by solving the equation of motion for the relative distance and orbital angular momentum,

$$\mu(R(t))\ddot{R} + \gamma_R(R(t))\dot{R}(t) = -\frac{\partial V(R(t))}{\partial R}, \quad (5)$$

$$\frac{dL}{dt} = \gamma_\theta(R(t))\left(\dot{\theta}R_{\rm eff}^2 - \dot{\theta}_1 R_{\rm 1eff}^2 - \dot{\theta}_2 R_{\rm 2eff}^2\right). \quad (6)$$

Here, $R(t)$ is the relative motion coordinate; $\dot{\mathbf{R}}(t)$ is the corresponding velocity; $\dot{\theta}$, $\dot{\theta}_1$, and $\dot{\theta}_2$ are angular velocities of the DNS and its fragments, respectively; γ_R and γ_θ are the friction coefficients for the relative motion along R and the tangential motion when two nuclei roll on each other's surfaces, respectively; $V(R)$ is the nucleus–nucleus potential; $\mu(R(t))$ is the reduced mass of the system; R_1 and R_2 are the fragment radii;

$$R_{\rm eff} = \frac{R+R_1+R_2}{2}, \qquad R_{1(2)\rm eff} = \frac{R_{1(2)}}{R_1+R_2}R,$$

where $R_{1(2)}$ is the nucleus radius (see Appendix A).

The friction coefficients $\gamma_R(\gamma_\theta)$, that is, the change in the nucleus–nucleus potential and reduced mass of relative motion during the interaction time t, are calculated from the estimation of the coupling term between the relative motion of nuclei and the intrinsic excitation of nuclei [21].

The nucleus–nucleus potential holding DNS for the given charge and mass asymmetry includes Coulomb ($V_{\rm C}$), nuclear ($V_{\rm nucl}$), and rotational ($V_{\rm rot}$) potentials:

$$V(\mathbf{R}) = V_{\rm C}(\mathbf{R}) + V_{\rm nucl}(\mathbf{R}) + V_{\rm rot}(\mathbf{R}) + \delta V(\mathbf{R}). \quad (7)$$

A change δV of the nucleus–nucleus potential during the interaction time t is taken into account (all details are in Appendix A). In the calculations, we took into account the dynamic contribution $\delta\mu(R)$ to the reduced mass:

$$\mu(R) = \delta\mu(R) + m_0 A_T A_P/A_{\rm tot} \quad (8)$$
$$\times\left(1 - \frac{2}{A_{\rm tot}}\int\frac{\rho_1^{(0)}(\mathbf{r}-\mathbf{r_1})\rho_2^{(0)}(\mathbf{r}-\mathbf{r_2})}{\rho_1^{(0)}(\mathbf{r}-\mathbf{r_1}) + \rho_2^{(0)}(\mathbf{r}-\mathbf{r_2})}d\mathbf{r}\right),$$

where $A_{\rm tot} = A_T + A_P$; $\rho_1^{(0)}$ and $\rho_2^{(0)}$ are nucleon densities of the DNS fragments (details are in Appendix B of paper [14]); $\mathbf{r}_1$ and $\mathbf{r}_2$ are coordinates of the fragment centers of mass; m_0 is the nucleon mass; and A_T and A_P are mass numbers of the target and projectile nucleus, respectively.

The nucleus–nucleus potential $V(R)$ depends on the mutual orientations of the symmetry axes of the deformed nuclei relative to $\mathbf{R}(t)$. Thus, it is possible to consider fusion at different initial orientations of the symmetry axes. The quadrupole (2^+) and octupole (3^-) collective excitations in spherical nuclei are taken into account. The final result is obtained by averaging over the contributions of different mutual orientations of the symmetry axes of the reacting nuclei.

The competition between fusion and quasifission is taken into account by the factor $P_{\rm CN}(E,\ell)$ (fusion factor, hereafter) which is calculated using the framework of the statistical model. This way was first used in [12]. The validity of using the statistical method is justified due to fact that, in quasifission, a full relaxation of the relative kinetic energy and mass (charge) asymmetry between the two fragments takes place [2–8].

The fact that mass and charge distribution can reach near-equilibrium values is seen from the experimental data on study of fusion–fission and quasifission reactions induced by ^{48}Ca and ^{58}Fe projectiles on ^{232}Th, ^{238}U, ^{248}Cm, and Cf targets [22, 23]. It was observed that products far from initial nuclei could be formed not only in the fission of a hot CN, but also in quasifission of the DNS, which lives long enough to reach mass equilibration in the subsequent

fission process. Experimentally, it is difficult to distinguish between fission of the CN and quasifission. Only analysis of correlation between reaction fragment mass and angular distributions allows us to estimate a ratio between contributions of quasifission and fusion–fission processes. These theoretical and experimental results on quasifission justify using a statistical approach to estimate competition of the complete-fusion and quasifission processes. According to statistical methods of calculation, the probability of realizing complete fusion (in competition with quasifission) is related to the ratio of the level densities, depending on the intrinsic fusion or quasifission barriers, by the expression

$$P_{\mathrm{CN}} = \frac{\rho(E^*_{\mathrm{DNS}} - B^*_{\mathrm{fus}})}{\rho(E^*_{\mathrm{DNS}} - B^*_{\mathrm{fus}}) + \rho(E^*_{\mathrm{DNS}} - B_{\mathrm{qf}})}, \quad (9)$$

where $\rho(E^*_{\mathrm{DNS}} - B^*_K)$ is the level density:

$$\rho(E^*_{\mathrm{DNS}} - B^*_K) = \frac{g(\varepsilon_{\mathrm{F}})K_{\mathrm{rot}}}{2\sqrt{g_1(\varepsilon_{\mathrm{F}})g_2(\varepsilon_{\mathrm{F}})}} \quad (10)$$
$$\times \frac{\exp\left[2\pi\sqrt{g(\varepsilon_{\mathrm{F}})(E^*_{\mathrm{DNS}} - B^*_K)/6}\,\right]}{\left[(3/2)g(\varepsilon_{\mathrm{F}})(E^*_{\mathrm{DNS}} - B^*_K)\right]^{1/4}(E^*_{\mathrm{DNS}} - B^*_K)\sqrt{48}}.$$

Here, B_{qf} is the quasifission barrier, and it is determined by the depth of well in the nucleus–nucleus potential well: this barrier must be overcome if the DNS decays in two fragments. E^*_{DNS} is the excitation energy of the DNS given by the difference between the beam energy $E_{\mathrm{c.m.}}$ and the minimum of the nucleus–nucleus potential ($E^*_{\mathrm{DNS}} = E_{\mathrm{c.m.}} - V(R_m)$); $g_{1,2}(\varepsilon_{\mathrm{F}})$ are the single-particle level densities of the fragments of the DNS: $g_i = A_i\varepsilon_{\mathrm{F}}^{-1}(i = 1, 2)$ [24], $\varepsilon_{\mathrm{F}} = 37$ MeV, and $g = g_1 + g_2$; K_{rot} is the enhancement factor of the level density which takes into account rotation of the DNS:

$$K_{\mathrm{rot}} = \frac{\sqrt{6(E^*_{\mathrm{DNS}} - B^*_K)/g(\varepsilon_{\mathrm{F}})}}{\pi}J_\perp, \quad (11)$$

where

$$J_\perp = (2/5m_0r_0^2A^{5/3})\,(1 + \beta_2/3) \quad (12)$$

is the rigid-body moment of inertia for rotation around an axis perpendicular to the line connecting the centers of the fragments. In (12), $r_0 = 1.18$ fm, and β_2 is the quadrupole deformation parameter, whose value was obtained from [19, 20]. The enhancement factor (11) of the level density describes an adiabatic limit in which intrinsic and rotational degrees of freedom are completely decoupled. This assumption ceases to be valid for higher excitation energies. Following [25, 26], we account for the damping of the rotational enhancement by multiplying the K_{rot} factor by

$$1 - Q_{\mathrm{rot}}\left(1 - \frac{1}{\hbar^2/(J_\perp T)}\right). \quad (13)$$

The advanced statistical model, described in detail in [27, 28], allows us to take into account the dynamical aspect of the fission–evaporation competition during the evolution of the CN along the deexcitation cascade. The model accounts exactly for the angular momentum, and parity coupling allows for neutron, proton, and α-particle multiple emission, as well as for the fission channel and full γ cascade in the residual nuclei.

Particular attention is given to the determination of the level densities. These are calculated in the nonadiabatic approach allowing for rotational and vibrational enhancements. These collective effects are gradually removed above a certain energy. In the case of rotational enhancement, this energy is related to the Coriolis force which couples intrinsic and collective motions. Our level densities acquire a dynamic aspect through the dependence of the Coriolis force and of the rotational enhancement on the nuclear shape, which is, in turn, obtained from the classical model of a rotating liquid drop. Intrinsic level densities are calculated using the Ignatyuk approach [29], which takes into account shell structure effects and pairing correlations. Use of the correct level densities is of fundamental importance for the present analysis as they determine the phase space available for each channel, the very essence that governs statistical decay.

In the case of ER production, one should also carefully consider the low-energy level densities since this is the energy interval where most of the ERs are formed. That is why we use the superfluid model of the nucleus [30] in our calculations, with the standard value of pairing correction $\Delta = 12/\sqrt{A}$. The yrast lines are automatically included in our calculations by the requirement that the total excitation energy should be higher than the rotational energy, otherwise the level density is set to zero.

For the fission barriers, we use the predictions of the rotating droplet model (angular momentum dependent) as parametrized by Sierk [31] and allow for angular momentum and temperature fade-out of the shell corrections [27]. This is expressed by the formula for the actual fission barrier used in our calculations:

$$B_{\mathrm{fis}}(J, T) = cB^m_{\mathrm{fis}}(J) - h(T)q(J)\delta W, \quad (14)$$

with

$$h(T) = \begin{cases} 1, & T \le 1.6\ \mathrm{MeV}, \\ k\exp(-mt), & T > 1.65\ \mathrm{MeV}, \end{cases}$$

$$q(J) = \{1 + \exp[(J - J_{1/2})/\Delta J]\}^{-1},$$

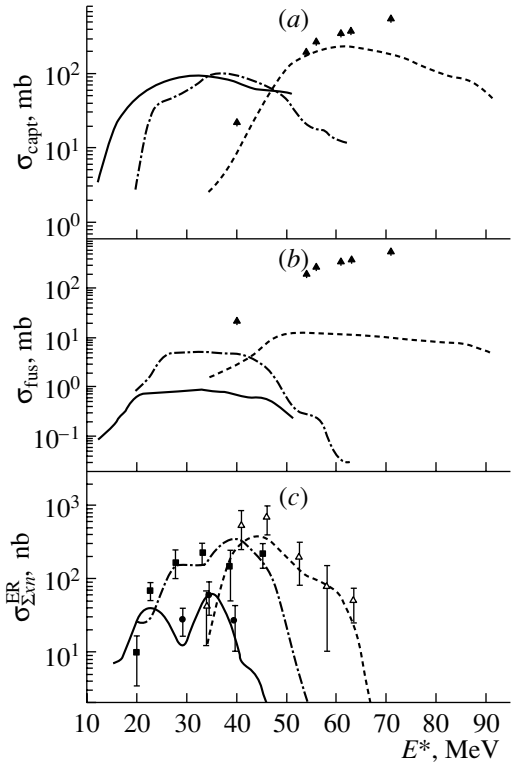

Fig. 2. Comparison of the calculated (*a*) capture, (*b*) fusion, and (*c*) evaporation residue excitation functions as well as the measured excitation functions of evaporation residue (*c*) for ^{40}Ar + ^{176}Hf (dashed curve, open triangles [37, 38], ^{124}Sn + ^{92}Zr (dash-dotted curve, closed squares [39], and ^{86}Kr + ^{130}Xe (solid curve, closed circles [36]) reactions leading to the ^{216}Th* CN. The closed triangles in (*a*) and (*b*) are the fission excitation functions obtained from the measurements of the two symmetric mass fragments for the ^{40}Ar+^{176}Hf reaction [38]; the curves are for the same reactions, as in (*c*).

where $B^m_{fis}(J)$ is the parametrized macroscopic fission barrier [31] depending on the angular momentum J; $\delta W = \delta W_{sad} - \delta W_{g.s} \simeq -\delta W_{g.s}$ is the shell correction (at saddle point and ground state) to the fission barrier taken from the tables [20]; and the constants for the macroscopic fission barrier scaling, temperature, and angular momentum dependences of the microscopic correction are chosen as follows: $c = 1.0$, $k = 5.809$, $m = 1.066$ MeV^{-1}, $J_{1/2} = 24\hbar$ for nuclei with $Z \simeq 80$–100 (or $J_{1/2} = 20\hbar$ for nuclei with $Z > 100$), and $\Delta J = 3\hbar$. This procedure also allows the shell corrections to become dynamical quantities.

Dissipation effects, which delay fission, are treated according to [32, 33]. These include the Kramers stationary limit [34] and an exponential factor applied to the Kramers fission width to account for the transient time, after which the statistical regime is reached. The systematics obtained by Bhattacharya *et al.* [35] allows us to take into account the dependences of the reduced dissipation coefficient β_{dis} on the incident energy per nucleon ϵ and compound-nucleus mass A_{CN} (β_{dis} is the ratio between the friction coefficient γ, which describes the coupling of the fission degree of freedom to the intrinsic degrees of freedom, and the reduced mass M of the system). This ratio characterizes the dissipative and diffusive motion. In the calculations, we used the simple form

$$\beta_{dis}(\epsilon, A_{CN}) = a\epsilon + bA^3_{CN}, \qquad (15)$$

where $a = 0.18$ and $b = 0.357 \times 10^{-6}$ [35]. For the investigated reactions, the β_{dis} values are (6–7) $\times$ 10^{21} s^{-1}.

In the present advanced statistical model calculations, the target–projectile fusion cross section was determined by formula (3).

3. COMPARISON OF DNS MODEL RESULTS AND EXPERIMENTAL DATA

The role of the entrance channel in the formation of the CN and ERs is the main focus of our interest. The qualitative difference between fusion excitation functions of reactions leading to the same CN allows us to analyze the effect of the shell structure on the fusion mechanism. Experimental excitation functions of the evaporation residues measured in the ^{86}Kr + ^{130}Xe [36], ^{40}Ar + ^{176}Hf [37, 38], and ^{124}Sn + ^{92}Zr [39] reactions for the ^{216}Th* CN and in the ^{32}S + ^{182}W and ^{60}Ni + ^{154}Sm [40] reactions for the ^{214}Th* CN have been compared with the results of calculation in the framework of the method presented in Section 2.1. It is shown that the effect of shell structure is revealed in a comparison of the differences in spin distributions of the CN formed by using different reactions.

3.1. The Reactions Leading to ^{216}*Th**

The experimental data reveal that the maximum value of the ER yield cross section for ^{40}Ar + ^{176}Hf (I) [37, 38] is 12 times larger than for ^{86}Kr + ^{130}Xe (II) [36] and 3 times larger than for ^{124}Sn + ^{92}Zr (III) [39] (see Fig. 2). The ^{40}Ar + ^{176}Hf reaction has a larger charge asymmetry ($\eta_Z = (Z_2 - Z_1)/(Z_1 + Z_2)$) in comparison with the two others (II), (III). The height of B^*_{fus} on the way to fusion (that is, in competition with quasifission) for this reaction is smaller than for (II), (III) (see table), joined with a higher value of the B_{qf} barrier (against quasifission) with respect to the B_{qf} values for the (II) and (III) reactions. The way to fusion is longer for the DNS, which has a more mass-symmetric configuration. In Figs. 2*a* and 2*b*, the excitation functions of the capture and fusion calculated in the framework of

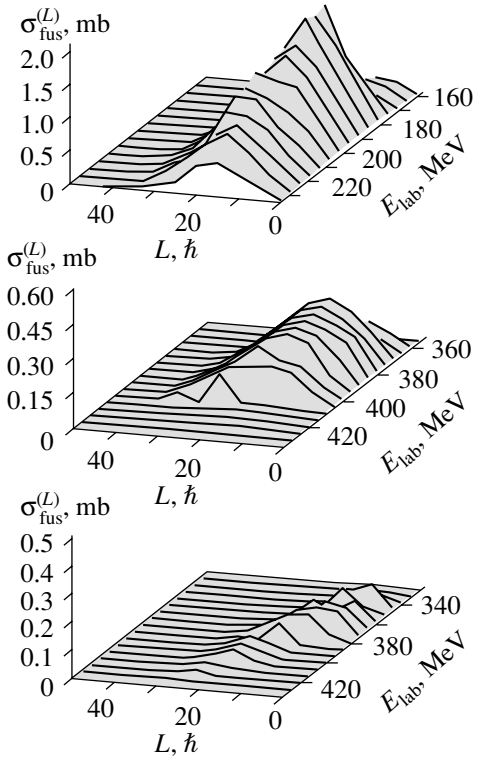

Fig. 3. The calculated spin distribution for the ^{40}Ar + ^{176}Hf (top panel), ^{124}Sn + ^{92}Zr (middle panel), and ^{86}Kr + ^{130}Xe (bottom panel) reactions at different beam energies E_{lab}.

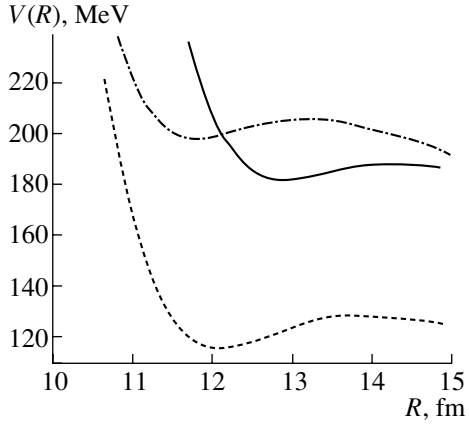

Fig. 4. The wells of nucleus–nucleus potential for the ^{40}Ar + ^{176}Hf (dashed curve), ^{124}Sn + ^{92}Zr (dash-dotted curve), and ^{86}Kr + ^{130}Xe (solid curve) reactions.

the DNS for the (I), (II), and (III) reactions are compared. The ER excitation functions calculated in the framework of the advanced statistical model [27] for those reactions are in good agreement with the experimental data (see Fig. 2*c*). In these calculations, the spin distributions for the CN estimated by the method presented in [14] were used.

However, there is an unusual phenomenon. The maximum value of the ER yield cross section for ^{124}Sn + ^{92}Zr is 4 times larger than for ^{86}Kr + ^{130}Xe near the same value of E^*_{CN}. These reactions lead to the same ^{216}Th CN. The mass asymmetry of the (III) reaction $((A_2 - A_1)/(A_1 + A_2) = 0.148)$ is smaller than the one of the (II) reaction (0.203). The phenomenon can be accounted for by a comparison of the driving potential calculated using binding energies obtained from the mass table [19] and those determined by the liquid-drop model (see Fig. 1, top and middle panels). The values of the driving potential corresponding to the ^{86}Kr + ^{130}Xe and ^{124}Sn + ^{92}Zr reactions in the top and middle panels are different. One can see that, in the top panel of Fig. 1, the value of B^*_{fus} for the ^{86}Kr + ^{130}Xe reaction is larger than the one of the ^{124}Sn + ^{92}Zr reaction. In this case, the fusion factor P_{CN} of the fusion cross section is smaller for the former reaction than for the latter. This corresponds to the observed phenomenon for these two reactions and discloses, even qualitatively, the difference between the values of B^*_{fus} for reactions (II) and (III). It can be seen from the middle panel of Fig. 1 that B^*_{fus}(II) $\approx B^*_{fus}$(III) when the driving potential is calculated using the binding energies B_1, B_2, and B_{CN} is calculated using the liquid-drop model. If the latter takes place, then a difference between the fusion excitation functions of the ^{86}Kr + ^{130}Xe and ^{124}Sn + ^{92}Zr reactions must be very small. This is in contradiction with experimental data, which means that the use of binding energies obtained in the liquid-drop model is not suitable in such an analysis.

As can be seen from the table for the reaction (II), B^*_{fus} is larger than for reaction (III) due to shell effects for the nuclear binding energy in the range of the charge number of the light fragment $Z = 30$–40. Another reason is seen from the analysis of spin distributions of the CN formed in these three reactions.

As seen in Fig. 3, the spin distribution of the CN formed in reaction (I) (top panel) has a larger volume in comparison with reactions (II) (bottom panel) and (III) (middle panel). It is an expected result. However, an unexpected result is that the volume of the spin

Charge asymmetry, intrinsic fusion (B^*_{fus}) and quasifission (B_{qf}) barriers, and the fusion factor (P_{CN}) for the reactions leading to ^{216}Th* CN

Reaction	η_Z	B^*_{fus}, MeV	B_{qf}, MeV	P_{CN}
^{40}Ar + ^{176}Hf (I)	0.60	2.31	7.12	0.580
^{86}Kr + ^{130}Xe (II)	0.20	12.31	2.35	0.014
^{124}Sn + ^{92}Zr (III)	0.15	9.87	1.35	0.081

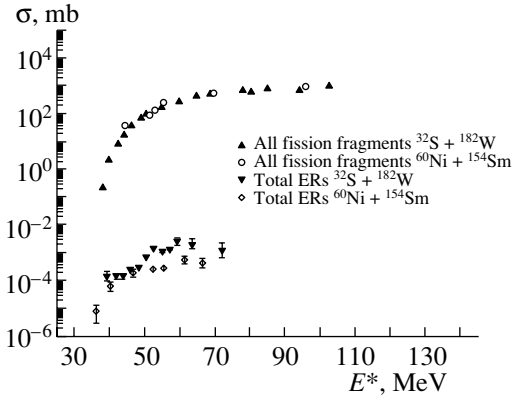

Fig. 5. The experimental data vs. the excitation energy, extracted from [40] and reduced at the E^* x axis for the ^{32}S + ^{182}W and ^{60}Ni + ^{154}Sm reactions leading to the ^{214}Th* CN.

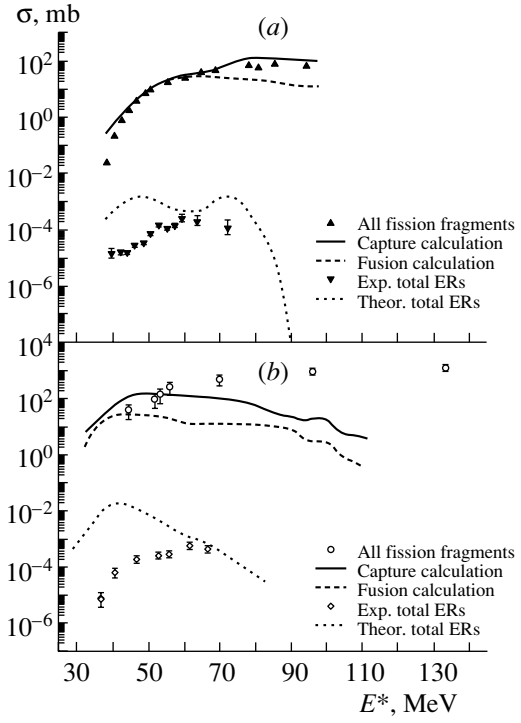

Fig. 6. The capture, fusion, and evaporation residue cross sections for (*a*) the ^{32}S + ^{182}W and (*b*) ^{60}Ni + ^{154}Sm reactions. We also represent, for a comparison, our calculations with the experimental data [40] for the fission fragments and evaporation residue formations already presented in Fig. 5.

distributions of the CN corresponding to reaction (III) is larger than that for reaction (II). This could be connected with $\sigma_\ell^{\text{capture}}(E)$ and P_{CN}, which determine partial fusion cross sections (3). The size of the potential well in the entrance channel (Fig. 4) determines the number of partial waves (number of angular momentum) that contribute to $\sigma_\ell^{\text{capture}}(E)$ and the height of $B_{\text{qf}}(\ell)$, which is one of two barriers characterizing P_{CN} (another is $B^*_{\text{fus}}(\ell)$). It must be stressed that $B_{\text{qf}}(\ell)$ and $B^*_{\text{fus}}(\ell)$ depend on orbital angular momentum: with an increase in ℓ, the quasifission barrier decreases, while the intrinsic fusion barrier increases. The factor P_{CN} (9) determining competition between complete fusion and quasifission is connected with the values of B^*_{fus} and B_{qf} (see Fig. 1) at the given excitation energy of the DNS and decreases with increasing ℓ.

The use of calculated friction coefficients leads to a gradual dissipation of kinetic and rotational energies [21]. The calculations showed that, in collisions of massive nuclei, despite continuous dissipation, capture becomes impossible at beam energy values larger than the Coulomb barrier. This is because of the small size of the well in the nucleus–nucleus potential. The dissipation is not sufficient to trap colliding nuclei in the potential well to create a necessary condition for fusion at low values of angular momentum, which allow the DNS to fuse.

At the largest values of beam energy, capture is possible only for high angular momentum. In this case, the formed DNS can exist in a molecular state, forming a superdeformed shape, or it undergoes quasifission because B^*_{fus} increases with angular momentum of the DNS. Therefore, the maximum of the calculated spin distributions has a tendency to move to larger values of angular momentum at beam energies well above the Coulomb barrier. It can be seen in the spin distributions for ^{124}Sn + ^{92}Zr and ^{86}Kr + ^{130}Xe reactions (Fig. 3). The driving potential is the same for all the reactions leading to the same compound nucleus. Therefore, the intrinsic fusion barriers for these reactions under discussion can be compared. In the top panel of Fig. 1, one can see from the curve of the driving potential that B^*_{fus} is smaller for reaction (III) than for (II). This is connected with the increase in the potential energy at $Z > 37$ due to the shell effects.

The fact that the measured excitation function of evaporation residues for the ^{86}Kr + ^{130}Xe reaction is lower than the one for the ^{124}Sn + ^{92}Zr reaction can be explained by the peculiarity of the shell structure of the nuclear fragments forming the DNS (see top panel of Fig. 1) that leads to a small Q_{gg} value decreasing the driving potential for this reaction. Due to the large difference between the Q values of these three reactions leading to the ^{216}Th* CN, the centers of their excitation functions (see Fig. 2) are placed at different values of excitation energy.

In these reactions under consideration, the ER cross sections are several orders of magnitude smaller than the fission cross sections. One can say that the

fusion cross section is approximately equal to the fission cross section. Comparision of the calculated fusion excitation function and the measured fission excitation function is intriguing when discussing the mechanism of fusion–fission reactions. This has been done for the $^{40}Ar + ^{176}Hf$ reaction (Fig. 2*b*). In [38], the fission excitation function was obtained from the detection of reaction products of symmetric masses. It should be stressed that those products could be formed not only in the fission of a hot CN, but in quasifission of the DNS, which lives long enough to reach mass equilibration in the subsequent reseparation process. Experimentally, it is difficult to distinguish between fission of the CN and quasifission. In [13], the calculations showed that a contribution of quasifission is increased with beam energy above the fusion barrier. For this reason, the measured fission data in the $^{40}Ar + ^{176}Hf$ reaction [38] are closer to the calculated capture cross section (Fig. 2*a*) that is a sum of fusion and quasifission cross sections.

Therefore, the fact that the measured fission cross section is higher than the fusion cross section (Fig. 2*b*) could be explained by the sizable contribution of quasifission products to the measured fission data [38]. The appearance of a difference between the measured fission and theoretical capture cross sections at energies higher than $E^* = 55$ MeV means that the fragments of the deep-inelastic collisions may be considered as fusion–fission reaction products. That is not excluded in the analysis of experimental data.

3.2. The Reactions Leading to $^{214}Th^*$

In this paper, we also consider experimental results of the $^{32}S+^{182}W$ and $^{60}Ni + ^{154}Sm$ reactions [40] (leading to the $^{214}Th^*$ CN) to show that the reduction of the fragment experimental data does not remove the ambiguity about the dynamical processes which contribute to the events related to the fragments. Of course, we present this case only as an example since in the literature there are many other cases showing the same problem.

If we plot the results from [40] vs. the excitation energy E^*, we obtain Fig. 5 for the two very different reactions in the entrance channel leading to the same $^{214}Th^*$ CN.

By such results regarding fragments and ERs of the two reactions, one can infer that, at the same excitation energy E^*, the capture cross sections are almost equal, the ER cross sections are similar too, and therefore the fusion cross sections also have the same values. Such a result does not seem to be realistic since the dynamical effects of the entrance channel are strongly different for the two considered reactions.

For comparison, we present our calculations of the capture, fusion, and ER cross sections for the $^{32}S + ^{182}W$ reaction (Fig. 6*a*) and for the $^{60}Ni + ^{154}Sm$ reaction (Fig. 6*b*).

As one can see, the fusion cross section is comparable with the capture cross section up to about $E^* = 60$ MeV for the $^{32}S + ^{182}W$ reaction, while at higher excitation energies the quasifission contribution overwhelms the complete-fusion contribution also in the case of the mass-asymmetric entrance channel (see Fig. 6*a*). In the case of a more massive beam and more symmetric entrance channel, as in the $^{60}Ni + ^{154}Sm$ reaction, the quasifission contribution overwhelms the complete-fusion contribution also at lower E^* excitation energies (see Fig. 6*b*). Of course, the shape and the yield of the total evaporation cross section for the latter reaction is also different in comparison with the $^{32}S + ^{182}W$ reaction.

Moreover, it is also important to note that, in our total ER calculation, we take into account all possible contributions into the final residue nuclei, whereas, by the experimental procedure, it is not possible to solve all contributions along the CN deexcitation cascade, and therefore the experimental result is underestimated.

In addition to the previous consideration, if we compare only the xn channel of the residue nuclei obtained by the two very different reactions in the entrance channel, it is not easy to come to some conclusion about the dynamical process for two reasons: (i) it is not possible experimentally to have unambiguous information on the complete-fusion formation, which is in competition with the quasifission process, because the rate is different for those two different reactions; (ii) the same CN formed at the same excitation energy E^* by the two very different entrance channels does not produce the same ER cross section due to a different fissility of the CN—since it is formed at a different angular momentum $\langle L \rangle$ distribution caused by the dynamical effects of the two very different reactions in the entrance channel (see, for example, Fig. 3).

Figure 6*b* also shows that the capture cross-section first increases and then decreases, increasing the beam energy (and therefore also increasing the excitation energy E^*) in the case of a more symmetric reaction with massive nuclei (the $^{60}Ni + ^{154}Sm$ reaction). This trend leads to the result that the complete-fusion cross section also decreases at higher beam energies.

4. THE FORMATION OF THE $^{296}116$ AND $^{297}118$ SUPERHEAVY ELEMENTS

A problem relevant to the synthesis of superheavy elements obtained by reactions with massive nuclei

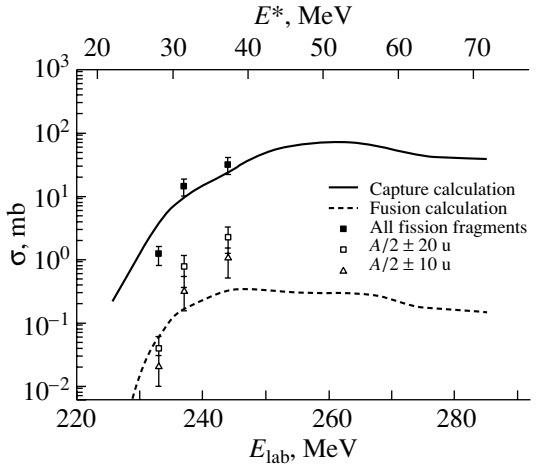

Fig. 7. The capture and fusion cross section calculation, in comparison with the experimental data [23, 41], for the ^{48}Ca + ^{248}Cm reaction leading to the ^{296}116 superheavy CN. The difference between the fusion calculation and more symmetric fragment yield ($A/2 \pm 10$ u) at higher excitation energy is related to the contribution of the quasifission process yielding more symmetric fragments.

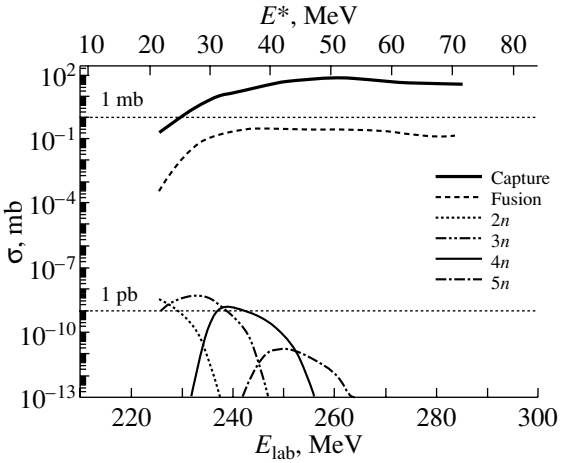

Fig. 8. The excitation functions for the evaporation residue nuclei obtained after the emission of 2–5 neutrons from the ^{296}116 CN by the ^{48}Ca + ^{248}Cm reaction. In the figure, we also represent the capture and fusion cross-section calculation.

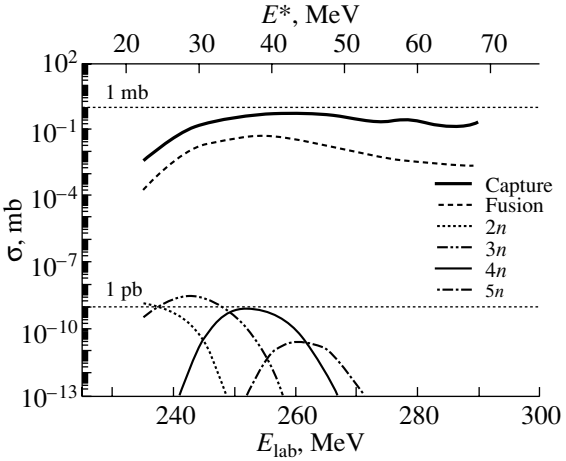

Fig. 9. The same as in Fig. 8, but for the ^{297}118 superheavy CN obtained by the ^{48}Ca + ^{249}Cf reaction. The capture, fusion, and evaporate residue cross sections are lower than the ones respectively obtained for the ^{296}116 CN by the ^{48}Ca + ^{248}Cm reaction.

is to find out unambiguously the quasifission contribution in respect to the complete-fusion contribution. An experimental assumption in the data analysis saying that symmetric fragments (with a large Δm interval) result from fission after fusion is not enough for correct estimation of the fusion cross section, because the quasifission process contributes into the asymmetric fragments as well as to the more symmetric fragments. Moreover, the analysis of the fragment angular distribution and the kinetic energy distribution of fragments also does not allow one to find out unambiguously the contribution of quasifission as compared with the fusion–fission contribution.

In this respect, if we consider as an example the experimental data [23] obtained in the analysis of the ^{48}Ca + ^{248}Cm reaction leading to the ^{296}116 compound nucleus, we can note that our calculation of the capture cross section (see Fig. 7) is in complete agreement with the experimental data for the production of all fragments, while the fusion cross-section calculation is not in agreement with the data for the symmetric mass fragments ($A/2$) when it is assumed that the mass interval is as large as ± 20 u.

Such a strong disagreement is connected with the contribution of the quasifission process in the range of the more symmetric fragments in which the contribution of the fusion–fission fragments is present. In fact, if one assumes for Δm an interval of ± 10 u (almost close to the $\sqrt{A/2}$ value) for selecting the symmetric fragment events, the fusion calculation will appear approximately in agreement (see dashed curve in Fig. 7) with the new selection of the experimental data (open triangles [41] in Fig. 7). Of course, also in this last-mentioned case, there is a relevant contribution of the quasifission process, or a contribution that cannot be neglected, in addition to the fusion–fission fragment formation. This is the reason why the new selection of the experimental data of fragments still slightly overestimates the fusion calculation at higher excitation energies. In our calculation, the capture and fusion cross sections are characterized by the $B^*_{\rm fus}$ intrinsic fusion barrier of 4.48 MeV and $B_{\rm qf}$ of 4.12 MeV.

In Fig. 8, we also present the excitation functions of the ERs obtained as a result of the emission of

2–5 neutrons from the $^{296}116$ CN. The maximum of the cross section is several picobarns for the $3n$ emission, and it is almost 2 pb for the maximum of the $4n$ emission.

We also made calculations for the $^{48}Ca + ^{249}Cf$ reaction leading to the $^{297}118$ CN, aiming at the evaluation of the fusion cross section and the excitation functions for the ER nuclei obtained as a result of the $x(2–5)$ neutron emission from the CN. For this reaction, we obtain the intrinsic fusion barrier B^*_{fus} of about 9 MeV and the quasifission barrier B_{qf} of about 4.5 MeV.

In Fig. 9, we show the capture cross section (lower than 1 mb) and the fusion cross section (with a maximum value of about 50 μb) vs. the beam energy. For the ER cross section, we find the maximum values of about 3.5 pb for the $3n$ channel, and about 0.8–0.9 pb for the $4n$ channel.

By comparing the results of the two last-mentioned reactions, namely, $^{48}Ca + ^{248}Cm$, ^{249}Cf (leading to the $^{296}116$ and $^{297}118$ CN, respectively), one can make a conclusion that the complete fusion decreases, as does the ER nuclei ($ER_{3n,4n}$) in the case of the $^{297}118$ nucleus formation.

5. CONCLUSIONS

The role of the entrance channel in fusion–fission reactions was studied with the intention of accounting for the difference between the experimental data for the $^{40}Ar + ^{176}Hf$, $^{86}Kr + ^{130}Xe$, and $^{124}Sn + ^{92}Zr$ reactions leading to the $^{216}Th^*$ CN and for the $^{32}S + ^{182}W$ and $^{60}Ni + ^{154}Sm$ reactions leading to the $^{214}Th^*$ CN. The combined dynamical and statistical model based on the DNS approach was used to estimate the excitation functions of quasifission, fusion, and formation of ER in fusion reactions with massive nuclei. The capture stage was calculated using the dynamical model. In calculation of the fusion stage by the statistical approach, the competition of complete fusion with quasifission was taken into account. The fusion excitation functions calculated in this way were used to estimate the survival probability of the formed CN relative to fission in the framework of the advanced statistical model for the deexcitation cascade. In calculations of the excitation function for capture, fusion, and ER, we used such relevant variables as potential energy surface, driving potential, spin distributions, and survival probability of CN, which are responsible for the mechanism of fusion–fission processes.

The results of the calculations in the framework of the DNS concept and advanced statistical model for ER cross sections for the sum of xn-channel contributions were compared with the experimental data measured in the $^{86}Kr + ^{130}Xe$ [36], $^{40}Ar + ^{176}Hf$ [37, 38], and $^{124}Sn + ^{92}Zr$ [39] reactions leading to the same excited isotope of $^{216}Th^*$. Moreover, we also compared the calculations with the experimental data of the $^{32}S + ^{182}W$ and $^{60}Ni + ^{154}Sm$ reactions [40] leading to the $^{214}Th^*$ CN.

An unusual phenomenon is that the measured maximum value of the ER for $^{124}Sn + ^{92}Zr$ (III) is 4 times larger than for $^{86}Kr + ^{130}Xe$ (II), nearly the same E^* value. Because the mass asymmetry ($\eta_A = 0.148$) of reaction (III) is smaller than reaction (II) (0.204), the fusion cross section for (III) seems to be smaller than that for (II). In fact, according to the DNS concept [12, 14, 42–44], the way to fusion by nucleon transfer from a light fragment to a heavy one is longer for the DNS, which has less mass-asymmetric configuration. However, the experimental results of ER of (III) in comparison to those of (II) are, at a glance, in contradiction with the above-mentioned statement of the DNS model if driving potential is calculated using binding energies of the liquid-drop model (see middle panel of Fig. 1). In this case, the fusion barrier B^*_{fus} for the $^{124}Sn + ^{92}Zr$ reaction is larger than the one for the $^{86}Kr + ^{130}Xe$ reaction, and the fusion cross section for the former reaction will be smaller than for the latter. Instead, if we also include the effects of shell structure in the DNS analysis, we will find an opposite rate for B^*_{fus} for these reactions: the value of B^*_{fus} is 9.87 MeV for (III), lower than 12.31 MeV for (II) (see table). This corresponds to the measured ratio between the ER cross sections for reactions (II) and (III).

We should like to stress that the driving potential calculated by including the binding energies of nuclei from [19] discloses, even qualitatively, the difference between the values of B^*_{fus} for reactions (II) and (III). As seen from the table for reaction (II), B^*_{fus} is larger than the one for reaction (III). Thus, only by a complete analysis of the role of the entrance channel and the effect of the shell structure is it possible to understand why the evaporation cross sections for the reaction of less mass asymmetry (III) ($\eta_{(\text{III})} = 0.148$) are larger than those for reaction (II), which has more mass asymmetry ($\eta_{(\text{II})} = 0.204$). The effect of the entrance channel on the spin distributions of the CN formed in these three reactions has been analyzed.

For the $^{32}S + ^{182}W$ reaction, the dynamical effect of the entrance channel (the quasifission process) begins at about $E^* = 60$ MeV, while, for the reaction with more massive nuclei ($^{60}Ni + ^{154}Sm$) leading to the same $^{214}Th^*$ CN, the quasifission contribution overwhelms the fusion cross section also at lower beam energies, which is in disagreement with the considered experimental data. Having analyzed the

^{48}Ca + ^{248}Cm reaction, we note that the quasifission process also contributes into the symmetric fragment formation at higher E^* excitation energies. Moreover, with increasing Z of superheavy elements from 116 to 118 obtained by the synthesis of nuclear reactions, the respective cross sections (capture, fusion, and ER nuclei) decrease.

ACKNOWLEDGMENTS

This work was performed partially under the financial support of the Russian Foundation for Basic Research (project no. 99-02-16447) and INTAS (grant no. 991-1344). A.I.M. and A.K.N. are grateful to the STCU Uzb-45, Uzbekistan State Scientific-Technical Committee (grant no. 7/2000) and Fund of the Uzbek Academy of Sciences for Support of Basic Research (grant no. 45-00) for partial support. A.K.N. would like to express his gratitude for the warm hospitality during his stay at the University of Messina (Italy). A.K.N. are also grateful to the Fondazione Bonino-Pulejo (FBP) of Messina for the support received in the collaboration with the Messina group.

APPENDIX A

The nucleus–nucleus potential is calculated as follows:

$$V_0(\mathbf{R}) = V_{\rm C}(\mathbf{R}) + V_{\rm nucl}(\mathbf{R}) + V_{\rm rot}(\mathbf{R}), \qquad (A.1)$$

where $V_{\rm C}(\mathbf{R})$, $V_{\rm nucl}(\mathbf{R})$, and $V_{\rm rot}(\mathbf{R})$ are the Coulomb, nuclear, and rotational potentials, respectively. The nuclear shape is important in the calculation of the Coulomb and the nuclear interactions between colliding nuclei. Thus, the Coulomb interaction of deformed nuclei (with a quadrupole deformation) can be calculated according to the following expression taken from [45]:

$$V_{\rm C}(R) = \frac{Z_1 Z_2}{R}e^2 + \frac{Z_1 Z_2}{R^3}e^2 \qquad (A.2)$$
$$\times \left\{ \left(\frac{9}{20\pi}\right)^{1/2} \sum_{i=1}^{2} R_{0i}^2 \beta_2^{(i)} \mathcal{P}_2(\cos\alpha_i') + \frac{3}{7\pi}\sum_{i=1}^{2} R_{0i}^2 \left[\beta_2^{(i)}\mathcal{P}_2(\cos\alpha_i')\right]^2 \right\},$$

where $\alpha_1' = \alpha_1 + \Theta$; $\alpha_2' = \pi - (\alpha_2 + \Theta)$; $\sin\Theta = |\mathbf{L}|/(\mu\dot{R}R)$; and Z_i, $\beta_2^{(i)}$, and α_i' are (for each fragment) the atomic number, the quadrupole deformation parameter, and the angle (see Fig. 3 in [14]) between the line connecting the centers of mass of the nuclei and the symmetry axis of the fragment $i (i = 1, 2)$, respectively. Here, $R_{0i} = r_0 A_i^{1/3}$, $r_0 = 1.18$ fm, and $\mathcal{P}_2(\cos\alpha_i')$ is the second term of the second type of Legendre polynomial.

The nuclear part of the nucleus–nucleus potential is calculated using the folding procedure between the effective nucleon–nucleon forces $f_{\rm eff}[\rho(x)]$ suggested by Migdal [46] and the nucleon density of the projectile and the target nucleus:

$$V_{\rm nucl}(R) = \int \rho_1^{(0)}(\mathbf{r} - \mathbf{R}_1) f_{\rm eff}[\rho] \rho_2^{(0)}(\mathbf{r} - \mathbf{R}_2) d\mathbf{r}, \qquad (A.3)$$

$$f_{\rm eff}[\rho] = 300\left(f_{\rm in} + (f_{\rm ex} - f_{\rm in})\frac{\rho(0) - \rho(r)}{\rho(0)}\right). \qquad (A.4)$$

Here, $f_{\rm in} = 0.09$, $f_{\rm ex} = -2.59$ are the constants of the effective nucleon–nucleon interaction; $\rho = \rho_1^{(0)} + \rho_2^{(0)}$; $\mathbf{R}_i$ $(i = 1, 2)$ is the position of the center of mass of the fragment i. The center of the coordinate system is placed at the center of mass of the target; therefore, $\mathbf{R}_2 = 0$ and $\mathbf{R}_1 = \mathbf{R}$, $\mathbf{R}$ being the relative distance between the center of mass of colliding nuclei. The nucleon densities are assumed to have a Fermi distribution:

$$\rho_i^{(0)}(\mathbf{r} - \mathbf{R}_i) = \rho_i^{(0)}(\mathbf{r}, \mathbf{R}_i(t), \beta_2^{(i)}, \beta_3^{(i)}) \qquad (A.5)$$
$$= \left\{1 + \exp\left[\frac{|\mathbf{r} - \mathbf{R}_i(t)| - \tilde{R}_i(\beta_2^{(i)}, \beta_3^{(i)})}{a_0}\right]\right\}^{-1},$$

$$\tilde{R}_i(\beta_2^{(i)}, \beta_3^{(i)}) = R_{0i}(1 + \beta_2^{(i)} Y_{20}(\alpha_i) + \beta_3^{(i)} Y_{30}(\alpha_i)), \qquad (A.6)$$

where $a_0 = 0.54$ fm. The shape of the nuclei of the DNS changes with the evolution of the mass-asymmetry degrees of freedom: $\beta_2 = \beta_2(Z, A)$ and $\beta_3 = \beta_3(Z, A)$. In order to calculate the potential energy surface as a function of the charge number, we use the values of $\beta_2^{(2^+)}$ from the data in [47] and the values of $\beta_3^{(3^-)}$ from the data in [48].

Expressions for the friction coefficients

$$\gamma_R(R(t)) = \sum_{i,i'} \left|\frac{\partial V_{ii'}(R(t))}{\partial R}\right|^2 B_{ii'}^{(1)}(t), \qquad (A.7)$$

$$\gamma_\theta(R(t)) = \frac{1}{R^2}\sum_{i,i'} \left|\frac{\partial V_{ii'}(R(t))}{\partial \theta}\right|^2 B_{ii'}^{(1)}(t), \qquad (A.8)$$

and the dynamic contribution to the nucleus–nucleus potential

$$\delta V(R(t)) = \sum_{i,i'} \left|\frac{\partial V_{ii'}(R(t))}{\partial R}\right|^2 B_{ii'}^{(0)}(t), \qquad (A.9)$$

were obtained in [21] by estimating the evolution of the coupling term between relative motion of nuclei and nucleon motion inside nuclei; $B^{(0)}_{ii'}(t)$ is given below by Eq. (A.11).

The dynamic correction of the reduced mass $\delta\mu(R(t))$ is calculated using the expression

$$\delta\mu(R(t)) = \sum_{i,i'} \left| \frac{\partial V_{ii'}(R(t))}{\partial R} \right|^2 B^{(2)}_{ii'}(t), \quad \text{(A.10)}$$

$$B^{(n)}_{ik}(t) = \frac{2}{\hbar} \int_0^t dt'(t-t')^n \quad \text{(A.11)}$$

$$\times \exp\left(\frac{t'-t}{\tau_{ik}}\right) \sin\left[\omega_{ik}\left(\mathbf{R}(t')\right)(t-t')\right] \times [\tilde{n}_k(t') - \tilde{n}_i(t')],$$

$$\hbar\omega_{ik} = \varepsilon_i + \Lambda_{ii} - \varepsilon_k - \Lambda_{kk}. \quad \text{(A.12)}$$

Here, $\tilde{n}_i$ is a diagonal matrix element of the density matrix that is calculated according to the model presented elsewhere [21, 49]; $\tau_{ik} = \tau_i\tau_k/(\tau_i + \tau_k)$; τ_i is the lifetime of the quasiparticle excitations in the single-particle state i of the nucleus. It determines the damping of single-particle motion. The value of τ_i is calculated using the results of the theory of quantum liquids [50] and the effective nucleon–nucleon forces from [46]:

$$\frac{1}{\tau_i^{(\alpha)}} = \frac{\sqrt{2}\pi}{32\hbar\varepsilon^{(\alpha)}_{\mathrm{F}_K}} \quad \text{(A.13)}$$

$$\times \left[(f_K - g)^2 + \frac{1}{2}(f_K + g)^2\right] \times \left[\left(\pi T_K\right)^2 + \left(\tilde{\varepsilon}_i - \lambda_K^{(\alpha)}\right)^2\right] \times \left[1 + \exp\left(\frac{\lambda_K^{(\alpha)} - \tilde{\varepsilon}_i}{T_K}\right)\right]^{-1},$$

where

$$T_K(t) = 3.46\sqrt{\frac{E^*_K(t)}{\langle A_K(t)\rangle}} \quad \text{(A.14)}$$

is the effective temperature determined by the amount of intrinsic excitation energy $E^*_K = E^{*(Z)}_K + E^{*(N)}_K$ and by the mass number $\langle A_K(t)\rangle$ (with $\langle A_K(t)\rangle = \langle Z_K(t)\rangle + \langle N_K(t)\rangle$). In addition, $\lambda^{(\alpha)}_K(t)$ and $E^{*(\alpha)}_K(t)$ are the chemical potential and intrinsic excitation energies for the proton ($\alpha = Z$) and neutron ($\alpha = N$) subsystems of the nucleus $K(K = 1$(projectile), 2(target)), respectively. Furthermore, the finite size of the nuclei and the difference between the numbers of neutrons and protons makes it necessary to use the following expressions for the Fermi energies [46]:

$$\varepsilon^{(Z)}_{\mathrm{F}_K} = \varepsilon_{\mathrm{F}}\left[1 - \frac{2}{3}(1 + 2f'_K)\frac{\langle N_K\rangle - \langle Z_K\rangle}{\langle A_K\rangle}\right], \quad \text{(A.15)}$$

$$\varepsilon^{(N)}_{\mathrm{F}_K} = \varepsilon_{\mathrm{F}}\left[1 + \frac{2}{3}(1 + 2f'_K)\frac{\langle N_K\rangle - \langle Z_K\rangle}{\langle A_K\rangle}\right],$$

where $\varepsilon_{\mathrm{F}} = 37$ MeV,

$$f_K = f_{\mathrm{in}} - \frac{2}{\langle A_K\rangle^{1/3}}(f_{\mathrm{in}} - f_{\mathrm{ex}}), \quad \text{(A.16)}$$

$$f'_K = f'_{\mathrm{in}} - \frac{2}{\langle A_K\rangle^{1/3}}(f'_{\mathrm{in}} - f'_{\mathrm{ex}}),$$

and $f_{\mathrm{in}} = 0.09$, $f'_{\mathrm{in}} = 0.42$, $f_{\mathrm{ex}} = -2.59$, $f'_{\mathrm{ex}} = 0.54$, $g = 0.7$ are the constants of the effective nucleon–nucleon interaction.

Finally, the rotational potential is

$$V_{\mathrm{rot}}(R) = \hbar^2\frac{l(l+1)}{2\mu R^2}. \quad \text{(A.17)}$$

APPENDIX B

The angles between the symmetry axis of the projectile and target nucleus and the beam direction are α_1 and α_2, respectively (Fig. 3 in [14]). The spherical coordinate system O with the vector $\mathbf{r}$ and angles θ and ϕ is placed at the center of mass of the target nucleus, and the Oz axis is directed opposite to the beam. In this coordinate system, the direction of the vector $\mathbf{R}$ connecting the centers of mass of the interacting nuclei has angles Θ and Φ. The coordinate system is chosen so that the planes in which the symmetry axes of nuclei are located cross the Oz line and form an angle Φ. For head-on collisions, $\Theta = 0$ and $\Phi = \phi$.

The nucleon distribution functions of interacting nuclei in the integrand (A.3) can be expressed using these variables in the same coordinate system O.

In the O system, the symmetry axis of the target nucleus is turned through an angle α_2, so its nucleon distribution function is as follows:

$$\rho^{(0)}_2(\mathbf{r}) = \rho_0\left\{1 + \exp\left[\frac{r - \tilde{R}_2(\beta^{(2)}_2, \beta^{(2)}_3; \theta'_2)}{a}\right]\right\}^{-1}, \quad \text{(A.18)}$$

$$\tilde{R}_2(\beta^{(2)}_2, \beta^{(2)}_3; \theta'_2) = R^{(2)}_0\left(1 + \beta^{(2)}_2 Y_{20}(\theta'_2) + \beta^{(2)}_3 Y_{30}(\theta'_2)\right),$$

where $\rho_0 = 0.17$ fm^{-3},

$$\cos\theta'_2 = \cos\theta\cos(\pi - \alpha_2)$$

$$+\sin\theta\sin(\pi-\alpha_2)\cos\phi. \qquad \text{(A.19)}$$

The center of mass of the projectile nucleus is shifted to the end of the vector **R**, and its symmetry axis is turned by the angle $\pi-\alpha_1$. According to the transformation formulas of the parallel transfer of vectors, the variables of the transferred system O' are as follows:

$$r'^2 = r^2 + R^2 - 2rR\cos(\omega_{12}), \qquad \text{(A.20)}$$

$$\cos(\omega_{12}) = \cos\theta\cos\Theta + \sin\theta\sin\Theta\cos(\phi-\Phi),$$

$$\cos\theta_1' = \frac{r\cos\theta - R\cos\Theta}{r'},$$

$$\cos\phi_1' = (1+\tan^2\phi_1')^{-1/2},$$

$$\tan\phi_1' = \frac{r\sin\phi\sin\theta - R\sin\Theta\sin\Phi}{r\cos\phi\sin\theta - R\sin\Theta\cos\Phi}.$$

In the coordinate system O', the deviation of the symmetry axis of projectile nuclei relative to the $O'z'$ axis is determined by the angle

$$\cos\theta_1'' = \cos\theta_1'\cos(\pi-\alpha_1) + \sin\theta_1'\cos\phi_1'. \qquad \text{(A.21)}$$

Now, the nucleon distribution function of the projectile nucleus looks like

$$\rho_1^{(0)}(\mathbf{r}') = \rho_0 \qquad \text{(A.22)}$$

$$\times\left\{1+\exp\left[\frac{r'-\tilde{R}_1(\beta_2^{(1)},\beta_3^{(1)};\theta_1')}{a}\right]\right\}^{-1},$$

$$\tilde{R}_1(\beta_2^{(1)},\beta_3^{(1)};\theta_1') = R_0^{(1)}\left(1+\beta_2^{(1)}Y_{20}(\theta_1')\right.$$

$$\left.+\beta_3^{(1)}Y_{30}(\theta_1')\right).$$

The nuclear part of the nucleus–nucleus potential was calculated by (A.3) using the folding procedure of the effective nucleon–nucleon forces by Migdal [46] with the nucleon distribution functions (A.18) and (A.22) of interacting nuclei.

REFERENCES

1. B. B. Back, R. R. Betts, K. Cassidy, *et al.*, Phys. Rev. Lett. **50**, 818 (1983).
2. B. B. Back, Phys. Rev. C **31**, 2104 (1985).
3. J. Tōke *et al.*, Nucl. Phys. A **440**, 327 (1985).
4. J. Tōke *et al.*, Phys. Lett. B **142B**, 258 (1984).
5. W. Q. Shen *et al.*, Europhys. Lett. **1**, 113 (1986).
6. W. Q. Shen *et al.*, Phys. Rev. C **36**, 115 (1987).
7. B. B. Back *et al.*, Phys. Rev. C **32**, 195 (1985).
8. B. B. Back, P. B. Fernández, B. G. Glagola, *et al.*, Phys. Rev. C **53**, 1734 (1996).
9. R. L. Hahn, K. S. Toth, Y. LeBeyec, *et al.*, Phys. Rev. C **36**, 2132 (1987).
10. R. L. Hahn, K. S. Toth, C. Cabot, *et al.*, Phys. Rev. Lett. **42**, 218 (1979).
11. A. C. Berriman, D. J. Hinde, M. Dasgupta, *et al.*, Nature (London) **413**, 144 (2001).
12. V. V. Volkov, N. A. Antonenko, E. A. Cherepanov, *et al.*, Phys. Lett. B **319**, 425 (1993); Phys. Rev. C **51**, 2635 (1995).
13. G. Giardina, F. Hanappe, A. I. Muminov, *et al.*, Nucl. Phys. A **671**, 165 (2000).
14. G. Giardina, S. Hofmann, A. I. Muminov, and A. K. Nasirov, Eur. Phys. J. A **8**, 205 (2000).
15. W. J. Swiatecki, Phys. Scr. **24**, 113 (1981); Nucl. Phys. A **376**, 275 (1982).
16. K. T. R. Davies, A. J. Sierk, and J. R. Nix, Phys. Rev. C **28**, 679 (1983).
17. P. Fröbrich, Phys. Rep. **116**, 337 (1984); Phys. Lett. B **215**, 36 (1988).
18. J. P. Blocki, H. Feldmeier, and W. J. Swiatecki, Nucl. Phys. A **459**, 145 (1986).
19. G. Audi and A. H. Wapstra, Nucl. Phys. A **595**, 509 (1995).
20. P. Möller and J. R. Nix, At. Data Nucl. Data Tables **39**, 213 (1988).
21. G. G. Adamian, R. V. Jolos, A. I. Muminov, and A. K. Nasirov, Phys. Rev. C **56**, 373 (1997).
22. A. A. Bogatchev *et al.*, in *Proceeding of the International Conference on Nuclear Physics at Border Lines, Lipari, Italy*, Ed. by G. Fazio, G. Giardina, F. Hanappe, *et al.* (World Sci., Singapore, 2002), p. 56.
23. M. G. Itkis *et al.*, in *Proceedings of the International Conference on Nuclear Physics at Border Lines, Lipari, Italy*, Ed. by G. Fazio, G. Giardina, F. Hanappe, *et al.* (World Sci., Singapore, 2002), p. 146.
24. O. Bohr and B. Mottelson, *Nuclear Structure* (Benjamin, New York, 1969, 1975), Vols. 1, 2.
25. S. E. Vigdor and H. J. Karwowski, Phys. Rev. C **26**, 1068 (1982).
26. A. D'Arrigo, G. Giardina, M. Herman, and A. Taccone, Phys. Rev. C **46**, 1437 (1992).
27. A. D'Arrigo, G. Giardina, M. Herman, *et al.*, J. Phys. G **20**, 365 (1994).
28. R. N. Sagaidak, V. I Chepigin, A. P. Kabachenko, *et al.*, J. Phys. G **24**, 611 (1998).
29. A. V. Ignatyuk, G. N. Smirenkin, and A. S. Tishin, Yad. Fiz. **21**, 485 (1975) [Sov. J. Nucl. Phys. **21**, 255 (1975)].
30. A. V. Ignatyuk, K. K. Istekov, and G. N. Smirenkin, Yad. Fiz. **29**, 875 (1979) [Sov. J. Nucl. Phys. **29**, 450 (1979)].
31. A. J. Sierk, Phys. Rev. C **33**, 2039 (1986).
32. P. Grange and H. A. Weidenmüller, Phys. Lett. B **96B**, 26 (1980).
33. E. M. Rastopchin, S. I. Mul'gin, Yu.V. Ostapenko, *et al.*, Yad. Fiz. **53** 1200 (1991) [Sov. J. Nucl. Phys. **53**, 741 (1991)].
34. H. A. Kramers, Physica **7**, 284 (1940).
35. C. Bhattacharya, S. Bhattacharya, and K. Krishan, Phys. Rev. C **53**, 1012 (1996).
36. Yu.Ts. Oganessian, A. Yu. Lavrentev, A. G. Popeko, *et al.*, Preprint No. E7-97-206, JINR (Joint Inst. for Nucl. Res., Dubna, 1997), p. 62.

37. D. Vermeulen, H.-G. Clerc, C.-C. Sahm, *et al.*, Z. Phys. A **318**, 157 (1984).
38. H.-G. Clerc, J. G. Keller, C.-C. Sahm, *et al.*, Nucl. Phys. A **419**, 571 (1984).
39. C.-C. Sahm, H.-G. Clerc, K.-H. Schmidt, *et al.*, Nucl. Phys. A **441**, 316 (1985).
40. S. Mitsuoka, H. Ikezoe, K. Nishio, and J. Lu, Phys. Rev. C **62**, 054603 (2000).
41. E. Kozulin, private communication.
42. E. A. Cherepanov, V. V. Volkov, N. A. Antonenko, and A. K. Nasirov, Nucl. Phys. A **583**, 165 (1995).
43. G. G. Adamian, N. A. Antonenko, W. Scheid, and V. V. Volkov, Nucl. Phys. A **633**, 409 (1998).
44. E. A. Cherepanov, in *Proceedings of the International Conference on Nuclear Physics "Shells-50," Dubna, Russia, 1999*, Ed. by Yu. Ts. Oganessian and R. Kalpakchieva (World Sci., Singapore, 2000), p. 266.
45. C. Y. Wong, Phys. Rev. Lett. **31**, 766 (1973).
46. A. B. Migdal, *Theory of the Finite Fermi Systems and Properties of Atomic Nuclei* (Nauka, Moscow, 1983) (in Russian).
47. S. Raman, C. H. Malarkey, W. T. Milner, *et al.*, At. Data Nucl. Data Tables **36**, 1 (1987).
48. R. H. Spear, At. Data Nucl. Data Tables **42**, 55 (1989).
49. G. G. Adamian, A. K. Nasirov, N. V. Antonenko, and R. V. Jolos, Fiz. Élem. Chastits At. Yadra **25** 1379 (1994) [Phys. Part. Nucl. **25**, 583 (1994)].
50. D. Pines and P. Noziéres, *Theory of Quantum Liquids* (Benjamin, New York, 1966).

Physics of Atomic Nuclei, Vol. 66, No. 6, 2003, pp. 1086–1094. From Yadernaya Fizika, Vol. 66, No. 6, 2003, pp. 1122–1130.

Competition of Fusion and Quasifission in Reactions Leading to Production of Superheavy Elements*

M. Veselsky**

Institute of Physics, Slovak Academy of Sciences, Bratislava, Slovakia

Received January 8, 2003

Abstract—The mechanism of fusion hindrance, an effect observed in the reactions of cold, warm, and hot fusion leading to production of superheavy elements, is investigated. A systematics of transfermium production cross sections is used to determine fusion probabilities. The mechanism of fusion hindrance is described as a competition of fusion and quasifission. Available evaporation residue cross sections in the superheavy region are reproduced satisfactorily. Analysis of the measured capture cross sections is performed and a sudden disappearance of the capture cross sections is observed at low fusion probabilities. A dependence of the fusion hindrance on the asymmetry of the projectile–target system is investigated using the available data. The most promising pathways for further experiments are suggested.

INTRODUCTION

In recent years, the heavy elements up to $Z = 112$ have been synthesized using cold fusion reactions with Pb and Bi targets in the evaporation channel with emission of one neutron [1]. Experimentalists had to face a steep decrease in cross sections down to the picobarn level due to increasing fusion hindrance, whose origin was unclear. The same level of cross sections has been reached in hot fusion reactions with emission of 3–4 neutrons using ^{48}Ca beams that lead to synthesis of relatively neutron-rich isotopes of elements 112, 114, and 116 [2–5]. Again, fusion hindrance was observed. The possibility of describing fusion hindrance in both cold and hot fusion in a unified way as a competition between formation of the compound nucleus and a fast-fission-like process (quasifission) was suggested in our article [6] using a simple phenomenological model. A comparison of the recent experimental results to the results of the model calculation is provided in the present article. Furthermore, additional investigations on the nature of the fusion process are carried out using available data on capture cross section. An additional dynamical fusion hindrance is predicted based on available experimental evaporation residue data from the reactions where heavy nuclei are produced in the symmetric projectile–target combinations approaching the asymmetry of the fission channel.

STATISTICAL MODEL FOR COMPETITION OF FUSION AND QUASIFISSION

In our previous article [6], we presented a simple statistical model for the description of production cross sections of superheavy nuclei in a wide range of excitation energies including cold, warm, and hot fusion. The model assumes that the fusion hindrance observed in cold fusion reactions, where only one neutron is emitted prior to the formation of evaporation residue (ER), can be explained by the competition of fusion with a fast fission-like process which can be identified with quasifission. It is not obvious what the role is of a traditional saddle configuration, used in description of fusion–fission, in quasifission. Therefore, the scission configuration was chosen as a final state in the fission channel. Then, the fusion probability can be expressed using the level densities in compound and scission configurations as

$$P_{\rm fus}^{\rm stat} = \frac{\rho(E^*_{\rm CN})}{\rho(E^*_{\rm CN}) + \rho(E^*_{\rm sc,eff})}. \qquad (1)$$

The excitation energy in the scission configuration is estimated empirically using the systematics of postscission neutron multiplicities. Proportionality of the number of neutrons emitted from the fission fragments to the intrinsic excitation energy in the scission configuration is assumed. Then the excitation energy in the scission configuration can be expressed as

$$E^*_{\rm sc,eff} = (\nu_n^{\rm s.f}(A_{\rm CN}) + \Delta\nu_n(E^*_{\rm CN}))E_n. \qquad (2)$$

The multiplicity of emitted neutrons in the spontaneous fission of heavy nuclei $\nu_n^{\rm s.f}(A_{\rm CN})$ is approximated by a linear extrapolation of the available

*This article was submitted by the author in English.

** e-mail: fyzimarv@savba.sk

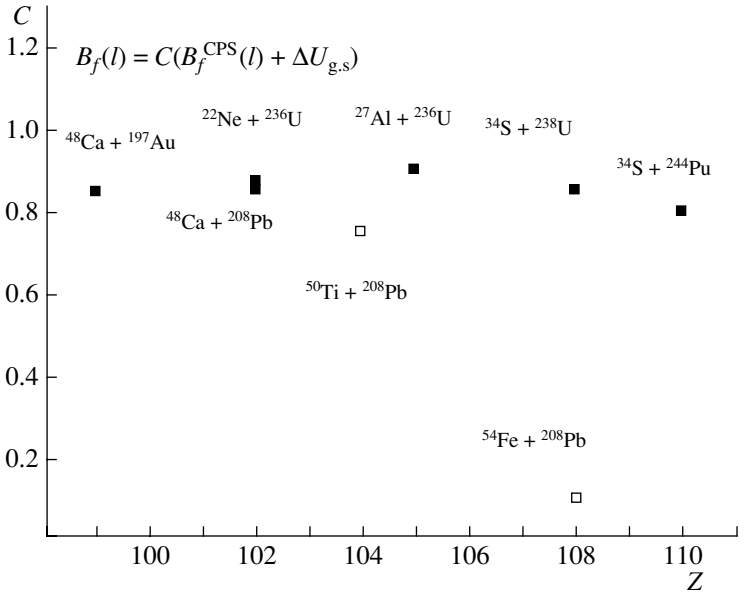

Fig. 1. Optimum values of parameter C necessary to reproduce experimental cross sections of hot fusion reactions (closed symbols) as a function of atomic number of residual nuclei. Open symbols are for cold fusion reactions.

spontaneous fission neutron multiplicity data to given A_{CN},

$$\nu_n^{s.f}(A_{CN}) = 3.316 + 0.0969(A_{CN} - 250). \quad (3)$$

An additional increase in the postscission neutron multiplicity at a given excitation energy $\Delta\nu_n(E^*_{CN})$ can be expressed approximately as

$$\Delta\nu_n(E^*_{CN}) = 0.035E^*_{CN}, \quad (4)$$

as follows from the available postscission neutron multiplicity data [7]. A proportionality factor E_n is the amount of intrinsic excitation energy per emitted neutron. This is a free parameter and it was estimated from the systematics of production cross sections of transfermium nuclei produced in cold and hot fusion.

The unhindered fusion cross sections have been calculated using a one-dimensional WKB approximation with a Gaussian barrier width distribution [8] implemented in the statistical code HIVAP [9]. Such an approximation proved quite successful despite its simplicity. The depth of the nuclear potential well is taken as $V_0 = 40$ MeV, the half-density radius is taken as $r_0 = 1.11$ fm, and the diffuseness is set to $d = 0.75$ fm. The width of barrier distribution ranges from 3% for reactions with the doubly magic nucleus ^{208}Pb to 5% for reactions with heavy deformed nuclei away from the shell closure.

The survival probabilities were calculated using a conventional statistical calculation. The competition of fission vs. particle emission was calculated using a modified version of the HIVAP code [9] with fission barriers expressed as [10]

$$B_f(l) = C(B_f^{LD}(l) + \Delta B_f^{shell}). \quad (5)$$

The liquid-drop component of the fission barrier (B_f^{LD}) has been calculated according to the rotating charged liquid-drop model of Cohen–Plasil–Swiatecki [11]. The shell component of the fission barrier (ΔB_f^{shell}) has been approximated by a value of the ground-state shell correction taken from the calculation of Möller *et al.* [12]. Such an approximation for the fission barriers proved successful for description of the ER cross sections in the region around neutron shell closure $N = 126$, where the parameter C proved to be virtually constant for a large set of ERs with values of the ground-state shell correction ranging from zero up to 8 MeV [10].

The shell corrections for transfermium nuclei are expected to be within the same range, while the liquid-drop fission barriers are virtually zero. The optimum values of parameter C necessary to reproduce experimental cross sections of the ERs with $Z > 100$ are given in Fig. 1 as a function of atomic number. One can see that the optimum values of C for the hot fusion reactions remain stable within $Z = 102$–110. The value of $C = 0.8$–0.9 is higher when compared to the $N = 126$ region and this difference could be most probably attributed to differences of saddle point configurations in both regions.

Unlike for the hot fusion products, the optimum values of the parameter C for the cold fusion reactions with a ^{208}Pb target increasingly fall out of the systematics at $Z > 104$, which can be attributed

Table 1. Comparison of several recently reported production cross sections of elements with $Z > 110$ [2–5] to the predictions published in [6]

Reaction	Experiment		Calculation	
	ER	σ_{ER}, pb	ER	σ_{ER}, pb
$^{48}Ca + ^{238}U$	$^{283}112$	5	$^{283}112$	1.5
$^{48}Ca + ^{242}Pu$	$^{287}114$	2.5	$^{286}114$	0.25
$^{48}Ca + ^{244}Pu$	$^{288}114$	0.7	$^{287}114$	0.1
$^{48}Ca + ^{248}Cm$	$^{292}116$	0.3	$^{291}116$	0.01

to emerging competition of fusion with quasifission. Thus, the fusion probabilities for cold fusion were obtained by comparing the measured evaporation residue cross sections with those calculated using C from the hot fusion systematics. The parametrization $E_n = 3.795 + 0.04(A_{CN} - 260)$ for the parameter in the formula (2) was obtained and used in further calculation for nuclei with $Z > 110$.

The alternative scenario of the fusion hindrance originating from tunneling through the barrier in the subbarrier region seems to be in contradiction with experimental ratios of the cross sections in $1n$ and $2n$ evaporation channels of reactions with a ^{208}Pb target [1], which increase from about 0.1 for ^{48}Ca beam ($Z = 102$) to 10 for ^{58}Fe beam ($Z = 108$). Such a situation suggests that, even at excitation energies corresponding to the $1n$ channel, the reaction cannot be considered as a subbarrier type.

Table 1 gives the production cross sections of several new superheavy nuclei [2–5], reported since our initial article [6] was published, compared to the maximum evaporation residue cross sections in xn channels estimated in [6]. No angular momentum dependence for description of the scission point was assumed, and the cross sections were evaluated at the maxima of the excitation functions obtained from statistical calculations with no fusion hindrance assumed. One can see that the calculation predicted production cross sections rather well for the reaction $^{48}Ca + ^{238}U$. For heavier systems the estimated cross sections are lower by up to one order of magnitude since the calculation exhibits a systematic shift in the dominating xn ER channel toward a higher number of emitted neutrons. The discrepancy observed can be attributed to the simplification used in the initial calculation, where the unhindered maximum production cross sections obtained using the HIVAP code were multiplied by the fusion probabilities with no angular momentum dependence assumed. Recently, the calculation was corrected [13] by implementing

Table 2. Comparison of recently reported production cross sections of elements with $Z > 110$ [2–5] to the results of the improved calculations [13]

Reaction	E_{lab}, MeV	ER	σ_{ER}, pb	
			exp.	calc.
$^{48}Ca + ^{238}U$	231	$^{283}112$	5	4
$^{48}Ca + ^{238}U$	238	$^{282}112$	≤ 7	8
$^{48}Ca + ^{242}Pu$	235	$^{287}114$	2.5	1.5
$^{48}Ca + ^{244}Pu$	236	$^{288}114$	0.7	2.0
$^{48}Ca + ^{248}Cm$	240	$^{292}116$	0.3	0.1

an angular momentum in the description of the compound nucleus and scission configuration and by introducing the fusion probability calculation for each partial wave into the HIVAP code. The moment of inertia of symmetric touching rigid spheres was used for the scission configuration. An improved version of the HIVAP code uses the fusion probability for each partial wave as a multiplication factor to the unhindered fusion cross section. This allows one to obtain more realistic shapes of excitation functions for ER channels.

Table 2 again gives the production cross sections of the recently synthesized superheavy nuclei compared to the results of an improved calculation [13]. The production cross sections track quite well with the reported ones. The new calculation reproduces reasonably well not only the absolute values but also the positions of the maxima and thus promises a possibility for further estimates. Concerning the recently reported [14] (and more recently corrected [15]) experimental results from the reaction $^{86}Kr + ^{208}Pb$, the calculation (as published in [13]) led to an estimated

Table 3. Predictions of production cross sections of elements with $Z > 116$ calculated using improved calculation [13] (reactions of stable beams with stable or long-lived targets have been taken into account)

Reaction	E^*, MeV	ER	σ_{ER}, pb
$^{48}Ca + ^{249}Cf$	47	$^{293}118$	0.1
$^{48}Ca + ^{249}Cf$	52	$^{292}118$	0.25
$^{48}Ca + ^{252}Cf$	46	$^{296}118$	0.02
$^{48}Ca + ^{252}Cf$	53	$^{295}118$	0.03
$^{58}Fe + ^{238}U$	48	$^{292}118$	0.2
$^{58}Fe + ^{244}Pu$	56	$^{297}120$	0.007
$^{64}Ni + ^{238}U$	56	$^{297}120$	0.007

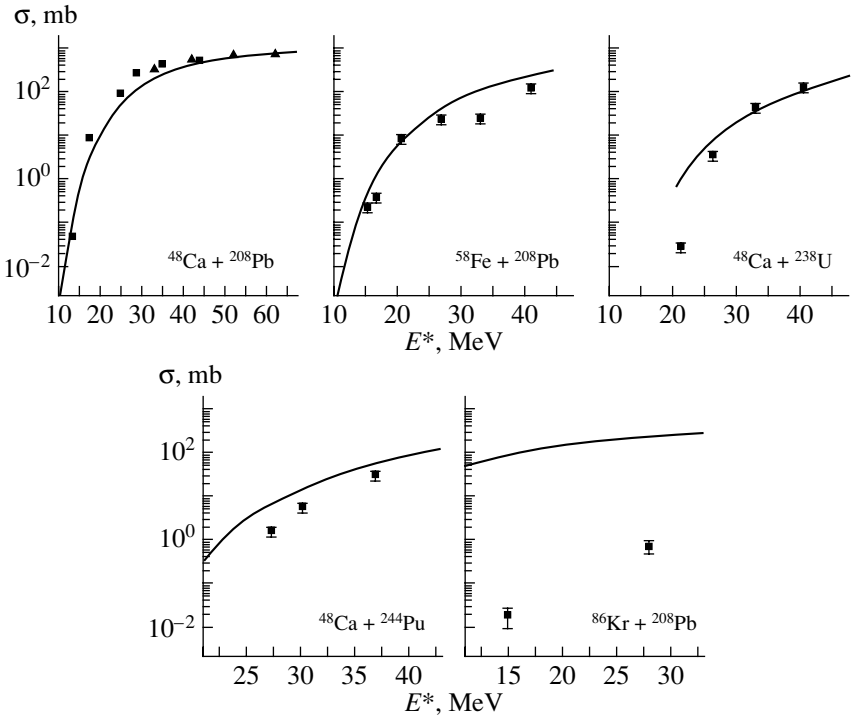

Fig. 2. Experimental capture cross sections [16] (symbols) and the fusion cross sections calculated using the WKB approximation with a Gaussian barrier distribution [8] (curves). Data from five different reactions are presented. The width of barrier distribution is assumed to be 3% for ^{208}Pb target and 5% for ^{238}U and ^{244}Pu targets.

production cross section for the $1n$ channel of approximately 10^{-4} pb. Such a value was in contradiction with the initial experimental cross section value of 2.2 pb [14], but it is consistent with the corrected experimental results. As stated above, the parametrization of E_n used was obtained using data from cold fusion only, and thus the estimated cross section for cold fusion is practically just an extrapolation of the cross-section trend. In any case, significant success of the extrapolation when used for hot fusion reactions virtually justifies its validity also for cold fusion reactions. Therefore, the cold fusion reactions do not seem to offer much promise for further progress in the synthesis of superheavy nuclei.

In Table 3, predictions are given for several reactions that may lead to the synthesis of even heavier nuclei. An improved calculation [13] was used in this case. Only reactions of stable beams with stable or long-lived targets have been taken into account. The reactions ^{48}Ca + ^{249}Cf and ^{58}Fe + ^{238}U give promise for the synthesis of the isotope ^{292,293}118 on the cross section level of 0.1–0.2 pb, which seems to be an experimental limit for the foreseeable future. Compared to the system ^{58}Fe + ^{238}U, the choice of heavier projectile ^{64}Ni or target ^{244}Pu leads to the drop in cross section by one and a half orders of magnitude. It is necessary to note that the quality of the estimate directly depends on the prediction of the masses and ground-state shell corrections [12] used in the calculation. The results given in Table 2 suggest that the masses and ground-state shell corrections used are quite realistic. Nevertheless, any discrepancies in further extrapolation will affect the cross-section estimates significantly.

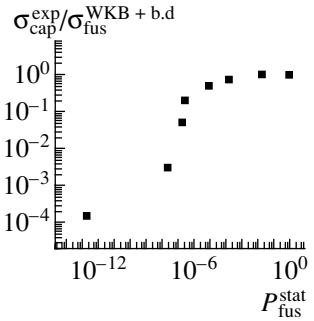

Fig. 3. Ratio of the experimental capture cross sections [16] to the fusion cross sections calculated using the WKB approximation with a Gaussian barrier distribution [8] (symbols) plotted as a function of the calculated fusion probability [6, 13]. The data points from Fig. 2 are used.

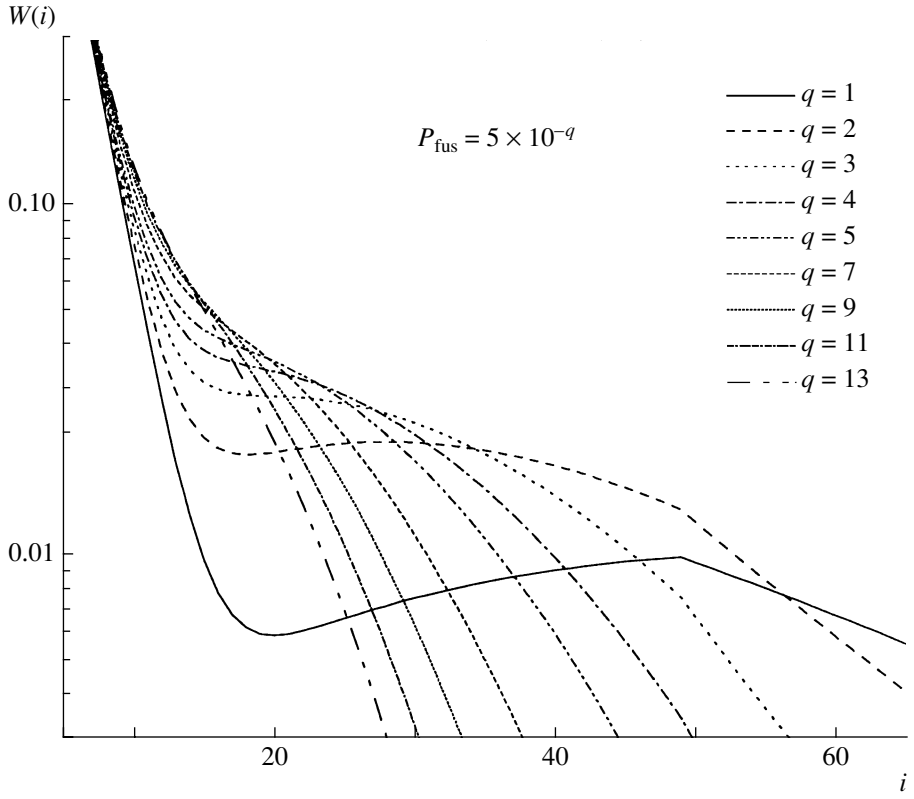

Fig. 4. "Toy model" description of the fusion–fission vs. quasifission competition during the dynamical evolution of the system. The exit probability density $W(i)$ is plotted as a function of step number i for several values of the resulting fusion probability P_{fus}. For details, see text.

CAPTURE CROSS SECTIONS

In order to understand the competition of fusion and quasifission, it is of great interest to investigate also the measured cross sections of fusion–fission and quasifission. Such an analysis was performed on the data on measured capture cross sections [16] (defined in the experiment as the cross section of the fission events with the total kinetic energy (TKE) and fragment masses outside of the quasielastic/deep-inelastic region of the TKE vs. mass matrix). The experimental setup used was optimized to detect fusion–fission for each specific reaction. A comparison of the experimentally determined capture cross sections [16] to the calculated unhindered fusion cross sections [8] and fusion probabilities [6, 13] is presented in Figs. 2 and 3. As one can see from Fig. 2, the calculated fusion cross sections track very well with the measured capture cross sections for the reactions ^{48}Ca + ^{208}Pb and ^{58}Ca + ^{208}Pb. For the heavier systems, the measured capture cross sections become smaller than the calculated fusion cross sections. Such an effect appears to increase with a decrease in the excitation energy of the compound nucleus. One can assume that such a discrepancy can be related to a decrease in the fusion probability for the heavier systems. Such an assumption is examined in Fig. 3, where the ratio of the measured capture cross sections to the calculated unhindered fusion cross sections is represented as a function of the fusion probability calculated as in [13]. One can observe a surprising abrupt disappearance of the measured capture cross section at fusion probabilities below 10^{-6}. Such an abrupt disappearance of the measured capture cross section when compared to the calculated fusion cross section seems to be rather global, and it may indicate a dramatic change in the properties of reaction products due to different dynamical evolution. A possibility of explaining the trend qualitatively is presented in Fig. 4 in the framework of a "toy model" mimicking a competition of multistep dynamical evolution toward fusion with a possibility of irreversible exit into the quasifission channel at each step. Fusion probability is treated as a product of N elementary subprobabilities $P(i)$ corresponding to elementary steps of the evolution toward fusion. The probability for the first step $P(1)$ is assumed to be one, later the probability decreases linearly until it reaches a minimum halfway toward fusion, then the probability starts to increase linearly,

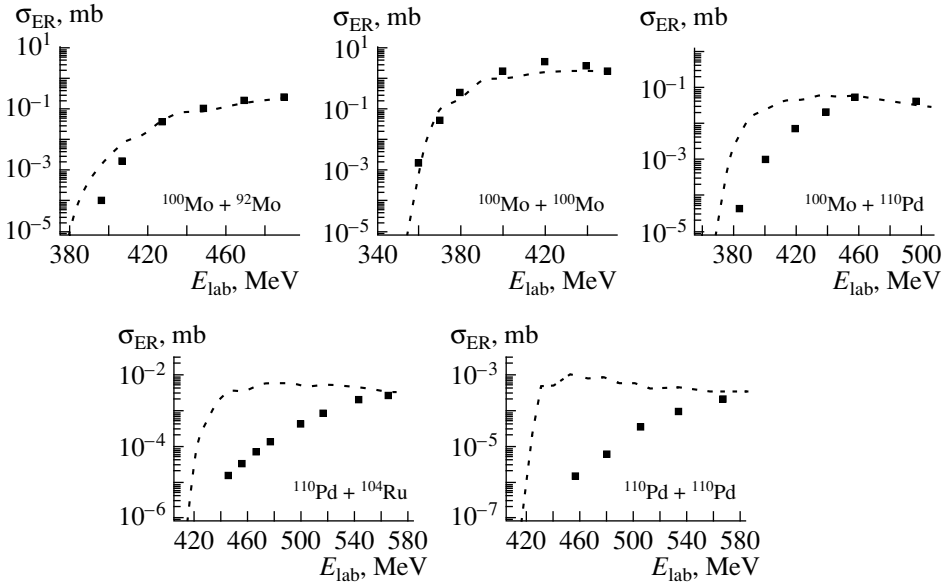

Fig. 5. Comparison of the measured [18, 19] and calculated evaporation residue cross sections for several symmetric systems.

and the probability of the last step is again assumed to be one. At each step, the quantity $1 - P(i)$ can be considered as the probability of exit into the quasifission channel. The resulting exit channel probability density of fusion–quasifission competition with 100 steps is superimposed onto the exit channel probability density of another process with the exit channel probability density quickly exponentially decreasing with step number. The latter process is considered 10 times more frequent. Such a procedure can simulate an interplay with the quasi-elastic/deep-inelastic reactions occurring at the partial waves close to the grazing angular momentum (and thus with higher cross section). As one can see, with decreasing fusion probability, the exit channel probability densities of the two processes increasingly overlap and at some point cannot be decomposed anymore. This can be a qualitative explanation for the situation in Fig. 3, where the measured capture cross section initially tracks with the calculated fusion cross section, but at some point this correspondence is abruptly disrupted. In the realistic process leading to either fusion or quasifission, the concentration of the probability density at the early stage of dynamical evolution may lead to kinematic properties of the fission fragments very different from fusion–fission. Such fragments can become undetectable using a given experimental setup optimized for detection of fusion–fission products. In any case, the disappearance of the measured capture cross sections in a given case can be understood as a signature of the interconnection of the fusion and the quasifission processes within the concept of their competition during the multistep dynamical evolution of the system.

SYMMETRIC SYSTEMS

Of great interest for the future prospects of synthesis of superheavy nuclei is the understanding of reaction dynamics in the case where both projectile and target are of comparable size. In order to investigate a possible fusion hindrance originating from increasing symmetry of the projectile–target system, we compared the calculated ER cross section in the four reactions leading to compound nucleus ^{246}Fm to the experimental cross sections from the work of Gäggeler *et al.* [17]. The calculation used was identical to [13]. The result is presented in Table 4. When looking at the results and taking into account the systematics in Fig. 1, where fusion hindrance occurs for cold fusion of compound nuclei with $Z > 104$, one can assume that there appear to exist additional fusion hindrances which emerge with increasing symmetry of the reaction.

Table 4. Comparison of the calculated ER cross section in the four reactions leading to compound nucleus ^{246}Fm to the experimental cross sections from the work of Gäggeler *et al.* [17]

Reaction	σ_{2n}, nb	
	exp.	calc.
$^{40}Ar + {}^{206}Pb$	3	1
$^{76}Ge + {}^{170}Er$	1	19
$^{86}Kr + {}^{160}Gd$	<0.3	26
$^{136}Xe + {}^{110}Pd$	<0.2	40

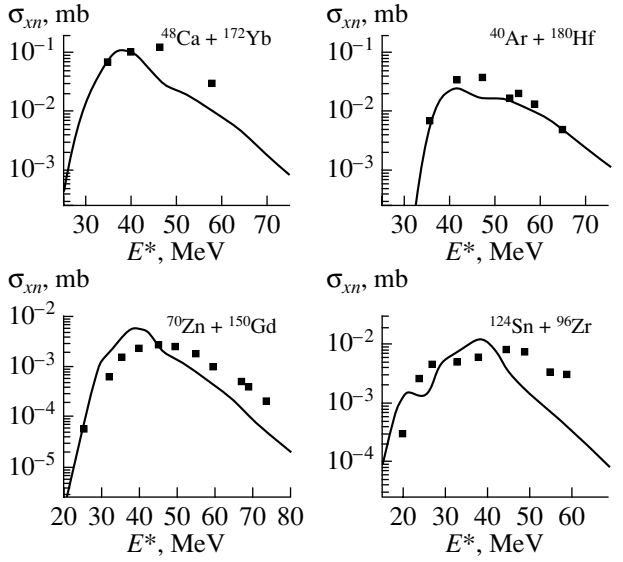

Fig. 6. Comparison of the measured [20–22] and calculated xn evaporation residue cross sections for several systems leading to the compound nucleus ^{220}Th.

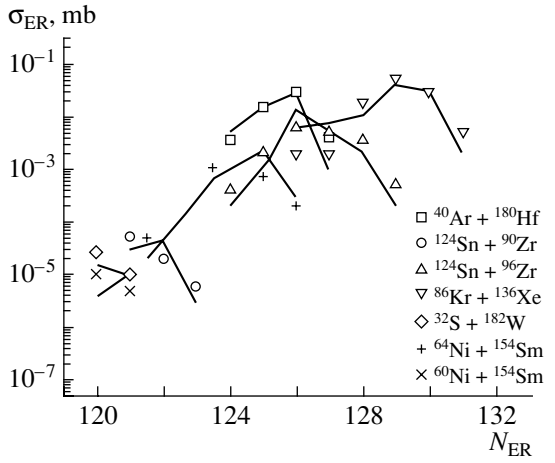

Fig. 7. Comparison of the measured [20, 21, 24–27] and calculated maximum xn evaporation residue cross sections for several systems leading to various Th compound nuclei.

In order to understand the possible nature of such hindrances, we carried out an analysis of the data in the Pb–U region [18, 19]. Using the fusion model with WKB and Gaussian barrier distribution [8] and fission channel parameters from the systematics for a given region [10] ($C \approx 0.65$), we observe an interesting behavior (see Fig. 5). For the reaction ^{100}Mo + ^{100}Mo, the ER cross section is described well. In the transition to ^{110}Pd + ^{110}Pd, there is an increasing hindrance at low excitation energies. The hindrance factor seems to increase with decreasing excitation energy. To some surprise, the same effect can also be seen in the transition from ^{100}Mo + ^{100}Mo to ^{100}Mo + ^{92}Mo (lighter system but with higher fissility). Also of interest is the fact that experimental cross-section data for Pd + Ru and Pd + Pd systems are only in the region above the calculated fusion barrier, where calculated fusion cross sections remain stable but disappear in the subbarrier region, where calculated cross sections start to drop quickly.

In order to test the fusion cross-section model, the measured and calculated xn ER cross sections for four systems leading to the compound nucleus ^{220}Th (^{40}Ar + ^{180}Hf [20], ^{124}Sn + ^{96}Zr [21], ^{48}Ca + ^{172}Yb, and ^{70}Zn + ^{150}Gd [22]) are given in Fig. 6. The calculations have been performed using the HIVAP code. The barrier distribution widths [8] used comply with the usual prescription (5% for Ar + Hf, Ca + Yb, and Zn + Gd since the (heavy) target is deformed and 4% for Sn + Zr since the (heavier) projectile is close to spherical). The shapes of xn excitation functions are reproduced reasonably well, especially the ascending/barrier part, and the maxima of xn excitation functions are reproduced acceptably. The fission barrier scaling parameter C [10] was equal for Ar + Hf and Ca + Yb ($C = 0.67$) and for Zn + Gd and Sn + Zr ($C = 0.61$). The discrepancy in C is not fully compliant with the concept of a compound nucleus, since it should be the same in all cases. Most probably, it is caused by the irregularities in alpha emission, where, especially in the symmetric systems, the memory of the entrance channel (e.g., deformation) may lead to enhanced emission of alpha particles and thus to reduction of xn cross sections. Experimental alpha-particle emission spectra [23] suggest alpha-emission barriers of about 90% of the alpha-particle fusion barrier, which is also used in calculations, but such a prescription is rather simplistic and may not account for dynamical effects in symmetric reactions. Apart from entrance channel memory, an admixture from incomplete fusion channels with emission of alpha particles is also possible. More detailed data will be necessary for complete understanding of the phenomena. In any case, the description of the fusion barrier by the approximation employed can be considered adequate.

Further comparisons of the calculated and experimental evaporation residue cross sections for reactions leading to various Th compound nuclei are given in Fig. 7. The maximum cross sections for various xn evaporation channels are considered. For the compound system ^{214}Th, where one can see a strong hindrance for the reaction ^{110}Pd + ^{104}Ru (see Fig. 5), the same cannot be concluded for the reaction ^{124}Sn + ^{90}Zr [24]. Also, for Th compound nuclei ranging from ^{214}Th to ^{222}Th, no hindrance can be observed for reactions including ^{32}S + ^{182}W [25], ^{60}Ni + ^{154}Sm [25],

^{64}Ni + ^{154}Sm [26], and ^{86}Kr + ^{136}Xe [27]. For ^{86}Kr + ^{136}Xe data, the xn cross sections are virtually constant from the $1n$ to the $6n$ channel, which is in conflict with extrapush theory [28]. As in the previous case, the fission barrier scaling parameter C varied from 0.6 to 0.67 and emission barriers were 10% lower than fusion barriers for a given light charged particle. The widths of the fusion barrier distribution were consistent with the above prescription. As one can see from Figs. 6 and 7, a statistical model calculation with fission barriers compliant with formula (5) (giving an equally good description for nuclei with and without strong ground-state shell corrections [10]) and with the fusion cross section calculated using the one-dimensional WKB approximation with fusion barrier distribution provides a very consistent description of the ER cross sections virtually without using free parameters. No fusion hindrance can be observed for a wide range of compound nuclei. Thus, one can conclude that the fusion hindrance in the Th region takes place only for the reactions leading to highly fissile compound nuclei with projectile–target asymmetry in a narrow region close to zero.

When looking for an explanation of the above behavior, one can turn attention to the properties of the fission fragments in the given region. Recent studies of low-energy fission in Ac–U region [29, 30] show that there is a systematic transition from asymmetric to symmetric fission around the mass 222–226. The Th compound nuclei studied above all fall into the region with symmetric fission mode. Thus, one can assume that an additional fission hindrance appears when the asymmetry of the fusion channel is close to the asymmetry of the fission channel. There, one can assume that immediate fission is highly favored dynamically over the long evolution toward fusion. For the heavier nuclei with masses above 226, the dominant fission mode at low excitation energies is the mode where one fragment (heavier one for lighter nuclei and lighter one for very heavy nuclei) is of the mass approximately 132 and the mass of the other fragment increases linearly with the mass of fissioning system [16]. The reaction ^{136}Xe + ^{110}Pd studied by Gäggeler *et al.* [17] is virtually an inverse fission and a dynamical fusion hindrance can be understood there. The reactions ^{76}Ge + ^{170}Kr and ^{86}Kr + ^{160}Gd are far away from the main fission mode but still match the superasymmetric mode (with the maximum yields of light fragments positioned around ^{82}Ge), which is usually necessary to reproduce the experimental mass distributions [31]. Thus, the knowledge of fission modes in the transfermium region seems to be essential information for the study of fusion probability. An interesting test for such an assumption would be a reaction ^{132}Sn + ^{96}Zr leading to compound nucleus ^{228}Th, which fissions asymmetrically, and thus it would be an inverse fission again and hindrance factors should appear. The nonhindered cross sections can be expected to be in the millibarn region, so already a relatively moderate beam of ^{132}Sn may be sufficient to show discrepancy. The use of a radioactive beam is essential in this case since no symmetric combination of a stable beam and target appears to reach Th isotopes beyond 222.

SUMMARY AND CONCLUSIONS

In summary, the possibilities for synthesis of new superheavy elements using stable or long-lived projectiles and targets seem to be rather restricted. The parametrization of model parameters able to reproduce existing experimental results predicts a possibility of synthesizing isotopes of element 118 in hot fusion reactions at the cross section level of 0.1 pb. Concerning the nature of the process, the analysis of the measured cross sections suggests that the competition of fusion and quasifission is a multistep dynamical process and that the low fusion probability is consistent with the fast reseparation of the reacting system even at low partial waves. For symmetric systems where the asymmetry of the projectile–target combination approaches the asymmetry of the fission channel, an additional fusion hindrance caused by dynamical dominance of immediate reseparation into the fission channel over a long evolution toward complete fusion seems to take place. Such a dynamical hindrance can strongly reduce the possible pathways toward superheavy elements. Knowledge of fission fragment asymmetry seems to be essential for further studies of synthesis of superheavy elements.

ACKNOWLEDGMENTS

I would like to thank S. Hofmann, A.V. Yeremin, J. Peter, R. Smolanczuk, G. Chubarian, E.M. Kozulin, W. Loveland, and G.A. Souliotis for fruitful discussions. Furthermore, I would like to thank Yu.Ts. Oganessian and M.G. Itkis for their interest in this work.

This work was supported through grant no. VEGA-2/1132/21.

REFERENCES

1. S. Hofmann, Rep. Prog. Phys. **61**, 639 (1998).
2. A. V. Yeremin *et al.*, Eur. Phys. J. A **5**, 63 (1999).
3. Yu. Ts. Oganessian *et al.*, Nature (London) **400**, 242 (1999).
4. Yu. Ts. Oganessian *et al.*, Phys. Rev. C **62**, 41604 (2000).
5. Yu. Ts. Oganessian *et al.*, Phys. Rev. C **63**, 11301 (2001).
6. M. Veselsky, Acta Phys. Slov. **49**, 101 (1999).

7. S. M. Lukyanov *et al.*, in *Proceedings of the International School of Heavy Ion Physics, Dubna, 1989* (JINR, Dubna, 1990), p. 225; D. Hilscher *et al.*, Yad. Fiz. **57**, 1255 (1994) [Phys. At. Nucl. **57**, 1187 (1994)].
8. W. Reisdorf *et al.*, Nucl. Phys. A **444**, 154 (1985).
9. W. Reisdorf, Z. Phys. A **300**, 227 (1981).
10. M. Veselsky, PhD Thesis (Comenius University, Bratislava, 1997); D. D. Bogdanov *et al.*, Yad. Fiz. **62**, 1794 (1999) [Phys. At. Nucl. **62**, 1794 (1999)].
11. S. Cohen, F. Plasil, and W. J. Swiatecki, Ann. Phys. (N.Y.) **82**, 557 (1974).
12. P. Möller *et al.*, At. Data Nucl. Data Tables **59**, 185 (1995).
13. M. Veselsky, *Progress in Research, 2000–2001, Cyclotron Institute, Texas A&M University*, p. II-30; http://cyclotron.tamu.edu/progress/2000-2001/2_a12.pdf.
14. V. Ninov *et al.*, Phys. Rev. Lett. **83**, 1104 (1999).
15. K. E. Gregorich *et al.*, nucl-ex/0201014.
16. M. G. Itkis *et al.*, in *Proceedings of the International Workshop on Fusion Dynamics at the Extremes, Dubna, Russia, 2000* (World Sci., Singapore, 2001), p. 93.
17. H. W. Gäggeler *et al.*, Z. Phys. A **316**, 291 (1984).
18. W. Morawek *et al.*, Z. Phys. A **341**, 75 (1991).
19. A. B. Quint *et al.*, Z. Phys. A **346**, 119 (1993).
20. D. Vermeulen *et al.*, Z. Phys. A **318**, 157 (1984).
21. C.-C. Sahm *et al.*, Z. Phys. A **319**, 113 (1984).
22. J. Peter *et al.*, in *Proceedings of the International Conference on Nuclear Physics at Border Lines, Lipari, Italy, 2001* (World Sci., Singapore, 2002), p. 257.
23. L. C. Vaz and J. M. Alexander, Z. Phys. A **318**, 231 (1984).
24. C.-C. Sahm *et al.*, Nucl. Phys. A **441**, 316 (1985).
25. S. Mitsuoka *et al.*, Phys. Rev. C **62**, 54603 (2000).
26. S. Mitsuoka *et al.*, Phys. Rev. C **65**, 54608 (2002).
27. R. N. Sagaidak *et al.*, in *Proceedings of the VI International School–Seminar on Heavy Ion Physics, Dubna, Russia, 1997* (World Sci., Singapore, 1998), p. 323.
28. J. Blocki, H. Feldmeier, and W. Swiatecki, Nucl. Phys. A **459**, 145 (1986).
29. K.-H. Schmidt *et al.*, Nucl. Phys. A **665**, 221 (2000).
30. I. V. Pokrovsky *et al.*, Phys. Rev. C **62**, 14615 (2000).
31. V. A. Rubchenya and J. Äystö, Nucl. Phys. A **701**, 127c (2002).

Physics of Atomic Nuclei, Vol. 66, No. 6, 2003, pp. 1095–1104. From Yadernaya Fizika, Vol. 66, No. 6, 2003, pp. 1131–1140.

Cold Valleys of Superheavy Elements with Deformed Targets and Projectiles*

Ş. Mişicu** **and W. Greiner**

Institut für Theoretische Physik, J.W. Goethe-Universität, Frankfurt am Main, Germany

Received August 28, 2002

Abstract—The dependence of the cold driving potential on the deformation of the incoming target and projectile is investigated in the case of the synthesis of the superheavy nuclei ^{256}No, ^{286}112, ^{292}114, ^{296}116, and ^{306}122. The occurrence of valleys in the driving potential as a function on the interfragment distance and the mass asymmetry is studied for different fixed orientations of the colliding nuclei such as the pole–pole, pole–equator, equator–equator, and equator–equator-crossed and compared to the case when the nuclei are assumed to be spherical or when the potential is averaged over the orientation.

1. INTRODUCTION

The cold fusion configuration after the capture took place and before the mass transfer between the colliding emergent nuclei is initiated can be pictured as a long- or short-lived dinuclear or quasimolecular system [1].

It was advocated a long time ago that, in the collision between a deformed target and a spherical projectile, the most favorable orientation of the deformed nucleus is the one in which its symmetry axis intersects the center of the spherical partner because it leads to a substantially lower fusion barrier than expected for a spherical nucleus of equal mass [2]. Thus, fusion becomes possible at lower bombarding energies, the probability for producing *cold* compound nuclei being enhanced.

More recently, it was invoked that fusion of two well-deformed nuclei in an equatorial–equatorial and equator–equator twisted orientation has been envisioned because such a configuration could be more compact than all other orientations of the two deformed nuclei [3].

There is no doubt that the way in which the superheavy elements are synthesized is also dependent on particular deformations and orientations, as already noted in [3]. In analogy to the cold fission of ^{252}Cf, we investigate the role of the fragment deformations and orientations on the driving potential of the superheavy nuclei ^{256}No, ^{286}112, ^{292}114, ^{296}116, and ^{306}122.

*This article was submitted by the authors in English.

**e-mail: misicu@th.physik.uni-frankfurt.de

2. DEFORMATION-DEPENDENT DRIVING POTENTIAL

The basic ingredient in the driving potential is represented by the heavy-ion interaction between the projectile and the target with densities ρ_1 and ρ_2 and center of masses separated by the distance $\mathbf{R}$, which is computed with the double-folding integral method (see [4] and references therein),

$$V(\mathbf{R}) = \int d\mathbf{r}_1 \int d\mathbf{r}_2 \rho_1(\mathbf{r}_1)\rho_2(\mathbf{r}_2)v(\mathbf{s}), \quad (1)$$

where $\mathbf{s} = \mathbf{R} + \mathbf{r}_2 - \mathbf{r}_1$.

Considering that the orientation of each nucleus is specified by the Euler angles $\omega_i = (\alpha_i, \beta_i, \gamma_i)$ as shown in Fig. 1 and assuming that the molecular axis is fixed in space, we arrive at the following expression of the projectile–target potential [5]:

$$\begin{aligned} V(\mathbf{R}) = \frac{1}{2}\sum_{\lambda_i\mu} V^{\mu-\mu0}_{\lambda_1\lambda_2\lambda_3}(R)(1+(-1)^{\lambda_1+\lambda_2-\lambda_3}) \quad (2)\\ \times \cos\mu(\alpha_2-\alpha_1) d^{\lambda_1}_{\mu0}(\beta_1) d^{\lambda_2}_{-\mu0}(\beta_2) \\ + \frac{1}{2}\sum_{\lambda_i\mu} V^{\mu-\mu0}_{\lambda_1\lambda_2\lambda_3}(R)(1-(-1)^{\lambda_1+\lambda_2-\lambda_3}) \\ \times \sin\mu(\alpha_2-\alpha_1) d^{\lambda_1}_{\mu0}(\beta_1) d^{\lambda_2}_{-\mu0}(\beta_2), \end{aligned}$$

where

$$\begin{aligned} V^{\mu_1\mu_2\mu_3}_{\lambda_1\lambda_2\lambda_3}(R) = \frac{1}{(2\pi)^3} i^{\lambda_1-\lambda_2-\lambda_3}\hat{\lambda}_1\hat{\lambda}_2\hat{\lambda}_3^2 \quad (3)\\ \times \begin{pmatrix} \lambda_1 & \lambda_2 & \lambda_3 \\ 0 & 0 & 0 \end{pmatrix} \begin{pmatrix} \lambda_1 & \lambda_2 & \lambda_3 \\ \mu_1 & \mu_2 & \mu_3 \end{pmatrix} F_{\lambda_1\lambda_2\lambda_3}(R) \end{aligned}$$

1063-7788/03/6606-1095$24.00

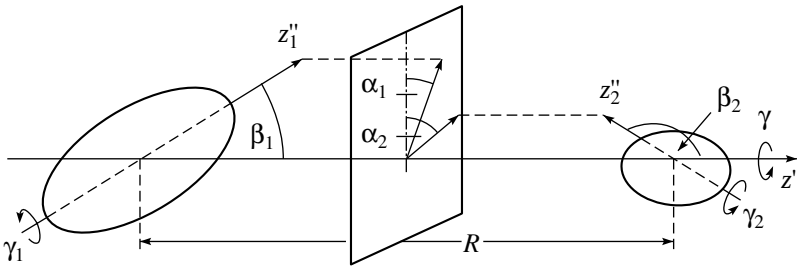

Fig. 1. The position and space orientation of two colliding nuclei is described by the center-to-center distance and the Euler angles α_i, β_i, γ_i. The axis z' is the third axis of the molecular (dinuclear) frame. The double-primed axes correspond to the intrinsic frame of each nucleus.

and $F_{\lambda_1\lambda_2\lambda_3}(R)$ is an oscillating integral whose integrand contains the multipolar components of the Fourier transforms of the projectile density (multipolarity λ_1) and target density (multipolarity λ_2), a spherical Bessel function j_{λ_3}, and the Fourier transform of the nucleon–nucleon potential. Due to the 3-j coefficient occurring in Eq. (3), with all the angular momentum projections equal to zero, the angular momenta must fulfill $\lambda_1 + \lambda_2 - \lambda_3 =$ even condition, otherwise the 3-j coefficient equals zero. Thus, the last sum in Eq. (2) cancels and the final expression of the double-folding potential reads

$$V(\mathbf{R}) = \sum_{\lambda_i\mu} V^{\mu-\mu0}_{\lambda_1\lambda_2\lambda_3}(R)\cos\mu(\alpha_2-\alpha_1) \times d^{\lambda_1}_{\mu0}(\beta_1)d^{\lambda_2}_{-\mu0}(\beta_2). \quad (4)$$

A very frequent way of considering the orientation of the projectile relative to the target when fusion is initiated is given by the so-called pole-to-pole (p–p) or nose-to-nose configuration [6]. In this case, $\alpha_1 = \alpha_2 = 0$ and $\beta_1 = \beta_2 = 0$, and Eq. (4) becomes

$$V(\mathbf{R}) = \sum_{\lambda_i} V^{000}_{\lambda_1\lambda_2\lambda_3}(R). \quad (5)$$

This configuration also arises in fission when the fragments are strongly polarized due to the nuclear forces and, accordingly, their symmetry axes are aligned. Only fluctuations around this axial symmetry configuration are allowed [7]. This is justified experimentally by the small forward anisotropy of the angular distribution of prompt γ rays.

As discussed in [3], for fusion reactions, there are also other relevant configurations. In the equator–equator (e–e) or belly-to-belly orientation, the axially symmetric fragments are in touching with their symmetry axis parallel to each other. Then $\alpha_1 = \alpha_2 = 0$, $\beta_1 = \beta_2 = \pi/2$, and the potential along the radial coordinate reads

$$V(\mathbf{R}) = \sum_{\lambda_i\mu}(-1)^{\frac{\lambda_1+\lambda_2}{2}}\sqrt{\frac{(\lambda_1+\mu-1)!!(\lambda_1-\mu-1)!!}{(\lambda_1+\mu)!!(\lambda_1-\mu)!!}\frac{(\lambda_2+\mu-1)!!(\lambda_2-\mu-1)!!}{(\lambda_2+\mu)!!(\lambda_2-\mu)!!}} \times \delta_{\lambda_1+\lambda_2,\text{even}}\delta_{\mu,\text{even}}V^{\mu-\mu0}_{\lambda_1\lambda_2\lambda_3}(R). \quad (6)$$

In the pole–equator (p–e) or the nose-to-belly orientation, $\alpha_1 = \alpha_2 = 0$, $\beta_1 = 0$, and $\beta_2 = \pi/2$. Hence,

$$V(\mathbf{R}) = \sum_{\lambda_i}(-1)^{\lambda_2/2}\sqrt{\frac{(\lambda_2-1)!!}{\lambda_2}}\delta_{\lambda_2,\text{even}}V^{000}_{\lambda_1\lambda_2\lambda_3}(R). \quad (7)$$

In the equator–equator-crossed (e–c) orientation $\alpha_1 = 0, \alpha_2 = \pi/2$, and $\beta_1 = \beta_2 = \pi/2$, and the heavy-ion potential reads

$$V(\mathbf{R}) = \sum_{\substack{\lambda_i-\text{even}\\ \mu-\text{even}}}(-1)^{\frac{\lambda_1+\lambda_2+\mu}{2}}\sqrt{\frac{(\lambda_1+\mu-1)!!(\lambda_1-\mu-1)!!}{(\lambda_1+\mu)!!(\lambda_1-\mu)!!}\frac{(\lambda_2+\mu-1)!!(\lambda_2-\mu-1)!!}{(\lambda_2+\mu)!!(\lambda_2-\mu)!!}} \times \delta_{\lambda_1+\lambda_2,\text{even}}\delta_{\mu,\text{even}}V^{\mu-\mu0}_{\lambda_1\lambda_2\lambda_3}(R). \quad (8)$$

To illustrate in a very simple way the influence of the orientation in fusion, we consider the projectile–target system ^{238}U + ^{48}Ca used in the synthesis of the superheavy nucleus $^{286}112$ [8], with the symmetry axes found in the same plane. In this case, the only degree of freedom describing the relative orientation is given by the angle $\beta_2 \equiv \theta$ between the molecular axis and the symmetry axis of the target. As one can see in Fig. 2, for each orientation of the ^{238}U target, pockets in the heavy-ion potential are possible. The difference is that the barrier increases with θ up to approximately 60°; afterward, the barrier decreases slightly. Cold fission is a reaction characterized by only one energy for each given fragmentation, i.e., the decay energy, and the scission configuration is shown to be of the type p–p [9]. This configuration minimizes the difference between the height of the Coulomb barrier and the Q value and, consequently, the tunneling probability. In cold fusion, when the projectile and target collide at different orientations, a certain range of values of the bombarding energy should be envisaged. For bombarding energies that are noticeably higher than the height of the p–p barrier, the fragments can scatter without undergoing mutual capture. When collision takes place for nonaxially symmetric configurations, the capture probability for higher energy will dominate over the one for lower energy. The essence of Fig. 2, in our opinion, is that a certain energy can lead to a hot fusion process for a p–p orientation, but for another one, say e–e, it can rather lead to a cold fusion process.

In the middle of the 1970s, one of us (W.G.) and collaborators proposed a method to determine the optimal projectile–target combinations for the synthesis of superheavy elements [10–12]. In that approach, we calculated the potential energy surface of a given compound nucleus for all possible projectile–target combinations as a function of the mass and charge asymmetries, $\eta = (A_1 - A_2)/(A_1 + A_2)$ and $\eta_Z = (Z_1 - Z_2)/(Z_1 + Z_2)$, at the touching point R_c, i.e., the point where the assumed spherical fragments come into contact and they interact only by means of the Coulomb force. The charges of the target and the projectile were determined by requiring that, for a fixed η, the potential $V(R, \eta, \eta_Z)$ attains a minimum in the η_Z direction; i.e., for every fixed mass pair (A_1, A_2) a single pair of charges is determined among all possible combinations. Next, minima of the potential on the two-dimensional (R, η) landscape were sought. From here, a criterion was inferred for cold fusion; i.e., the deep minima of the two-dimensional function $V(R, \eta)$ correspond to the projectile–target combinations where the compound nucleus has a minimum of excitation and deexcites to the ground state with the emission of a couple of neutrons.

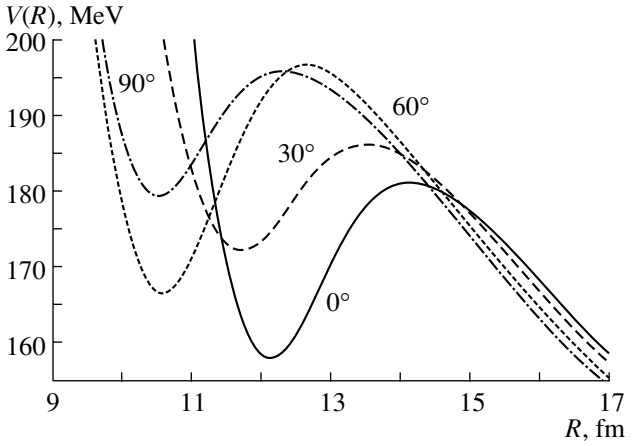

Fig. 2. The heavy-ion potential for the ^{238}U + ^{48}Ca system in four different orientations of the projectile, i.e., $\theta = 0°$ (pole–pole), 30°, 60°, and 90° (equator–equator).

It is a well-understood fact that the mass-asymmetry valleys which appear in the fragmentation potential are due to the shell effects. They are responsible for the maximum of cross sections for the same compound system obtained by different projectile–target combinations. It was advocated in [13], using the framework of fragmentation theory, that, due to the existence of different mass-asymmetry valleys for the same compound system, a new, highly asymmetric fission mode appears in which one of the fragments is close to the doubly magic nucleus ^{208}Pb. In all these calculations from the mid-1970s, the projectile and the target are considered to be spherical and therefore the orientation plays no role.

In what follows, we consider only the s channel in the fusion reactions; i.e., the orbital angular momentum is 0, and projectile and target are allowed to approach each other with various orientations specified by the Euler angles $\omega_i = (\theta_i, \phi_i)$, $i = 1, 2$. In order to avoid confusion between the second Euler angle and the deformation, we introduced a new notation for the angles (α, β), that is, (ϕ, θ). Then, the driving potential is defined as [14]

$$V_{\text{driv}} = V(R, Z_1, A_1, \{\beta^{(1)}\}_{2,3,4}, \{\beta^{(2)}\}_{2,3,4}, \omega_1, \omega_2) + B_1 + B_2 - B_{\text{CN}}. \quad (9)$$

Here, B_1, B_2, and B_{CN} are the binding energies of the projectile, target, and compound superheavy nucleus. The driving potential also depends on the charges, masses, the distance between the centers of mass of the two nuclei, mutual orientations, and the quadrupole, octupole, and hexadecapole deformations through the heavy-ion potential V defined in (4).

In the study of formation of dinuclear molecules, when the target is deformed and the projectile is

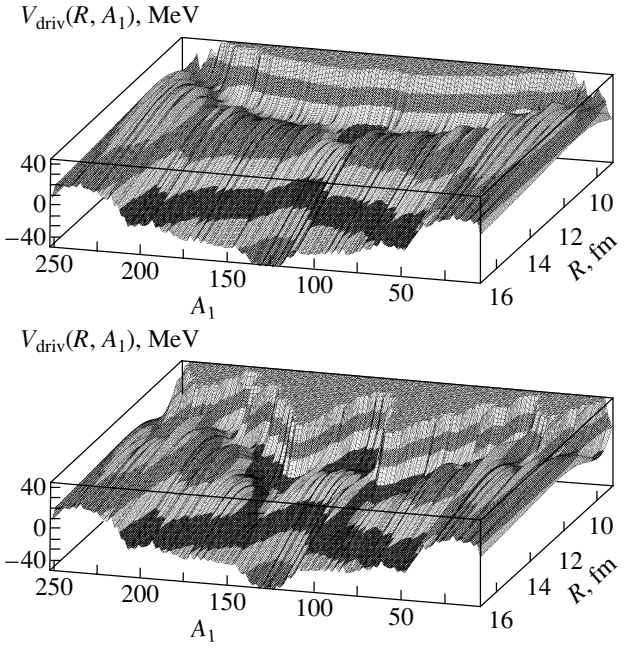

Fig. 3. Surface plot of the driving potential as a function of the projectile mass A_1 and the radius for the element ^{256}No. Upper panel corresponds to spherical nuclei, whereas the lower panel corresponds to deformed fragments in pole–pole orientation.

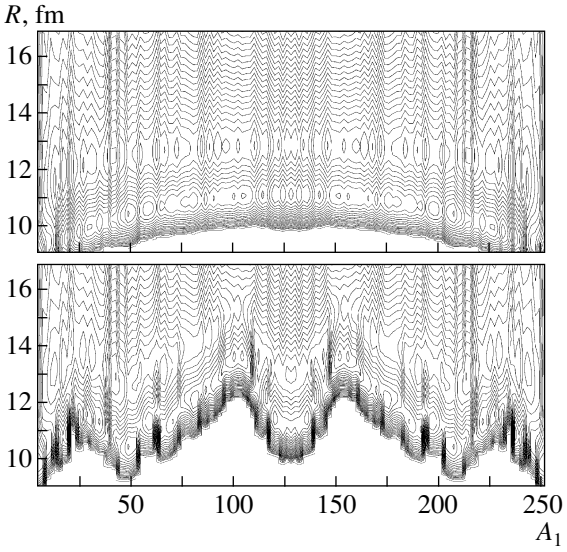

Fig. 4. Contour plot of the driving potential as a function of the projectile mass A_1 and the radius for the element ^{256}No. Upper panel corresponds to spherical nuclei, whereas the lower panel corresponds to deformed fragments in pole–pole orientation.

spherical, the subbarrier fusion cross section is computed by replacing the deformed nucleus with a series of spherical nuclei of different radii [15, 16]. The potential is then averaged over the angles of orientation to get an effective potential. In the present case, when both projectile and target can be deformed, the averaging formula reads

$$\bar{V}_{\mathrm{driv}} = \frac{\int V_{\mathrm{driv}}(\omega_1, \omega_2) d\omega_1 d\omega_2}{\int d\omega_1 d\omega_2}. \qquad (10)$$

A simple evaluation of the above integral using the multipolar decomposition of the double-folding potential (4) leads us to the result that the orientation-averaged driving potential $\bar{V}_{\mathrm{driv}}$ coincides with the monopolar component of the driving potential. For this reason, we expect similarities between the orientation-averaged driving potential of two deformed nuclei and the driving potential in the approximation of spherical nuclei.

We follow the same procedure as in [10] and search first for minima of the driving potential in the landscape (Z_1, Z_2) for a fixed mass pair (A_1, A_2). As a result, we obtain for each orientation (ω_1, ω_2) the driving potential as a function of the center-to-center distance R and the mass number of the projectile (target).

3. COLD VALLEYS OF SUPERHEAVY NUCLEI

As a case study, we compute the cold fusion driving potentials of the superheavy nuclei ^{256}102, ^{286}112, ^{292}114, ^{296}116, and ^{306}122, which were recently investigated by the group from FLNR, Dubna [17]. The target nuclei ^{208}Pb, ^{238}U, ^{244}Pu, and ^{248}Cm were bombarded with ^{48}Ca projectiles for the first four superheavy nuclei mentioned above. For element 122, the projectile ^{56}Fe was used to bombard ^{248}Cm. For ^{256}102, the mass distribution contains a broad peak centered on the symmetric region and a very asymmetric narrow but high peak centered apparently on ^{48}Ca. For the other four investigated superheavy nuclei, it was observed that the mass distribution of fission fragments of compound nuclei is asymmetric in shape with the light fragment mass on average being 132–134.

3.1. The Nucleus ^{256}No

As a function of R and A_1, the driving potential (9) is represented in Fig. 3 as a surface plot and in Fig. 4 as a contour plot. The upper panel corresponds to the case with spherical fragments, and the lower one to deformed nuclei and in p–p orientation. The differences between the spherical and the deformed case are noticeable. First of all, switching on the deformation induces valleys that are not found in the spherical case. The symmetric valley that occurs for spherical fragments is replaced by an asymmetric

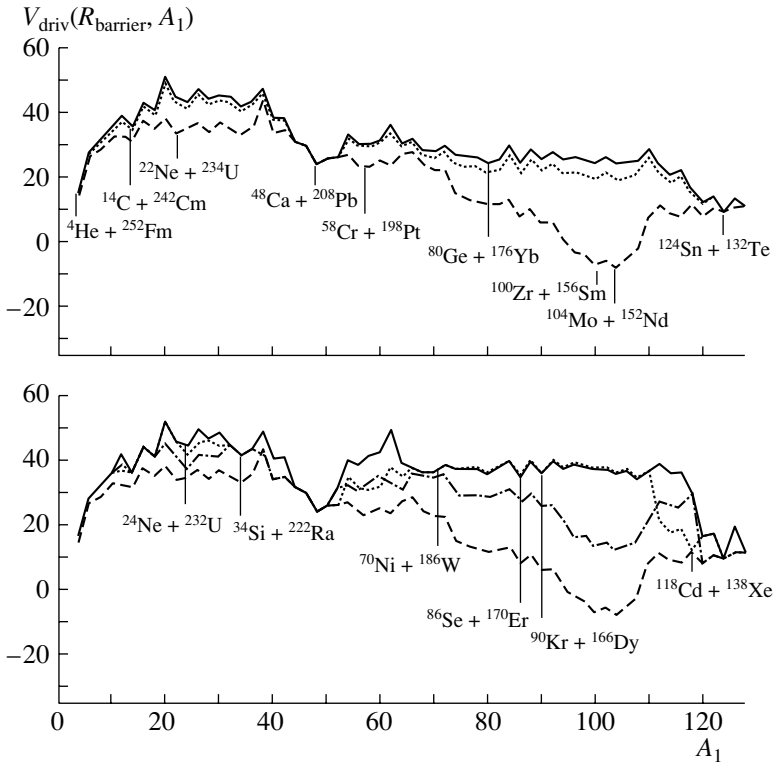

Fig. 5. Driving potential as a function of the projectile mass A_1 for the nucleus ^{256}No. In the upper panel, the driving potential along the A_1 coordinate at $R = R_{barrier}$ is represented for spherical fragments (solid line), for deformed fragments oriented in nose-to-nose configuration (dashed line), and for the averaged orientation (dotted lines). In the lower panel, the four curves correspond to the orientations nose-to-nose (dashed line), belly-to-belly (solid line), crossed bellies (dotted line), and nose-to-belly (dash-dotted line).

valley. As can be inferred from the contour plot, the valley corresponding to ^{48}Ca survives in both cases.

In Fig. 5, we represented a cut along the mass-asymmetry coordinate of the driving potential. In the upper panel, we compare the spherical, average-oriented, and p–p cases. The first two cases are very similar and the main valleys associated to them are ^{48}Ca + ^{208}Pb and ^{124}Sn + ^{132}Te. In between, there is a weakly developed valley centered on ^{80}Ge + ^{176}Yb. In the cluster radioactivity region, we note the valleys of ^{14}C, ^{24}Ne, and ^{34}Si.

The p–p orientation produces a different structure of valleys. The symmetric valley vanishes and its place is taken by a very pronounced valley centered on Mo–Zr. In a cold compound fission yield mass distribution, one should see high yields in this region. The fission mass distribution observed in the recent experiment from Dubna at excitation energy $E^* \approx 33$ MeV provides a pattern that better resembles the other two cases, i.e., spherical and orientation-averaged.

In the lower panel of Fig. 5, we compared the four deformed cases, i.e., p–p, p–e, e–e, and e–c. The e–e case bears many similarities to the spherical and orientation averaged cases, the valleys of Pb and Sn being even more pronounced.

3.2. The Nucleus ^{286}112

From the inspection of the driving potential contour plot of the nucleus ^{286}112 (see Fig. 6), we observe changes in the structure of minima compared to ^{256}No. In Fig. 7, we represented a cut along the mass-asymmetry coordinate of the driving potential.

From the inspection of Fig. 7, we note the differences in the driving potential when the target and the projectile are spherical and when they are deformed. In all the calculations, we included quadrupole, octupole, and hexadecapole deformations. The Ca valley (with heavy partner U) is more pronounced when one takes spherical fragments or when the fragments come into contact in e–e or e–c orientations. The valleys corresponding to the cluster radioactivity (superasymmetric valleys) occur with some differences: for p–p, the most pronounced are ^{14}C, ^{22}Ne, and ^{28}Mg, whereas for e–c we note ^{24}Ne, ^{30}Mg, and ^{36}Si.

For p–p-oriented fragments, the valley centered on ^{62}Cr is separated by a high barrier from what we

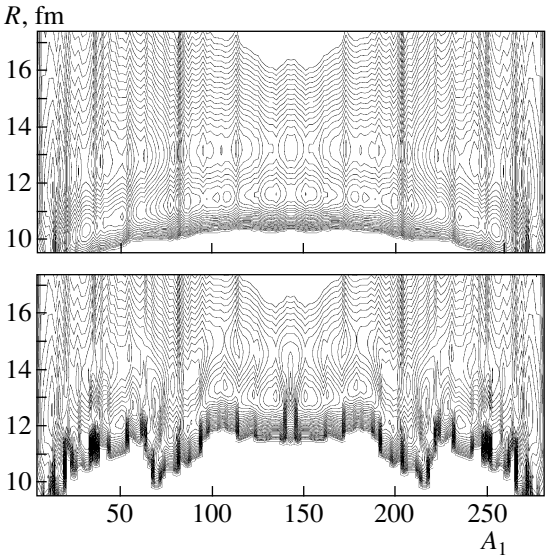

Fig. 6. The same as in Fig. 4, but for the element $^{286}112$.

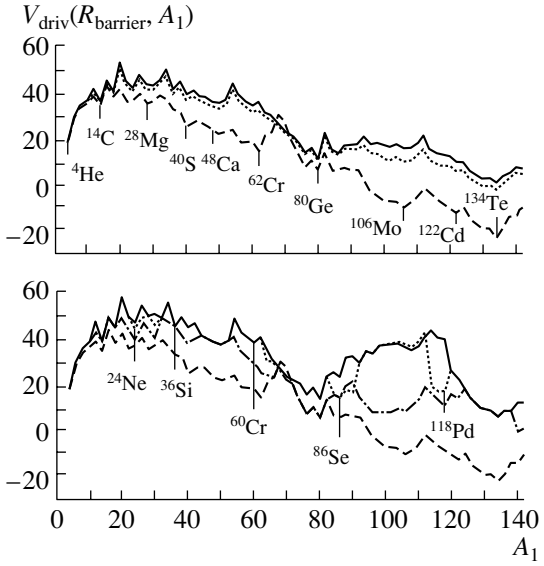

Fig. 7. The same as in Fig. 5, but for the nucleus $^{286}112$.

call the Pb valley centered on ^{76}Zn and ^{80}Ge, and obviously for such configurations, the tendency of the initial cold strong asymmetric system to move in the symmetric direction, before undergoing quasifission, is hindered.

The p–e orientation presents features common to the p–p but also to the e–e and e–c orientations. Similar to the p–p case, the valley for Ca is less pronounced and the Mo valley is broader and the target ^{96}Sr will give a minimum in the potential for this orientation.

For the e–c orientation, we notice a valley, coming after the Pb valley, centered on ^{86}Se, which also contains ^{90}Kr. For this orientation, there is an additional valley centered on ^{118}Pd, which is connected to the prolate-to-oblate transition in this mass region of the target, as can be observed in the top left panel of Fig. 8, and the region of negative hexadecapole deformations (slightly necked shapes) of both projectile and target (see the top left panel of Fig. 9). This valley also occurs for the elements 114 and 116 for the same reasons. For e–e orientations, these two valleys disappear. Between the Pb valley and the valley centered on ^{134}Te, which also contains Sn, a huge barrier appears, which determines an even stronger hindrance to symmetric quasifission compared to p–p orientation.

The orientation-averaged potential follows very closely the spherical one, the differences in the barrier height being more sensitive in the weak asymmetric and symmetric regions. This characteristic is the same for all superheavy nuclei studied in this paper.

3.3. The Nucleus $^{292}114$

For the driving potential of the superheavy nucleus $^{292}114$ (see Fig. 10), we note a similar structure of p–p and e–e valleys as for $^{286}112$: a nearly symmetric valley with the minimum displaced at ^{140}Xe for the p–p configuration, a broad asymmetric valley centered on ^{106}Mo (which also contains Zr isotopes and arising only for p–p orientations), the deep Cr valley (in combination with U), a very asymmetric shallow valley centered on ^{84}Ge + ^{208}Pb for the p–p orientation, and a deep valley centered on ^{86}Se for the e–e and e–c orientations. In other calculations, this valley is assigned to Kr [18]. One should note that the occurrence of this deep valley is motivated by the transition to oblate deformations of the target, as can be observed in the top right panel of Fig. 8. In the present study, a few of the Kr isotopes occur in the e–e and e–c valleys. The valley corresponding to ^{48}Ca (in combination with ^{248}Cm) is less pronounced for the p–p orientations, but when the fragments are constrained to be spherical or to collide in the belly-to-belly or crossed-belly orientation, this valley becomes more pronounced.

As for the p–e orientation, we note the increase in importance of the ^{98}Sr nucleus simultaneously with the disapperance of the minimum centered on Mo. The Cr valley, which occurred for the p–p orientation, is now shifted to ^{64}Fe such that we deal with the Fe valley frequently invoked in the literature.

3.4. The Nucleus $^{296}116$

For the nucleus $^{296}116$, the new features are the entrance in competition with the Cr–Fe valley of

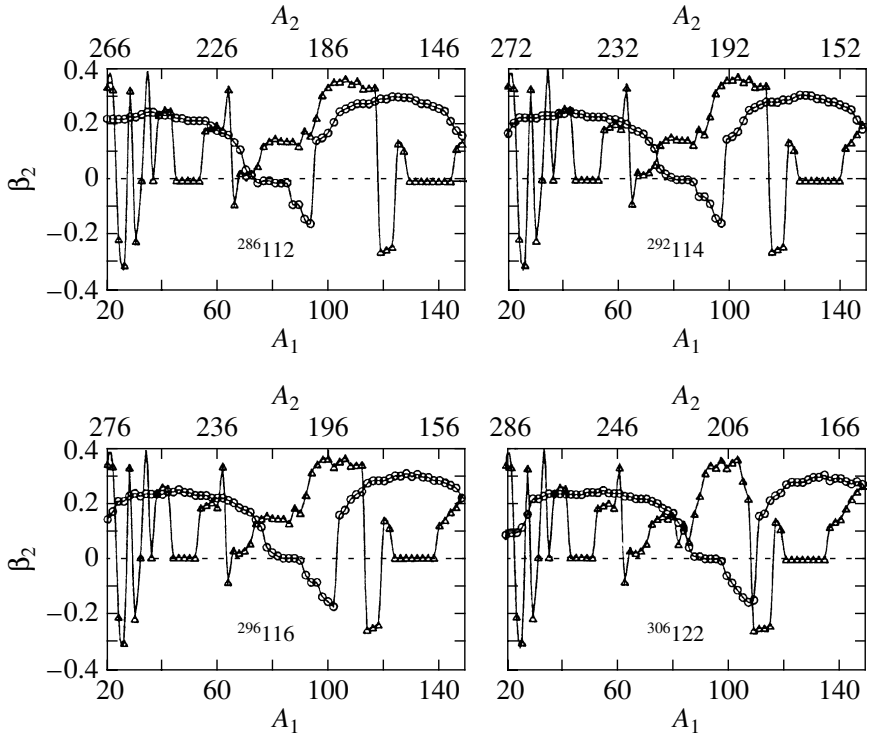

Fig. 8. Quadrupole deformations of the projectile A_1 (triangles) and target A_2 (circles) for the four superheavy nuclei studied in the present paper.

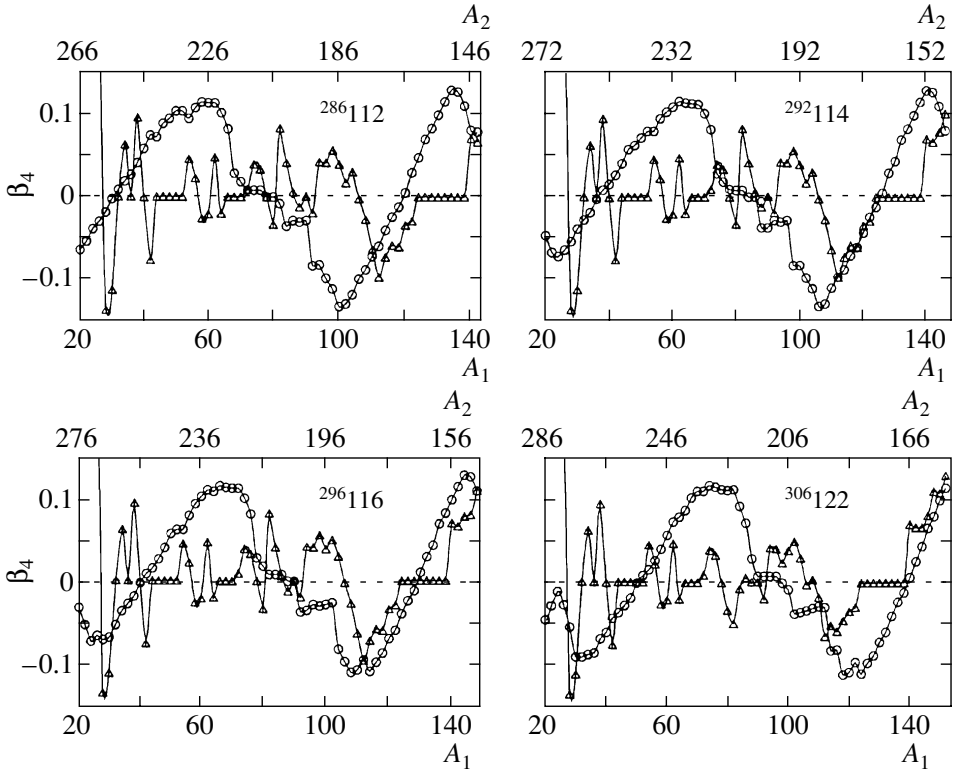

Fig. 9. Hexadecapole deformations of the projectile A_1 (triangles) and target A_2 (circles) for the four superheavy nuclei studied in the present paper.

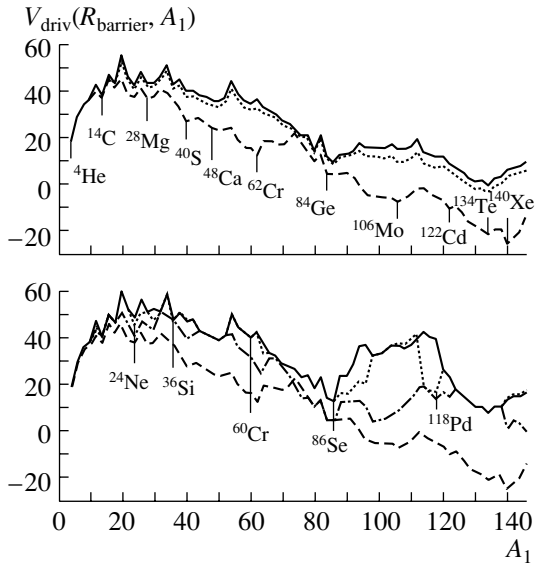

Fig. 10. The same as in Fig. 5, but for the nucleus $^{292}114$.

a neighboring valley centered on ^{74}Zn for the p–p orientation, the entrance of ^{90}Kr in competition with ^{86}Se for the Pb valley in e–e and e–c orientations, and the occurrence of a second minimum (^{100}Zr) in the Mo valley for the p–p orientations (see Fig. 11). As in the previous case, the accentuation of the Pb valley for the e–e and e–c orientations is a consequence of the prolate-to-oblate transition of the target (bottom left panel of Fig. 8) and small negative hexadecapole deformations of both nuclei.

Contrary to the cases of nuclei $^{286}112$ and $^{292}114$, for $^{296}116$ an absolute minimum occurs for full-symmetric fragmentation, i.e., ^{148}Ce + ^{148}Ce in the p–p configuration.

In the case of the p–e orientation, the Fe valley gains more stability.

3.5. The Nucleus $^{306}122$

We next go six units higher in charge, to the superheavy nucleus $^{306}122$, in order to investigate possible deviations from the above-observed pattern of formation of cold fusion valleys.

From Fig. 12, we observe a new arrangement of valleys and minima compared to ^{256}No and $^{286}112$.

For the p–p orientation, we notice two main valleys, one corresponding to Mo–Zr, already observed for the previous superheavy nuclei, and another one corresponding to Ge (see Fig. 13). This last valley gains in importance in comparison to the previously superheavy nuclei due to the occurrence of large deformations of the Th target. In this case, the Pb valley melts with the Mo–Zr valley since Pb comes in combination with Zr. For the orientations p–e and e–e, it is only the Pb part of this valley which survives, whereas for e–c it vanishes.

The tendency observed for $^{296}116$ to form a valley for total symmetry ($\eta = 0$) and p–p orientation will now be even more accentuated, which could lead to a high quasifission yield for symmetric separation if the p–p scenario would work for cold fusion.

For the e–c orientation, we obtain a new valley centered on ^{112}Ru. In this region, both projectile and targets have negative hexadecapole deformations, as can be noticed from the bottom right panel of Fig. 8.

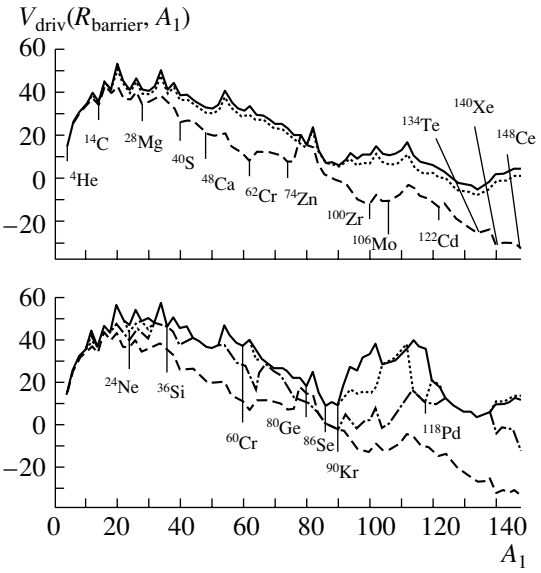

Fig. 11. The same as in Fig. 5, but for the nucleus $^{296}116$.

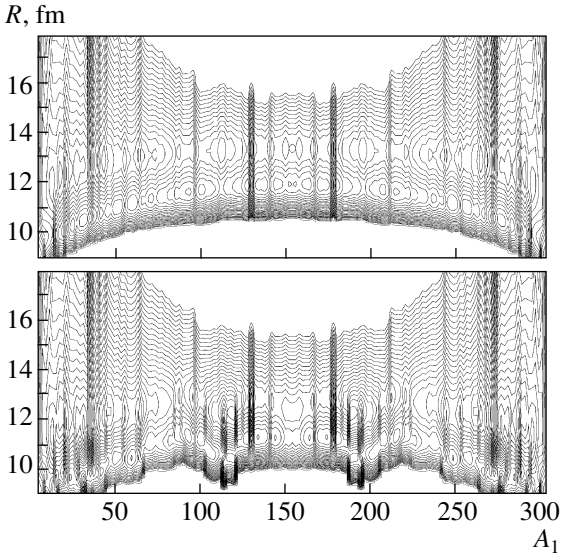

Fig. 12. The same as in Fig. 4, but for the element $^{306}122$.

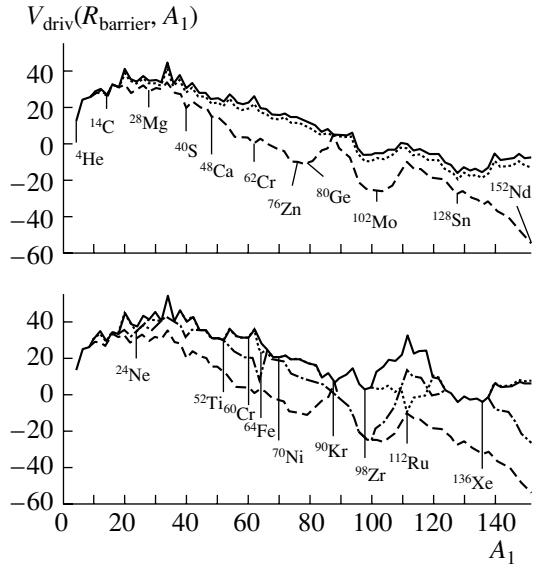

Fig. 13. The same as in Fig. 5, but for the nucleus $^{306}122$.

For the p–e orientation, we note the constancy of the valley centered on ^{64}Fe and the fact that the leading role in the Mo–Zr valley, specific for the p–p orientation, will now be taken over by ^{100}Zr, which comes in combination, with the doubly magic ^{208}Pb. This valley will be separated from the total symmetric valley by a broad barrier, contrary to the p–p case.

In the cluster radioactivity region, we notice the occurrence of a narrow valley for ^{32}Si.

4. CONCLUSIONS

The task of the present study was to understand the role of mutual orientation of fragments in the formation of cold fusion valleys. Especially due to the existence of quadrupole and hexadecapole deformations, the various orientations will produce different valley structures in the fusion potential.

According to earlier calculations in which the fragments are endowed only with quadrupole deformations and the barrier is constructed by using the nuclear proximity potential [19], for the elements 112, 114, and 116, two valleys are substantiated, one corresponding to Fe and the other one to Pb. The deformations used in the present study are provided by recent improved calculations of the macroscopic–microscopic model [20] that also take into account octupole and hexadecapole distortions of the nuclear shape.

The main reason for the importance of the Mo valley, for all superheavy nuclei studied in this paper, in the p–p orientation is the existence of noticeable prolate deformations for both projectile and target. In what concerns the Ge valley, things are different. Only the target has not too large a deformation for the nucleus $^{286}112$, and the reason why ^{80}Ge dominates a very shallow valley can be explained by the sensitive decrease in the Q value for the reaction $^{80}\mathrm{Ge} + {}^{206}\mathrm{Hg} \rightarrow {}^{286}112$. For the synthesis of $^{306}122$, the isotope Ge will enter in combination with well-prolate deformed isotopes of Th, and therefore the corresponding valley will gain in importance. However, it should be noted that, for spherical projectile target pairs or for e–e and e–c orientations, the Ge valley disappears.

We also noted the occurrence of Sn isotopes in a weak asymmetric valley, but not of the doubly magic ^{132}Sn. As for the doubly magic nucleus ^{208}Pb, we arrived at the conclusion that the corresponding valleys in the driving potential are especially pronounced for the e–e and e–c orientations and to a lesser extent for p–e. In contrast to these orientations, the p–p driving potential exhibits a very shallow Pb valley.

We also showed that the orientation-averaged driving potential resembles very much the driving potential with spherical projectile–target pairs.

It is obvious from the inspection of driving potential cuts along the mass-asymmetry coordinate that the p–p orientation is unlikely to explain the experimental observation of asymmetric distribution of fission fragments. Deep cold valleys including the light fragments with mass 132–134 were found in the present study for all studied configurations, including the orientation averaged case, except the p–p case. This can be understood, according to our opinion, whether by the realization of the orientation-averaged scenario for quasifission fragments, not for the fission fragments, or by the fission of the compound nucleus along channels other than the p–p one. This last scenario, in contrast to the scenario widely accepted for the cold fission of ^{252}Cf, when the fragments emerge in the p–p configuration, may be for the moment justified only qualitatively by the possibility of populating the states from the oblate well due to the available excitation energy in the compound nucleus. The decisive answer to this challenging problem naturally requires more experimental information.

Although some of the predicted fusion valleys are not found in previous works, we should note that several of the neutron-rich isotopes creating these valleys (^{100}Zr, ^{106}Mo, ^{112}Ru, ^{148}Ce, ^{140}Xe) were recently recorded in the cold binary fission of ^{252}Cf [21]. In the cluster radioactivity region, we note the valleys for ^{14}C, ^{24}Ne, and ^{28}Mg, clusters which were earlier observed to be emitted from the parent nuclei ^{224}Ra, ^{234}U, and ^{238}Pu (see [22] and references therein).

As noted in [3], it was Nörenberg who first suggested the use of two well-deformed rare-earth nuclei

in an equator–equator twisted orientation in fusion, for the simplest reason that such an orientation leads to the most compact touching configuration out of all possible orientations of two deformed nuclei. In this paper, we showed quantitatively the occurrence of fusion cold valleys for such orientations in all cases. For the superheavy nuclei $^{286}112$, $^{292}114$, and $^{296}116$, this valley corresponds to ^{118}Pd, whereas for $^{306}122$ the valley is centered on ^{112}Ru .

It should be noted that, according to the relativistic mean field theory, the nucleus with proton number $Z = 120$ and neutron number $N = 172$ is predicted to be doubly magic. Nuclei near this value of N and Z are also expected to be spherical, and therefore the argument that collisions in the equator–equator twisted orientation are geometrically more suitable in the synthesis of a spherical superheavy nucleus than the pole-to-pole one seems to be justified.

ACKNOWLEDGMENTS

One of the authors (Ş.M.) would like to acknowledge the financial support from the European Community through a Marie Curie fellowship. He is also grateful to Prof. A. Săndulescu, Dr. F. Cârstoiu, and Dr. A. Nasirov for enlightening discussions. Both authors express thanks to Dr. Th. Bürvenich, who read the manuscript and expressed critical remarks. The technical assistance of Ms. Astrid Steidl in designing Fig. 1 is kindly acknowledged.

REFERENCES

1. W. Greiner, J. Y. Park, and W. Scheid, *Nuclear Molecules* (World Sci., Singapore, 1995).
2. R. Bass, *Nuclear Reactions with Heavy Ions* (Springer-Verlag, Berlin, 1980).
3. A. Iwamoto, P. Möller, J. Rayford Nix, and H. Sagawa, Nucl. Phys. A **596**, 329 (1996).
4. A. Săndulescu, Ş. Mişicu, F. Cârstoiu, and W. Greiner, Fiz. Élem. Chastits At. Yadra **30**, 908 (1999) [Phys. Part. Nucl. **30**, 386 (1999)].
5. Ş. Mişicu and W. Greiner, Phys. Rev. C **66**, 044606 (2002).
6. P. O. Hess and W. Greiner, Nuovo Cimento A **83**, 77 (1984).
7. Ş. Mişicu, A. Săndulescu, G. M. Ter-Akopian, and W. Greiner, Phys. Rev. C **60**, 034613 (1999).
8. Yu. Ts. Oganessian, Nucl. Phys. A **682**, 108c (2001).
9. Ş. Mişicu, A. Săndulescu, and W. Greiner, Phys. Rev. C **64**, 044610 (2001).
10. A. Săndulescu, R. K. Gupta, W. Scheid, and W. Greiner, Phys. Lett. B **60B**, 225 (1977).
11. R. K. Gupta, A. Săndulescu, and W. Greiner, Phys. Lett. B **67B**, 257 (1977).
12. R. K. Gupta, C. Pârvulescu, A. Săndulescu, and W. Greiner, Z. Phys. A **283**, 217 (1977).
13. A. Săndulescu and W. Greiner, J. Phys. G **3**, L189 (1977).
14. G. Giardina, S. Hofmann, A. I. Muminov, and A. K. Nasirov, Eur. Phys. J. A **8**, 205 (2000).
15. R. G. Stokstad and E. E. Gross, Phys. Rev. C **23**, 281 (1981).
16. T. Arctaedius and Chr. Bargholz, Z. Phys. A **335**, 315 (1990).
17. M. G. Itkis *et al.*, in *Proceedings of the International Workshop on Fusion Dynamics at the Extremes,* Ed. by Yu. Ts. Oganessian and V. I. Zagrebaev (World Sci., Singapore, 2001), p. 93.
18. R. K. Gupta, M. Balasubramanian, G. Münzenberg, *et al.*, J. Phys. G **27**, 867 (2001).
19. A. Săndulescu and W. Greiner, Rep. Prog. Phys. **55**, 1423 (1992).
20. P. Möller, J. R. Nix, W. D. Myers, and W. J. Swyatecki, At. Data Nucl. Data Tables **59**, 185 (1995).
21. A. V. Ramayya *et al.*, in *Proceedings of the Second International Conference "Fission and Properties of Neutron Rich Nuclei",* Ed. by J. H. Hamilton, W. R. Phillips, and H. K. Carter (World Sci., Singapore, 1999), p. 246.
22. R. K. Gupta and W. Greiner, Int. J. Mod. Phys. E **3** (1 Suppl.), 335 (1994).

Physics of Atomic Nuclei, Vol. 66, No. 6, 2003, pp. 1105–1113. From Yadernaya Fizika, Vol. 66, No. 6, 2003, pp. 1141–1149.

Analysis of Fusion–Fission Process with Neutron Evaporation in Superheavy Mass Region*

Y. Aritomo[1),2)**] **and M. Ohta**[3)]

[1)] *Flerov Laboratory of Nuclear Reactions, Joint Institute for Nuclear Research, Dubna, Moscow oblast, 141980 Russia*

[2)] *Department of Physics, University of Tokyo, Japan*

[3)] *Department of Physics, Konan University, Okamoto, Japan*

Received August 28, 2002

Abstract—The fusion–fission process for the synthesis of superheavy elements is discussed on the basis of fluctuation–dissipation dynamics. Recently, experiments at Dubna on fission of superheavy nuclei were carried out, and the mass and total kinetic energy distributions of fission fragments were measured. The fusion–fission cross section was derived from the experiments. We analyze the data using a three-dimensional Langevin calculation. We present a clear understanding of the competition between the fusion and the quasifission. We emphasize that a one- or two-dimensional model of Langevin calculation is not sufficient to estimate the fusion cross section in the superheavy mass region. Also, experiments on the emission of neutrons in correlation with fission fragments were conducted. It is useful to investigate the fusion–fission dynamics. We take into account the neutron emission with a Langevin calculation and compare it with experimental data. Finally, we discuss the evaporation residue cross section for superheavy elements. © *2003 MAIK "Nauka/Interperiodica".*

1. INTRODUCTION

Unceasing efforts have been devoted to synthesizing superheavy elements. Recently, a group from Dubna announced the production of superheavy elements $Z = 114$ in the reactions $^{48}\mathrm{Ca} + {}^{244}\mathrm{Pu}$ and $^{48}\mathrm{Ca} + {}^{242}\mathrm{Pu}$ [1]. Moreover, they presented the observation of the first decay events of $^{292}116$ in the reaction $^{48}\mathrm{Ca} + {}^{248}\mathrm{Cm}$ [2]. Now, they are carrying out the experiment of synthesizing $Z = 118$ in the reaction $^{48}\mathrm{Ca} + {}^{249}\mathrm{Cf}$ [3].

Also, experiments at Dubna on the fission of superheavy nuclei were carried out [4]. The mass and total kinetic energy (TKE) distributions of the fission fragments were measured. The fusion–fission cross section of compound nuclei was derived from the mass symmetric fission fragments ($A/2 \pm 20$), where A denotes the mass number of the compound nucleus. They also measured the emission of neutrons and gamma rays in correlation with fission fragments in the decay of superheavy compound systems.

In order to understand the mechanism of the fusion–fission process and synthesizing superheavy elements, we treat the whole process from touching of two colliding nuclei to the formation of a compound nucleus, and further to their reseparation. We divide the whole dynamical process into three stages. The first stage is the approaching process, and the second stage is the process from the point corresponding to the touching of two colliding nuclei to the formation of a compound nucleus. The third stage is decay process of the compound nucleus under the competition between fission and neutron evaporation.

In the second stage, the trajectory calculations with friction are performed [5–7]. In the superheavy mass region, the mean trajectories cannot overcome the extra barrier only by adding extra energy due to strong fusion hindrance [5–7]. Therefore, it is necessary to solve a full dissipative dynamics or a fluctuation–dissipation dynamics with the Fokker–Planck equation or with the Langevin equation [8–12]. We can describe the competition between the fusion–fission and quasifission process in the dynamical calculation.

Using the three-dimensional Langevin equation, we try to reproduce the experimental data. The purpose of the present paper is to elucidate the mechanism of the fusion–fission process and present the fusion–fission cross section and evaporation residue cross section by theoretical calculation. We also take into account the neutron emission with the Langevin calculation and discuss the neutron multiplicity in

*This article was submitted by the authors in English.

**E-mail: aritomo@jinr.ru

1063-7788/03/6606-1105$24.00

the fusion–fission process, where the reaction mechanism should be clarified.

In Section 2, we explain our framework and model. In Section 3, we discuss the mass distribution and TKE distribution of the fission fragments. We present our results for the excitation function of the fusion–fission cross section in the reactions ^{48}Ca + ^{244}Pu and ^{48}Ca + ^{249}Cf in Section 4. We discuss the fusion probability and survival probability. In Section 5, we present the neutron multiplicity in correlation with fission fragments. Also, we discuss the synthesis of superheavy elements when one neutron evaporates on the fusion process. A summary is presented in Section 6.

2. MODEL

We estimate the fusion–fission cross section $\sigma_{\rm CN}$ as

$$\sigma_{\rm CN} = \frac{\pi\hbar^2}{2\mu_0 E_{\rm c.m.}} \sum_{l=0}^{\infty} (2l+1) T_0(E_{\rm c.m.}, l) P_{\rm CN}(E^*, l), \tag{1}$$

where μ_0 denotes the reduced mass in the entrance channel. $E_{\rm c.m.}$ and E^* denote the incident energy in the c.m. frame and the excitation energy of the composite system, respectively. $P_{\rm CN}(E^*, l)$ is the probability of forming a compound nucleus in competition with quasifission. $T_0(E_{\rm c.m.}, l)$ is the barrier penetration coefficient of the lth partial wave through the potential barrier. $T_0(E_{\rm c.m.}, l)$ is calculated with a parabolic approximation of the combined Coulomb potential and proximity potential [13, 14],

$$T_0(E_{\rm c.m.}, l) = \left[1 + \exp\left(2\pi \frac{B_l - E_{\rm c.m.}}{\hbar\omega_l}\right)\right]^{-1}. \tag{2}$$

Here, B_l is the fusion barrier height for the partial wave with angular momentum l, and ω_l denotes the oscillator frequency.

Also, we estimate the evaporation residue cross section $\sigma_{\rm ER}$ as

$$\sigma_{\rm ER} = \frac{\pi\hbar^2}{2\mu_0 E_{\rm c.m.}} \sum_{l=0}^{\infty} (2l+1) T_0(E_{\rm c.m.}, l) \times P_{\rm CN}(E^*, l) W(E^*, l), \tag{3}$$

where W is the survival probability of the compound nuclei during deexcitation.

When we treat the fusion–fission process of the superheavy mass region, we have to take into account the competition between quasifission and fusion [10, 12, 15–17]. In order to treat the process precisely, we use the fluctuation–dissipation model. Fluctuation–dissipation dynamics can be described with the Langevin equation or with the Fokker–Planck equation [18]. In this research, we employ the Langevin equation. We adopt a three-dimensional nuclear deformation space with two-center parametrization [19, 20]. The neck parameter ϵ is fixed at 1.0 in the present calculation. The three collective parameters to be described by the Langevin equation are treated as follows: z_0 (distance between two potential centers), δ (deformation of fragments), and α (mass asymmetry of the colliding partner); $\alpha = (A_1 - A_2)/(A_1 + A_2)$, where A_1 and A_2 denote the mass number of target and projectile, respectively.

The multidimensional Langevin equation is given in the following form:

$$\frac{dq_i}{dt} = \left(m^{-1}\right)_{ij} p_j, \tag{4}$$

$$\frac{dp_i}{dt} = -\frac{\partial V}{dq_i} - \frac{1}{2}\frac{\partial}{\partial q_i}\left(m^{-1}\right)_{jk} p_j p_k - \gamma_{ij}\left(m^{-1}\right)_{jk} p_k + g_{ij} R_j(t),$$

where summation over repeated indices is tacitly assumed; V is the potential energy; and m_{ij} and γ_{ij} are the shape-dependent collective inertia and dissipation tensors, respectively. The normalized random force $R_i(t)$ is assumed to be a white noise, i.e., $\langle R_i(t)\rangle = 0$ and $\langle R_i(t_1) R_j(t_2)\rangle = 2\delta_{ij}\delta(t_1 - t_2)$. The strength of random force g_{ij} is given by $\gamma_{ij} T = \sum_k g_{ij} g_{jk}$, where T is the temperature of the compound nucleus calculated from the intrinsic energy of the composite system as $E_{\rm int} = aT^2$ with a denoting the level density parameter. The temperature dependent potential energy is defined as follows:

$$V(q, l, T) = V_{\rm DM}(q) + \frac{\hbar^2 l(l+1)}{2I(q)} + V_{\rm shell}(q)\Phi(T), \tag{5}$$

$$V_{\rm DM}(q) = E_S(q) + E_{\rm C}(q), \tag{6}$$

where $I(q)$ is the moment of inertia of a rigid body at deformation q, $V_{\rm shell}$ is the shell correction energy at $T = 0$, and $V_{\rm DM}$ is the potential energy of the finite range droplet model. E_S and $E_{\rm C}$ denote a generalized surface energy [21] and Coulomb energy, respectively. The centrifugal energy with a moment of inertia of the rigid body is also considered. The temperature-dependent factor Φ is parametrized as $\Phi = \exp\{-aT^2/E_d\}$ following the work of Ignatyuk *et al.* [22]. The shell-damping energy E_d is chosen to be 20 MeV. A hydrodynamical inertia tensor is adopted with the Werner–Wheeler approximation for the velocity field, and the wall-and-window one-body dissipation is adopted for the dissipation tensor [23–25]. Intrinsic energy of the composite system $E_{\rm int}$ is calculated for each trajectory as

$$E_{\rm int} = E^* - \frac{1}{2}\left(m^{-1}\right)_{ij} p_i p_j - V(q, l, T), \tag{7}$$

where E^* is the excitation energy of the composite system, which is given as $E^* = E_{\text{c.m.}} + Q$ with Q denoting the Q value of the reaction. At $t = 0$, each trajectory starts from the contact configuration with the initial velocity in the z_0 direction.

3. MASS AND TKE DISTRIBUTION OF FISSION FRAGMENTS

In this section, we discuss the mass and TKE distribution of fission fragments in the superheavy mass region. When we deal with the fusion–fission process in the superheavy mass region, the competition between the fusion and quasifission is very important. Such competition has great influence on the the mass and TKE distribution of fission fragments. We estimate them by the simulation in solving the Langevin equation. The experimental data of the mass and TKE distribution of fission fragments are shown in [26]. These data depend on the incident energy. In the case of $Z = 102$, at each incident energy, the mass-symmetric fission fragments are dominant. In the case of $Z = 110$, when the incident energy is low, mass asymmetric fission and deep inelastic collision are dominant. When the incident energy is large, mass symmetric fission is dominant. We try to estimate the experimental data with our model.

Figure 1 shows mean trajectories at each energy on the potential energy surface for $^{256}102$ and $^{272}110$. The potential energy surface is calculated by the liquid-drop model in nuclear deformation space with $l = 0$, which is calculated using the code from [27, 28]. Here, the excitation energy of the compound nucleus is found to correspond to the values of the incident energy.

Nuclear shapes are described with the two-center potential parametrization. In Fig. 1, the abscissa denotes z and the ordinate denotes the mass asymmetry α. The coordinate z is defined as $z = z_0/(R_{\text{CN}}B)$, where z_0 and R_{CN} denote the distance between two potential centers and the radius of the spherical compound nucleus, respectively. The parameter B is defined as $B = (3 + \delta)/(3 - 2\delta)$. By this scaling, we can save a great deal of computation time. The position at $z = \alpha = 0$ corresponds to a spherical compound nucleus. The cross point (+) denotes the touching point of the system. We start the Langevin calculation at the touching point.

In the case of $Z = 102$, all mean trajectories at each excitation energy go to mass symmetric fission. However, in the case of $Z = 110$, the mean trajectory at low excitation energy goes to mass asymmetric fission.

In this model, we have one unknown parameter. We start the Langeven calculation at the touching point. In fact, during approaching process, the relative kinetic energy of the colliding system dissipates through the friction force [29]. We need information on how much kinetic energy dissipates at the touching point. For example, in order to get this information, we employ the surface friction model. However, we are not sure about applying the surface friction model in the superheavy mass region. Therefore, at this point, we deal with it as a parameter.

The results of the mass distribution of fission fragments in the system ^{48}Ca + ^{208}Pb, ^{52}Cr + ^{208}Pb, and ^{64}Ni + ^{208}Pb are shown in Fig. 2. When we assume that 25% of kinetic energy dissipates during the process up to the touching point, the results agree rather well with experimental data. When we take 100% of kinetic energy dissipation, the mass distribution shows two sharp peaks around the mass region of the target and projectile, which means the DIC process. The calculation with the surface friction model shows that 100% of kinetic energy dissipates during the process up to the touching point. This means that the energy dissipation calculated by the surface friction model is too strong.

Figure 3 shows the TKE distribution of fission fragments in the same system as Fig. 2. The tendency of the results agrees with experimental data.

4. FUSION–FISSION CROSS SECTION AND EVAPORATION RESIDUE CROSS SECTION

4.1. Fusion–Fission Cross Section

In order to check the validity of our model, we analyzed the fusion–fission cross section in the reaction ^{48}Ca + ^{208}Pb. The details of the calculation are presented in [16]. The excitation function of the fusion–fission cross section shows good agreement with experimental data.

Next, we present an analysis of the ^{48}Ca + ^{244}Pu reaction. Figure 4 shows the samples of the trajectory at $E^* = 33$ MeV in the three-dimensional coordinate space. Nuclear shapes at each point are denoted in Fig. 4. The box in Fig. 4 is a fusion box that is defined as the inside of the fission saddle point. The probability of the mass asymmetric fission process is 93.12%, which corresponds to the quasifission process (QF). The trajectory for the mass-symmetric fission occupies 6.8% of all trajectories. However, almost all trajectories of mass symmetric fission do not enter the fusion box. They move in the direction of the large deformation of fragments due to the steep potential slope. We call such a trajectory a "deep quasifission process" (DQF) [15, 16]. That is to say, the deep quasifission process contributes to the yield of the mass-symmetric fission fragments [15, 16, 30]. In fact, at $E^* = 33$ MeV, only 0.08% of all trajectories

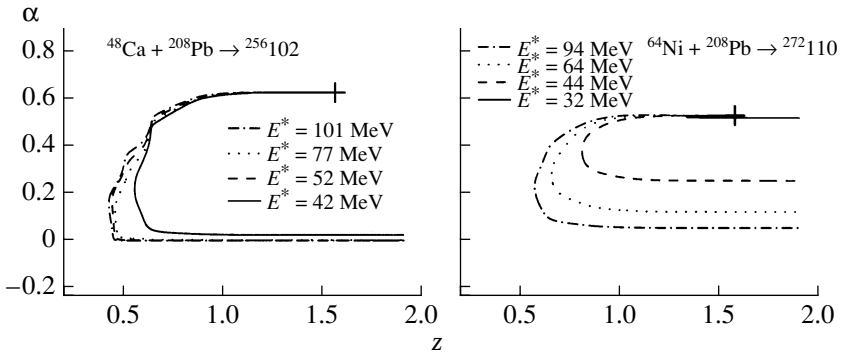

Fig. 1. The mean trajectories at each energy on the potential energy surface for ^{256}102 and ^{272}110. The potential energy surface is calculated by the liquid-drop model in nuclear deformation space. The abscissa and the ordinate denote the separation between two potential centers and the mass asymmetry, respectively. The marks (+) indicate the contact configuration of each system.

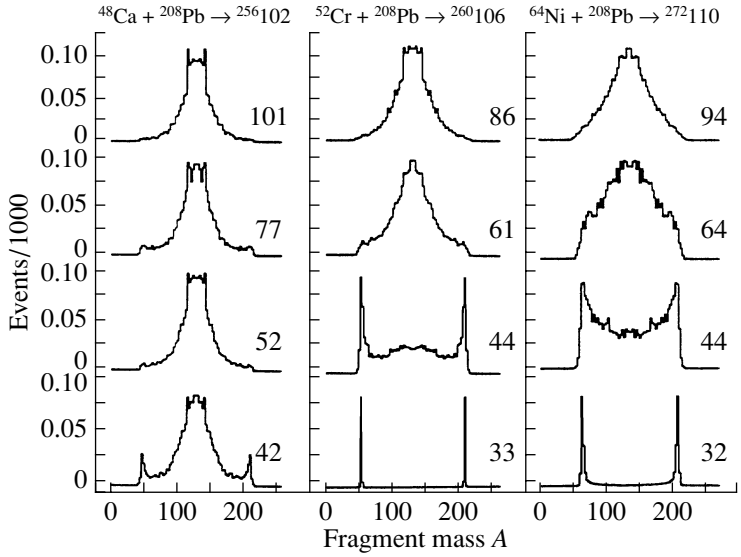

Fig. 2. The mass distribution of fission fragments in each system. The excitation energies are denoted by figures. Here, we assume that 25% of kinetic energy dissipates at the touching point.

can enter the spherical region of fusion box, which is represented by CN in Fig. 4.

When we calculate the trajectories for the fusion–fission process, we have to pay attention to the dynamical deformation of fragments, because a lot of trajectories go in the $+\delta$ direction. We would like to emphasize that a one- or two-dimensional calculation is not sufficient to describe the fusion–fission process in the superheavy mass region. Three- or higher dimensional models should be used to calculate the fusion–fission probability.

Figure 5*a* shows the excitation function of the cross section in the reaction ^{48}Ca + ^{244}Pu. Both our calculations and the experimental data are presented. The open and closed diamonds denote the capture cross section $\sigma_{\rm cap}$ and the cross section $\sigma_{A/2\pm20}$ derived by the yield of the mass symmetric fission fragments with $A/2 \pm 20$ in the experiments, respectively [4]. The theoretical value of $\sigma_{A/2\pm20}$ is denoted by the solid curve. We can see very good agreement with the experimental data and our calculations. The calculated fusion–fission cross section $\sigma_{\rm CN}$ is denoted by the dashed curve. This cross section $\sigma_{\rm CN}$ is derived from the trajectory crossing the three-dimensional fusion box. The calculated fusion–fission cross section $\sigma_{\rm CN}$ is one or two orders of magnitude smaller than the cross section $\sigma_{A/2\pm20}$ beyond the Bass barrier region. We see that the cross section $\sigma_{A/2\pm20}$ includes the deep quasifission events. Such information is very important for estimating the evaporation residue cross section.

We calculate the fusion–fission cross section in

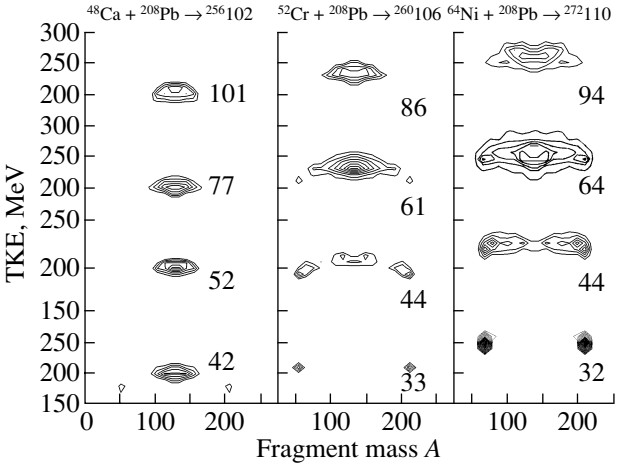

Fig. 3. The total kinetic energy distribution of fission fragments in the same system as Fig. 2.

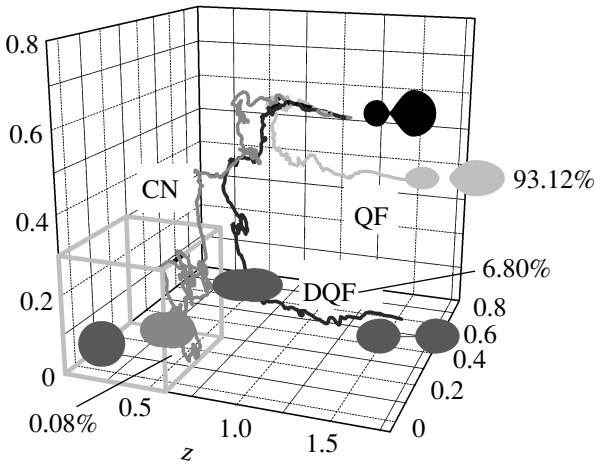

Fig. 4. The samples of the trajectory in the three-dimensional coordinate space at $E^* = 33$ MeV in the reaction ^{48}Ca + ^{244}Pu.

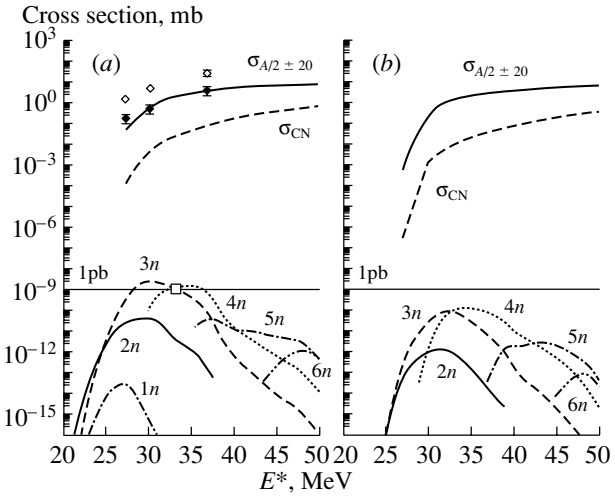

Fig. 5. The excitation functions of the fusion–fission cross section and evaporation residue cross section in the reactions (*a*) ^{48}Ca + ^{244}Pu and (*b*) ^{48}Ca + ^{249}Cf. Symbols are given in the text.

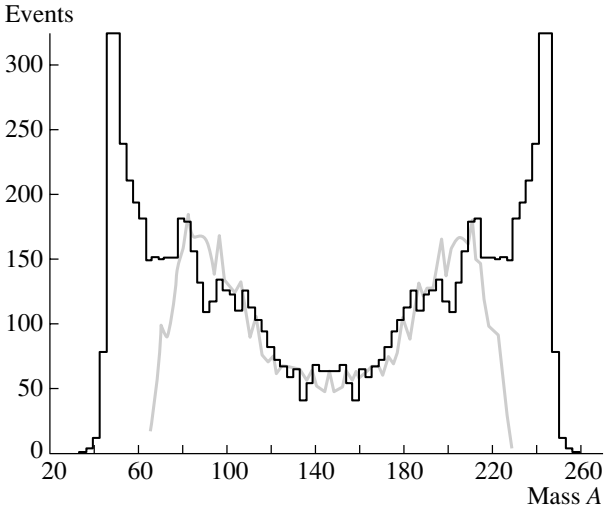

Fig. 6. Mass distribution of fission fragments in the reaction ^{48}Ca + ^{244}Pu at $E^* = 37$ MeV. Black and gray lines denote the calculation and experiments [4], respectively.

the reaction ^{48}Ca + ^{249}Cf, which is shown in Fig. 5*b*. The calculation for the fusion–fission cross section σ_{CN} is also one or two orders of magnitude smaller than the cross section $\sigma_{A/2\pm20}$ beyond the Bass barrier region.

4.2. Evaporation Residue Cross Section

Using the results of the fusion–fission cross section, we try to estimate the evaporation residue cross section in Eq. (3). Survival probability for the compound nucleus is calculated using a theoretical formula based on Γ_n/Γ_f [31]. The details of the calculation are reported in [32, 33].

The excitation functions of the evaporation residue cross section for ^{48}Ca + ^{244}Pu and ^{48}Ca + ^{249}Cf are shown in Fig. 5. The open square in Fig. 5*a* denotes the experimental data at Dubna [1]. The evaporation residue cross sections from calculations are shown to be several pb. Our calculations give the same order of magnitude as the experimental results. However, this calculation has several ambiguities of parameters, for example, the level density parameter, the shell correction energy, the shell dumping energy, and the collective enhancement [30, 33]. We have to continue to investigate more precisely.

The mass distribution of fission fragments in the reaction ^{48}Ca + ^{244}Pu at $E^* = 37$ MeV is shown in Fig. 6. Black and gray lines denote the calculation and

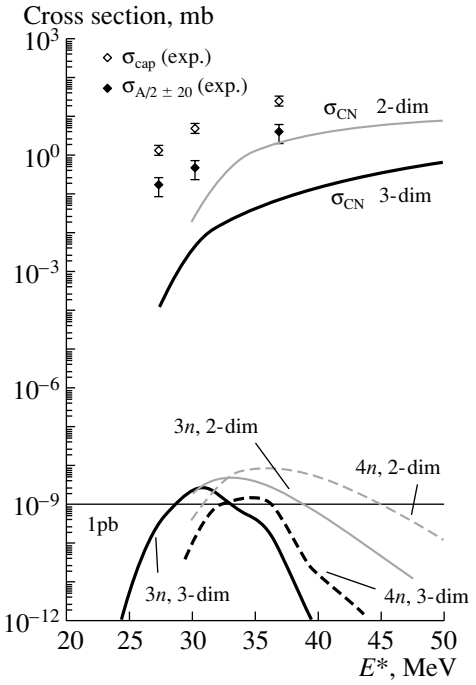

Fig. 7. The fusion cross section and evaporation residue cross section in the reaction ^{48}Ca + ^{244}Pu. Gray curves and black curves denote the calculations by the two-dimensional model [34, 35] and our three-dimensional model, respectively. The evaporation residue cross sections are shown in the $3n$ and $4n$ channels.

experimental data [4], respectively. Our calculation includes the DIC events.

Here, in the three-dimensional Langevin calculation, we can see that the parameter of the deformation of fragments is very important. Almost all of the trajectories go to quasifission due to the large deformation of fission fragments. It originates in large Coulomb repulsion for large charge number of superheavy elements. In the superheavy mass region, we should not ignore the degree of freedom on the deformation of fragments.

As Abe presented in these proceedings [34], in the two-dimensional calculation on z–α coordinate space, the fusion cross section agrees very well with experimental data. Here, the experimental fusion cross section is derived from mass symmetric fission events. However, our three-dimensional calculation shows that the fusion probability is about two orders of magnitude smaller than such experimental data, because a lot of mass symmetric fission events come from the quasifission process in our calculation. Figure 7 shows the comparison of our three-dimensional calculation results with the two-dimensional results [34, 35]. Gray curves and black curves denote the calculations by the two- and three-dimensional models, respectively. The evaporation residue cross sections are shown in the $3n$ channel and $4n$ one. In Fig. 7, the discrepancy in the fusion cross section between the two-dimensional calculation and the three-dimensional one is about 1.5 orders of magnitude, but finally the evaporation residue cross section of both calculations shows rather good agreement with the experimental data. It means that the difference between the two calculations is caused by the survival probability.

We compare the survival probability of the compound nucleus with another calculation. Our results show good agreement with Zagrebaev and Cherepanov [36] when we use the same parameters [30]. The survival probability calculated by Abe *et al.* [34, 35] is 1.5 orders of magnitude larger than in the former three cases, because Abe *et al.* manipulate the absolute value of the shell correction energy [37] diminishing it by a factor of 3. Finally, we can reproduce the experimental data by both models, but the ingredients of the formation probability and the survival probability are very different.

5. DYNAMICS FOR FUSION–FISSION PROCESS WITH NEUTRON EVAPORATION

The experiment performed at Dubna in the reaction ^{48}Ca + ^{244}Pu at excitation energy $E^* \sim 33$ MeV [1] corresponds to the (HI, $3n$) reaction. However, if one neutron evaporates on the fusion process, that is to say, if one neutron evaporates before the trajectory enters the fusion box, the situation changes drastically. In the decay process of the compound nucleus, which is estimated on the basis of the statistical model, we have to consider the $2n$ channel instead of the $3n$ channel. In this case, the survival probability is proportional to $(\Gamma_n/\Gamma_f)^2$ and also Γ_f decreases not only due to decreasing excitation energy of the compound nucleus by the first neutron evaporation but also due to the recovery of the shell correction energy. As a result, the survival probability increases.

Emission of neutrons in the correlation with fission fragments in the fusion–fission process and decay process of the superheavy mass region at excitation energies near or below the Coulomb barrier has been studied at Dubna [4]. Such investigations are useful for additional identification of the fusion–fission and the quasifission process. Moreover, the information about neutron multiplicity of fission fragments may be used in the identification of superheavy elements.

Thus, it is very interesting to investigate the effect of neutron evaporation on the fusion process and to estimate how to change the survival probability or evaporation residue cross section. We take into account the neutron evaporation in the fusion process with the Langevin calculation. In the Langevin calculation with neutron evaporation, we employ the

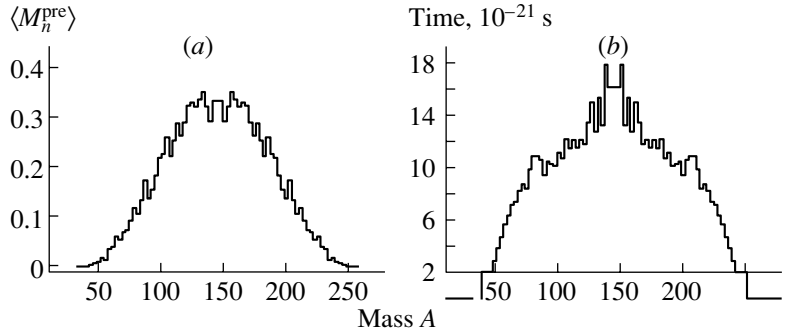

Fig. 8. (*a*) The average of prescission neutron multiplicity in the fusion–fission process for ^{48}Ca + ^{244}Pu at E^* = 33 MeV. The horizontal axis denotes the mass number of fission fragments. (*b*) The mean time that the system needs to reach the scission point.

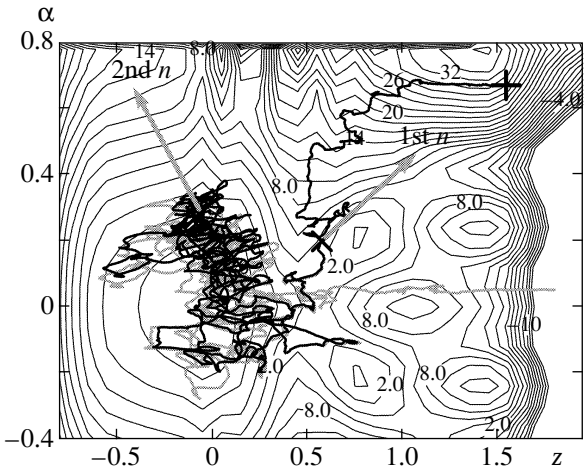

Fig. 9. A sample trajectory on the z–α coordinate space. On the black trajectory, the first neutron is emitted in the fusion process and the second neutron is emitted inside the fusion box. The gray trajectory denotes the case without neutron evaporation in the fusion process.

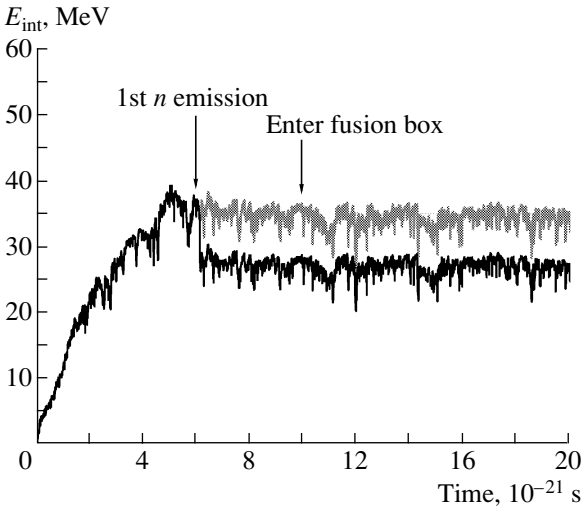

Fig. 10. Time dependence of the intrinsic energy of two trajectories in Fig. 9. The black and gray curves denote the case of taking into account neutron emission and without neutron emission, respectively.

calculation method that was suggested by Fröbrich *et al.* [38].

In order to check our code, first we try to estimate the neutron multiplicity in the fusion–fission process for the reaction ^{58}Ni + ^{208}Pb which was measured by the DéMoN group [39]. In the experiment, the neutron multiplicity has two peaks. It is considered that the first peak comes from the quasifission process and the second one comes from the fusion–fission process. Our calculation results could reproduce two such peaks of neutron multiplicity. The details are presented in this conference [40].

We calculate the average of prescission neutron multiplicity in the fusion–fission process for ^{48}Ca + ^{244}Pu at E^* = 33 MeV. Figure 8*a* shows the results. The horizontal axis denotes the mass number of fission fragments. The neutron multiplicity from the mass symmetric region is larger than the one from the mass asymmetric region. Figure 8*b* shows the mean time that the system needs to reach the scission point. In the mass symmetric fission region, it takes a long time for a trajectory to reach the scission point. In this case, it has more chances that neutrons are emitted in the the fusion–fission process. On the other hand, in the mass asymmetric fission region, the trajectory takes a short time to reach the scission point, and it does not have as many chances that neutrons are emitted.

Figure 9 shows a sample trajectory on the z–α coordinate space, which evaporates the first neutron on the fusion process and the second neutron in the fusion box. We prepare 500 000 trajectories in the Langevin calculation, and the trajectory in Fig. 9 is one of them. The black curve denotes the trajectory and the cross points attached by the arrow denote the position of the first neutron evaporation and the

second one. When we do not take into account the neutron evaporation in the fusion process, the trajectory is denoted by the gray curve. By the neutron evaporation, the temperature of the system decreases and the landscape of the potential energy surface changes due to the recovery of shell correction energy. Also, the strength of the random force changes by the Einstein relation. Therefore, the trajectory with neutron evaporation (black curve) and the one without neutron evaporation (gray curve) represent different behaviors after one neutron is emitted.

Figure 10 shows the time dependence of the intrinsic energy of the two trajectories in Fig. 9. In the case of taking into account the neutron emission, which is denoted by the black curve, after the first neutron emission, the excitation energy decreases from about 33 to 26 MeV. Without neutron emission, the excitation energy, which is denoted by the gray curve remains around 33 MeV. In this case, we can see that, when one neutron is emitted, the emitted neutron removes about 7 MeV from the excitation energy of the composite system.

We try to estimate the survival probability. At the excitation energy $E^* = 33$ MeV, the survival probability of the $3n$ channel is about 7×10^{-9} for $l = 0$. However, if one neutron evaporates on the fusion process, the compound nucleus is $^{291}114$ and the excitation energy is about 26 MeV in the sample of Fig. 9. In this case, due to one neutron emission on the fusion process, the survival probability of the compound nucleus increases about two orders of magnitude.

We estimate the probability of neutron emission on the fusion process. In the reaction $^{48}\mathrm{Ca} + {}^{244}\mathrm{Pu}$ at $E^* = 33$ MeV, we prepare 500 000 trajectories in the Langevin calculation; 1986 of these trajectories can enter the fusion box. We can say that they are the fusion trajectories. And only 13 trajectories of the fusion trajectories emit a neutron before they enter the fusion box. That is to say, the probability of one neutron emission on the fusion process is 0.65%.

We try to estimate this probability in another way. With the statistical model, we can estimate the lifetime of neutron emission of the fusion process,

$$\tau_n \sim 10^{-18}\ \mathrm{s}.$$

We can know the required time for a trajectory to reach the fusion box in the Langevin calculation,

$$t_{\mathrm{fus}} \sim 6 \times 10^{-21}\ \mathrm{s}.$$

We can estimate the probability of one neutron evaporation on the fusion process as follows:

$$t_{\mathrm{fus}}/\tau_n \sim 6 \times 10^{-3} = 0.6\%.$$

Both of the estimates give similar results. We can say that, for the $3n$ channel, the probability of one neutron emission on the fusion process is about 0.6%.

6. SUMMARY

The fusion–fission process for synthesis of superheavy elements is studied on the basis of the fluctuation–dissipation dynamics. We take into account the competition between the fusion of the compound nucleus and quasifission. The mass and TKE distribution of fission fragments in the superheavy mass region are investigated. The fusion–fission cross section is calculated and compared with the experimental data.

Using the three-dimensional Langevin calculation, we found that the substantial quasifission process contributes to the yield of the mass symmetric fission fragments. We call such a trajectory a "deep quasifission process." When we calculate the trajectory on the fusion–fission process, we have to pay attention to the deformation of fragments. In the superheavy mass region, it is important because a lot of trajectories go in the direction of the large deformation of the fragment. We remark that a one- or two-dimensional calculation is not sufficient to describe the fusion probability. We should estimate the fusion–fission probability using a three- or higher dimensional model. Actually, the present calculation shows that the fusion–fission cross section σ_{CN} is one or two orders of magnitude smaller than the cross section $\sigma_{A/2\pm20}$, that is to say, the cross section $\sigma_{A/2\pm20}$ may include a lot of quasifission processes.

Then, we discussed the neutron emission on the fusion process. We employed the Langevin calculation with a statistical model. In the reaction $^{48}\mathrm{Ca} + {}^{244}\mathrm{Pu}$ at $E^* = 33$ MeV, we estimated the prescission neutron multiplicity in correlation with fission fragments. The probability of one neutron emission on the fusion process is about 0.6%, and in this case, the survival probability increases by two orders of magnitude compared with no neutron emission on the fusion process.

As the next step, we would like to investigate the fusion process more precisely, before and just touching of two nuclei especially. We need to take into account the nuclear-structure and nucleon-transfer effects. We would like to introduce the friction tensor calculated by a microscopic model, for example, linear response theory [41–43]. Also, we have to estimate the evaporation residue cross section more precisely.

ACKNOWLEDGMENTS

We are grateful to Prof. Zagrebaev and Prof. Yu.Ts. Oganessian for their helpful suggestions and valuable discussions throughout the present work. We thank Prof. T. Wada, Dr. Tokuda, and Mr. K. Okazaki, who developed the calculation code of the three-dimensional Langevin equation. Also, we would like to thank Dr. S. Yamaji, Dr. A. Iwamoto,

and their collaborators, who developed the calculation code of potential energy with two-center parametrization.

REFERENCES

1. Yu. Ts. Oganessian *et al.*, Nature (London) **400**, 242 (1999); Yu. Ts. Oganessian *et al.*, Phys. Rev. Lett. **83**, 3154 (1999).
2. Yu. Ts. Oganessian *et al.*, Phys. Rev. C **63**, 011301(R) (2001).
3. Yu. Ts. Oganessian, this Conference.
4. M. G. Itkis *et al.*, in *Proceedings of the International Workshop on Fusion Dynamics at the Extremes, Dubna, Russia, 2000* (World Sci., Singapore, 2001), p. 93; M. G. Itkis *et al.*, in *Proceedings of the International Conference on Nuclear Physics at Border Lines, Lipari, Italy, 2001* (World Sci., Singapore, 2002), p. 146.
5. W. J. Swiatecki, Phys. Scr. **24**, 113 (1981); Nucl. Phys. A **376**, 275 (1982).
6. S. Bjørnholm and W. J. Swiatecki, Nucl. Phys. A **391**, 471 (1982).
7. J. P. Blocki, H. Feldmeier, and W. J. Swiatecki, Nucl. Phys. A **459**, 145 (1986).
8. C. E. Aguiar *et al.*, Nucl. Phys. A **491**, 2301 (1989); C. E. Aguiar *et al.*, Nucl. Phys. A **514**, 205 (1990).
9. T. Wada, Y. Abe, and N. Carjan, Phys. Rev. Lett. **70**, 3538 (1993).
10. Y. Aritomo, T. Wada, M. Ohta, and Y. Abe, Phys. Rev. C **55**, R1011 (1997); T. Wada, T. Tokuda, K. Okazaki, *et al.*, in *Proceedings of DANF98, Slovakia, 1998* (World Sci., Singapore, 1999), p. 77; Y. Aritomo, T. Wada, M. Ohta, and Y. Abe, Phys. Rev. C **59**, 796 (1999); M. Ohta, K. Okazaki, T. Wada, *et al.*, Acta Phys. Hung. New Ser.: Heavy Ion Phys. **10**, 253 (1999).
11. T. Tokuda, T. Wada, and M. Ohta, Prog. Theor. Phys. **101**, 607 (1999).
12. Y. Aritomo, T. Wada, M. Ohta, and Y. Abe, in *Proceedings of the International Workshop on Fusion Dynamics at the Extremes, Dubna, Russia, 2000* (World Sci., Singapore, 2001), p. 123.
13. R. Bass, Nucl. Phys. A **231**, 45 (1974).
14. J. Blocki *et al.*, Ann. Phys. (N. Y.) **105**, 427 (1977).
15. Y. Aritomo, in *Proceedings of the International Conference on Nuclear Physics at Border Lines, Lipari, Italy, 2001* (World Sci., Singapore, 2002), p. 38; submitted to Phys. Rev. C.
16. Y. Aritomo, in *Proceedings of the International Conference on Exotic Nuclei, Baikal, Russia, 2001* (World Sci., Singapore, 2002) (in press).
17. V. I. Zagrebaev, Phys. Rev. C **64**, 034606 (2001).
18. Y. Abe, S. Ayik, P.-G. Reinhard, and E. Suraud, Phys. Rep. **275**, 49 (1996).
19. J. Maruhn and W. Greiner, Z. Phys. **251**, 431 (1972).
20. K. Sato, A. Iwamoto, K. Harada, *et al.*, Z. Phys. A **288**, 383 (1978).
21. H. J. Krappe, J. R. Nix, and A. J. Sierk, Phys. Rev. C **20**, 992 (1979).
22. A. V. Ignatyuk, G. N. Smirenkin, and A. S. Tishin, Yad. Fiz. **21**, 485 (1975) [Sov. J. Nucl. Phys. **21**, 255 (1975)].
23. J. Blocki, Y. Boneh, J. R. Nix, *et al.*, Ann. Phys. (N.Y.) **113**, 330 (1978).
24. J. R. Nix and A. J. Sierk, Nucl. Phys. A **428**, 161c (1984).
25. H. Feldmeier, Rep. Prog. Phys. **50**, 915 (1987).
26. R. Bock *et al.*, Nucl. Phys. A **388**, 334 (1982).
27. S. Suekane, A. Iwamoto, S. Yamaji, and K. Harada, JAERI-MEMO No. 5918 (1974).
28. A. Iwamoto, S. Yamaji, S. Suekane, and K. Harada, Prog. Theor. Phys. **55**, 115 (1976).
29. D. H.E. Gross and H. Kalinowski, Phys. Rep. **45**, 175 (1978).
30. V. I. Zagrebaev, Y. Aritomo, M. G. Itkis, *et al.*, Phys. Rev. C **65**, 014607 (2002).
31. R. Vandenbosch and J. R. Huizenger, *Nuclear Fission* (Academic, New York, 1973), p. 233.
32. M. Ohta, in *Proceedings of the International Workshop on Fusion Dynamics at the Extremes, Dubna, Russia, 2000* (World Sci., Singapore, 2001), p. 110.
33. M. Ohta, Y. Aritomo, V. I. Zagrebaev, and E. A. Cherepanov, in *Proceedings of the International Conference on Exotic Nuclei, Baikal, Russia, 2001* (World Sci., Singapore, 2002); Y. Aritomo and M. Ohta, Phys. Rev. C (in press).
34. Y. Abe, this Proceedings.
35. G. I. Konsenko, C. Shen, and Y. Abe, J. Nucl. Radiochem. Sci. **3**, 19 (2002).
36. V. I. Zagrebaev and E. A. Cherepanov, private communication.
37. P. Möller *et al.*, At. Data Nucl. Data Tables **59**, 185 (1995).
38. N. D. Mavlitov, P. Fröbrich, and S. I. Gonchar, Z. Phys. A **342**, 195 (1992).
39. L. Donadille *et al.*, Nucl. Phys. A **656**, 259 (1999).
40. T. Materna, this Proceedings.
41. H. Hofmann, Phys. Rev. **284**, 137 (1997).
42. S. Yamaji, F. A. Ivanyuk, and H. Hofmann, Nucl. Phys. A **612**, 1 (1997).
43. F. A. Ivanyuk, H. Hofmann, V. V. Pashkevich, and S. Yamaji, Phys. Rev. C **55**, 1730 (1997).

Physics of Atomic Nuclei, Vol. 66, No. 6, 2003, pp. 1114–1117. From Yadernaya Fizika, Vol. 66, No. 6, 2003, pp. 1150–1153.

Reaction Dynamics at the Barrier for Heavy Compound Systems*

D. Ackermann

Gesellschaft für Schwerionenforschung GSI, Darmstadt, Germany
Institut für Physik, Johannes-Gutenberg-Universität, Mainz, Germany

Received August 28, 2002

Abstract—To investigate basic properties of the fusion reaction dynamics for heavy compound systems, the partial wave distribution σ_ℓ extracted from measured γ multiplicities can be employed as an alternative to the classically used fusion/fission excitation functions. A variety of reactions leading to compound nuclei in the Pb region can be used to investigate features like the fusion–fission competition, the role of deformation in the fusion of heavy systems, and a possible effect of the $Z = 82$ shell on the enhancement of evaporation residue production. The measured spin distribution can provide information on the single partial wave cross sections, which is hidden in the integral fusion cross section. Moreover, it can reveal signatures in the high-spin region, which could be an indication of a stabilization due to an increase in the potential hole by shell correction energies E_{shell} in the vicinity of a closed shell. The systematic investigation and understanding of the fusion–fission reaction dynamics, together with the understanding of the structure of transfermium nuclei, which are stabilized only via shell effects, are essential for a successful program aiming at the synthesis of new elements at GSI, Dubna, or elsewhere. We started a series of experiments to measure those properties for the reactions at the Laboratori Nazionali di Legnaro, Italy. In order to extract the compound nucleus spin distribution, γ multiplicities are measured using the γ-detector array GASP and its inner ball in the multiplicity filter mode. © *2003 MAIK "Nauka/Interperiodica"*.

INTRODUCTION

The assumption that shell effects in the compound nucleus (CN) could favor the survival probability of the evaporation residue (ER) could not be confirmed for the $N = 126$ neutron shell [1]. Nevertheless, in particular, with respect to the recent results for the elements 114 [2] and 116 [3] in Dubna, the possibility is discussed that the shell stabilization close to the next higher proton shell could favor the survival of heavy nuclei in its vicinity. Here, various observed decay chains for ^{48}Ca-induced reactions on ^{244}Pu and ^{248}Cm were interpreted as $3n$ or $4n$ reactions leading to isotopes of element 114 and 116. The peculiarity of these observations is a more or less constant cross section in the picobarn range, which breaks the trend of a steep decrease with Z that was observed for all other reactions leading to ER with $Z \geq 102$. One way to let the excited compound system feel the underlying shell structure could be putting a considerable part of its excitation energy into rotation. A deeper potential hole due to a shell energy E_{shell} shifts the critical angular momentum ℓ_{crit} to higher spins as shown in Fig. 1. In this case, a clear signature would be the observation of an enhanced population of high-spin states or the enhancement of the high-spin part of the spin distribution measured for the surviving ER. Deformation of one reaction partner could enhance this effect due to the increased moment of inertia in the entrance channel. The actinide targets used in Dubna are well deformed, and the isotopes that have been interpreted as the observed reaction products by Yu.Ts. Oganessian and collaborators are close to a region where, according to theoretical expectations (see, e.g., [4]), a region of stabilization starts.

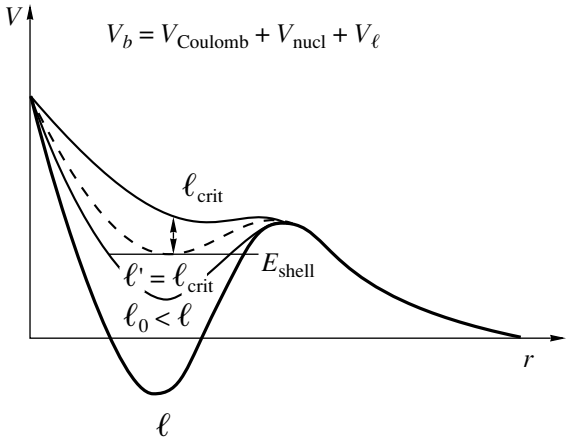

Fig. 1. Schematic illustration of the variation of the fusion barrier as function of the angular momentum and the influence of the shell correction energy E_{shell}.

*This article was submitted by the author in English.

1063-7788/03/6606-1114$24.00

NUCLEAR STRUCTURE EFFECTS

The importance of the nuclear structure of the participants in fusion reactions on the reaction cross section has been intensively studied throughout the last two decades in various laboratories [5–7]. It has been shown that the vibrational and the rotational structure have great influence on the fusion excitation function. The effect of low-lying excitation levels as well as the deformation could be shown, in particular, by precisely measured fusion excitation functions via the fact that experimental access to the fusion barrier distribution became possible [5]. Particularly clear signatures are produced by deformed reaction partners, which in some cases were observed on a different slope of the fusion excitation function as early as the late 1970s for reactions with ^{16}O on various Sm isotopes [8]. It has also been suggested that the deformation in the entrance channel could favor the fusion of very heavy systems [9]. On the other hand, as already mentioned, reactions with a deformed reaction partner could be expected to favor the population of high-spin states due to its high momentum of inertia in the entrance channel.

THE FUSION–FISSION COMPETITION

From fusion reactions for medium and light compound systems, we have learned that nuclear deformation strongly affects the near- and subbarrier fusion dynamics [5]. This aspect of heavy-ion fusion processes has been extensively studied via the extraction of an experimental representation of the barrier distribution (ERBD) governing fusion [10]. In a recent experiment C.R. Morton and coworkers were able to observe the same behavior for the up to now heaviest system (^{34}S + ^{168}Er), where nuclear deformation was investigated thus far in terms of the ERBD [11]. They measured ER and fission yields vs. bombarding energy as well as the fusion/evaporation excitation function (Fig. 2*a*). From the total fusion excitation function (Fig. 2*b*), the ERBD was obtained as the second energy derivative of the function $E\sigma_{\text{fus}}$ using the point difference formula [11] (Fig. 2*c*). It has the expected shape for the large quadrupole deformation of ^{168}Er as also shown in Fig. 2*c*. For modeling the measured fission anisotropies, the main goal of that work, they needed the fusion angular momentum distribution as an input for a statistical model description. That was deduced from the fusion barrier data. In this context, the direct measurement of the spin distribution can serve as a cross-check, apart from yielding information on the fusion process as described in this section.

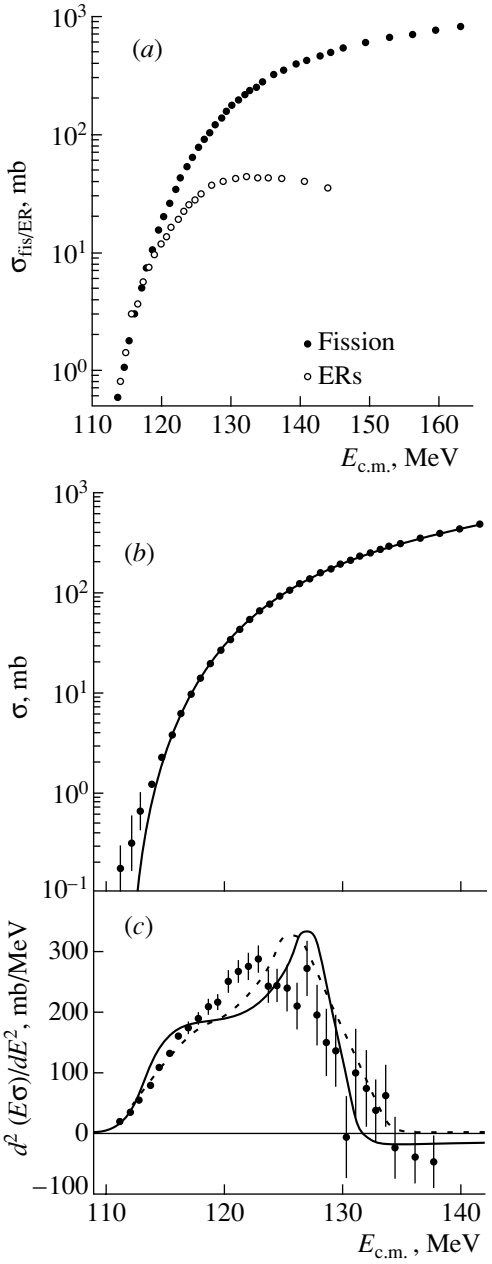

Fig. 2. Fusion/fission data for the reaction ^{34}S + ^{168}Er [11]: (*a*) fission and ER excitation functions, (*b*) total fusion excitation function compared to a calculation using a geometrical model with $\beta_2 = 0.338$, and (*c*) measured and calculated fusion barrier distributions obtained from the calculation in (*b*) (solid curve) and from a coupled channel calculation (dashed curve).

SPIN DISTRIBUTION

The coupled channels model describes the experimental findings on the effect of the entrance channel properties on fusion in most cases satisfactorily. The second derivative of the function $E\sigma_{\text{fus}}(E)$ has proven to be a useful tool for investigating the barrier distribution which governs the reaction dynamics [5]. One

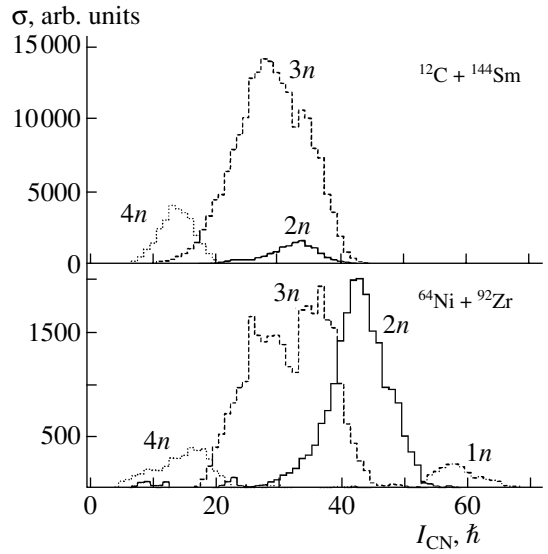

Fig. 3. Evaporiation residue distribution on the CN-spin distribution for the reactions ^{12}C + ^{144}Sm and ^{64}Ni + ^{92}Zr [13] ($E^* = 47.0$ MeV).

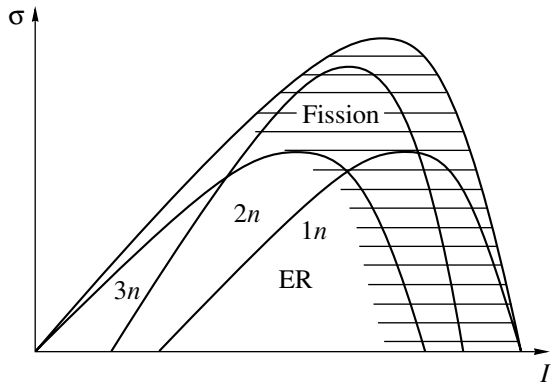

Fig. 4. Schematic picture of the partial wave spin distributions with the integral spin distribution of the ER and the effect of fission at high angular momenta.

can show that the same information can be obtained from the CN-spin distribution [12]. At each energy, the function $\sigma_\ell(E)$, in fact, contains information on the single partial wave cross section, which is otherwise hidden in the integral σ_{fus}:

$$\sigma_{\text{fus}}(E) = \frac{\pi\hbar}{2\mu E}\sum(2\ell+1)T_\ell = \sum\sigma_\ell(E). \quad (1)$$

For each partial wave, the energy $E_{\text{rot}} = \ell(\ell+1)\hbar^2/2\mu R^2$ is used by the rotation of the system up to a critical angular momentum ℓ_{crit}, above which fusion is energetically forbidden. Thus, the high end of the spin distribution reflects the region of fusion barriers. This is also reflected in the distribution of the ER as a function of spin shown in Fig. 3 [13]. The higher the spin and, accordingly, the energy dissipation in rotation, the lower the number of evaporated particles. After dividing the function

$$\sigma_\ell(E) = \frac{(2\ell+1)\pi\hbar^2}{2\mu E}T_\ell(E) \quad (2)$$

by the geometrical term $((2\ell+1)\pi\hbar^2)/(2\mu E)$ and after transformation of the transmission function T_ℓ,

$$T_\ell(E) = \frac{1}{\pi R^2}\frac{d(E\sigma_{\text{fus}})}{dE}, \quad (3)$$

into $T_{E'}$ ($E' = E - E_{\text{rot}}(\ell)$), one obtains the fusion barrier distribution D_B by differentiation:

$$D_B = \frac{1}{\pi R^2}\frac{d^2(E\sigma_{\text{fus}})}{dE^2} = \frac{dT_{E'}}{dE'}. \quad (4)$$

This shows that the first derivative of the spin distribution after the given transformation is equivalent to the second derivative of the function $E\sigma_{\text{fus}}$. The latter is widely used in medium-mass systems [5]. For increasing mass of the compound system, fission comes into play as a relevant reaction channel. In particular, for the production of the heaviest elements, the competition between fission and particle evaporation is decisive for the survival of the ER. To understand the two-step process of fusion and deexcitation, the necessity arises to have a comprehensive description of both the entrance channel properties of the system and the role of the fission barrier in the exit channel. The effect of fission on the spin distribution has been qualitatively shown in [14]. The spin distribution at three near- and above-barrier energies has been measured for the system ^{64}Ni + ^{100}Mo using the Argonne/Notre Dame BGO array. A clear change of the slope at high angular momenta has been observed at energies where fission becomes the main reaction channel. This is interpreted as fission setting in high angular momentum. Therefore, the CN-spin distribution can serve as a tool to study the structure of the fission barrier. It would be particularly interesting to investigate this as a function of the fissility of the system in a mass region where fission becomes important with respect to ER production. In Fig. 4, a schematic picture of the CN-spin distribution is drawn showing the distribution of ER channels and the effect of fission.

The spin distribution itself can be extracted from measured γ multiplicities M_γ with a multiplicity filter like the inner ball of the γ-ray array GASP of the LNL, consisting of 80 BGO crystals with a total efficiency of $\approx$80%, or the Darmstadt–Heidelberg crystal ball:

$$\ell_{\text{CN}} = (M_\gamma - M_{\gamma s})\Delta\ell_\gamma + M_{\gamma s}\Delta\ell_{\gamma s} + \sum_i M_i\Delta\ell_i + \Delta\ell_{\text{g.s}/m}, \quad i = p, n, \alpha. \quad (5)$$

Here, M_γ, $\Delta\ell_\gamma$ and $M_{\gamma s}$, $\Delta\ell_{\gamma s}$ denote the multiplicity and spin taken away by the yrast cascade (γ) and the statistical γ rays in the early stage of the deexcitation (γs). The sum $\sum_i M_i \Delta\ell_i, i = p, n, \alpha$, takes into account the spin removed by the evaporated protons, neutrons, and alphas, and $\Delta\ell_{\mathrm{g,s}/m}$ is the spin of the ground state or an isomeric state of the final nucleus. The number of evaporated particles is defined by pinning down the ER via characteristic transmissions with the highly resolving part of the γ-ray array, consisting of 40-Ge detectors in the case of GASP. By modeling the deexcitation cascade with the statistical model and comparing the theoretical and experimental mass distribution, the number of statistical γ rays and the spin removed by them and the evaporated particles can be determined. The ground/isomeric state spin and the spin removed by the yrast gammas can be taken from the literature. In the case of $^{34}\mathrm{S} + {}^{168}\mathrm{Er}$, the experimental spin distribution can be used as a direct cross-check with the data of Morton *et al.* [11] for the fusion barrier data, as well as a direct input for the evaluation of the fission anisotropies. In the context of fission competing with particle evaporation, it is very interesting to investigate, which partial waves contribute to the ER production. As mentioned above, for a detailed understanding of the survival of the CN, higher partial waves could be important. Here, a substantial part of the excitation energy is stored in the rotation, and for nuclei that are stabilized only by their shell structure, shell correction energies of the order of a few MeV could be felt by the compound system and lead to higher survival probabilities. The investigation of ER-spin distributions would reveal such an effect if present. As mentioned above, a qualitative effect of the influence of fission on the high-spin part at higher energies has been observed [14]. This confirms, on one hand, the feasibility of the method and provides, on the other hand, information on the fusion–fission dynamics, which is experimentally not accessible otherwise.

EXPERIMENTAL PROGRAM

All three aspects, investigation of the $Z = 82$ shell, the role of deformed reaction partners, and fusion–fission reaction dynamics, can be combined by choosing suitable projectile–target combinations. We started a series of experiments studying the spin distribution of reactions leading to nuclei in the vicinity of the $Z = 82$ proton shell as well as fusion/fission excitation functions in terms of ER production and fission yields. In this context, a first run has been performed by Sagaidak *et al.* [15] for the measurement of ER and fission excitation function for the reactions $^{48}\mathrm{Ca} + {}^{168,170}\mathrm{Er} \rightarrow {}^{216,218}\mathrm{Ra}^*$ using LNL's electrostatic deflector MAIALE and the fission detector setup CORSET [16], respectively. The residues of these reactions cross, as a function of the kinetic energy, the $N = 126$ shell at ^{214}Ra. To study the spin distribution, γ multiplicities will be measured with the Ge-BGO detector array GASP at the Laboratori Nazionali di Legnaro using the 80 BGO crystals of the inner ball as a multiplicity filter. In a first series of experiments, the reactions $^{34}\mathrm{S} + {}^{168,170}\mathrm{Er} \rightarrow {}^{202}\mathrm{Po}$ and $^{48}\mathrm{Ca} + {}^{144,154}\mathrm{Sm} \rightarrow {}^{188,198}\mathrm{Pb}$ will be investigated. Future plans are to complete the systematics by studying a number of reactions scanning the Pb region.

ACKNOWLEDGMENTS

These investigations have been prepared in collaboration with S. Hofmann, F.P. Heßberger, and G. Münzenberg (also Mainz University) from GSI; S. Antalic and G. Berek from Bratislava University; M. Axiotis, L. Corradi, G. De Angelis, A. Gadea, A. Latina, T. Martinez, A.M. Stefanini, S. Szilner, and M. Trotta from the LNL; D. Bazzacco, S. Beghini, E. Farnea, R. Menegazzo, C. Rossi-Alvarez, C. Ur, G. Montagnoli, and F. Scarlassara from INFN Padova and Padova University; and M.G. Itkis, G.N. Kniajeva, E.M. Kozulin, Yu.Ts. Oganessian, and R.N. Sagaidak from the JINR FLNR, Dubna.

REFERENCES

1. D. Vermeulen *et al.*, Z. Phys. A **318**, 157 (1984).
2. Yu. Ts. Oganessian *et al.*, Phys. Rev. C **62**, 041604 (2000).
3. Yu. Ts. Oganessian *et al.*, Phys. Rev. C **63**, 011301 (2001).
4. M. Bender *et al.*, Preprint No. 2001-09, GSI (May 2001).
5. M. Dasgupta *et al.*, Annu. Rev. Nucl. Part. Sci. **48**, 401 (1998).
6. K.-H. Schmidt and W. Moraweck, Rep. Prog. Phys. **54**, 949 (1991)
7. W. Reisdorf, J. Phys. G **20**, 1297 (1994)
8. R. G. Stokstad *et al.*, Phys. Rev. C **21**, 2427 (1980).
9. A. Iwamoto and P. Möller, Nucl.Phys. A **605**, 334 (1996).
10. N. Rowley *et al.*, Phys. Lett. B **245**, 25 (1991).
11. C. R. Morton *et al.*, Phys. Rev. C **62**, 024607 (2000).
12. D. Ackermann, Acta Phys. Pol. B **26**, 517 (1995).
13. F. Heller, PhD Thesis (University of Heidelberg, 1995).
14. D. Ackermann *et al.*, Nucl. Phys. A **630**, 442c (1998).
15. R. N. Sagaidak *et al.* (in press).
16. I. V. Pokrovsky *et al.*, Phys. Rev. C **60**, 041304 (1999).

Physics of Atomic Nuclei, Vol. 66, No. 6, 2003, pp. 1118–1124. From Yadernaya Fizika, Vol. 66, No. 6, 2003, pp. 1154–1160.

Fusion–Fission of Heavy and Superheavy Nuclei*

M. G. Itkis[1)], S. Beghini[2)], A. A. Bogatchev[1)], L. Corradi[3)], O. Dorvaux[4)], A. Gadea[3)], G. Giardina[5)], A. A. Goverdovski[6)], F. Hanappe[7)], I. M. Itkis[1)], M. Jandel[1)], J. Kliman[1)], G. N. Kniajeva[1)], N. A. Kondratiev[1)], I. V. Korzyukov[1)], E. M. Kozulin[1)], L. Krupa[1)], L. Latina[3)], T. Materna[7)], G. Montagnoli[2)], K. J. Moody[8)], Yu. Ts. Oganessian[1)], I. V. Pokrovsky[1)], V. A. Ponomarenko[1)], E. V. Prokhorova[1)], N. Rowley[4)], A. Ya. Rusanov[9)], F. Scarlassara[2)], A. M. Stefanini[3)], L. Stuttgé[4)], S. Szilner[3)], M. Trotta[3)], A. M. Vinodkumar[3)], and V. M. Voskressensky[1)]**

[1)] *Flerov Laboratory of Nuclear Reactions, Joint Institute for Nuclear Research, Dubna, Moscow oblast, 141980 Russia*

[2)] *Dipartimento di Fisica, Università di Padova, Italy*

[3)] *Laboratorio Nazionali di Legnaro, Istituto Nazionale di Fisica Nucleare, Legnaro (Padova), Italy*

[4)] *Institut de Recherches Subatomiques, Strasbourg, France*

[5)] *Dipartimento di Fisica dell' Università di Messina, Italy*

[6)] *Institute for Physics & Power Engineering, Obninsk, Russia*

[7)] *Universite Libre de Bruxelles, Brussels, Belgium*

[8)] *University of California, Lawrence Livermore National Laboratory, USA*

[9)] *Institute of Nuclear Physics of the National Nuclear Center, Almaty, Kazakhstan*

Received August 28, 2002

Abstract—The process of fusion–fission of heavy and superheavy nuclei (SHE) with $Z = 82$–122 formed in the reactions with ^{48}Ca and ^{58}Fe ions at energies near and below the Coulomb barrier has been studied. The experiments were carried out at the U-400 accelerator of the Flerov Laboratory of Nuclear Reactions (JINR) and at the XTU Tandem accelerator of the National Laboratory of Legnaro (LNL) using the time-of-flight spectrometer of fission fragments CORSET and the neutron multidetector DEMON. As a result of the experiments, mass and energy distributions (MED) of fission fragments; fission, quasifission, and evaporation residue cross sections; and multiplicities of neutrons and γ-quanta and their dependences on the mechanism of formation and decay of compound systems have been studied. © *2003 MAIK "Nauka/Interperiodica".*

1. INTRODUCTION

The interest in the study of the fission process of superheavy nuclei (SHE) is connected mainly with the possibility of obtaining information on the cross section of compound nuclei production at excitation energies of ≈15–30 MeV (i.e., when the influence of shell effects on the fusion and the decay characteristics of the composite system is considerable), which is of basic importance concerning the synthesis of new heavy nuclides. Thus, it helps to predict the probability of the SHE composite system surviving after evaporating one, two, or three neutrons, i.e., in "cold" or "warm" fusion reactions. However, a much deeper insight into the mechanism of the fission process is needed to be able to so. In particular, better knowledge of the fission–quasifission cross-section ratio as a function of the reaction entrance channel and excitation energy, the multiplicities of the pre- and postfission neutrons, the peculiarities of the mass and kinetic-energy distributions of the fragments originated from fission and quasifission could clarify the situation. Undoubtedly all these aspects are of great independent interest to nuclear fission physics.

This work presents the results of experiments aimed at studying the fission process in the reactions ^{48}Ca + ^{154}Sm, ^{168}Er, ^{208}Pb, ^{238}U, ^{244}Pu, ^{248}Cm and ^{58}Fe + ^{208}Pb, ^{244}Pu, ^{248}Cm. The choice of the underlined reactions was inspired by the recent experiments on producing the isotopes ^{283}112, ^{289}114, and ^{283}116 at Dubna [1, 2] using the same reactions, while the

*This article was submitted by the authors in English.

**e-mail: itkis@flnr.jinr.ru

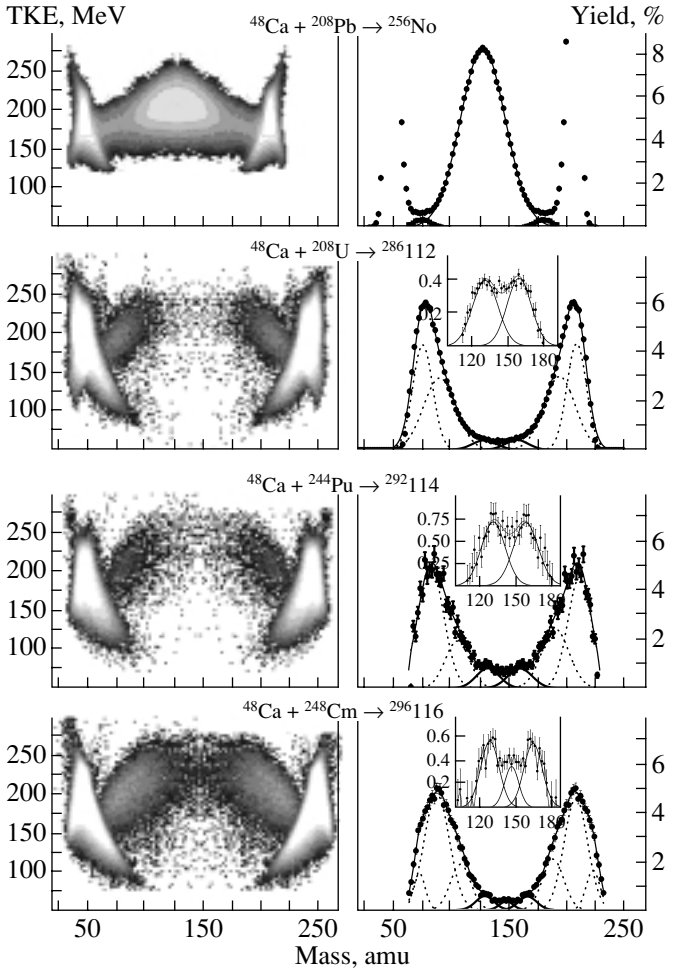

Fig. 1. Double-differential cross sections $\partial^2\Omega/\partial M\partial E_k$ [two-dimensional matrices $N(M, E_k)$] (left-hand side panels) and mass yields (right-hand side panels) of fission fragments of ^{256}No, ^{286}112, ^{292}114, and ^{296}116 nuclei produced in the reactions with ^{48}Ca at the excitation energy $E^* \approx 33$ MeV.

^{58}Fe projectile was chosen since the corresponding projectile–target combinations lead to the synthesis of even heavier elements.

2. MED CHARACTERISTICS OF FISSION FRAGMENTS OF SHE

Figure 1 shows the data on mass and energy distributions (MED) of fission fragments of the ^{256}102, ^{286}112, ^{292}114, and ^{296}116 nuclei produced in the reactions with ^{48}Ca at one and the same excitation energy $E^* \approx 33$ MeV. The main peculiarity of the data is the sharp transition from the predominant compound nucleus fission in the case of ^{256}102 to the quasifission mechanism of decay in the case of the ^{286}112 and heavier nuclei. It is very important to note that, despite the dominating contribution of the quasifission process in the case of nuclei with $Z = 112$–116, in the symmetric region of fission fragment masses ($A/2 \pm 20$), the process of fusion–fission of compound nuclei, in our opinion, prevails. It

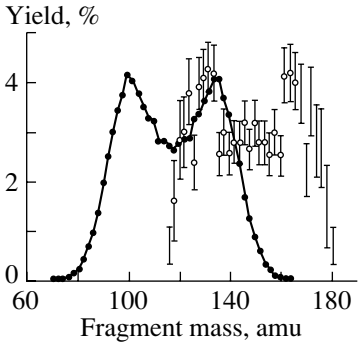

Fig. 2. Mass spectra of fission fragments of ^{238}U at the excitation energy $E^* \approx 30$ MeV (solid circles) and those of the SHE ^{296}116 produced in the reaction ^{48}Ca + ^{248}Cm (open circles).

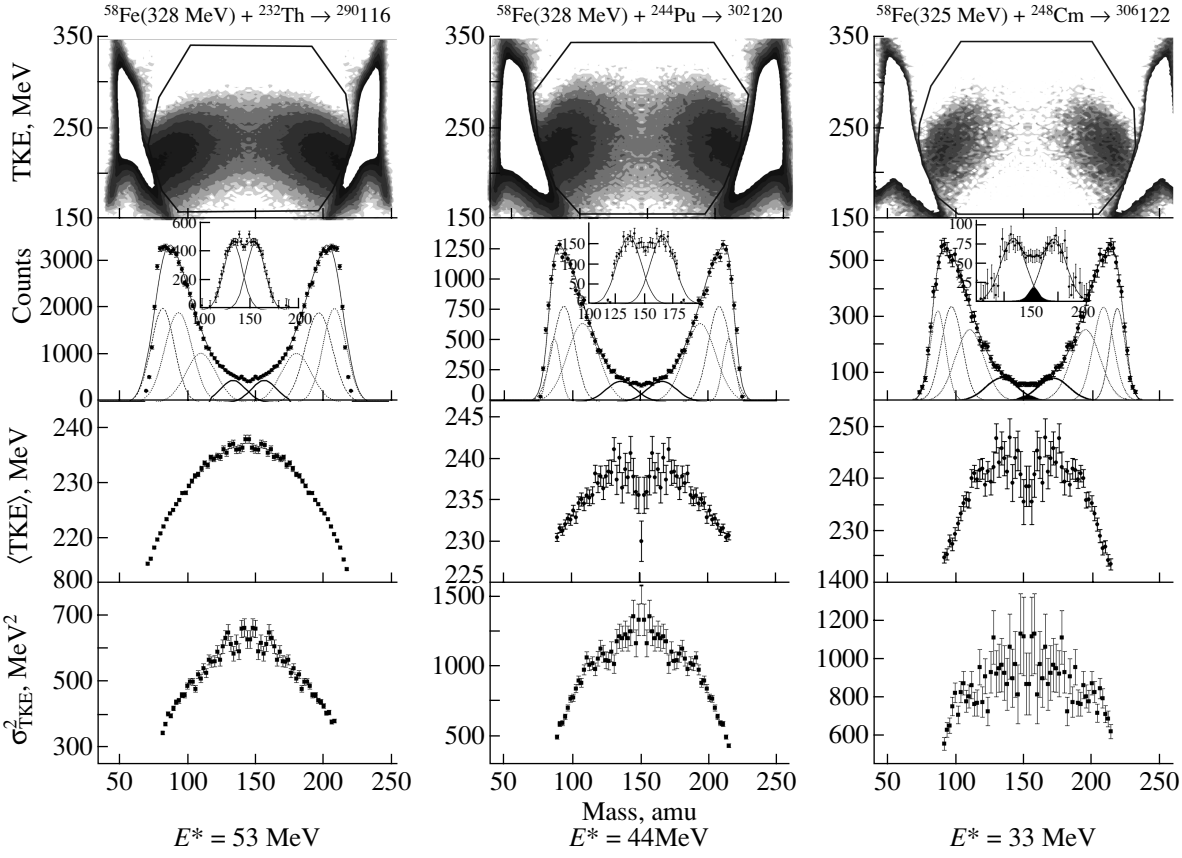

Fig. 3. Two-dimensional matrices $N(M, E_k)$, the mass yields, average TKE, and the variances σ^2_{TKE} as functions of the mass of fission fragments of ^{290}116, ^{302}120, and ^{306}122 produced in the reactions with ^{58}Fe ions.

is demonstrated in the framings (see the right-hand panels of Fig. 1), where one can see that the mass distribution of fission fragments of compound nuclei is asymmetric in shape with the light fission fragment mass at about 132–134 amu.

The position of the light-fragment peak of the mass distribution in the region of ~132 reflects the decisive role of shell effects, which is characteristic of SHE fission. It is worthwhile to draw a phenomenological analogy between the heavy element fission and that of SHE. Indeed, nuclear fission fragments belonging to the region of the spherical neutron shell $N = 82$ can be observed in all cases of the synthesized SHE with $Z > 110$. Here, the fission process can be understood on the basis of the multimodal fission concept. The fission fragments belonging to the so-called standard I [3] channel make the light-mass group in the case of SHE nuclear fission, instead of the heavy-mass group, as is in the case with the actinides. In the case of SHE, the number of nucleons in the heavy-fission fragment may not be quite sufficient for the subsequent neutron shell $N = 126$ to manifest itself substantially. It looks as if the role of the valley ($N = 82$, $Z = 50$–52) is decisive in the formation of the structure of the potential barrier of heavy nuclei as well as of SHE. Sticking to such an assumption, one can determine the reflected fission analog of the ^{296}116 isotope. Simple calculations show that it should be ^{240}U, where the light fission fragment peak reflected about 132–134 yields the heavy fission fragment peak observed in the fission of ^{296}116. Fortunately, there are detailed and reliable studies of the fission fragment properties performed using the reaction $^{238}\mathrm{U} + n$ in a wide neutron energy range. Direct comparison of the two data sets is presented in Fig. 2 [4]. It is worthwhile mentioning that, in the case of uranium, it was taken into account that we were dealing with a nucleus undergoing fission at different excitation energies due to the multichance character of the process. That is why from all the available data we chose a spectrum at $E_n = 50$ MeV, characterized by a mean excitation energy of ~30 MeV. As can be seen from the figure, the mass spectra in the overlapped region practically coincide within the error bars. In the case of ^{238}U, the two-humped fission mass distribution is governed mainly by the doubly magic heavier fragment ^{132}Sn, which plays the role of a lighter fragment in the

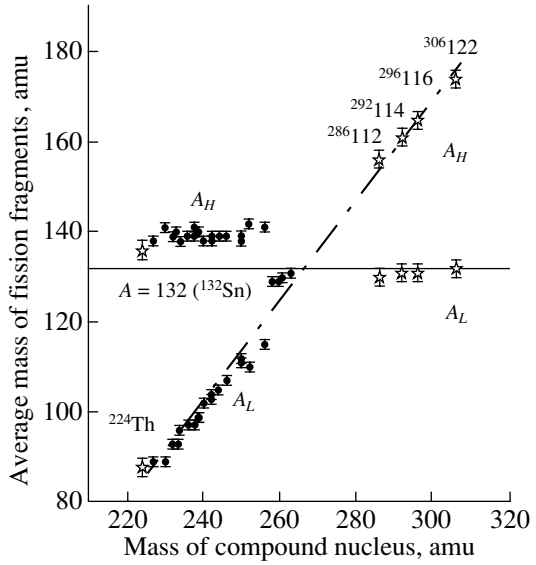

Fig. 4. The average masses of the light (A_L) and heavy (A_H) fission fragments versus the compound nucleus mass. The asterisks show the data of this work; the solid circles, the data from [7].

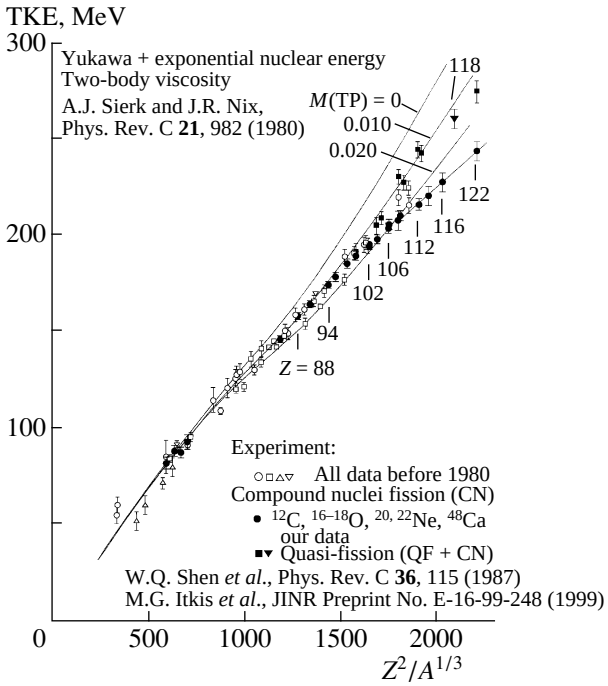

Fig. 5. The dependence of TKE on the Coulomb parameter $Z^2/A^{1/3}$.

case of fission of a $^{296}116$ nucleus at low excitation energies. This means that the symmetric region of fission fragment masses seems to originate mainly from the regular fusion–fission process in the reaction ^{48}Ca + ^{248}Cm [5]. The rigidity q of the potential connected with the corresponding fission valley is unknown. That is why any further consideration demands the use of new data.

Figure 3 shows the data for the reactions of ^{58}Fe projectile on ^{232}Th, ^{244}Pu, and ^{248}Cm targets, leading to the formation of the compound system $^{290}116$ and the heaviest compound systems $^{302}120$ and $^{306}122$ (where $N = 182–184$), i.e., to the formation of a spherical compound nucleus, predicted by theory [6]. As seen from Fig. 3, in these cases, we observe an even stronger manifestation of the asymmetric mass distributions of $^{306}122$ and $^{302}120$ fission fragments with the light-fragment mass at about 132. The corresponding structures are well seen from the dependence of the mean TKE on the fragment mass. Only for the reaction ^{58}Fe + ^{232}Th $\rightarrow$ $^{290}116$ ($E^* =$ 53 MeV) does the valley in the region of $M = A/2$ in the mean TKE dependence disappears. This fact is connected with a reduction of the influence of shell effects at such high excitation. Summing up all that was said above, one can draw two main regularities in the characteristics of the mass and energy distributions of SHE fission fragments:

(i) Figure 4 shows the dependence of the average light- and heavy-fragment masses on the compound nucleus mass. One can see that, in the case of SHE, the light spherical fragment with mass 132–134 plays a stabilizing role, in contrast to the region of actinide nuclei, where the heavy fragment is the spherical one.

(ii) Figure 5 shows the TKE dependence on the Coulomb parameter $Z^2/A^{1/3}$. One can see that, for nuclei with $Z > 100$, the TKE value is much smaller in the case of fission as compared with the quasifission process.

3. MED CHARACTERISTICS OF HEAVY-ELEMENT FISSION FRAGMENTS

The reactions ^{48}Ca + ^{154}Sm, ^{168,170}Er were investigated in order to understand the competition between fission and evaporation residue production processes depending on the reaction entrance channel. Thus, the fission cross section was measured together with the evaporation residue cross section in a wide energy range of ^{48}Ca [8]. At the same time, the MED of the fission fragment are of great independent interest. In recent years, our effort was concentrated on the investigation of the multimodal structure of the fission fragment MED in the region of transition nuclei $213 < A_{CN} < 226$, which so far had been poorly studied. Thus, MED of the ^{216,218,220}Ra compound nuclei produced in reactions with ^{12}C were studied. It was found [9] that the yield of the asymmetric fission did not exceed the value of 5%. The result obtained for

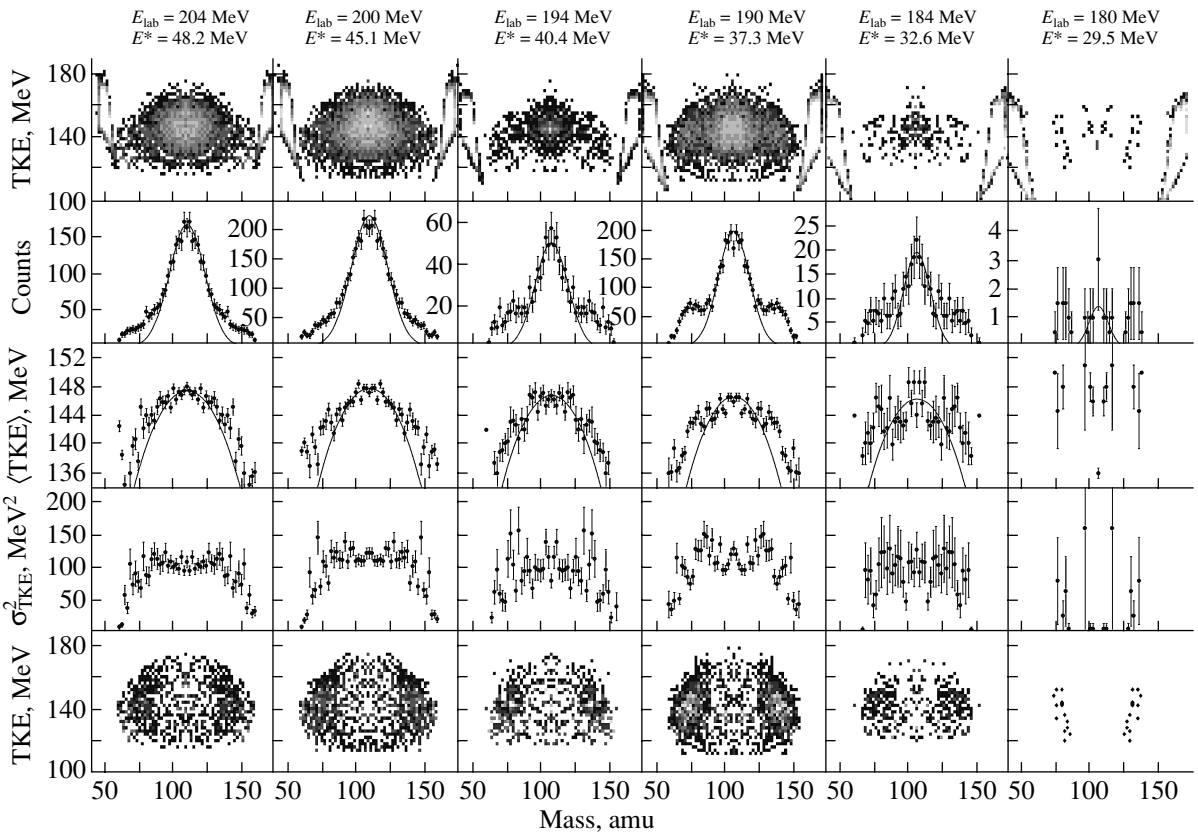

Fig. 6. From top to bottom: double-differential cross sections of the reaction ^{168}Er(^{48}Ca, f) products; mass yields of fission fragments; average TKE, and the variances σ^2_{TKE}; double-differential cross sections of the quasifission process versus the mass of fission fragments.

the reactions ^{48}Ca + ^{168,170}Er, leading to the same compound nuclei ^{216,218}Ra, turned out to be rather unexpected.

Figure 6 shows the data for the ^{48}Ca + ^{168}Er reaction. In the matrix $N(M, \mathrm{TKE})$ shown at the top of Fig. 6, the reaction products having masses close to those of the projectiles and target nuclei are identified as quasi-elastic and deep-inelastic events, and we shall not consider them. The mass range 55–160 of the reaction products can be identified as totally relaxed events, i.e., as fragments, and we shall consider only the properties of these events. Mass distributions for this reaction are shown right under the matrices. The contribution of the asymmetric mode manifesting itself in the form of wide "shoulders" increases with decreasing excitation energy. The shapes of the obtained curves of $\langle \mathrm{TKE} \rangle(M)$ and $\sigma^2_{\mathrm{TKE}}(M)$ are far from being parabolic. The symmetric fission component was described using the statements of [10] and was subtracted from the experimental MED. The results of these subtractions are shown at the bottom of Fig. 6. One can see that the yield of the asymmetric component is quite high even at the highest excitations. Let us note that, for the reaction ^{48}Ca + ^{170}Er, the situation is exactly the same. Moreover, in the ^{48}Ca + ^{154}Sm reaction, leading to the compound

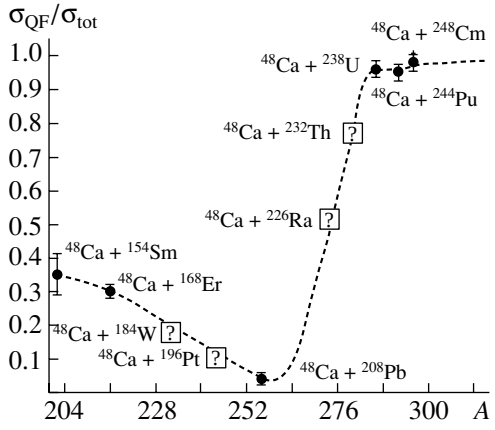

Fig. 7. The quasifission cross section (σ_{QF}) to the capture cross section (σ_{tot}) ratio dependence on the mass number of compound nuclei produced in the reactions with ^{48}Ca at the same excitation energy $E^* \sim 33$ MeV. Solid circles are the measured reactions; the question marks are the combinations to be measured.

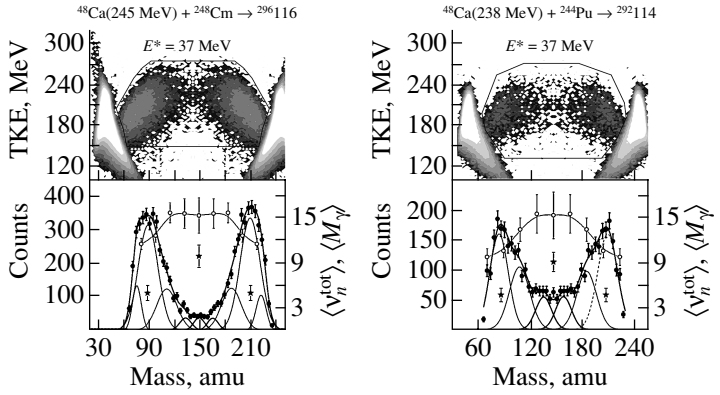

Fig. 8. Two-dimensional matrices $N(M, E_k)$ (top panels); the mass yields (solid circles) and neutron (stars), and γ-ray multiplicities (open circles) as a function of the fission fragment mass (bottom panels) for the reactions ^{48}Ca + ^{248}Cm and ^{48}Ca + ^{244}Pu.

nucleus ^{202}Pb, the relative yield of the asymmetric component is even higher. We have interpreted such a sharp increase in the asymmetric yield in the reaction with ^{48}Ca as a manifestation of the quasifission process, where the influence of the shell effects is clearly seen in the MED of reaction products [11].

Summing up all the data, we plot the dependence of the quasifission relative yield as a function of the mass of compound nuclei produced in reactions with ^{48}Ca at the same excitation energy $E^* \sim 33$ MeV (Fig. 7). Our prediction on the behavior of this curve is shown with a line. The most probable explanation of such a nontrivial behavior of the ratio $\sigma_{QF}/\sigma_{tot}(A)$ is the corresponding probability of formation of the different spherical shells during the decay of the composite system.

4. NEUTRON AND GAMMA-RAY MULTIPLICITIES IN THE FISSION OF SHE

Formerly, emission of neutrons and γ rays in correlation with fission fragments in the decay of superheavy compound systems at excitation energies near or below the Coulomb barrier had not been extensively studied. At the same time, such investigations may be extremely useful for an additional identification of the fusion–fission and quasifission processes and consequently for a more precise determination of the cross sections of these processes in the total yield of fragments. On the other hand, the knowledge of the value of the fission fragment neutron multiplicity can be used in the identification of SHE in experiments aimed at their synthesis.

The results of such investigations are presented in Fig. 8 for the reactions ^{48}Ca + ^{248}Cm, ^{244}Pu at energies near the Coulomb barrier. As seen from the figures, in all cases, the total neutron multiplicity $\langle\nu_n^{tot}\rangle$ is considerably lower (by more than a factor of 2) for the region of fragment masses where the mechanism of quasifission predominates as compared with the region of fragment masses where, in our opinion, the process of fusion–fission prevails (in the symmetric region of fragment masses). Another important feature of the obtained data is the large values of $\langle\nu_n^{tot}\rangle \approx 9.2$ and 9.9 for the fission of ^{292}114 and ^{296}116 compound nuclei, respectively. Considerable differences have been observed in the values of γ-ray multiplicities for different mechanisms of SHE decay as well as for $\langle\nu_n^{tot}\rangle$.

5. CONCLUSIONS

As a result of the experiments carried out, for the first time, the properties were studied of the fission of the compound nuclei ^{202}Pb, ^{216,218}Ra, ^{256}No, ^{266}Hs, ^{286}112, ^{292}114, ^{296}116, ^{302}120, and ^{306}122 produced in reactions with ^{48}Ca and ^{58}Fe at energies close to and below the Coulomb barrier.

On the basis of these data, a number of novel important physics results were obtained:

(i) It was found that the mass distributions of fission fragments for the compound nuclei ^{286}112, ^{292}114, ^{296}116, ^{302}120, and ^{306}122 are asymmetric ones, whose nature, in contrast to the asymmetric fission of actinides, is determined by the shell structure of the light fragment with an average mass of 132–134. It was established that TKE and neutron and γ-ray multiplicities for fission and quasifission of SHE are significantly different.

(ii) The dependence of the capture (σ_c) and fusion–fission (σ_{ff}) cross sections for the nuclei ^{202}Pb, ^{216,218}Ra, ^{256}No, ^{266}Hs, ^{286}112, ^{292}114, ^{296}116, and ^{306}122 on excitation energy in the range 15–60 MeV has been studied. It should be emphasized

that the fusion–fission cross section for the compound nuclei produced in reaction with ^{48}Ca and ^{58}Fe ions at excitation energy of ~30 MeV only slightly depends on the reaction partners; that is, as one goes from ^{286}112 to ^{306}122, σ_{ff} changes by no more than a factor of 4–5. This property seems to be of considerable importance in planning and carrying out experiments on the synthesis of SHE with $Z > 114$ in reaction with ^{48}Ca and ^{58}Fe ions.

ACKNOWLEDGMENTS

This work was supported by the Russian Foundation for Basic Research (project no. 99-02-17981) and by INTAS (grant nos. 11929 and 00-655).

REFERENCES

1. Yu. Ts. Oganessian *et al.*, Eur. Phys. J. A **5**, 63 (1999).
2. Yu. Ts. Oganessian *et al.*, Nature **400**, 242 (1999).
3. U. Brosa *et al.*, Phys. Rep. **197**, 167 (1990).
4. A. Goverdovskii, private communication.
5. M. G. Itkis *et al.*, Phys. Rev. C **65**, 044602 (2002).
6. Z. Patyk and A. Sobiczewski, Nucl. Phys. A **533**, 132 (1991).
7. M. G. Itkis *et al.*, Sov. J. Part. Nucl. **19**, 301 (1988).
8. R. N. Sagaidak *et al.* (in press).
9. I. V. Pokrovsky *et al.*, Phys. Rev. C **60**, 041304 (1999).
10. I. V. Pokrovsky *et al.*, Phys. Rev. C **62**, 014615 (2000).
11. A. Yu. Chizhov *et al.*, Phys. Rev. C **67**, 011603(R) (2003).

Physics of Atomic Nuclei, Vol. 66, No. 6, 2003, pp. 1125–1130. From Yadernaya Fizika, Vol. 66, No. 6, 2003, pp. 1161–1166.

Accuracy of the Chemical Data Evaluated from One-Atom-at-a-Time Experiments*

I. Zvára**

Flerov Laboratory of Nuclear Reactions, Joint Institute for Nuclear Research, Dubna, Moscow oblast, 141980 Russia

Received August 28, 2002

Abstract—Studies of chemistry of the transactinoid elements, which are available only as single atoms, by gas (thermo)chromatographic techniques can provide the adsorption enthalpies of the atoms or molecules. These values serve the ultimate goal—to characterize bulk volatility of the species in terms like sublimation enthalpies. The paper attempts an in-depth discussion of the statistical significance of the adsorption enthalpies derived in such experiments. Usually, the counting statistics are very poor and one faces nonstandard problems in evaluating the confidence intervals for the values of parameters. Here, a most efficient way seems to be the Bayesian approach, realized, when necessary, by Monte Carlo simulations of the counting results. Necessarily, the adsorption enthalpy is not evaluated based on the second law of thermodynamics but through accepting an a priori value of the adsorption entropy. More additional assumptions about the mechanisms and parameters involved are needed. This may produce systematic errors in the quantitative conclusions; the analysis of some recent works with elements 106 and 108 corroborates this concern. Despite such problems, it is possible to reveal qualitative differences in the adsorption behavior of a transactinoid and its expected known congeners as well as to use chemistry for an independent assignment of the atomic numbers of transactinoid nuclides. © *2003 MAIK "Nauka/Interperiodica".*

1. INTRODUCTION

When studying chemical properties of transactinoids on one-atom(per shift, day or week)-at-a-time level, experimenters inevitably experience the subconscious temptation to draw more definite and numerous conclusions than such poor statistics allow; one must be aware of this danger. It is difficult to evaluate the actual accuracy of the values measured on the basis of a few counts using the formulas of the traditional statistics. The Bayesian approach seems much more appropriate and suitable [1–3]. Also, the specific conditions of performing the experiments and radiation measurements often make hardly possible the analytical evaluation of the required conditional likelihoods and then confidence intervals (CI). Here Monte Carlo modeling of the chemical and counting procedures becomes the leading tool.

We are concerned with some typical results of the experiments on gas phase chemistry of transactinoids. These aimed at providing values of the adsorption energies of molecules on some surfaces, which could serve to judge the bulk properties of the substances.

The gas phase techniques are, essentially, two alternatives of gas chromatography [4]:

Isothermal chromatography (IC): the (usually open) column is kept at constant temperature; at its exit, one detects the atoms that have not decayed during the retention time. Measurements must be done at two or more temperatures!

Thermochromatography (TC): a negative longitudinal temperature gradient is imposed on the column so that the migration velocity of the adsorbable molecules strongly decreases downstream; they come to a practical stop, and the radioactive nuclei decay in some temperature range that depends on the lifetimes and the adsorption energy of the molecules. The column must be made of a material capable of detecting the radiation!

2. BAYESIAN APPROACH TO STATISTICAL TREATMENT

With the standard approach, one actually asks: "Once we have obtained some data, D, what will be the probability density distribution of the data if the experiment is repeated many times?" It is difficult to answer convincingly when, say, just two counts were detected. With the Bayesian approach, the question is: "What is, e.g., the 95% CI containing the true

*This article was submitted by the author in English.

** e-mail: zvara@sungraph.jinr.ru

1063-7788/03/6606-1125$24.00

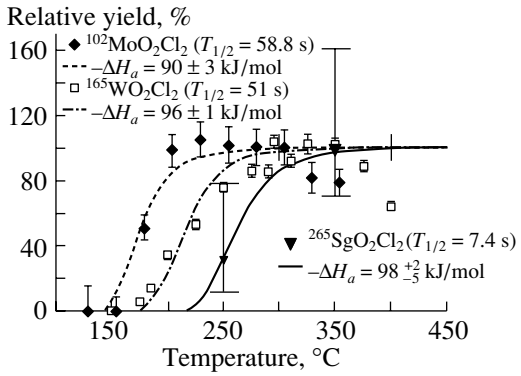

Fig. 1. Isothermal chromatography experiments with Mo, W, and Sg isotopes. The curves are the best fit (as to the enthalpy value) of the data [5] by Eq. (2).

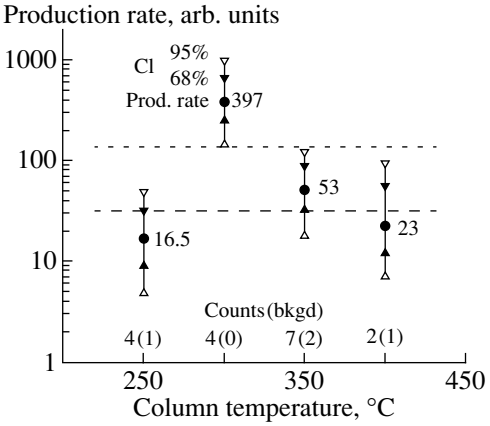

Fig. 2. Numbers (per some unit beam dose) of the Sg atoms surviving at the column exit as a function of the temperature. The 68 and 95% (weighted) Bayesian CI are given.

value of the parameter, θ, inferred by the observation of the data?"

To proceed in this way, one needs, first, the likelihood of observing the data given the parameter value, $L(D|\theta)$. It is known for some simple cases like Poisson and binomial distributions or can be evaluated numerically by Monte Carlo simulations of the model for the data. Second is the prior probability density function for the parameter, $F_{\text{prior}}(\theta)$. Commonly, it is suggested that the probability is uniform over some physically acceptable range ("total ignorance"). Now, the answer to the original question is to be found from the posterior probability density function,

$$F_{\text{post}}(\theta|D) = \frac{L(D|\theta)F_{\text{prior}}(\theta)}{\int L(D|\theta)F_{\text{prior}}(\theta)d\theta}, \qquad (1)$$

with summation rather than integration in the denominator if the parameter is a discrete quantity.

The experimenter often tries to answer the very serious questions like whether there is a significant difference in properties of a very heavy element and its lighter congener(s) and, if so, whether it is a manifestation of the so-called "relativistic effects in chemical properties." A 68% or 1σ CI for a measured quantity, which means to bet only 2 : 1 that the true value is within it, will hardly be convincing. Meanwhile, the posterior probability density function is usually asymmetric and, say, the 95% CI is much wider than 2σ and its limits may even become uncertain (see below)!

3. ISOTHERMAL CHROMATOGRAPHY

One has to measure the number of atoms surviving at the column exit at several column temperatures to find the temperature interval in which the adsorption retention time increases from practically zero to a value comparable with the average lifetime of the nuclide under study, $1/\lambda$. Then, the ratio of the normalized yields—N_∞ at a "high" temperature, T_∞, and N at a "low" T—is a measure of the retention time, t_R:

$$r \equiv N/N_\infty = \exp(-\lambda t_R). \qquad (2)$$

In turn,

$$t_R = [l \cdot (s/Q)\exp(\Delta S/R)]\exp(-\Delta H/RT),$$

where l is the column length, s is the column surface area per unit length, Q is the flow rate, ΔS is the adsorption entropy change, and ΔH is the adsorption enthalpy change.

Let

$$A \equiv \lambda l \cdot (s/Q)\exp(\Delta S/R). \qquad (3)$$

Then,

$$r = \exp[-A\exp(-\Delta H/RT)/T]$$

and

$$-\Delta H = RT\ln(-T\ln r/A). \qquad (4)$$

The number of the theoretical plates in the utilized IC columns is usually rather large, so Eq. (2) is expected to be closely followed. The problem with poor statistics is the precision of the experimental value of r. We shall demonstrate this by an analysis of a recent publication [5] on the oxochloride of Sg—element 106. Figure 1 shows the data as they were presented in the paper; the curves are those calculated by Eq. (2). The point at 350°C for Sg is actually the sum of the measurements at 300, 350, and 400°C placed at 350°C. For a sound analysis, such a folding seems hasty. We started with the primary data: the numbers of counts detected and the expected background. Most of them were presented in [6] and are given in Fig. 2, above the particular temperatures, with the

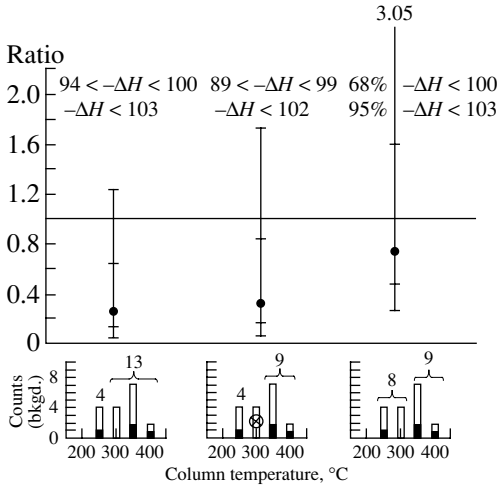

Fig. 3. Evaluation of the PSI data [5] from Fig. 1. Confidence intervals for the N/N_∞ values (bars) for different combinations of experimental points and corresponding CI for $-\Delta H$ in kJ/mol (numerical data).

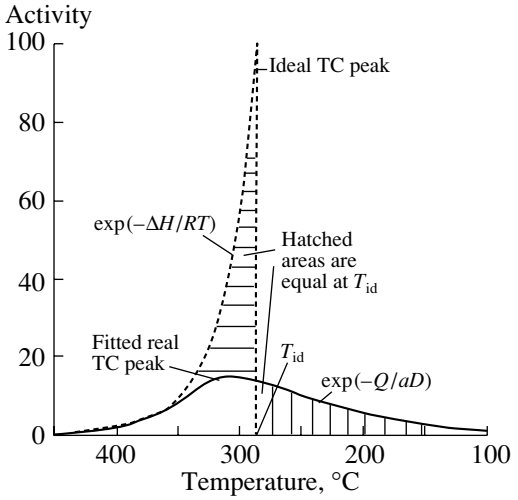

Fig. 4. Adsorption zones in real and ideal thermochromatography.

background in parentheses. The beam doses were different at different temperatures. Figure 2 presents our evaluation of the yield rates (per unit beam dose) using the reported [6, 7] counting efficiencies. The yield rate at 300°C obtained with a very low dose was extremely high, so we use a logarithmic scale to present the data. It is evident that the possibility of fitting the data using the prescription of Eq. (2) is questionable. Then, one can try to combine the data because only two points, N and N_∞, are needed. The possible combinations are schematically shown in the bottom of Fig. 3.

The authors, when putting their two points in Fig. 1, argued that the measurements at 300, 350, and 400°C "within the error limits yielded about the same production rate" [5], but it is not true (cf. Fig. 2)—the huge 95% error bars of the 300°C data still do not overlap with those at the other two temperatures, while even the 68% CIs at 250, 350, and 400°C do overlap!

One might prefer just to omit this strange result at 300°C—see the next combination.

To avoid any prejudice, two pairs of points can be taken.

For each of the combinations, we evaluated the "weighted" [7] Bayesian intervals for r, which are shown in the middle of Fig. 3. One can see that, even for the "most favorable" case, the 95% CI extends above $r = 1$; i.e., the yield rates do not significantly differ! The other two, more reasonable, choices of points give even a less significant difference. Now, using Eq. (1), we can evaluate the CI for the values of $-\Delta H$, which are presented in the top lines of Fig. 3. It shows that, at a confidence level of 95%, one can set only the upper limit for $-\Delta H$ but not the lower one. Moreover, for the first combination (that from [5]), the "narrowest" 95% CI encompasses both $r = 0$ and $r = 1$, thus yielding just $-\Delta H < \infty$!

4. THERMOCHROMATOGRAPHY

The theory of "ideal" thermochromatography suggests that, at any point down the column, there exists thermodynamical (adsorption) equilibrium between the gas phase and surface concentrations of the adsorbable molecules. The ideal *elution* TC, like the ideal IC, of nonradioactive species would yield a narrow band at some T_{id}—a function of ΔH and ΔS, of the processing time and temperature profile. Figure 4 illustrates different situations. In the ideal *frontal* thermochromatography, the high temperature branch of the TC peak must obviously approach an adsorption isobar,

$$N \sim \exp(-\Delta H/RT),$$

and the zone would abruptly terminate at the same T_{id} as above. The integral of the isobar from T_∞ to T_{id} equals the total number of detectable atoms.

If by analogy with the definition (3) for IC

$$A_{TC} \equiv \lambda \cdot (T/g)(s/Q)\exp(\Delta S/R),$$

where g (>0) is the temperature gradient, then

$$\mathrm{Ei}^*(-\Delta H/RT_{id}) = 1/A,$$

where Ei* is the integral exponential function. After approximations,

$$-\Delta H = RT_{id}\ln\left[\frac{-\Delta H/RT_{id}}{A(1 - RT_{id}/\Delta H)}\right]. \qquad (5)$$

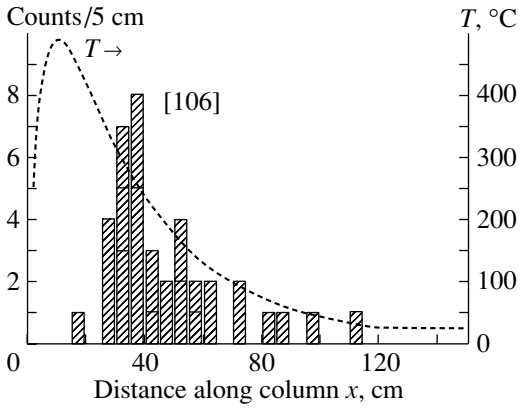

Fig. 5. TC experiment on Sg oxochloride in JINR [9]. The column (silica) surface served as the fission fragment track detector.

Here, we discuss experiments with short-lived nuclides; nominally, they last much longer than the nuclide half-lives. In such tests, the "adsorption zone" is seen as a distribution of coordinates of the detected decay events. In the first approximation, one can consider it as a result of frontal chromatography with an effective duration of about $1/\lambda$. Already, the random lifetimes must broaden the zone. Moreover, short half-lives require a high linear velocity of the carrier gas, which prevents reaching equilibrium as the temperature drops. All this makes it difficult to calculate the shapes of the TC adsorption zones. The scatter in behavior of a few molecules having different concrete lifetimes in rather short TC columns evidently calls for a mathematical model of the migration histories of molecules and Monte Carlo simulations. A versatile procedure [8] describes the history as a sequence of relatively long (compared with column radius), exponentially distributed random jumps down the column, each of which is followed by a random number of elementary adsorption—desorption events at the same coordinate. The latter events realize the retention time. Though the actual jump length distribution is much more complicated, the approximation yields profiles consistent with the analytical solution of a simple IC problem. The mean "deposition length" of irreversibly adsorbed molecules from the established laminar flow in a cylindrical channel is $\approx 0.1Q/G$, where Q is the true (pressure- and temperature-dependent) flow rate, and G is the true diffusion coefficient. Thus, the mean length does not depend on the channel diameter! The effective mean value of the equivalent jump for Monte Carlo simulations proves to be about 80% of the deposition length. The simulations provide quite satisfactory fits to real TC zones [9] like that depicted in Fig. 4. Its right branch corresponds to the exponentially distributed deposition lengths for irreversible adsorption.

When the statistics are sufficient, e.g., a total of 40 Sg decays in Fig. 5 from [9], one can do Monte Carlo simulation of the zones with various ΔH values and a very large "number of atoms" in the experiment to obtain an almost smooth profile. If the profiles can be described by a (semi)empirical formula with ΔH as the only parameter, one can look for the best ΔH value to fit the experimental data. It is not yet clear how to evaluate the rather narrow CIs within this procedure. With the poor statistics, the experimental data, i.e., the distribution of counts over sections of the column (see below), can be simulated a great number of times and Monte Carlo can be used to evaluate the $L(D|\Delta H)$ for use with Eq. (1).

As an example, we consider the recent chemical identification of element 108—hassium (Hs) [10, 11]. The tetroxide (presumably) of the element was detected in a TC column made of charged particle detectors to register decays occurring at different tem-

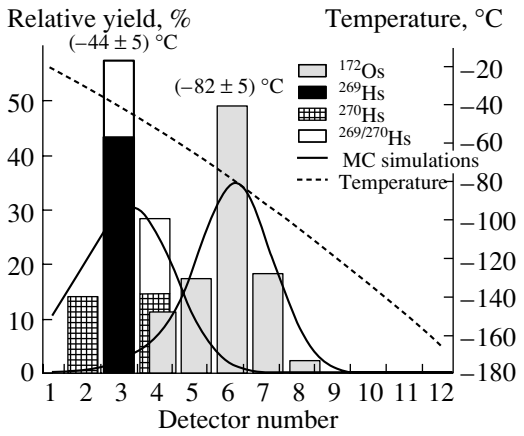

Fig. 6. Thermochromatography of the tetroxide of hassium [10, 11].

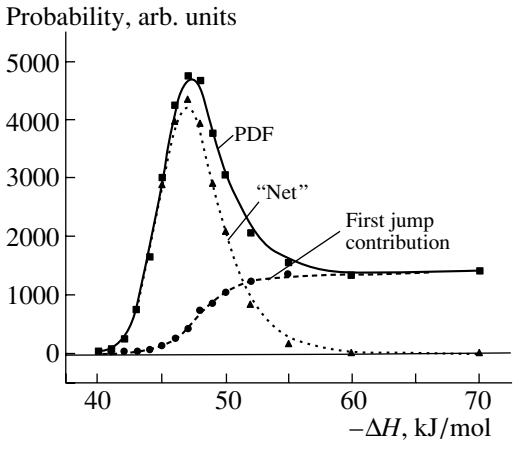

Fig. 7. The Bayesian posterior for the adsorption enthalpy of HsO_4. The "net" curve is the difference between the other two.

peratures. The experimental data are shown in Fig. 6. Seven decays were detected but only three of them were used for evaluation of ΔH because they were due to ^{269}Hs, while the half-lives of other isotopes are not yet known. All three counts occurred in the third section of the column. By using the Monte Carlo simulations, the authors of [10, 11] arrived at $\Delta H(HsO_4) = (-46 \pm 3)$ kJ/mol (95% CI); no additional comments are given.

We performed a similar analysis by following 500 000 histories for each of 15 values of $-\Delta H(HsO_4)$ in the range 40 to 70 kJ/mol. The relative frequencies of the success (when all three events decayed within the third section) are plotted in Fig. 7. A peculiar feature is the constant "tail" toward high $-\Delta H$. So, the curve cannot be normalized nor can CI be defined. One may only rely upon some physical considerations. First, a considerable fraction of the successes proved to be due to the molecules that got to the third section by a sole first jump from the column inlet, i.e., without been chromatographed (see the dotted curve in Fig. 7). This is why this fraction becomes independent of $-\Delta H$ with its higher values. Second, the column was preceded by a long gas duct kept at ambient temperature and overly "nonvolatile" molecules would deposit in the duct not reaching the inlet of the column. But one does not know ΔH on various surfaces and their interrelations. Hence, a quantitative estimate of the upper limit of $-\Delta H$ on the column material is impossible. Another ambiguity stems from the fact that the first section detectors did not work properly, so one does not know whether or not some decays of ^{269}Hs happened within it. Zero would be very informative. Our (still deliberate) conclusion is that $-\Delta H$ is hardly less than 42 kJ/mol but that nothing definite can be said about the upper limit.

5. SYSTEMATIC ERRORS

We have seen that the extremely low yields force one to abandon the use of the second law procedures (plotting equilibrium characteristics against inverse temperature) for measurement of enthalpies. Then, what are the possible systematic errors in ΔH when using Eqs. (4) and (5) due to ambiguities in estimating entropy and other parameters? The equations can be rewritten as

$$-\Delta H/RT = \ln(-T \ln r) - \ln A \qquad (6)$$

and

$$-\Delta H/RT_{id} = \ln(-\Delta H/RT_{id}) - \ln A, \qquad (7)$$

respectively, taking into account that $-RT_{id}/\Delta H \ll 1$. Meanwhile, A is proportional to s—the true surface per centimeter of column length—and also to $\exp(\Delta S/R)$; the latter, in turn, is proportional to τ_0—the period of vibration of the adsorbed molecule perpendicular to the surface [12]. One seldom knows the true specific surface. Using an electron scanning microscope, we found patterns of 0.05 to 1 μm in size for most capillaries; the patterns are of quite variable appearance in different batches of tubes. Figure 8 displays an atomic force microscopy scan of the inner surface of a fused silica capillary [13] with even better resolution. Very probably, there is some "roughness" down to nanometers. It means that the actual surface per column unit length may be order(s) of magnitude larger than that for a smooth cylinder. Also, τ_0 seems to be but an effective value describing the complex adsorption phenomena and must depend on the adsorption mechanism, energetics, and dynamics. Meanwhile, in the transactinoid gas chromatography studies, it is usually taken as 2×10^{-13} or 1×10^{-12} s for any molecule on any surface! But again, one cannot be certain even with orders of magnitude, and the possible bias in the ΔH value may be very large. As can be seen from Eqs. (6) and (7), at temperatures of 200, 350, and 500 K, a mere error in A by a factor of 10 changes the evaluated ΔH value by around 2, 3, and 4 kJ/mol, respectively.

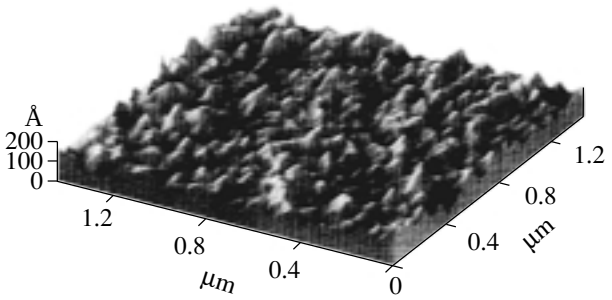

Fig. 8. Real surface of a quartz capillary visualized by atomic force microscopy [13].

Last but not least, all the evaluations are based on the assumption that the column surface is homogeneous in adsorption properties. But in practice, this is very seldom true. As for silica, Fig. 8 makes such an assumption very dubious. To date, in transactinoid studies, this problem has been left almost untouched.

6. CONCLUSION

We conclude that one cannot pretend to obtain a "good" value of the adsorption enthalpy in the experiments under discussion not only because of poor precision but also—or, maybe, mostly—due to possible large systematic errors. Furthermore, it is questionable to make any serious conclusions based on the agreement or disagreement between the "experimental" and "theoretical" (quantum chemistry) values.

On the other hand, just finding experimentally a difference in the values for the analogous compounds of congeners is an important piece of data, if statistically significant.

Even with poor statistics, the chemical experiments can bring results of crucial importance when one is searching for a qualitative difference in behavior of the compared elements, for instance, if it is possible to produce two chemical fractions and determine into which of them goes the new element. This has been accomplished in the work on chemical identification of element 112 presented at this meeting [14, 15] when it was asked whether the element behaves like mercury or rather like radon.

REFERENCES

1. O. Helene, Nucl. Instrum. Methods Phys. Res. A **228**, 120 (1984); **390**, 383 (1997).
2. H. B. Prosper, Nucl. Instrum. Methods Phys. Res. A **241**, 236 (1985).
3. A. de Angelis and M. Iori, Nucl. Instrum. Methods Phys. Res. A **260**, 451 (1987).
4. I. Zvara, Isotopenpraxis **26**, 251 (1990).
5. A. Türler *et al.*, Angew. Chem. Int. Ed. Engl. **38**, 2212 (1999).
6. A. Türler *et al.*, Phys. Rev. C **57**, 1648 (1998).
7. R. Dressler *et al.*, in *Extended Abstracts of the 1st International Conference "Chemistry and Physics Transactinide Elements," Seeheim, 1999*, Contribution P-M-9.
8. I. Zvara, Radiochim. Acta **38**, 95 (1985).
9. I. Zvara *et al.*, Radiochim. Acta **81**, 179 (1998).
10. Ch. E. Düllmann *et al.*, submitted to Nature; PSI Science Report 2001, Vol. 1, p. 123.
11. A. Türler, this Conference.
12. B. Eichler and I. Zvara, Radiochim. Acta **30**, 233 (1982).
13. J. J. Bonvent *et al.*, J. Chromat. A **756**, 233 (1996).
14. A. B. Yakushev *et al.*, Radiochim. Acta **89**, 743 (2001).
15. A. B. Yakushev *et al.*, this Conference.

Physics of Atomic Nuclei, Vol. 66, No. 6, 2003, pp. 1131–1136. From Yadernaya Fizika, Vol. 66, No. 6, 2003, pp. 1167–1172.

Heavy Element Nuclear Chemistry at JAERI*

Y. Nagame**, **M. Asai**, **H. Haba**[1)], **K. Tsukada**, **I. Nishinaka**, **S. Goto**[2)], **A. Toyoshima**, **K. Akiyama**, **M. Sakama**[3)], **Y. L. Zhao**[4)], **S. Ichikawa**, and **H. Nakahara**

Advanced Science Research Center, Japan Atomic Energy Research Institute, Tokai, Japan

Received August 28, 2002

Abstract—The present status of heavy element nuclear chemistry research at JAERI (Japan Atomic Energy Research Institute) is reviewed. Production of the transactinide nuclei ^{261}Rf and ^{262}Db via the reactions of ^{248}Cm(^{18}O,5n) and ^{248}Cm(^{19}F, 5n), respectively, at the JAERI tandem accelerator is reported. Study of the aqueous chemistry of Rf is being carried out with a newly developed rapid ion-exchange separation apparatus. Anion-exchange behavior of Rf in acidic solution is briefly discussed. Recent experimental results on decay studies of neutron-deficient actinide nuclei using the gas-jet coupled JAERI-ISOL are given. We also discuss characteristics of nuclear deformation properties at scission in symmetric and asymmetric fission of actinides. Prospects for studies in the near future are briefly considered. © *2003 MAIK "Nauka/Interperiodica".*

1. INTRODUCTION

Nuclear chemistry study of the transactinide elements in Japan is currently being performed using the JAERI tandem accelerator. We have developed some experimental apparatuses: a beam-line safety system for the usage of the gas-jet coupled radioactive target and recoil chamber, a rotating wheel catcher apparatus for the measurement of α and spontaneous fission (SF) decay of transactinides, and an automated rapid ion-exchange separation apparatus based on high-performance liquid chromatography coupled with an on-line α-particle detection system [1].

The 78-s ^{261}Rf and 34-s ^{262}Db transactinide nuclei, which were commonly used for recent chemical studies of elements 104 and 105, have been successfully produced for the first time in Japan through the reactions of ^{248}Cm(^{18}O, 5n) and ^{248}Cm(^{19}F, 5n), respectively. The production cross sections for each reaction have been accurately measured with the newly developed rotating wheel catcher apparatus MANON (Measurement system for Alpha particle and spontaneous fissioN events ON-line) [2].

On-line anion-exchange experiments of Rf together with the group-4 elements Zr and Hf in acidic solution have been conducted with AIDA (Automated Ion-exchange separation apparatus coupled with the Detection system for Alpha spectroscopy). The results have clearly shown that ion-exchange behavior of Rf is quite similar to that of Zr and Hf and is different from that of the tetravalent pseudo-homologue Th, indicating that Rf is a member of the group-4 elements [3].

Studies of α/EC(electron capture)-decay properties of neutron-deficient actinide nuclei have been carried out using the gas-jet coupled JAERI-ISOL system, and recently the new isotopes ^{233,236}Am and ^{237}Cm have been unambiguously identified [4–6].

From the systematic study of scission properties in a wide range of actinide fission [7, 8], it has been revealed that the bimodal fission observed in SF of the heavy actinides is interpreted as the result of the presence of two fission paths, symmetric and asymmetric fission [9].

In this paper, the present status of nuclear chemistry studies of heavy elements and research plans for the near future at JAERI are summarized.

2. TRANSACTINIDE CHEMISTRY

2.1. Production of ^{261}Rf and ^{262}Db

A ^{248}Cm target of 590 μg/cm^2 in thickness prepared by electrodeposition onto a 2.2-mg/cm^2-thick beryllium backing foil was bombarded by ^{18}O and ^{19}F beams delivered from the JAERI tandem accelerator.

*This article was submitted by the authors in English.

[1)] Present address: RIKEN (The Institute of Physical and Chemical Research), Saitama, Japan.

[2)] Permanent address: Department of Chemistry, Niigata University, Niigata, Japan.

[3)] Permanent address: Department of Radiologic Science and Engineering, University of Tokushima, Japan.

[4)] Permanent address: Institute of High Energy Physics, Chinese Academy of Science, Beijing, China.

**e-mail: nagame@popsvr.tokai.jaeri.go.jp

1063-7788/03/6606-1131$24.00

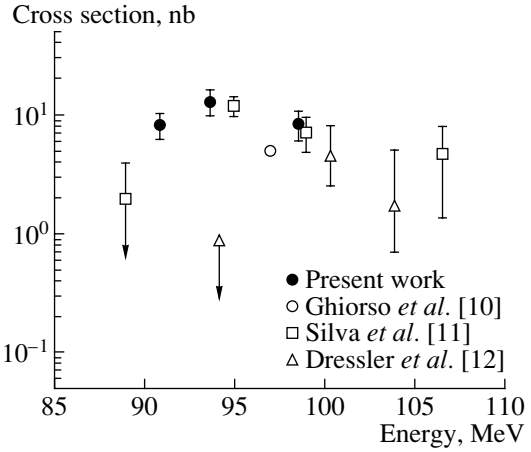

Fig. 1. Cross sections of the ^{248}Cm(^{18}O, $5n$)^{261}Rf reaction as a function of the ^{18}O bombarding energy. The data taken from the literature are also shown.

The reaction products recoiling out of the target were stopped in He gas (~1 bar), attached to KCl aerosols, and were transported through a Teflon capillary to the rotating wheel apparatus MANON. The transported nuclei were deposited on polyethylene terephthalate foils of 120 μg/cm^2 in thickness. The wheel was periodically rotated to position the foils between six pairs of Si PIN photodiodes for α-particle detection. The production cross sections were evaluated from the mother–daughter correlations of α energies between ^{261}Rf and ^{257}No, and ^{262}Db and ^{258}Lr. The experimental details are described in [2].

In Fig. 1, the measured cross sections in the ^{248}Cm(^{18}O, $5n$)^{261}Rf reaction are plotted as a function of the ^{18}O bombarding energy together with the literature data [10–12], where the relative cross section values in [11] are normalized to the present results. The data except for the value <0.9 nb at 94.2 MeV in [12] are smoothly connected with the maximum cross section of about 13 nb at around 94 MeV.

The production cross section of ^{262}Db was evaluated to be 1.3 ± 0.4 nb at the ^{19}F energy of 106 MeV [2].

2.2. Aqueous Chemistry of Rf

Study of the chemical properties of the transactinide elements is challenging both experimentally and theoretically [13]. Due to increasingly strong relativistic effects in the transactinide elements, increasing deviations from the periodicity of the chemical properties based on extrapolations from the lighter homologues in the Periodic Table are predicted [14]. Thus, the experimental approach should involve a detailed comparison of the chemical properties of the transactinides with those of their lighter homologues under identical conditions. We have investigated the anion-exchange behavior of Rf together with the lighter homologues Zr and Hf in the same on-line experiments [3].

To perform fast and repetitive ion-exchange separation of Rf, we have developed the apparatus AIDA that consists of a modified ARCA (Automated Rapid Chemistry Apparatus) which is a miniaturized computer-controlled liquid chromatography system [15] and an automated on-line α-particle detection system. In the modified ARCA as shown in Fig. 2, there are two different paths to supply solutions; the first eluent goes through the collection port to the micro column, while the other one is directed to the column without going through the collection port.

In the following, we briefly introduce the experiment and a part of the result on the anion-exchange behavior of Rf in HCl solution. 78-s ^{261}Rf was produced in the 94-MeV ^{18}O-induced reaction of ^{248}Cm. The reaction products recoiling out of the target were transported by the He/KCl gas-jet system to the collection site of AIDA, where the products were dissolved with 170 μl of hot (~80 °C) 11.5 M HCl and were fed onto the $\varnothing$ 1.6 mm $\times$ 7 mm chromatographic column filled with the anion-exchange resin MCI GEL CA08Y (particle size of about 20 μm) at a flow rate of 1.0 ml/min. Then, the products were eluted with 290 μl of 4.0–10.5 M HCl. The effluent collected on a Ta disk was evaporated to dryness, and the products remaining in the column were eluted with 250 μl of 4.0 M HCl. The pair of Ta disks were automatically subjected to α spectrometry with eight 600-mm^2 passivated ion-implanted planar silicon (PIPS) detectors.

Figure 3 shows the adsorption behavior of Rf, Zr, and Hf as a function of HCl concentration. The result clearly indicates that the adsorption behavior of Rf is quite similar to that of the group-4 elements Zr and Hf, while it was different from that of the tetravalent pseudo-homologue Th in HCl concentration of >8 M. This means that the anionic chloride complexes of tetravalent Rf, Zr, and Hf are formed in concentrated HCl. Another interesting feature is observed in the adsorption trend on the anionic-exchange resin among Rf, Zr, and Hf as shown in Fig. 3. The adsorption order that reflects the stability of chloride complexation is Rf > Zr > Hf. Presently, we are conducting relativistic molecular orbital calculations to understand the present results and to see whether the anion-exchange behavior of Rf is affected by relativistic effects.

Non-Th(IV)-like and non-Pu(IV)-like behavior of Rf was also probed with anion-exchange experiments in 8 M HNO_3 with AIDA. Although Th(IV)

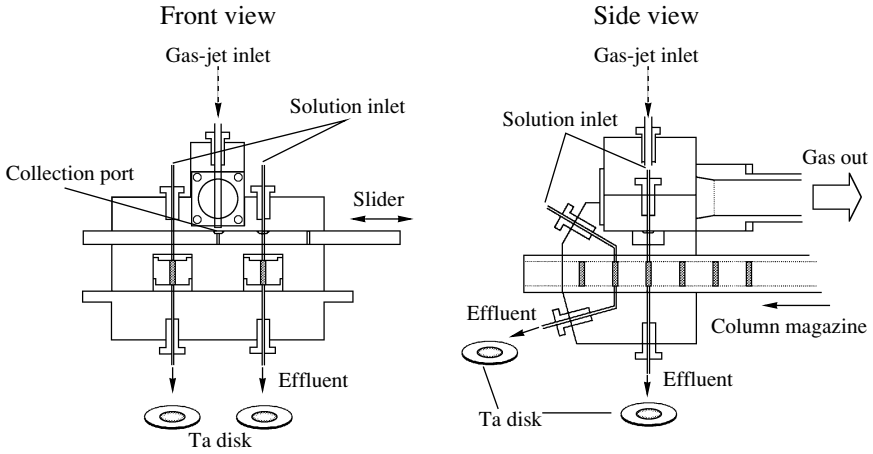

Fig. 2. Schematic of the modified ARCA in AIDA.

and Pu(IV) formed anionic complexes and were adsorbed on the anion-exchange resin, Rf was eluted from the column with 8 M HNO_3 as expected for a typical group-4 element [3].

3. α/EC-DECAY STUDIES OF NEUTRON DEFICIENT ACTINIDES

There still remain many unknown isotopes to be discovered in the region of neutron-deficient actinides which predominantly decay through EC. Decay properties of these nuclides lead to considerable advances in the understanding of proton-excess heavy nuclei: verification of the proton drip line, nuclear structure of large deformed nuclei such as hexadecapole deformation, and fission barrier heights of neutron-deficient nuclei far from stability.

To search for new isotopes and to study α/EC-decay properties of neutron-deficient actinides, we have developed a composite system consisting of a gas-jet transport apparatus and a thermal ion source in the on-line isotope separator (JAERI-ISOL) [16, 17]. This gas-jet coupled JAERI-ISOL system enables us to determine mass number simultaneously via the isotope separator and atomic number by the measurement of x rays associated with the EC/$\beta^{\pm}$ decay of a nucleus.

The experimental setup is schematically drawn in Fig. 4. The ^{6}Li beams delivered from the JAERI tandem accelerator bombarded the ^{233,235}U and ^{237}Np targets set in a multiple target chamber. The reaction systems used were ^{233}U(^{6}Li, xn)$^{233-235}$Am, ^{235}U(^{6}Li, $5n$)^{236}Am, and ^{237}Np(^{6}Li, xn)^{237,238}Cm. The reaction products recoiling out of the targets were thermalized in He gas loaded with PbI_2 aerosol clusters. The products attached to the aerosols were swept out of the target chamber and transported to the thermal ion source of ISOL through a Teflon capillary (1.5-mm i.d. and 8 m in length). The transported nuclides were ionized in the thermal ion source, and mass-separated atoms were collected on an aluminum-coated Mylar tape in a tape transport system or a rotating catcher foil apparatus. In the tape transport system, we used Ge detectors for the x/γ-ray measurement, and Si PIN photodiode detectors set in the rotating catcher foil apparatus were employed for the measurement of α particles.

In the table, the half-lives, α-decay energies, and α-decay branching ratios measured with JAERI-ISOL are summarized.

4. NUCLEAR FISSION STUDIES OF ACTINIDES

The presence of two kinds of deformation paths in low-energy fission of actinides has been demonstrated by examining the correlation among saddle-point configurations, scission configurations, and

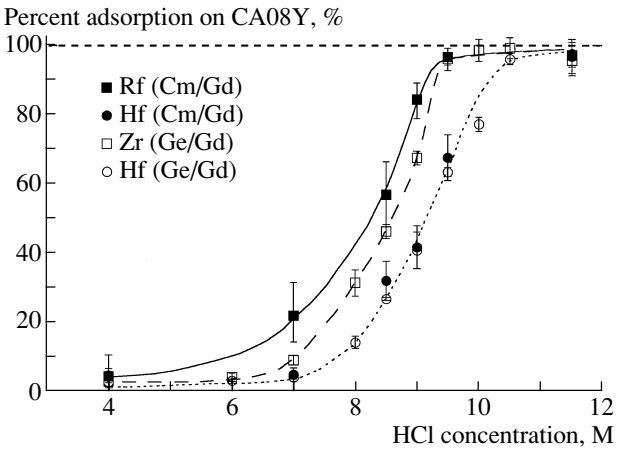

Fig. 3. Adsorption behavior of Rf, Zr, and Hf as a function of HCl concentration [3].

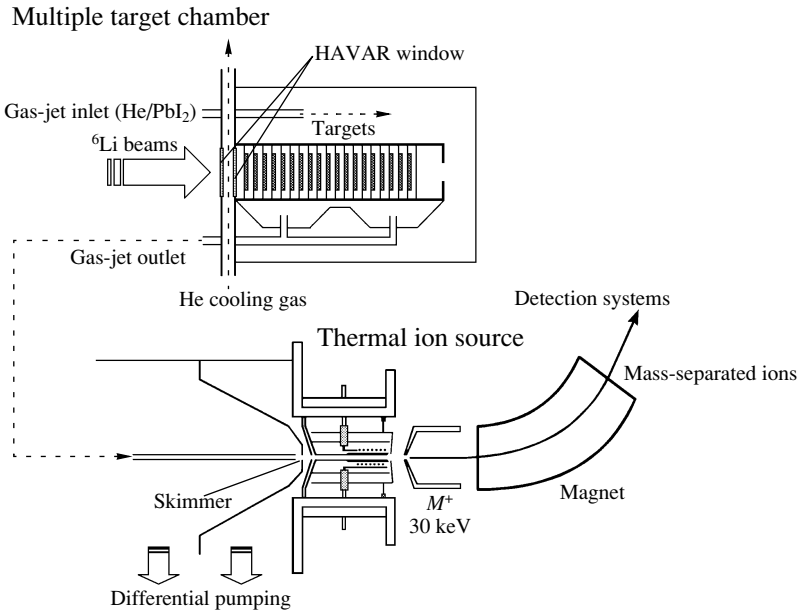

Fig. 4. Schematic view of the gas-jet coupled JAERI-ISOL [16, 17].

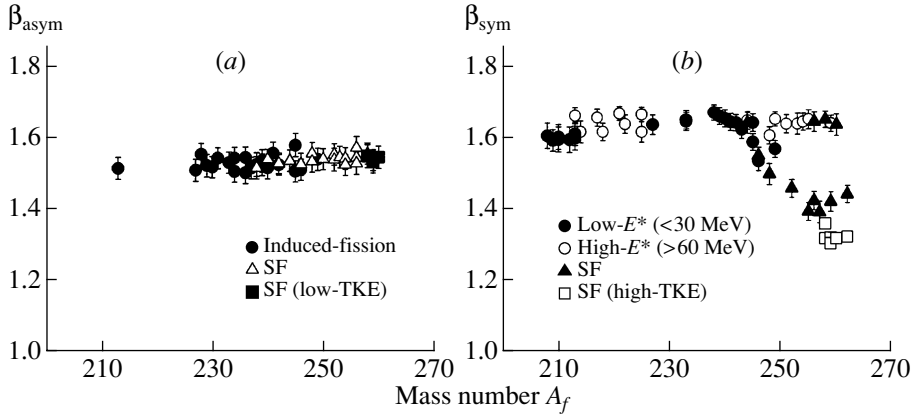

Fig. 5. Degree of deformation of the scission configurations as a function of A_f, (a) asymmetric fission mode and (b) symmetric fission mode [7, 8].

mass-yield distributions [18]. The first path is initiated at higher threshold energy and ends with an elongated scission configuration, giving a final mass yield centered around symmetric mass division, the symmetric fission path. In the second path, a fissioning nucleus experiences a lower threshold energy. This results in a more compact scission configuration, which gives a double-humped mass-yield distribution always centered around the heavy fragment mass number $A = 140$, the asymmetric fission path.

In the following, we discuss the systematic variation of the elongated and compact scission configurations in terms of shape elongation evaluated from the experimental fragment total kinetic energy (TKE) values. The shape elongation parameter β [7, 8] reflecting the degree of deformation at scission is defined as $\beta = D/D_0$, where D_0 indicates the distance between charge centers of two touching spheres. The distance D between the two charge centers of the complementary fragments is evaluated from the average experimental TKE values by assuming that TKE originates from Coulomb repulsion energy.

The β_{asym} values for the scission configurations leading to the asymmetric mass division that produce the typical heavier fragment mass of $A_H = 140$ are plotted in Fig. 5*a* as a function of mass number of the fissioning nuclei A_f [7, 8]. It is found that the β_{asym} shows nearly the same value of 1.53 for both the particle-induced fission and SF, indicating that the degree of deformation at scission for the asymmetric fission mode is independent of the excitation energy

α/EC-decay properties of the neutron-deficient Am and Cm isotopes measured with JAERI-ISOL

Nuclide	Half-life, min	α energy, MeV	α branching ratio, %
^{233}Am	3.2 ± 0.8 [5]	6.780 ± 0.017 [5]	>3 [5]
^{234}Am			<0.04 [17]
^{235}Am	10.3 ± 0.6 [17]	6.457 ± 0.014 [17]	0.40 ± 0.05 [17]
^{236g}Am	3.6 ± 0.2 [6]	6.150 [17]	0.004 [17]
^{236m}Am	2.9 ± 0.2 [6]		
^{237}Cm		6.660 ± 0.010 [6]	
^{238}Cm		6.560 ± 0.010 [6]	

(E^*) of the fissioning nucleus. It is also interesting to note that the β_{asym} values evaluated from the low-TKE component in the bimodal fission (closed squares) [19, 20] are equal to those in the preactinide and actinide region. This means that the ordinary asymmetric fission mode passing through the asymmetric valley is evident even in the heavy actinide region.

Figure 5*b* shows the β_{sym} values evaluated from the TKE data for the symmetric mass division [7, 8]. It is clear that two extreme types of β_{sym} exist. The first one is for the low-E^* fission in the region from the preactinide through the actinide until $A_f \sim 245$ (solid circles) and for the high-E^* fission (open circles) in a wide range of A_f, where β_{sym} is nearly a constant of 1.65. It has been reported that the value of $\beta_{\text{sym}} = 1.65$ corresponds to that expected from the dynamical calculations based on the liquid-drop model [8]. The other type of behavior is for SF in the region of $A_f \sim 260$, at which β_{sym} is decreased to a constant value of 1.33 (open squares), which corresponds to that evaluated from the high-TKE component in the bimodal fission [19, 20]. The smaller elongation at the scission would be related to the effects of spherical fragment shells of $N = 82$ and $Z = 50$ on the mass-symmetric deformation. Note that β_{sym} in the low-E^* fission and SF gradually becomes smaller beyond $A_f \sim 245$, approaching the value of 1.33. Thus, the feature of the symmetric fission mode with the liquid-drop-like elongated scission configuration in the light actinides and preactinides gradually shifts to that of the narrow symmetric mass distribution with the compact scission configuration that is strongly affected by the spherical shell structure of $Z = 50$ and $N = 82$ for both of the complementary fragments. It is also found that, due to washing out of shell effects in hot nuclei, β_{sym} in the high-E^* fission observed in $A_f \geq 245$ keeps the value of 1.65.

From the systematic analysis of the deformation at scission, we can interpret the so-called bimodal fission of the heavy actinides as essentially the two-mode fission seen in the light actinides. The point of difference between the two-mode and the bimodal fission is the liquid-drop-like elongated symmetric scission configuration in the two-mode and the compact symmetric scission configuration due to the strong fragment shell effect in the bimodal fission. The asymmetric fission mode still competes with the strongly shell-affected symmetric fission mode even in the bimodal fission process.

The above inference is supported by the theoretical calculations by Ćwiok *et al.* [21] and Möller *et al.* [22]. The detailed description of the characteristics of the two fission modes has been reported in [8, 9].

5. FUTURE PLANS

In the study of Rf aqueous chemistry, anion-exchange experiments in HF solution are being conducted. Plans for additional experiments are also being made to understand the complex structure of Rf together with Zr and Hf in HNO_3, HCl, and HF solutions. Measurements of XAFS (X-ray Absorption Fine Structure) spectra of Zr and Hf compounds in these solutions will be performed at the KEK (High Energy Accelerator Research Organization) Photon Factory. Relativistic molecular orbital calculations are being carried out to gain an understanding of complex chemistry of Rf and to see whether there are unexpected differences within the group-4 elements.

In the next stage of aqueous chemistry, we plan to conduct Db ion-exchange experiments. Improvements to the overall production rates and a possible multiple target system are being considered to study the short-lived 34-s ^{262}Db produced in the ^{248}Cm(^{19}F, $5n$) reaction with the small cross section of about 1.5 nb. Development of a new ion-exchange separation apparatus, an improved AIDA system, is

being performed. Gas phase chemistry of the transactinide elements is also planned. Although some experimental data on the gas chemistry of the transactinide elements have been reported [13], there are still conflicting results. An apparatus based on isothermal gas chromatography is now under construction.

Experiments on $\alpha-\gamma$ spectroscopy and on SF and α-decay properties of heavy and transactinide nuclei will be conducted with the gas-jet coupled JAERI-ISOL, an $\alpha-\gamma$ spectrometry apparatus, and MANON coupled with a gas chemistry separator system.

ACKNOWLEDGMENTS

The present study has been carried out in collaboration with Niigata University, Osaka University, Tokyo Metropolitan University, University of Tokushima, Kanazawa University, Nagoya University, Hiroshima University, Gesellschaft für Schwerionenforschung (GSI), Mainz University, Paul Scherrer Institut (PSI), Bern University, and Institute of High Energy Physics (Beijing). We would like to acknowledge the crew of the JAERI tandem accelerator for providing the stable and intense beams. This work was partly supported by the JAERI tandem accelerator collaboration program and the Program on the Scientific Cooperation between JAERI and GSI in Research and Development in the Field of Ion Beam Application.

REFERENCES

1. H. Haba, K. Tsukada, M. Asai, *et al.*, Radiochim. Acta **89**, 733 (2001).
2. Y. Nagame, M. Asai, H. Haba, *et al.*, J. Nucl. Radiochem. Sci. **3**, 85 (2002).
3. H. Haba, K. Tsukada, M. Asai, *et al.*, J. Nucl. Radiochem. Sci. **3**, 143 (2002).
4. K. Tsukada, S. Ichikawa, Y. Hatsukawa, *et al.*, Phys. Rev. C **57**, 2057 (1998).
5. M. Sakama, K. Tsukada, M. Asai, *et al.*, Eur. Phys. J. A **9**, 303 (2000).
6. M. Asai, M. Sakama, K. Tsukada, *et al.*, J. Nucl. Radiochem. Sci. **3**, 187 (2002).
7. Y. L. Zhao, I. Nishinaka, Y. Nagame, *et al.*, Phys. Rev. Lett. **82**, 3408 (1999).
8. Y. L. Zhao, Y. Nagame, I. Nishinaka, *et al.*, Phys. Rev. C **62**, 014612 (2000).
9. Y. Nagame, Y. L. Zhao, I. Nishinaka, *et al.*, Radiochim. Acta **89**, 681 (2001).
10. A. Ghiorso, M. Nurmia, K. Eskola, and P. Eskola, Phys. Lett. B **32B**, 95 (1970).
11. R. J. Silva, P. F. Dittner, M. L. Mallory, *et al.*, Nucl. Phys. A **216**, 97 (1973).
12. R. Dressler, PhD Thesis (University of Bern, 1999).
13. J. V. Kratz, *Heavy Elements and Related New Phenomena* (World Sci., Singapore, 1999), p. 129.
14. B. Fricke and W. Greiner, Phys. Lett. B **30B**, 348 (1969).
15. M. Schädel, W. Brüchle, E. Jäger, *et al.*, Radiochim. Acta **48**, 171 (1989).
16. S. Ichikawa, K. Tsukada, M. Asai, *et al.*, Nucl. Instrum. Methods Phys. Res. B **187**, 548 (2002).
17. M. Sakama, M. Asai, K. Tsukada, *et al.* (in preparation).
18. Y. Nagame, I. Nishinaka, K. Tsukada, *et al.*, Phys. Lett. B **387**, 26 (1996).
19. E. K. Hulet, J. F. Wild, R. J. Dougan, *et al.*, Phys. Rev. Lett. **56**, 313 (1986).
20. E. K. Hulet, J. F. Wild, R. J. Dougan, *et al.*, Phys. Rev. C **40**, 770 (1989).
21. S. Ćwiok, P. Rozmej, and A. Sobiczewski, Nucl. Phys. A **491**, 281 (1989).
22. P. Möller, D. G. Madland, A. J. Sierk, and A. Iwamoto, Nature (London) **409**, 785 (2001).

Physics of Atomic Nuclei, Vol. 66, No. 6, 2003, pp. 1137–1145. From Yadernaya Fizika, Vol. 66, No. 6, 2003, pp. 1173–1181.

New Outlook on the Possible Existence of Superheavy Elements in Nature*

A. Marinov[1], S. Gelberg[1], D. Kolb[2], R. Brandt[3], and A. Pape[4]**

[1] *Racah Institute of Physics, Hebrew University, Jerusalem, Israel*
[2] *Department of Physics, University GH Kassel, Germany*
[3] *Kernchemie, Philipps University, Marburg, Germany*
[4] *IReS–UMR7500, IN2P3–CNRS/ULP, Strasbourg, France*

Received November 19, 2002

Abstract—A consistent interpretation is given to some previously unexplained phenomena seen in nature in terms of the recently discovered long-lived high-spin super- and hyperdeformed isomeric states. The Po halos seen in mica are interpreted as being due to the existence of such isomeric states in corresponding Po or nearby nuclei that eventually decay by γ or β decay to the ground states of ^{210}Po,^{214}Po, and ^{218}Po nuclei. The low-energy 4.5-MeV α-particle group observed in several minerals is interpreted as being due to a very enhanced α transition from the third minimum of the potential-energy surface in a superheavy nucleus with atomic number $Z = 108$ (Hs) and atomic mass number around 271 to the corresponding minimum in the daughter. © *2003 MAIK "Nauka/Interperiodica"*.

1. INTRODUCTION

The theoretical predictions in the 1960s [1–8] of the possible existence of very long-lived superheavy elements around $Z = 114$ and $N = 184$ stirred a lot of excitement among the nuclear scientific community and initiated the search for the possible existence of superheavy elements in nature. In the present paper, we concentrate on two independent well-established experimental results that are impossible to understand under the present common knowledge of nuclear physics. These puzzling data are, first, the observation, in mica minerals, of certain halos that have been attributed to the α decay of the short-lived ^{210}Po,^{214}Po, and ^{218}Po nuclei [9–11] and, second, the observation in several minerals of a low-energy α-particle group with an energy of about 4.5 MeV [12–15].

Halos in mica, which consist of tiny concentric rings, have been known for a long time [16, 17]. For most of them, the measured radii of the rings fit within the known ranges of the various α-particle groups from ^{238}U or ^{232}Th decay chains. Therefore, they were correctly interpreted back in 1907 [16, 17] as being due to the existence of very small grains of ^{238}U or ^{232}Th in the centers of the corresponding halos, which have been decaying, through their characteristic decay chains, since the time of crystallization of the crust of the Earth. However, other types of halos were discovered back in 1939 [9] and were thoroughly studied by Gentry [10]. These are the ^{210}Po, ^{214}Po, and ^{218}Po halos, which consist of, respectively, one, two, and three concentric rings, with radii equal to the ranges of the α-particle groups from the decay chains of the corresponding Po isotopes.[1)] These Po isotopes belong to the ^{238}U decay chain. However, their half-lives, as well as the half-lives of their β-decay parents, are short, and since rings belonging to their long-lived precursors are absent, their appearance in nature is puzzling [18].

Another puzzling phenomenon is the low-energy α-particle group, around 4.5 MeV, which has been seen in molybdenite [12], in thorite [13], in magnetite [14], and in OsIr [15]. The cleanest spectrum, where this group appears without observed residues from U isotopes decays, was obtained by Cherdyntsev *et al.* [14]. Based on chemical behavior (having volatile oxides) of the α emitter, it has been suggested that it might be due to a decay of an isotope of Eka–Os, the superheavy element with $Z = 108$ (Hs).[2)]

*This article was submitted by the authors in English.

**e-mail: marinov@vms.huji.ac.il

[1)] Colored pictures of various halos are given in [11].

[2)] Actually Cherdyntsev suggested naming element 108 sergenium, based on part of the great silk road in Kazakhstan (name Serika) where the studied mineral molybdenite was found (private communication from Yu. Lobanov).

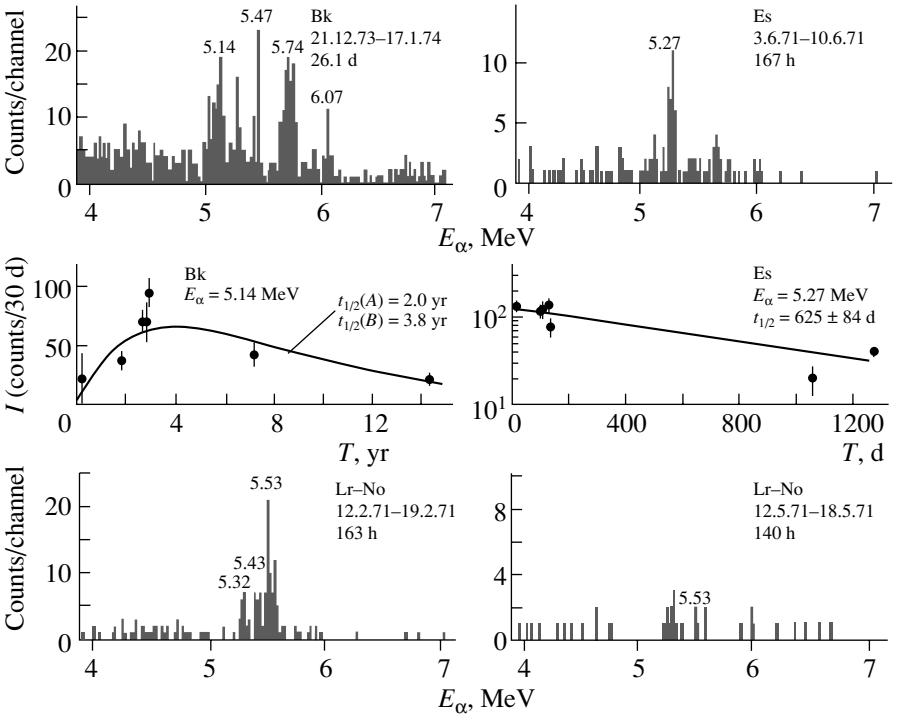

Fig. 1. Left, top: α-particle spectrum obtained with the Bk source. Right, top: α-particle spectrum obtained with the Es source. Left, center: decay curve obtained with the 5.14-MeV group seen with the Bk source (left, top above). {See Note (a) in Table 2 regarding the growing half-life of 2.0 yr [24].} Right, center: decay curve obtained with the 5.27-MeV group seen with the Es source (right, top above). Left, bottom: α-particle spectrum obtained with the Lr—No source. Right, bottom: the same as the previous one but taken about 3 months later. From a comparison of the two spectra a half-life of 26 ± 7 d was deduced for the 5.53-MeV group [24].

Since it was usually found together with ^{247}Cm and ^{239}Pu, it has been suggested [15] that this low-energy α-particle group is due to an isotope of element 108 which is a precursor of ^{247}Cm and its descendant ^{239}Pu. The half-life of this activity has been estimated to be around $(2.5 \pm 0.5) \times 10^8$ yr [12].

With the current common knowledge of nuclear physics, it seemed impossible to understand these data. The predicted energies of ground-state to ground-state α transitions for β stable Hs nuclei with atomic masses of 274 to 286 are between 9.5 and 6.7 MeV [19–21], and the predicted half-lives for these energies are between 3×10^{-2} s and 3×10^2 yr [22, 23], as compared to a half-life of about 5×10^{16} yr for 4.5 MeV. The question is why the nucleus decays with such a low-energy α-particle when a much higher energy, with a penetrability factor of at least 14 orders of magnitude higher, is available.

A second question is how the nucleus can decay with a lifetime that is about eight orders of magnitude shorter than what is predicted [22, 23] from energy versus lifetime relationships for a normal 4.5-MeV α-transition (experimentally estimated at 2.5×10^8 yr as compared to the predicted value of 5×10^{16} yr). (A lifetime in the region of 10^{16} yr is certainly impossible, since it implies the existence of about 100 mg of material in the studied samples.)

In the following sections, similar effects seen in the study of various actinide fractions [24] produced via secondary reactions [25], and also in the study of the ^{16}O + ^{197}Au [26, 27] and the ^{28}Si + ^{181}Ta [28] heavy ion reactions, are summarized. Based on the results of all these experiments, a consistent interpretation for the puzzling phenomena seen in nature is suggested (see also [29]).

2. UNIDENTIFIED α-PARTICLE GROUPS IN ACTINIDES

In a study of actinide fractions from a W target that had been irradiated with 24-GeV protons, long-lived isomeric states were found in the neutron-deficient ^{236}Am and ^{236}Bk nuclei with respective half-lives of 0.6 yr and $\geq$30 d [30]. Their character, however, was not clear, being far from closed shell nuclei, where high-spin isomers are known, and living much longer than the known fission isomers. In addition, several unidentified α-particle groups were

Table 1. The energies and half-lives of several unidentified α-particle groups seen in various actinide sources as compared to theoretical predictions

Source	$E_\alpha^{\exp}$, MeV	$t_{1/2}^{\exp}$, yr	$t_{1/2}^{\mathrm{cal}}$, yr [23]	Enhancement factor[c]	E_α (g.s. $\rightarrow$ g.s.), MeV[a]	$t_{1/2}^{\mathrm{cal}}$, s[b]
Bk	5.14	3.8	1.7×10^5 [d]	4.5×10^4	6–7	2.2×10^9
Es	5.27	1.7	2.7×10^6 [e]	1.6×10^6	7–8	1.9×10^6
No–Lr	5.53	0.07	1.1×10^6 [f]	1.5×10^7	8–9	2.4×10^2

[a] Typical values from [33].

[b] Calculated for the lower energy of column 6 according to formulas given in [23].

[c] The ratio of column 4 to column 3.

[d] Calculated for ^{238}Am. See below.

[e] Calculated for ^{247}Es. See below.

[f] Calculated for ^{252}No. See below.

found in some actinide sources. Thus, 5.14-MeV ($t_{1/2} = 3.8 \pm 1$ yr), 5.27-MeV ($t_{1/2} = 625 \pm 84$ d), and 5.53-MeV ($t_{1/2} = 26 \pm 7$ d) groups were found, respectively, in the Bk, Es, and Lr–No sources [24, 30] (see Fig. 1 and Table 1). Similar to the situation with the 4.5-MeV group seen in nature, also here in the case of the latter unidentified groups, one cannot understand their relatively low energies [e.g., 5.53 MeV in Lr–No as compared to typical ground-state to ground-state transitions of around 8 MeV (column 6 of Table 1), which have penetrability factors about 11 orders of magnitude larger (the ratio of column 4 to column 7 in Table 1)] and their very enhanced character, having a factor of 10^5–10^7 shorter half-lives than predicted from the systematics of energy versus the half-life relationship for normal α decays [22, 23] (see column 5 in Table 1). The deduced evaporation-residue cross sections [24], in the mb region, are also several orders of magnitude larger than expected.

3. STUDY OF THE ^{16}O + ^{197}Au REACTION AND LONG-LIVED HIGH-SPIN SUPERDEFORMED ISOMERIC STATES

A possible explanation for the above puzzling data comes from the study of the ^{16}O + ^{197}Au reaction at $E_{\mathrm{lab}} = 80$ MeV, which is around the Coulomb barrier [26, 27], and of the ^{28}Si + ^{181}Ta reaction at $E_{\mathrm{lab}} = 125$ MeV [28], about 10% below the Coulomb barrier. In the first reaction, a 5.2-MeV α-particle group with a half-life of about 90 min has been found in ^{210}Fr. This group has the same unusual properties as the abnormal α-particle groups found in the actinides and produced via secondary reactions, and of the 4.5-MeV group found in nature. 5.2 MeV is a low energy as compared to 6.5 MeV, the ground-state to ground-state transition from ^{210}Fr, and the 90-min half-life is about 4×10^5 enhanced as compared to the prediction [22, 23] for normal α particles of this energy from ^{210}Fr. However, the 5.2-MeV group has been found in coincidence with γ rays which fit the energies of superdeformed band transitions. Therefore, the α decay is through a barrier of a superdeformed nucleus, and the large enhancement can quantitatively be understood [26] if one takes into account typical superdeformed radius parameters in the penetrability calculations. The data were consistently interpreted [26] in terms of production of a long-lived high-spin isomeric state in the second well of the potential energy surface of ^{210}Fr which decays, by a very enhanced α transition, to a high-spin state in the second well of ^{206}At.

The predicted [31, 32] excitation energies of the second minima in ^{210}Fr and nearby nuclei are above the proton separation energies [33]. Therefore, the decay of isomeric states from the second minima, by emitting protons, is in principle possible. In a separate study of the same ^{16}O + ^{197}Au reaction [27], long-lived proton radioactivities with half-lives of about 5.8 and 67.3 h have been discovered. They were interpreted as being due to very retarded decays from superdeformed isomeric states in the parent nuclei to normal deformed or to the ground states of the daughters. In particular, the indicated line with $E_p = 2.19$ MeV [27] may be associated with the predicted [31] ($E_p = 2.15$ MeV) second minimum to ground state transition from ^{198}Tl, which can be produced by three consecutive superdeformed to superdeformed α-transitions from ^{210}Fr.

4. STUDY OF THE ^{28}Si + ^{181}Ta REACTION AND LONG-LIVED HIGH-SPIN HYPERDEFORMED ISOMERIC STATES

The ^{28}Si + ^{181}Ta reaction has been studied at $E_{\mathrm{lab}} = 125$ MeV, which is about 10% below the

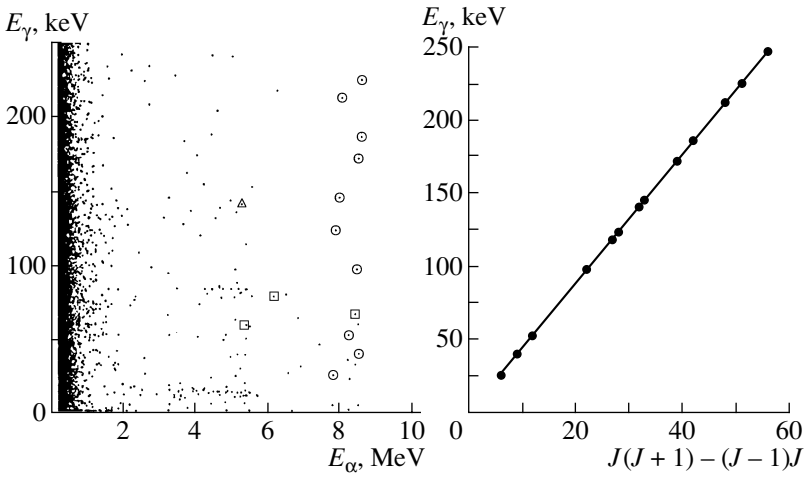

Fig. 2. Left: α–γ coincidence plot from one measurement of the ^{28}Si + ^{181}Ta reaction. $E_{\rm lab} = 125$ MeV, with 200-μg/cm^2 C catcher foil, taken for 76.8 d, starting 77.4 d after the end of irradiation. The γ-ray energies of the encircled events fit with SDB transitions. The squared events fit with known characteristic x rays and the events in triangles are identified with known γ-ray transitions (see [28]). Right: E_γ vs. $J(J+1)-(J-1)J$ for the γ rays seen in coincidence with 7.8–8.6 MeV α-particles. (The encircled events in the left figure plus similar events obtained in a second measurement [28].) The slope of the straight line is 4.42 keV.

Coulomb barrier, and at $E_{\rm lab} = 135$ MeV [28]. A fusion cross section of about 10 mb is predicted at 125 MeV using a coupled-channel deformation code [34] with deformation parameters $\beta_2 = 0.41$ for ^{28}Si and $\beta_2 = 0.26$ for ^{181}Ta [35] and allowing for 2^+ and 3^- excitations in ^{28}Si. Only 2μb is predicted when no deformations are included in the calculations. For 135 MeV, the corresponding predicted fusion cross sections are 95 mb with deformations and 40 mb without.

Figure 2 (left) shows an α–γ two-dimensional coincidence plot obtained at $E_{\rm lab} = 125$ MeV. Quite a few coincidence events are seen between a relatively high energy α-particle group around 8.6 MeV and various γ rays. The half-life of this coincidence group has been measured [28] to be 40 d $\leq t_{1/2} \leq$ 2.1 yr. Figure 2 (right) shows that the γ rays which are in coincidence with these high-energy α particles fit nicely with a $J(J+1)$ law assuming $E_x = 4.42 \times J(J+1)$ keV and $\Delta J = 1$. On the basis of the observation of a Pt x ray in coincidence with the 8.6-MeV alphas and on kinematic arguments, it was suggested [28] that the α transition is from ^{195}Hg to ^{191}Pt. (^{195}Hg may be produced via $1p1n$ evaporation reaction and three consecutive III$^{\rm min} \to$ III$^{\rm min}$ α decays, see below.) An energy parameter of 4.42 keV is typical to superdeformed band γ-ray transitions in this region of nuclei.

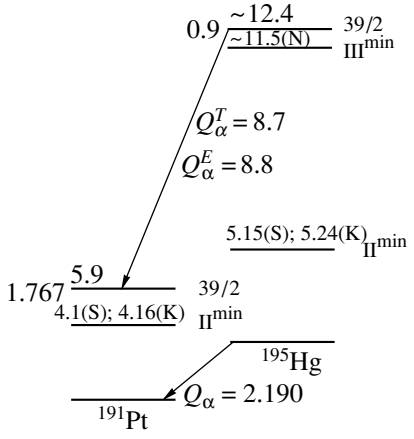

Fig. 3. Proposed decay scheme deduced from the observation of the 8.6-MeV α particles seen in coincidence with superdeformed band transitions. S—Satula *et al.* [31]; K—Krieger *et al.* [32]; N—Nazarewicz [37].

An α energy of 8.6 MeV is a very high energy for ^{195}Hg, which does not decay by emitting α particles, and its ground-state to ground-state Q_α value is 2.190 MeV [33]. A half-life of 40 d is about 13 orders of magnitude too long as compared to the systematics of energy vs. half-life relationship [23], which predicts $t_{1/2} \approx 6 \times 10^{-8}$ s. Since the α particles are in coincidence with superdeformed band γ-ray transitions, the α decay is to the superdeformed well of the daughter nucleus. However, it could not be a II$^{\rm min} \to$ II$^{\rm min}$ transition, since such a transition is very enhanced as opposed to the large retardation measured in the experiment. A consistent interpretation, both from the point of view of the high energy of the α particles and their very long lifetime, is that the decay is from a long-lived high-spin ($J \approx 39/2$) isomeric state in the III$^{\rm min}$, the hyperdeformed minimum [36–39] of

Table 2. A comparison between the experimental α-particle energies and values deduced from the predictions of [36] for some superdeformed (SD) to superdeformed and hyperdeformed (HD) to hyperdeformed isomeric transitions. (The last column shows the corresponding experimental ground-state to ground-state transitions [33].)

Source	$E_\alpha^{\exp}$, MeV	Isotope	Transition	E_α^{cal}, MeV [36]	$E_\alpha^{\mathrm{g.s}\to\mathrm{g.s}}$, MeV
Bk	5.14	^{238}Am[a]	SD → SD	5.13	5.94
Es	5.27	^{247}Es	HD → HD	5.27	7.32
No–Lr	5.53	^{252}No	HD → HD	≈5.6[b]	8.42

[a] Since the intensity of the 5.14-MeV group (Fig. 1) grew at the beginning with time, it was assumed here [24], similar to the situation with the isomeric states in ^{236}Bk and ^{236}Am [30], that ^{238}Bk decayed by EC or β^+ transitions to ^{238}Am.

[b] Extrapolated value. See [24].

Table 3. Experimental and predicted half-lives for superdeformed (SD) to superdeformed and hyperdeformed (HD) to hyperdeformed transitions [24]

Mother isotope	E_α, MeV	Transition	β_2[a]	β_3[a]	β_4[a]	$t_{1/2}^{\mathrm{cal}}$, yr[b]	$t_{1/2}^{\exp}$, yr
^{238}Am	5.14	SD → SD	0.71	0.0	0.09	10.9	3.8 ± 1.0
^{247}Es	5.27	HD → HD	1.05	0.19	0.0	1.15	1.7 ± 0.2
^{252}No	5.53	HD → HD	1.2	0.19	0.0	0.22	0.07 ± 0.02

[a] β_2 and β_4 values were deduced from the ϵ_2 and ϵ_4 values given in [36] using Fig. 2 of [40]. The value of β_3 was taken equal to ϵ_3.

[b] Calculated according to formulas given in [24]. Calculated half-lives for other deformation parameters are given in [24].

^{195}Hg, which decays by strongly retarded transition to the II$^{\min}$ of the potential in ^{191}Pt [28]. As seen in Fig. 3 the predicted Q_α value for such a transition is about 8.7 MeV, taking into account an extrapolated value from [37] for the excitation energy of the III$^{\min}$ in ^{195}Hg and the predictions of [31, 32] for the excitation energy of the II$^{\min}$ in ^{191}Pt. This value fits rather nicely with the measured Q_α value of about 8.8 MeV. (The excitation energy of the state in the third minimum of ^{195}Hg was assumed to be around the rotational 39/2 state with estimated energy of $E_x = 2.2 \times J(J+1)$ keV [39].)

5. SUPER- AND HYPERDEFORMED ISOMERIC STATES IN THE ACTINIDE REGION

Based on the discovery of the long-lived super- and hyperdeformed isomeric states (Sections 3 and 4), a consistent interpretation has been given [24] to the unidentified α-particle groups seen in the actinide sources and described in Section 2 above. II$^{\min}$ → II$^{\min}$ and III$^{\min}$ → III$^{\min}$ α-particle transition energies have been deduced from the predicted [36] excitation energies. Table 2 shows that the low-energy 5.14-, 5.27-, and 5.53-MeV groups, seen in the Bk, Es, and No–Lr sources can consistently be interpreted as being due to the low-energy II$^{\min}$ → II$^{\min}$ transition from ^{238}Am and III$^{\min}$ → III$^{\min}$ transitions from ^{247}Es and ^{252}No, respectively. Their energies are considerably lower than the corresponding ground-state to ground-state transitions (column 6 in Table 2).

Table 3 shows that the very enhanced measured half-lives of the low-energy α-particle groups seen in the various actinide sources are consistent with

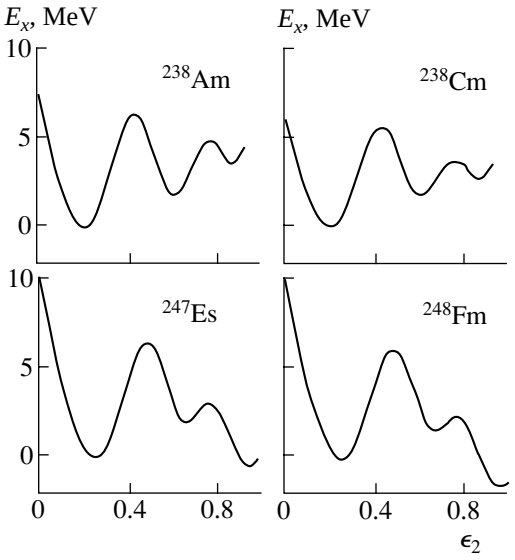

Fig. 4. Potential energies as function of quadrupole deformations for four nuclei according to [36].

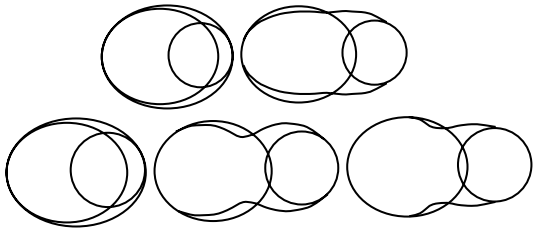

Fig. 5. Calculated shapes of two compound nuclei at various configurations together with the shapes of the corresponding projectile and target nuclei. Top, left: $A_{CN} = 239$ in the normal ground state; $\beta_2 = 0.2$; $\beta_4 = 0.08$ [36]. Top, right: $A_{CN} = 239$ in the second minimum; $\beta_2 = 0.77$; $\beta_4 = 0.1$ [36]. In both figures, $A_{heavy} = 186$; $\beta_2 = 0.22$ [35]. $A_{light} = 53$; β_2, β_3, $\beta_4 = 0$. Bottom, left: $A_{CN} = 253$ in the normal ground state; $\beta_2 = 0.28$; $\beta_4 = 0.01$ [36]. Bottom, center: $A_{CN} = 253$ in the third minimum; $\beta_2 = 1.2$; $\beta_4 = 0$ [36]. Bottom, right: $A_{CN} = 253$ with parameters of the third minimum of ^{232}Th; $\beta_2 = 0.85$; $\beta_3 = 0.35$; $\beta_4 = 0.18$ [38]. In the three figures at the bottom, $A_{heavy} = 186$; $\beta_2 = 0.22$ [35]. $A_{light} = 67$; β_2, β_3, $\beta_4 = 0$.

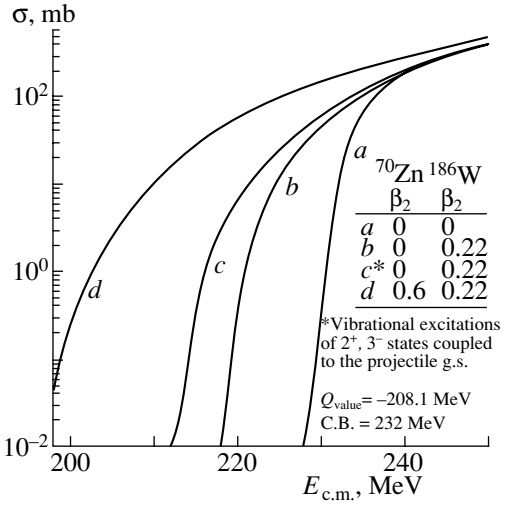

Fig. 6. Calculated fusion cross sections using the code CCDEF [34] for the ^{70}Zn + ^{186}W reaction assuming various quadrupole deformations of the projectile and target nuclei (see text, Section 5).

calculated values [24], taking into account in the penetrability calculations the deformation parameters of the superdeformed and hyperdeformed isomeric states.

The potential energies as function of quadrupole deformations, taken from [36], are shown in Fig. 4 for the ^{238}Am, ^{238}Cm, ^{247}Es, and ^{248}Fm nuclei. It is seen that, in ^{238}Am, the inner and the outer barriers of the second minimum are quite large, while in ^{247}Es and ^{248}Fm the outer barriers of the second minima are small, and the inner barriers of the third minima are large. In fact, the third minima in ^{247}Es and ^{248}Fm are predicted to be the ground states of these nuclei, being 0.61 and 1.76 MeV below the normal, slightly deformed, ground states. Unfortunately there are no predictions in these cases for the potential at even larger deformations, beyond the third minimum. (In the case of ^{232}Th [38], the outer barrier in the third minimum is quite high.)

In [24], detailed estimates for the various production cross sections of the actinide nuclei, as well as of the superheavy element with $Z = 112$ and $N \simeq 160$, are given. It is argued that the relatively large fusion cross sections, in the millibarn region, are due to two effects. First, the compound nucleus is produced in an isomeric state in the second or third minimum of the potential, rather than in the normal ground state. As shown in Fig. 5, much less overlapping and penetration are needed under these conditions, and therefore the compound nucleus formation probability increases drastically. Secondly, in the secondary reaction experiment, the projectile is a fragment that has been produced within 2×10^{-14} s before interacting with another W nucleus in the target. During this short time, it is at high excitation energy and quite deformed. Figure 6 gives the results of couple-channel calculations [34] for the fusion cross section as a function of bombarding energy for the ^{70}Zn + ^{186}W reaction, taking into account the known deformation of ^{186}W and various deformations of the projectile. In Fig. 6, curve *d* shows the results when the projectile has a deformation that is typical for the second minimum of the potential. It is seen that, due to the reduced Coulomb repulsion between the two nuclei for the tip to tip configuration, the cross section decreases very slowly with decreasing bombarding energy.

An idea about the relative importance of the above two effects can be deduced from the following arguments: the difference from a typical cross section of about 1 pb [41] obtained in the ^{70}Zn + ^{208}Pb reaction producing the nucleus ^{277}112 in its ground state to a cross section of about 20 nb producing $^{271(2)}$112 in an isomeric state via the ^{88}Sr + ^{184}W reaction [42] is due to the first effect. The additional difference from 20 nb to about 3.8 mb [24] of producing element 112 in an isomeric state via secondary reactions is due to the second effect.

6. SUMMARY OF THE PROPERTIES OF THE SUPER- AND HYPERDEFORMED ISOMERIC STATES

Figure 7 summarizes the results obtained about the super- and hyperdeformed isomeric states. The nucleus may have a long lifetime in its ground state, but also in long-lived isomeric states in the second

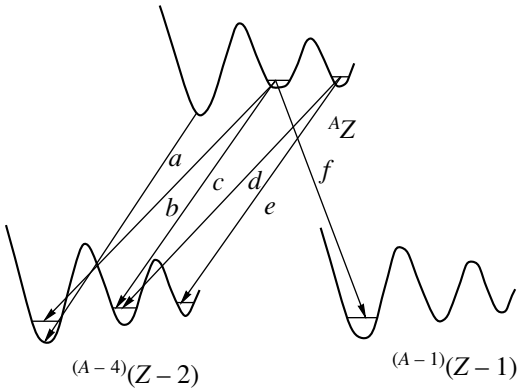

a) $I^{min} \to I^{min}$ normal α's.

b) $II^{min} \to I^{min}$ retarded α's:
$^{190}Ir \to {}^{186}Re$ [28].

c) $II^{min} \to II^{min}$ enhanced α's:
$^{210}Fr \to {}^{206}At$ [26].
$\sim {}^{238}Am \to {}^{234}Np$ [24].

d) $III^{min} \to II^{min}$ retarded α's:
$^{195}Hg \to {}^{191}Pt$ [28].

e) $III^{min} \to III^{min}$ enhanced α's:
$\sim {}^{247}Es \to {}^{243}Bk$ [24].
$\sim {}^{252}No \to {}^{248}Fm$ [24].

f) $II^{min} \to I^{min}$ retarded protons[27, 28]:
$^{198}Tl \to {}^{197}Hg$(?) [27].
$^{205}Fr \to {}^{204}Rn$(?) [28].

Fig. 7. Summary of abnormal particle decays seen in various experiments.

and third minima of the potential-energy surfaces. Long-lived superdeformed isomeric states may decay by very enhanced α particles to superdeformed states in the daughter nuclei or by strongly retarded α particles to the normal deformed states in the corresponding nuclei. It also may decay by very retarded proton radioactivity. Similarly, hyperdeformed isomeric states may decay by strongly enhanced α-particle decay to the hyperdeformed potential well in the daughter or by very retarded α decay to the superdeformed minimum in the same nucleus. All these extremely unusual decay properties have been discovered experimentally as summarized in Fig. 7.

It should be mentioned that the half-lives of the newly discovered isomeric states are longer than those of their corresponding ground states. Such a comparison for the isomeric states in the actinide region is presented in Table 4.

It should be mentioned that, back in 1969 [44], a new type of fission isomeric state was predicted for nuclei with $N \approx 144$–150. A specialization energy in excess of 4 MeV for the second barrier was predicted for a $[505]\frac{11^-}{2}$ state, which is associated with a factor of about 10^{15} increase in the half-life of a normal fission shape isomer.

7. SUPER- AND HYPERDEFORMED ISOMERIC STATES AND THE PUZZLING PHENOMENA SEEN IN NATURE

The discovered super- and hyperdeformed long-lived isomeric states enable one to understand the previously puzzling phenomena seen in nature (see the Introduction).

The source for the Po halos [9, 10] may be such isomeric states in isotopes with $Z \simeq 84$ that decayed, by β or γ decays, to the ground states of ^{210}Po, ^{214}Po, and ^{218}Po.

The low-energy α particles around 4.5 MeV [12–15] can consistently be interpreted as being due to a very enhanced $III^{min} \to III^{min}$ transition in $Z \sim 108$ and $A \sim 271$. The predicted [24, 26] half-life in this case is around 10^9 yr, as seen in Table 5. This resolves the first difficulty in understanding these data, namely, the lifetime about eight orders of magnitude shorter

Table 4. Half-lives of some isomeric states and their ratios to the half-lives of their corresponding normal-deformed ground states

Isotope	$t_{1/2}^{g.s}$	$t_{1/2}^{i.s}$	$t_{1/2}^{i.s}/t_{1/2}^{g.s}$
^{236}Bk	42.4 s[a]	$\geq$ 30 d[b]	$\geq 6.1 \times 10^4$
^{236}Am	3.6 min[c]	219 d[b]	8.8×10^4
^{238}Am[d]	98 min[e]	3.8 yr	2.0×10^4
^{247}Es[f]	4.55 min[e]	625 d	2.0×10^5
^{252}No[g]	2.3 s[e]	26 d	9.8×10^5

[a] Predicted by Möller *et al.* [19].

[b] Ref. [30].

[c] Nagame *et al.*, these Proceedings.

[d] Assuming that the 5.14-MeV group is from ^{238}Am (see Tables 1 and 3).

[e] Ref. [43].

[f] Assuming that the 5.27-MeV group is from ^{247}Es (see Tables 1 and 3).

[g] Assuming that the 5.53-MeV group is from ^{252}No (see text).

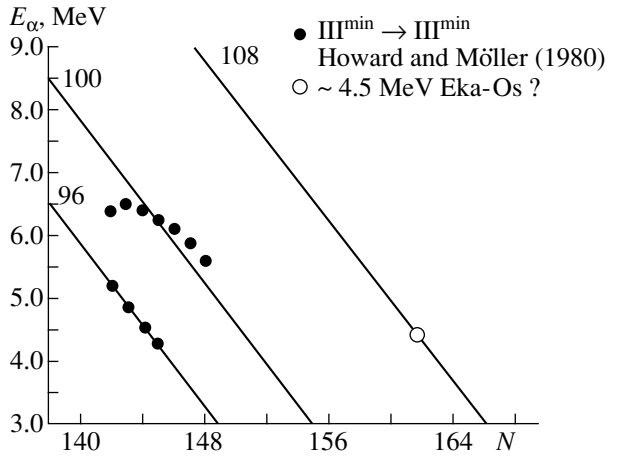

Fig. 8. Predictions [36], and extrapolations from these predictions, of the $III^{min} \rightarrow III^{min}$ α-particle energies. The black dots are the predictions for various isotopes of $Z = 96$ and $Z = 100$. The straight lines are extrapolations from these predictions. The open circle shows the position of 4.5-MeV α particles in $Z = 108$.

than what is predicted [22, 23] from the energy versus lifetime relationship for a normal α transition. (About 2.5×10^8 yr estimated experimentally as compared to 5×10^{16} yr. See the Introduction.)

In addition, an extrapolation of the deduced α energies for $III^{min} \rightarrow III^{min}$ transitions from the predictions of [36] shows that, for $Z = 108$, E_α of about 4.5 MeV corresponds to $N \sim 162$ (see Fig. 8). This is consistent with the suggestion [15] that ^{247}Cm may be a descendent of the superheavy element with $Z = 108$ which decays by 4.5-MeV α particles, since ^{247}Cm can be obtained from $^{271}_{108}Hs_{163}$ by six successive α decays. Another possibility is that the long-lived isotope is ^{267}Hs, which decays by two β^+ or electron capture decays to ^{267}Sg, which is then followed by five successive α decays to ^{247}Cm. It should, however, be mentioned that, in principle, the above 4.5-MeV α particles may also be due to a strongly retarded $II^{min} \rightarrow I^{min}$ or $III^{min} \rightarrow II^{min}$ transition in the region of Os itself. (For normal 4.5-MeV α particles in Os, the expected [22, 23] half-life is about 1 yr. Such a short-lived nuclide cannot exist in nature.)

Table 5. Calculated half-lives for hyperdeformed to hyperdeformed α-particle transition of 4.5 MeV from ^{271}Hs assuming various deformation parameters [24]

β_2	β_3	β_4	$t_{1/2}$, yr
1.2[a]	0.0[b]	0.0[a]	1.8×10^{11}
1.2[a]	0.19[c]	0.0	4.6×10^9
0.85[d]	0.35[d]	0.18[d]	1.3×10^8

[a] ϵ_2 and ϵ_4 values for ^{248}Fm were taken from [36] and converted to β_2 and β_4 values according to [40].

[b] Assuming $\beta_3 = 0$.

[c] Assuming $\beta_3 = \epsilon_3$ of [36].

[d] Parameters given in [38] for ^{232}Th.

8. SUMMARY

It was shown that the newly discovered long-lived super- and hyperdeformed isomeric states can provide consistent interpretations to two previously unexplained phenomena seen in nature. Thus, the Po halos can be understood as being due to the existence of such isomeric states in nuclei with Z values around 84 and atomic masses in the region of 210–218. The observed 4.5-MeV α-particle group can be understood as being due to a low-energy and strongly enhanced hyperdeformed to hyperdeformed transition in a nucleus with $Z = 108$ and $A \simeq 271$.

It seems to us that the existence of superheavy elements in nature is not impossible.

ACKNOWLEDGMENTS

We appreciate very much the valuable discussions with J.L. Weil and N. Zeldes.

REFERENCES

1. V. M. Strutinsky, Yad. Fiz. **3**, 614 (1964) [Sov. J. Nucl. Phys. **3**, 449 (1964)].
2. W. D. Myers and W. J. Swiatecki, Nucl. Phys. **81**, 1 (1966).
3. A. Sobiczewski, F. A. Gareev, and B. N. Kalinkin, Phys. Lett. **22**, 590 (1966).
4. V. M. Strutinsky, Nucl. Phys. A **95**, 420 (1967).
5. C. L. Wong, Phys. Rev. Lett. **19**, 328 (1967).
6. Yu. A. Muzychka, V. V. Pashkevich, and V. M. Strutinsky, Preprint No. R7-3733, JINR (Joint Inst. for Nucl. Res., Dubna, 1968).
7. S. G. Nilsson, J. R. Nix, A. Sobiczewski, *et al.*, Nucl. Phys. A **115**, 545 (1968).
8. J. Grumann, U. Mosel, B. Fink, and W. Greiner, Z. Phys. **228**, 371 (1969).
9. G. H. Henderson and F. W. Sparks, Proc. R. Soc. London, Ser. A **173**, 238 (1939).
10. R. V. Gentry, Science **160**, 1228 (1968).
11. R. V. Gentry, *Creation's Tiny Mystery* (Earth Sci. Associates, Knoxville, Tennessee, 1992).
12. V. V. Cherdyntsev and V. F. Mikhailov, Geochemistry, No. 1, 1 (1963).
13. R. D. Chery, K. A. Richardson, and J. A. S. Adams, Nature **202**, 639 (1964).
14. V. V. Cherdyntsev, V. L. Zverev, V. M. Kuptsov, and G. I. Kislitsina, Geochemistry, No. 4, 355 (1968).
15. H. Meier, W. Albrecht, D. Börche, *et al.*, Z. Naturforsch. **25**, 79 (1970).

16. J. Joly, J. Phil. Mag. **13**, 381 (1907).
17. O. Mugge, Zent. Mineral. **1907**, 397 (1907).
18. N. Feather, Cumm. Roy. Soc. Edinburgh, No. 11, 147 (1978).
19. P. Möller, J. R. Nix, and K.-L. Kratz, At. Data Nucl. Data Tables **66**, 131 (1997).
20. H. Koura, M. Uno, T. Tachibana, and M. Yamada, Nucl. Phys. A **674**, 47 (2000); RIKEN-AF-NP-394 (2001).
21. S. Liran, A. Marinov, and N. Zeldes, Phys. Rev. C **62**, 047301 (2000); nucl-th/0102055.
22. V. E. Viola, Jr. and G. T. Seaborg, J. Inorg. Nucl. Chem. **28**, 741 (1966).
23. G. Royer, J. Phys. G **26**, 1149 (2000).
24. A. Marinov, S. Gelberg, D. Kolb, and J. L. Weil, Int. J. Mod. Phys. E **10**, 209 (2001).
25. A. Marinov, C. J. Batty, A. I. Kilvington, *et al.*, Nature **229**, 464 (1971).
26. A. Marinov, S. Gelberg, and D. Kolb, Mod. Phys. Lett. A **11**, 861 (1996).
27. A. Marinov, S. Gelberg, and D. Kolb, Mod. Phys. Lett. A **11**, 949 (1996).
28. A. Marinov, S. Gelberg, and D. Kolb, Int. J. Mod. Phys. E **10**, 185 (2001).
29. A. Marinov, S. Gelberg, D. Kolb, *et al.*, in *Proceedings of the 3rd International Conference on Exotic Nuclei and Atomic Masses, Hämeenlinna, Finland, 2001*, Ed. by J. Äysto *et al.*, p. 380.
30. A. Marinov, S. Eshhar, and D. Kolb, Phys. Lett. B **191**, 36 (1987).
31. W. Satula, S. Ćwiok, W. Nazarewicz, *et al.*, Nucl. Phys. A **529**, 289 (1991).
32. S. J. Krieger, P. Bonche, M. S. Weiss, *et al.*, Nucl. Phys. A **542**, 43 (1992).
33. G. Audi and A. H. Wapstra, Nucl. Phys. A **565**, 66 (1993).
34. J. Fernández-Neillo, C. H. Dasso, and S. Landowne, Comput. Phys. Commun. **54**, 409 (1985).
35. S. Raman, C. H. Malarkey, W. T. Milner, *et al.*, At. Data Nucl. Data Tables **36**, 1 (1987).
36. W. M. Howard and P. Möller, At. Data Nucl. Data Tables **25**, 219 (1980).
37. W. Nazarewicz, Phys. Lett. B **305**, 195 (1993).
38. S. Ćwiok, W. Nazarewicz, J. X. Saladin, *et al.*, Phys. Lett. B **322**, 304 (1994).
39. A. Krasznahorkay, M. Hunyadi, M. N. Haraken, *et al.*, Phys. Rev. Lett. **80**, 2073 (1998).
40. W. Nazarewicz and I. Ragnarsson, *Handbook of Nuclear Properties*, Eds. by D. N. Poenaru and W. Greiner (Clarendon Press, Oxford, 1996), p. 80.
41. S. Hofmann, V. Ninov, F. P. Hessberger, *et al.*, Z. Phys. A **354**, 229 (1996).
42. A. Marinov, S. Gelberg, and D. Kolb, in *Conference "Nuclei Far from Stability/Atomic Masses and Fundamental Constants," 1992*, p. 437.
43. R. B. Firestone, V. S. Shirley, C. M. Baglin, *et al.*, *Table of Isotopes* (Wiley-Interscience, 1996).
44. S. G. Nilsson, G. Ohlén, C. Gustafsson, and P. Möller, Phys. Lett. B **30B**, 437 (1969).

Physics of Atomic Nuclei, Vol. 66, No. 6, 2003, pp. 1146–1151. From Yadernaya Fizika, Vol. 66, No. 6, 2003, pp. 1182–1187.

Perspective for the Determination of Chemical Properties of Element 112*

R. Eichler** **and S. Soverna**
(for a PSI–University Bern–GSI–TU Munich–FLNR–University Mainz–IMP Collaboration)[1)]

Paul Scherrer Institute, Villigen, Switzerland
University of Bern, Switzerland

Received August 28, 2002

Abstract—We present here results of thermochromatographic model studies with Rn and Hg, conducted in order to prepare future gas-adsorption chromatographic investigations of element 112. The adsorption properties of Rn on various transition metals were investigated by vacuum thermochromatography. From the results of these experiments, predictions have been deduced for the adsorption behavior of hypothetically noble-gas-like elements 112 and 114. Empirical predictions of the adsorption interaction of a noble metallic element 112 and its lighter homologues with transition metal surfaces are given in the literature. The results of these calculations are compared with experimental data obtained in thermochromatographic model experiments with Hg. The most efficient way to chemically identify element 112 is the use of a cryo-on-line detector (COLD)-like setup, which was already successfully applied in the chemical investigation of hassium. Modifications of this device needed for the on-line thermochromatographic investigation of element 112 are presented together with results of test experiments with short-lived isotopes of Rn and Hg.

1. INTRODUCTION

From the systematics given by the periodic table, the elements with the atomic numbers 112 (E112) and 114 (E114) have their outermost valence electrons in the $7s$ and $7s7p_{1/2}$ orbitals, respectively. Increasing nuclear charges causes progressively growing relativistic effects in the electron shells influencing the chemical behavior of the heaviest elements [1, 2]. The primarily occurring stronger binding of the electrons in the spherical relativistic orbitals s and $p_{1/2}$ is predicted to have a strong impact on the properties of heavy elements that have valence electrons in these orbitals. In 1973, Pitzer [3] suggested that the element 112 should behave as a noble gas. Noble-gas-like behavior would give evidence of chemically inert E112 and E114 related to strong relativistic shell stabilizations in the $7s$ and $7s7p_{1/2}$ orbitals, respectively. However, a metallic behavior due to relativistically destabilized $6d$ electron orbitals as the outermost is also possible. In 1976, Eichler [4] predicted a noble metallic behavior of element 112 closer to Hg. Thus, the primary scientific goal of the chemical investigation of E112 and E114 must be the differentiation between a noble metallic character and a noble-gas-like behavior. This differentiation is the matter of recent experiments, which endeavor to study the gas adsorption properties of these elements on metal surfaces. In preparation of the challenging experimental studies of E112 and E114, model experiments with Hg and Rn are essential. Ranges of experimental parameters are deduced, which have to be covered by experiments with the transactinides. These model studies are the topic of this work.

*This article was submitted by the authors in English.

[1)] W. Brüchle (*Gesellschaft für Schwerionenforschung, Darmstadt, Germany*), R. Dressler (*Paul Scherrer Institute, Villigen, Switzerland*), C.E. Düllmann (*Paul Scherrer Institut, Villigen, Switzerland; Labor für Radio- und Umweltchemie, Universität Bern, Switzerland*), B. Eichler (*Paul Scherrer Institut, Villigen, Switzerland*), N.W. Gäggeler (*Paul Scherrer Institut, Villigen, Switzerland; Paul Scherrer Institute, Villigen, Switzerland*), E. Jäger (*Gesellschaft für Schwerionenforschung, Darmstadt, Germany*), D. Piguet (*Paul Scherrer Institute, Villigen, Switzerland*), M. Schädel (*Gesellschaft für Schwerionenforschung, Darmstadt, Germany*), E. Schimpf (*Gesellschaft für Schwerionenforschung, Darmstadt, Germany*), P. Törle (*Institut für Kernchemie, Universität Mainz, Germany*), N. Trautmann (*Institut für Kernchemie, Universität Mainz, Germany*), A. Türler (*Institut für Radiochemie, TU München, Germany*), A.B. Yakushev (*Flerov Laboratory of Nuclear Reactions, JINR, Dubna, Russia*), Z. Qin (*Institute of Modern Physics, Lanzhou, China*).

** e-mail: `robert.eichler@psi.ch`

1063-7788/03/6606-1146$24.00 © 2003 MAIK "Nauka/Interperiodica"

2. NOBLE-GAS-LIKE BEHAVIOR OF TRANSACTINIDE ELEMENTS E112 AND E114: MODEL STUDIES WITH Rn*

Adsorption properties of Rn on transition metal surfaces have been determined using vacuum thermochromatography. The method of vacuum thermochromatography was already successfully applied for the separation of volatile elements and compounds at the on-line mass separator OSIRIS [5–7] and for adsorption studies of various elements on metallic surfaces [8–11]. Figure 1 shows a schematic view of the vacuum thermochromatography setup used in this work.

The vacuum chamber (*1*) was evacuated by a turbo molecular pump setup (*2*) and by a modified double-stage cryogenic pump (*3*) to a pressure of about 3×10^{-5} Pa. The pressure was monitored using an ionization gauge (*4*). A copper tube (*5*) was mounted on top of the cold head of the cryogenic pump. The thermochromatography experiments were carried out in quartz tubes (*6*), which were covered inside by thin metal foils (*7*). The quartz tube was then placed into the copper tube. A temperature gradient from $T_1 = 273$ K to $T_4 = 20$ K was obtained outside along the copper tube. The upper temperature (T_1) was forced by an oven (*8*). The stability of this temperature gradient was monitored by stationary thermocouples (T_1, T_2, T_4). The temperature gradient from 230 to 60 K obtained inside of the chromatography columns was monitored by a movable Teflon® insulated thermocouple (T_3). Temperature equilibrium conditions were established along the chromatographic column over about 15 h. By opening the valve (*12*) to the emanation source (*11*), the experiment was started.

Either $^{\text{nat.}228/232}ThO_2$ (2 g as powder), emanating ^{220}Rn ($T_{1/2} = 55.6$ s), or $^{227}Ac_2O_3$ (about 2×10^{-3} μg, deposited on a Pt-foil), emanating ^{219}Rn ($T_{1/2} = 3.96$ s), was used as the Rn source. The emanating Rn isotopes entered the chromatographic column. During the experiments ^{220}Rn and ^{219}Rn decayed to much less volatile daughter nuclides. These decay products were instantly deposited or kept adsorbed on the chromatographic surface. Hence, the distribution of the Rn isotopes along the temperature gradient was "frozen." Afterward, the chromatography column was removed from the vacuum chamber and the γ emission of the nuclides ^{212}Pb ($E_\gamma =$ 238 keV) or ^{211}Bi ($T_{1/2} = 2.17$ min, $E_\gamma = 351$ keV, the equilibrium daughter activity of ^{211}Pb) was measured using an HPGe (high-purity germanium) γ detector through a 1-cm lead collimator. The original result of each thermochromatography experiment is an internal thermochromatogram (e.g., black bars in Fig. 2) representing the distribution of the adsorbate along the chromatographic column.

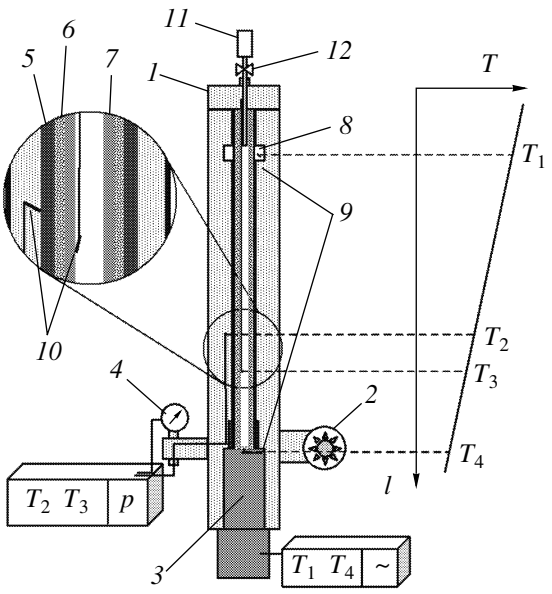

Fig. 1. Schematic view of the vacuum thermochromatography setup and the temperature gradient.

From deposition temperatures, T_{dep}, observed in the experiment and from the selected experimental parameters, the adsorption enthalpy of Rn on the metal surfaces at zero surface coverage, ΔH_{ads}(ther.), was evaluated, using a thermodynamic equilibrium model of vacuum thermochromatography, based on principles of ideal linear gas chromatography [10]. Furthermore, similar to the Monte Carlo simulation of gas thermochromatography [12], a Monte Carlo simulation of idealized microscopic adsorption and desorption processes of single atoms in an evacuated cylindrical tube [13] was used to determine independently the adsorption enthalpy of Rn on the metal surfaces, ΔH_{ads}(kin.). The resulting

Table 1. The enthalpies of adsorption of Rn on polycrystalline metal surfaces

Metal	Rn			Xe
	$-\Delta H_{ads}$ (ther.), kJ/mol	$-\Delta H_{ads}$ (kin.), kJ/mol	$-\Delta H^M_{ads}$, kJ/mol	$-\Delta H^M_{ads}$, kJ/mol
Cu	37 ± 2	40 ± 2	25 ± 2	21
Ag	20 ± 2	23 ± 2	26 ± 2	21.5
Au	29 ± 2	33 ± 2	33 ± 2	27.5
Pd	37 ± 2	41 ± 2	35 ± 2	29
Ni	39 ± 2	43 ± 2	37 ± 2	31

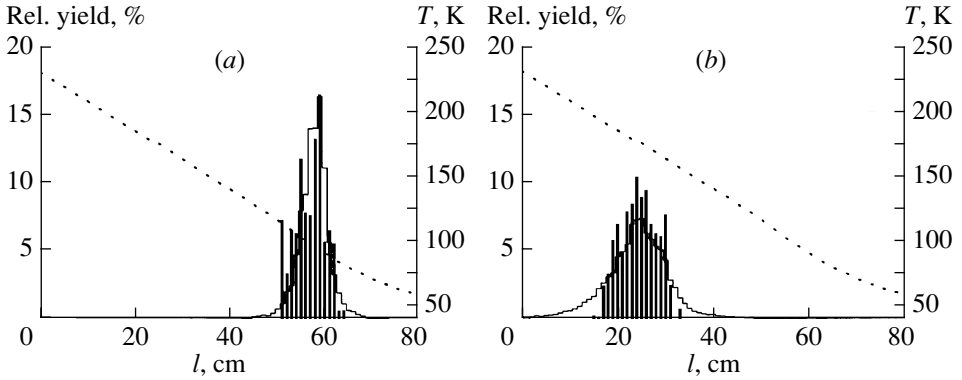

Fig. 2. Thermochromatograms: the distribution of (*a*) ^{219}Rn on silver (3 h experimental duration) and (*b*) ^{220}Rn on nickel (50 h experimental duration) are shown as black bars; the stepped line represents the distribution calculated by the Monte Carlo model; the temperature gradient is indicated (dotted lines).

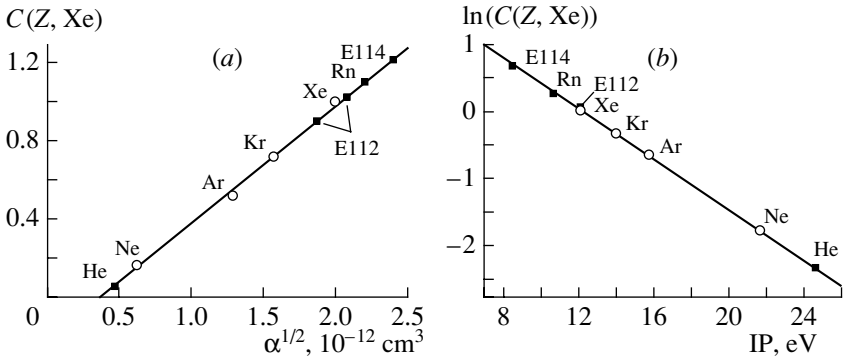

Fig. 3. Empirical correlations of $C(Z, \mathrm{Xe})$ for the light noble gases with physical properties as (*a*) polarizability (α) or (*b*) ionization potential (IP). Extrapolation of $C(\mathrm{Rn}, \mathrm{Xe})$ and into the unknown region of transactinide elements ($C(\mathrm{E112}, \mathrm{Xe})$ and $C(\mathrm{E114}, \mathrm{Xe})$), assuming a noble-gas-like behavior of E112 and E114.

simulated thermochromatograms are shown in Fig. 2 (stepped lines).

The adsorption enthalpies of Rn on the transition metal surfaces are compiled in Table 1 (ΔH_{ads}(kin.) and ΔH_{ads}(ther.)). Both adsorption models applied in this analysis yield similar results for ΔH_{ads}. The adsorption enthalpies of Rn on the polycrystalline surfaces of the metals Cu, Ag, Au, and Ni were determined experimentally for the first time. The evaluated adsorption enthalpy of Rn on Pd agrees very well with the data obtained by gas thermochromatography (-37 ± 4 kJ/mol) [14]. Similar deposition temperatures measured on the same metal for different experimental durations indicate the metallic surfaces to be stable at the given vacuum conditions, which is a crucial point for the scientific and experimental concept of the investigation of E112 and E114.

Exact calculations exist only for the interaction of closed shell atoms with hypothetical metal surfaces (e.g., [15–18]). Miedema and Nieuwenhuys [19] presented an empirical model used to estimate theoretical adsorption enthalpies of Rn on transition metal surfaces. They assumed the adsorption enthalpy of noble gases on metal surfaces as being proportional to the energy of adhesion. The calculated adsorption enthalpies of Xe on metal surfaces agree with literature data within an error range of about $\pm 5\%$. On the basis of the calculations for the lighter noble gases, the authors suggest a linear dependence between the adsorption enthalpies of Ne, Ar, and Kr on metal surfaces and the empirically calculated adsorption enthalpies of Xe on the same metal surfaces:

$$\Delta H^{M}_{\mathrm{ads}}(Z) = C(Z, \mathrm{Xe}) \Delta H^{M}_{\mathrm{ads}}(\mathrm{Xe}). \qquad (1)$$

We found empirically correlations between the factors $C(Z, \mathrm{Xe})$ for $Z =$ Ne, Ar, Kr, and Xe and the enthalpies of sublimation, polarizabilities, and the ionization potentials (see, e.g., Fig. 3) [13]. Subsequently, the factors $C(Z, \mathrm{Xe})$ for the calculation of the adsorption enthalpies ($\Delta H^{M}_{\mathrm{ads}}$) of closed shell atoms Z ($Z =$ He, Rn, E112, and E114) on different metal surfaces have been obtained by extrapolation (Fig. 3). The $\Delta H^{M}_{\mathrm{ads}}$ of Rn on the metal surfaces of Cu, Ag, Au,

Pd, and Ni were calculated using Eq. (1). The results are included in Table 1 (Rn, $-\Delta H^M_{ads}$).

With exception of Cu, the results for the Rn adsorption from this extended empirical model are obviously in very good agreement with our experimental results. This encouraged us to use this model for a prediction of the adsorption enthalpies of E112 and E114 on different metal surfaces, assuming hypothetically a noble-gas-like behavior of these elements. For the empirical deduction of C(E112, Xe) and C(E114, Xe), predicted properties of the elements E112 and E114 have been used, e.g., the polarizabilities (α) [20] and the ionization potentials (IP) [21, 22] (Fig. 3). The predicted values for the adsorption enthalpies of E112G and E114G on Cu, Ag, Au, Pd, and Ni are presented in Fig. 4.

These values have to be distinguished from the adsorption enthalpies calculated with the Miedema model for metal–metal interactions [23], which was applied to transactinide elements assuming a metallic behavior of E112M and E114M [24]. The predicted values have been inserted into Fig. 4 for comparison. The metallic interaction of the elements E112 and E114 with transition metal surfaces are expected to be much stronger and much more dependent on the nature of the metal surface (see Section 3).

3. METALLIC BEHAVIOR OF TRANSACTINIDE ELEMENTS E112 AND E114: MODEL STUDIES WITH Hg

A high volatility of element 112 has been predicted by Eichler [4], using extrapolations of the sublimation enthalpies along the groups of the periodic table. The metallic character was quantified from the sublimation enthalpies and the dissociation enthalpies of homonuclear dimers. These empirical extrapolations led to the assumption of a noble metallic behavior for element 112 even closer to Hg than to Rn. In order to cover also these predicted chemical properties of E112, gas thermochromatography experiments with tracer nuclides of Hg were carried out. ^{192,193}Hg were produced at the PSI SINQ spallation neutron source at PSI applying the NAA "rabbit" system and using the fast-neutron-induced activation reaction ^{nat}Pb$(n, xn)^{192,193}$Pb $\rightarrow ^{192,193m}$Hg. We prepared ^{192,193m}Hg samples using a one-step volatilization-adsorption sequence in a 50-ml/min H_2/Ar gas flow (Fig. 5*a*), which allowed us to separate carrier-free ^{192,193m}Hg at 600°C from the bulk of lead. The volatile mercury was adsorbed in a cooled trap on Au foils, which served afterward in the thermochromatography experiments as Hg sources.

A thermochromatography setup (Fig. 5*b*) was used to study adsorption properties of Hg on different metals. The chromatography columns were

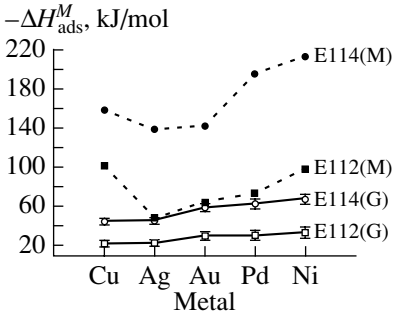

Fig. 4. Prediction of adsorption properties of E112 and E114 on transition metal surfaces.

prepared in the same way as for the vacuum thermochromatography experiments with radon. A temperature gradient was established along the thermochromatography column between 600 and −10°C (Fig. 6). The adsorption properties of Hg on Au, Pt, and Pd have been investigated. The resulting thermochromatograms of Hg on Au and Pd are shown in Fig. 6. From the distribution of Hg along the chromatography column, the adsorption enthalpies of Hg on Au, Pd, and Pt have been determined by a Monte Carlo simulation based on a microscopic description of adsorption chromatography [12].

Interestingly, all thermochromatograms of Hg on the metals showed two deposition maxima. Therefore, two adsorption enthalpies of Hg on the metals were determined (Table 2).

The ΔH_{ads} were compared with results calculated using the Eichler–Miedema model (Table 2, ΔH^M_{ads}) from [25]. We note better agreement of the calculated adsorption enthalpies of Hg on the metals evaluated from the higher deposition temperature. But still these values are smaller than predicted. The deposition in two peaks is still under discussion. Further experiments are envisaged.

4. SIMULTANEOUS STUDIES OF Hg AND Rn

On-line experiments with short-lived Hg and Rn isotopes have been conducted at PSI. The Hg isotopes were produced in the nuclear fusion reaction

Table 2. Adsorption enthalpies (in kJ/mol) of Hg on metal surfaces

Metal	$-\Delta H_{ads}(1)$	$-\Delta H_{ads}(2)$	$-\Delta H^M_{ads}$
Au	100	86	114
Pt	133	108	167
Pd	148	128	206

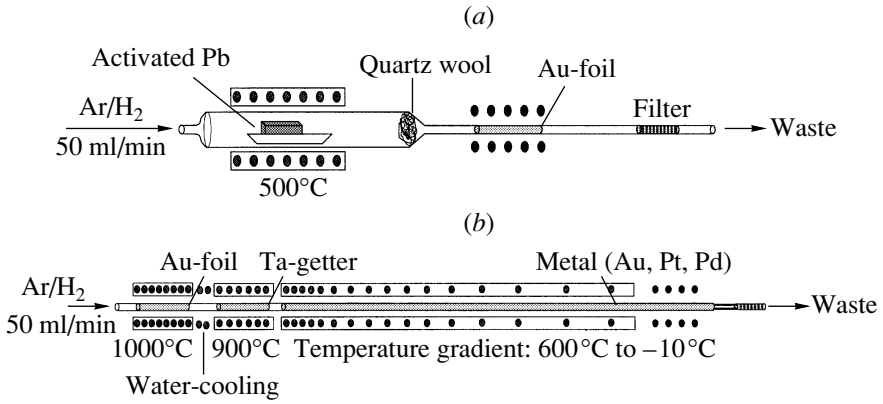

Fig. 5. Setup for the offline experiments with ^{192,193m}Hg: (*a*) Preparation of carrier-free Hg samples. (*b*) Thermochromatography of Hg in metal columns.

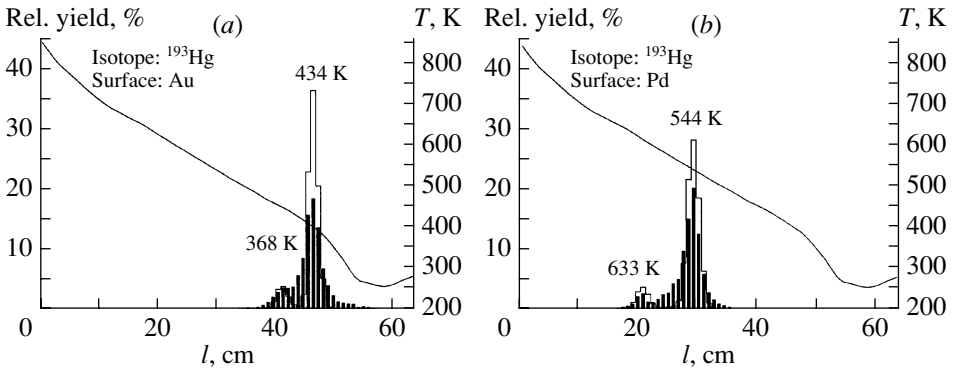

Fig. 6. Thermochromatograms of Hg on noble *d*-metals (*a*) Au and (*b*) Pd. Duration of the experiments 1 h. The Hg deposition along thermochromatographic column (black bars) is presented together with results of a Monte Carlo simulation of the gas chromatographic process (stepped line). The temperature gradient is indicated (solid curve).

^{168}Yb(^{20}Ne, (6–8)n)$^{180-182}$Hg. The recoiling reaction products were thermalized in a 500-ml/min He gas flow. The volatile reaction products, mainly the Hg isotopes, remained in the gas phase and were thus continuously swept out of the target chamber.

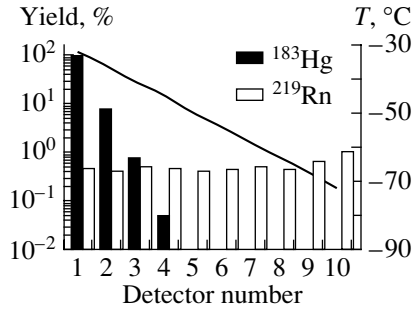

Fig. 7. Thermochromatogram of Hg and Rn in the 2π-COLD setup. The assumed temperature gradient is indicated (solid curve).

An emanation source containing ^{227}Ac was connected to the carrier gas stream emanating the ^{219}Rn ($T_{1/2} = 3.9$ s). The target chamber was connected directly to the cryo-on-line detector (COLD) through a 2-mm Teflon capillary. A new 2π-COLD device was built. This thermochromatography device (COLD II) consists of a special arrangement of 3×1 cm^2 PIN diodes and glass plates facing each other and forming a rectangular channel. The surfaces of the glass plates were covered with gold, which was deposited using a sputtering technique. Hence, the spontaneous deposition of Hg and the adsorption properties of Rn on Au could be studied simultaneously. ^{219}Rn and its α-decaying daughter nuclides were used for an on-line α-spectroscopic calibration. A resulting chromatogram of one experiment is presented in Fig. 7.

It represents a typical picture of a diffusion-driven deposition of Hg on the Au surface. The beginning deposition of Rn on Au at −70°C can be observed. For further on-line experiments, we improved the COLD

II setup. A better coupling of the cryo-unit to the detector array was developed in order to obtain a temperature gradient from 25°C to −190°C, which is needed to cover the whole prediction interval of the expected E112 deposition on Au. A direct coverage of the copper channel opposite to the PIN diodes with Au will provide a more reproducible, stable, and directly measurable temperature gradient.

5. CONCLUSIONS

The low-temperature vacuum thermochromatography technique is shown to be usable for the investigation of adsorption interactions of very volatile atoms and molecules on a wide variety of surfaces.

The gas thermochromatographic experiments with Hg yielded a less strong adsorption interaction of Hg with noble metal surfaces than expected and a two-peak deposition. Further experiments are envisaged to clarify this phenomenon.

The predicted adsorption enthalpies of E112 on transition metals, if it behaves as a noble gas element or as a noble metal E112, allow us to select the best-suited experimental conditions for on-line gas phase chemical studies. If E112 behaves as a noble gas, it could not be separated from Rn. If E112 behaves as a noble metal, it can clearly be separated chromatographically from the bulk of Rn using the COLD device. However, the α background of decaying Rn daughters in the detectors will obstruct the unambiguous detection of E112 by genetically linked α-decay chains. Therefore, physical separation methods such as a gas-filled recoil separator or a velocity filter should assist in effectively preseparating E112 from Rn. The vacuum thermochromatography technique will then provide an excellent choice when coupled to such physical separators, which work at low gas pressures or even under vacuum conditions.

Using the presented COLD II setup, without physical preseparation, investigations of the spontaneously fissioning isotope $^{283}112$, for which the decay modes of the Rn daughter isotopes do not interfere, are envisaged.

ACKNOWLEDGMENTS

We would like to thank the staff of the PSI Philips Cyclotron and of the PSI SINQ facility.

This work was supported in part by the Swiss National Science Foundation.

REFERENCES

1. B. Fricke and J. T. Waber, Act. Rev. **1**, 433 (1971).
2. P. Pyykkö, Chem. Rev. **88**, 563 (1988).
3. K. Pitzer, J. Chem. Phys. **63** (2), 1032 (1975).
4. B. Eichler, Kernenergie **19** (10), 307 (1976).
5. L. Westgaard *et al.*, J. Inorg. Nucl. Chem. **31**, 3747 (1969).
6. B. Grapengriesser and G. Rudstam, Radiochim. Acta **20**, 85 (1973).
7. G. Rudstam and B. Grapengriesser, Radiochim. Acta **20**, 97 (1973).
8. B. Eichler *et al.*, Kernenergie **30**, 11 (1987).
9. N. Hildebrand *et al.*, Nucl. Instrum. Methods Phys. Res. A **260**, 407 (1987).
10. H. Gäggeler *et al.*, Radiochim. Acta **40**, 137 (1986).
11. B. Eichler *et al.,* J. Phys. Chem. A **104** (14), 3126 (2000).
12. I. Zvara, Radiochim. Acta **38**, 95 (1985).
13. R. Eichler and M. Schädel, J. Phys. Chem. B **106** (21), 5413 (2002).
14. B. Eichler and K. Son Chun, Isotopenpraxis **21** (5), 180 (1985).
15. S. Clarke *et al.*, Phys. Rev. B **63**, 85416 (2001).
16. G. G. Kleiman and U. Landmann, Phys. Rev. Lett. **31**, 707 (1973).
17. E. Zaremba and W. Kohn, Phys. Rev. B **13**, 2270 (1976).
18. E. Zaremba and W. Kohn, Phys. Rev. B **15**, 1769 (1977).
19. A. R. Miedema and B. E. Nieuwenhuys, Surf. Sci. **104**, 491 (1981).
20. M. Seth *et al.*, J. Chem. Phys. **106** (9), 3623 (1997).
21. E. Eliav *et al.*, Phys. Rev. A **52**, 2765 (1995).
22. A. Landau *et al.*, J. Chem. Phys. **114** (7), 2977 (2001).
23. A. R. Miedema and J. W. F. Dorleijn, Surf. Sci. **95**, 447 (1980).
24. B. Eichler, PSI Report No. 00-09 (Paul Scherrer Institute, Villigen, 2000).
25. B. Eichler and H. Rossbach, Radiochim. Acta **33**, 121 (1983).

Physics of Atomic Nuclei, Vol. 66, No. 6, 2003, pp. 1152–1162. From Yadernaya Fizika, Vol. 66, No. 6, 2003, pp. 1188–1198.

Accuracy and Efficiency of Modern Methods for Electronic Structure Calculation on Heavy- and Superheavy-Element Compounds*

A. V. Titov**, **N. S. Mosyagin, T. A. Isaev, and A. N. Petrov**

Petersburg Nuclear Physics Institute, Russian Academy of Sciences, Gatchina, 188300 Russia

Received November 27, 2002

Abstract—The methods that are actively used for electronic structure calculations of low-lying states of heavy- and superheavy-element compounds are briefly described. The advantages and disadvantages of the Dirac–Coulomb–Breit Hamiltonian, Huzinaga-type potential, shape-consistent Relativistic Effective Core Potential (RECP), and Generalized RECP are discussed. The nonvariational technique of the electron-structure restoration in atomic cores after the RECP calculation of a molecule is presented. The features of the approaches accounting for electron correlation, the configuration interaction and coupled cluster methods, are also described. The results of calculations on E113, E114, U, and other heavy-atom systems are presented. © *2003 MAIK "Nauka/Interperiodica".*

1. INTRODUCTION

High-precision calculations of molecules with heavy and superheavy atoms that provide "chemical accuracy" (1 kcal/mol or 350 cm^{-1}) for excitation and dissociation energies of low-lying states are extremely time-consuming. Employing the latest theoretical and program developments is necessary at the following stages:

(A) selection of an effective spin-dependent Hamiltonian;

(B) basis set optimization;

(C) appropriate way of accounting for correlation.

In order to minimize the computational efforts necessary to provide a given accuracy in calculation of properties, it is important to achieve the equivalent (balanced) level of accuracy in each of these stages in the most economical way. Moreover, too high an accuracy which can be formally attained at the first two stages by, e.g., (a) employing an effective Hamiltonian, in which inactive core electrons are treated explicitly, or/and (b) using a too large a basis set can result in abnormal requirements on computers at the last stage.

In the present paper, the main attention is paid on items (A) and (C). The Dirac–Coulomb–Breit (DCB) Hamiltonian and the Relativistic Effective Core Potential (RECP) method, which are widely employed [at stage (A)], are described in Sections 2 and 3. The Configuration Interaction (CI) and Coupled Cluster (CC) methods, which are most popular in correlation calculations [at stage (C)], are presented in Sections 4 and 5. In contrast to the density functional approaches, the CI and CC methods allow one to study excited electronic states of a given symmetry with high level of accuracy.

2. DIRAC–COULOMB–BREIT HAMILTONIAN

It is well known that the Dirac–Coulomb (DC) Hamiltonian with the Breit interaction and other Quantum ElectroDynamic (QED) corrections taken into account provides a very high accuracy of calculations of heavy atoms and heavy-atom molecules. The DC Hamiltonian has the form (in atomic units, $e = m = \hbar = 1$, where e and m are the electron charge and mass, and $\hbar$ is Planck constant)

$$\mathbf{H}^{\mathrm{DC}} = \sum_p \mathbf{h}^{\mathrm{D}}(p) + \sum_{p>q} \frac{1}{r_{pq}}, \qquad (1)$$

where indices p, q run over all the electrons in an atom or molecule; r_{pq} is the distance between electrons p and q; and the one-electron Dirac operator $\mathbf{h}^{\mathrm{D}}$ is

$$\mathbf{h}^{\mathrm{D}} = c(\boldsymbol{\alpha} \cdot \mathbf{p}) + mc^2(\beta - 1) + V^{\mathrm{nucl}}, \qquad (2)$$

where c is the speed of light; V^{nucl} is the nuclear potential including the effect of finite nuclear size, etc.; $\mathbf{p} = -i\boldsymbol{\nabla}$ is the electron momentum operator; and $\boldsymbol{\alpha}$ and β are the 4×4 Dirac matrices.

The lowest order QED correction includes the interelectronic exchange by one transverse photon

*This article was submitted by the authors in English.

**e-mail: Titov@pnpi.spb.ru; url: http://qchem.pnpi.spb.ru

Table 1. Transition energies of the tin ($Z = 50$), lead ($Z = 82$), and eka-lead ($Z = 114$) atoms calculated by the DHF method with Coulomb and Coulomb–Gaunt two-electron interaction for states with the ns^2np^2 configuration (in cm^{-1})

Configuration	J	DC	DCG	Absolute difference	Relative difference, %
			Tin		
$(5s^2_{1/2}5p^2_{1/2})$	0	3113	3153	40	1.3
$(5s^2_{1/2}5p^1_{1/2}5p^1_{3/2})$	1	0	0	0	0
$(5s^2_{1/2}5p^1_{1/2}5p^1_{3/2})$	2	5143	5139	−4	−0.1
$(5s^2_{1/2}5p^2_{3/2})$	2	5941	5893	−48	−0.8
$(5s^2_{1/2}5p^2_{3/2})$	0	15 873	15 820	−53	−0.3
			Lead		
$(6s^2_{1/2}6p^2_{1/2})$	0	0	0	0	0
$(6s^2_{1/2}6p^1_{1/2}6p^1_{3/2})$	1	4752	4644	−108	−2.3
$(6s^2_{1/2}6p^1_{1/2}6p^1_{3/2})$	2	9625	9514	−111	−1.2
$(6s^2_{1/2}6p^2_{3/2})$	2	18 826	18 592	−234	−1.2
$(6s^2_{1/2}6p^2_{3/2})$	0	28 239	27 995	−244	−0.9
			Eka-lead		
$(7s^2_{1/2}7p^2_{1/2})$	0	0	0	0	0
$(7s^2_{1/2}7p^1_{1/2}7p^1_{3/2})$	1	27 198	26 806	−392	−1.4
$(7s^2_{1/2}7p^1_{1/2}7p^1_{3/2})$	2	30 775	30 391	−384	−1.2
$(7s^2_{1/2}7p^2_{3/2})$	2	66 068	65 225	−843	−1.3
$(7s^2_{1/2}7p^2_{3/2})$	0	74 527	73 674	−853	−1.1

in the Coulomb gauge and leads to the so-called Dirac–Coulomb–Breit Hamiltonian

$$\mathbf{H}^{\mathrm{DCB}} = \mathbf{H}^{\mathrm{DC}} + \sum_{p>q} B_{pq}, \tag{3}$$

where

$$B_{pq}(\omega_{pq}) = -(\boldsymbol{\alpha}_p\cdot\boldsymbol{\alpha}_q)\frac{\cos(\omega_{pq}r_{pq})}{r_{pq}} \tag{4}$$
$$+ (\boldsymbol{\alpha}_p\cdot\boldsymbol{\nabla}_p)(\boldsymbol{\alpha}_q\cdot\boldsymbol{\nabla}_q)\frac{\cos(\omega_{pq}r_{pq})-1}{\omega^2_{pq}r_{pq}},$$

ω_{pq} designating the frequency of the photon exchanged between electrons p and q. A low-frequency expansion of the cosines yields the incomplete Breit interaction $B_{pq}(0)$:

$$B_{pq}(0) = -(\boldsymbol{\alpha}_p\cdot\boldsymbol{\alpha}_q)/r_{pq} \tag{5}$$
$$+\frac{1}{2}\left[\boldsymbol{\alpha}_p\cdot\boldsymbol{\alpha}_q - (\boldsymbol{\alpha}_p\cdot\mathbf{r}_{pq})(\boldsymbol{\alpha}_q\cdot\mathbf{r}_{pq})/r^2_{pq}\right]/r_{pq}.$$

These terms describe the instantaneous magnetostatic interaction and classical retardation of the electric interaction between electrons. The contribution from the first term (called Gaunt interaction) to transition energies and hyperfine structure (HFS) constants can be observed in atomic Dirac–Hartree–Fock (DHF) calculations [1] (Tables 1 and 2).

The one-electron basis functions in calculations with the DC(B) Hamiltonian are the four-component Dirac spinors. The DC(B)-based calculations have the following disadvantages:

Too many electrons are treated explicitly in heavy-atom systems and too large a basis set of Gaussians is required for accurate description of the large number of radial oscillations that valence spinors have in the case of a heavy atom.

The need for working with the four-component Dirac spinors leads to a serious complication of calculations as compared to the nonrelativistic case.

3. RELATIVISTIC EFFECTIVE CORE POTENTIALS

In calculations on heavy-atom molecules, the DC and DCB Hamiltonians are usually replaced by an

Table 2. HFS constants in the indium ($Z = 49$), thallium ($Z = 81$), and eka-thallium ($Z = 113$) atoms calculated by the DHF method with Coulomb and Coulomb–Gaunt interaction for different configurations (in MHz)

Configuration	DC	DCG	Absolute difference	Relative difference, %
		Indium		
$(5s^2_{1/2}5p^1_{1/2})$	1913	1900	−13	−0.7
$(5s^2_{1/2}5p^1_{3/2})$	288	287	−1	−0.3
$(5s^2_{1/2}5d^1_{3/2})$	4.41	4.40	−0.01	−0.2
$(5s^2_{1/2}5d^1_{5/2})$	1.88	1.88	0	0
$(5s^2_{1/2}6s^1_{1/2})$	1013	1011	−2	−0.2
		Thallium		
$(6s^2_{1/2}6p^1_{1/2})$	18 918	18 691	−227	−1.2
$(6s^2_{1/2}6p^1_{3/2})$	1403	1391	−12	−0.9
$(6s^2_{1/2}6d^1_{3/2})$	20.8	20.8	0	0
$(6s^2_{1/2}6d^1_{5/2})$	8.72	8.70	−0.02	−0.2
$(6s^2_{1/2}7s^1_{1/2})$	7826	7807	−19	−0.2
		Eka-thallium*		
$(7s^2_{1/2}7p^1_{1/2})$	150 168	147 538	−2630	−1.8
$(7s^2_{1/2}7p^1_{3/2})$	2007	1983	−24	−1.2
$(7s^2_{1/2}7d^1_{3/2})$	34.3	34.2	−0.1	−0.3
$(7s^2_{1/2}7d^1_{5/2})$	13.5	13.5	0	0
$(7s^2_{1/2}8s^1_{1/2})$	28 580	28 473	−107	−0.4

* The magnetic moment μ_N and spin I for the eka-thallium nucleus were taken as those for thallium. The presented results can be easily recalculated as only the proper values of μ_N and I are known because they just include the μ_N/I coefficient.

effective Hamiltonian

$$\mathbf{H}^{\text{eff}} = \sum_{p_v} [\mathbf{h}^{\text{Schr}}(p_v) + \mathbf{U}^{\text{eff}}(p_v)] + \sum_{p_v > q_v} \frac{1}{r_{p_v q_v}} \quad (6)$$

written only for valence or "valence-extended" (when some outermost core shells are treated explicitly) subspace of electrons denoted by indices p_v and q_v; $\mathbf{U}^{\text{eff}}$ is an RECP operator simulating, in particular, interactions of the explicitly treated electrons with those which are excluded from the RECP calculation. In Eq. (6)

$$\mathbf{h}^{\text{Schr}} = -\frac{1}{2}\boldsymbol{\nabla}^2 + V^{\text{nucl}} \quad (7)$$

is the one-electron operator of the nonrelativistic Schrödinger Hamiltonian. Contrary to the four-component wave function used in DC(B) calculations, the pseudowave function in the RECP case can be both two- and one-component.

3.1. Huzinaga-Type Potential

When forming chemical bonds in heavy-atom molecules, states of core electrons are practically unchanged. To reduce computational efforts in expensive molecular calculations, the "frozen core" approximation is often employed.

In order to "freeze" core (c) spinors, the energy level shift technique can be applied. Following Huzinaga *et al.* [2], one should add the effective core operator $\mathbf{U}^{\text{eff}}_{\text{Huz}}$ containing the Hartree–Fock (HF) field operators, the Coulomb ($\mathbf{J}$) and spin-dependent exchange ($\mathbf{K}$) terms, over these core spinors together with the level shift terms to the one-electron part of the Hamiltonian:

$$\mathbf{U}^{\text{eff}}_{\text{Huz}} = (\mathbf{J}-\mathbf{K})[\varphi_{n_c lj}] + \sum_{n_c,l,j} B_{n_c lj} |\varphi_{n_c lj}\rangle\langle\varphi_{n_c lj}| \quad (8)$$

$$(\text{i.e., } \varepsilon_{n_c lj} \to \varepsilon_{n_c lj} + B_{n_c lj}),$$

where n_c, l, and j are the principal, orbital-angular momentum, and total-angular momentum quantum numbers; the $B_{n_c lj}$ parameters are at least of order $|2\varepsilon_{n_c lj}|$; and $\varepsilon_{n_c lj}$ is the one-electron energy of the core spinor $\varphi_{n_c lj}$ that is frozen. Such nonlocal terms are needed in order to prevent collapse of the valence electrons to the frozen core states. As will be shown below, all the terms with the frozen core spinors (the level shift operator and exchange interactions) can be transformed to the spin–orbit representation in addition to the spin-independent Coulomb term.

3.2. Shape-Consistent Radially Local RECPs

In other RECP versions, the valence spinors are smoothed in the core regions. Consider the shape-consistent radially local (or semilocal) RECP developed by Pitzer's group [3, 4]. The nodeless numerical pseudospinors $\widetilde{\varphi}_{n_v lj}(r)$ are constructed of the large components $f_{n_v lj}(r)$ of the valence (v) DHF spinors (one pseudospinor for each l and j):

$$\widetilde{\varphi}_{n_v lj}(r) = \begin{cases} f_{n_v lj}(r), & r \geq R_c, \\ r^\gamma \sum\limits_{i=0}^{5} a_i r^i, & r < R_c, \end{cases} \qquad (9)$$

where r is the distance between the nucleus and electron. The matching (or core) radius, R_c, is chosen near the outermost extremum for the large component, and the a_i coefficients are taken such that the pseudospinors are normalized, smooth, and nodeless. The power γ is typically chosen higher than $l+1$ to ensure an efficient ejection of the valence electrons from the core region.

To derive the RECP components U_{lj}, the HF equations are inverted for the valence pseudospinors so that $\widetilde{\varphi}_{n_v lj}$ become solutions to the nonrelativistic-type HF equations (but with j-dependent potentials) for a "pseudoatom" with removed core electrons [5]:

$$U_{lj}(r) = \widetilde{\varphi}^{-1}_{n_v lj}(r)\left(\frac{1}{2}\frac{d^2}{dr^2} - \frac{l(l+1)}{2r^2}\right. \qquad (10)$$
$$\left. + \frac{Z^*}{r} - \widetilde{\mathbf{J}}(r) + \widetilde{\mathbf{K}}(r) + \varepsilon_{n_v lj}\right)\widetilde{\varphi}_{n_v lj}(r),$$

where $Z^* = Z - N_c$, Z is the nuclear charge, N_c is the number of excluded core electrons, $\widetilde{\mathbf{J}}$ and $\widetilde{\mathbf{K}}$ are the Coulomb and exchange operators on the pseudospinors $\widetilde{\varphi}_{n_v lj}$, and $\varepsilon_{n_v lj}$ are their one-electron energies (the same as for the original spinors). The radially local RECP operator $\mathbf{U}^{\text{eff}}_{\text{rloc}}$ can be written in the form

$$\mathbf{U}^{\text{eff}}_{\text{rloc}} = \frac{N_c}{r} + U_{LJ}(r) \qquad (11)$$
$$+ \sum_{l=0}^{L} \sum_{j=|l-1/2|}^{l+1/2} \left[U_{lj}(r) - U_{LJ}(r)\right]\mathbf{P}_{lj},$$

$$\mathbf{P}_{lj} = \sum_{m_j=-j}^{j} |ljm_j\rangle\langle ljm_j|,$$

where $J = L + 1/2$, $L = l_c^{\max} + 1$, and $l_c^{\max}$ is the highest orbital-angular momentum of the core spinors, and m_j is the projection of the total momentum.

Using the identities for the $\mathbf{P}_{lj}$ projectors [6]

$$\mathbf{P}_{l,j=l\pm1/2} = \frac{1}{2l+1}\left[\left(l + \frac{1}{2} \pm \frac{1}{2}\right)\mathbf{P}_l \pm 2\mathbf{P}_l \mathbf{l}\cdot\mathbf{s}\mathbf{P}_l\right],$$
$$\mathbf{P}_l = \sum_{m_l=-l}^{l} |lm_l\rangle\langle lm_l|, \qquad (12)$$

the RECP operator can be rewritten in the spin–orbit representation, where $\mathbf{l}$ and $\mathbf{s}$ are operators of the orbital-angular and spin momenta, and m_l is the projection of the orbital-angular momentum. Similar to Huzinaga-type potentials, the shape-consistent radially local RECPs already allow one to exclude chemically inactive electrons from the RECP/SCF stage of calculations. Moreover, they have the following advantages:

(1) The oscillations of the explicitly treated spinors are smoothed in the core regions of heavy atoms when generating nodeless pseudospinors. Therefore, the number of one-electron Gaussian basis functions may be minimized, thus reducing dramatically both the number of two-electron integrals and the computational time.

(2) The small components of the four-component spinors are eliminated and the nonrelativistic kinetic energy operator is used. The RECP method allows one to use a well-developed nonrelativistic technique of calculation and relativistic effects are taken into account with the help of spin-dependent semilocal potentials. Breit and other two-electron QED interactions can be efficiently treated within the one-electron RECPs.

(3) In principle, correlations of the explicitly treated electrons with those which are excluded from the RECP calculation can be considered within "correlated" RECP versions. Reducing the number of explicitly correlated electrons with the help of the correlated RECPs is a very promising way to minimize efforts when performing high-precision molecular calculations.

The disadvantages of the semilocal RECPs are as follows:

(1) At present, different versions of the radially local RECPs provide a comparable level of accuracy for the same number of explicitly treated electrons. It is clear that the explicit inclusion of the outer core electrons into the RECP calculation is the way to increase the accuracy. However, the extension of the space of these electrons beyond some limit does not

improve the accuracy, as is obtained in all our calculations with RECPs. The RECP errors still range up to 1000–3000 cm^{-1} and more even for the dissociation of the lowest lying states and for energies of transition between them.

(2) The reliability of the radially local RECP versions is not high for transitions with the excitations in d and f shells in transition metals, lanthanides, actinides, etc.

(3) Moreover, the direct calculation of such properties as electron densities near heavy nuclei, HFS, and matrix elements of other operators singular on heavy nuclei is impossible as a result of smoothing the spinors in the core regions of heavy elements.

To overcome the above disadvantages, the Generalized RECP (GRECP) method (see Subsection 3.3) and the One-Center Restoration (OCR) procedures (see Subsection 3.4) were developed.

3.3. Generalized RECP

It was shown in [7] that a requirement for pseudospinors to be nodeless is not necessary to generate the shape-consistent RECP components. In the case of pseudospinors with nodes, the RECP components are singular because division by zero appears in Eq. (10). This problem is overcome in the GRECP method by interpolating the potentials in the vicinity of these nodes. It was shown both theoretically and computationally that the interpolation errors are small enough. This allows one to generate different potentials, $U_{n_c lj}$ and $U_{n_v lj}$, for outer core and valence pseudospinors, unlike the conventional RECP approach.

The GRECP operator is written in the form [8]

$$\mathbf{U}^{\mathrm{GRECP}} = \frac{N_c}{r} + U_{n_v LJ}(r) \qquad (13)$$
$$+ \sum_{l=0}^{L} \sum_{j=|l-1/2|}^{l+1/2} \left[U_{n_v lj}(r) - U_{n_v LJ}(r)\right] \mathbf{P}_{lj}$$
$$+ \sum_{n_c} \sum_{l=0}^{L} \sum_{j=|l-1/2|}^{l+1/2} \Big\{ \left[U_{n_c lj}(r) - U_{n_v lj}(r)\right] \widetilde{\mathbf{P}}_{n_c lj}$$
$$+ \widetilde{\mathbf{P}}_{n_c lj} \left[U_{n_c lj}(r) - U_{n_v lj}(r)\right] \Big\}$$
$$- \sum_{n_c, n_c'} \sum_{l=0}^{L} \sum_{j=|l-1/2|}^{l+1/2} \widetilde{\mathbf{P}}_{n_c lj}$$
$$\times \left[\frac{U_{n_c lj}(r) + U_{n_c' lj}(r)}{2} - U_{n_v lj}(r) \right] \widetilde{\mathbf{P}}_{n_c' lj},$$
$$\widetilde{\mathbf{P}}_{n_c lj} = \sum_{m_j=-j}^{j} |\widetilde{n_c l j m_j}\rangle \langle \widetilde{n_c l j m_j}|.$$

The new nonlocal terms (3–6 lines in the above equation) were added to the conventional semilocal RECP operator. These terms take into account the difference between the effective potentials acting on the outer core and valence electrons with the same l and j quantum numbers.

The GRECP method allows one to improve the accuracy of calculations in a regular manner when including more outer core shells explicitly in the GRECP calculations. More details on the GRECP method can be found in [9, 10]. To compare different effective potential versions by accuracy, we carried out both all-electron calculations with the DC Hamiltonian and calculations with RECPs of different groups. The RECP errors in reproducing the DHF all-electron results are studied in [9, 10], etc. One can see from our atomic HF calculations [11] and correlation calculations on the Hg [12] and Pb [13] atoms that the accuracy of the GRECP is up to an order of magnitude higher than that of the other tested RECPs even for the cases when the same number of outermost core shells is treated explicitly.

Results for the eka-thallium atom (E113) are presented in Table 3. The GRECP errors are collected into two groups. The errors for transitions without change in the occupation number of the $6d$ shell are rather small. The errors for transitions with change in the occupation number of the $6d$ shell are about 400 cm^{-1}. The latter errors have a systematic nature and are connected with the fact that the $6d$ shell in the present GRECP version is described with the help of nodeless pseudospinors. Of course, these errors can be reduced significantly if one includes the $5d$ electrons explicitly in the GRECP calculations. The Self-Consistent (SfC) RECP method was suggested in [9, 15]; it allows one to minimize the above-mentioned errors without extension of space of explicitly treated electrons. New terms with an operator of the occupation number of the outermost d (or f) shell are added to the RECP operator. This method is most optimal for studying compounds of transition metals, lanthanides, and actinides. The comparison of accuracy of different RECP versions in calculations on the uranium atom can be found in Table 4 and in [9, 15].

A technique for the "Correlated" GRECP (CGRECP) generation was proposed in [9] and essential improvements in this technique were made in [10]. The CGRECP for mercury was generated in the framework of the relativistic CC (RCC) method [19]. The GRECP components were constructed for $5s$, $5p$, $5d$, $6s$, $6p$, $6d$, $5f$, $5g$ electrons of the Hg atom. The $5s$, $5p$ pseudospinors are "frozen" in calculations with this CGRECP {in fact, they are completely excluded from the calculations with the help of the level shift technique (see Section 3.1 and [9, 20])}, and only 12 external electrons of the

Table 3. Transition energies between low-lying configurations of the eka-thallium (E113) atom derived from all-electron calculations and the errors of their reproduction in calculations with different RECP versions (all values are in cm^{-1})

Configuration	All-el. DHFG*	Gaunt contrib.	21e-GRECP**	21e-RECP of Nash *et al.***
	transition energies	DHFG−DHF	absolute errors	
$6d^4_{3/2}6d^6_{5/2}7s^2_{1/2}7p^1_{1/2}(J=1/2) \rightarrow$				
$6d^4_{3/2}6d^6_{5/2}7s^2_{1/2}7p^1_{3/2}(J=3/2)$	25 098	347	−23	282
$6d^4_{3/2}6d^6_{5/2}7s^2_{1/2}8s^1_{1/2}(J=1/2)$	34 962	374	0	−186
$6d^4_{3/2}6d^6_{5/2}7s^2_{1/2}6f^1$ (nonrel. av.)	50 316	395	6	148
$6d^4_{3/2}6d^6_{5/2}7s^2_{1/2}5g^1$ (nonrel. av.)	52 790	395	6	148
$6d^4_{3/2}6d^6_{5/2}7s^2_{1/2}7d^1$ (nonrel. av.)	45 215	395	6	161
$6d^4_{3/2}6d^6_{5/2}7s^2_{1/2}(J=0)$	57 180	395	6	148
$6d^4_{3/2}6d^6_{5/2}7s^1_{1/2}7p^2_{1/2}(J=1/2)$	61 499	−60	32	4830
$6d^4_{3/2}6d^6_{5/2}7s^1_{1/2}7p^1_{1/2}7p^1_{3/2}$ (rel. av.)	83 177	248	−4	5177
$6d^4_{3/2}6d^6_{5/2}7s^1_{1/2}7p^2_{3/2}$ (rel. av.)	112 666	624	−9	5729
$6d^4_{3/2}6d^6_{5/2}7s^1_{1/2}7p^1_{1/2}$ (rel. av.)	115 740	268	−2	5161
$6d^4_{3/2}6d^6_{5/2}7s^1_{1/2}7p^1_{3/2}$ (rel. av.)	149 526	678	−10	5811
$6d^4_{3/2}6d^6_{5/2}7s^1_{1/2}(J=1/2)$	234 385	796	−4	6151
$6d^4_{3/2}6d^5_{5/2}7s^2_{1/2}7p^2_{1/2}(J=5/2)$	47 410	−778	403	−2389
$6d^4_{3/2}6d^5_{5/2}7s^2_{1/2}7p^1_{1/2}7p^1_{3/2}$ (rel. av.)	74 932	−424	341	−2089
$6d^4_{3/2}6d^5_{5/2}7s^2_{1/2}7p^2_{3/2}$ (rel. av.)	110 435	−6	306	−1556
$6d^3_{3/2}6d^6_{5/2}7s^2_{1/2}7p^2_{1/2}(J=3/2)$	78 862	−416	375	−2272
$6d^3_{3/2}6d^6_{5/2}7s^2_{1/2}7p^1_{1/2}7p^1_{3/2}$ (rel. av.)	104 097	−86	405	−1968
$6d^3_{3/2}6d^6_{5/2}7s^2_{1/2}7p^2_{3/2}$ (rel. av.)	137 083	306	473	−1436
$6d^4_{3/2}6d^5_{5/2}7s^2_{1/2}7p^1_{1/2}$ (rel. av.)	110 139	−407	380	−2317
$6d^4_{3/2}6d^5_{5/2}7s^2_{1/2}7p^1_{3/2}$ (rel. av.)	150 116	45	338	−1679
$6d^3_{3/2}6d^6_{5/2}7s^2_{1/2}7p^1_{1/2}$ (rel. av.)	139 841	−65	439	−2184
$6d^3_{3/2}6d^6_{5/2}7s^2_{1/2}7p^1_{3/2}$ (rel. av.)	177 157	361	506	−1541
$6d^4_{3/2}6d^5_{5/2}7s^2_{1/2}(J=5/2)$	239 509	158	408	−1603
$6d^3_{3/2}6d^6_{5/2}7s^2_{1/2}(J=3/2)$	267 208	481	579	−1431

* All-electron Dirac–Hartree–Fock–Gaunt (DHFG) calculation with Fermi nuclear charge distribution for $A = 297$.

** GRECP generated in the present work from DHFG calculation.

*** RECP from [14] (generated from DHF calculation without Gaunt iteration).

Hg atom should be explicitly correlated instead of 34 in the case of the DC calculations because the correlations for the $4f$, $5s$, $5p$ electrons and between the $4f$, $5s$, $5p$ and $5d$, $6s$, $6p$ electrons are taken into account by the CGRECP. It allows one to reduce drastically the computational efforts necessary for the "chemical" accuracy in calculations of mercury compounds. Results of our test calculations are presented in Table 5. One can see that energies of the one-electron excitations in calculations of the Hg atom with the all-electron DC Hamiltonian for 34 external electrons correlated explicitly by the RCC method (DC/34e-RCC) can be reproduced with the accuracy within 270 cm^{-1} in the 12e-RCC calculations when

Table 4. Transition energies between states of U (averaged over nonrelativistic configurations) derived from all-electron DHF calculations and the errors of their reproduction in calculations with different RECP versions (all values are in cm^{-1})

	DHF	RECP of Ermler *et al.* [16]	Energy-adjusted PP*	SfC GRECP	Quadratic SfC GRECP	"Frozen core"	
						(f^3)	(f^2)
Num. of electrons	all	14	32	24	24	24	24
Configuration	tr. energy	absolute error					
$5f^37s^26d^1 \rightarrow$							
$5f^37s^27p^1$	7383	387	−498	−35	−33	2	14
$5f^37s^2$	36 159	332	130	4	6	3	16
$5f^37s^16d^2$	13 299	−192	−154	−3	−5	−1	−16
$5f^37s^16d^17p^1$	17 289	144	−621	−31	−31	−1	−5
$5f^36d^2$	54 892	−121	−398	−14	−15	1	−21
$5f^37s^26d^1 \rightarrow$							
$5f^47s^2$	16 483	176	788	−723	0	54	187
$5f^47s^2 \rightarrow$							
$5f^47s^16d^1$	15 132	−738	−87	11	−11	−16	−35
$5f^47s^17p^1$	15 016	90	−443	−37	−26	−1	−2
$5f^46d^2$	34 022	−1287	−153	28	−13	−26	−62
$5f^46d^17p^1$	32 341	−794	−457	−11	−23	−17	−39
$5f^37s^26d^1 \rightarrow$							
$5f^27s^26d^2$	3774	3096	−748	−17	−17	90	−96
$5f^27s^26d^2 \rightarrow$							
$5f^27s^26d^17p^1$	12 646	−441	−626	−16	−15	−5	0
$5f^27s^26d^1$	42 638	−498	155	24	25	−5	1
$5f^27s^16d^3$	10 697	608	−240	−10	−10	13	1
$5f^27s^16d^27p^1$	19 319	390	−826	−26	−26	6	0
$5f^37s^26d^1 \rightarrow$							
$5f^17s^26d^3$	29 597	11 666	−1526	−896	−104	466	48
$5f^17s^26d^3 \rightarrow$							
$5f^17s^26d^27p^1$	18 141	−1367	−778	46	49	−2	−2
$5f^17s^26d^2$	49 158	−1355	173	70	73	−3	−2
$5f^17s^16d^4$	7584	1655	−331	−39	−40	22	14
$5f^17s^16d^37p^1$	21 154	779	−1055	−11	−11	16	10
$5f^37s^26d^1 \rightarrow 5f^5$	100 840	430	1453	−1860	22	105	291

* Pseudopotential (PP) from [17] (generated from all-electron calculation in the framework of Wood–Boring [18] approximation).

using the present CGRECP. Contribution of the core correlation effects can be seen from comparison of the DC/12e-RCC and DC/34e-RCC results or of the GRECP and CGRECP results. Further development of this technique is in progress.

3.4. Nonvariational One-Center Restoration of Electronic Structure in Cores of Heavy-Atoms in a Molecule (NOCR)

In the valence region, the electronic density obtained from the two-component GRECP (pseudo)wave function very accurately reproduces the

Table 5. Transition energies from all-electron DC and different GRECP calculations of the lowest lying states of the mercury atom and its ions in the [7, 9, 8, 6, 7, 7] correlation basis set from [12] for the 12 and 34 correlated electrons* by the RCC method (all values are in cm^{-1})

State (leading conf., term)	DC 34e-RCC	DC 12e-RCC	GRECP 12e-RCC	CGRECP 12e-RCC
$5d^{10}6s^2(^1S_0) \rightarrow$				
$5d^{10}6s^16p^1(^3P_0)$	37 471	37 208	37 244	37 742
$5d^{10}6s^16p^1(^3P_1)$	39 318	38 992	39 025	39 573
$5d^{10}6s^16p^1(^3P_2)$	44 209	43 675	43 710	44 453
$5d^{10}6s^16p^1(^1P_1)$	55 419	54 769	54 780	55 466
$5d^{10}6s^1(^2S_{1/2})$	84 550	83 885	83 919	84 744
$5d^{10}6s^1(^2S_{1/2}) \rightarrow$				
$5d^{10}6p^1(^2P_{1/2})$	52 025	51 515	51 559	52 059
$5d^{10}6p^1(^2P_{3/2})$	61 269	60 476	60 532	61 320
$5d^{10}(^1S_0)$	151 219	150 132	150 202	151 262

* This number is smaller by one or two for Hg^+ or Hg^{2+} ions, respectively.

corresponding all-electron four-component density. In the core region, the pseudospinors are smoothed, so that the electron density with the (pseudo)wave function is not correct.

The following restoration scheme was developed (see [21, 22] and references):

Generation of equivalent basis sets of atomic (one-center) four-component spinors

$$\left\{ \begin{pmatrix} f_{nlj}(r)\chi_{ljm_j} \\ g_{nlj}(r)\chi_{l'jm_j} \end{pmatrix} \right\}$$

(where f_{nlj}, g_{nlj} are the radial parts, χ_{ljm_j} are the spin-angular parts of the atomic Dirac spinors, and $l' = 2j - l$) and two-component pseudospinors $\{\tilde{f}_{nlj}(r)\chi_{ljm_j}\}$ by atomic finite-difference (numerical) all-electron DHF and two-component GRECP/HF calculations of the same valence configurations of the atom and its ions.

The molecular pseudospin orbitals $\tilde{\phi}_i$ are then expanded in the basis set of the one-center two-component atomic pseudospinors (for $r \le R_c^{\rm rest}$, where $R_c^{\rm rest} \ge R_c$),

$$\tilde{\phi}_i(\mathbf{x}) \approx \sum_{l=0}^{L_{\max}} \sum_{j=|l-1/2|}^{l+1/2} \sum_{n,m_j} c^i_{nljm_j} \tilde{f}_{nlj}(r)\chi_{ljm_j}, \quad (14)$$

where $\mathbf{x}$ denotes spatial and spin variables.

Finally, the atomic two-component pseudospinors are replaced by the equivalent four-component spinors in the molecular basis and the expansion coefficients $c^i_{nljm_j}$ from Eq. (14) are preserved:

$$\phi_i(\mathbf{x}) \approx \sum_{l=0}^{L_{\max}} \sum_{j=|l-1/2|}^{l+1/2} \sum_{n,m_j} c^i_{nljm_j} \begin{pmatrix} f_{nlj}(r)\chi_{ljm_j} \\ g_{nlj}(r)\chi_{l'jm_j} \end{pmatrix}. \quad (15)$$

The molecular four-component spinors constructed in this way are orthogonal to the inner core spinors of the heavy atom, as the atomic basis functions used in Eq. (15) are generated with the inner core electrons treated as frozen. The properties described by the operators singular close to (heavy) nuclei are calculated with the restored bispinors ϕ_i. A more advanced technique of the variational restoration is proposed in [22].

4. CONFIGURATION INTERACTION

The many-electron wave function $\Psi^{\rm CI}$ in the CI method is presented by a linear combination of determinants D_I,

$$\Psi^{\rm CI} = \sum_I C_I^{\rm CI} D_I, \quad (16)$$

where $C_I^{\rm CI}$ are some numbers (CI coefficients). In turn, each determinant is an anti-symmetric production of N one-electron basis functions, where N is the number of electrons in the considered system. The CI equations are written as

$$\sum_J H_{IJ} C_J^{\rm CI} = E^{\rm CI} C_I^{\rm CI}, \quad (17)$$

where H_{IJ} are Hamiltonian matrix elements in the basis set of the determinants and E^{CI} is the CI energy. To find the coefficients and the energy in the CI method, one should diagonalize the Hamiltonian matrix.

If all possible determinants are considered, then the method (called Full-CI) will provide the "exact" solution in the framework of a given one-electron basis set and an employed Hamiltonian. However, requirements on the computational resources in the Full-CI case are usually so huge that such calculations are practically impossible for systems of interest except for cases of very small numbers of correlated electrons and basis functions. In almost all the CI calculations, only some selected (the most important) determinants are explicitly considered. To take into account the effect of the unselected determinants, various semiempirical corrections (e.g., the Davidson correction [23]) can be employed. In precise calculations, the number of selected determinants reaches a few million or more; therefore, a very large Hamiltonian matrix should be diagonalized. The iterative diagonalization (Davidson) method is then used to obtain a few low-lying roots of this matrix.

There are two main categories of the CI method [24]:

"Conventional CI": the Hamiltonian matrix elements are calculated once and saved in memory.

"Direct CI": only those Hamiltonian matrix elements are calculated at each step of the diagonalization procedure which are required at the moment.

The CI method has the following advantages:

(1) The method is simple; solutions always exist independently of the number of open shells.

(2) It describes well "static" (avoided crossing of terms) and "nondynamical" electron correlations.

The disadvantages of the CI method are the following:

(1) It works poorly for a large number of correlated electrons (when semiempirical corrections on unselected determinants are large).

(2) Unsmoothness of potential curves is a result of selection of determinants by some thresholds.

(3) The above semiempirical energy corrections cannot be used when calculating other than spectroscopic properties.

5. THE COUPLED-CLUSTER APPROACHES

The complete space of $\{D_I\}$ is divided into two subspaces:

$\mathcal{M}_0$, model space, consists of small number (M) of the most important determinants $\{D_m\}_{m=1}^{M}$ to describe static and nondynamical correlations, which are taken into account exactly on $\mathcal{M}_0$;

$\mathcal{M}_0^{\perp}$, rest of space (usually very large), is included approximately to account for dynamical correlations (i.e., correlations at small interelectron distances, "Coulomb holes").

The eigenstates of interest are represented as

$$|\Psi^{\mathrm{CC}}\rangle = \sum_{m=1}^{M} C_m \exp[T^{(m)}]|D_m\rangle, \qquad (18)$$

where $T^{(m)} \equiv T_1^{(m)} + T_2^{(m)} + \dots$ is the cluster operator:

$$\begin{cases} T_1^{(m)} = \sum\limits_{i,a} \{\mathbf{a}_a^+ \mathbf{a}_i\}\, t_{i,a}^{(m)}, \\ T_2^{(m)} = \dfrac{1}{2} \sum\limits_{ij,ab} \{\mathbf{a}_b^+ \mathbf{a}_a^+ \mathbf{a}_j \mathbf{a}_i\}\, t_{ij,ab}^{(m)}, \\ \dots, \end{cases} \qquad (19)$$

where $\mathbf{a}_a^+$ and $\mathbf{a}_i$ are the creation and annihilation operators (their combination $\mathbf{a}_a^+ \mathbf{a}_i$ will replace the ith one-electron state in the determinant by the ath one). The coefficients $\{t_{i,a}^{(m)}, t_{ij,ab}^{(m)}\}$, etc., are called the cluster amplitudes and are calculated by solving Bloch equations:

$$\mathbf{UHU} = \mathbf{HU}, \qquad (20)$$

$$\mathbf{U} \equiv \sum_{m=1}^{M} \exp[T^{(m)}]|D_m\rangle\langle D_m|.$$

The coefficients C_m and final energy E^{CC} are obtained from diagonalization of some effective Hamiltonian $\mathbf{H}^{\mathrm{eff}}$ on the model space:

$$\mathbf{H}^{\mathrm{eff}} \sum_{m=1}^{M} C_m|D_m\rangle = E^{\mathrm{CC}} \sum_{m=1}^{M} C_m|D_m\rangle \qquad (21)$$

$$(\mathbf{H}_{nm}^{\mathrm{eff}} \equiv \langle D_n|(\exp[-T^{(m)}]\mathbf{H}\exp[T^{(m)}])|D_m\rangle).$$

If all the $T_k^{(m)}$ are considered in the $T^{(m)}$ operator, then the CC method is equivalent to the Full-CI one. However, in practical calculations, the third and following terms in $T^{(m)}$ (three-body and higher order cluster amplitudes) are usually neglected. Such a CC version is called CC–SD. There are three basic CC categories [25]:

One-state or state-selective;

Fock-space or valence universal methods;

Hilbert-space or state-universal approaches.

The CC method has the following advantages:

(1) It is a size-extensive method; i.e., the energy of the system is scaled properly with an increase in the number of electrons (whereas the CI method is not size-extensive in a general case).

(2) The CC–SD method takes into account the contributions not only from the determinants obtained from the model space by applying the $(1 + T_1^{(m)} + T_2^{(m)})$ operator but also approximately from all the rest of the determinants (whereas the CI method with the same number of unknown coefficients does not).

(3) The CC method is one of the best methods for accounting for the dynamical correlation.

The disadvantages of the CC method are the following:

(1) This is a nonvariational method; i.e., the CC energy is not an upper bound to the exact energy of the system (whereas the CI energy is).

(2) The CC equations are nonlinear and the effective Hamiltonian is non-Hermitian.

(3) Intruder states (i.e., such states from the $\mathcal{M}_0^{\perp}$ subspace, which are lying within the $\mathcal{M}_0$ subspace energy span) destroy the convergence of the CC iterations. Alleviation of the problem is in using incomplete model space procedures; energy shifting, RLE [26], DIIS [27, 28], and IPM [29] procedures.

6. SOME PRACTICAL CALCULATIONS

Calculations of the spectroscopic constants for the ground and lowest excited states of the HgH molecule and for the ground state of the HgH^+ ion were carried out with the help of the GRECP and RCC [19] methods in [30]. The results are within a few mbohr from the experimental data for bond lengths and tens of wave numbers for excitation energies and vibrational frequencies. It is demonstrated that the triple cluster amplitudes for the 13 outermost electrons and corrections for the Basis Set Superposition Errors (BSSE) [31, 32] are necessary to obtain accurate results for this molecule. The accurate GRECP/CI calculations of the spectroscopic constants for the ground state of the TlH molecule are presented in [20], in which the reliability of the semiempirical energy corrections is, in particular, investigated.

The NOCR scheme was applied in the GRECP/RCC calculations of the P,T-odd properties for the TlF molecule [21]. The corresponding GRECP/HF/NOCR results are in good agreement with the all-electron DHF results of other groups. Inclusion of electron correlation has changed the values by 20%. The previous NOCR version was employed in the GRECP calculations of the P,T-odd parameters and HFS constants for the YbF [33, 34] and BaF [35] molecules. A reasonable agreement with the experimental data for the HFS constants was attained. It was demonstrated that the spin-correlation effects of the unpaired electron with the deeply lying outer core $5s$ and $5p$ shells should be taken into account in order to perform accurate calculations of the HFS and P,T-odd constants.

ACKNOWLEDGMENTS

We are grateful to the US Civilian Research & Development Foundation for the Independent States of the Former Soviet Union (CRDF), grant no. RP2-2339-GA-02. A.T. and N.M. were supported in part by the Scientific Program of the St. Petersburg Scientific Center of RAS. T.I. is grateful to INTAS (grant no. YSF 2001/2-164) for financial support. A.P. is grateful to the Ministry of Education of the Russian Federation (grant no. PD02-1.3-236) and to the St. Petersburg Committee of Science (grant no. PD02-1.3-236).

This work was also supported in part by the Russian Foundation for Basic Research (project no. 03-03-32335).

REFERENCES

1. The new version of the HFD code, was developed by I. I. Tupitsyn and A. N. Petrov.
2. V. Bonifacic and S. Huzinaga, J. Chem. Phys. **60**, 2779 (1974).
3. Y. S. Lee, W. C. Ermler, and K. S. Pitzer, J. Chem. Phys. **67**, 5861 (1977).
4. P. A. Christiansen, Y. S. Lee, and K. S. Pitzer, J. Chem. Phys. **71**, 4445 (1979).
5. W. A. Goddard III, Phys. Rev. **174**, 659 (1968).
6. P. Hafner and W. H. E. Schwarz, Chem. Phys. Lett. **65**, 537 (1979).
7. A. V. Titov, A. O. Mitrushenkov, and I. I. Tupitsyn, Chem. Phys. Lett. **185**, 330 (1991).
8. I. I. Tupitsyn, N. S. Mosyagin, and A. V. Titov, J. Chem. Phys. **103**, 6548 (1995).
9. A. V. Titov and N. S. Mosyagin, Int. J. Quantum Chem. **71**, 359 (1999).
10. A. V. Titov and N. S. Mosyagin, Russ. J. Phys. Chem. **74** (Suppl. 2), S376 (2000).
11. N. S. Mosyagin, A. V. Titov, and Z. Latajka, Int. J. Quantum Chem. **63**, 1107 (1997).
12. N. S. Mosyagin, E. Eliav, A. V. Titov, and U. Kaldor, J. Phys. B **33**, 667 (2000).
13. T. A. Isaev, N. S. Mosyagin, M. G. Kozlov, *et al.*, J. Phys. B **33**, 5139 (2000).
14. C. S. Nash, B. C. Bursten, and W. C. Ermler, J. Chem. Phys. **106**, 5133 (1997).
15. A. V. Titov and N. S. Mosyagin, Struct. Chem. **6**, 317 (1995).

16. W. C. Ermler, R. B. Ross, and P. A. Christiansen, Int. J. Quantum Chem. **40**, 829 (1991).
17. W. Küchle, M. Dolg, H. Stoll, and H. Preuss, J. Chem. Phys. **100**, 7535 (1994).
18. J. H. Wood and A. M. Boring, Phys. Rev. B **18**, 2701 (1978).
19. U. Kaldor and E. Eliav, Adv. Quantum Chem. **31**, 313 (1999).
20. A. V. Titov, N. S. Mosyagin, A. B. Alekseyev, and R. J. Buenker, Int. J. Quantum Chem. **81**, 409 (2001).
21. A. N. Petrov, N. S. Mosyagin, T. A. Isaev, *et al.*, Phys. Rev. Lett. **88**, 073001 (2002).
22. A. V. Titov, Int. J. Quantum Chem. **57**, 453 (1996).
23. E. R. Davidson, *The World of Quantum Chemistry* (Reidel, Dordrecht, 1974), p. 17.
24. S. Krebs and R. J. Buenker, J. Chem. Phys. **103**, 5613 (1995).
25. J. Paldus, *Methods in Computational Molecular Physics* (Plenum Press, New York, 1992), p. 99.
26. G. D. Purvis III and R. J. Bartlett, J. Chem. Phys. **75**, 1284 (1981).
27. P. Pulay, Chem. Phys. Lett. **73**, 393 (1980).
28. P. Pulay, J. Comput. Chem. **3**, 556 (1982).
29. N. S. Mosyagin, E. Eliav, and U. Kaldor, J. Phys. B **34**, 339 (2001).
30. N. S. Mosyagin, A. V. Titov, E. Eliav, and U. Kaldor, J. Chem. Phys. **115**, 2007 (2001).
31. M. Gutowski, J. H. Van Lenthe, J. Verbeek, *et al.*, Chem. Phys. Lett. **124**, 370 (1986).
32. B. Liu and A. D. McLean, J. Chem. Phys. **91**, 2348 (1989).
33. A. V. Titov, N. S. Mosyagin, and V. F. Ezhov, Phys. Rev. Lett. **77**, 5346 (1996).
34. N. S. Mosyagin, M. G. Kozlov, and A. V. Titov, J. Phys. B **31**, L763 (1998).
35. M. G. Kozlov, A. V. Titov, N. S. Mosyagin, and P. V. Souchko, Phys. Rev. A **56**, R3326 (1997).

Physics of Atomic Nuclei, Vol. 66, No. 6, 2003, pp. 1163–1167. From Yadernaya Fizika, Vol. 66, No. 6, 2003, pp. 1199–1203.

Probing Fission Time Scales with Neutrons and GDR Gamma Rays*

R. P. Schmitt[1)], T. Botting[1)], G. G. Chubarian[1)], K. L. Wolf[1)], B. J. Hurst[1)], H. Jabs[1)], M. Hamelin[1)], A. Bacak[1)], Yu. Ts. Oganessian[2)], M. G. Itkis[2)], E. M. Kozulin[2)], N. A. Kondratiev[2)], V. S. Salamatin[2)], I. V. Pokrovsky[2)], F. Hanappe[3)], E. de Goès Brennand[3)], A. Huck[4)], L. Stuttgé[4)], E. Liatard[5)], J. Beene[6)], R. Varner[6)], M. Halbert[6)], and N. Gan[6)]**

[1)] *Cyclotron Institute, Texas A&M University, College Station, TX, USA*

[2)] *Flerov Laboratory of Nuclear Reactions, Joint Institute for Nuclear Research, Dubna, Moscow oblast, 141980 Russia*

[3)] *Universite Libre de Bruxelles, Brussels, Belgium*

[4)] *CRN, Strasbourg, France*

[5)] *ISN, Grenoble, France*

[6)] *ORNL, Oak Ridge, TN, USA*

Received August 28, 2002

Abstract—The time scales for nuclear fission have been explored using both pre- and postfission neutrons and GDR gamma rays. Four systems were investigated: 133-MeV ^{16}O + ^{176}Yb and ^{208}Pb and 104-MeV ^{4}He + ^{188}Os and ^{209}Bi. Fission fragments were measured in coincidence with PPACs. The neutrons were detected using eight detectors from the DEMON array, while gamma rays were measured using the US BaF_2 array. The pre- and postfission gamma rays were determined using moving source fits parallel and perpendicular to the fission fragment emission directions. The time scales for fission for the neutrons were determined using the neutron clock technique. The gamma-ray data were fitted using a statistical model calculation based on the code CASCADE. The results of the fits from both data types were used to extract nuclear friction coefficients, γ, and fission time scales. The γ values ranged from 7 to 20, while the fission times were $(31-105) \times 10^{-21}$ s. © *2003 MAIK "Nauka/Interperiodica".*

1. INTRODUCTION

The question of fission time scales has been actively explored for a number of years using a variety of techniques including pre- and postfission neutron [1, 2] and light charged particle emission [3] and GDR γ-ray emission [2, 4]. Some newer studies have utilized crystal blocking techniques [5]. Using the various decay modes has met with limited success. In particular, the time scales obtained by the various methods have differed by an order of magnitude or more [2]. This situation indicates that further work is needed to reconcile these differences. The motivation for the current work is intended to distinguish effects attributable to experimental techniques, the underlying physics, and systematic model analysis. Two of the major tools for determining the time scale for the fission process have been employed here: neutron emission and GDR γ-ray emission.

In the case of neutron measurements, the time scale for fission, τ, can be approximated by

$$\tau = \tau_{\text{form}} + \tau_{\text{sadd}} + \tau_{\text{sci}} + \tau_{\text{acc}},$$

where τ_{form} represents the formation time of the fissioning species, τ_{sadd} is the time to achieve quasistatic equilibration at the saddle point, τ_{sci} is the time to evolve from saddle to scission, and τ_{acc} is the time required for the fragments to achieve their asymptotic velocities. Analogously, for GDR emission the fission time can be expected to follow

$$\tau = \tau_{\text{form}} + \tau_{\text{sadd}} + \tau_{\text{sci}},$$

where the latter term is absent.

The quantity τ_{sadd} is of particular interest as it is the so-called fission time delay or transient time. Determination of this quantity is expected to provide the value of the nuclear friction coefficient. Following Kramer's work in 1940 [6], the effective fission decay width including dissipative effects is expected to be smaller than the standard Bohr–Wheeler decay width according to the viscosity of the system according to

$$\Gamma_{\text{eff}} = \Gamma_{\text{BW}}((\gamma^2 - 1)^{1/2} - \gamma),$$

*This article was submitted by the authors in English.

** e-mail: schmitt@tamu.edu

1063-7788/03/6606-1163$24.00

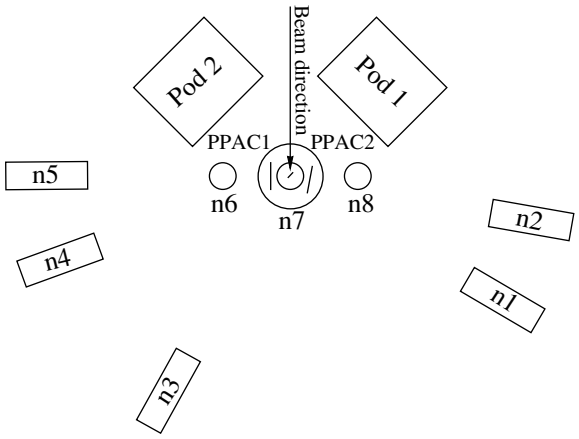

Fig. 1. Schematics of the experimental apparatus.

where Γ_{eff} is the effective fission decay width, Γ_{BW} is the Bohr–Wheeler decay width [7], and γ is the nuclear friction coefficient. In the past, γ has been associated with a fission time delay. However, this interpretation is not so clear. Values of γ vary considerably depending on the system, experimental technique, and analysis, yielding a range of fission time scales. For example, neutron clock measurements have given values of fission times as small as 5–100 zs. Studies involving GDR γ rays have given times as low as 30 zs and as large as 290 zs. For a summary of these various results, see [2].

The motivation for the present work is to compare the two above-mentioned methods using the same apparatus and same statistical model code to check the consistency of the two approaches. We find that the extracted γ values range from about 7–20, while the fission ranges from about 30 to 105 zs. The neutron clock method analysis yields somewhat higher values than the GDR technique. However, the difference is not large given the errors in the data and the associated errors. Thus, we find fission times that are consistent within a factor of 2.

2. EXPERIMENTAL PROCEDURE

A diagram of the experimental setup is shown in Fig. 1. As depicted, the beam from the Texas A&M K = 500 cyclotron impinged on the target in a thin walled chamber, constructed in Dubna. Neutrons were detected with two arrays from the DEMON array. As indicated in the diagram, five of the counters were placed in the reaction plane, while three more were located approximately 90° out of plane. Gamma rays where detected using two clusters of BaF_2 each consisting of 72 hexagonal counters of the US BaF_2 gamma array positioned at about 130°. The fission counters consisted of two thin start detectors placed 2 cm from the target and two position sensitive PPACs about 8 cm from the target, allowing for the kinematical reconstruction of the fission fragment masses via time of flight.

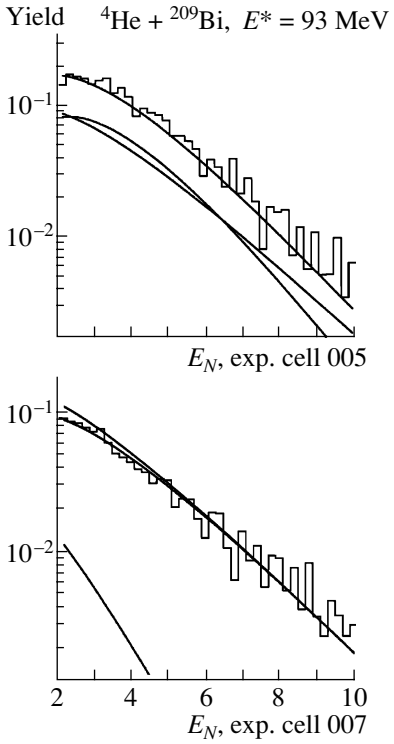

Fig. 2. Neutron energy spectra for parallel (top) and perpendicular (bottom) neutron counters with respect to the fission axis for the ^{4}He + ^{209}Bi reaction. The data are represented by histograms, while the solid lines reflect fits from the compound system, the fragments, and the total yield from moving source fits.

The response of the neutron counters was determined using standard γ-ray sources. The dynamic ranges of the γ-ray detectors were set using cosmic rays. The energy calibrations were established using an Am–Be source. The energy thresholds were set at about 1 MeV. The fission detectors were tested using a ^{252}Cf source.

3. DATA ANALYSIS

The neutron data were analyzed using the usual technique of moving source fits [8]. Unfortunately, because of the long cable delays needed to make the coincidence with the γ array, the neutron energy thresholds were about 2 MeV. Nevertheless, good fits were obtained for the neutron energy spectra. An example is shown in Fig. 2. One clearly sees that the spectra can be decomposed in two components: one component is strongly focused along the fragment direction, while the second component from the compound nucleus is essentially isotropic. The results of

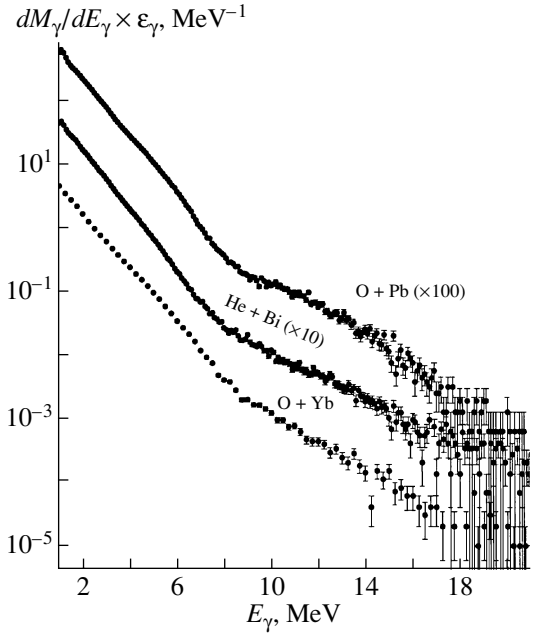

Fig. 3. Gamma-ray spectra for the indicated reactions.

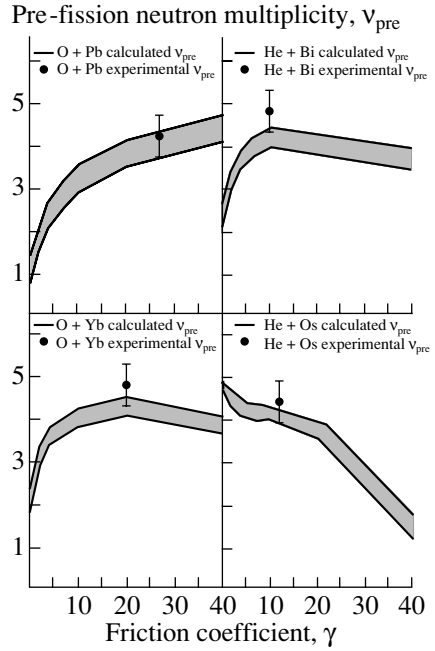

Fig. 4. Prefission neutron multiplicities as a function of the friction coefficient for various reactions. The points correspond to the experimental values, while the lines are the result to statistical model calculations.

the fits were used to extract the pre- and postfission neutron multiplicities using the code TIMCASC [9].

Because of the long delays used in the trigger, it was not possible to use pulse-height discrimination to separate neutrons and gammas in the BaF_2 counters. However, because of their excellent timing properties, the time of flight proved sufficient to perform the separation. In analyzing the gamma data, only central hits were considered. In other words, events in which deposited energy in the other most crystals were rejected. This made a significant difference in the energy spectra in the GDR region of the spectra. Figure 3 shows the random corrected spectra for three of the systems. The GDR bump is clearly visible in these three cases. Unfortunately, it was not possible to obtain a statistically significant spectrum for the ^{4}He + ^{188}Os system because of the low fission yield. The γ-ray energy spectra were also analyzed using TIMCASC coupled with fitting code MINUIT [9].

In order to restrict the decay of the compound nucleus to the fission channel, the code TIMCASC follows the decay in time-reversed fashion. This approach allows one to follow the decay of both the fragments and the fissioning compound system. In contrast, ordinary versions of CASCADE terminate the decay chain at the fission point. Another feature of the code is that it incorporates a time-dependent fission decay width following the work of Weidenmüller and Zhang [10]. The details of the calculation are described extensively in [9] and will not be given here.

4. RESULTS

Extraction of the friction coefficient and the associated fission times from the neutron data is relatively straight forward. The code TIMCASC was run for various values of the nuclear friction coefficient and the prefission neutron multiplicities were extracted. When the calculated values agreed with the experimental values, the corresponding times were extracted. Because the calculated values varied only slightly with the GDR parameters (see below), the calculations were run assuming a spherical compound nucleus with ground-state GDR behavior. Figure 4 shows the results of this procedure for the various systems. The points reflect the experimental values, while the lines represent the calculated values. The shaded region reflects the use of different level density parameters ($a = A/7 - A/10$). The times

Table 1. Summary of the neutron data

Reaction	γ	τ, zs
^{16}O + ^{208}Pb	20	105 ± 10
^{4}He + ^{209}Bi	10	72 ± 7
^{16}O + ^{176}Yb	20	112 ± 12
^{4}He + ^{188}Os	10	31 ± 4

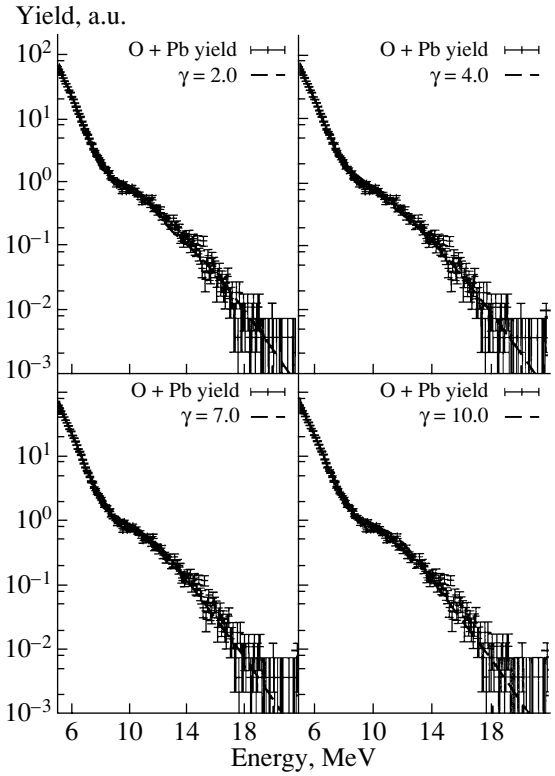

Fig. 5. Fits (lines) to the γ-ray data (points) using the procedure described in the text for the indicated parameters for the $^{16}O + ^{208}Pb$ reaction. The best χ^2/N fits are given in the lower left panel.

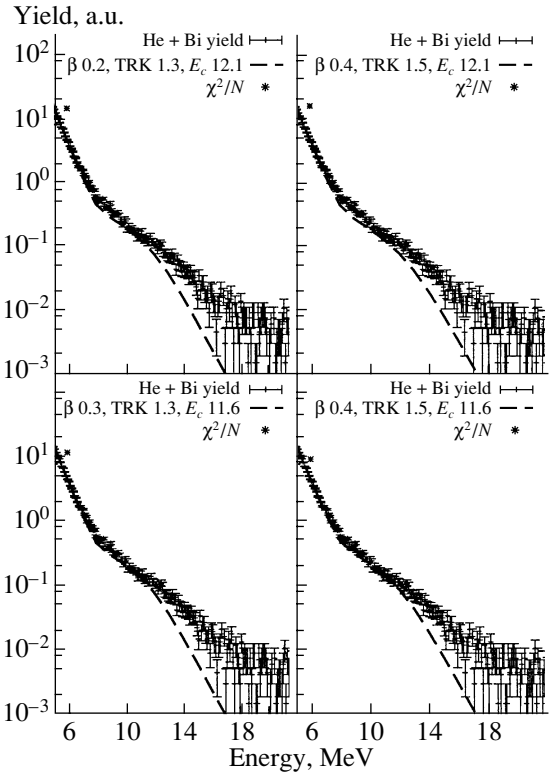

Fig. 6. Same as Fig. 5 for the $^{4}He + ^{209}Bi$ reaction.

taken for fission used $a = A/8$. The results of the procedure are summarized in Table 1.

Fitting the GDR data proved much more challenging due to the existence of many parameters used to describe the GDR. In the calculations, the GDR was described by two Lorentzian components with centroids $E_\perp$ and $E_{||}$, which can describe prolate, oblate, and spherical shapes. The average energy E_{cen} of the two components was taken as an average of the energies weighted by their fractional strengths, $S_\perp$ and $S_{||}$. Initially, the total strength was taken to be 100% of the TRK sum rule. However, this proved to be inadequate for the less fissile systems. In this case, the total strength was taken as a fitting parameter. The widths Γ_i of the components were taken to be a fraction c of the square of the energy centroids:

$$\Gamma_i = cE_i^2.$$

The deformation, β, which is related to the energy centroids of the two components [9], was treated as a free parameter.

Given the above constraints, there are a total of four fitting parameters: E_{cen}, $S_\perp$, c, and β. Early in the analysis, it was found that the fits converged to constant values of E_{cen} and c; these were held fixed in the fits. The value of c was taken to be 0.03 for all the reactions, while E_{cen} was initially taken to be 12.0, 12.1, and 12.7 for the reactions $^{16}O + ^{208}Pb$, $^{4}He + ^{209}Bi$, and $^{16}O + ^{176}Yb$, respectively.

Fits to the $^{16}O + ^{208}Pb$ data are shown in Fig. 5. The agreement is excellent. The best χ^2/N value is obtained with a friction coefficient of 7 and a β value of 0.554. In this case, 100% of the TRK sum rule was used. The other fits seem about of equal quality, but they require much more deformed shapes. For example, using a friction coefficient $\gamma = 2.0$ requires a β value of -1.257, which seems unreasonable. Results for the other two systems are less satisfactory. It was found that it was not possible to fit the data in the GDR region using 100% of the sum rule and the E_{cen} values quoted above. Increasing the sum rule value to

Table 2. Summary of the GDR results

Reaction	γ	τ, zs
$^{16}O + ^{208}Pb$	7	67 ± 10
$^{4}He + ^{209}Bi$	20	45 ± 9
$^{16}O + ^{176}Yb$	20	84 ± 16

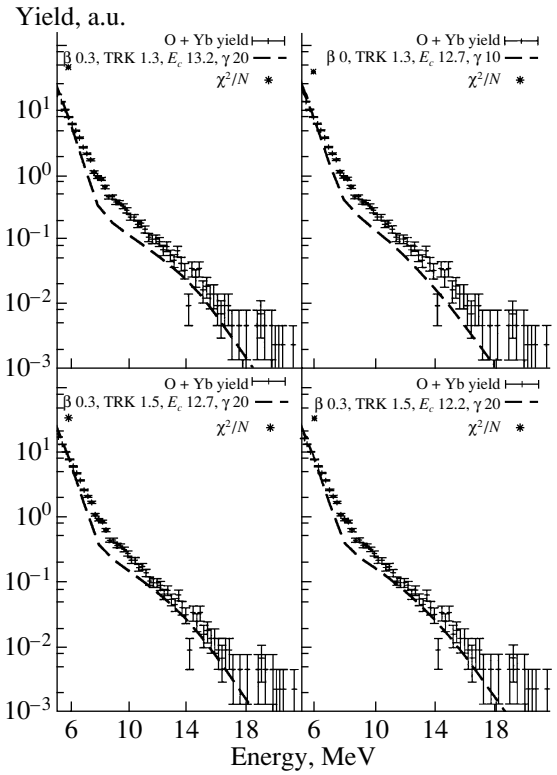

Fig. 7. Same as Fig. 5 for the $^{16}O + {}^{176}Yb$ system.

150% was necessary to obtain any kind of reasonable fits to the data.

Figure 6 shows some fits to the $^4He + {}^{209}Bi$ reaction. The agreement is reasonable up to about 12 MeV. However, at this point, the data shows an enhancement with respect to the fitted spectrum. The reason for this behavior is unclear. Possibly this is due to the presence of an internuclear bremsstrahlung component. Alternately, the deviation could also reflect quasideuteron formation. Both could explain the deviation from the sum rule. Neither of these effects is considered in the statistical model calculations.

Some fits for the $^{16}O + {}^{176}Yb$ system are shown in Fig. 7. Again, the fits are less than satisfactory but for a different reason. Using 150% of the sum rule gives reasonable agreement in the GDR region of the spectrum. However, the calculation underestimates the yield from about 6 to 10 MeV. Since the fragment's γ rays have a significant contribution in this region, this discrepancy could be due to a poor description of the fragment's decay. As shown in previous works, the γ-ray spectra are quite sensitive to the exit channel mass asymmetry.

Tables 1 and 2 summarize the results of both the neutron and the γ-ray measurements. Several trends are observed. The extracted friction coefficients are consistent to within about a factor of three, which seems reasonable considering the uncertainties in the analysis. The time scales vary from 31 to 112 zs. The shortest fission time is observed for the least fissile system, namely, $^4He + {}^{188}Os$. This could be expected due to the high chance for first chance fission. The longest times are seen for the ^{16}O-induced reactions. This is not unexpected since the $^{16}O + {}^{208}Pb$ system continues to be fissile even after the emission of several neutrons. The less fissile $^{16}O + {}^{176}Yb$ presumably involves high partial waves and does not fission until several neutrons are emitted. The $^4He + {}^{209}Bi$ reaction corresponds to an intermediate situation. There is an overall tendency for the GDR measurements to give shorter times than the neutron measurements. This suggests that the two methods sample different stages in the fission process. Of course, this difference could reflect the model dependence of the analysis.

5. SUMMARY

In conclusion, fission time scales have been investigated for a number of systems using both neutrons and GDR γ rays. The results have been analyzed using a code that incorporates both the nuclear friction coefficient and the time-dependent fission widths. The results give friction coefficients in the range of 7–20. The extracted fission times vary from 31 to 112 zs. The shortest times are associated with the least fissile system, while the longest times are observed for the more fissile systems. The neutron measurements tend to give somewhat longer times than the GDR results. Possibly, this is due to sampling different stages of the fission process.

REFERENCES

1. D. J. Hinde *et al.*, Phys. Rev. C **45**, 1229 (1992).
2. T. Botting, PhD Dissertation (Texas A&M University, 1999).
3. M. Gui *et al.*, Phys. Rev. C **48**, 1791 (1993).
4. P. Paul and M. Thoennessen, Annu. Rev. Nucl. Part. Sci. **44**, 65 (1994).
5. M. Morjean *et al.*, Nucl. Phys. A **630**, 200c (1998).
6. H. A. Kramers, Physica **7**, 284 (1940).
7. N. Bohr and J. A. Wheeler, Phys. Rev. **56**, 426 (1939).
8. D. Ward *et al.*, Nucl. Phys. A **403**, 189 (1983).
9. G. van't Hof *et al.*, Nucl. Phys. A **638**, 613 (1998).
10. H. A. Weidenmüller and Zhang Jing-Shang, Phys. Rev. C **29**, 879 (1984).

Physics of Atomic Nuclei, Vol. 66, No. 6, 2003, pp. 1168–1172. From Yadernaya Fizika, Vol. 66, No. 6, 2003, pp. 1204–1208.

Tracking Dissipation in Capture Reactions*

T. Materna[1)], C. Schmitt[2)], Y. Aritomo[3),4)], J. Bartel[2)], B. Benoit[1)], A. A. Bogatchev[4)], E. de Goès Brennand[1)], O. Dorvaux[2)], G. Giardina[5)], F. Hanappe[1)], M. G. Itkis[4)], I. M. Itkis[4)], J. Kliman[4)], G. N. Kniajeva[4)], N. A. Kondratiev[4)], E. M. Kozulin[4)], L. Krupa[4)], Yu. Ts. Oganessian[4)], I. V. Pokrovsky[4)], E. V. Prokhorova[4)], N. Rowley[2)], K. Siwek-Wilczynska[6)], and L. Stuttgé[2)]**

[1)] *PNTPM, Université Libre de Bruxelles, Brussels, Belgium*

[2)] *Institut de Recherches Subatomiques, IReS, Strasbourg, France*

[3)] *Department of Physics, University of Tokyo, Tokyo, Japan*

[4)] *Flerov Laboratory of Nuclear Reactions, Joint Institute for Nuclear Research, Dubna, Moscow oblast, 141980 Russia*

[5)] *INFN and Dipartimento di Fisica dell' Università di Messina, Messina, Italy*

[6)] *Warsaw University, Warsaw, Poland*

Received September 27, 2002

Abstract—Nuclear dissipation in capture reactions is investigated using backtracing, a new analysis protocol. Combining analysis procedure with dynamical models, the difficult and long-standing problem of competition and mixing between quasifission and fusion–fission is solved for the first time. The nature of the relevant dissipation is determined as one-body dissipation. At low excitation energy where shell effects are strongly effective, the shape of the mass distribution could be a powerful check of the nature and the magnitude of the dissipation. © *2003 MAIK "Nauka/Interperiodica".*

INTRODUCTION

Introduced by Kramers [1] very early after the discovery of nuclear fission, the role of dissipation was only recognized in the 1970s with the emergence of deep inelastic collisions. Its nature, one-body dissipation (OBD) or two-body dissipation (TBD) and its magnitude and evolution with different parameters like shape or temperature, is still a matter of controversy.

A lot of experimental data obtained in most of the cases by the observation of pre- and postscission emission of particles or gamma rays have been devoted to the determination of the dissipation. But still recently, depending on the experiments but also deeply on the models used to extract the dissipation coefficient (Kramers γ coefficient), a dispersion of the results covering at least two orders of magnitude is observed. Different behaviors are extracted for the evolution with the temperature and no definite conclusions can be drawn.

Even if coherent experimental data [2] are selected and analyzed by the same dynamical model [3], a large spreading of values for the dissipation coefficient is observed. For example, in Fig. 1, adapted from [4], the evolution with the temperature of the dissipation coefficient is presented for different reactions

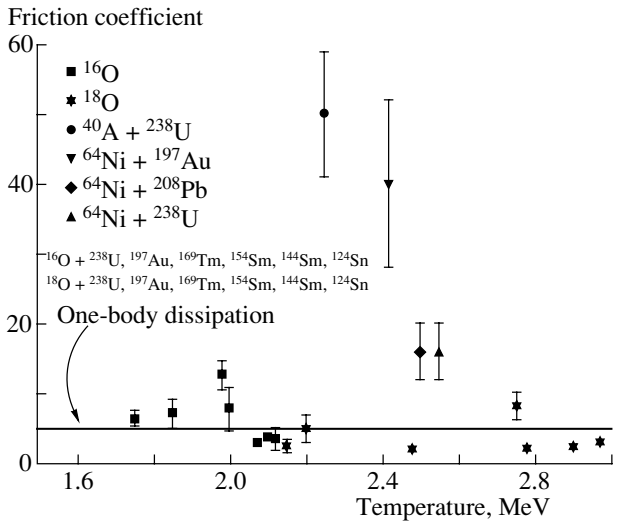

Fig. 1. Evolution of the dissipation coefficient as a function of the temperature for different reactions. Data from Hinde *et al.* [2].

*This article was submitted by the authors in English.

**e-mail: tmaterna@ulb.ac.be;aspirantFNRS.

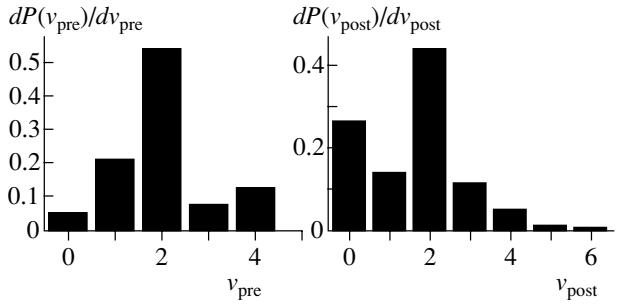

Fig. 2. Pre- and postscission neutron multiplicity distributions for ^{126}Ba obtained by backtracing.

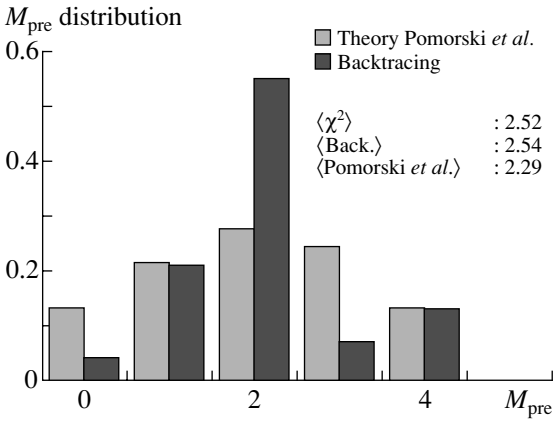

Fig. 3. Comparison between the experimental prescission neutron multiplicity distribution obtained by backtracing for the ^{28}Si + ^{98}Mo reaction at 204 MeV and the prediction of the model of Pomorski [8].

channels leading to very different fissioning systems. As pointed out by the authors, on one had, for true fusion–fission systems ($Z_1Z_2 \ll 1600$), the deduced γ coefficient ranges from 2 to 10 and is clearly compatible with OBD. No particular evolution with the temperature is observed. On the other hand, for systems with $Z_1Z_2 > 1600$, the γ values are considerably larger and clearly not compatible with OBD. This puzzling behavior for these systems is assumed to be due to TBD or to the expected mixing of mass-symmetric fragments coming from the different reaction mechanisms of capture reactions: quasifission and fusion–fission. Indeed, no separation between the two mechanisms was available and only the mean value of the multiplicity for neutron pre- and postscission emission could be obtained using the classical χ^2 minimization.

In this report, we will show how a more powerful analysis protocol, backtracing [5], which is able to provide not only mean values but also correlations and distributions, can help us to solve this long-standing problem.

Recently applied to the Ni + Pb [6] and Ca + Th [7] reactions leading to isotopes of $Z = 110$, the backtracing procedure allowed one for the first time to clearly disentangle, at least intuitively, the contributions of quasifission and fusion–fission in the neutron prescission multiplicity distribution. A complete description of the backtracing procedure and its application to our cases is described in [6–8].

A SIMPLE CASE: FUSION–FISSION REACTION LEADING TO ^{126}Ba

In order to validate the backtracing application to the determination of the distribution of pre- and postscission neutron multiplicity, we will first present results obtained for the ^{28}Si + ^{98}Mo reaction at 204 MeV.

This system has been investigated [8] at the VIVITRON, IReS, Strasbourg, using, as for all the data presented here, the DEMON neutron detector associated to parallel plates or CORSET setups for the observation of the reaction fragments.

In such a low-mass system, obtained in a reaction with such a low Z_1Z_2 product, only the fusion–fission mechanism is expected to contribute to the mass-symmetric fragment distribution.

Figure 2 shows the distributions of the pre- and postscission neutron multiplicity as obtained by the backtracing. It must be noted that the mean values obtained here are in complete agreement with the ones deduced from the conventional χ^2 minimization. For instance, the mean values for the neutron prescission multiplicity are 2.52 and 2.54 for χ^2 and backtracing, respectively (see Fig. 3). Figure 3 presents, in addition to the backtraced distribution, the theoretical results obtained using the dynamical model of Pomorski *et al.* [9]. This model, based on the resolution of the one-dimensional Langevin equation, is able to describe only the fusion–fission process and is thus well adapted to this ^{126}Ba system. The excellent observed agreement between experimental data and model calculations is obvious; in particular, one notes that the zero-neutron multiplicity channel is well reproduced. The model uses OBD (wall and window formula) and the agreement confirms that, at least when only the fusion–fission reaction is concerned and even if the model is not perfect, for instance, no dependence on temperature is included, there is no need to introduce TBD to reproduce the experimental data.

To our knowledge, this is the first time that the neutron prescission multiplicity distribution has been experimentally observed and compared with such good agreement with dynamical calculations.

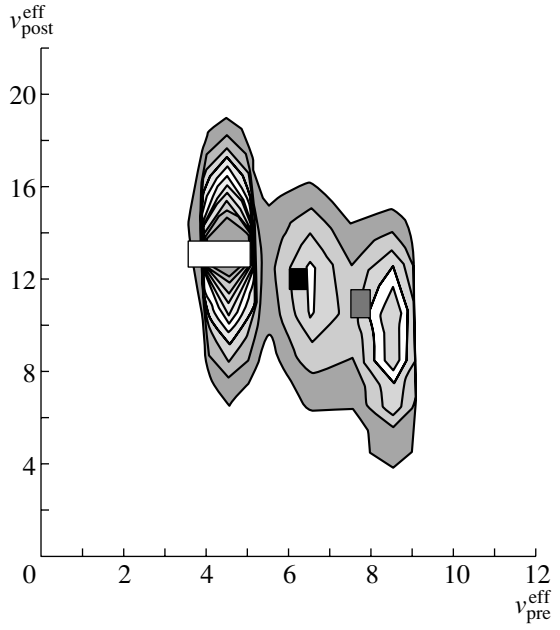

Fig. 4. Pre- and postscission neutron multiplicity correlation for the system ^{58}Ni + ^{208}Pb at 186 MeV of excitation energy. Results of calculations using HICOL + DYNSEQ from Siwek-Wilczynska *et al.* [3] are also shown. The rectangle to the left represents quasifission ($30 < l < 120$) with only one-body dissipation. The two squares stand for fusion–fission ($0 < l < 30$) with OBD (left) and two times OBD (right).

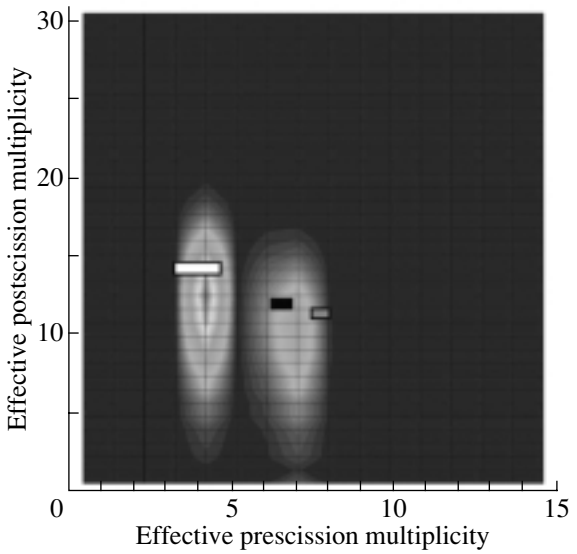

Fig. 5. Pre- and postscission neutron multiplicity correlation for the system ^{40}Ca + ^{232}Th at 166 MeV of excitation energy. Results of calculations using HICOL + DYNSEQ from Siwek-Wilczynska *et al.* [3] are also shown. The rectangle to the left represents quasifission ($36 < l < 110$) with only one-body dissipation. The two squares stand for fusion–fission ($0 < l < 36$) with OBD (left) and two times OBD (right).

A MORE COMPLEX CASE: $Z = 110$

In this case, the fused $Z = 110$ nucleus is obtained by two different entrance channels (^{40}Ca or ^{58}Ni projectiles on ^{232}Th or ^{208}Pb targets) leading to the same high excitation energy ranges, from around 60 MeV to more than 160 MeV. For such (super)heavy systems, competition between quasifission and fusion–fission is expected to populate the symmetric part of the fragment mass distribution, and until now there was no real way to disentangle these two contributions at these excitation energies. The experiments have been carried out at SARA, Grenoble [6, 7].

Neutron pre- and postscission multiplicities (mean values) were first obtained by χ^2 minimization and, as usual, led to the same difficulties as before: large values for γ are deduced using dynamical models. It must be noted that, when it was possible, our experimental results were compared to and found to be in complete agreement with those of Hinde *et al.* [2].

In a second step, backtracing was applied and provided us with neutron pre- and postscission multiplicity distributions at least for the highest excitation energy for both systems. Indeed, backtracing requires very high statistics and has been applied only in these two cases.

Figures 4 and 5 presents the backtracing results for Ni + Pb and Ca + Th, respectively. In both cases, the neutron pre- and postscission correlations exhibit two well-defined regions corresponding essentially to two different distributions for the pre-scission neutrons. Intuitively, we can think that each separated distribution can be attributed to each of the capture reactions. As expected, a low mean value (of the order of 4) of the neutron prescission multiplicity distribution can be associated to quasifission (faster mechanism), a larger mean value (around 7) to fusion–fission (slower mechanism).

Now, using the same HICOL + DYNSEQ code as the one used by K. Siwek-Wilczynska to deduce the dissipation coefficient for the Hinde *et al.* data, we can reproduce our experimental backtraced correlations by two different scenarios: quasifission and fusion–fission (see rectangles and squares in Figs. 4 and 5). They correspond to different angular momentum ranges obtained in HICOL by comparison with the experimental mass distribution. In both systems, the same dissipation coefficients are needed to reproduce the experimental distributions ($\gamma = 5$ for quasifission and ranges from 5 to 11 for fusion–fission). This spectacular and first-time agreement with OBD (or with a value between OBD and 2 OBD) reconciles completely these data with the ones corresponding to fusion–fission only and clearly supports the conclusion that, as soon as one is able to distinguish be-

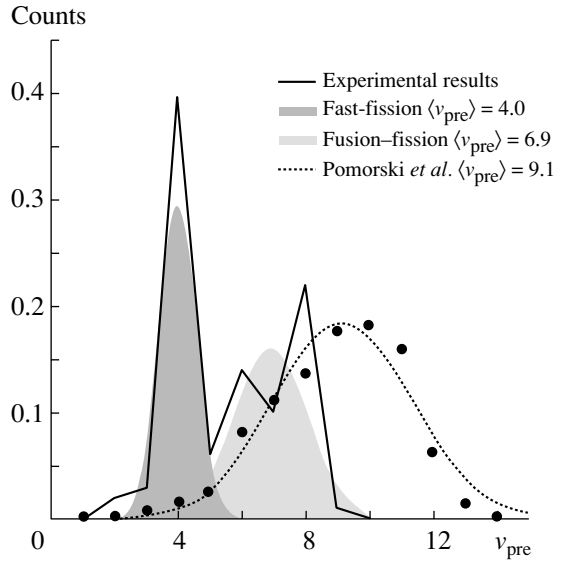

Fig. 6. Comparison between the experimental prescission neutron multiplicity distribution obtained by backtracing for the ^{58}Ni + ^{208}Pb system at 186 MeV of excitation energy (black line) and the prediction of the model of Pomorski [8] (points). The full Gaussian curves are a fit to the experimental distribution, while the dotted Gaussian curve is a fit to the model.

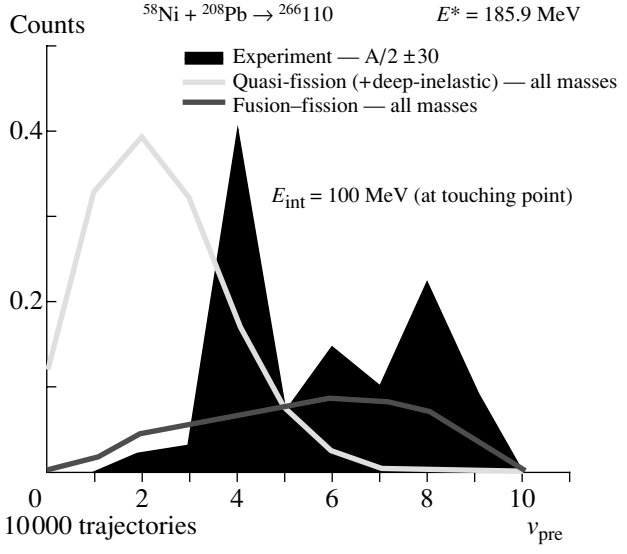

Fig. 7. Comparison between the experimental prescission neutron multiplicity distribution for the ^{58}Ni + ^{208}Pb system at 186 MeV of excitation energy for fragment masses in the range $A/2 \pm 30$ (full black line) and the prediction of the model of Aritomo [12] for quasifission and fusion–fission for the whole mass range of deep-inelastic, quasifission, and fusion–fission processes.

tween quasifission and fusion–fission, no discrepancy remains and OBD is large enough to reproduce the experimental data.

COMPARISON WITH LANGEVIN EQUATION MODELS

Figure 6 shows the distribution of prescission multiplicity for the Ni + Pb system. Two free Gaussian curves have been fitted on the experimental backtraced distribution (full curves) and are now considered to represent the distribution to be attributed to quasifission and fusion–fission reactions. Calculations for the fusion–fission part, performed by Schmitt [10] using the Pomorski model, are also given in this figure (dotted curve). One can note that the mean value and the width obtained in this model are a little bit too high, but the agreement can be considered satisfactory with this OBD (only) symmetric fission model if one takes into account that it does not contain dissipation in the entrance channel and that no dependence of friction on shape or temperature is considered. These points are under consideration.

Recently, a three-dimensional Langevin equation model has been developed and applied to the dynamics of capture reactions, in particular, in the superheavy region [11]. A first comparison of these calculations with our experimental result for the Ni + Pb reaction is presented in Fig. 7 [12].

If one takes into account that these preliminary calculations include all the events associated not only with quasifission and fusion–fission but also with deep-inelastic processes, the overall agreement is satisfactory. It seems obvious that, as soon as the experimental mass and TKE cuts are included in the calculations, the agreement will be better. Indeed, deep-inelastic processes are known to be low prescission multiplicity events, and the symmetric fusion–fission process corresponds to the largest multiplicity.

AT LOW EXCITATION ENERGY

Low excitation energies, which mean the ones required for superheavy synthesis, represent a very serious problem in the determination of the dynamical aspects of capture reactions. Indeed, regardless of the decreasing the cross section, which is already a severe limitation, the prescission multiplicity will also drop and can represent a real difficulty for backtracing since it requires very high statistics in the neutron experimental observables.

But low excitation energies also mean shell effects that will strongly determine the shape of the mass distributions in capture reactions.

From the work of the DEMON–CORSET team in Dubna [13], we know that quasifission and fusion–fission can presumably be sorted by a careful examination of the mass distributions of the so-called symmetric fragments in a lot of different ^{48}Ca-induced

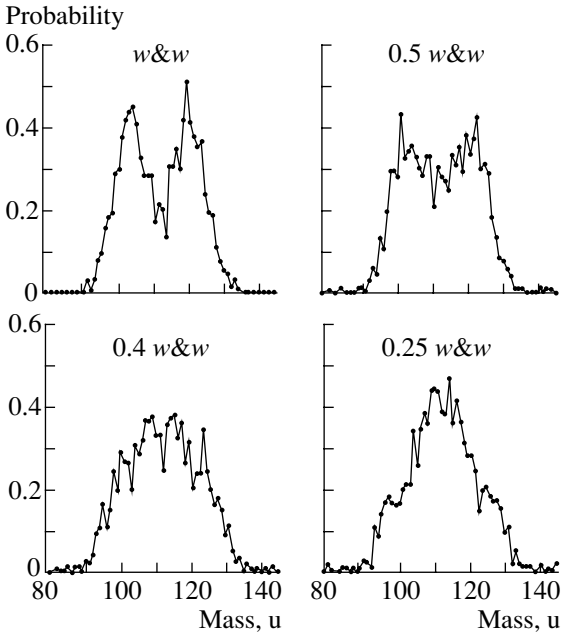

Fig. 8. Evolution of the mass distribution of the fragments in the system $^{18}O + ^{209}Bi$ at 26 MeV of excitation energy as a function of the one-body dissipation (1.0, 0.5, 0.4, and 0.25 times the wall and window formula, respectively).

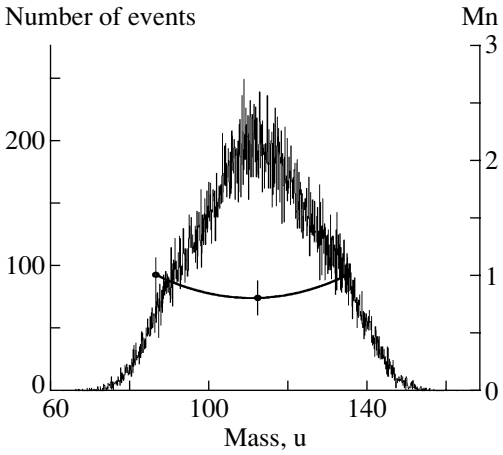

Fig. 9. Experimental fission fragment mass distribution for the system $^{18}O + ^{209}Bi$ at 26 MeV of excitation energy (black curve) with the mean prescission neutron multiplicity Mn.

reactions at energies close to the barrier. In such a case, where statistical errors could inhibit the use of the backtracing protocol, if the quasifission and fusion–fission mechanisms are already identified, the χ^2 minimization procedure remains valid for obtaining the dynamical properties by looking at the mean values of the prescission multiplicities. Of course, it would be nice to obtain at least for a selected case, a complete backtracing analysis that could remove any ambiguity.

Shell effects are also responsible for the occurrence of bimodal fission in the transition region. Arguments based on the evolution of the neutron prescission multiplicity (obtained by χ^2 minimization) as a function of the mass of the fission fragments have already been used to confirm the bimodal character of the induced fission of ^{226}Th at low excitation energy [13, 14]. At the present time, such a low value of the neutron prescission multiplicity cannot be reproduced by a dynamical model that includes assumptions for the emission that are valid at only high excitation energy. But, as has been pointed out recently [10] (see Fig. 8), the shape of the mass distribution obtained in a Langevin bidimensional model strongly depends on the magnitude of the dissipation and could thus also be used to deduce the magnitude and the nature of the dissipation. In Fig. 9, the experimental mass distribution corresponding to the calculation in Fig. 7 is shown. The mean prescission neutron multiplicity is also displayed.

Combining the different approaches, it would be possible to obtain here clear evidence for the origin of the nuclear dissipation.

ACKNOWLEDGMENTS

This work has been supported in part by INTAS, project nos. 97-11929 and 00-655.

REFERENCES

1. H. Kramers, Physica **7**, 284 (1940).
2. D. Hinde *et al.*, Phys. Rev. C **45**, 1229 (1992).
3. K. Siwek-Wilczynska *et al.*, Phys. Rev. C **51**, 2054 (1995).
4. J. Wilczynski *et al.*, Phys. Rev. C **54**, 325 (1996).
5. P. Désesquelles *et al.,* Nucl. Phys. A **604**, 183 (1996).
6. L. Donadille *et al.*, Nucl. Phys. A **656**, 259 (1999).
7. B. Benoit, PhD Dissertation (Unversité Libre de Bruxelles, 2000).
8. E. de Goès Brennand, PhD Dissertation (Université Libre de Bruxelles, 2000).
9. K. Pomorski *et al.*, Nucl. Phys. A **679**, 25 (2000).
10. C. Schmitt, PhD Dissertation (Université Louis Pasteur, Strasbourg, 2002).
11. Y. Aritomo, in *Proceedings of the 2001 Exotic Nuclei, Lake Baikal, 2001*, Ed. by Yu. E. Penionzhkevich and E.A. Cherepanov, p. 106.
12. Y. Aritomo and T. Materna, work in progress.
13. M. Itkis *et al.*, this Proceedings.
14. A. Kelic *et al.*, Europhys. Lett. **47**, 552 (1999).

Physics of Atomic Nuclei, Vol. 66, No. 6, 2003, pp. 1173–1177. From Yadernaya Fizika, Vol. 66, No. 6, 2003, pp. 1209–1213.

The Complex Trajectory Method and Dissipation in Fission*

F. F. Karpeshin**

Fock Institute of Physics, St. Petersburg University, St. Petersburg, 198504 Russia, and Universidade de Coimbra, Departamento de Física, Coimbra, Portugal

Received August 28, 2002

Abstract—The sensitivity of the muon attachment probabilities to the light fragments of prompt fission W_l on the fission dynamics is discussed. It is shown that the final W_l value consists of two contributions: one from the point of scission and a second from avoided crossing of the levels. The relative contribution from the prescission phase turns out to be higher for more asymmetric fission. © *2003 MAIK "Nauka/Interperiodica".*

1. DISSIPATION IN FISSION

A feature of fundamental interest of nuclear matter is dissipation of the collective energy. This feature is manifested in nuclear fission. From the experimental viewpoint, the dissipation is studied in the fusion–fission reaction, where emitted prefission gammas and neutrons and, sometimes, light charged particles play a role of a natural time scale.

Another situation is in low-energy fission, e.g., induced by thermal neutrons. In this case, no prefission gammas or neutrons have been positively observed. It is known that neutrons are emitted from fully accelerated fragments. And it can be concluded from this fact that prefission time $t_{sc} \lesssim 10^{-19}$ s [1]. This upper limit still remains two orders of magnitude higher than the concluded duration of around a few units of 10^{-21} s for the saddle-to-scission descent found in the case of heavy-ion collisions [2].

Some hopes had been related to ternary fission, accompanied by emission of light charged particles, but they were also not quite realized [3].

Usually, one considers two mechanisms of dissipation: one-body dissipation and two-body viscosity. The former comes from collisions of the nucleons with the moving walls of the fissile nucleus. The other is due to collisions between the nucleons. The one-body mechanism is generally characterized with a more compact scission configuration and, as a consequence, with less primary kinetic energy of the nascent fragments, smaller deformation energy, and larger Coulomb potential energy (Fig. 1). At first sight, all these features could be immediately revealed in the total kinetic energy (TKE) of the fragments, their excitation energy, and the number of emitted neutrons and the radiated energy leaving with gamma quanta. However, all these three characteristic quantities are not independent, being mutually related by the conservation of energy. Thus, less primary kinetic energy is compensated by larger Coulomb potential energy, so that at infinity the TKE becomes the same for both scission configurations. Analogously, smaller deformation energy is balanced by higher intrinsic energy (that is, higher temperature) at the scission point. Therefore, measuring the TKE provides us with limited information about the scission configuration of the fragments. Furthermore, measuring the energy carried off by the neutrons, gammas, or light charged particles, in correlation with the TKE of the same fragments, provides the most of any conceivable information about the scission characteristics. However, again, only the sum of the deformation plus intrinsic energy of the fragment energy can be extracted in this way—in view of the conservation of their total value. There always remains a corridor of uncertainty for the R_{sc} value. An independent source of information is therefore needed if one wants to know the scission configuration more precisely. Muon-induced prompt fission can serve as a tool capable of providing unique information about the scission configuration versus its TKE.

Prompt fission occurs as a result of a radiationless transition to the $1s$ state in a muonic atom [4–7]. Its study also offers a way of probing the fission dynamics.

As a result of prompt fission, the muon is usually entrained on the heavy fragment, forming a muonic atom. This gives rise to different processes and effects, such as muonic conversion of the γ rays of the fragment, muon capture by the fragment, muonic x-ray of the fragment, augmentation of the fission barrier due to the presence of the muon, and many

*This article was submitted by the author in English.

** e-mail: karpesh@snoopy.phys.spbu.ru

1063-7788/03/6606-1173$24.00

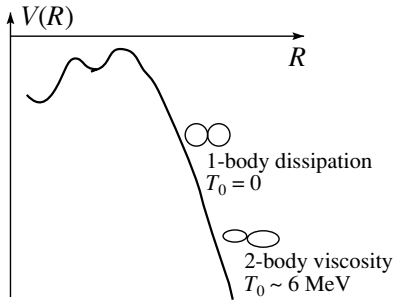

Fig. 1. Two possible scission configurations answering the same final TKE of the fragments. In the case of a more elongated configuration, smaller repulsion energy can be compensated by higher primary collective energy T_0 of the nascent fragments.

others ([4–21] and references therein). Of these topics, the problem of the muon attachment probability to the light fragment W_L has been considered in many papers ([8–21] and references therein). Some calculations (e.g., [10, 21]) lead to a conclusion that is of great interest from the viewpoint of studying the fission dynamics, namely, that the W_L value may be sensitive to the amount of dissipated energy. At first sight, this conclusion contradicts results of other calculations performed within the more traditional quasimolecular method by making use of the Born–Oppenheimer expansion in the adiabatic basis [8, 11–13, 15, 16]. Below, we show a way to overcome it.

The way is offered by the Landau method of complex trajectories. It is shown that the final muon attachment amplitude is a result of the interplay of the contributions from the point of scission and avoided crossing of the terms. This presents a unique possibility of rather definitely localizing, at least in principle, the scission point and knowing the primary velocity of the nascent fragments at scission in experiment. This becomes possible because the scission point may be treated as a point with violated analyticity of the Hamiltonian (e.g., [22]) with respect to the time variable. We recall that, in [23], it has been shown that scission is accompanied with a density reorganization, specifically resulting in the appearance of a thin external barrier.

2. SEMICLASSICAL CHARACTER OF THE COLLECTIVE MOTION

Separation of the fragments generally occurs with a large Massey parameter of adiabaticity, which is only broken at the point of avoided crossing of the $1s\sigma$ and $2p\sigma$ levels [24]. The transition amplitude can be found by means of the Born–Oppenheimer expansion in the adiabatic basis of the two quasimolecular states and solving the resulting set of differential equations {like Eq. (1) in [16]} for the population amplitudes C_1 and C_2. The equations are solved with the initial condition

$$C_i = \delta_{i1} \quad \text{for} \quad R = R_i, \tag{1}$$

denoting that the muon is in the ground state at the starting point R_i. Note that, due to adiabaticity, we can set in the equations $C_1 = 1$ for a first approximation, which results in virtually identical final muon attachment probabilities in the cases considered below. C_2 is then found by simple quadrature

$$C_2(R \to \infty) \approx \int_{R_s}^{\infty} F_{21}(R')dR'. \tag{2}$$

Equation (2) facilitates the analytical continuation into the complex plane. It is used in the calculations of $C_2(R)$ in the complex plane.

3. THE COMPLEX TRAJECTORY METHOD

This method can be used to better understand the real influence of fission dynamics on the attachment probability by means of the Landau method of complex trajectories of the transition [25]. According to this method, the path $R(t)$ corresponding to the trajectory of relative motion of the fragments from $R = 0$ to $R \to \infty$ can be deformed and shifted to the upper half-plane of complex R values, with the exception of irregular points. Among the latter ones, the point of avoided crossing of the $1s\sigma$ and $2p\sigma$ levels is of most importance. Another one is the initial point (1), for which we assume a value corresponding to the outer saddle: $R_i = R_s$. At this point, the mass asymmetry of the fragments starts to develop, which gives rise to the onset of the nonadiabatic coupling.

The third point is the point of scission $R_{\rm sc}$. The region of necking is usually small in comparison with the characteristic size of the fission path. This allows one to idealize the picture of scission conventionally, contracting the area to the scission point. At this point, the dependence of the velocity on time changes, which also breaks the analytical dependence of the Hamiltonian on time (e.g., [22]). Explicitly, we suppose for the relative velocity of the fragments the following expression:

$$V(R) = \begin{cases} \sqrt{\dfrac{2}{\mu}\left(\mathrm{TKE} - \dfrac{Z_1 Z_2}{R}\right)} & \text{for } R \geq R_{\rm sc}, \\ V(R_{\rm sc})\sqrt{\dfrac{1-(R_s/R)^2}{1-(R_s/R_{\rm sc})^2}} & \text{for } R < R_{\rm sc}, \end{cases} \tag{3}$$

where TKE is the total kinetic energy of both fragments and μ is their reduced mass.

Therefore, $V(R = R_s) = 0$. This rules out shaking effects of sudden switching on a perturbation related to beginning of motion. Furthermore, $V(R)$ has a point $R = R_{sc}$ where its derivative is discontinuous, and, therefore, analyticity is violated. This discontinuity thus turns out to be an inherent physical property of any realistic scenario of fission. Below, we discuss consequences of this conclusion for the muon distribution of fragments in finer detail.

The two vertical cuts in Fig. 2 fix the trajectory at the scission point, not allowing one to move it from the real axis of R.

We note that nonanaliticity of the trajectory $R(t)$ as a function of time can be concluded from a very simple consideration. At large distances, $R(t)$ can be considered to be unambiguously defined by the Coulomb repulsion and, therefore, the same for every couple of fragments if they have the same TKE for $R \to \infty$. Were $R(t)$ an analytical function, that would also uniquely define the whole trajectory $R(t)$, including the position of R_{sc} and the prefission scenario. This is not the case, however. First, we know that the position of R_{sc} is determined randomly. Second, the prefission scenario, as we saw in the introduction, may also be very different, depending on the friction, which is obviously not the case for $R > R_{sc}$. The obtained contradiction proves that $R(t)$ appears not to be an analytical function in the entire trajectory.

An advantage of the method is that the contributions from the line segments 2 and 5 are expected to vanish for $R \to \infty$ [25]. As a result, the resulting transition amplitude becomes a sum of several terms. The contribution from the line segment 1 in Fig. 2 may be naturally interpreted as coming from the beginning of the collective motion [13]. That is not expected to be significant, being proportional to $|V(R_i)|^2$. In turn, the combined contribution from segments 3 and 4 may be attributed to the point of scission. Furthermore, the contributions from segments 6 and 7 may be ascribed to the pseudocrossing point. Further details of the complex trajectory calculation are presented elsewhere [26].

Contributions from segments 3 and 4 partly cancel one another, being of the opposite sign. Were the scission point a regular point of the trajectory, the cancellation would be complete, and this point would give no contribution to the transition amplitude.

Relative contributions of the scission and pseudocrossing points turn out to be different, depending on the mass split of the fragments. The first contribution is several times smaller than the second one in the case of the most probable mass split. In the case of larger asymmetry, the contribution from scission holds approximately. In contrast, the contribution from the avoided crossing decreases exponentially. For this reason, the attachment probability becomes relatively more sensitive to the prefission scenario for more asymmetric fission, though its absolute value decreases. This circumstance was noted in [18, 22], where a higher sensitivity for larger asymmetry was predicted as a consequence of approaching the pseudocrossing point to the prefission area.

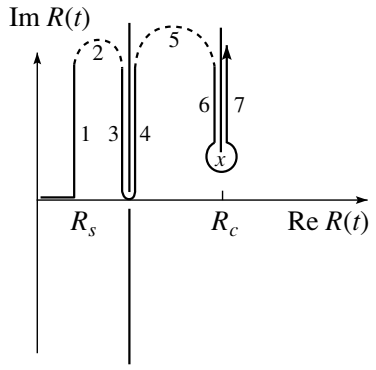

Fig. 2. The complex trajectory. The point $R = 0$ corresponds to the united atom limit. The onset of population of the $2p\sigma$ level is at the saddle point R_s. The scission point R_{sc} and that of avoided crossing R_c are the other singular points, where the integration contour is fixed.

The seeming contradiction of the results noted above concerning sensitivity to the fission dynamics also finds a simple explanation in the complex trajectory approach. The only point that rules the dissipation is the position of R_{sc} in Eq. (3) for the velocity. In [16, 17], all the variations of the prescission time were made with a fixed R_{sc} value and, therefore, with the same velocity at this point. Moreover, this variation was performed for the fragments with usual mass split. In view of what was said previously, no considerable effect should be expected in this case, in agreement with the results obtained.

4. NUMERICAL RESULTS FOR THE FINAL MUON ATTACHMENT PROBABILITIES

The final muon attachment probabilities for various values of the scission point R_{sc} and the TKE of the fragments have been obtained by solving numerically the set of differential Eqs. (1) of [16] in the two-state basis $|1s\sigma\rangle$ and $|2p\sigma\rangle$, with the initial condition (1) at the outer saddle point. Some results of the calculation are listed in the table for representative fission fragments with the most probable charge split, $Z = 52 + 40$, and with a high charge asymmetry, $Z = 57 + 35$. One can see that, as the fission becomes more asymmetric, the related variation of the calculated attachment probability against the position of

Calculated attachment probabilities to the light fragments, W_L (%), for the fragments with the charge numbers $Z_1 = 52$, $Z_2 = 40$

TKE, MeV	R_{sc}, fm				Experiment [19, 20]
	20	22	24	26	
$Z = 52 + 40$	5.11	4.58	4.11	3.94	6.8
$Z = 57 + 35$	0.42	0.25	0.15	0.13	0.56
T_0, MeV	20				

R_{sc} reaches an order of magnitude. The sensitivity to the dynamics thus increases, as expected on the basis of the previous discussion.

Were the values of $V(R) = \text{const}$ used for $R < R_{sc}$ instead of Eq. (3) [24], the variations of W_L against R_{sc} would be still 2–3 times stronger than those in the table. In contrast, the values in the table would remain practically unchanged in the case of usual mass asymmetry $Z_1 = 52$, $Z_2 = 40$. This agrees with the relative contributions of the starting point R_s to the final amplitude, found in the previous section, which turns out to be substantial in the first case and negligible in the second one. This also gives, as noted above, an explanation of the results of [16, 17] where the final transition amplitude has been found to be independent of the fission time t_{sc}. The explanation that the velocity at the scission point in those papers (together with the position of R_{sc}) was not varied. Finally, this is also in accordance with a strong dependence of W_L on the position of the starting point in an example discussed in [16] (see Fig. 3 therein).

5. CONCLUSION

The main results of the present consideration and prospects for further investigation can be formulated as follows.

The muon attachment probability to the light fragments depends on the velocity of the saddle-to-scission descent. This dependence turns out to be relatively more prominent in the case of strongly asymmetric fission. The above arguments founded on the analytical properties of the population amplitudes provide a physical basis for this conclusion. Therefore, a challenging task for experiment is to concentrate efforts on this point and to measure the muon distribution with good accuracy as a function of the atomic number and the TKE of the fragments, paying particular attention to fission with strong mass asymmetry.

ACKNOWLEDGMENTS

I would like to acknowledge fruitful discussions with H.Ye. Belovitzky and D.F. Zaretsky. I would also like to express my gratitude to J. da Providencia and P. David for stimulating interest in the paper. I am grateful to F.B. Malik for fruitful discussions and to M.R. Harston for his help in preparing the manuscript.

The present paper was started within the framework of a fellowship from the Heinrich Hertz Foundation. It was completed through support from the NATO Science Program.

REFERENCES

1. Yu. P. Gangrsky, B. Dalkhsurén, and B. N. Markov, *Nuclear Fission Debris* (Énergoatomizdat, Moscow, 1986).
2. V. A. Rubchenya, these Proceedings.
3. F. Gönnenwein, in *Proceedings of the International Conference on Fission Dynamics in Atomic Clusters and Nuclei, Luso, Portugal, 2000*, Ed. by J. da Providencia, F. B. Malik, F. F. Karpeshin, and D. Brink (Nova Sci., Singapore, 2001).
4. J. A. Wheeler, Phys. Rev. **73**, 1252 (1948).
5. D. F. Zaretsky and V. M. Novikov, Nucl. Phys. **14**, 540 (1959); **28**, 177 (1961).
6. E. Teller and M. S. Weiss, Trans. N. Y. Acad. Sci. **40**, 222 (1980).
7. F. F. Karpeshin and V. O. Nesterenko, J. Phys. G **17**, 705 (1991).
8. Yu. N. Demkov, D. F. Zaretsky, F. F. Karpeshin, *et al.*, Pis'ma Zh. Éksp. Teor. Fiz. **28**, 287 (1978) [JETP Lett. **28**, 263 (1978)].
9. V. A. Karnaukhov, Yad. Fiz. **28**, 319 (1978) [Sov. J. Nucl. Phys. **28**, 621 (1978)].
10. J. A. Maruhn, V. E. Oberacker, and V. Maruhn-Rezwany, Phys. Rev. Lett. **44**, 1576 (1980).
11. P. Leander, S. G. Nilsson, and P. Möller, Phys. Lett. B **90B**, 193 (1980).
12. Z. Y. Ma, X. Z. Wu, G. S. Zhang, *et al.*, Nucl. Phys. A **348**, 446 (1980).
13. F. F. Karpeshin and V. N. Ostrovsky, J. Phys. B **14**, 4513 (1981).
14. Z. Y. Ma, X. Z. Wu, G. S. Zhang, *et al.*, Phys. Lett. B **106B**, 159 (1981).
15. F. F. Karpeshin, M. Kaschiev, and V. A. Kaschiev, Yad. Fiz. **36**, 336 (1982) [Sov. J. Nucl. Phys. **36**, 195 (1982)].
16. F. F. Karpeshin, M. Kaschiev, and V. A. Kaschiev, Yad. Fiz. **45**, 1556 (1987) [Sov. J. Nucl. Phys. **45**, 965 (1987)].
17. L. Bracci and G. Fiorentini, Nucl. Phys. A **423**, 429 (1984).
18. F. F. Karpeshin, J. Phys. G **16**, 1195 (1990).
19. F. Risse, W. Bertl, P. David, *et al.*, Z. Phys. A **339**, 427 (1991).

20. P. David, Ch. Rösel, F. F. Karpeshin, *et al.*, in *Proceedings of the Workshop on Muonic Atoms and Molecules, Monte Verita, Ascona, 1992*.
21. V. E. Oberacker *et al.*, Phys. Lett. B **293**, 270 (1992).
22. F. F. Karpeshin, Yad. Fiz. **55**, 29 (1992) [Sov. J. Nucl. Phys. **22**, 18 (1992)].
23. M. A. Hooshyar and F. B. Malik, Phys. Lett. B **55B**, 144 (1975); I. Reichstein and B. Malik, Ann. Phys. (N.Y.) **98**, 322 (1976).
24. F. F. Karpeshin, Yad. Fiz. **63**, 799 (2000) [Phys. At. Nucl. **63**, 729 (2000)].
25. L. D. Landau and E. M. Lifshitz, *Quantum Mechanics: Non-Relativistic Theory* (Nauka, Moscow, 1989, 4th ed.; Pergamon, London, 1958).
26. F. F. Karpeshin, to be published in Izv. RAN, Ser. Fiz., No. 5 (2003).

Physics of Atomic Nuclei, Vol. 66, No. 6, 2003, pp. 1178–1181. From Yadernaya Fizika, Vol. 66, No. 6, 2003, pp. 1214–1217.

Fission Paths in Fm Region Calculated with the Gogny Forces*

M. Warda[1),2)], J. L. Egido[1)], L. M. Robledo[1)], and K. Pomorski[2),3)]

[1)] *Departamento de Física Teórica, Universidad Autónoma de Madrid, Spain*

[2)] *Katedra Fizyki Teoretycznej, Uniwersytet M. C. Skłodowskiej, Lublin, Poland*

[3)] *IReS–IN_2P_3–CNRS and Université Louis Pasteur, Strasbourg, France*

Received November 22, 2002

Abstract—The fission barriers of the nuclei ^{256}Fm and ^{258}Fm are investigated in a fully microscopic way up to the scission point. The analysis is based on the constrained Hartree–Fock–Bogolyubov theory and Gogny's D1S force. The quadrupole, octupole, and hexadecapole moments, as well as the number of nucleons in the neck region, are used as constraints. Two fission paths, corresponding to bimodal fission, are found. The difference between fission of ^{256}Fm and ^{258}Fm is explained. © *2003 MAIK "Nauka/Interperiodica".*

1. INTRODUCTION

The spontaneous fission of nuclei in the Fm region shows some very interesting features. There is an abrupt transition that occurs from ^{254}Fm to ^{258}Fm in the mass and kinetic energy distributions of the fission fragments as well as in the spontaneous fission half-lives of Fm isotopes (see, e.g., the review articles [1, 2]). The spontaneous fission half-lives of the ^{258}Fm and heavier isotopes decrease relative to ^{256}Fm by several orders of magnitude. Also, the fission-fragment mass distribution changes rapidly from asymmetric for ^{256}Fm to symmetric for ^{258}Fm.

It was found experimentally by Hulet *et al.* [3, 4] that the nucleus ^{258}Fm exhibits bimodal fission with high (230 MeV) and low (205 MeV) components in the total kinetic energy (TKE) yield of the fission fragments. In the both fission modes, the mass distribution is symmetric with a single peak around $A = 128$. On the other hand, the ^{256}Fm isotope exhibits rather strong asymmetry in the fission fragment masses ($A_L/A_H = 112/141$), and only the low energy peak is observed in the TKE distribution.

There is a number of theoretical papers devoted to the bimodal fission of ^{258}Fm (see references in [5]). The majority of them are based on the mean-field single-particle potential and the Strutinsky shell-correction method. Two fission valleys were found on the potential energy surface: one leading to the elongated forms of fission fragments (EF) and the second one corresponding to two nearly spherical fragments, which is usually referred to as the compact fission (CF) valley. These two valleys were identified as the paths leading to the low and to the high TKE modes, respectively.

The fission barrier shapes of the isotopes ^{256}Fm and ^{258}Fm are analyzed in this paper. The results are based on the constrained Hartree–Fock–Bogolyubov (HFB) calculations with the Gogny D1S force.

2. THEORY

The Gogny density-dependent effective nucleon–nucleon forces have been taken in the following form [6]:

$$V_{12} = \sum_{i=1}^{2}(W_i + B_i\hat{P}_\sigma - H_i\hat{P}_\tau - M_i\hat{P}_\sigma\hat{P}_\tau)e^{-\frac{(\mathbf{r}_1-\mathbf{r}_2)^2}{\mu_i^2}} + iW_{\rm LS}(\overleftarrow{\nabla_1 - \nabla_2}) \times \delta(\mathbf{r}_1-\mathbf{r}_2)(\overrightarrow{\nabla_1 - \nabla_2})(\boldsymbol{\sigma}_1+\boldsymbol{\sigma}_2) + t_0(1+x_0\hat{P}_\sigma) \times \delta(\mathbf{r}_1-\mathbf{r}_2)\left[\rho\left(\frac{\mathbf{r}_1+\mathbf{r}_2}{2}\right)\right]^\gamma + V_{\rm C}. \quad (1)$$

We have used the D1S [7, 8] parametrization of the Gogny interaction. The microscopic self-consistent HFB equations have been solved [9] by expanding the quasiparticle creation and annihilation operators in a finite basis of the axially symmetric deformed harmonic oscillator eigenfunctions. The $N_0 = 15$ shells in the direction perpendicular to the symmetry axis and the $N_z = 22$ shells in the z direction were used. This ensures that very elongated shapes which appear during the fission process of the considered nuclei are described with a sufficient accuracy.

*This article was submitted by the authors in English.

1063-7788/03/6606-1178$24.00

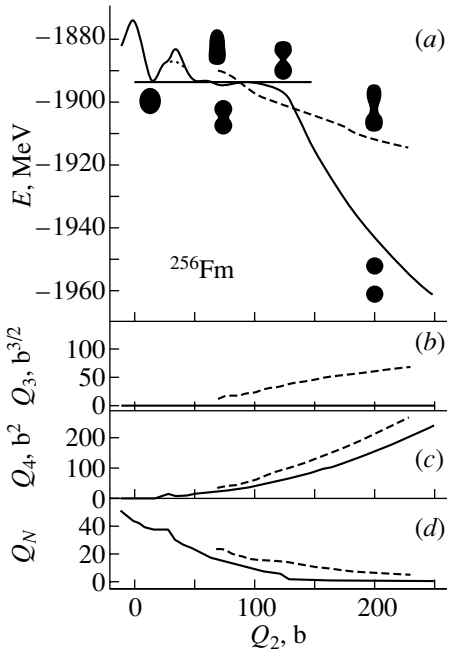

Fig. 1. *(a)* The fission barrier of ^{256}Fm as a function of the axial quadrupole moment Q_2. The solid curve corresponds to the CF path and the dashed curve to the elongated one (EF). The dotted curve shows the reduction of the first barrier due to the nonaxial degrees of freedom. The shapes of the nucleus at density of $\rho_0 = 0.08$ fm^{-3} are depicted for several values of Q_2 for both the CF and the EF path (note that the EF path leads to shapes with octupole deformation). Additionally, in (*b*)–(*d*), the octupole and the hexadecapole moment and the neck parameter Q_N are plotted, respectively.

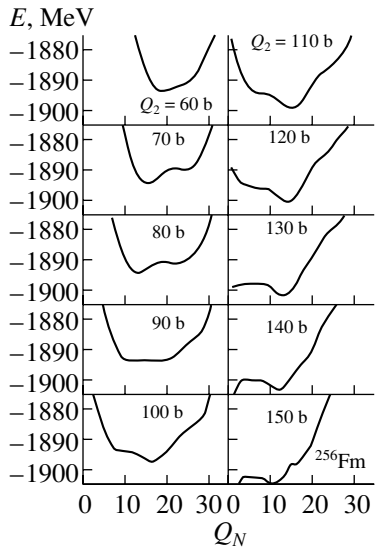

Fig. 2. The cross section of the potential energy surface of ^{256}Fm for different values of Q_2 as a function of the neck parameter Q_N.

In order to study different paths to fission, we have used the following constraints: axial (Q_2) and nonaxial (Q_{22}) quadrupole, octupole (Q_3), and hexadecapole (Q_4) moments as well as the number of nucleons in the neck region (Q_N). The corresponding operators are given by

$$\hat{Q}_\lambda = r^\lambda P_\lambda(\cos(\theta)), \quad \hat{Q}_N = \exp\left(\frac{-z^2}{a_N^2}\right), \quad (2)$$

with $a_N = 1$ fm.

3. RESULTS

The ground states of nuclei in the Fm region are well deformed with the deformation parameter $\beta_2 \approx 0.25$ [5]. Typically the ground-state minimum is separated from the scission point by a barrier that is around 10 MeV high. The fission barriers are decreased by a few MeV as far as triaxial shapes are concerned. It seems that the last effect plays rather a minor role in the spontaneous fission of the nuclei considered; namely, it was found in [10] that the least action trajectory, or, in other words, the dynamical path to fission, leads only through the axially symmetric shapes of the fissioning nucleus. It is due to the increase in the collective inertia with growing nonaxiality that significantly reduces the effect of triaxiality on the fission half-lives. At $Q_2 \approx 50$ b, one can find in Fm nuclei a superdeformed minimum with energy similar to the ground state. This minimum is separated from the scission point by a small second barrier. The shape of this barrier, as will be shown in the following subsections, plays a fundamental role when one evaluates the fission half-lives.

3.1. ^{256}*Fm*

The potential energy obtained for ^{256}Fm [5] is plotted in Fig. 1*a* as a function of the quadrupole moment. The solid curve represents the CF path, whereas the dashed curve shows the EF path. The shapes of the nucleus at some quadrupole deformations are also plotted in this panel. The dotted curve shows the reduction of the first barrier due to the triaxial degrees of freedom (typically, γ does not exceed 8°). This nucleus has two superdeformed minima: one at $Q_2 = 50$ b and another one, separated by a tiny hill, at 70 b. The deeper minimum at $Q_2 = 70$ b is situated 2 MeV below the ground-state energy. The second hump of the barrier is only 2 MeV high in this case. The fission products corresponding to this path are two identical and spherical ^{128}Sn nuclei. In [11], this path was called the CF path. The octupole moment along this path is equal to zero, which can be seen in Fig. 1*b*. It is in contrast to the second path, on which the nucleus has pearlike shapes with nonzero octupole moment. This path, called in [11] the EF path,

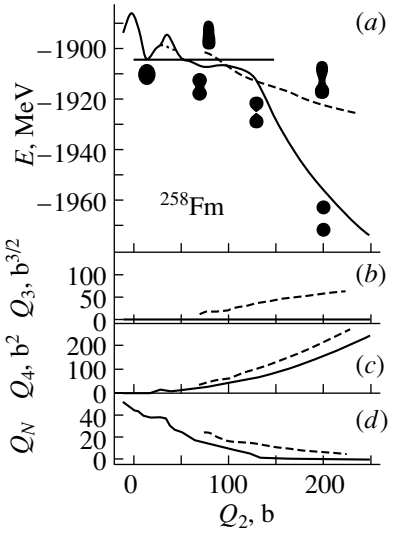

Fig. 3. The same as in Fig. 1, but for the ^{258}Fm nucleus.

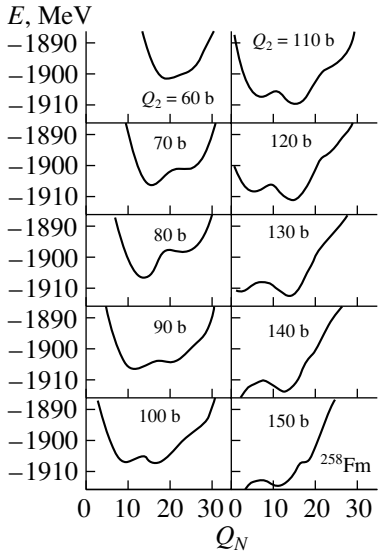

Fig. 4. The same as in Fig. 2, but for the ^{258}Fm nucleus.

begins at $Q_2 = 70$ b and goes with a gentle slope to very high deformations. Both fission paths differ significantly in the hexadecapole moments (Fig. 1*c*) and in the number of nucleons in the neck region (Fig. 1*d*). Apart from the two valleys described above, a few other paths were found. All of them are located much higher in energy than the CF and EF paths, and it is rather improbable that the fissioning nucleus will follow one of them.

The cross sections of the potential energy surface for various quadrupole moments are plotted in Fig. 2 as a function of the neck parameter Q_N. One can see there that the transition from the CF to the EF path cannot take place at $Q_2 < 90$ b because the EF path begins first at $Q_2 = 70$ b on a shoulder 5 MeV above the CF valley. At $Q_2 = 90$ b, the depths of both paths are already comparable and the transition to the EF path can take place here or at higher quadrupole moments, where the minimum corresponding to the CF valley becomes only a shoulder. This means that ^{256}Fm cannot continue fission in the CF mode and it will proceed along the EF path. This effect explains the low TKE of the fission fragments born from this nucleus. The minimum corresponding to the CF valley appears again at $Q_2 = 140$ b, where two fragments are already separated.

At higher elongations, the ^{256}Fm nucleus fissioning along the EF path consists of two parts: one nearly spherical and the other one with a big deformation. Both parts correspond to nearly equal masses. This result is inconsistent with the experimental mass distribution, which shows a significant mass asymmetry: $A_H/A_L \sim 141/112$ [12]. This disagreement may partially originate from the fact that the dynamical effects, which play a certain role in the fission process, are neglected in our static calculations. The other problem is that the neck of the ^{256}Fm nucleus at the EF path is quite long and one cannot determine exactly the point of splitting into two fragments.

3.2. ^{258}*Fm*

The nucleus ^{258}Fm exhibits the bimodal fission [3, 4]. In contrast to ^{256}Fm, mass distributions in both modes are symmetric and both fission paths have similar abundance. In Fig. 3*a*, the CF (solid curve) and the EF (dashed curve) fission barriers are displayed [5]. Figures 3*b*, 3*c*, and 3*d* present the octupole and hexadecapole moments, and the number of nucleons in the neck region Q_N for the two paths. At first glance, this figure is very similar to Fig. 1 for ^{256}Fm, but there are some important differences that change the fission features of these nuclei.

First, the second hump of the fission barrier on the CF path is only 0.5 MeV above the superdeformed minimum and the whole second barrier is placed below the ground-state energy. The next distinction between ^{258}Fm and ^{256}Fm can be observed in Fig. 4. One can see there that both minima corresponding to the CF and to the EF coexist along the fission path. The ridge that separates them is at the most 1.5 MeV high. This means that the nucleus ^{258}Fm could continue fission via the CF valley or change its path and proceed with elongated fission. The transfer to the EF path can take place between $Q_2 = 90$ and 120 b. Such a configuration of the EF and CF paths seems to ensure (because we do not include here the dynamical effects) that both modes can be intensified

similarly. This result is in agreement with the conclusions of [3, 4], where the comparable abundance of the two modes was found.

The shapes of the ^{258}Fm nucleus on both paths are similar to those in Fig. 1 for ^{256}Fm, which explains the symmetric mass distribution observed in both modes. The CF path can be identified as the one leading to the high TKE mode. On this path, the distance between the centers of masses of the spherical fragments at the scission point is relatively small. This means that the Coulomb repulsion is strong and it gives the high value of TKE of fragments. On the EF path, the distance between the centers of charges of the spherical and elongated parts is larger than on the CF path. It means that the energy of Coulomb repulsion at the scission point is weaker and the fragments can have smaller TKE.

4. CONCLUSIONS

In conclusion, one can say that the potential energy surfaces of fissioning even–even nuclei in the ^{258}Fm region are characterized by a two-humped barrier. The first hump is similar for all the nuclei considered, whereas the differences in the second one have a big influence on the fission properties. There are two paths leading to fission. The first one goes through compact shapes and is responsible for the high total kinetic energy mode in fission. The other path, going through elongated shapes, gives the low total kinetic energy mode.

In ^{256}Fm, fission follows only the elongated fission path. The mass asymmetry in this nucleus is not explained by our static calculation. The mechanism of bimodal fission in ^{258}Fm has been described properly: we have found that fission can take place along both elongated and compact fission paths. Contrary to the majority of papers describing the bimodal fission, we have simultaneously reproduced the right distributions of the TKE and the masses of the fission fragments born from ^{258}Fm. We have shown that, in spite of the large asymmetry of shapes of fragments on the EF path, they have the same masses. This is a new feature that could be discovered only in the HFB type of calculations with the Gogny or δ-pairing forces which distinguish between orbitals in different fragments.

ACKNOWLEDGMENTS

This work is partly sponsored by the Spanish Interministerial Commission of Science and Technology, ref. SB99-BA6182184, DGICyT, Spain, under project PB97-0023, and the Polish Committee of Scientific Research, grant no. 2P 03B 115 19.

One of the authors (M.W.) is grateful to the Bogolyubov–Infeld Program for financial support during the VII International School–Seminar on Heavy Ion Physics 2002 in Dubna.

REFERENCES

1. D. C. Hoffman, Nucl. Phys. A **502**, 21c (1989).
2. F. Gönnenwein, Nucl. Phys. A **654**, 855c (1999).
3. E. K. Hulet, J. F. Wild, R. J. Dougan, *et al.*, Phys. Rev. Lett. **56**, 313 (1986).
4. E. K. Hulet, J. F. Wild, R. J. Dougan, *et al.*, Phys. Rev. C **40**, 770 (1989).
5. M. Warda, J. L. Egido, L. M. Robledo, and K. Pomorski, Phys. Rev. C (in press); nucl-th/0203057.
6. J. Dechargé and D. Gogny, Phys. Rev. C **21**, 1568 (1980).
7. J. F. Berger, M. Girod, and D. Gogny, Nucl. Phys. A **428**, 23c (1984).
8. J. F. Berger, M. Girod, and D. Gogny, Comput. Phys. Commun. **63**, 365 (1991).
9. J. L. Egido, L. M. Robledo, and R. R. Chasman, Phys. Lett. B **393**, 13 (1997).
10. A. Baran, K. Pomorski, A. Łukasiak, and A. Sobiczewski, Nucl. Phys. A **361**, 83 (1981).
11. S. Ćwiok, P. Rozmej, A. Sobiczewski, and Z. Patyk, Nucl. Phys. A **491**, 281 (1989).
12. R. Vandenbosch and J. R. Huizenga, *Nuclear Fission* (Academic, New York, 1973).

Physics of Atomic Nuclei, Vol. 66, No. 6, 2003, pp. 1182–1189. From Yadernaya Fizika, Vol. 66, No. 6, 2003, pp. 1218–1225.

Fission Dynamics with the 4π Detector 8πLP*

E. Vardaci[1),2)], A. Brondi[1),2)], G. La Rana[1),2)], R. Moro[1),2)], A. Ordine[2)], A. Boiano[2)], M. A. DiMeo[1),2)], A. Scherillo[1),2)], D. Fabris[3)], M. Lunardon[3)], G. Nebbia[3)], G. Viesti[3)], M. Cinausero[4)], E. Fioretto[4)], G. Prete[4)], N. Gelli[5)], and F. Lucarelli[5)]**

[1)] *Dipartimento di Scienze Fisiche, Università di Napoli "Federico II," Italy*

[2)] *Istituto Nazionale di Fisica Nucleare, Napoli, Italy*

[3)] *Dipartimento di Fisica and Istituto Nazionale di Fisica Nucleare, Padova, Italy*

[4)] *Laboratori Nazionali di Legnaro, Istituto Nazionale di Fisica Nucleare, Legnaro (Padova), Italy*

[5)] *Dipartimento di Fisica and Istituto Nazionale di Fisica Nucleare, Firenze, Italy*

Received December 15, 2002

Abstract—A 4π light charged particle spectrometer, named 8πLP, is in operation at the Laboratori Nazionali di Legnaro (Italy) for the study of the reaction mechanisms produced in low-energy heavy-ion reactions. The spectrometer has recently been used in a study of fission dynamics that involves the detection of light charged particles in the fission and evaporation residue channel in a system of intermediate fissility, as well as in a study of multinucleon transfer to heavy target. Data on the system 240 MeV $^{32}S + {}^{100}Mo$ are presented. Dynamical effects extracted as a consequence of the comparison of the data to the statistical model calculations are discussed. © *2003 MAIK "Nauka/Interperiodica".*

INTRODUCTION

Fission dynamics has been the subject of a large variety of studies in the last two decades [1–16]. As the time scale of fission is thought to be affected by nuclear dissipation [17], the main goal of these studies has been the use of GDR γ rays and light-particle emissions as probes for the dynamical evolution of the composite nuclear system from the equilibrium to the scission point. The presence of dynamical effects in the fission decay is inferred on the basis of the standard statistical model [2]. It is widely found that there exists an energy domain [16] above which multiplicities of neutrons, protons, alpha particles, and GDR γ-rays yields associated to the prescission are underpredicted by the statistical model, and the extent of the gap usually grows with increasing excitation energy.

The overall picture, suggested at first in studies involving only neutron emission [2], is that the collective flow of mass from equilibrium to scission is slowed down by nuclear viscosity in such a way that fission cannot compete effectively in the early stages of the decay with the other open decay channels. Consequently, fission is hindered and particles and GDR γ-ray emissions are more favored than what it is expected from statistical considerations only.

To account for such a delayed fission, several interesting modifications of the statistical model have been proposed in the literature [4, 5, 9, 12, 18, 19]. Following the initial idea of the "neutron clock," the path from equilibrium to the scission point is usually split into two regions, the pre- and the postsaddle. The total fission time is defined as $\tau_f = \tau_d + \tau_{\rm ssc}$, where τ_d is the presaddle delay, namely, the characteristic time necessary for the buildup of the collective motion toward the saddle point, and $\tau_{\rm ssc}$ is the time to travel the path from saddle to scission. The relevant observables are computed using τ_d and $\tau_{\rm ssc}$ as free parameters, along with the other input parameters relative to the specific ingredients of the model (i.e., level density, shell corrections, fission barriers, etc.), and fit to the experimental data. On the basis of systematics [5], it is expected that τ_d is almost constant ($\approx 10 \times 10^{-21}$ s) for a large range of fissility values, while $\tau_{\rm ssc}$ increases linearly from about 3×10^{-21} to 50×10^{-21} s for systems with fissility in the range 0.70–0.85.

Estimates of the fission time scales are, however, still quite controversial, not easily comparable on a common physical ground, and weakened by the fact that different sets of input parameters can result in equally good fits within the same model. Other important open questions remain the delicate and blurred separation between pre- and postsaddle emissions, the change in the strength of the viscosity in the pre-

*This article was submitted by the authors in English.

**e-mail: Emanuele.Vardaci@na.infn.it

and postsaddle, and its dependence on the temperature and deformation [12, 13].

A more complete understanding of the aspects related to the time scale in the fission decay requires the consideration of systems spanning a wide range of fissilities and the use of complementary observables and probes. We have started a research program at LNL with the apparatus 8πLP aimed at studying the fission dynamics in systems of intermediate fissility using light charged particles as probes and the fission dynamics on heavier systems by means of transfer reactions on heavy targets [15]. Since through multinucleon transfer reactions it is possible to populate heavy target-like fragments (TLF) of a wide range of fissility, excitation energy, and angular momentum, the study of the fission probability of the TLF is interesting because it provides a direct measure of the probability of survival of the populated TLF, which is strongly affected by nuclear viscosity. Results on a study of this kind have been published previously in [15].

This paper is organized as follows. First, a short review of the 8πLP apparatus is given. Second, we present the study of the fission time scale in the system $^{32}S + {}^{100}Mo$ at 240 MeV.

THE 8πLP APPARATUS

The 8πLP apparatus [20], shown schematically in Fig. 1, is a light charged particle detector assembly that fulfills the following requirements:

(a) angular coverage close to 4π;

(b) compact and flexible arrangement to accommodate different trigger detectors;

(c) low identification energy thresholds;

(d) high granularity;

(e) measurement of energy of light charged particles from heavy ion reactions up to 20 A MeV of incident energy.

8πLP consists of two detector subsystems, each made of two-stage telescopes: the WALL and the BALL. The WALL contains 116 telescopes and is placed 60 cm from the target. Each of the WALL telescopes consists of a 300-μm Si detector backed by a 15-mm CsI(Tl) crystal and has an active area of 25 cm^2, which corresponds to an angular opening of about 4°. The WALL covers the angular range from 2° to 24°. The BALL has a diameter of 30 cm and consists of seven rings placed coaxially around the beam axis. Each ring contains 18 telescopes and covers an angular opening of about 17°. The telescopes of the BALL are made of a 300-μm Si detector mounted in the flipped configuration (particle entering from the ohmic side) backed by a 5-mm CsI(Tl) crystal. The BALL has a total of 126 telescopes and covers the angular range from 34° to 177°. The rings are labeled from A to G going from backward to forward angles.

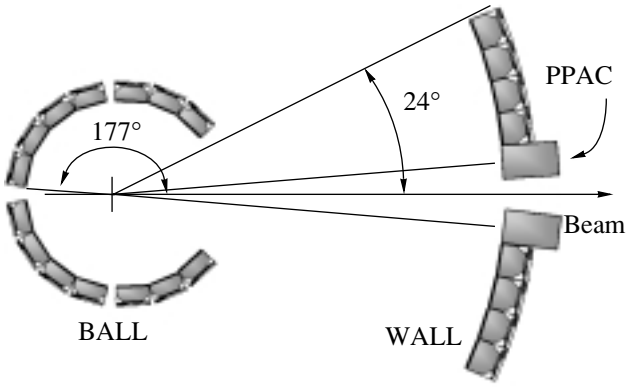

Fig. 1. Schematic layout of the 8πLP apparatus.

Particle identification is carried out by the ΔE–E method for the ions that are not stopped in the ΔE stage. The particles stopping in the first stage are identified by the TOF method in the case of the WALL telescopes and by the pulse shape discrimination (PSD) technique in the case of the BALL telescopes. In this configuration, we are able to measure energies up to 64 A MeV in the WALL and 34 A MeV in the BALL with energy thresholds of 0.5 MeV for protons and 2 MeV for alpha particles.

Heavy fragments can be detected in the telescopes of the BALL. The PSD technique allows the separation between heavy fragments and light particles stopping in the same detector but does not provide any information about the mass or charge of the fragments. The selection between symmetric and asymmetric mass splitting can nevertheless be achieved on a kinematics ground, as will be shown later. A more selective trigger detector based on a MWPC is presently under test and will be installed in the near future.

In the 8πLP setup, it is also possible to detect evaporation residues (ER). The WALL detectors between 2.5° and 7.5° around the beam axis are in fact replaced by four parallel plate avalanche counter (PPAC) modules, each one subtending a solid angle of about 0.3 msr. Each module consists of two coaxial PPACs mounted and operating in the same gas volume at a distance of 15 cm from each other. By adjusting the gas pressure, it is possible to stop the ER between the two PPACs and let the fission fragments and elastic scattered ions impinge on the second PPAC. Consequently, ER are sorted out from the first PPAC signals using the signals from the second PPAC as a veto.

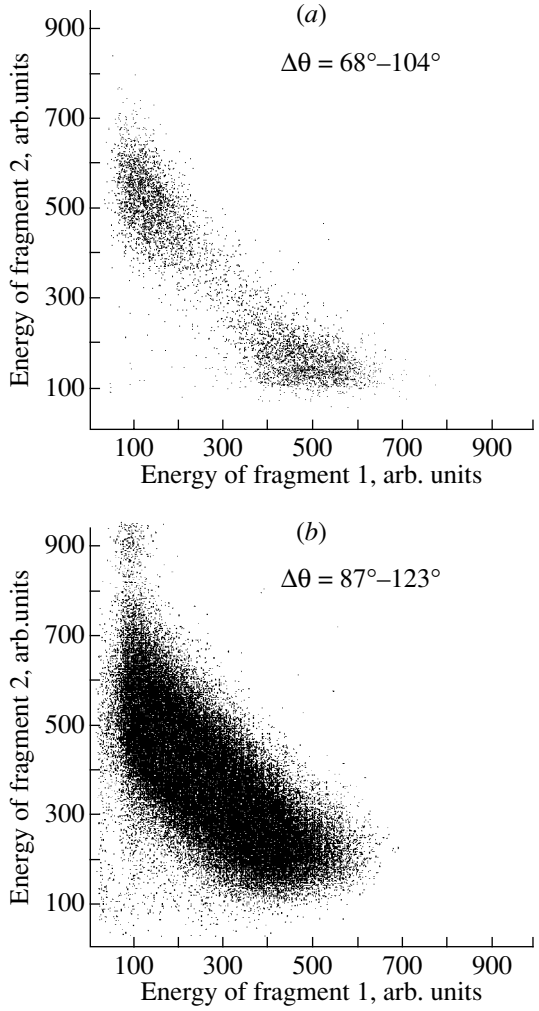

Fig. 2. Energy–energy correlation matrix of the measured fragments: (*a*) both fragments in ring G; (*b*) one fragment in ring F and the other in ring G.

The acquisition system is based on a newly designed readout FAIR bus [21] and is capable of handling the whole set of input signals (about 1000 between energy and time). The on-line analysis of all the default 1D histograms and of about 800 2D matrices is handled by commercial VME CPUs. The whole acquisition system is accessible via Ethernet since is designed on a client/server architecture.

DYNAMICAL EFFECTS IN THE SYSTEM $^{32}S + {}^{100}Mo$ AT 240 MeV

At the moment, there are not many studies on systems of intermediate fissility ($\chi = 0.5$–0.6), although they offer some advantages. These systems are characterized by an ER cross section comparable to or larger than the fission cross section and by a relatively higher probability for charged particle emission in the prescission channel. In a theoretical framework in which time scale estimates rely on statistical model calculations, the additional analysis of particle emission in the ER channel allows one to put more constraints on the statistical model input parameters. Furthermore, light charged particles and, especially, alpha particles are sensitive to the emitter deformation as well as to the yrast line at high-angular momentum. Therefore, clues on the system deformation can be conveniently cumulated with the ones extracted by GDR γ-rays studies [12, 13].

An additional advantage comes from the fact that the potential energy surface is characterized by a shorter path from the saddle to scission [22]. This means that the role of the presaddle dynamics relative to the saddle to scission one is enhanced, and consequently, some of the ambiguities on the not-well-identified separation and interplay between pre- and postsaddle might be reduced in the interpretation of the data.

Recently, the charged particle emission in both evaporation residue and prescission channels has been used to extract the fission delay [23] for the systems 180 MeV $^{32}S + {}^{109}Ag$ [14], 905 MeV $^{121}Sb + {}^{27}Al$ [6], and 247, 337 MeV $^{40}Ar + {}^{nat}Ag$ [1]. A wide interval of time delays was obtained with values ranging from 4 to 27×10^{-21} s.

The experiment on the system $^{32}S + {}^{100}Mo$ at 240 MeV was performed at the XTU Tandem–ALPI Superconducting LINAC accelerator complex of the Laboratori Nazionali di Legnaro. A 240-MeV pulsed beam of ^{32}S of about 1 p nA intensity was used to bombard a self-supporting ^{100}Mo target, 300 $\mu g/cm^2$ thick. A beam burst with frequency of about 1.25 MHz and duration of about 2 ns was used. We took full advantage of the performance of the 8πLP apparatus. Energy spectra of protons and alpha particles, in coincidence with evaporation residues and fission fragments, were measured with low-energy thresholds and with an almost 4π geometry. Heavy fragments were detected in the telescopes of the ring F and G of the BALL, and the ER were detected by the four PPAC modules mentioned earlier.

Data were collected requiring the OR mode between the following conditions: (a) coincidence between any PPAC and any particle detector, to select events corresponding to light particles emitted in the ER channel; (b) twofold event in the F and G ring detectors, to select events with two fission fragments; and (c) coincidence between one detector of the F or G ring and all other particle detectors. During the data taking, the acquisition rate was about 1.5k events per second with dead time of ~15% mainly due to the conversion time and the storage of events on tape. The replay of the data tape, data sorting, and

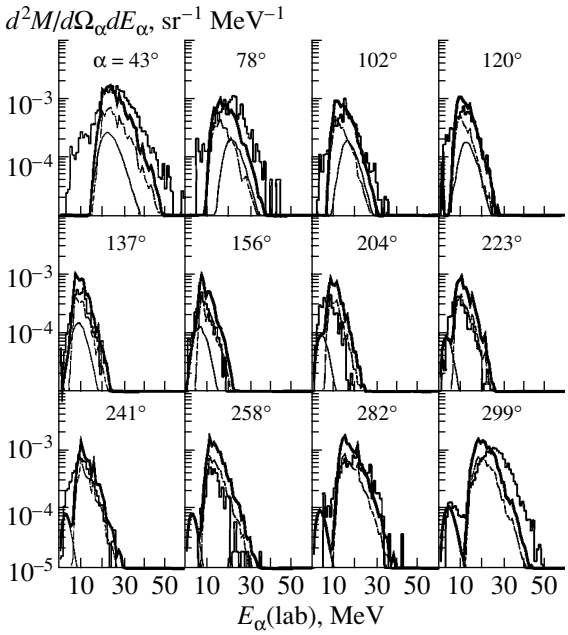

Fig. 3. In-plane ($\beta = 0$) multiplicity spectra of the alpha particles in the fission channel.

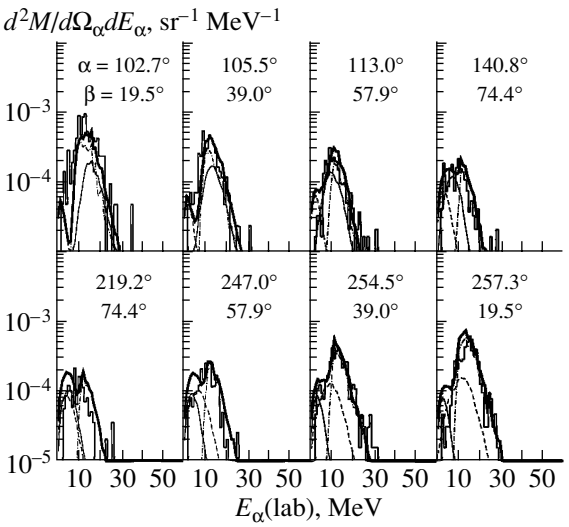

Fig. 4. Out-of-plane multiplicity spectra of the alpha particles in the fission channel (ring D).

analysis were handled by the software package VISM [24].

DATA ANALYSIS

The main goal of the data analysis presented is the extraction of the prescission multiplicity of the alpha particles from which we estimate the fission time scale. Data on proton and alpha particles in the ER channel have also been obtained in order to further constrain the statistical model parameters. Results reported here refer to the data collected by the BALL section of the 8πLP apparatus.

Selection of the Fission Fragments

Fission fragments have been sorted out from the possible binary reaction products by means of the fragment–fragment coincidences. In Figs. 2*a* and 2*b*, we show the fragment–fragment energy correlation of the two fragments detected by two different telescopes in the same ring G and in the rings F–G, respectively. Due to the detector openings, in the first case (ring G only), the measurable folding angle of two fragments can span the range 68°–104°, whereas, in the second case (one fragment in ring F and one in ring G), the range of the possible folding angle can be 87°–123°. The data have been summed over all the combinations of detectors belonging to the ring G (Fig. 2*a*) and to the rings F and G (Fig. 2*b*).

The energy distribution in Fig. 2*a* is compatible with the presence of deep inelastic collisions (DIC), which produces target-like and projectile-like fragments. A simulation of the DIC, performed by the code GANES [25, 26], gives for the folding angle distribution a bell shape centered around 88°, ranging from 75° to 100°. As regards the fission process, the code predicts a bell-shaped distribution centered around 100°, ranging from 90° to 110°. From this simulation and from the pattern observed in Fig. 2, it is clear that the combination of the rings F and G favors the selection of fragments from the symmetric splitting of the intermediate composite system. The events of Fig. 2*b* correspond to an angular range centered around the most probable folding angle for fission, and one can be confident that most of these events are associated with fission fragments. This conclusion is supported by the fact that the multiplicity of pre- and postscission alpha particles, extracted by the procedure described in the following, does not change significantly when the event selection is restricted to the region in which the two fragments have nearly the same energy.

Alpha-Particle Emission in the Fission Channel

Laboratory energy spectra of the alpha particles in triple coincidence (fragment–fragment–particle) were extracted for all the correlation angles allowed by the geometry (12 in plane and 56 out of plane). Some of the multiplicity spectra are shown as histograms in Figs. 3–6. Figure 3 refers to the 12 in-plane angle correlations, while Figs. 4–6 refer to the out-of-plane multiplicity distributions.

The position of each particle detector with respect to the beam has been translated to a position relative to a trigger plane (defined by the position of the

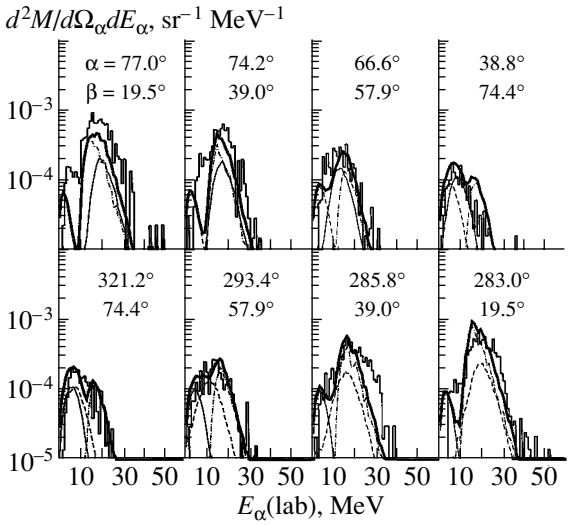

Fig. 5. Out-of-plane multiplicity spectra of the alpha particles in the fission channel (ring E).

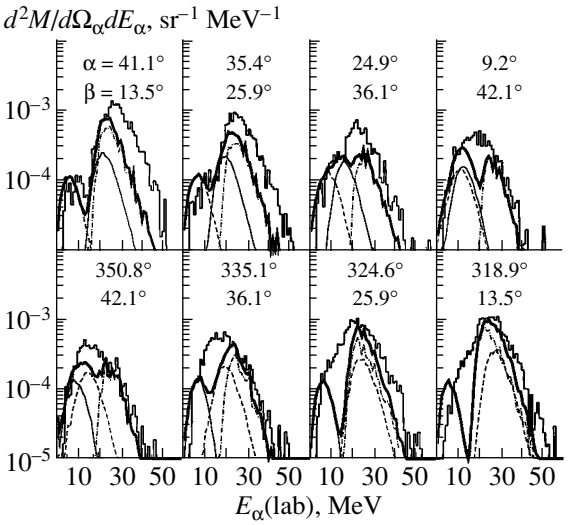

Fig. 6. Out-of-plane multiplicity spectra of the alpha particles in the fission channel (ring G).

two fired fragment detectors) using the in-plane α and the out-of-plane β angles. The values of these angles, ranging from 0° to 360° and from 0° to 90°, respectively, are shown in Figs. 3–6. Rings D and E cover the same out-of-plane angular range, which is the largest with respect to the other rings, and ring G is positioned at the most forward in-plane angles. Each alpha-particle spectrum has been obtained as the sum of the alpha-particle spectra corresponding to the same in-plane and out-of-plane angles and normalized to the number of its corresponding trigger fragment–fragment events.

To extract the pre- and postscission integrated multiplicities, alpha-particle spectra have been analyzed considering three evaporative sources: the composite nucleus prior to scission (CE—composite emission) and the two fully accelerated fission fragments F1 and F2 (FE—fragment emission). We have used a well-established procedure that employs the Monte Carlo statistical code GANES [1, 6, 25, 26]. Alpha-particle evaporative spectra are computed separately for each source of emission in the trigger configuration defined in the experiment, taking into account the detection geometry. Afterward, the calculated spectra are normalized to the experimental ones, and the integrated multiplicities are evaluated for each emitting source.

The curves superimposed on the histograms in Figs. 3–6 represent calculated multiplicity spectra for CE (dash-dotted curves), F1 (thin solid line), and F2 (dashed line) components, along with their sum (thick solid line). A large deformation of the composite system prior to scission was necessary to fit simultaneously the energy spectra and the angular distribution. The deformation of the emitter affects both the mean energy of the evaporated charged particles (because of the change in the evaporation barriers) and the out-of-plane angular distribution (because of the increase in the moment of inertia). In our data, the best fit to the energy spectra provides for the CE component a prolate shape with axis ratio $b/a = 3$. This emitter deformation results in mean energies of the alpha particles that are $\approx$2 MeV lower than those expected for the case of a spherical emitter.

Although the bulk of the experimental spectra is very well reproduced, also considering the wide angular coverage of the detecting array, there are some important deviations that indicate contributions not accounted for by the CE and FE components, which are mainly of two kinds: an excess of high-energy alpha particles at the most forward angles and a surplus of particles with energies intermediate between those corresponding to CE and FE components. These two types of contributions have already been observed in other experiments of the same kind as presented here [1, 6, 14] and have been ascribed to preequilibrium and near-scission emission [27–29], respectively. It is interesting to take advantage of the detailed angular coverage of our data to discuss briefly these observations and give support to the above conclusions.

The in-plane angular distribution in Fig. 3 and the out-of-plane one in ring G (Fig. 6) are most suited to clarify the pattern of the excess at higher energies. In the in-plane spectra (Fig. 3), this excess disappears when going from forward to backward angles; in Fig. 6, the top and bottom rows show clearly the gradual disappearance of the higher energy component when the detection position moves to larger out-of-plane angles. The angular patterns observed in-plane and, more noticeably, out-of-plane are com-

patible with a preequilibrium mechanism of emission strongly related to the entrance channel.

In some of the spectra of ring G (Fig. 6), an excess of particles with energies in between the mean energies corresponding to the CE and FE components is also quite evident. A similar excess is also found in the spectra of ring C (not shown), but not in rings D and E (Figs. 4 and 5), and is partially visible at some angles in the in-plane spectra (Fig. 3).

The angular and energy dependence of such a component is consistent with the well-established pattern for the near-scission emission: enhanced emission at angles perpendicular to the scission axis [27] with energies characteristic of emission barriers lower than those measured in the CE component. This correlation with the scission axis is remarkably evident when we compare the spectrum of ring D (Fig. 4) at $\alpha = 105.5°$ and $\beta = 39.0°$ with the spectrum in ring G (Fig. 6) at $\alpha = 9.2°$ and $\beta = 42.1°$. The first position favors the detection of particles emitted out-of-plane along the direction of the scission axis; the second one favors the detections of particles emitted perpendicularly to the scission axis. In spite of the almost equal out-of-plane angles, we notice a dramatic difference in the intermediate energy component.

From the fit to experimental spectra, alpha-particle multiplicities of 0.040 ± 0.006 and 0.014 ± 0.002, for prescission and postscission emissions, respectively, have been deduced.

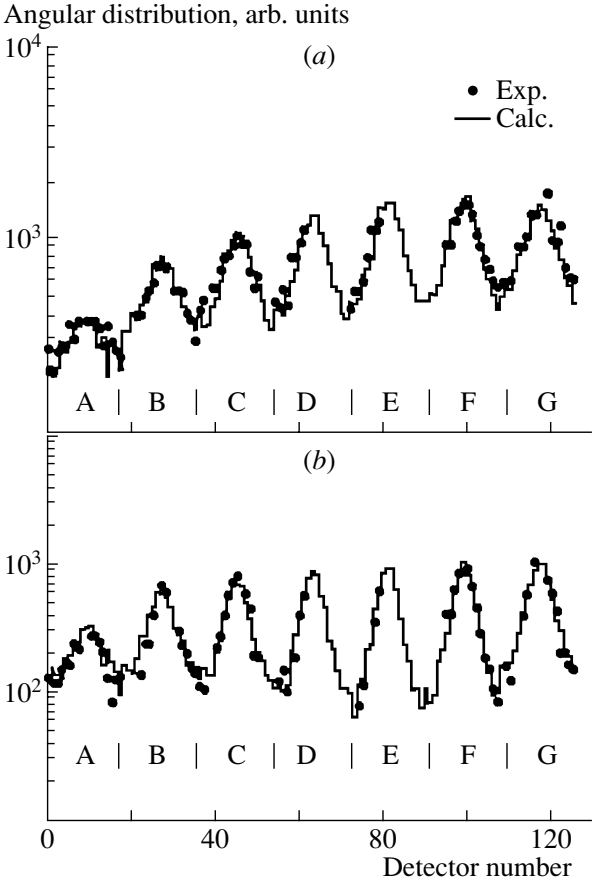

Fig. 7. Yield distribution of the protons (a) and alpha particles (b) in coincidence with the evaporation residues as a function of the BALL detector number. A number has been assigned to each detector of the BALL in order to easily group the detectors by rings.

Evaporation Residue Channel

Evaporation residues were detected by four PPAC modules of the type described earlier. In Fig. 7, we show, as points, the number of protons and alpha particles detected in coincidence with one of the PPAC vs. the identification number of the BALL detectors. The result of the simulation performed with the code PACE 2, in which the detailed geometry of the detecting system has been properly included, is shown as solid lines. For each ring, we observe a strong dependence of the intensity on the detector position resulting from the different correlation angles with respect to the trigger detector, both for protons and alpha particles. The same pattern of Fig. 7 is also observed in the case of the other three trigger positions. The code PACE 2 reproduces very well the observed pattern, independently of the ratio a_f/a_ν parameter, where a_f and a_ν are the level density parameters governing fission and particle evaporation, respectively. This ratio is an input parameter of the statistical model which strongly affects the competition between fusion–fission and fusion–evaporation. Consequently, it is expected that the particle multiplicities in the ER channel show a dependence on the value of the ratio a_f/a_ν.

We have extracted an estimate of the proton-to-alpha particle multiplicity ratio, with the help of statistical model calculations. This also allowed us to optimize the ratio a_f/a_ν needed to analyze the prescission multiplicity. Since the calculations reproduce very well the shape of the angular distributions in Fig. 7, independently of the ratio a_f/a_ν, an estimate of the above multiplicity ratio can be obtained by the code PACE 2, provided that the model is also able to reproduce the absolute values of the measured angular distribution of the two particles with a unique normalizing factor. Such a condition depends strongly upon the ratio a_f/a_ν. It was found that the value $a_f/a_\nu = 1.08$ provides the same normalizing factor within 30% and a multiplicity ratio equal to 1.48. The implications of the use of such a value of a_f/a_ν in the model are discussed in the next section.

Table 1. Calculated alpha particle prescission multiplicities (M_α^{PRE}) for different values of the a_f/a_ν parameter and delay time τ_d

τ_d, 10^{-21} s	a_f/a_ν					
	1.00	1.02	1.04	1.06	1.08	1.10
0	0.049	0.035	0.026	0.019	0.015	0.010
2	0.049	0.043	0.035	0.030	0.030	0.031
4	0.088	0.090	0.096	0.100	0.100	0.110

STATISTICAL MODEL ANALYSIS AND CONCLUSIONS

We have analyzed the prescission alpha-particle multiplicity M_α^{PRE} on the basis of the statistical model as implemented in the code PACE 2. A fission delay time parameter τ_d has been included in the code, so that the fission probability is zero up to the time τ_d and has full statistical value subsequently. Since we expect that the particle multiplicities are sensitive to the value of the ratio a_f/a_ν and to the delay time τ_d, we performed a grid of calculations for $1.00 \le a_f/a_\nu \le 1.10$ and $0 \le \tau_d \le 4 \times 10^{-21}$ s. The results for M_α^{PRE} are given in Table 1. The calculations show that the measured M_α^{PRE} value of 0.040 can be reproduced with $\tau_d = 0$ and $a_f/a_\nu = 1.0$. If we take into account the result of the analysis in the ER channel, we should consider $a_f/a_\nu = 1.08$ and $\tau_d \approx (2\text{–}3) \times 10^{-21}$ s as our optimal delay time. A further increase in τ_d is not compatible with our data because it would produce a rapid increase in M_α^{PRE}.

On the basis of our simple static calculation, we should conclude that there is no evidence of significant dynamical effects in the alpha particle prescission emission in the 240-MeV $^{32}\mathrm{S} + {}^{100}\mathrm{Mo}$ system. However, from the systematics on the threshold excitation energy for the onset of a nonstatistical behavior of the fission decay [16], we would expect a sizable deviation from the statistical description in the prescission particle multiplicities. The extrapolation of the data of [16] to lower composite system masses would give a value of 80 MeV as the threshold energy for our system, to be compared to the excitation energy of 152 MeV in the present experiment.

The same conclusion has been withdrawn for the system of similar fissility Ar + Ag [23], for which measurements exist at two excitation energies, $E_x =$ 128, 194 MeV [1]. Even though these energies are well above the threshold expected on the basis of the predictions in [16], short delay times have been found: $\tau_d = 4$ and 5×10^{-21} s for the two excitation energies, respectively, [23]. It has been argued [1, 23] that, since, in the system Ar + Ag at both energies, the critical angular momentum for fusion is larger than angular momentum l_{Bf} for which the fission barrier vanishes, the presence of fast fission [30] might be responsible for the overall lowering of the measured fission time.

To find out about the presence of fast fission in the system 240 MeV $^{32}\mathrm{S} + {}^{100}\mathrm{Mo}$, we performed calculations of the cross sections for the production of ER, for the fission and fast fission decays, at different incident energies, using the code PACE 2. We used the critical angular momentum for fusion deduced by the Bass model [31] and the value of l_{Bf} from the FRLD model [32]. Results are reported in Table 2.

Taking the values in Table 2 as a guide for our speculation, it seems that, at 240 MeV, fast fission may play a significant role. In fact, the calculated critical angular momentum for fusion is $90\hbar$, which is greater than the angular momentum at which the fission barrier vanishes ($83\hbar$). On the contrary, at 200 MeV, we find the drastic reduction of the fast fission cross section and the increase in the fission and evaporation cross sections. On the basis of these considerations, we have planned an experiment at 200 MeV.

Table 2. Calculated cross sections (in mb) for the $^{32}\mathrm{S} + {}^{100}\mathrm{Mo}$

E_{lab}, MeV	Evaporation	Fission	Fast fission
160	994	32	
170	1010	130	
200	904	353	47
240	779	268	410

REFERENCES

1. R. Lacey, N. N. Ajitanand, J. M. Alexander, *et al.*, Phys. Rev. C **37**, 2540 (1988).
2. D. J. Hinde, D. Hilscher, H. Rossner, *et al.*, Phys. Rev. C **45**, 1229 (1992).
3. H. Ikezoe, Y. Nagame, I. Nishinaka, *et al.*, Phys. Rev. C **49**, 968 (1994).

4. J. P. Lestone, J. R. Leigh, J. O. Newton, *et al.*, Nucl. Phys. A **559**, 277 (1993).
5. A. Saxena, A. Chatterjee, R. Choudhury, *et al.*, Phys. Rev. C **49**, 932 (1994).
6. W. E. Parker, M. Kaplan, D. J. Moses, *et al.*, Nucl. Phys. A **568**, 633 (1994).
7. A. Chatterjee, A. Navin, S. Kailas, *et al.*, Phys. Rev. C **52**, 3167 (1995).
8. L. Fiore, G. D'Erasmo, D. Di Santo, *et al.*, Nucl. Phys. A **620**, 71 (1997).
9. R. Butsch, D. J. Hofman, C. P. Montoya, *et al.*, Phys. Rev. C **44**, 1515 (1991).
10. D. J. Hofman, B. B. Back, and P. Paul, Phys. Rev. C **51**, 2597 (1995).
11. V. A. Rubchenya, A. V. Kuznetsov, W. H. Trzaska, *et al.*, Phys. Rev. C **58**, 1587 (1998) .
12. I. Diószegi, N. P. Shaw, I. Mazumdar, *et al.*, Phys. Rev. C **61**, 24613 (2000).
13. N. P. Shaw, I. Diószegi, I. Mazumdar, *et al.*, Phys. Rev. C **61**, 44612 (2000).
14. E. Vardaci, G. La Rana, A. Brondi, *et al.*, in *Proceedings of the International Conference on Dynamical Aspects of Nuclear Fission, Casta-Papiernicka, Slovak Republic, 1998*, Ed. by Yu. Ts. Oganessian, J. Kliman, and S. Gmuca (World Sci., Singapore, 2000), p. 261.
15. A. Saxena, D. Fabris, G. Prete, *et al.*, Phys. Rev. C **65**, 64601 (2002).
16. M. Thoennessen and G. F. Bertsch, Phys. Rev. Lett. **71**, 4303 (1993).
17. A. Kramer, Physica (Amsterdam) **7**, 284 (1940).
18. V. A. Rubchenya, in *Proceedings of the International Conference "Large-Scale Collective Motion of Atomic Nuclei", Brolo Messina, Italy, 1996*, Ed. by G. Giardina, G. Fazio, and M. Lattuada (World Sci., Singapore, 1997), p. 534.
19. G. Giardina, in *Proceedings of the 6th International School–Seminar on Heavy Ion Physics, Dubna, Russia, 1997*, Ed. by Yu. Ts. Oganessian and R. Kalpakchieva (World Sci., Singapore, 1998), p. 628.
20. E. Fioretto, M. Cinausero, M. Giacchini, *et al.*, IEEE Trans. Nucl. Sci. **44**, 1017 (1997).
21. A. Ordine, A. Boiano, E. Vardaci, *et al.*, IEEE Trans. Nucl. Sci. **45**, 873 (1998).
22. M. G. Itkis and A. Ya. Rusanov, Part. Nucl. **29**, 160 (1998).
23. G. La Rana, E. Vardaci, A. Brondi, *et al.*, in *Proceedings of the International Conference on Nuclear Reaction Mechanisms, Varenna, Italy, 2000.*
24. E. Vardaci, VISM: a Computer Program for Nuclear Data Analysis, *Ann. Rep. Carnegie Mellon University* (Pittsburgh, USA, 1989).
25. N. N. Ajitanand, R. Lacey, G. F. Peaslee, *et al.*, Nucl. Instrum. Methods Phys. Res. A **243**, 111 (1986).
26. N. N. Ajitanand, G. La Rana, R. Lacey, *et al.*, Phys. Rev. C **34**, 877 (1986).
27. E. Duek, N. N. Ajitanand, J. M. Alexander, *et al.*, Phys. Lett. B **131B**, 297 (1983).
28. L. Schad, H. Ho, G.-Y. Fan, *et al.*, Z. Phys. A **318**, 179 (1984).
29. E. Vardaci, M. Kaplan, W. E. Parker, *et al.*, Phys. Lett. B **480**, 239 (2000).
30. C. Ngô, C. Grégoire, B. Remaud, and E. Tomasi, Nucl. Phys. A **400**, 259c (1983).
31. R. Bass, *Nuclear Reactions with Heavy Ions* (Springer-Verlag, New York, 1980).
32. A. J. Sierk, Phys. Rev. C **33**, 2039 (1986).

Physics of Atomic Nuclei, Vol. 66, No. 6, 2003, pp. 1190–1197. From Yadernaya Fizika, Vol. 66, No. 6, 2003, pp. 1226–1233.

Isotopic Invariance of Fission Fragment Charge Distributions for Actinide Nuclei at Excitation Energies above 10 MeV*

D. M. Gorodisskiy, S. I. Mulgin, A. Ya. Rusanov, and S. V. Zhdanov**

Institute of Nuclear Physics, National Nuclear Center, Almaty, Kazakhstan

Received August 28, 2002

Abstract—The fragment mass and energy distributions from the proton-induced fission of compound nuclei ^{233}Pa, ^{234,236,237,239}Np, ^{239,240,241,243}Am, and ^{245}Bk at proton energy $E_p = 10.3$ and 22.0 MeV have been experimentally studied. It was revealed that the shapes of the asymmetric fission mass distributions are mainly defined by the proton numbers of compound nuclei and demonstrate only a weak dependence on the neutron ones. The detailed study of the fission fragment mass yields for compound nuclei Np and Am isotopic chains has shown that the asymmetric fission fragment charge distributions calculated within the unchanged charge density hypothesis for nuclei with equal Z_C practically coincide. © *2003 MAIK "Nauka/Interperiodica".*

1. INTRODUCTION

It is common knowledge that the fragment mass yields from the low-energy-particle-induced fission of actinide nuclei are asymmetric due to the shell properties of fissile nuclei. Numerous experimental investigations of actinide nuclei fission showed that shapes of the fragment mass yield curves can change drastically as a function of the nucleonic composition and excitation energy of fissioning nuclei. A wide variety of mass yield shapes can be explained within a multimodal approach to describing the fragment mass and energy distributions (MEDs) [1–5]. In the framework of this approach, it is usually assumed that an experimentally observed MED consists of different MEDs of four independent fission modes: one symmetric (S) and three asymmetric—Standard 1 ($S1$), Standard 2 ($S2$), and Standard 3 ($S3$). Mode S is mainly formed by liquid drop properties of nuclear matter, and, therefore, its most probable values of fragment masses M are close to $A/2$. Asymmetric mode $S1$ with average masses of heavy fragments $M_H \approx 134$ and high kinetic energies is conditioned by the formation of spherical heavy fragments with Z_{FH} and N_{FH} close to magic numbers 50 and 82, accordingly. Mode $S3$ is also due to the spherical shell closures $Z = 28$ and $N = 50$ but formed in light fragments.

The origin of predominant asymmetric mode $S2$ is usually associated with the deformed neutron shell closure $N \approx 88$ [6] in heavy fragments. However, the attempts (for example, [6, 7]) to describe the experimental fragment mass yields for actinide nuclei in a large range of their nucleonic composition by using the shell $N \approx 88$ properties did not remove all doubts about the validity of such an explanation of the origin of this predominant part of the asymmetric fission.

We supposed that a comparative analysis of fragment mass yields from fission of nuclei with equal Z_C, but different N_C, and vice versa, i.e., for isotopic and isotonic nuclear chains, could help to answer the question about the origin of the asymmetric modes.

2. EXPERIMENT

The fragment MEDs from the proton-induced fission of compound nuclei ^{233}Pa, ^{234,236,237,239}Np, ^{239,240,241,243}Am, and ^{245}Bk at proton energy $E_p =$ 10.3 and 22.0 MeV have been measured with the external proton beams from the Almaty isochronous cyclotron. Targets from chlorides of enriched isotopes with thickness of working layers 20–40 μg/cm^2 evaporated on backings from Al_2O_3 with thickness 60 μg/cm^2 have been used. The measurements were fulfilled by fast spectrometry and timing of the pulses from a pair of Si–Au surface-barrier detectors with the subsequent "time-of-flight" selection of fragments belonging to one fission event [8, 9]. The detectors were calibrated with the ^{252}Cf spontaneous fission fragment spectra [10], and the MEDs were calculated from the measured pulse distributions according to a standard procedure [11]. Since experimental information on the pre- and postfission neutron emission numbers for the majority of the reactions studied here is absent, corrections for the

*This article was submitted by the authors in English.

** e-mail: zhdanov@inp.kz

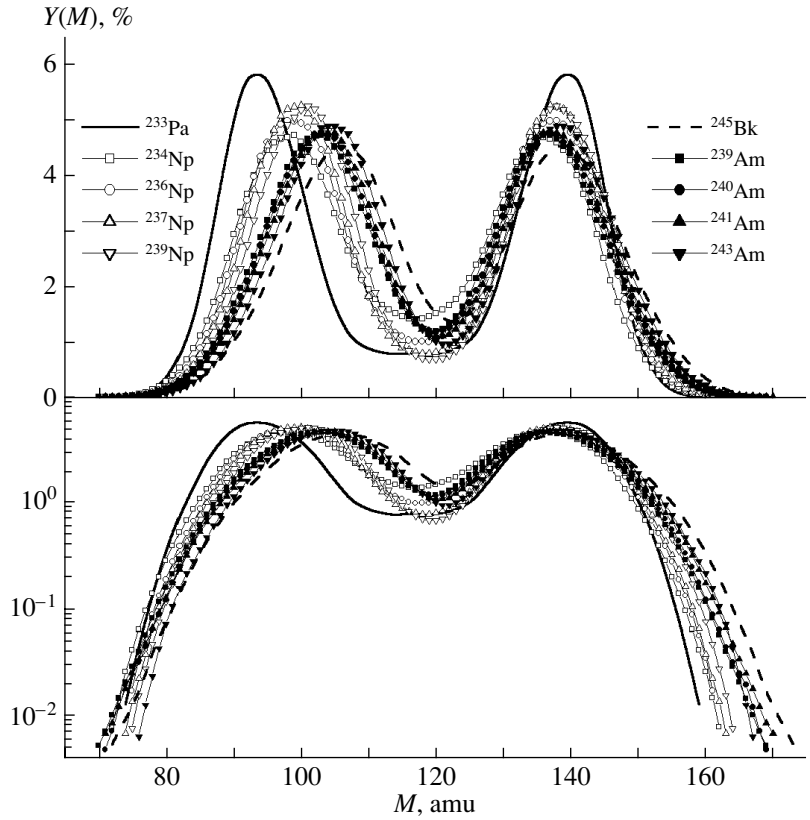

Fig. 1. The fragment mass yields $Y(M)$ measured at $E_p = 10.3$ MeV.

neutron emission have not been introduced. However, as will be shown below, this does not influence the effects being discussed, since, for our comparative analysis, only the differences in the neutron emission numbers are significant, but not their absolute values.

Thus, in the present work, the desired set of MEDs for ten actinide compound nuclei including two isotopic chains with $Z_C = 93$, 95 (^{234,236,237,239}Np and ^{239,240,241,243}Am), three isotonic pairs with $N_C =$ 144, 146, 148 (^{237}Np–^{239}Am, ^{239}Np–^{241}Am, ^{243}Am–^{245}Bk), and ^{233}Pa, as well, has been obtained.

3. RESULTS AND DISCUSSION

The experimental fragment mass yields $Y(M)$ measured at a proton energy of 10.3 MeV are shown in Fig. 1 on linear (upper part) and logarithmic (lower part) scales. One can see that, for all studied compound nuclei, the contribution of symmetric fission is rather small, and the shapes of the MEDs are mainly defined by shell effects responsible for the formation of asymmetric fission. The heavy fragment mass yield curves, in accordance with well-known fact, are similar for all studied nuclei, and the maximal yield values are achieved at $M_H \approx 140$. For nuclei with higher asymmetric peaks, the contributions of symmetric fission are lower.

From Fig. 1, one can note that, whereas on the right wings of heavy fragments the mass yields diverge, on the left wings of light fragments all measured yields virtually converge at masses $M_L \approx 80$. The character of the yield curve divergence at masses $M_H > 155$ is also of interest. One can see that, for nuclei from the Np and Am isotopic chains, the difference in the compound neutron numbers N_C (4–5 u) results in the shifts of equal yields along the fragment mass axis less than the difference in the compound atomic numbers Z_C (2 u). Almost the same situation could be observed in the light fragment asymmetric peak positions. The Z_C dependence of the peak positions is stronger than the dependence on N_C. Some effect of grouping of the yield curves could be seen on the left and right slopes of the light fragment yields for the Np and Am isotopic chains. These findings allow one to conclude that, at excitation energies above 10 MeV, the Z_C dependence of the fragment mass distributions is stronger than the N_C dependence.

In order to study both of these dependences in more detail, we converted the experimental mass yields $Y(M)$ into the yields of the fragment proton $Y(Z_F)$ and neutron $Y(N_F)$ numbers. We used the unchanged charge density (UCD) hypothesis within which the proton and neutron numbers of fragments

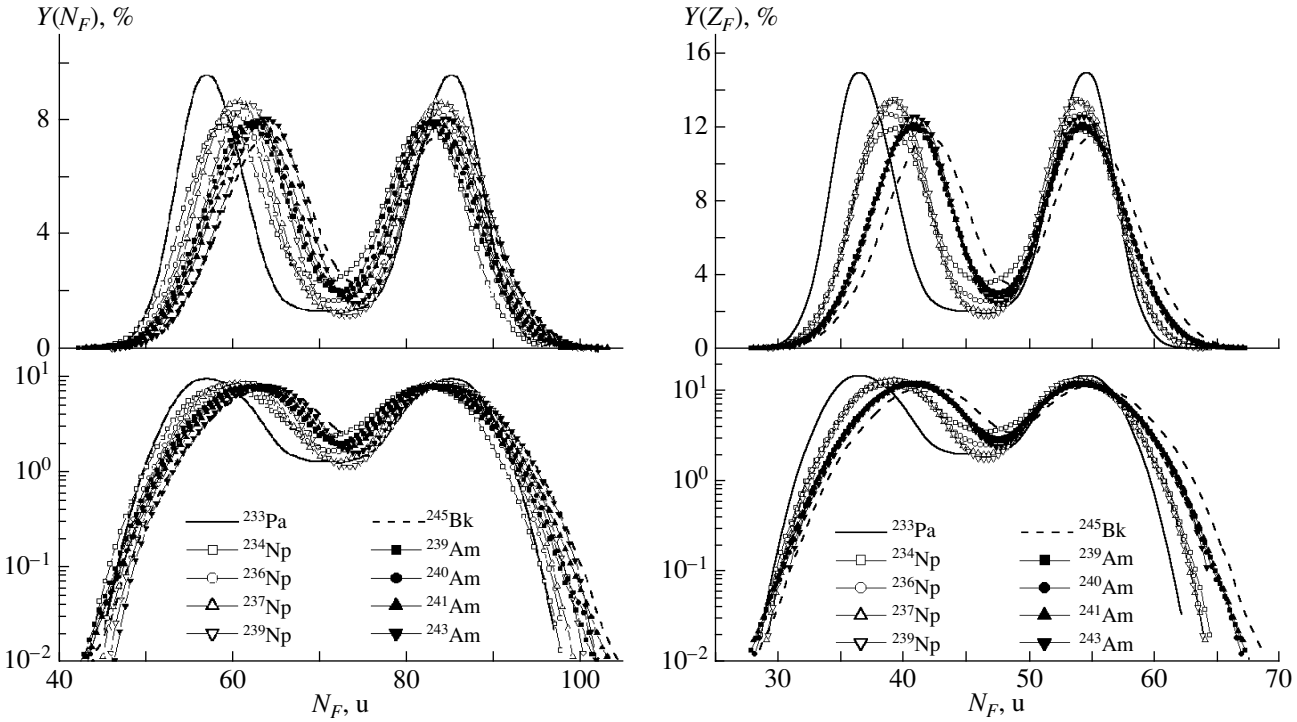

Fig. 2. The UCD fragment neutron $Y(N_F)$ and proton $Y(Z_F)$ number distributions at $E_p = 10.3$ MeV.

are defined by the relations $Z_F = M^*(Z_C/A_C)$ and $N_F = M^*(N_C/A_C)$.

The yields of the fragment proton $Y(Z_F)$ and neutron $Y(N_F)$ numbers for the 10.3-MeV reactions are presented in Fig. 2 on linear (upper parts) and logarithmic (lower parts) scales. One can see that, at the transition from $Y(M)$ to $Y(N_F)$ (left parts), the grouping effect of fragment yields from fission of isotopes belonging to either Np or Am chains practically disappears. A radically different situation takes place at the transition to $Y(Z_F)$ (right parts), for which this grouping effect becomes definite.

This interesting finding can be confirmed by comparing our calculated $Y(Z_F)$ for the Np and Am isotopic chains to the results of direct measurements of fragment charge distributions from fission of ^{229,230,231,232}Pa, for which the numerical data have been taken from [12]. This comparison has been done in Fig. 3. One can see that the behavior of these three isotopic groups of yields is very similar, and the small divergences in $Y(Z_F)$ for the isotopes at $Z_F \approx Z_C/2$ and on tops of the asymmetric peaks seem to be due to the differences in the symmetric fission contributions and do not change the picture as a whole. Incidentally, we may conclude that, in the present work, the use of both the experimental data on yields of the provisional fragment masses without corrections for postfission neutron emission and the UCD hypothesis for calculating fragment proton and neutron numbers is quite acceptable.

In order to study the yield grouping effect found in asymmetric fission in more detail, we subtracted the contributions of the symmetric fission from the experimental mass yields. This was done on the basis of decomposing the experimental matrices of mass and total kinetic energies of coincident fragments $N(M, E_k)$ on the matrices for independent modes $S1$, $S2$, $S3$, and S in the framework of the multimodal analysis method proposed in [13]. After the decomposition, the matrix for symmetric mode S was subtracted from the experimental one, and the fragment mass, charge, and neutron number distributions for the "pure" asymmetric fission were calculated.

In Fig. 4, the widths of the asymmetric mass peaks from fission of all nuclei studied in reactions with 10.3-MeV protons are shown as a function of the compound nuclei masses A_C. Lines represent values of $\sigma^2_{M,a}$ averaged over the nuclei from one (Np or Am) isotopic chain. It can easily be seen that the increase in Z_C by 2 u results in rather significant ($\sim$10 amu^2) growth of $\sigma^2_{M,a}$, whereas, for the increase in N_C by 4–5 u, the values of $\sigma^2_{M,a}$ for the Np and Am nuclei stay approximately constant. In other words, the widths of the asymmetric peaks strongly depend on Z_C and are practically independent of N_C.

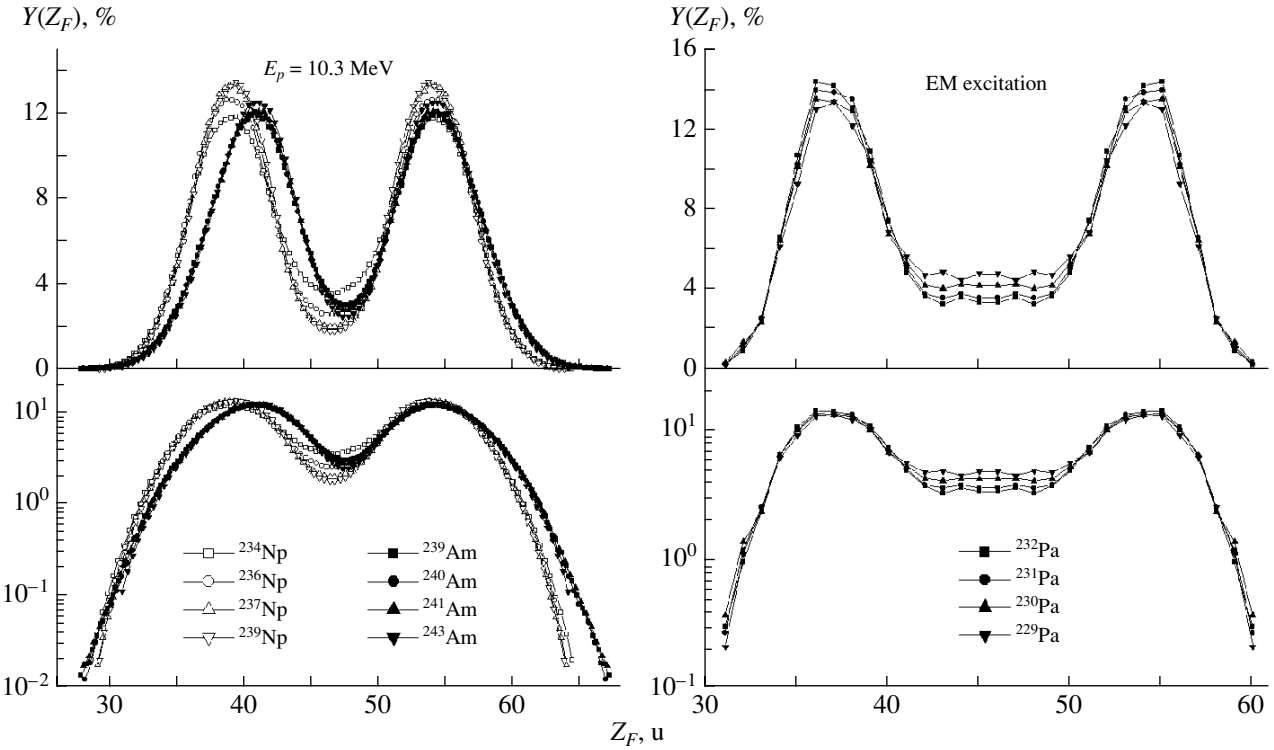

Fig. 3. The UCD fragment proton number distributions $Y(Z_F)$ at $E_p = 10.3$ MeV for compound nuclei from the Np and Am isotopic chains and the experimental fragment charge distributions from the electromagnetic-induced fission of ^{229,230,231,232}Pa taken from [12].

In Figs. 5 and 6, the fragment neutron $Y_a(N_F)$ and proton $Y_a(Z_F)$ number distributions for the "pure" asymmetric fission at $E_p = 10.3$ and 22.0 MeV are given on linear (upper part) and logarithmic scales. It is clearly seen that the $Y_a(Z_F)$ curves for all studied nuclei virtually coincide both for light fragments with $Z_F \approx 30$, which is rather close to magic number $N = 28$, and for heavy fragments with $Z_F \approx 50$ (see arrows). Roughly speaking, the mass distributions for actinide nuclei are packed between fragments with $Z_{\mathrm{FL}} \approx 28$ and $Z_{\mathrm{FH}} \approx 50$, and, therefore, the widths of these distributions are mainly defined by the value $\Delta Z \sim Z_C$ (28–50), almost independently of N_C. Recently, this global yield grouping effect was revealed in [14, 15] in thermal-neutron-induced fission of actinide nuclei. In those works, this effect was interpreted as a manifestation of the determinative influence of spherical shell closures formed in light and heavy fragments on the wings of the fragment mass yields.

In addition, in both Figs. 5 and 6, the $Y_a(Z_F)$ curves for isotopes from the Np and Am chains coincide with good accuracy in the whole range of Z_F. Contrary to the global and isotopic grouping effects clearly seen in $Y_a(Z_F)$, the $Y_a(N_F)$ curves do not demonstrate any visible coincidences of the yield values, including in the vicinities of magic neutron numbers 50 and 82 marked in these figures with arrows.

The difference in the influence of fragment proton and neutron numbers on the shapes of $Y_a(Z_F)$ and $Y_a(N_F)$ is shown in more detail in Fig. 7, where these yields from fission of ^{237,239}Np and ^{239,241}Am at $E_p = 10.3$ MeV are presented. This set of compound nuclei consists of two isotopic ($Z_C = 93, 95$) and two isotonic ($N_C = 144, 146$) pairs. Whereas the charge yields inside both isotopic pairs practically coincide in the whole range of fragment proton numbers, the

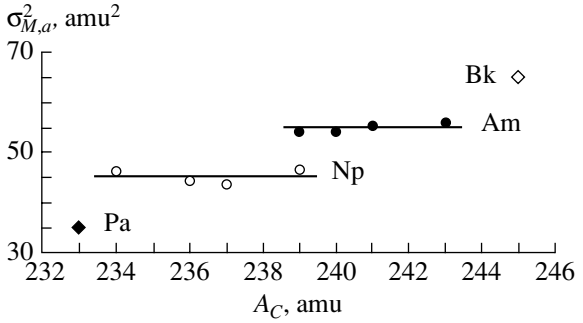

Fig. 4. The dispersions $\sigma^2_{M,a}$ of the asymmetric fission fragment mass distributions at $E_p = 10.3$ MeV as a function of the compound nucleus masses A_C.

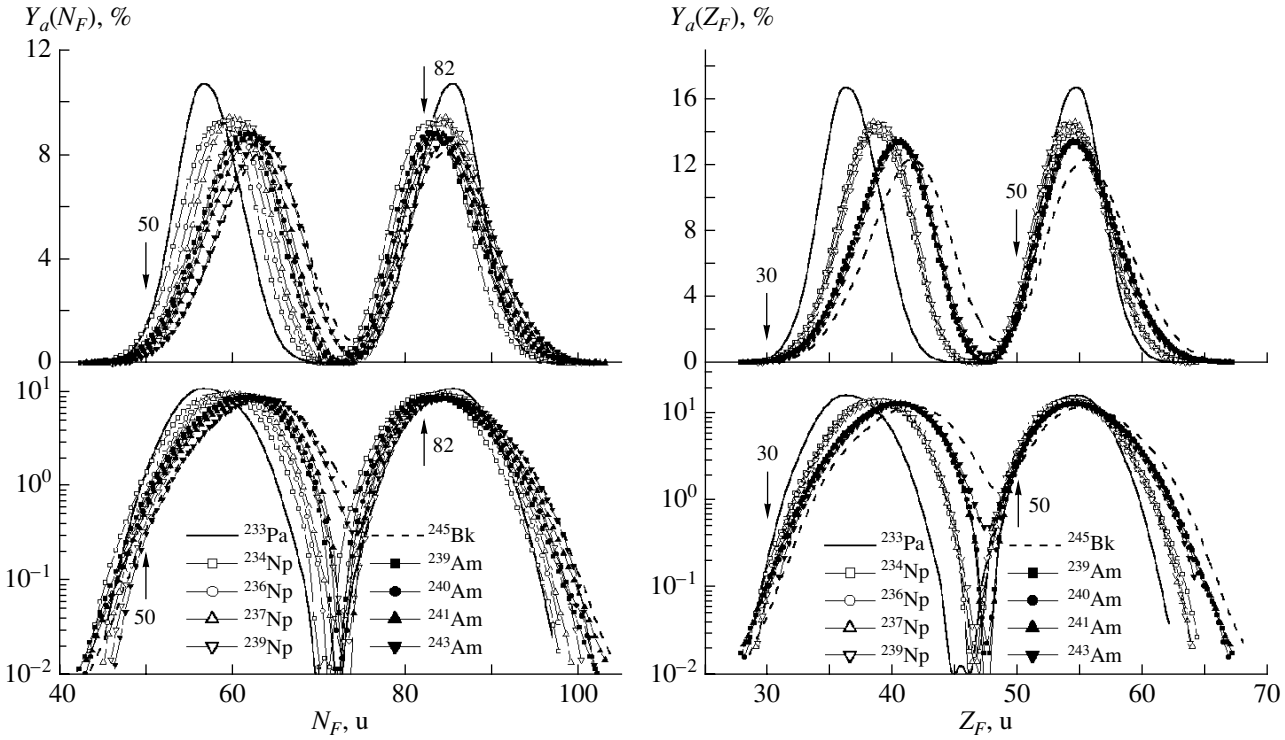

Fig. 5. The UCD fragment neutron $Y_a(N_F)$ and proton $Y_a(Z_F)$ number distributions from asymmetric fission at $E_p =$ 10.3 MeV.

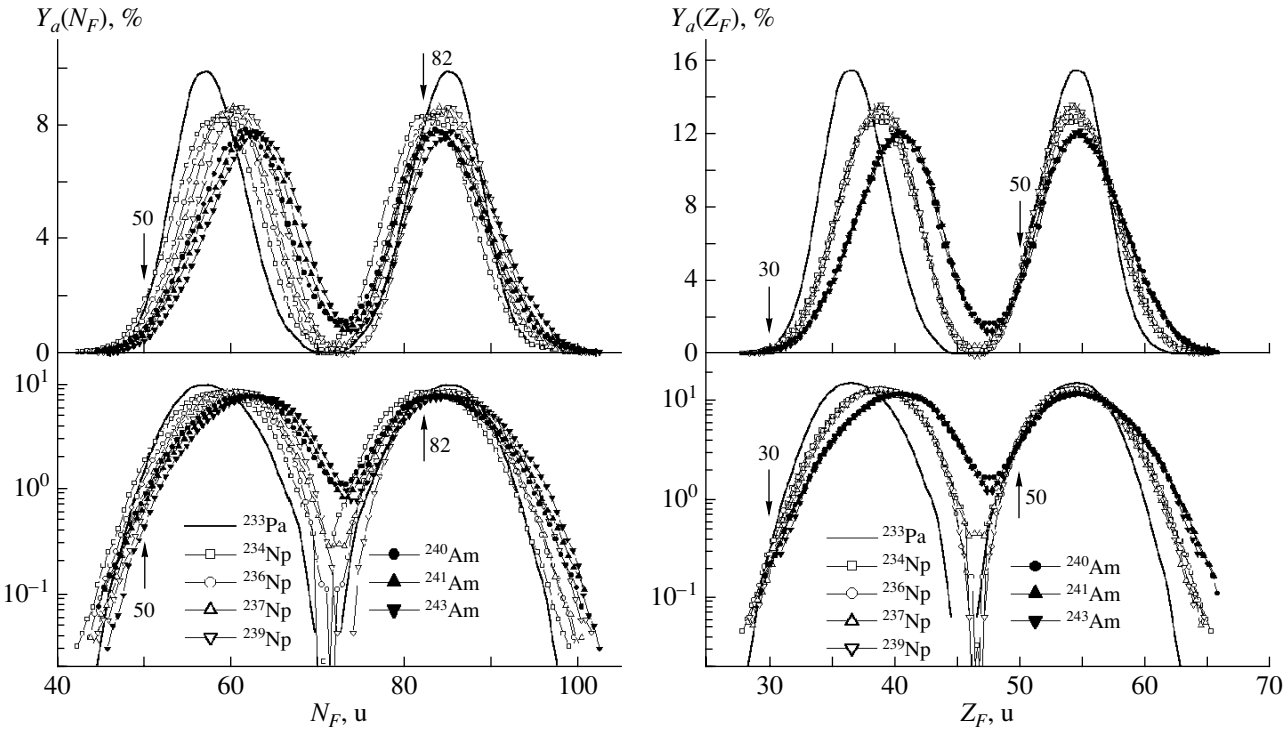

Fig. 6. The UCD fragment neutron $Y_a(N_F)$ and proton $Y_a(Z_F)$ number distributions from asymmetric fission at $E_p =$ 22.0 MeV.

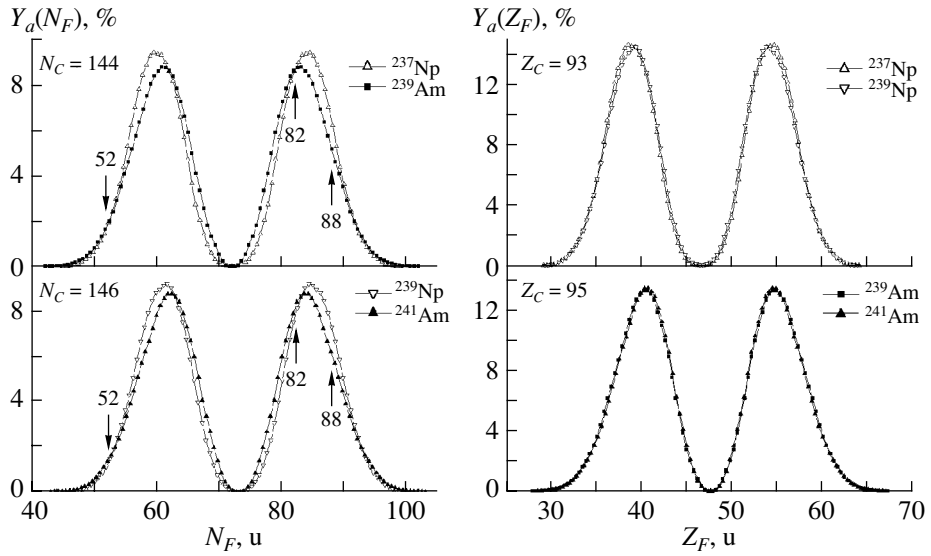

Fig. 7. The UCD fragment neutron $Y_a(N_F)$ and proton $Y_a(Z_F)$ number distributions from asymmetric fission at $E_p = 10.3$ MeV for the isotopic $Z_C = 93, 95$ and isotonic $N_C = 144, 146$ pairs.

$Y_a(N_F)$ curves for both these isotonic pairs coincide only in narrow vicinities of neutron numbers 52 and 82. In other areas of fragment neutron numbers, the difference in the yields is rather substantial, including in the vicinity of $N = 88$ (dashed arrows). As was mentioned above, the deformed neutron shell 88 is usually involved in attempts to explain the properties of predominant asymmetric mode $S2$. But if that is the case, one could expect to see some stabilizing influence of this shell on the positions and/or shapes of the heavy fragment asymmetric distributions, at least for nuclei with equal N_C. Instead, we observe very strong stabilizing effects in $Y_a(Z_F)$ for nuclei with equal Z_C.

Thus, resuming all considerations mentioned above, one may conclude that, at excitation energies above 10 MeV, the asymmetric fission mass distributions are governed by proton shell closures.

In our opinion, both revealed grouping effects, namely, the virtual coincidence of the charge yields at their left light and heavy wings for all studied nuclei as well as the isotopic invariance in the asymmetric fission fragment yields, would agree to the dumbbell prescission configuration concept discussed in [16, 17] if one supposes that this configuration is conditioned by two proton spherical clusters with $Z = 28$, 50 and the corresponding number of neutrons joined by an elongated variable cross section neck formed by the remaining nucleons. Then, the prescission configurations of all nuclides from the actinide region differ, in principle, only in the neck volume. For all compound nuclei, the appearance of light fission fragments with $Z_F < 28$ and heavy ones with $Z_F < 50$ requires one to destroy these very stable spherical shell closures that must lead to common limitations for all nuclei of the Z_F region available for asymmetric fission. For nuclei from one isotopic chain, the spatial distributions of protons in the prescission configuration should be similar, and, therefore, one can expect the similarity in the distributions of the neck rupture probability along the nucleus elongation axis that leads to the observed grouping effect in the fragment charge yields of isotopes. Thus, this dumbbell prescission configuration concept could be useful for qualitative explanation of some features of asymmetric fission. However, we should note that these notions do not explain the experimental fact that, in the asymmetric fission of actinides, the most probable Z_{FH} approximately equals 54 [18].

We would like to note that all effects discussed above reflect the commonality in properties of fragment yields from asymmetric fission as a whole. At the same time, as was mentioned above, the MEDs of asymmetric fission can be performed as a superposition of several independent fission modes ($S1$, $S2$, and $S3$). At first sight, these two notions about asymmetric fission formation are hardly compatible. Indeed, if the origin of high-energy mode $S1$ with heavy fragment masses close to $M_H = 132$ is obviously associated with the formation of fragments close to doubly magic ^{132}Sn, the assumption that predominant mode $S2$ is also due to the same heavy cluster is not so clear.

Some indications in favor of this assumption can be obtained from [13, 19], where it was shown that, at excitation energies of compound nuclei above 10 MeV, the contribution of mode $S1$ is not too big ($\sim$10%), and $Y_{S1}(M)$, even at its maximum at

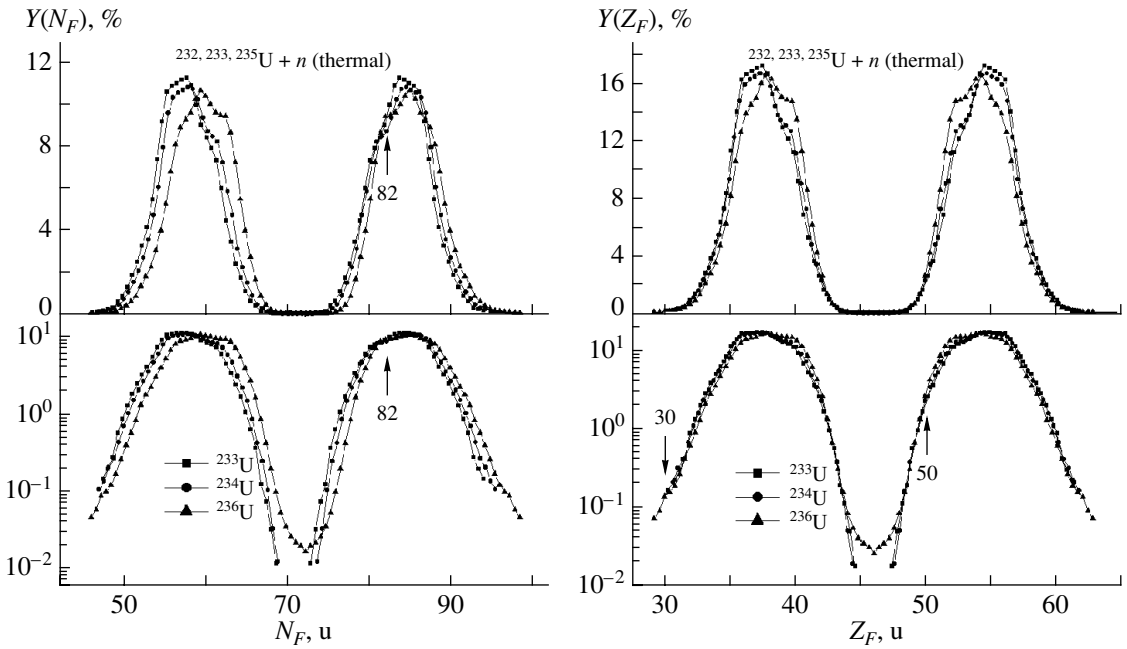

Fig. 8. The UCD fragment neutron $Y(N_F)$ and proton $Y(Z_F)$ number distributions from the thermal-neutron-induced fission of ^{232,233,235}U. The experimental data on the fragment mass distributions have been borrowed from [8, 22].

$M_H \approx 134$, does not exceed 30% of $Y_a(M)$. This means that the grouping of $Y_a(M_H)$ at $Z_{\rm FH} = 50$ is mainly due to mode $S2$.

Additional arguments in favor of both $S1$ and $S2$ being generated by the same shell closures can be obtained from new results of our multicomponent analysis of these MEDs [20]. According to these results, there are strong correlations in the behavior of the basic characteristics of modes $S1$ and $S2$ (contributions, average masses, and mass yield widths) as a function of the nucleonic composition and excitation energies of fissioning nuclei.

For large mass asymmetry, according to [13], in mass yields of light fragments with $M_L \approx 83$, one also can observe the appearance of high-energy mode $S3$ associated with the closeness of these light fragments to doubly magic nucleus ^{78}Ni.

Hence, one can suppose that, in actinide nucleus fission, two main types of nucleus configurations are realized: a strongly deformed one inherent in mode S and the dumbbell configuration responsible for asymmetric fission as a whole. The maximal probability of this asymmetric configuration rupture corresponds to $Z_{\rm FH} \approx 54$ (due to some not quite clear reasons) and the relatively late descent stage of the fissioning nucleus (mode $S2$). At earlier stages, there is some probability of the neck rupture close to either heavy or light clusters that could explain the appearance of high-energy modes $S1$ and $S3$.

We should especially note that the conclusions discussed above have been made from the data obtained at excitation energies $E \geq 10$ MeV. In the spontaneous fission of Pu isotopes at the transition from ^{236}Pu to ^{244}Pu [21], strong alterations of shapes of the mass yields have been observed, and, therefore, corresponding charge distributions also strongly depend on N_C. Our analysis of the data on the thermal-neutron-induced fission of ^{232,233,235}U borrowed from [8, 22] (see Fig. 8) has shown that the UCD charge distributions $Y(Z_F)$ for these nuclei coincide only on their wings, but in the yield maxima, significant deviations are observed. At the same time, the UCD fragment neutron number distributions diverge on their wings, but the distinctions of $Y(N_F)$ in the vicinities of their tops are smaller than that of $Y(Z_F)$. Thus, one can suppose that, in the cold and low-energy fission of actinides, the shapes of the asymmetric fission fragment distributions are governed by both proton and neutron shell closures. But why does even a modest increase in excitation energy of the fissioning nucleus from 6 to about 10 MeV lead to such a significant decrease in the neutron shell influence, whereas that of proton ones remains visible at much higher energies? In our opinion, it is worth additional experimental and theoretical efforts to answer this question.

4. CONCLUSIONS

(i) At excitation energies above 10 MeV, the widths of the asymmetric fission mass distributions

are strongly dependent on the proton numbers of compound actinide nuclei and practically independent of the neutron ones.

(ii) The asymmetric fission fragment charge distributions for nuclei with equal Z_C practically coincide, which is conditioned by the determinative role of proton shell closures in the formation of asymmetric fission fragment yields.

(iii) A sharply expressed grouping of the asymmetric fission charge yields at $Z_{\mathrm{FH}} \approx 50$ in heavy fragments and at $Z_{\mathrm{FL}} \approx 30$ in light ones has been observed.

(iv) The observed features agree with the well-known "dumbbell" scission configuration concept if one assumes the spherical proton clusters with $Z = 28, 50$ joined by an elongate neck.

(v) An unexpected sharp decrease in the influence of neutron shells on the shapes of asymmetric fission fragment yields with a growth of excitation energy from 6 to about 10 MeV has been revealed.

REFERENCES

1. M. G. Itkis *et al.,* Z. Phys. A **320**, 433 (1985); Fiz. Élem. Chastits At. Yadra **19**, 701 (1988) [Sov. J. Part. Nucl. **19**, 301 (1988)].
2. Ch. Straede *et al.*, Nucl. Phys. A **462,** 85 (1987).
3. U. Brosa *et al.*, Phys. Rep. **197,** 167 (1990).
4. P. Siegler *et al.*, Nucl. Phys. A **594,** 45 (1995).
5. F.-J. Hambsch *et al.*, Nucl. Phys. A **679,** 3 (2000).
6. B. D. Wilkins *et al.*, Phys. Rev. C **14,** 1832 (1976).
7. J. Benlliure *et al.*, Nucl. Phys. A **628,** 458 (1998).
8. M. Asghar *et al.*, Nucl. Phys. A **311,** 205 (1978).
9. N. A. Kondrat'ev *et al.*, Prib. Tekh. Éksp., No. 2, 62 (1990).
10. S. I. Mulgin *et al.*, Nucl. Instrum. Methods Phys. Res. A **388**, 254 (1997).
11. H. W. Schmitt *et al.*, Phys. Rev. B **137**, 837 (1965).
12. S. Steinhäuser, PhD Dissertation (Technische Universität, Darmstadt, 1997).
13. S. I. Mulgin *et al.*, Phys. Lett. B **462,** 29 (1999).
14. F. Gönnenwein *et al.*, in *Proceedings of the International Conference "Nuclear Shells—50 Years," Dubna, Russia, 1999* (World Sci., Singapore, 2000), p. 76.
15. I. Tsekhanovich *et al.*, Nucl. Phys. A **688,** 633 (2001).
16. H. O. Denschlag and S. M. Qaim, Z. Naturforsch. A **24**, 2000 (1969).
17. K. Wildermuth and Y. C. Tang, *A Unified Theory of the Nucleus* (Vieweg, Brounschweig, 1977).
18. K.-H. Schmidt *et al.*, Nucl. Phys. A **665,** 221 (2000); **693**, 169 (2001).
19. I. V. Pokrovsky *et al.*, Phys. Rev. C **62,** 014615 (2000).
20. D. M. Gorodisskiy *et al.*, in *Proceedings of the Fifth International Conference on Dynamical Aspects of Nuclear Fission, Časta-Papiernička, Slovak Republic, 2001*, Ed. by J. Kliman (World Sci., Singapore, 2002), p. 287.
21. L. Dematte *et al.*, Nucl. Phys. A **617,** 331 (1997).
22. M. Asghar *et al.*, Nucl. Phys. A **368,** 328 (1981).

Physics of Atomic Nuclei, Vol. 66, No. 6, 2003, pp. 1198–1202. From Yadernaya Fizika, Vol. 66, No. 6, 2003, pp. 1234–1239.

The Effect of the Entrance Channel on the Fission of ^{216}Ra*

I. V. Pokrovsky[1)], A. Yu. Chizhov[1)], M. G. Itkis[1)], I. M. Itkis[1)], G. N. Kniajeva[1)], E. M. Kozulin[1)], N. A. Kondratiev[1)], R. N. Sagaidak[1)], V. M. Voskressensky[1)], L. Corradi[2)], A. M. Stefanini[2)], M. Trotta[2)], A. M. Vinodkumar[2)], S. Beghini[3)], G. Montagnoli[3)], F. Scarlassara[3)], A. Ya. Rusanov[4)], F. Hanappe[5)], O. Dorvaux[6)], N. Rowley[6)], and L. Stuttgé[6)]**

[1)] *Flerov Laboratory of Nuclear Reactions, Joint Institute for Nuclear Research, Dubna, Moscow oblast, 141980 Russia*

[2)] *Laboratori Nazionali di Legnaro, Istituto Nazionale di Fisica Nucleare, Legnaro (Padova), Italy*

[3)] *Dipartimento di Fisica, Universita di Padova, Padova, Italy*

[4)] *Institute of Nuclear Physics, National Nuclear Center, Almaty, 480082 Kazakhstan*

[5)] *Université Libre de Bruxelles, PNTPM, Brussels, Belgium*

[6)] *Institut de Recherches Subatomiques, Universitè Louis Pasteur, Strasbourg, France*

Received August 28, 2002

Abstract—We have studied mass-energy distributions (MED) of fission fragments using two projectile–target combinations, ^{12}C + ^{204}Pb and ^{48}Ca + ^{168}Er, leading to the same compound nucleus ^{216}Ra at the excitation energy $E^* \sim 40$ MeV. It has been found that the contribution of the asymmetric mode in the case of the former reaction is 1.5%, and it is 30% in the case of the latter one. We connect such a sharp increase in the yield of asymmetric products in the ^{48}Ca + ^{168}Er reaction with the quasifission process, the MED of which have a clearly expressed shell structure. The characteristics of the fission fragment MED are of such a kind that they can be interpreted by analogy with the low-energy fission of heavy nuclei as a manifestation of an independent mode of nuclear decay which competes with the classical fusion–fission process. © *2003 MAIK "Nauka/Interperiodica".*

The fact that the mass-energy distributions (MED) of fission fragments (FF) in low-energy and spontaneous fission of heavy nuclei have a multimodal nature has been widely recognized today [1–4]. In the recent years, our effort has been concentrated on the investigation of the multimodal structure of the fission fragment MED in the region of transition nuclei $213 < A_{CN} < 226$, which so far has been poorly studied. In [5–7], we studied the properties of the ^{220}Ra* [5], ^{219}Ac*, and ^{220,224,226}Th* [6, 7] fission fragment MED. In this work, we report on the properties of MED of ^{216}Ra* fission fragments, which were investigated, in contrast to previous experiments [5–7], in two projectile–target combinations, namely, ^{12}C + ^{204}Pb and ^{48}Ca + ^{168}Er. The result has turned out to be rather unexpected.

The experiment was carried out using the ion beams of the Tandem + ALPI accelerator complex of the Laboratori Nazionali di Legnaro in the beam energy range $E_{lab} = 56$–90 MeV in the case of ^{12}C ions and $E_{lab} = 180$–208 MeV in the case of ^{48}Ca ions. Both fission and evaporation residues cross sections have been measured. In this work, we present only results on the fission fragment MED measurements for the energies $E_{lab} = 73$ MeV (^{12}C) and $E_{lab} = 194$ MeV (^{48}Ca), which lead to about the same initial excitation energy $E^* = 40.5$ MeV of the ^{216}Ra compound nucleus (CN).

Reaction products were detected with the use of the double-arm time-of-flight spectrometer CORSET [5, 7, 8], each arm of which consisted of a compact start detector, composed of microchannel plates, and a stop position-sensitive (x, y-sensitivity) detector, 6×4 cm in size, also composed of microchannel plates. The minimal flight path was 14 cm. The mass resolution of the spectrometer was estimated at 3–5 amu [5, 8]. Targets of highly enriched isotopes ^{204}Pb and ^{168}Er, about 170 μg/cm^2 in thickness, were fabricated by means of evaporation of these elements onto carbon backings, 15–20 μg/cm^2 in thickness. A standard method presupposing the selection of a

*This article was submitted by the authors in English.

**e-mail: pokrovsk@cv.jinr.ru

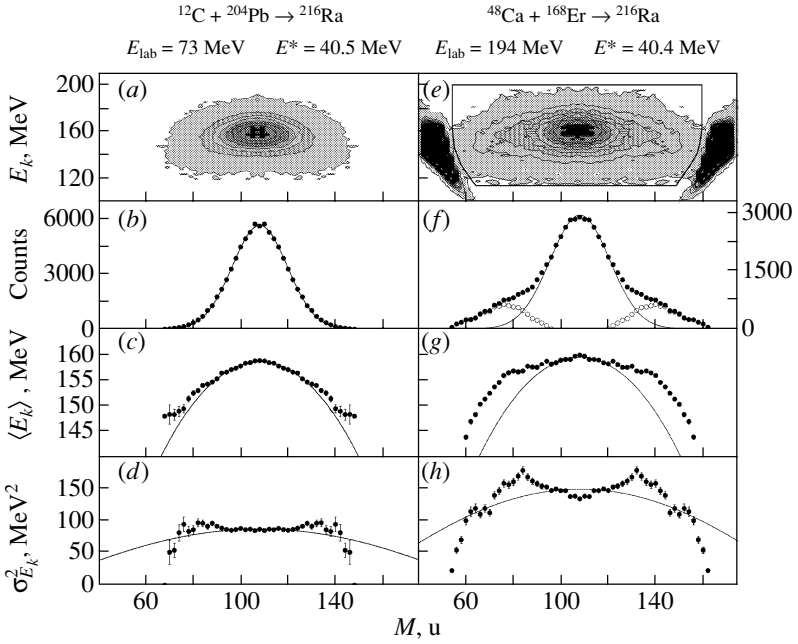

Fig. 1. (a, e) Two-dimensional matrices $N(M, E_k)$ of the fragments for both studied reactions. (b, f) Mass distributions for both reactions. Solid curves are the descriptions of the symmetric component with Gaussians. Open symbols denote the extracted asymmetric component. (c, g) Mean total kinetic energy ($\langle E_k \rangle$) as a function of fragment mass. Solid curves are the descriptions of the symmetric component with the parabola $E_{k,s}$ [7]. (d, h) Variance of the total kinetic energy ($\sigma^2_{E_k}$) as a function of fragment mass. Solid curves are the descriptions of the symmetric component with the dependence following from the expression $E^2_{k,s}(M)/\sigma^2_{E_{k,s}}(M) = \text{const}$ [7].

two-body process by using the folding angle correlations was employed in the data processing.

Figure 1 shows the main characteristics of the fission fragment MED for both reactions. Figure 1a demonstrates a two-dimensional matrix of the total kinetic energy (E_k) vs. the fragment mass (M) for the reaction $^{12}C + ^{204}Pb$. Figure 1b shows a corresponding fission fragment mass distribution (MD). A nearly triangular shape of the matrix and a practically Gaussian shape of the MD indicate that the influence of shell effects is rather small in this case. It is precisely these MDs that can be predicted by the liquid-drop model [9] or the diffusion model [10] in the case of a rather heated nucleus. The average total kinetic energy ($\langle E_k \rangle$) and its variance ($\sigma^2_{E_k}$) are shown in Figs. 1c and 1d, respectively, as a function of the mass of the fission fragment. One can see that $\langle E_k \rangle$ for the heavy (and complementary light) fission fragment masses, starting from $M_H \sim 128$, slightly deviates from a parabola (becomes higher than the latter), describing well the symmetric part of the dependence (Fig. 1c). In the dependence $\sigma^2_{E_k}(M)$, there are slight peaks in these mass regions. Since the energy characteristics of fission fragments are quite strongly sensitive to the presence of the asymmetric fission mode [1, 4, 5, 7], the observed irregularities point to an insignificant contribution of this mode estimated at $\sim$1.5%. It is exactly this contribution that was predicted for the nucleus under discussion proceeding from the systematics of the asymmetric fission yields as a function of the nucleon composition [1, 5]. Thus, in the reaction $^{12}C + ^{204}Pb$, we observed the symmetric fission of $^{216}Ra^*$, which is in agreement with our expectations.

Note that the fission of this nucleus was investigated in [11] using the giant dipole resonance at the near-barrier excitation energies $E^* \sim 11$–15 MeV. Similar to our case, any substantial contribution of the asymmetric fission to the total yield was not observed.

Figures 1e–1h show the same characteristics of the fission fragment MED as in Figs. 1a–1d, but for the reaction $^{48}Ca + ^{168}Er$. One can see that all the distributions discussed above differ rather strongly from those observed in the $^{12}C + ^{204}Pb$ reaction. Let us discuss in more detail the results shown in Figs. 1e–1h. In the matrix $N(M, E_k)$ of Fig. 1e, the reaction products having masses close to those of the projectile and target nuclei are identified as quasielastic and deep-inelastic events, and we will not consider those. The mass range 55–160 of the reaction products can be identified as totally relaxed events, i.e., as fragments. We have outlined them, and we shall be considering only the properties of these events. Mass distribution for this reaction is shown in Fig. 1f. The great contribution ($\sim$30%)

of the asymmetric fission mode manifesting itself in the form of wide "shoulders" draws attention immediately. The symmetric fission component described by a Gaussian is wider than that for the reaction with ^{12}C (compare the variance values for the symmetric mass distribution $\sigma_M^2 = 132$ amu^2 and $\sigma_M^2 = 156$ amu^2 for the ^{12}C and ^{48}Ca induced reactions, respectively). This increase in the variance value is in conformity with the results of [12], where it has been shown that an increase in the angular momentum of the fissioning nucleus leads to an increase in σ_M^2 of the symmetric fission nearly proportionally to $\langle l^2 \rangle$. Since the critical angular momentum calculated according to [13] is $l_{cr} = 31\hbar$ for the $^{12}C + ^{204}Pb$ reaction and $l_{cr} = 54\hbar$ for the $^{48}Ca + ^{168}Er$ reaction, the revealed increase in the σ_M^2 value is quite an expected effect in the case of the classical symmetric fission of the excited CN. The shape of the obtained curve $\langle E_k \rangle(M)$ (Fig. 1*g*) is far from being parabolic, and it is much higher than the parabola presented in Fig. 1*c*. As for the $\sigma_{E_k}^2(M)$ curve, the peaks in the region of masses 130–140 are more distinguished. Thus, in the case of the reaction with ^{48}Ca ions, we experimentally observed a sharp increase (by ~20 times) in the contribution of the asymmetric component to the yields of fission fragment masses as compared to the ^{12}C induced reaction, and it is reflected in the energy distributions of the fission fragments. We would like to put an emphasis on the fact that this effect has been observed at all energies of the ^{48}Ca projectiles studied in this work (these cases are not considered here).

Let us try to analyze the obtained results. In the case of classical fission proceeding through the stage of CN formation, it is quite problematic to explain the results; considering only a change in the angular momentum—when $l \ll l_{cr}$ ($B_f = 0$), where B_f is the fission barrier—cannot lead to such a dramatic change in the shell structure of the potential energy surface (fission valleys) of the fissioning nucleus. In our opinion, in the case of such a massive ion as ^{48}Ca, the most acceptable explanation of the observed effects, as opposed to the case of the reactions with ^{12}C, is the contribution of quasifission (QF)—the process proceeding without the stage of classical CN formation. This conclusion can be supported by the results of [14, 15], where it was found that there was a clearly expressed asymmetry in the backward and forward direction in different ranges of fission fragment masses in the reactions $^{58}Ni + ^{165}Ho$ [14] and $^{48}Ti + ^{166}Er$ and $^{60}Ni + ^{154}Sm$ [15], which points to the nonequilibrium nature of the process, i.e., to the QF. A decomposition of the integral mass yields into the compound and QF components was also performed in the above-mentioned works. In our case, the processes of classical FF (the symmetric component of the yield) and QF (the asymmetric component of the yield) also compete with each other, and in the experiment, we observe a combined effect of the two reaction channels. Thus,

$$Y_{exp} = Y_{FF} + Y_{QF}, \tag{1}$$

where Y_{exp} is the total (experimental) MD and Y_{FF} and Y_{QF} are the MD of the classical fission and QF processes, respectively. Y_{FF} was described with a Gaussian and is shown in Fig. 1*f* by the solid curve. Y_{QF} obtained from Eq. (1) is shown by the open symbols in Fig. 1*f*.

As we see in Fig. 1*f*, the QF fragment MD has two humps, and as surprising as it may be, its shape reminds one of a standard picture of mass yields in the low-energy fission of actinide nuclei (only a slightly wider one), since the average mass of the heavy fragment $M_H \cong 140$. It is well known that, in the classical low-energy fission of heavy nuclei, two principal modes (components)—symmetric (s) and asymmetric (a) ones—are realized with typical yields (Y_i) and energy characteristics for each of the modes $\langle E_k \rangle_i$ and $\sigma_{E_k,i}^2$ ($i = s$ or a). In our case, in a first approximation, one can speak about two modes, i.e., QF and FF. Thus, there is a formal analogy with the low-energy fission—the modes are different, but note that their nature is absolutely different too. If we follow this logic, we have to admit that the experimentally observed fragments in the region where the FF and QF modes overlap may have the same mass, as well as the same E_k, but they must be born in those two competing processes. In this case, a standard procedure of MED decomposition into two independent modes [1] can be applied. Apart from Eq. (1), we add the following ones:

$$E_{k(exp)} = E_{k(FF)}(Y_{FF}/Y_{exp}) + E_{k(QF)}(Y_{QF}/Y_{exp}), \tag{2}$$

$$\begin{aligned}(\sigma_{E_k}^2)_{exp} &= (\sigma_{E_k}^2)_{FF}(Y_{FF}/Y_{exp}) \\ &+ (\sigma_{E_k}^2)_{QF}(Y_{QF}/Y_{exp}) \\ &+ (E_{k(FF)} - E_{k(QF)})^2(Y_{FF}Y_{QF}/Y_{exp}^2).\end{aligned} \tag{3}$$

In Eqs. (1)–(3), it is the dependence on M that is naturally assumed in all the cases. The maximum in the $\sigma_{E_k}^2$ value is achieved at $Y_{FF} \cong Y_{QF}$. As can be seen in Fig. 1*f*, for the heavy fragments, the extracted QF component has a yield equal to that of the FF process (a Gaussian) near $M_H \approx 132$, i.e., exactly where the value of the variance $(\sigma_{E_k}^2)_{exp}$ is maximal. Thus, our assumption on the superposition of two modes (FF and QF) formed independently is quite justified, and proceeding from what was said above,

let us decompose the experimental distributions into two components.

Figure 2 show the results of such a decomposition for the $^{12}C + ^{204}Pb$ reaction (left panels) and the $^{48}Ca + ^{168}Er$ reaction (right panels). The solid curves show the characteristics of the symmetric component (same as in Fig. 1), and the filled circles denote the extracted asymmetric component. In the first case, it is a classical asymmetric fission, i.e., the FF process; in the second case, an overwhelming contribution of the QF process to the asymmetric component. The QF characteristics slightly differ from those of the FF process—the $(\sigma^2_{E_k})_{QF}$ value increases in the direction torward symmetry, and the curve $E_{k(QF)}(M)$ is about equidistant from the $E_{k(FF)}$ curve and is parabolic; the yield of the QF component (Y_{QF}) has a much broader distribution than those for the FF component. However, now we will not dwell on all the differences between the characteristics in question, but will point out the most essential things. A hypothesis explaining the main properties of the QF process is the supposition of quite a strong manifestation of shell effects in this process. The arrows in Fig. 2 show positions of closed spherical shells with $Z = 28$, 50 and $N = 50$, 82 and complimentary masses, derived from a simple assumption on the proportionality of charge to mass (the reaction with ^{48}Ca). As we have seen, the major part of the QF component fits into the region of the above-mentioned shells, and the maximum of Y_{QF} is a "compromise" between $Z = 28$, $N = 50$ and $N = 82$. Thus, it is clear that the shell structure of the formed fragments in the mass ranges $M_L = 65$–68 and $M_H = 130$–150 strongly influences the QF process, the shells of the light as well as the heavy fragments playing their important roles.

Let us recall that the problem of the shell effect manifestation in the QF process has long been discussed in a number of experimental and theoretical papers [16–22], but typically the cases in which massive projectiles interacted with actinide targets (or U ions in the reactions in inverse kinematics) have been considered. In this kind of reactions, the manifestation of doubly magic lead with $M_H \sim 208$ ($Z \sim 82$, $N \sim 126$) has been observed in the MD of fission fragments; however, the interpretation of such MD is not unambiguous. For example, the authors of [17, 18] studied the ^{40}Ar, $^{48}Ca + ^{238}U$ reactions and came to the conclusion that the "lead" peak appearing due to the "washing out" of events in the mass region $M_H = 215$–230 was the result of sequential fission. At the same time, the authors of [19], having studied the $^{40}Ar + ^{232}Th$ reaction, stick to the opinion that it is still a manifestation of the strong lead shell. Reverting to our results obtained from the $^{48}Ca + ^{168}Er$ reaction proceeding at $E^* \sim$ 40.5 MeV, one can say that, in this case, sequential fission is scarcely probable since the fission probability of fission fragments of any masses approaches zero [23]. An interesting situation occurs in the $^{164}Ho + ^{58}Ni \rightarrow ^{223}Am^*$ reaction [14]. In the yield of the reaction products at the forward and backward angles, some maxima in the yields of fission fragment masses in the range $M_H = 120$–140 and the complimentary ones are clearly seen, but at higher excitation energies.

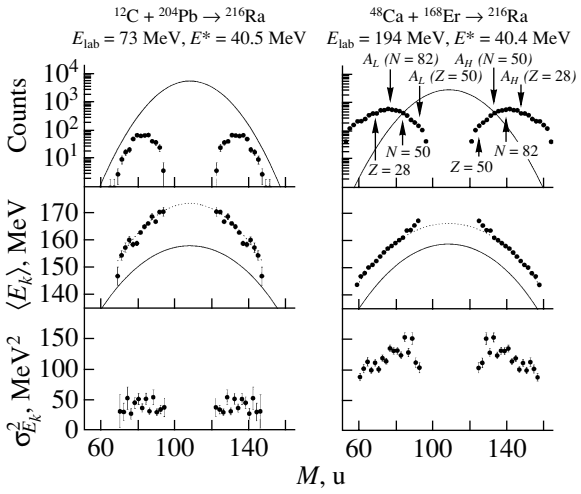

Fig. 2. The characteristics of the extracted asymmetric components for both studied reactions. From top to bottom, the mass distributions and $\langle E_k \rangle(M)$, $\sigma^2_{E_k}(M)$ as a function of fragment mass are shown. The solid curves denote the symmetric components (the same as in Fig. 1). For the reaction $^{48}Ca + ^{168}Er$, downward arrows show the positions of the close spherical shells. Upward arrows shows the positions of the fragments complementary to the above-mentioned spherical ones.

Recently, in the $^{48}Ca + ^{208}Pb$, ^{238}U, ^{244}Pu, ^{248}Cm reactions [24–27], we have observed the effect of magic shells on the properties of QF at $E^* \sim 30$ MeV. It was found that the shell structure of heavy fission fragments (nuclei in the vicinity of ^{208}Pb), as well as of the light ones (nuclei in the vicinity of ^{78}Ni), played an important role. It is interesting to note that, in the $^{48}Ca + ^{208}Pb$ reaction, the main decay channel is the classical symmetric fission, and the QF process manifests itself in the form of asymmetric "shoulders," whose relative yield is much lower [25, 26] than what has been found in this work. We connect this fact with the circumstance that, in the fission of ^{256}No, only the light fragment in the "quasifission shoulders" is in the vicinity of magic numbers.

A question arises—Why do shell effects in the case of one and the same nucleus (for example, $^{216}Ra^*$ in this work) powerfully manifest themselves in the QF process and quite weakly in the FF process? This

phenomenon can be explained using the dinuclear system (DNS) concept [21], originally elaborated for deep-inelastic reactions and then applied to QF, or using the "hybrid" model [22], based on the same DNS concept. In these models, the DNS potential energy plays an important role and depends on the fragment masses formed in the QF process. The potential energy surface (PES) of a DNS is strongly modulated by shell effects. The minima of the PES lie near the doubly magic numbers, which play an important role in fission. The DNS excitation energy is counted from the valley in the PES for each particular mass instead of the ground state of the CN. Since it is usually slightly higher than the ground state of the CN, the excitation energy of separate fission fragments is lower on the average. Thus, in these models, the QF process is much "colder" than the classical fission, and the sensitivity to the shell structure is higher. It is most likely that this circumstance explains the observed effect.

Summing up, we have studied mass-energy distributions of fission fragments in two projectile–target combinations—^{12}C + ^{204}Pb and ^{48}Ca + ^{168}Er—leading to the same compound nucleus ^{216}Ra* at the initial excitation energy $E^* \sim 40$ MeV. We have found that the contribution of the asymmetric fission mode in the former reaction is 1.5%, and it is ~30% in the case of the latter one. We have interpreted such a sharp increase in the yield of asymmetry in the reaction with ^{48}Ca as a manifestation of the QF process, where the influence of the shell effects is clearly seen in the MED of the reaction products. We have interpreted the properties of quasifission fragments by analogy with the low-energy fission of heavy nuclei as a manifestation of an independent mode of nuclear decay, competing with the classical FF process. It is possible to explain this phenomenon using the dinuclear system concept.

ACKNOWLEDGMENTS

The work has been supported by the Russian Foundation for Basic Research (project no. 99-02-17891) and by INTAS (grant no. 00-655).

REFERENCES

1. M. G. Itkis, V. N. Okolovich, A. Ya. Rusanov, and G. N. Smirenkin, Fiz. Élem. Chastits At. Yadra **19**, 701 (1988) [Sov. J. Part. Nucl. **19**, 301 (1988)]; Nucl. Phys. A **502**, 243 (1989).
2. E. K. Hulet *et al.*, Phys. Rev. Lett. **56**, 313 (1986); Phys. Rev. C **40**, 770 (1989).
3. U. Brosa, S. Grossmann, and A. Müller, Phys. Rep. **197**, 167 (1990).
4. F.-J. Hambsch, F. Vives, P. Siegler, and S. Oberstedt, Nucl. Phys. A **679**, 3 (2000).
5. V. Pokrovsky, L. Calabretta, M. G. Itkis, *et al.*, Phys. Rev. C **60**, 041304 (1999).
6. M. G. Itkis *et al.*, in *Proceedings of the Tours Symposium on Nuclear Physics III, Tours, France, 1997*, Ed. by M. Arnould *et al.*; AIP Conf. Proc. **425**, 189 (1998).
7. V. Pokrovsky *et al.*, Phys. Rev. C **62**, 014615 (2000); G. G. Chubarian, M. G. Itkis, N. A. Kondratiev, *et al.*, Phys. Rev. Lett. **87**, 052701 (2001).
8. N. A. Kondratiev, *et al.*, in *Proceedings of the Fourth International Conference on the Dynamical Aspects of Nuclear Fission, Časta-Papernička, Slovak Republic, 1998*, Ed. by Yu. Ts. Oganessian *et al.* (World Sci., Singapore, 1999), p. 431.
9. J. R. Nix and W. J. Swiatecki, Nucl. Phys. **71**, 1 (1965); J. R. Nix, Nucl. Phys. A **130**, 241 (1969).
10. G. D. Adeev, I. I. Gonchar, V. V. Pashkevich, *et al.*, Sov. J. Part. Nucl. **19**, 529 (1988); G. D. Adeev and V. V. Pashkevich, Nucl. Phys. A **502**, 405 (1989).
11. K.-H. Schmidt *et al.*, Nucl. Phys. A **665**, 221 (2000).
12. M. G. Itkis and A. Ya. Rusanov, Fiz. Élem. Chastits At. Yadra **29**, 389 (1998) [Phys. Part. Nucl. **29**, 160 (1998)].
13. R. Bass, Phys. Rev. Lett. **39**, 265 (1977).
14. M. A. Butler, S. S. Datta, R. T. de Souza, *et al.*, Phys. Rev. C **34**, 2016 (1986).
15. B. B. Back, P. B. Fernández, B. G. Glagola, *et al.*, Phys. Rev. C **53**, 1734 (1996).
16. R. Kalpakchieva, Yu. Ts. Oganessian, Yu. E. Penionzhkevich, and H. Sodan, Z. Phys. A **283**, 253 (1977).
17. G. Guarino, A. Gobbi, K. D. Hildenbrand, *et al.*, Nucl. Phys. A **424**, 157 (1984).
18. G. J. Mathews, L. G. Sobotka, G. J. Wozniak, *et al.*, Z. Phys. A **290**, 407 (1979).
19. P. Gippner, K. D. Schilling, W. Seidel, *et al.*, Z. Phys. A **325**, 335 (1986).
20. P. Gippner, U. Brosa, H. Feldmeier, and R. Schmidt, Phys. Lett. B **252**, 198 (1990).
21. Díaz Torres, G. G. Adamian, N. V. Antonenko, and W. Sheid, Nucl. Phys. A **679**, 410 (2001); Phys. Rev. C **64**, 024604 (2001).
22. V. I. Zagrebaev, Phys. Rev. C **64**, 034606 (2001).
23. V. Ignatyuk, G. N. Smirenkin, M. G. Itkis, *et al.*, Fiz. Élem. Chastits At. Yadra **16**, 709 (1985) [Sov. J. Part. Nucl. **16**, 307 (1985)].
24. M. G. Itkis *et al.*, Nuovo Cimento A **111**, 783 (1998).
25. M. G. Itkis *et al.*, in *Proceedings of the 7th International Conference on Clustering Aspects of Nuclear Structure and Dynamics, Rab Island, Croatia, 1999*, Ed. by J. Korolija *et al.* (World Sci., Singapore, 2000), p. 368.
26. M. G. Itkis *et al.*, *Fission and Properties of Neutron-Rich Nuclei, St. Andrews, Scotland, 1999*, Ed. by J. H. Hamilton *et al.* (World Sci., Singapore, 2000), p. 268.
27. M. G. Itkis *et al.*, in *Proceedings of the International Conference on Nuclear Physics at Border Lines, Lipari, Messina, Italy, 2001*, Ed. by G. Fazio *et al.* (World Sci., Singapore, 2002), p. 146.

Physics of Atomic Nuclei, Vol. 66, No. 6, 2003, pp. 1203–1210. From Yadernaya Fizika, Vol. 66, No. 6, 2003, pp. 1240–1248.

Reduction Coefficient in Surface-Plus-Window Dissipation: Analysis of Experimental Data from Fusion–Fission Reactions within a Stochastic Approach*

P. N. Nadtochy[1)], A. V. Karpov[1)], D. V. Vanin[2)], and G. D. Adeev[1)]**

[1)] *Department of Theoretical Physics, Omsk State University, Omsk, 644077 Russia*

[2)] *Flerov Laboratory of Nuclear Reactions, Joint Institute for Nuclear Research, Dubna, Moscow oblast, 141980 Russia*

Received August 28, 2002

Abstract—A stochastic approach based on three-dimensional Langevin equations was applied to detailed study of fission dynamics in fusion–fission reactions. The reduction coefficient in surface-plus-window dissipation is deduced by analyzing the available experimental data on various observable quantities in fusion–fission reactions. Analysis of the results shows that not only characteristics of the mass-energy distribution of fission fragments but also the mass and kinetic-energy dependence of the prescission and postscission neutron multiplicities, the angular anisotropy, and fission probability can be reproduced using surface-plus-window dissipation with the reduction coefficient from a wall formula $k_s = 0.25$–0.5 for compound nuclei lighter than ^{224}Th. The analysis performed reveals that the coordinate-independent reduction coefficient k_s is not compatible with the simultaneous description of the main fission characteristics for fissioning systems heavier than ^{224}Th. © *2003 MAIK "Nauka/Interperiodica".*

1. INTRODUCTION

The most detailed and systematic information on large-scale collective nuclear motion presently available from heavy-ion reactions has been accumulated from measuring the multiplicities of evaporated particles, especially neutrons, in fusion–fission reactions in coincidence with mass and kinetic-energy distributions of fission fragments [1–3]. Analysis of these data and further references are presented in the review [4]. Three-dimensional Langevin calculations of the fission fragment mass-energy distributions (MED) have been carried out quite recently [5–7]. In the elaborated dynamical model [5–7], the evolution of the three most important shape parameters, elongation, constriction, and mass asymmetry, is described by the coupled Langevin equations. Along each stochastic Langevin trajectory, evaporation of light particles is considered. The results of these calculations show that the three-dimensional Langevin dynamics makes it possible to describe comprehensively characteristics of the MED and the mean prescission neutron multiplicity. The above-mentioned results can be considered as promising and encouraging for further development and extension of the stochastic approach to fission dynamics based on the three-dimensional Langevin equations.

The mass and kinetic-energy dependence of the prescission and postscission neutron multiplicities have been studied in experiments [1–4] in addition to the parameters of the MED. On the other hand, descriptions and explanations of such exclusive data as the mass and kinetic-energy dependence of the prescission neutron multiplicities have not been undertaken in full extent so far. It is a crucial test for theoretical models including the stochastic approach based on the Langevin equations. Thus, the available experimental data on the prescission and postscission neutron multiplicities as functions of the fragment mass asymmetry and kinetic energy have to be compared more closely with theoretical findings by means of three-dimensional Langevin dynamical calculations. In the present paper, we extend the investigations recently carried out in [5–7] to calculate the mass and kinetic-energy dependence of the prescission and postscission neutron multiplicities and the dependences of the mean prescission neutron multiplicity $\langle n_{\rm pre}\rangle$, fission probability P_f, and some other observables on excitation energy.

The aim of our study is twofold. First, we would like to analyze and elucidate correlations between the prescission and postscission neutron multiplicities and the fission fragment MED, and, second, to investigate the mean prescission neutron multiplicities

*This article was submitted by the authors in English.

** e-mail: vanin@nrsun.jinr.ru

1063-7788/03/6606-1203$24.00

$\langle n_{\rm pre}\rangle$, the fission probability P_f (or survival probability), and the fission fragment angular anisotropy in a broad range of excitation energy.

Although the influence of dissipation on the fission process is now well established [4, 8, 9], conclusions about its deformation and/or temperature dependence are still controversial [4, 10–12]. It is symbolic that compilations of available estimates for the friction coefficient obtained both from more or less a priori theories and from analysis of different experimental data are presented in [13] on a logarithmic scale. The elucidation of the mechanism of nuclear dissipation in fission and reliable estimation of its value continue being essentially open problems. The systematics of the parameters of fission fragment kinetic energy (mean value of the kinetic energy and its variance) were fairly well reproduced [8, 9, 11] using both the two-body and the one-body mechanisms of nuclear viscosity. However, it was shown [4, 11] that one-body dissipation is preferable in order to describe the prescission neutron multiplicity data. The assumption that the mechanism of nuclear viscosity has the nature of one-body dissipation is physically better justified. Making some simplifications to the mechanism of collision of nucleons with the surface of the nucleus, Blocki, Swiatecki, and others [8, 9] derived simple expressions for the one-body dissipation (so called wall and wall-and-window formulas). A quantum treatment of the one-body dissipation showed that the wall formula strongly overestimates nuclear viscosity, reproducing correctly the dependence of the one-body dissipation on a change in the shape of the nucleus. Therefore, in the modified surface-plus-window dissipation mechanism, the contribution from the wall formula was appreciably reduced by the reduction coefficient $k_s = 0.2$–0.3 [12]. The reduction coefficient value changes in the limits from 0 to 1. The value of k_s could depend upon both the excitation energy and the type of collective motion. Therefore, one of the main goals of the present analysis that applied to many observable quantities in fusion–fission reactions is to determine the value of the reduction factor k_s of surface-plus-window dissipation by comparing the experimental data with our calculated results.

2. RESULTS AND DISCUSSIONS

The dynamical model used in the calculations has been described in detail in our previous papers [5–7]. Since the details of the model have already been published (see, in particular, [5, 7]), we do not give any equations here, but only discuss the sensitivity of various observable quantities on the reduction coefficient k_s. We also discuss some related works from the literature in comparison with our findings. In this paper, we use the same notation and all input parameters of our dynamical model as in [5, 7].

We have carried out calculations of the mass-energy distributions of fission fragments; the anisotropy of the fission fragment angular distribution; the prescission, postscission, and total neutron multiplicities; and fission probabilities for the following fusion–fission reactions:

^{18}O + ^{154}Sm → ^{172}Yb ($E_{\rm lab} = 158.8$ MeV) [2],

^{18}O + ^{144}Sm → ^{162}Yb ($E_{\rm lab} = 158.8$ MeV) [2],

^{16}O + ^{170}Er → ^{186}Os ($E_{\rm lab} = 102$–165 MeV) [14–17],

^{16}O + ^{182}W → ^{198}Pb ($E_{\rm lab} = 102$–165 MeV) [14, 16],

^{12}C + ^{194}Pt → ^{206}Po ($E_{\rm lab} = 99$ MeV) [18],

^{36}Ar + ^{169}Tm → ^{205}Fr ($E_{\rm lab} = 205$ MeV) [3],

^{4}He + ^{209}Be → ^{213}At ($E_{\rm lab} = 100$ MeV) [14],

^{18}O + ^{197}Au → ^{215}Fr ($E_{\rm lab} = 158.8$ MeV) [2],

^{16}O + ^{208}Pb → ^{224}Th ($E_{\rm lab} = 82.8$–215 MeV) [19–27],

^{12}C + ^{232}Th → ^{244}Cm ($E_{\rm lab} = 97$ MeV) [28],

^{16}O + ^{232}Th → ^{248}Cf ($E_{\rm lab} = 90$–160 MeV) [23, 28],

^{18}O + ^{238}U → ^{256}Fm ($E_{\rm lab} = 158.8$ MeV) [2],

^{20}Ne + ^{232}Th → ^{252}Fm ($E_{\rm lab} = 215$ MeV) [29],

^{20}Ne + ^{240}Pu → ^{260}Rf ($E_{\rm lab} = 174$ MeV) [18].

In these calculations, we have varied the value of k_s from 0.1 to 1. The value $k_s = 1$ corresponds to the classic wall-and-window formula [8] that has been used in numerous studies [11, 30].

The standard transition state model [31] has been used to analyze the fission fragment angular distribution. It is assumed that the equilibrium distribution on the K degree of freedom (K is the projection of the compound nucleus spin I on the symmetry axis) is established at the transition state that is usually assumed to be the saddle point. The classical Halpern–Strutinsky expression has been applied to calculate the angular distribution of fission fragments.

It should be mentioned that the main difference of our three-dimensional model from the usually used one-dimensional models consists in the following: there is only one transition state for each angular momentum in the one-dimensional model, whereas a set of conditional saddle points forms an ensemble of transition states in the three-dimensional one. The volume of the phase space available for the system

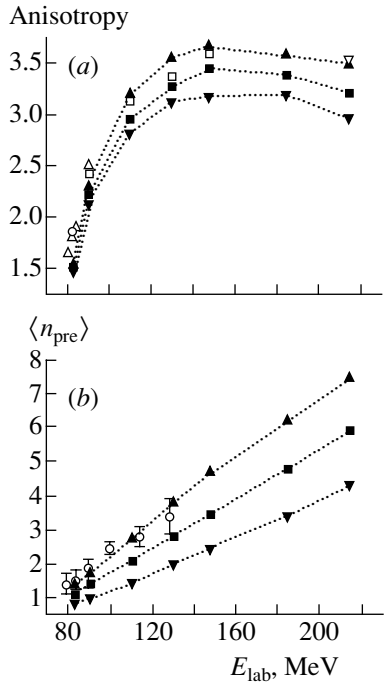

Fig. 1. The anisotropy of the fission fragment angular distribution (a) and the mean prescission neutron multiplicity (b) as functions of the projectile laboratory energy for the reaction $^{16}O + {}^{208}Pb \rightarrow {}^{224}Th$. The calculations have been carried out with different values of the reduction coefficient: $k_s = 0.25$ (inverted filled triangles), $k_s = 0.5$ (filled squares), and $k_s = 1$ (filled triangles). The calculated points are connected by dotted lines to guide the eye. The open symbols are the experimental data: a—[19] (circle), [20] (triangles), [23] (squares), and [24] (inverted triangle); b—[25].

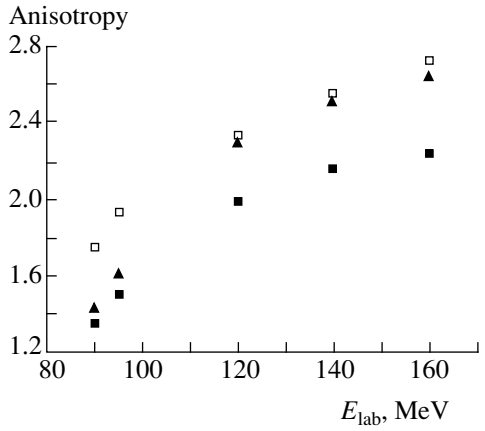

Fig. 2. The anisotropy of the fission fragment angular distribution as a function of the projectile laboratory energy for the reaction $^{16}O + {}^{232}Th \rightarrow {}^{248}Cf$. The calculations have been carried out with $k_s = 0.5$ (filled squares) and $k_s = 2$ (filled triangles). The open symbols are the experimental data from [23].

on the ridge grows with increasing excitation energy and/or fissility of the compound nucleus. Therefore, the influence of the model dimension has to be most significant in the region of heavy nuclei and/or high excitation energies.

There are three factors determining the anisotropy of the angular distribution: the initial spin distribution, the nuclear temperature, and the nuclear deformation at the transition state. The last two can be taken into account correctly only within the dynamical approach. We have used the reaction $^{16}O + {}^{208}Pb \rightarrow {}^{224}Th$ as a representative example to investigate the influence of the neutron emission on the anisotropy of the fragment angular distribution. The calculated results of the mean prescission neutron multiplicity $\langle n_{pre} \rangle$ and the anisotropy of the fragment angular distribution are shown in Fig. 1. One can see from Fig. 1a that the values of the anisotropy of the angular distribution obtained with $k_s = 0.5$–1.0 are in a good qualitative agreement with the experimental data. It is also seen from Fig. 1b that the experimental data on $\langle n_{pre} \rangle$ can be reproduced with $k_s = 0.5$–1.0 too. It indicates a correlation between the neutron evaporation and the values of the anisotropy of the angular distribution. We can assert that the reproduction of the experimental data on $\langle n_{pre} \rangle$ is one of the necessary conditions to reproduce the data on the angular anisotropy.

The calculation of the angular anisotropy has been carried out for the reaction $^{16}O + {}^{232}Th \rightarrow {}^{248}Cf$ in order to analyze the effect of inclusion into the model of three collective coordinates. We have chosen this reaction because the compound nucleus ^{248}Cf is a heavy nucleus and, according to our supposition, the influence of the model dimension would be considerable. The experimental data on $\langle n_{pre} \rangle$ can be reproduced for this reaction with $k_s = 1.5$–2. It is well known that the value of the reduction coefficient k_s cannot exceed 1 [32]. Nevertheless, we have used $k_s > 1$ because it has been shown above that the reproduction of the anisotropy of the angular distribution demands the reproduction of the mean prescission neutron multiplicity. Therefore, in this case, we treated the coefficient k_s only as a free parameter determining the strength of nuclear dissipation (see the similar analysis [33]).

It is clearly seen from Fig. 2 that, in the energy region $E_{lab} < 100$ MeV, the calculated values of the angular anisotropy with $k_s = 2$ are significantly smaller than the experimental ones. On the contrary, the deviation of the calculated values from the experimental data decreases with increasing of the excitation energy, and in the region $E_{lab} > 120$ MeV, a good quantitative agreement with the data on the anisotropy of the angular distribution has been obtained.

It should be mentioned that, in the recent work [34], the evaporation of the presaddle neutrons was

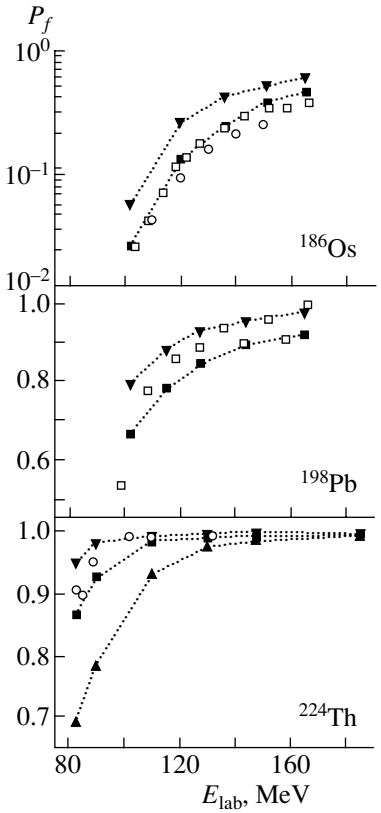

Fig. 3. The fission probability as a function of the projectile laboratory energy for the reactions $^{16}O + {}^{170}Er \rightarrow {}^{186}Os$, $^{16}O + {}^{182}W \rightarrow {}^{198}Pb$, and $^{16}O + {}^{208}Pb \rightarrow {}^{224}Th$. The results obtained with different values of k_s are marked at the same order as in Fig. 1. The calculated points are connected by dotted lines to guide the eye. The open symbols are the experimental data: for the compound nucleus ^{186}Os—[16] (squares) and [17] (circles); for the compound nucleus ^{198}Pb—[16]; for the compound nucleus ^{224}Th—see the text.

taken into account to calculate the anisotropy of the angular distribution. Good agreement with the experimental data has been achieved for systems like $^{16}O + {}^{208}Pb$ within the one-dimensional model. At the same time, for the system $^{16}O + {}^{232}Th$, an appreciable deviation of the theoretical predictions from the experiment has been obtained in the whole energy interval. Moreover, the difference between the theoretical and experimental values of the angular anisotropy increases with decreasing excitation energy, which is in qualitative agreement with the results of our calculation. The three-dimensional approach allows one to describe the experimental anisotropy of the fragment angular distributions better than in the framework of the one-dimensional model. In our three-dimensional model, the difference between the calculated and experimental values of the anisotropy of the angular distribution decreases more rapidly than in the one-dimensional model, due to taking into account the ensemble of the transition states.

Our model allows us to study another important characteristic of the fission process—the fission probability P_f. The calculated results for P_f are shown in Fig. 3 for the reactions $^{16}O + {}^{170}Er \rightarrow {}^{186}Os$, $^{16}O + {}^{182}W \rightarrow {}^{198}Pb$, and $^{16}O + {}^{208}Pb \rightarrow {}^{224}Th$. The experimental values of the fission probabilities for the last reaction have been obtained by the relation $P_f = \sigma_{fis}/(\sigma_{fis} + \sigma_{ER})$, where the data on σ_{ER} are taken from [19, 21] and the data on σ_{fis} are taken from [19, 22, 23]. Some values of P_f have been estimated for σ_{ER} and σ_{fis} measured at unequal projectile energies due to the experimental data taken from different works. The difference in energy is 3.6 MeV for the point at $E_{lab} = 133.6$ MeV, and it does not exceed 1 MeV for the other points. The energy dependence of the evaporation residue cross section for the last reaction has been studied in detail in [35]. It has been shown there that the evaporation residue cross section (fission probability) is a very sensitive characteristic to nuclear dissipation. One can see from Fig. 3 that the results of our calculations with $k_s = 0.25$–0.5 are in a quantitative agreement with the experimental data in the entire energy interval and also that the fission probability is in fact strongly influenced by the magnitudes of nuclear dissipation especially at low energies.

We have carried out calculations of the prescission, postscission, and total neutron multiplicities and their dependences on the mass and kinetic energies of fission fragments. Very detailed and systematized data [2] show a parabolic mass dependence of the prescission neutron multiplicities $\langle n_{pre}(M)\rangle$ with a maximum value $\langle n_s\rangle$ for symmetric fission and a decrease for asymmetric fission. The dependence of $\langle n_{pre}(M)\rangle$ can be parametrized by [4]

$$\langle n_{pre}(M)\rangle = \langle n_s\rangle - c_{pre}\,(M_s - M)^2\,, \qquad (1)$$

where M_s is the fission fragment mass for the symmetric mass division.

The calculated dependences $\langle n_{pre}(M)\rangle$ were approximated by a parabolic polynomial expression given by Eq. (1) using the least-squares method. The calculated values of c_{pre} are presented in the table. The reasons for one decrease in the prescission neutron multiplicities with the fragment mass asymmetry was considered in our previous paper [7] and they are not discussed here.

H. Rossner *et al.* [3] found an unexpected increase in $\langle n_{pre}\rangle$ with E_K. However, it soon turned out [1] that the deduced unexpected dependence $\langle n_{pre}(E_K)\rangle$ was an artifact due to the recoil effect imparted by the emitted neutrons to the fission fragments. After the correction of this effect, it was found [1, 2]

Table

Compound nucleus	E^*, MeV	k_s	$c_{\rm pre}$, 10^{-4}	$c_{\rm tot}$, 10^{-4}	$dn_{\rm post}/dM$, 10^{-2}	$-dn_{\rm tot}/dE_K$, MeV^{-1}	$\langle n_{\rm pre}\rangle$	$\langle n_{\rm post}\rangle$	$\langle n_{\rm tot}\rangle$
^{162}Yb	114	0.25	8	−1	3.2	0.054	1.8	2.6	7
		0.5	11	−3	2.7	0.058	2.4	2.3	7
Expt. [2]			12	1	3.5	–	2.45	1.7	5.85
^{172}Yb	121	0.25	20	12	3.6	0.038	3.4	3	9.4
		0.5	32	8	2.7	0.052	4.5	2.4	9.3
Expt. [2]			14	10	3.6	0.056	4.4	2	8.4
^{205}Fr	77	0.25	1.3	8	2.6	0.039	0.4	3.4	7.2
		0.5	1.9	11	2.7	0.041	0.9	3.2	7.3
Expt. [3]			0	9.5	1.8	0.046	1.2	–	–
^{215}Fr	111	0.25	5.1	4.8	4.3	0.037	3	3.2	9.4
		0.5	7.1	6	4.1	0.041	4.3	3	10.3
Expt. [2]			6.5	4.4	3.8	0.047	4.1	2.7	9.5
^{256}Fm	101	0.25	1.6	6.6	4.3	0.046	2	6.2	15.5
		0.5	3.6	6.5	4.1	0.066	3.1	5.8	14.7
Expt. [2]			8.2	5.4	4.1	–	5.1	4.25	13.6
^{252}Fm	140	0.25	2.7	2.2	5.4	0.052	2.7	7	16.7
		0.5	3.6	4	4.8	0.061	4.0	6.5	17
Expt. [29]			0	2.4	5	–	6.95	3.83	14.6

Note. The columns contain (from left to right) the compound nucleus; the excitation energy (E^*); the reduction coefficient of surface-plus-window dissipation k_s; the coefficients ($c_{\rm pre}$, $c_{\rm tot}$, $dn_{\rm post}/dM$, and $-dn_{\rm tot}/dE_K$); and the mean prescission ($\langle n_{\rm pre}\rangle$), postscission ($\langle n_{\rm post}\rangle$), and total ($\langle n_{\rm tot}\rangle$) neutron multiplicities.

that $\langle n_{\rm pre}(E_K)\rangle$ is independent of E_K. In our calculations, the mean fission time $\langle t_f(E_K)\rangle$ and, as a result, $\langle n_{\rm pre}(E_K)\rangle$ are nearly independent of E_K and slightly decrease only in the region of small E_K for all compound nuclei considered in this paper.

The postscission neutron multiplicity is determined by the excitation energy of fission fragments that was calculated using the energy conservation law

$$Q_f + E_{\rm coll}(t_{\rm sc}) - V(\mathbf{q}_{\rm sc}) - E_K = E^{(1)}_{\rm def} + E^{(2)}_{\rm def}, \quad (2)$$

where $E_{\rm coll}$ is the kinetic energy of the collective degrees of freedom at the instant of scission, $V(\mathbf{q})$ is the potential energy, E_K is the kinetic energy of fission fragments, and $E^{(1)}_{\rm def}$ and $E^{(2)}_{\rm def}$ are the deformation energies of fission fragments. The excitation energies of fission fragments are calculated as a sum of the thermal excitation energies and deformation energies. It was assumed that the thermal excitation energy of the compound nucleus at scission is divided between the fission fragments proportional to their masses. The shapes of the fission fragments were parametrized using the prescission shape of the compound nucleus that was divided into two parts by the plane $z = z_{\rm neck}$, where $z_{\rm neck}$ is the coordinate of the minimal neck thickness. The calculated deformation energies for such shapes do not satisfy the energy conservation law (2) due to the crude approximation of the fission fragment shapes. The values of $E^{(1)}_{\rm def}$ and $E^{(2)}_{\rm def}$ were reduced according to the relation $E^{(1)}_{\rm def}/E^{(2)}_{\rm def} = E^{(1')}_{\rm def}/E^{(2')}_{\rm def}$, where $E^{(1')}_{\rm def}$ and $E^{(2')}_{\rm def}$ are the deformation energies that satisfied the energy conservation law (2). The calculated dependences of the postscission neutron multiplicities on the mass and kinetic energy of fission fragments are presented in Figs. 4 and 5 for the compound nucleus ^{205}Fr. Here, we also have calculated the total neutron multiplicity and its dependence on the mass and kinetic energy of the fission fragments. The mass dependence of the total neutron multiplicity was calculated using

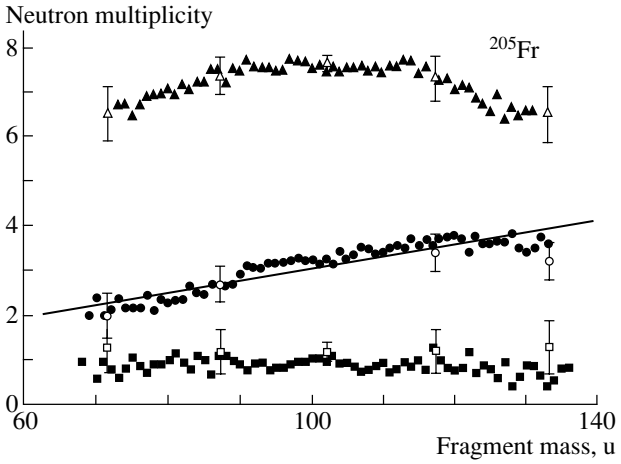

Fig. 4. The mass dependence of the prescission (squares), postscission (circles), and total (triangles) neutron multiplicities. The open symbols are the experimental data [3]. The filled symbols are the calculated results with $k_s = 0.5$.

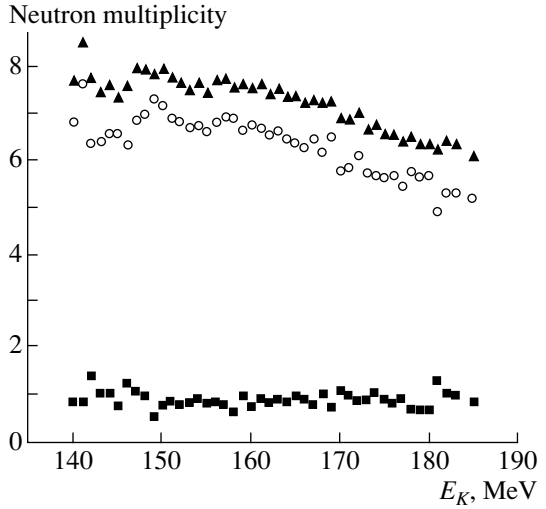

Fig. 5. The kinetic-energy dependence of the prescission (squares), postscission (circles), and total (triangles) neutron multiplicities calculated with $k_s = 0.5$.

the following relation:

$$\langle n_{\rm tot}(M)\rangle = \langle n_{\rm pre}(M)\rangle + \langle n_{\rm post}(M)\rangle + \langle n_{\rm post}(A_{\rm CN} - M)\rangle.$$

The mass dependence of the total neutron multiplicity was approximated by the parabolic expression with the coefficient $c_{\rm tot}$ as in the case of the mass dependence of the prescission neutron multiplicity. The dependences $\langle n_{\rm pre}(M)\rangle$ and $\langle n_{\rm tot}(M)\rangle$ could differ from each other due to the postscission neutron multiplicity. Our calculations show that the mass dependence of the postscission neutron multiplicity is determined mainly by the Q_f values, as was noted

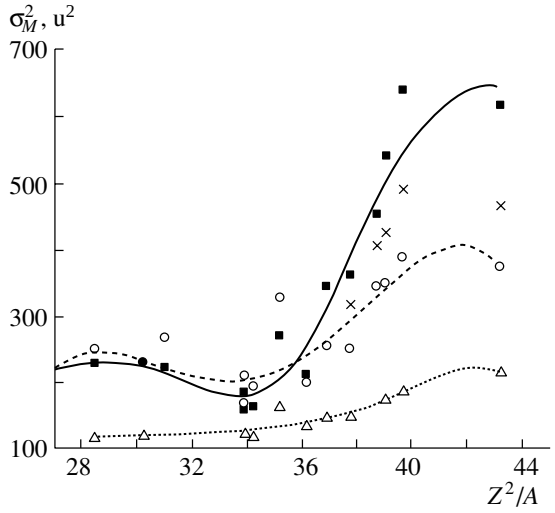

Fig. 6. The variance of the mass distribution as a function of the parameter Z^2/A. The filled squares fitted by the solid curve are the experimental data; the open triangles fitted by the dotted curve are the calculated results with $k_s = 1$; the open circles fitted by the dashed curve are the calculated results with $k_s = 0.25$; the crosses are the calculated results with $k_s = 0.1$.

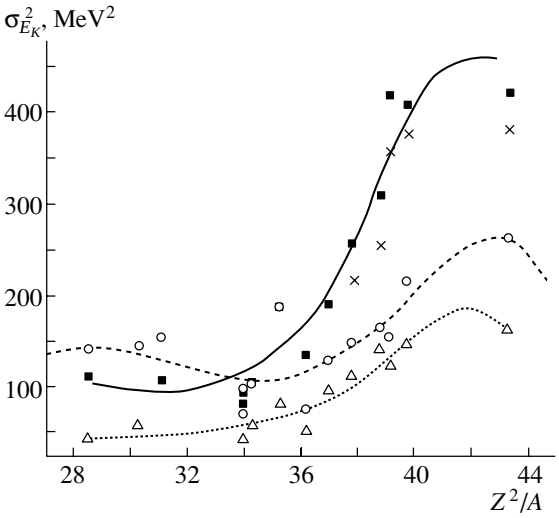

Fig. 7. The variance of the kinetic-energy distribution as a function of the parameter Z^2/A. The notation is the same as in Fig. 6.

early in [36]. The Q_f values are maximal for the fragments with neutron and/or proton numbers close to the magic numbers, and this fact provides the nonlinear dependence of the postscission neutron multiplicity on M (see Fig. 4). The calculated coefficients of the mass dependence of the prescission, postscission, and total neutron multiplicities, $c_{\rm pre}$, $dn_{\rm post}/dM$, and $c_{\rm tot}$, are presented in the table.

The dependence of the postscission neutron mul-

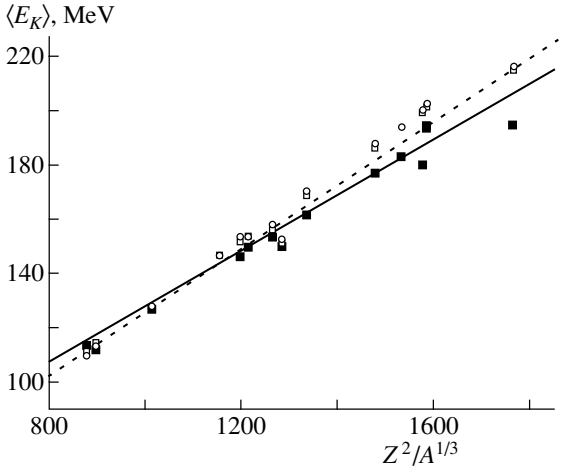

Fig. 8. The mean kinetic energy of fission fragments as a function of the parameter $Z^2/A^{1/3}$. The filled squares are the experimental data; the open squares are the calculated results with $k_s = 0.5$; and the open circles, with $k_s = 0.25$. The solid line is the systematics from [27], and the dashed line, from [37].

tiplicity on the kinetic energy of fission fragments is mainly determined by the E_K value according to the energy conservation law (2). The increase in E_K leads to a decrease in the deformation energies of fission fragments. The kinetic-energy dependence of the total neutron multiplicity is mainly determined by the postscission neutron multiplicity, because the prescission neutron multiplicity is approximately independent of E_K. As can be seen from the table, the experimental coefficients $\left(-\dfrac{dn_{\rm tot}}{dE_K}\right)$ are reproduced in our calculations with the reduction coefficient $k_s = 0.25$–0.5. Also, the experimental mean prescission, postscission, and total neutron multiplicities are reproduced with $k_s = 0.25$–0.5 for all fissioning nuclei considered here except for ^{256,252}Fm. Our calculations underestimate the mean prescission neutron multiplicity and overestimate the postscission one for these nuclei.

We have calculated the two-dimensional fission fragment MED in the three-dimensional Langevin dynamics. The calculated parameters of the fission fragment MED are presented in Figs. 6–8. It is evident from Fig. 8 that the calculated values of $\langle E_K \rangle$ are in good quantitative agreement with the experimental data and the well-known systematics [27, 37]. This quantity hardly depends on the value of the reduction coefficient of the contribution from the wall formula [32], k_s. On the contrary, the variances of the mass and energy distributions are sensitive to the strength of the nuclear dissipation. We have found that good quantitative agreement of the calculated results with the experimental data on the variances of the mass (σ_M^2) and kinetic-energy ($\sigma_{E_K}^2$) distributions could be obtained at the values of the reduction coefficient $k_s = 0.25$–0.5 for the light fissioning compound systems with the parameter $Z^2/A < 35$. For the heavier compound nuclei, the simultaneous description of the mean prescission neutron multiplicities and the variances of the mass and kinetic energy distributions is impossible with a constant value of the reduction coefficient k_s. The experimental data on the variances σ_M^2 and $\sigma_{E_K}^2$ could be reproduced at the value of $k_s \simeq 0.1$, whereas one should use $k_s > 1$ for the quantitative description of the mean prescission neutron multiplicities. The results of our calculations prove the need for further investigating of the mechanism of nuclear dissipation.

3. CONCLUSIONS AND OUTLOOK

The three-dimensional stochastic approach to fission dynamics that has been successfully applied [5–7] for studying the parameters of the MED, the mean prescission neutron multiplicity, fission probability, and anisotropy of angular distributions has been developed and extended to calculations of the mass and kinetic-energy dependences of the postscission and total neutron multiplicities. The modified one-body mechanism of nuclear dissipation (the so-called surface-plus-window dissipation) was used to determine the dissipative forces of the Langevin equations. Under the assumption of the surface-plus-window dissipation mechanism of nuclear viscosity, the only variable parameter is the reduction coefficient of the contribution from the wall formula, k_s.

The calculated parameters of the MED and the dependences of the prescission, postscission, and total neutron multiplicities on the mass and kinetic energy of fission fragments have been found to be in good quantitative agreement with the available experimental data at values of the reduction coefficient of the contribution from the wall formula $k_s = 0.25$–0.5 for the fissioning compound nuclei lighter than ^{224}Th. For the compound nuclei heavier than ^{224}Th, a simultaneous description of the main fission characteristics with coordinate-independent reduction coefficient k_s is impossible.

In summary, we have applied the surface-plus-window dissipation to detailed and systematic analysis of the data from fusion–fission reactions and have come to the following conclusions: (i) the strength of the wall formula has to be reduced by the coefficient $k_s = 0.5$ for lighter fissioning systems, (ii) $k_s = 0.1$–0.2 for the heaviest ones in order to get a good fit of the parameters of the fission fragment MED, and (iii) a good quantitative description of the

mean prescission neutron multiplicities and angular anisotropy could be achieved for such systems at the values $k_s = 0.5–1.0$. Probably, this is an indication that the reduction coefficient k_s might depend not only on the fissility parameter, as was noted in our previous publications [5, 7], but also on the collective coordinates and excitation energy. The wall formula applies to the high temperature (chaotic) regime, while the low temperature (ordered) regime is dominated by effects of symmetries. Neither this nor the intermediate regime has been properly addressed and they remain challenging problems for future studies. It is extremely interesting to derive the coordinate and/or temperature dependences of the reduction coefficient k_s from the microscopic approaches [38–41] and to use them in an analysis as presented in our study.

ACKNOWLEDGMENTS

We are grateful to Dr. A.Ya. Rusanov and Dr. V.A. Drozdov for numerous enlightening discussions and correspondence.

REFERENCES

1. H. Rossner, D. Hilscher, and D. J. Hinde, Phys. Rev. C **43**, 2434 (1991).
2. D. J. Hinde, D. Hilscher, H. Rossner, *et al.*, Phys. Rev. C **45**, 1229 (1992).
3. H. Rossner, D. Hilscher, D. J. Hinde, *et al.*, Phys. Rev. C **40**, 2629 (1989).
4. D. Hilscher and H. Rossner, Ann. Phys. (Paris) **17**, 471 (1992).
5. A. V. Karpov, P. N. Nadtochy, D. V. Vanin, and G. D. Adeev, Phys. Rev. C **63**, 054610 (2001).
6. P. N. Nadtochy, A. V. Karpov, and G. D. Adeev, Yad. Fiz. **65**, 832 (2002) [Phys. At. Nucl. **65**, 799 (2002)].
7. P. N. Nadtochy, G. D. Adeev, and A. V. Karpov, Phys. Rev. C **65**, 064615 (2002).
8. J. Blocki, Y. Boneh, J. R. Nix, *et al.*, Ann. Phys. (N.Y.) **113**, 330 (1978).
9. A. J. Sierk and J. R. Nix, Phys. Rev. C **21**, 982 (1980).
10. P. Paul and M. Thoenessenn, Ann. Rev. Nucl. Part. Sci. **44**, 65 (1994).
11. Y. Abe, S. Ayik, P.-G. Reinhard, and E. Suraud, Phys. Rep. **275**, 49 (1996).
12. J. R. Nix and A. J. Sierk, in *Proceedings of the International School–Seminar on Heavy Ion Physics, Dubna, USSR, 1986*, Ed. by M. I. Zarubina and E. V. Ivashkevich (JINR, Dubna, 1987), p. 453.
13. D. Hilscher, I. I. Gontchar, and H. Rossner, Yad. Fiz. **57**, 1255 (1994) [Phys. At. Nucl. **57**, 1187 (1994)].
14. F. Plasil, D. S. Burnett, H. C. Britt, and S. G. Thompson, Phys. Rev. **142**, 696 (1966).
15. M. G. Itkis, Yu. A. Muzychka, Yu. Ts. Oganessian, *et al.*, Yad. Fiz. **58**, 2140 (1995) [Phys. At. Nucl. **58**, 2026 (1995)].
16. T. Sikkeland, Phys. Rev. **135**, B669 (1964).
17. J. van der Plicht, H. C. Britt, M. M. Fowler, *et al.*, Phys. Rev. C **28**, 2022 (1983).
18. G. G. Chubaryan, M. G. Itkis, S. M. Lukyanov, *et al.*, Yad. Fiz. **56** (3), 3 (1993) [Phys. At. Nucl. **56**, 286 (1993)].
19. C. R. Morton, D. J. Hinde, J. R. Leigh, *et al.*, Phys. Rev. C **52**, 243 (1995).
20. E. Vulgaris, L. Grodzins, S. G. Steadman, and R. Ledoux, Phys. Rev. C **33**, 2017 (1986).
21. K.-T. Brinkmann, A. L. Caraley, B. J. Fineman, *et al.*, Phys. Rev. C **50**, 309 (1994).
22. F. Videbaek, R. B. Goldstein, L. Grodzins, and S. G. Steadman, Phys. Rev. C **15**, 954 (1977).
23. B. B. Back, R. R. Betts, J. E. Gindler, *et al.*, Phys. Rev. C **32**, 195 (1985).
24. L. C. Vaz, D. Logan, E. Duek, *et al.*, Z. Phys. A **315**, 169 (1984).
25. H. Rossner, D. J. Hinde, J. R. Leigh, *et al.*, Phys. Rev. C **45**, 719 (1992).
26. M. G. Itkis, Yu. Ts. Oganessian, G. G. Chubarian, *et al.*, in *Proceedings of the XV EPS Conference on Low Energy Nuclear Dynamics (LEND-95), St. Peterburg, 1995*, Ed. by Yu. Ts. Oganessian, R. Kalpakchieva, and W. von Oertzen (World Sci., Singapore, 1995), p. 177.
27. A. Ya. Rusanov, M. G. Itkis, and V. N. Okolovich, Yad. Fiz. **60**, 773 (1997) [Phys. At. Nucl. **60**, 683 (1997)].
28. M. G. Itkis, S. M. Lukyanov, V. N. Okolovich, *et al.*, Yad. Fiz. **52**, 23 (1990) [Sov. J. Nucl. Phys. **52**, 15 (1990)].
29. D. J. Hinde, H. Ogata, M. Tanaka, *et al.*, Phys. Rev. C **39**, 2268 (1989).
30. H. Feldmeier, Rep. Prog. Phys. **50**, 915 (1987).
31. R. Vandenbosch and J. R. Huizenga, *Nuclear Fission* (Academic, New York, 1973).
32. J. R. Nix and A. J. Sierk, in *Proceedings of the 6th Adriatic Conference on Nuclear Physics: Frontiers of Heavy Ion Physics, Dubrovnik, Yugoslavia, 1987*, Ed. by N. Cindro, R. Caplar, and W. Greiner (World Sci., Singapore, 1990), p. 333.
33. J. Wilczynski, K. Siwek-Wilczynska, and H. W. Wilschut, Phys. Rev. C **54**, 325 (1996).
34. A. M. Samant, S. Kailas, A. Chatterjee, *et al.*, Eur. Phys. J. A **7**, 59 (2000).
35. P. Fröbrich and I. I. Gontchar, Nucl. Phys. A **563**, 326 (1993).
36. G. I. Kosenko, D. V. Vanin, and G. D. Adeev, Yad. Fiz. **61**, 416 (1998) [Phys. At. Nucl. **61**, 356 (1998)].
37. V. E. Viola, K. Kwiatkowski, and M. Walker, Phys. Rev. C **31**, 1550 (1985).
38. F. A. Ivanyuk, H. Hofmann, V. V. Pashkevich, and S. Yamaji, Phys. Rev. C **55**, 1730 (1997).
39. S. Pal and T. Mukhopadhyay, Phys. Rev. C **54**, 1333 (1996).
40. T. Mukhopadhyay and S. Pal, Phys. Rev. C **56**, 296 (1997).
41. S. Pal and T. Mukhopadhyay, Phys. Rev. C **57**, 210 (1998).